UNIVERSITÀ DI PARMA

UNIVERSITA' DEGLI STUDI DI PARMA

DOTTORATO DI RICERCA IN

" *Scienze e Tecnologie dei Materiali* "

CICLO XXXVII

Supramolecular systems for novel applications: from calix[6]arene-encapsulated dyes to electrochemical studies of interlocked structures

Coordinatore:

Chiar.mo Prof. Enrico Dalcanale

Tutore:

Chiar.mo Prof. Andrea Secchi

Dottoranda: Caterina Baccini

Anni Accademici 2021/2022 – 2023/2024

Abstract

The advancement of modern molecular nanotechnology presents increasing complexities and demands. Deep understanding and precise manipulation of properties at the molecular level are critical to designing materials with desired chemical and physical properties. This thesis introduces novel methodologies across various areas of supramolecular chemistry, including molecular receptors and photo and electro-responsive materials. The key aspects of this research are outlined as follows.

The first chapter of this thesis is structured into two sections. The first section addresses the investigation of orientational pseudorotaxane isomers formed between a calix[6]arene derivative and a series of stilbazolium dyes. The second section focuses on the complexation of stilbazolium-based dyes immobilized on the surface of gold nanoparticles (AuNPs) with the calix[6]arene macrocycle. In the initial section, the aim was to study the influence of structural modifications of the stilbazolium dyes on their complexation behavior with the calix[6]arene derivative. The effect of temperature on the formation of two distinct orientational isomers was analyzed, and the fluorescence properties of the dyes were characterized both before and after complexation. Kinetic studies were conducted to gain deeper insights into the threading process that leads to the formation of the two orientational isomers. The second section explores the complexation of stilbazolium dyes with the calix[6]arene macrocycle on the surface of gold nanoparticles, with the aim of developing a "switch off-on" system. This system leverages the plasmonic properties of the gold nanostructures together with the complexation within the calix[6]arene macrocycle.

Chapter 2 presents the synthesis and calix[6]arene complexation of thiazo[5,4-*d*]thiazole-based dyes. Both symmetric and asymmetric novel thiazo[5,4-*d*]thiazole dyes were synthesized, incorporating variations in chain length and counterions. The interaction with a calix[6]arene derivative was systematically investigated, revealing significant findings related to the formation of higher-order adducts and alterations in fluorescence properties upon complexation.

Chapter 3 presents a study focused on enhancing the optical properties of a near-infrared (NIR) cyanine-based dye through complexation with calix[6]arene derivatives and its interaction with gold nanomaterials. Complexation studies conducted in solution demonstrated a strong affinity between the cyanine dye and the calix[6]arene macrocycle, resulting in a significant enhancement of the dye's fluorescence.

Chapter 4 details the synthesis of novel heptamethine cyanine dyes designed for covalent attachment to the surface of gold nanoparticles. Fluorescence studies were performed to assess the influence of plasmonic resonances on the optical properties of the cyanine dyes. Additionally,

the interactions between the cyanine dyes and the gold surface were systematically investigated to elucidate the nature of their binding and its effects on the system's behavior.

Chapter 5 reports the synthesis of a series of calix[6]arene-based supramolecular cages, with cavities defined by *N*-phenylureido groups designed to interact with guest molecules. The synthetic strategy involved the formation of ureido and imine bonds through reactions between complementary calix[6]arene macrocycles, either with each other or with linker molecules. The resulting supramolecular cages were evaluated for their complexation properties with a range of organic guest molecules.

Chapter 6 deals with the investigation of supramolecular electroactive systems, focusing on the synthesis and characterization of multi-functional interlocked structures exploiting host-guest recognition mechanisms driven by radical pairing interactions induced by external redox stimuli. Various systems were conceptualized and synthesized, ranging from simple complexes comprising a viologen dumbbell and the blue box macrocycle to more intricate structures incorporating multi-functionalized molecules.

Glossary of terms

Axle: an acyclic (thread-shaped) molecule, or molecular unit, that can be surrounded by a macrocyclic host to yield rotaxane-type structures.

Lower rim: The region of a calixarene where the phenolic groups are located. The term narrow rim is synonymous.

Molecular machine: a particular type of molecular device in which the relative position of the component parts can change as a result of some external stimulus.

Pseudorotaxane: a supramolecular architecture consisting in a macrocycle ("rota") threaded with a linear axle ("axis") and held together by non-covalent interactions. The pseudorotaxane is in equilibrium with its separated components.

Rotaxane: a molecular architecture consisting of a macrocycle ("rota") and an axle ("axis") mechanically interlocked and kinetically trapped with one another due to the presence of large moieties ("stoppers") at the ends of the axial component which prevent disassociation (dethreading) of the components.

Stopper: a bulky molecular unit incorporated in the components of rotaxanes and catenanes that limits the amplitude of intercomponent movements. Typically, stoppers are the terminal units of the axle component in a rotaxane.

Upper rim: The region of the calixarene at the para position of the phenolic OH. The term wider rim is synonymous.

Wheel: a macrocyclic (ring-shaped) molecule that can surround an acyclic guest to yield rotaxane-type structures.

Viologen: a 4,4’-bipyridinium moiety.

Abbreviations and Acronyms

ACN: acetonitrile

AIE: Aggregation Induced Emission

AMPs: Artificial molecular pumps

Ar: Aromatic

AuNPs: gold nanoparticles

BE: Binding energy

CDI: 1,1'-carbonyldiimidazole

CT: Charge-transfer

CV: Cyclic voltammetry

Cy: cyanine

DCC: *N,N'*-Dicyclohexylcarbodiimide

DCM: Dichloromethane (CH_2Cl_2)

DIC: *N,N'*-Diisopropylcarbodiimide

DIPEA: Diisopropylethylamine

DLS: dynamic light scattering

DMF: Dimethylformamide

DMSO: Dimethyl sulfoxide

DMP: Dess-Martin Periodinane

DOV: Dioctyl viologen

DPV: Differential pulse voltammetry

EC: Electrochromism

EFC: Electrofluorochromism

EDC: 1-Ethyl-3-(3-dimethylaminopropyl)carbodiimide

EtOAc: Ethyl Acetate

EtOH: Ethanol

ESI-MS: Electron Spray Ionization Mass Spectroscopy

FRET: Förster resonance energy transfer

HOMO: Highest occupied molecular orbital

HR-MS: High resolution mass spectrometry

HSQC: Heteronuclear single quantum coherence

ICT: Intramolecular charge-transfer

ISC: inter-system crossing

LSPR: Localized Surface Plasmon Resonances

LSV: Linear sweep voltammetry

LUMO: Lowest unoccupied molecular orbital

MALDI: Matrix-Assisted Laser Desorption Ionization

MeOH: Methanol

MOs: Molecular orbitals

NHS: *N*-hydroxysuccinimide

NIR: Near-infrared

NLO: Non-linear optical

NMR: Nuclear Magnetic Resonance

PEF: Plasmon-enhanced fluorescence

PEG: Polyethylene glycol

PBS: Phosphate-buffered saline

PDT: Photodynamic Therapy

PS: Photosensitizer

PTT: Photothermal Therapy

ROESY: Rotating frame overhause Effect spectroscopy

ROS: Reactive oxygen species

SCE: Saturated calomel electrode

SEC: spectro-electrochemistry

SPB: surface plasmon band

TBATsO: Tetrabutylammonium tosylate

TCE: Tetrachoroethane

TEA: Triethylammine

$TEAPF_6$: tetraethylammonium hexafluorophosphate

TEM: Transmission electron microscopy

TFA: Trifluoroacetic acid

TICT: Twisted intramolecular charged transfer

THF: Tetrahydrofuran

TLC: Thin Layer Chromatography

TsO: Tosylate

UV-VIS: Ultraviolet-visible spectroscopy

VB: Valence bond

VT: Variable temperature

XPS: X-ray photoelectron spectroscopy

Table of contents

Introduction

Chromophores

Organic dyes can be categorized based on their chemical structure, optical properties, or applications. In this thesis, two primary classes of organic dyes will be studied: cyanine dyes and thiazo[5,4-*d*]thiazole dyes.

Cyanine dyes

Cyanine dyes are extensively investigated compounds. The first cyanine dye was synthesized in 1856 by Charles Hanson Greville Williams, who produced a quinoline-based dye by reacting the distillate of cinchonine with amyl iodide and ammonia (**Figure 1**).[1] This compound, named Quinoline Blue, due to its intense blue color, marked the beginning of a significant expansion in the study of cyanine dyes, driven in part by their broad range of applications.

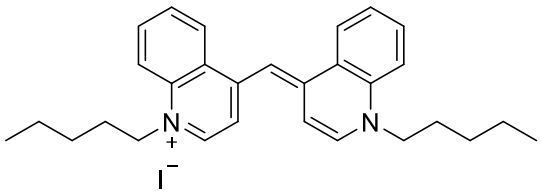

Quinoline Blue

Figure 1. Structure of the first cyanine-based dye.

The general structure of cyanine dyes is characterized by two nitrogen atoms at the ends of a conjugated system composed of alternating double and single bonds along a carbon chain (**Figure 2**). This chain, composed of sp^2-hybridized carbon atoms, forms a conjugated system where π-electrons are delocalized between the two nitrogen end groups. Cyanine dyes can be classified into three subcategories based on the nature of the terminal groups (**Figure 2**): closed-chain cyanine dyes (with heterocycles on both end groups), hemicyanine dyes (one heterocycle and an acyclic group), and streptocyanine dyes (acyclic groups on both ends). Common end groups in cyanine dyes include indole, benzoxazole, benzothiazole, and quinoline.[2] The end groups can be identical, resulting in a symmetric cyanine dye, or they can differ, leading to the formation of an asymmetrical cyanine dye.

Closed-chain cyanine dyes

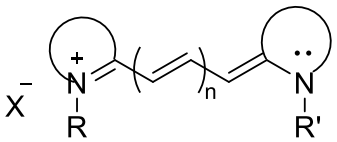

Hemicyanine dyes

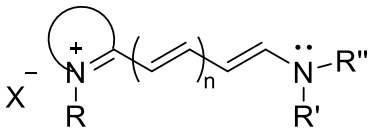

Streptocyanine dyes

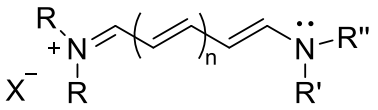

Figure 2. Representation of the three cyanine classes: closed-chain cyanine dyes (top), hemicyanine dyes (middle), and streptocyanine dyes (bottom).

One key feature of cyanine dyes is the tunability of their optical properties by adjusting the length of the conjugated carbon chain. Increasing the length of this carbon chain shifts the absorption wavelength of the dye to longer wavelengths, i.e., to lower energies. Each methine group typically contributes approximately 100 nm to the bathochromic shift in the absorption spectrum of cyanine dyes. Consequently, cyanine dyes can absorb and emit light across a broad range of the electromagnetic spectrum, from the visible to the infrared region. This aspect will be discussed in more detail in the following section.

The nomenclature of cyanine dyes is determined by the length of the conjugated carbon chain, specifically by the number of methine groups in the chain. A cyanine dye with a single methine group is called a monomethine cyanine. Similarly, dyes with 2, 3, 5, or 7 methine groups are named dimethine, trimethine, pentamethine, or heptamethine cyanine, respectively.

Heptamethine cyanine dyes

Heptamethine cyanine dyes, commonly referred to as **Cy7** dyes, are a distinct class of cyanine compounds characterized by the presence of a seven-carbon atom polymethine chain. These dyes typically exhibit absorption within the near-infrared (NIR) region of the electromagnetic spectrum, specifically within the 700-900 nm wavelength range. The classical heptamethine cyanine dyes (**I**) can exist as cis-trans isomers in the ground state; however, they predominantly adopt an all-trans stereoisomer configuration (**Figure 3**). It has been shown that substituents R_1 can enhance the stability of the dye.[3] Strekowski and colleagues demonstrated that introducing a chlorocyclohexenyl ring into the center of the polymethine chain significantly improves the dye's photostability.[4] Consequently, many cyanine dyes are synthesized with a central cyclohexenyl ring (**II**). Moreover, depending on the heteroatom in the *meso* position of the cyclohexenyl ring, it can result in the

formation of a neutral cyanine dye (**III**).[5] Additionally, modifying the R_2 and R_3 substituents allows for the tuning of the dye's solubility and hydrophobic interactions.

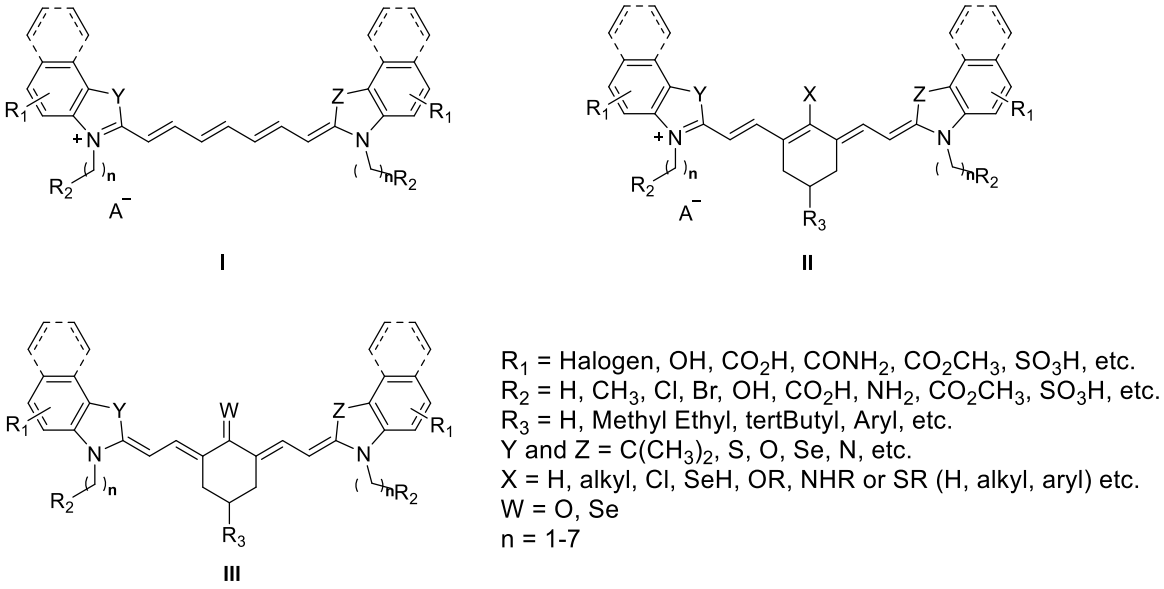

Figure 3. General structure of heptamethine cyanine dyes **Cy7**: classic (**I**), incorporating a cyclohexenyl unit (**II**), and neutral (**III**).

The synthesis of heptamethine cyanine dyes typically involves a Knoevenagel reaction, a modified aldol condensation that creates a carbon-carbon bond *via* nucleophilic addition between an aldehyde or ketone and an active hydrogen compound in the presence of a base. Chloro-heptamethine cyanine dyes, usually referred as to **Cy7-Cl**, are generally synthesized through the condensation of a positively charged nitrogen group with a bisaldehyde (**Scheme 1**). Common bases employed in this reaction include sodium acetate, triethylamine, piperidine, or pyridine, with acetic anhydride or ethanol used as solvents.

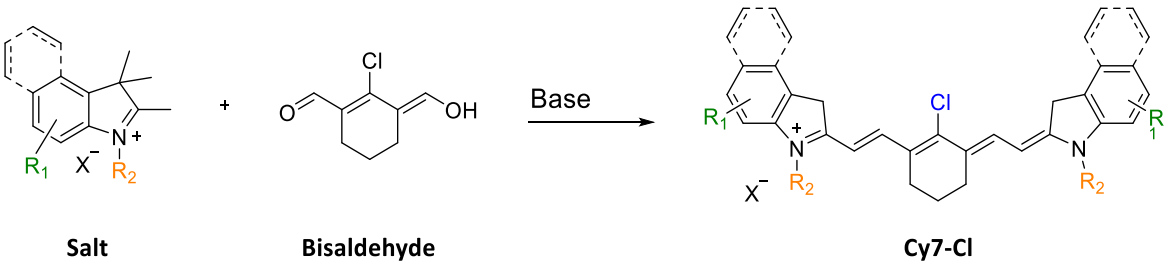

Scheme 1. General synthesis of heptamethine cyanine dye **Cy7-Cl**.

For symmetric heptamethine cyanine dyes, the reaction utilizes two equivalents of positively charged nitrogen salts and one equivalent of the linker, enabling the formation of the dye in a single step. In contrast, the synthesis of asymmetric cyanine dyes requires the use of two different salts, with one equivalent of each employed.

Heptamethine cyanine dyes containing a chlorocyclohexenyl ring in the *meso* position can undergo nucleophilic substitution of the chlorine atom when exposed to various nucleophilic reagents, such as amines, thiols, and aromatic alcohols. The most widely recognized reaction mechanism for this process is the $S_{RN}1$ mechanism,[6] wherein the nucleophilic species transfers an electron to the cyanine dye. This mechanism is favored in the presence of polar aprotic solvents, such as DMF or DMSO, as these solvents do not reduce the concentration of radical anions formed during the reaction (**Scheme 2**).

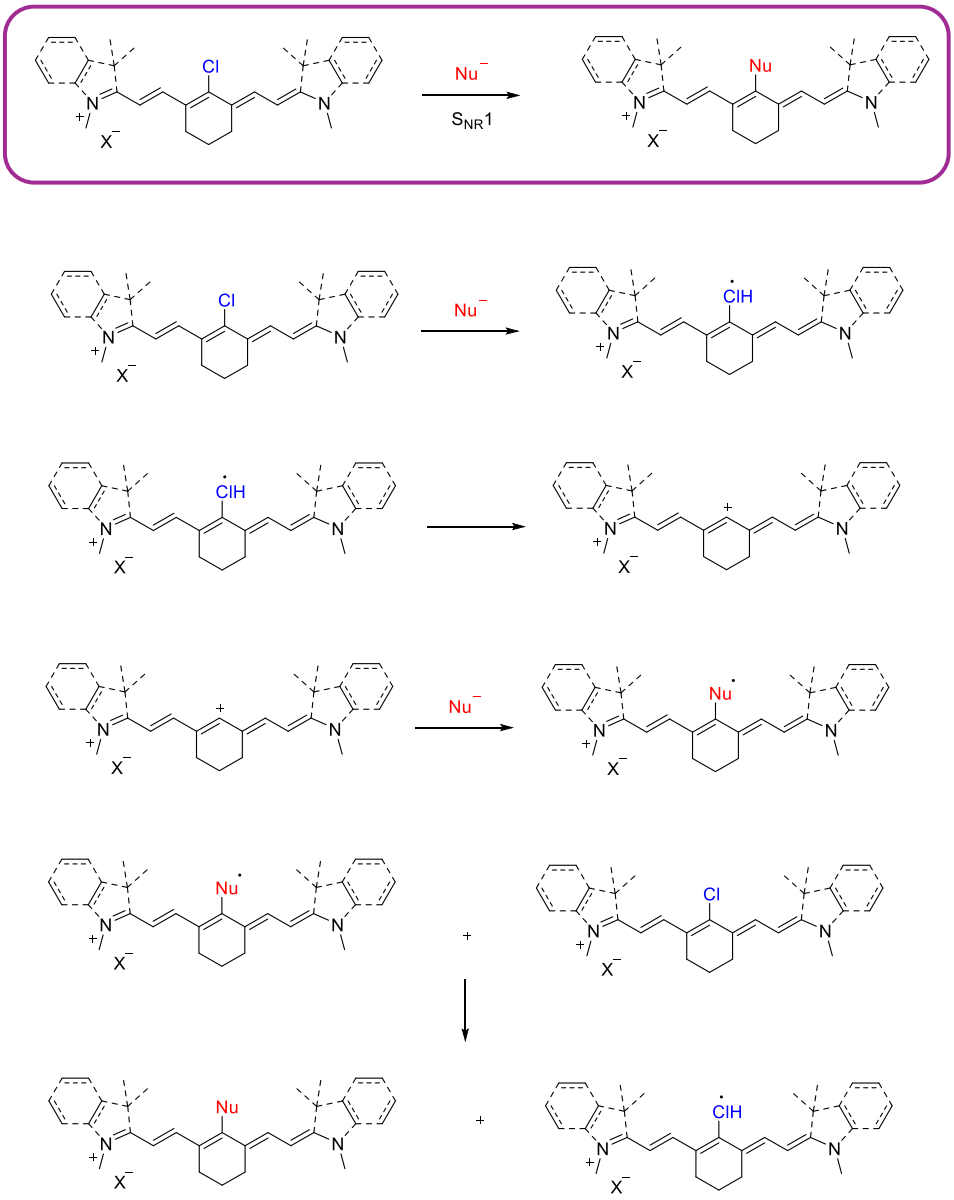

Scheme 2. Schematic representation of the mechanism of the nucleophilic substitution in *meso* position of heptamethine cyanine dyes.

Optical properties. As seen in the previous section, the optical properties of cyanine dyes can be tailored by modifying the length of the carbon chain, the substituents on the aromatic ring, or by altering the extent of the aromatic conjugated system. Typically, heptamethine cyanine dyes (**Cy7**)

are generally characterized by absorption maxima in the near-infrared (NIR) region of the spectrum. Additionally, the incorporation of groups with positively charged nitrogen atoms can influence the absorption maximum of the dye. Commonly used positively charged nitrogen groups are shown in **Figure 4**. When indolium and benzo[e]indolium salts are replaced with quinolinium- or benzo[c,d]indolium-based heterocyclic systems, a bathochromic shift of approximately 100-200 nm is observed.[4]

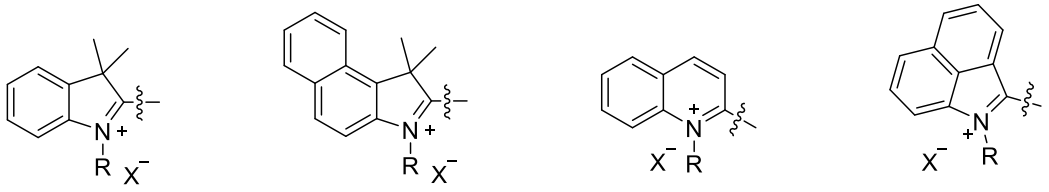

Indolium ring **Benzo[e]indolium ring** **Quinolinium ring** **Benzo[c,d]indolium ring**

Figure 4. Representation of most common positively charged nitrogen groups.

The presence of a cyclohexenyl ring at the *meso* position of **Cy-7** dyes not only increases their photostability, but also enhances the fluorescence quantum yield and lifetime by rigidifying the structure. Moreover, substituting the chlorine atom at the *meso* position may alter the optical properties of the dye. In 1998, Soper *et al.*[7] demonstrated that the fluorescent lifetime can be tuned by manipulating the heavy-atom effect, increasing the fluorescent lifetime in the sequence F<Cl<Br<I. Moreover, they showed that the heavy-atom modification can influence the intersystem crossing, with heavier atoms promoting a higher rate of this transition. Indeed, substituting carbon with sulfur or selenium within the ring system facilitated the intersystem crossing.[8] Moreover, the fluorescence lifetime can also be tuned by varying the length of the polymethine chain. Kasatani and Sato reported that the fluorescence lifetime decreases in the order pentamethine < heptamethine < trimethine.[9] Cyanine dyes exhibit sensitivity to solvent polarity, with fluorescence lifetime generally increasing as solvent polarity decreases, following the order: water < MeOH < EtOH < acetone < DMSO < DCM < $CHCl_3$.[4]

Cyanine dyes, including **Cy7** compounds, exhibit a pronounced tendency to aggregate in apolar media, driven by π-π interactions and electrostatic forces. These interactions can lead to the formation of two distinct types of aggregates: *H*-aggregates and *J*-aggregates. *J*-aggregates consist of chromophores arranged in an ordered "head-to-tail" configuration, whereas *H*-aggregates feature a "face-to-face" arrangement of chromophores (**Figure 5**).

J- and *H*- aggregates have completely different photophysical properties in respect to the monomers. *J*-aggregation results in narrow, bathochromically shifted absorption and emission bands, along with increased molar absorption coefficients (ε) and quantum yields (ϕ), and small

Stokes shifts. In contrast, *H*-aggregation is characterized by hypsochromically shifted absorption and emission spectra. *J*-aggregates have been widely used for the development of optoelectronic devices[10] and in biomedical applications.[11]

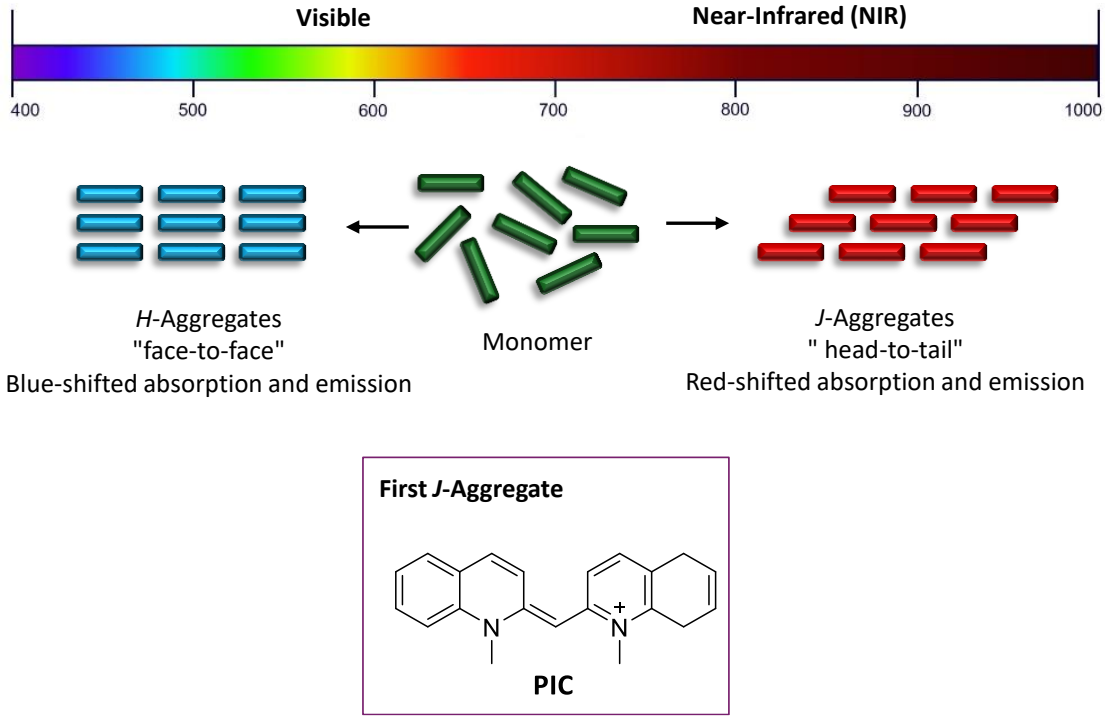

Figure 5. Top: schematic illustration of *H*- and *J*-aggregates and their features; bottom: structure of the first discovered *J*-Aggregate pseudoisocyanine chloride (**PIC**).

Optical sensing. Organic chromophores are widely used for monitoring molecular interactions in biochemical, medical, and environmental fields.[1] Heptamethine cyanines, for instance, have been broadly used as sensors to detect cations and anions. In 2018, Liu *et al*.[12] developed a sensor for cyanide anion based on a heptamethine cyanine dye (**T-Cy**) having a triphenylamine moiety at the *meso* position (**Figure 6**), which detected cyanide *via* nucleophilic addition. This process suppressed the fluorescence and varied the color of the solution from green to yellow, indicating cyanide presence.

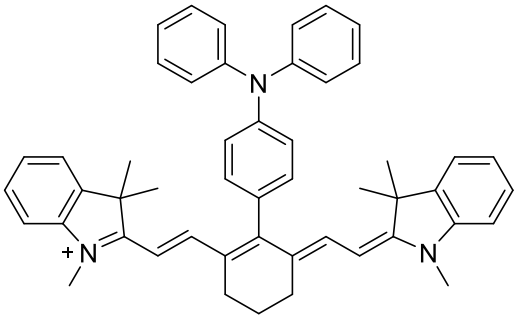

T-Cy

Figure 6. Structure of heptamethine cyanine-based dye **T-Cy**.

Heptamethine cyanine dyes are also used for the detection of small molecules like biothiols such as cysteine (Cys), homocysteine (Hcy), and glutathione (GSH). The control of the levels of biothiols in the blood is fundamental since both low and high levels may result in diseases. In 2014,[13] a first heptamethine cyanine dye (**IV**) was developed for the targeting of mitochondrial GSH with NIR fluorescence (**Figure 7**). The initial nitroazo cyanine dye (**IV**) was non-fluorescent, but upon reaction with GSH, fluorescence increased selectively toward GSH over Cys/Hcy. In 2018, Liu *et al*.[14] developed another heptamethine cyanine derivative (**V**) with NIR absorption and emission capable of detecting GSH and its oxidized form (GSSG) in the blood (**Figure 7**).

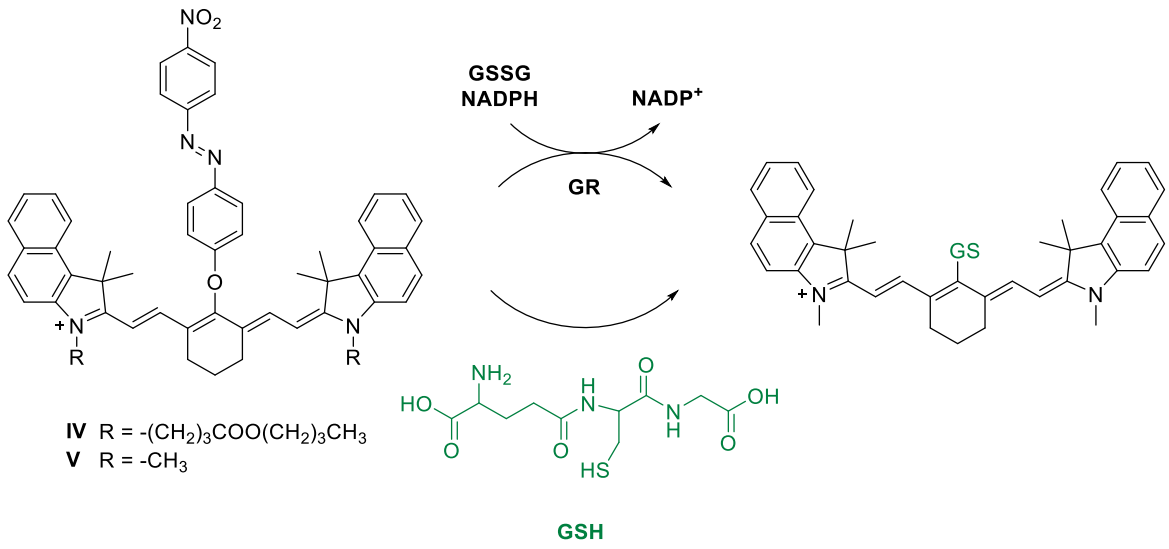

Figure 7. Heptamethine cyanine dyes **IV** and **V** for the detection of GSH and GSSG.

Drug delivery. The advent of targeted therapies has significantly minimized the off-target toxicities commonly associated with traditional cytotoxic agents. To enhance target specificity, ligands such as organic molecules, aptamers, antibodies, or fluorescent dyes can be conjugated to the drug, directing it toward the target cells. The use of fluorescent dyes offers the distinct advantage of

enabling light-based system activation, which is more efficient than conventional chemical activation methods. Heptamethine cyanine dyes, particularly those derived from modifications of **IR-780**, **IR-783**, **MHI-148**, and **DZ1** dyes, are frequently utilized in drug delivery applications (**Figure 8**). Typically, these modifications focus on the alkyl side chain, while the polymethine backbone is preserved to maintain tumor selectivity.[15]

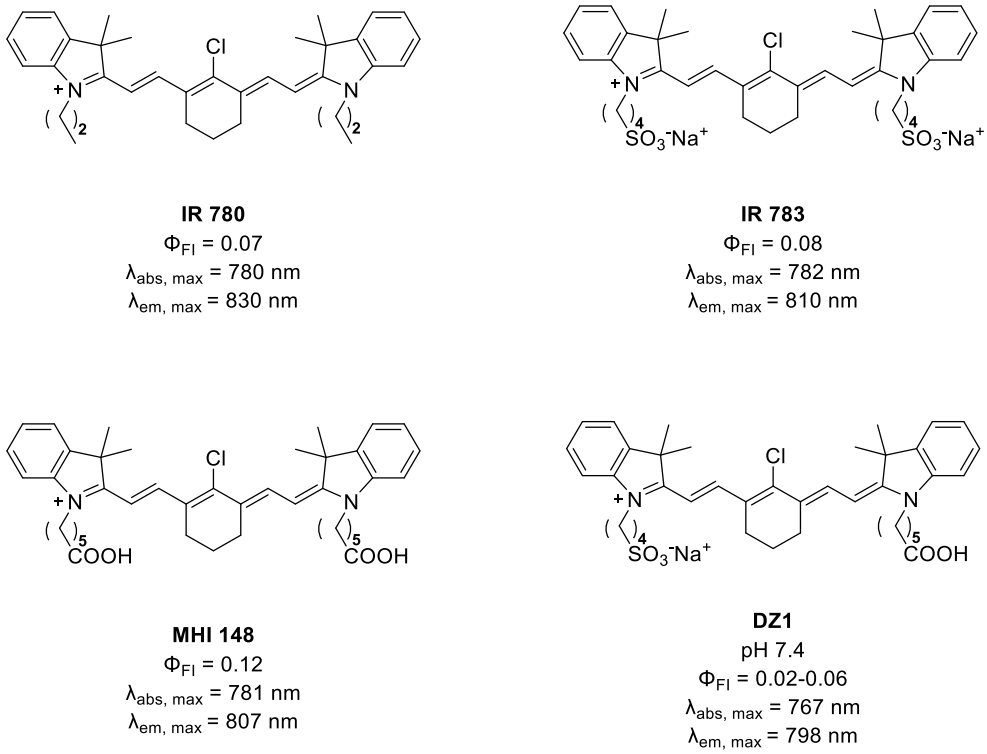

Figure 8. Structure and optical data for heptamethine cyanine dyes **IR-780**, **IR-782**, **MHI-148**, and **DZ1**.

A significant challenge in delivering small molecules to the brain is their inability to traverse the blood-brain barrier (BBB). Gemcitabine, a chemotherapeutic agent used in the treatment of various cancers, is unable to penetrate the BBB, thus limiting its efficacy against brain tumors. In 2015, Wu *et al.*[16] developed a **DZ1**-based conjugate (**VI**) with gemcitabine that accumulates selectively within brain tumor cells (**Figure 9**, top left). Similarly, Choi *et al*.[17] synthesized a conjugate of **IR 786** with crizotinib (**VII**), which is an inhibitor of anaplastic lymphoma kinase (ALK) and gene ROS1, which encodes a type I integral membrane protein with tyrosine kinase activity (**Figure 9**, top right). This conjugate exhibited a 110-fold increase in potency compared to crizotinib alone. Other notable conjugates were reported by Lv *et al*.,[18] where **MHI 148** was conjugated with isoniazid (**VIII** and **IX**) (**Figure 9**, bottom) for dual purposes: mitochondrial targeting and monoamine oxidase A (MAOA) inhibition. MAOA, a mitochondrial enzyme involved in developing chemotherapy resistance, is inhibited irreversibly by isoniazid, which is also employed as a treatment for tuberculosis. These conjugates demonstrated a 700-fold enhancement in cytotoxic activity against PC-3 prostate cancer cells, significantly increasing the potency of isoniazid.

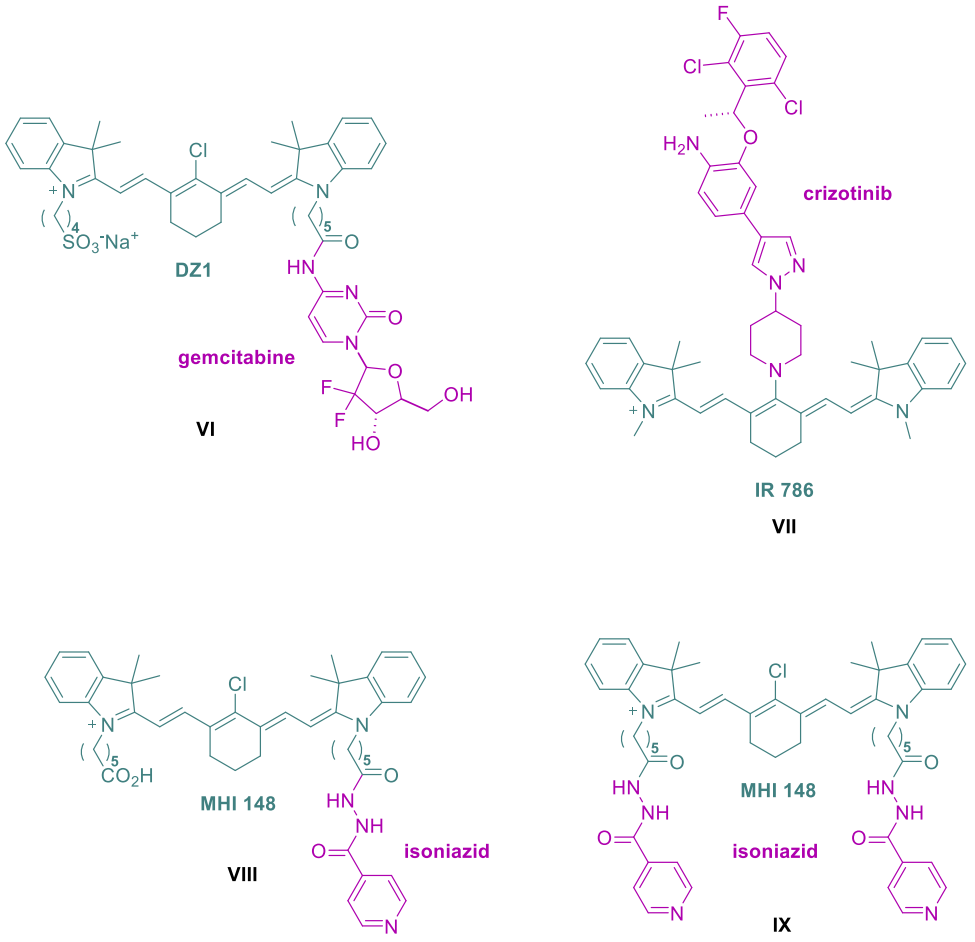

Figure 9. Structure of heptamethine cyanine-based dyes **VI**, **VII**, **VIII** and **IX**.

Bioimaging. Bioimaging is a technique that enables real-time visualization of biological processes and the structural organization of organisms, allowing for the non-invasive clarification of various biological functions. The applications of bioimaging range from observing subcellular structures to entire multicellular organisms. Various imaging modalities can be employed, including light, fluorescence, electron microscopy, ultrasound, X-ray, and magnetic resonance imaging. In fluorescence imaging, biological processes are highlighted by labeling specific molecules or structures with fluorescent dyes. Therefore, organic dyes with high biocompatibility, low toxicity, and strong fluorescence are highly desirable. Heptamethine cyanine dyes, which absorb and emit in the NIR region of the spectrum, are particularly valued in biological imaging due to their ability to achieve deep tissue penetration and their minimal background fluorescence. Numerous examples of cyanine dyes utilized in bioimaging have been reported in the literature. In 2020, Li *et al.*[19] developed a novel cyanine dye designed to improve stability, reduce dye aggregation, and enhance pharmacokinetics. Specifically, the researchers engineered a linear heptamethine polyene with a *meso*-aryl group, which features two shielding arms extending over the cyanine core (**s755z**)

(**Figure 10**). This shielded configuration significantly improved the dye's photophysical, physicochemical, and bioimaging properties.

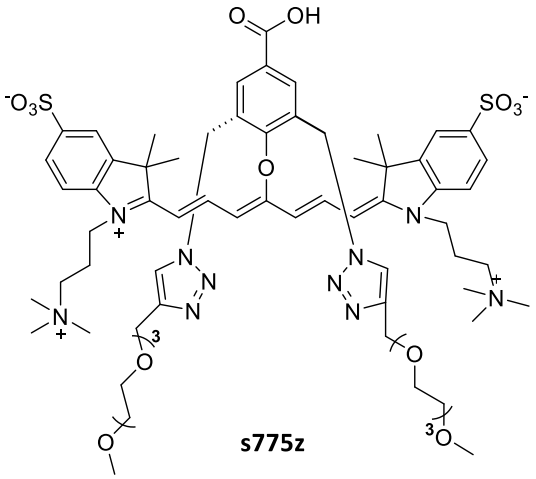

Figure 10. Structure of linear heptamethine polyene cyanine **s775z**.

More recently, in 2023, a liposome-encapsulated cyanine dye for fluorescence imaging in the second near-infrared window (NIR-II, 1000-1700 nm) was developed.[20] The authors encapsulated cyanine dyes within liposomes by sequestering the dyes in the hydrophobic pockets of lipids. The **ICG** dye, when encapsulated in liposomes (**S-Lipo-ICG**), demonstrated significantly increased NIR-II brightness, facilitating cerebrovascular imaging. Additionally, two other cyanine dyes (**IR780** and **FD1080**) were also encapsulated in liposomes, enabling NIR-II dual-color imaging (**Figure 11**).

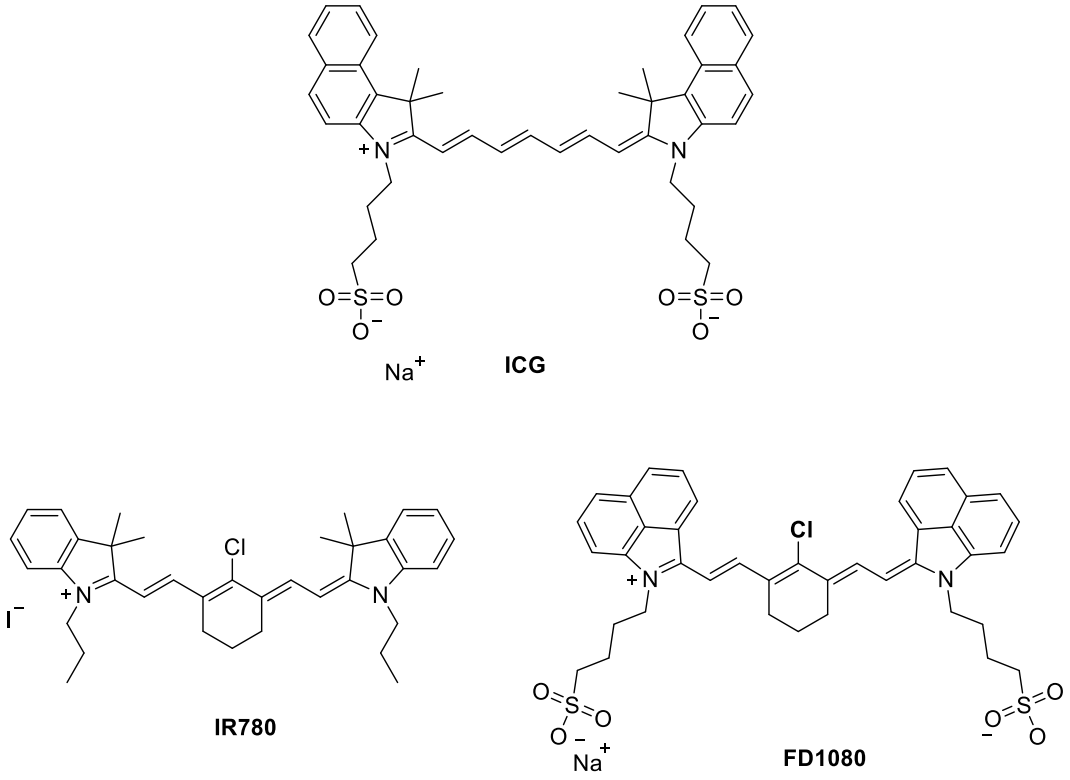

Figure 11. Representation of heptamethine cyanine dyes **ICG**, **IR780** and **FD1080**.

Photothermal (PPT) and Photodynamic (PDT) Therapy. Phototherapy is currently regarded as a promising alternative to conventional tumor treatments due to its non-invasive nature and high therapeutic efficacy. Cyanine dyes are extensively utilized in phototherapeutic applications due to their advantageous properties, including a broad absorption spectral range, high extinction coefficients, absorbance bands typically located within the phototherapeutic window (NIR region), and excellent biocompatibility.[21-23] PTT and PDT are effective cancer treatment modalities that leverage the unique properties of photosensitizers (PS). The versatile nature of cyanine dyes allows them to function in both PDT and PTT, making them valuable tools in phototherapy. PTT and PDT rely on combining a PS and targeted light irradiation. The therapies are designed to be localized to the treatment area where the light is focused, thereby minimizing off-target effects. The efficacy of these therapies is determined mainly by the light absorption characteristics of biological tissues. For PDT, the optimal spectral region, known as the biological window, ranges from 600 to 800 nm, while PTT typically utilizes light within the 650 to 1100 nm range. **Figure 12** illustrates the mechanisms of thermal and oxidative damage induced by photothermal and photodynamic effects. Upon light absorption, the PS is excited from its ground state (S_0) to an excited singlet state (S_1). From this excited state, the system can either return to the ground state *via* fluorescence or non-radiative processes, such as heat release, or transition to a more stable excited triplet state (T_1). The return to the ground state through vibrational relaxation or heat dissipation is the basis for thermal damage in PTT. If the PS transitions to the triplet state through inter-system crossing (ISC), it can undergo either type I or II photochemical reactions. In type I reactions, the PS interacts with nearby molecules, generating reactive oxygen species (ROS), such as hydroxyl radicals, hydrogen peroxide, or superoxide anions, through electron transfer processes. In type II reactions, the PS interacts with molecular oxygen ($^3O_2$) to produce singlet oxygen ($^1O_2$), which induces oxidative damage, a hallmark of PDT.

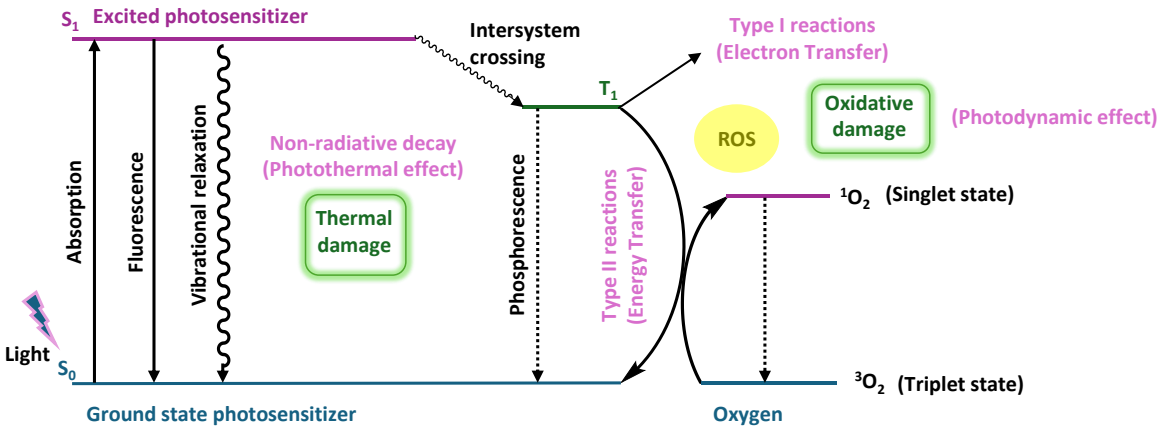

Figure 12. Schematic representation of the thermal and oxidative damage mechanism induced by PTT and PDT.

PDT has been extensively studied in recent years, with cyanine dyes finding numerous applications. For example, in 2017, Ryu *et al.*[24] designed a water-soluble, highly photostable indocyanine derivative (**IR-Pyr**) exhibiting strong mitochondrial targetability and PDT efficiency (**Figure 13**). The incorporation of a pyridinium moiety on the indolinium ends enhances the water solubility of **IR-Pyr** and contributes to its high photostability. Additionally, the formation of micellar aggregates with hyaluronic acid (HA) enabled targeted PDT against cancer mitochondria.

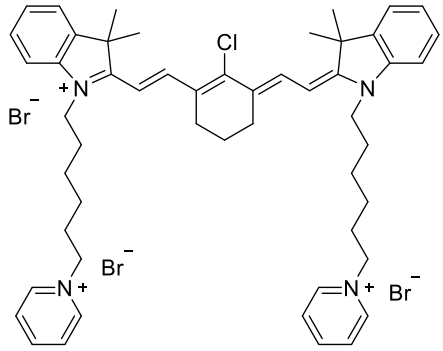

IR-Pyr

Figure 13. Structure of cyanine **IR-Pyr** for mitochondrial targeting and PDT.

Like PDT, PTT is extensively utilized in tumor treatment, but unlike the former, PTT does not require oxygen, making it particularly effective in hypoxic conditions. In 2022, a novel strategy was developed to enhance the efficacy of PTT by combining it with starvation therapy.[25]

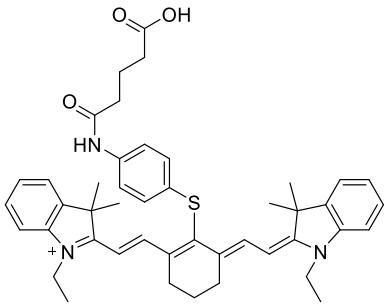

X

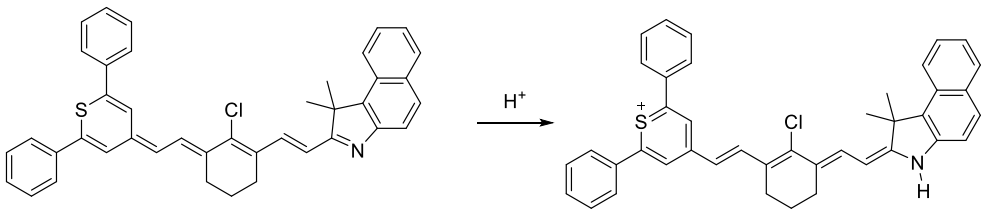

NSCy-1015 **NSCyH-1015**

Figure 14. Top: structure of cyanine derivative for the bioconjugation with **GOx**; bottom: activation of **NSCy-1015** by acidic conditions.

In this approach, the authors leveraged the catalytic activity of glucose oxidase (GOx) within tumor cells to deplete oxygen. Through a bioconjugation reaction, a **Cy7** derivative **X** (**Figure 14**, top) was

conjugated with the *N*-termination of GOx, forming **Cy-GOx**. This conjugation inhibited fluorescence and intersystem crossing, causing the absorbed photon energy to be released *via* non-radiative decay, thereby enhancing the photothermal effect of PTT. A recent study reported the development of cyanine dyes designed for high-contrast *in vivo* imaging and therapy using an H^+/viscosity-responsive system (**Figure 14**, bottom).[26] These cyanine dyes (**NSCy**) were activated through a "dual-key-and-lock" mechanism, enabling fluorescence switching from off to on, which enhances photothermal performance. Specifically, the cyanine dye **NSCy-1015**, upon acid activation, was employed to effectively kill bacteria *via* the PTT process under continuous laser irradiation.

Styryl dyes

Styryl dyes represent a subclass of cyanine dyes characterized by an electron-rich aromatic ring system covalently bonded to an electron-deficient heteroaromatic ring system *via* one or more conjugated double bonds.[27] This molecular architecture establishes a push-pull system, wherein electron donor (**D**) and electron acceptor (**A**) groups are interconnected through a π-conjugated framework. The resulting donor-π-acceptor (**D-π-A**) configuration (**Figure 15**, left) facilitates intramolecular charge-transfer (ICT) interactions, which are fundamental for the dyes' non-linear optical properties.

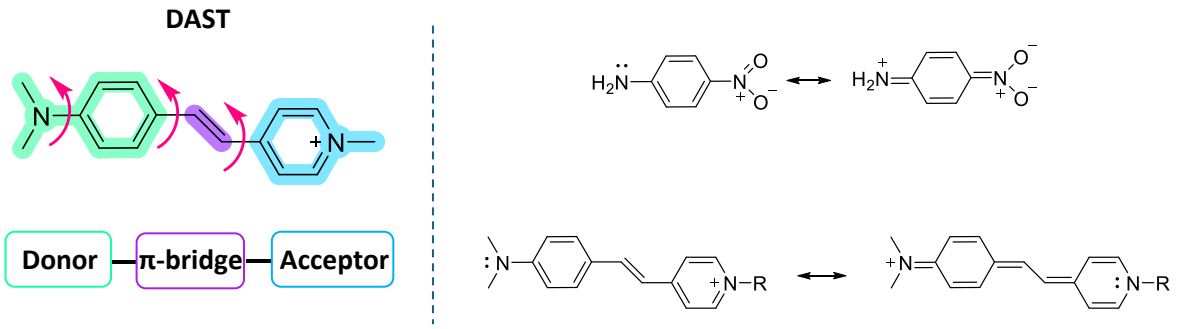

Figure 15. Left: structure of **DAST** showing the possible locations of twisting; right: limited resonance structures for linear model **D-π-A** systems.

The ICT mechanism induces polarization within the dye molecule, generating a molecular dipole that can be described by two limiting resonance forms (**Figure 15**, right). The ICT process in such dyes is due to a torsional motion of the molecular backbone around a single bond connecting the **D** and **A** units, known as twisted intramolecular charged transfer (TICT) state (**Figure 16**).[28] This motion causes large polarizability changes upon excitation, giving rise to second- and third-order optical non-linearities (NLO). For example, the known 4-*N*,*N*-dimethylamino-4′′-*N*′-methylstilbazolium tosylate (DAST) offers three different twisting modes: around the single bond of the dimethylamino group and the two single bonds adjacent to the π-bridge (**Figure 15**, left). By

tracking transient Raman signatures of the photoexcited DAST, Dasgupta and coworkers demonstrated that the twist in the ICT state occurs near the ethylenic π -bridge.[29]

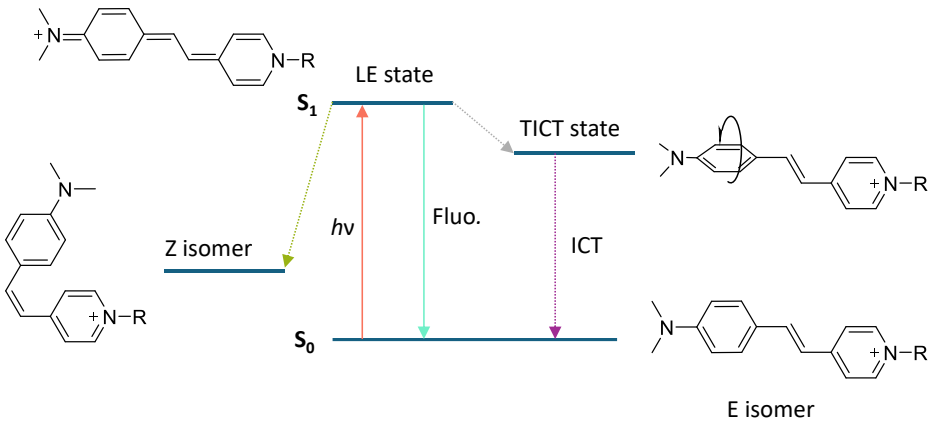

Figure 16. Deactivation pathways of excited styryl structure (simplified energy diagram). LE state = locally excited state, TICT state = twisted intramolecular charged transfer state, ICT = intramolecular charge transfer.

The study of NLO phenomena has gained increasing interest due to their broad range of applications. On a microscopic scale, when an NLO chromophore is exposed to a strong electric field, its material response, known as nonlinear polarization, can be described by a power series expansion of the electric field strength:

$$P = \alpha E + \beta EE + \gamma EEE + \cdots$$

where α represents the linear polarizability, β the first hyperpolarizability, and γ the second hyperpolarizability. The β term is particularly significant, as it is associated with key phenomena such as second-harmonic generation (SHG) and electro-optic (EO) effects. Therefore, achieving high β values is crucial for enhancing NLO properties. There are two primary strategies for maximizing β values: i) optimizing the π-bridge structure for a given combination of donor and acceptor groups; ii) optimizing the donor and acceptor groups for a selected π-bridge structure. Thus, careful selection of donor/acceptor groups and π-bridges is essential for designing effective NLO chromophores.

Common **D** groups in push-pull systems include substituents such as hydroxyl (OH), amino (NH_2), alkoxy (OR), and dialkylamino (NR_2) groups, as well as heterocyclic moieties like thiophene and aromatic pyridines. Conversely, typical **A** groups encompass nitro (NO_2), cyano (CN), formyl (CHO) groups, and electron-deficient heterocyclic compounds such as (di)azines, benzothiazole, pyridinio, and imidazole. In 2020, Ruzicka *et al*.[30,31] conducted a systematic study on how the electron-donating capacity of donor groups and the extension of the π-conjugated system affect the properties of styryl dyes. Specifically, in compounds **XI**-**XIII**, the acceptor unit (dicyanoimidazole, DCI) was held constant, while the donor group was varied (**Figure 17**, top). By analyzing the HOMO and LUMO energy levels, the authors observed that while the LUMO levels remained relatively

unchanged, significant shifts occurred in the HOMO energies. These variations indicated different electronic behaviors depending on the donor group. Substituting hydrogen with more electron-donating groups, such as MeO or NMe_2, increased the HOMO energy, leading to a reduced HOMO-LUMO energy gap. Consequently, the HOMO-LUMO gap can be easily tuned by modifying the donor group's electron-donating strength.

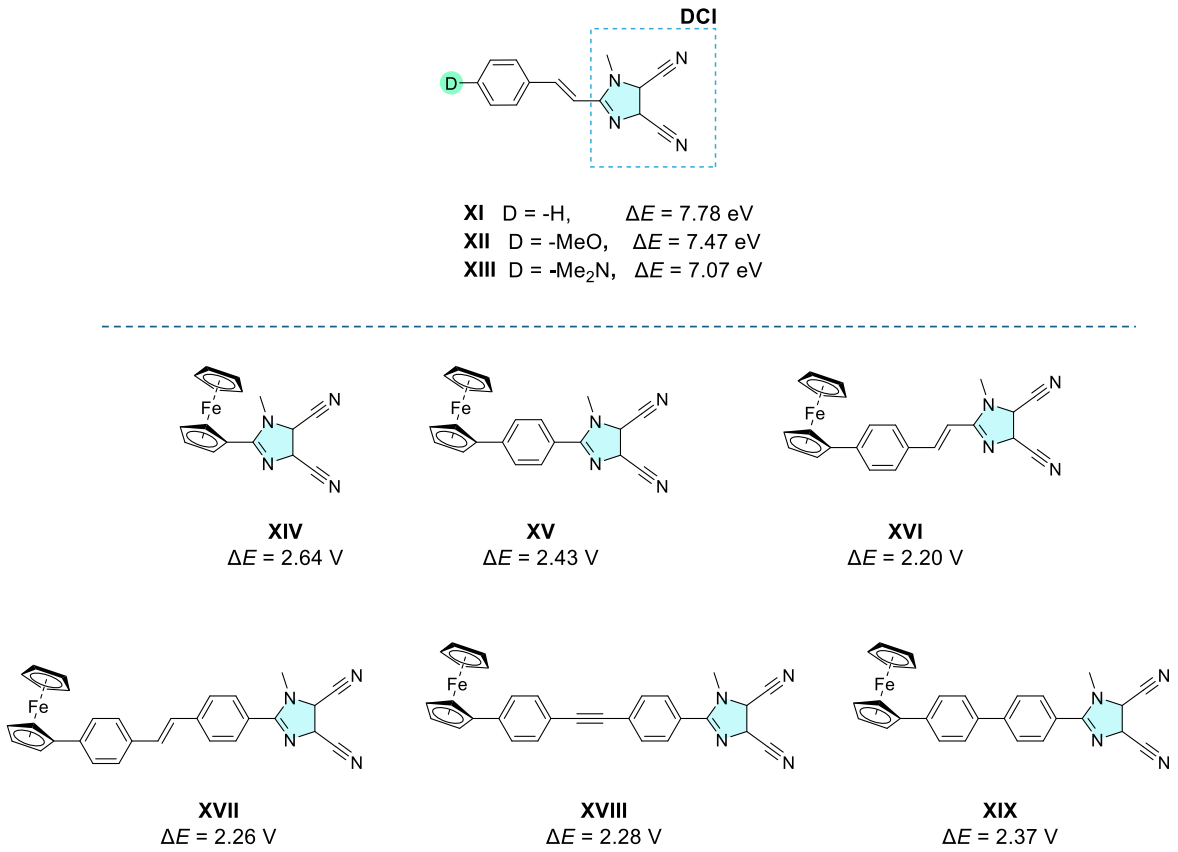

Figure 17. Top: chemical modification of the donor group, keeping the acceptor group (DCI) fixed; bottom: structures of dyes with the same donor and acceptor groups but different π-bridge.

Similarly, the extension of the *π*-conjugated system can effectively modulate the optical properties of the dyes. In the same study,[30,31] Ruzicka and colleagues demonstrated that, by maintaining the donor and acceptor units constant, the optical properties of the dye could be tuned by altering the length, composition, and spatial arrangement of the π-system (**Figure 17**, bottom). Extending the π-conjugation allowed the modulation of the HOMO-LUMO band gap by up to 0.95 eV, while the maximum absorbance wavelength shifted from 293 nm to 381 nm.

Similar to donor group modification, the acceptor group can also be altered to influence the properties of dyes. In 1991, Cheng *et al*.[32,33] investigated the effect of varying the acceptor group in amino-substituted styrenes (**Figure 18**, left). They found that nitro and cyano groups promoted a more efficient ICT process, thereby enhancing the first-order hyperpolarizability. More recently, in 2012,[34] Blanchard-Desce and colleagues explored the impact of different acceptor groups in

thiophene-based dyes (**Figure 18**, right), further elucidating how acceptor modifications can modulate the dye's properties.

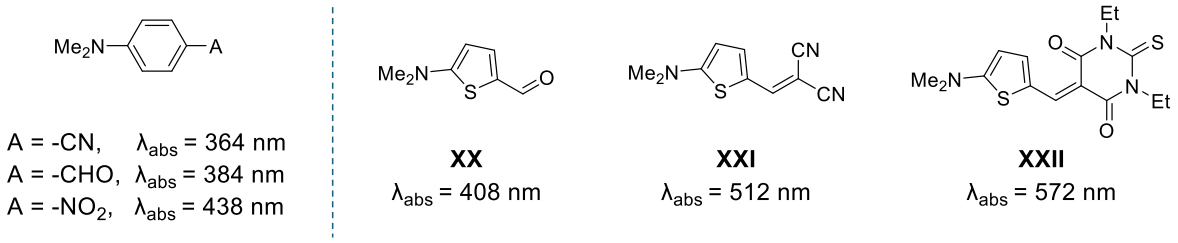

Figure 18. Left: styrene derivatives with different acceptor groups; right: thiophene-based dyes having different acceptors.

Another modification to the π-conjugated backbone involves replacing common aromatic rings with heteroaromatic ones. The incorporation of heterocyclic moieties can enhance the polarizability, improve chemical and thermal stability, and fine-tune the optical and NLO properties of the dye. In 2012, Kulhánek *et al*.[35] investigated the effect of substituting the conventional 1,4-phenylene unit with a 2,5-thiophene unit (**Figure 19**). This transition from compound **XXIII** to compound **XXIV** reduced the LUMO energy levels, decreasing the energy gap from 1.51 eV to 1.34 eV. Compound **XXV** exhibited LUMO energy levels similar to those of compound **XXIV**. As expected, this modification led to a red-shift in the absorbance spectrum from compounds **XXIII** to **XXIV** and **XXV**.

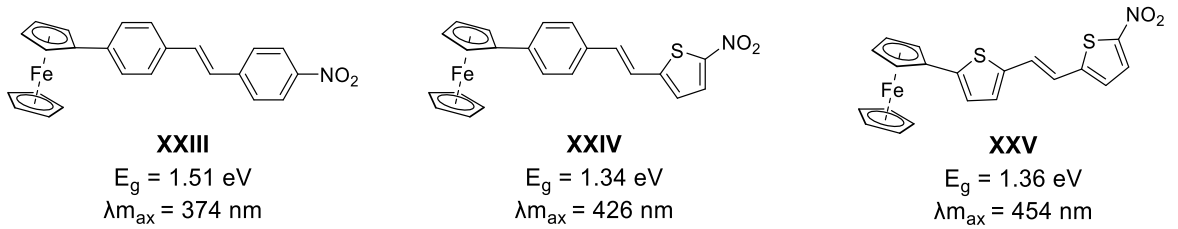

Figure 19. Structure of 2,5-thiophene dye derivatives, their band gap values and absorption maxima.

In 2009, Wang *et al*.[36] conducted a study investigating the impact of five-membered aromatic heterocycles containing oxygen, sulfur, and selenium as heteroatoms in the design of push-pull dyes for application in dye-sensitized solar cells (DSSCs) (**Figure 20**). The results demonstrated that dyes incorporating furan rings exhibited higher efficiencies compared to those with thiophene, while dyes containing selenophene showed even greater efficiency than those with thiophene. Additionally, the optical properties of the dyes were significantly influenced by the specific heteroatom present in the aromatic ring.

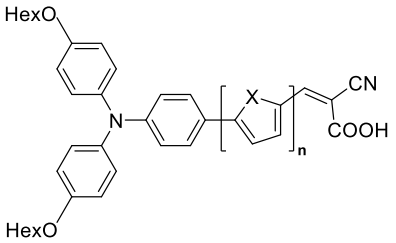

29a, n = 1, X = O E_g = 1.74, λ_{abs} = 506 nm, λ_{em} = 689 nm
29b, n = 2, X = O E_g = 1.62, λ_{abs} = 522 nm, λ_{em} = 716 nm
29c, n = 1, X = S E_g = 1.67, λ_{abs} = 514 nm, λ_{em} = 715 nm
29d, n = 2, X = S E_g = 1.57, λ_{abs} = 523 nm, λ_{em} = 723 nm
29e, n = 1, X = Se E_g = 1.66, λ_{abs} = 525 nm, λ_{em} = 720 nm
29f, n = 2, X = Se E_g = 1.53, λ_{abs} = 549 nm, λ_{em} = 772 nm

Figure 20. Structure of modified heterocyclic stilbazolium dyes.

NLO properties. As previously discussed, styryl dyes are extensively employed for their NLO properties. In 2017 Avhad *et al.*[37] investigated the NLO behavior of 3-styryl and 3-vinyl coumarin dyes (**Figure 21**) using density functional theory (DFT) calculations, which revealed high first hyperpolarizability (β) values. Furthermore, the study demonstrated that increasing the donor group strength in the order H < OCH_3 < $N(CH_2CH_3)_2$ resulted in a significant enhancement of both the charge transfer characteristics and the NLO response.

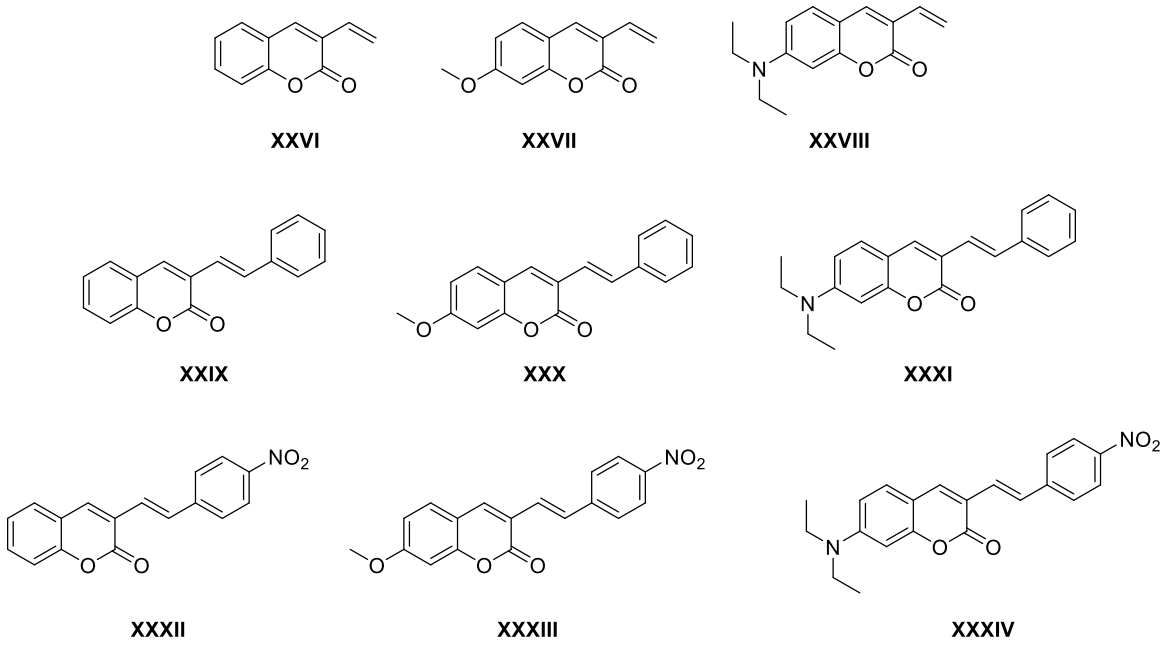

Figure 21. Representation of styryl and vinyl coumarin dyes investigated.

In 2018, Sekar *et al*.[38] conducted an investigation into the NLO properties of a series of carbazole-based styryl dyes (**Figure 22**) utilizing both solvatochromic analysis and computational methods. The results from both approaches highlighted the significant influence of solvent polarity on the NLO behavior of the dyes (see data in **Figure 22**). The two-photon absorption cross-section (σ_{2PA}) values were determined from the solvatochromic data, with dye **XXXVII** exhibiting lower σ_{2PA} value. This reduction in σ_{2PA} was attributed to the presence of a twisted phenyl ring, which alters the charge transfer pathway within the molecule.

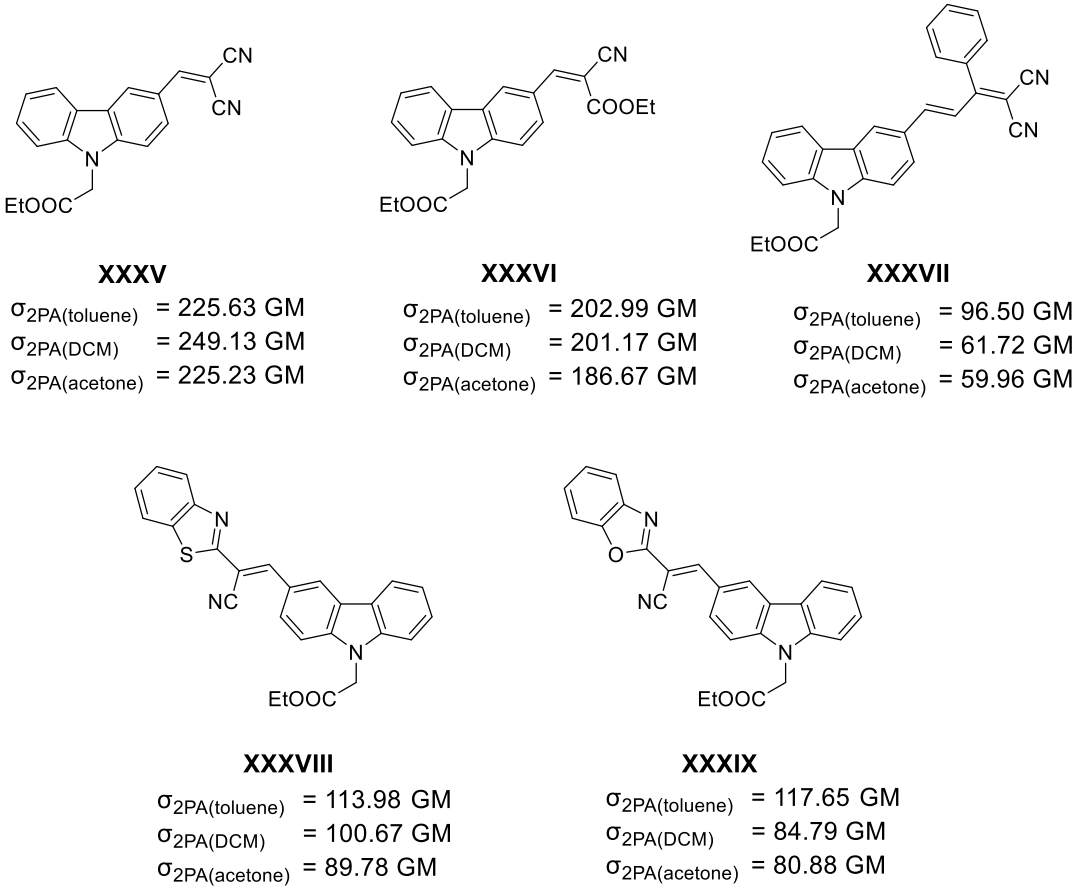

Figure 22. Structures of carbazole-based styryl dyes and their σ_{2PA} values in different solvents.

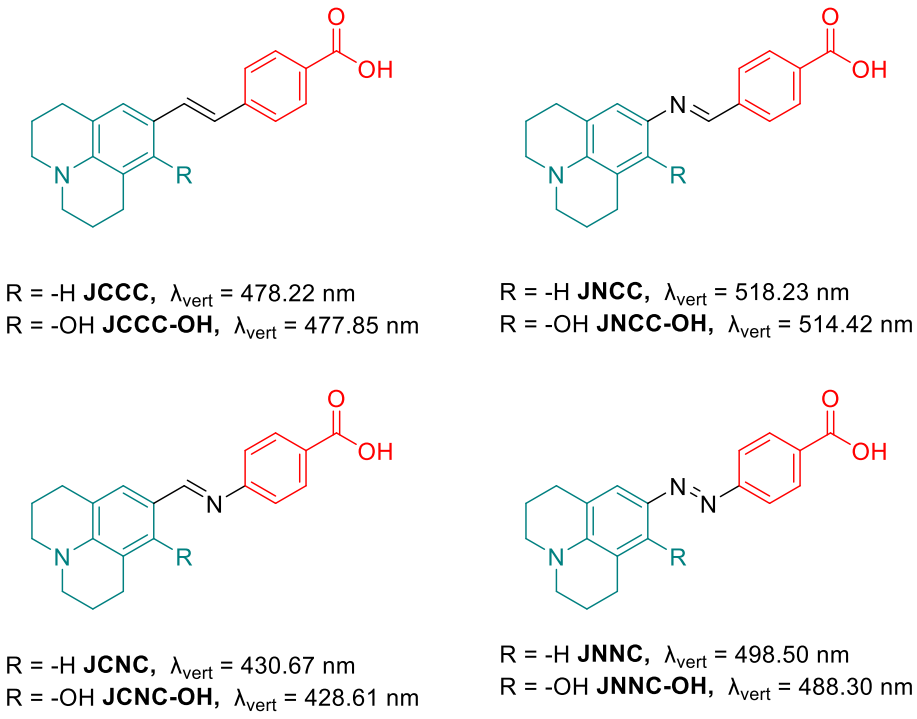

Figure 23. Structure of julolidine-based styryl dyes and vertical absorption maximum values in DMF.

In 2023, the same research group extended their investigation to the NLO properties of a series of julolidine-based styryl dyes (**Figure 23**) and their potential use as sensitizers in dye-sensitized solar cells (DSSC).[39] Their findings revealed that the CT characteristics of these dyes were influenced by the symmetry of the π-bridge, with less symmetrical π-bridges leading to altered CT behavior. Additionally, time-dependent density functional theory (TD-DFT) calculations demonstrated that the vertical absorption maximum exhibits a red shift when nitrogen atoms were incorporated into the styryl backbone (see data in **Figure 23**).

Bioimaging. For fluorescence targeting and cellular imaging, the development of novel dyes with enhanced optical properties is essential. Styryl dyes represent a class of fluorophores that exhibit significant potential due to their easy synthesis, high photostability, tunable optical characteristics, and strong fluorescence. These dyes are frequently employed in DNA duplex binding because their positive charge facilitates electrostatic interactions with DNA's negatively charged phosphodiester backbone. Various examples of such interactions have been reported. In 2022, Vilaivan *et al.*[40] reported the design of novel dicationic styryl dyes with enhanced binding affinity and improved optical response towards target nucleic acids compared to their mono-cationic counterparts (**Figure 24**).

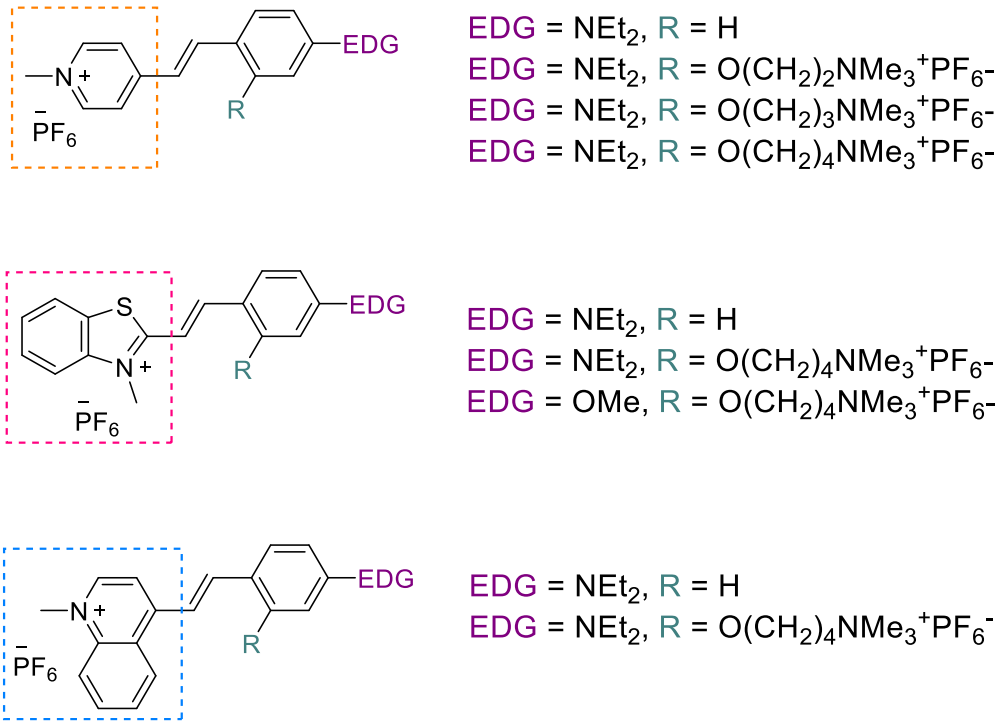

Figure 24. Structures of a series of styryl dyes for DNA targeting.

The same year, Wagenknecht *et al.*[41] introduced a fluorescent DNA probe utilizing styryl dyes, employing a click chemistry modification strategy. This system exploited an energy transfer process, significantly enhancing fluorescence output. In 2023, Kamkaew *et al.*[42] synthesized two cationic

styryl derivatives that demonstrated fluorescence intensification upon DNA binding *via* electrostatic interactions (**Figure 25**). These styryl dyes also exhibited selective targeting of cancer cells and certain bacterial strains.

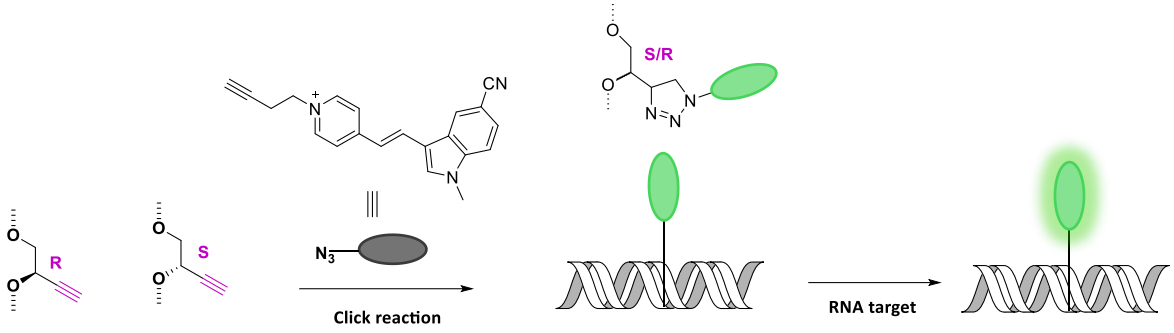

Figure 25. Hybridization-sensitive oligonucleotide probes.

In 2023, Wijesinghe *et al.*[43] reported the synthesis of two regioisomeric styryl dyes, **1a** and **1b**, exhibiting NIR emission (**Figure 26**). Probe **1b** displayed a bathochromic shift relative to **1a**, attributed to the regioisomeric effect. These dyes demonstrated a strong capability for visualizing bacteria and yeast using fluorescence microscopy.

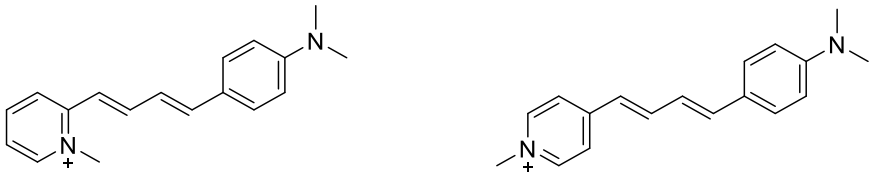

1a
λ_{abs} = 541 nm
λ_{em} = 678 nm
φ_{fl} = 0.61

1b
λ_{abs} = 561 nm
λ_{em} = 706 nm
φ_{fl} = 0.72

Figure 26. Structures of probes **1a** and **1b** with their optical characteristic in dichloromethane.

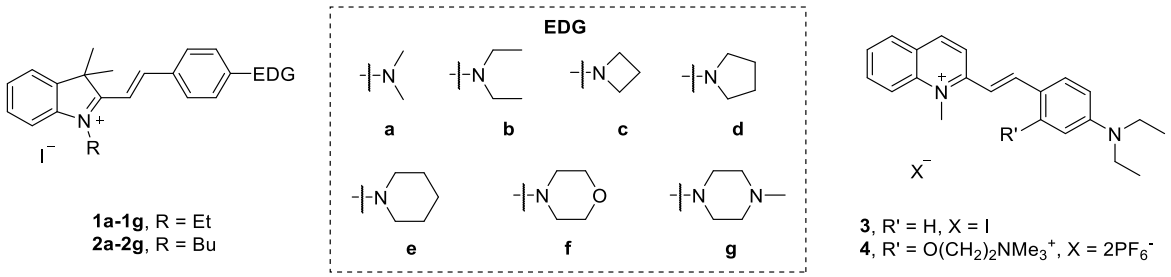

Figure 27. Structures of styryl dyes for *tau* protein targeting.

In 2024, Aonbangkhen *et al.*[44] reported a series of novel styryl dyes designed to investigate their binding interactions with *tau* protein aggregates both in vitro and in cellular models (**Figure 27**). *Tau*, a protein implicated in Alzheimer's disease, is associated with neurodegenerative pathology due to its abnormal accumulation in the brain, making effective binding to *tau* aggregates of critical

importance. Among the dyes, compound **4** exhibited a 28-fold increase in fluorescence emission upon binding to *tau* aggregates, as observed in both *in vitro* assays and *in cells*, with confocal fluorescence microscopy confirming these results.

Thiazo[5,4-d]thiazole dyes

Thiazo[5,4-*d*]thiazole-based dyes (**TTz**) belong to the class of fused (bi)heterocyclic compounds (**Figure 28**), distinguished by their rigid planar structure and extended π-conjugated electronic system. In contrast to their thieno[3,2-*b*]thiophene analogs (**T**), the thiazothiazole ring contains two nitrogen atoms, rendering it more electron-deficient and thus conferring greater oxidative stability compared to the thiophene ring (**Figure 28**, left). For instance, the derivative **TTz-T$_{12}$** (**Figure 28**, right), reported by Aso *et al*.,[45] exhibited a higher oxidation potential than its corresponding thiophene derivative **T$_4$**.[46]

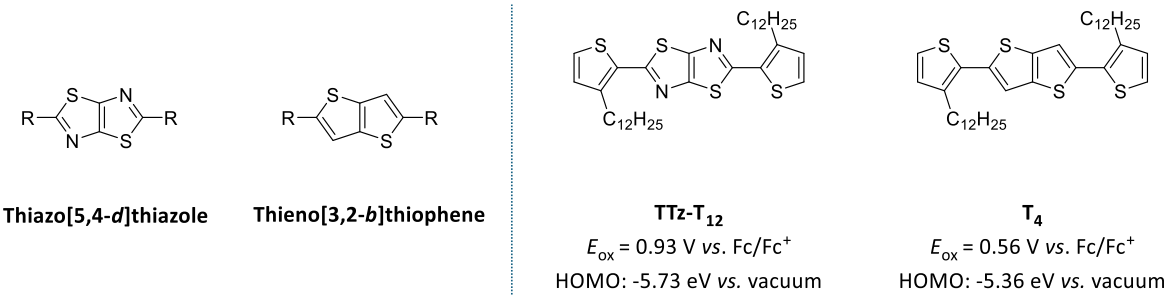

Figure 28. Left: general structure of thiazo[5,4-*d*]thiazole and thieno[3,2-*b*]thiophene system; right: structure of **TTz-T$_{12}$** and **T$_4$** with their oxidative potential and Homo values. The energy level of the Fc/Fc$^+$ couple was assumed to be -4.8 eV to vacuum.

Due to their enhanced oxidative stability, strong π-π stacking interactions, and effective orbital overlap in the solid state, which promotes efficient electron and hole mobilities, these dyes have garnered significant interest in the field of organic electronics. They are extensively utilized in various optoelectronic devices, including organic light-emitting diodes (OLEDs),[47,48] organic field-effect transistors (OFETs),[49,50], organic solar cells (OSCs),[51,52] and dye-sensitized solar cells (DSSCs).[53,54] The earliest synthesis of a compound containing the thiazolo[5,4-*d*]thiazole (**TTz**) ring system dates back to 1891, when Ephraim prepared 2,5-diphenylthiazolo[5,4-d]thiazole *via* the condensation of benzaldehyde with dithiooxamide.[55] However, the precise structure of the condensation product was not elucidated until 1960, when Johnson and Ketcham accurately determined its molecular configuration (**Figure 29**).[56]

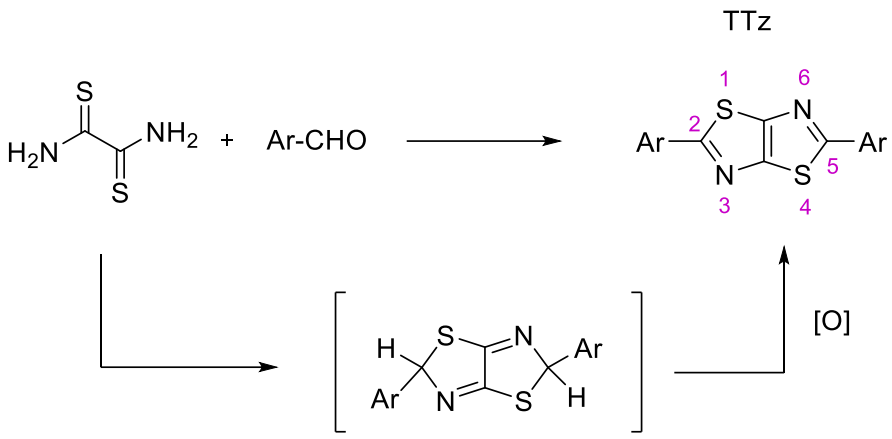

Figure 29. Scheme of the synthesis of a generic symmetric **TTz**-based dye.

Electrochromic properties. Electrochromism (EC) refers to the phenomenon where the application of an electrochemical potential to a dye species induces a color change, which is driven by a redox transformation of the species. This color change can appear both in the absorbance and fluorescence spectra. The latter phenomenon is termed electrofluorochromism (EFC). The earliest recorded instance of electrochromism dates back to 1966,[57] while the EFC was first demonstrated in 1993,[58] when J.M. Lehn utilized the redox state of a quinone derivative to toggle the fluorescence of a ruthenium-bipyridine complex. In EFC, materials typically exhibit strong fluorescence in their neutral state but become non-emissive upon applying an electric bias. In addition to EC and EFC, photochromism represents another related process wherein a material undergoes a color change upon exposure to light. **TTz**-based dyes have emerged as promising candidates for both EC and EFC applications, primarily due to their high fluorescence quantum yield. These symmetric **TTz**-based dyes, much like viologen salts, undergo two reversible redox processes corresponding to the successive one-electron reductions of the **TTz** core (**Figure 30**).

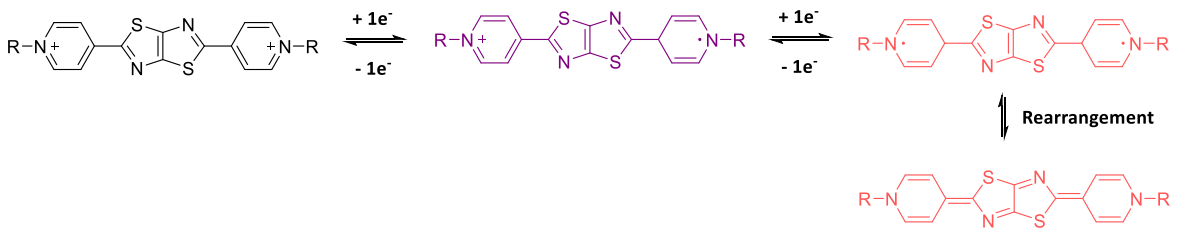

Figure 30. Redox process for a generic **TTz**-based dye.

In 2023, Chakraborty *et al.*[59] reported a thiazo[5,4-*d*]thiazole-containing polymer that showed both EC and EFC in the NIR region. The polymer, named **P-TTz**, exhibited a *quasi*-reversible single-electron reduction, resulting, during electrochromism, in a transition color from pale yellow to black in the NIR region. Also, it switched from a red-to-quenched fluorescence during EFC within a low

potential window of −1.7 to +0.6 V (**Figure 31**). This material represents a significant example of tunable absorption from the visible to NIR, alongside on-off fluorescence modulation.

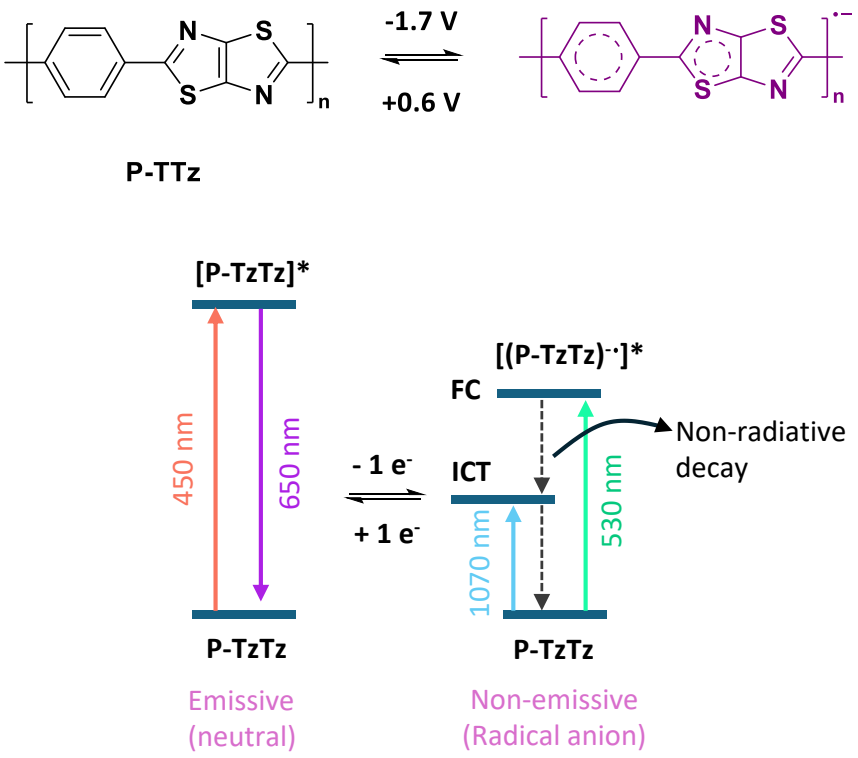

Figure 31. Top: radical-anionic structure of **P-TTz** during EC process; bottom: schematic representation of potential non-radiative decay pathways. The radical-anion species induces the formation of a low-energy intramolecular charge transfer (ICT) state. This low-energy ICT state facilitates non-radiative deactivation, leading to fluorescence quenching. FC corresponds to the Franck-Condon state.

In 2019, Gao *et al.*[60] reported an example of photochromism and fluorescence photomodulation, marking the first instance of photochromism observed in **TTz** derivatives. In this study, a metal-organic framework (MOF) containing a **TTz**-based ligand was synthesized (**Figure 32**). The reversible photochromism was attributed to interframework donor-acceptor interactions, which facilitated electron transfer between the carboxylate and **TTz** moieties. Additionally, the fluorescence of the **TTz** species exhibited photomodulable behavior, further contributing to the dynamic fluorescence response of the system.

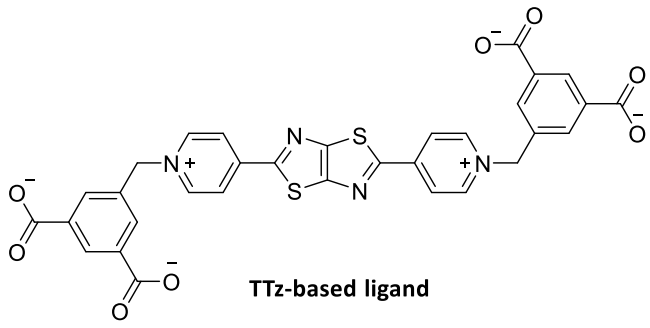

Figure 32. Structure of **TTz**-based ligand for a MOF.

In 2021, Walter and colleagues[61] reported a **TTz**-based system exhibiting multiple functionalities, including EC, EFC, and photochromism. The system involved a water-based hydrogel configured as FTO/hydrogel/FTO, utilizing water-soluble **TTz**-based dyes combined with polyvinyl alcohol (PVA)/borax polyelectrolyte hydrogel (**Figure 33**). This design enabled the development of multifunctional chromogenic devices (CGDs) that demonstrated significant EC and EFC responses and photochromic activity.

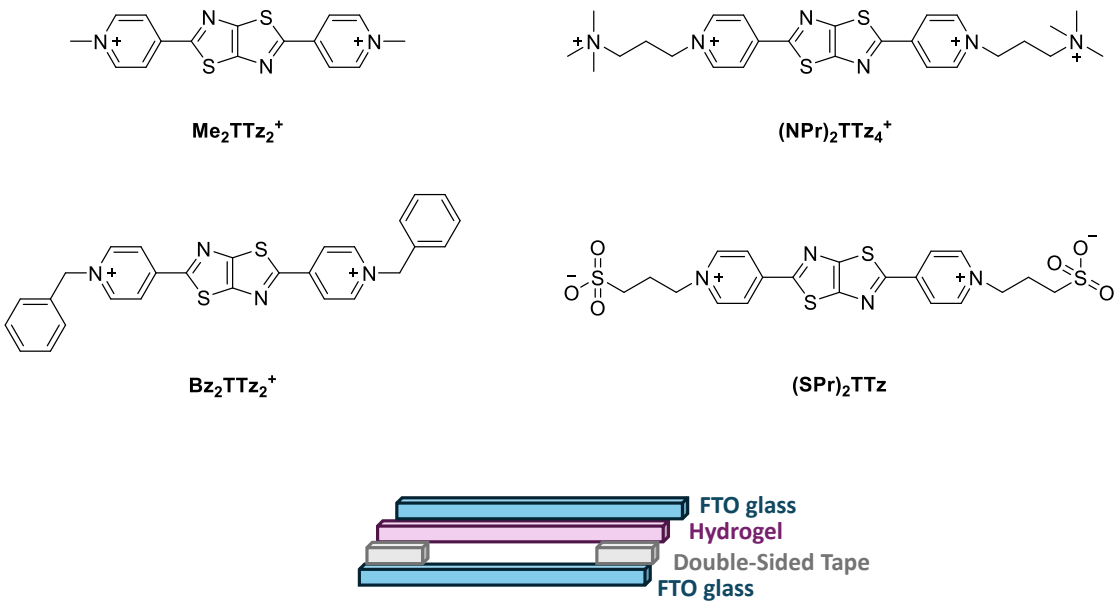

Figure 33. Top: structure of investigated **TTz**-based dye; bottom: schematic illustration of CGDs used.

Organic Solar Cells (OSCs).[57] Organic solar cells (OSCs), which utilize organic semiconductors, are of significant interest due to their ease of fabrication, low production costs, and compatibility with flexible substrates. As a result, they are attracting increasing attention in the field of renewable energy. Typically, OSCs are based on a "bulk-heterojunction" (BHJ) architecture, which consists of four main components (**Figure 34** ***a***): (1) a transparent electrode, commonly composed of glass coated with conductive indium-tin-oxide (ITO); (2) a photoactive layer, where two organic materials function as the electron donor and acceptor; (3) an electron-blocking and hole-conducting layer; and (4) a cathode capable of accepting electrons from the active layer.

The operational mechanism of the device is driven by sunlight, which activates the active layer. In this process, the donor material absorbs a photon, promoting an electron from the HOMO to the LUMO, resulting in the generation of an exciton, a bound electron-hole pair. Upon reaching the donor-acceptor interface, charge separation occurs: the electron is transferred to the acceptor material and subsequently transported to the metallic cathode, while the hole is conveyed through the conductive layer (PEDOT:PSS) to the anode. The electrons then travel through the external circuit, where they recombine with the holes, generating an electric current (**Figure 34** ***b***). For

optimal device performance, two critical factors must be considered: the efficiency of photon absorption by the donor material and the formation of a donor-acceptor network with well-defined domains. This structural arrangement ensures efficient exciton diffusion, allowing the excitons to reach the interface and facilitate charge separation with minimal obstacles.

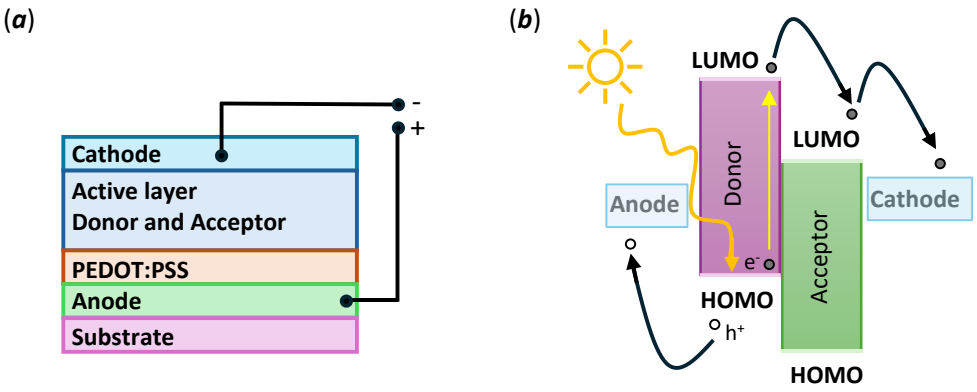

Figure 34. (***a***) Schematic representation of a BHJ solar cell; (***b***) scheme of the operating mechanism of BHJ solar cell.

TTz-based materials have demonstrated significant potential as highly efficient OSCs due to their molecular structure. Photovoltaic active materials typically comprise conjugated systems incorporating both electron-donor (**D**) and electron-acceptor (**A**) units. Materials containing heterocyclic components exhibit enhanced ICT and charge delocalization, which promotes efficient exciton transport. The **TTz** ring system, in particular, serves as a versatile building block in the design of various materials for high-performance OSCs. Both **TTz**-based polymers and small molecules can be employed to achieve this efficiency. Since 2010,[63] the **TTz** ring system has been increasingly utilized in BHJ solar cells. Typically, the **TTz** unit is incorporated into copolymers by combining it with other heterocyclic units, resulting in materials with donor-acceptor characteristics. Despite the diversity of structural compositions, copolymers designed for OSCs generally exhibit an alternating structure, where electron-rich groups, such as thiophene and related heterocycles, are coupled with the electron-withdrawing **TTz** moiety. **TTz**-based copolymers frequently achieve high power conversion efficiencies (PCE), which is defined as the ratio of the electrical power generated by the solar cell to the incident light power.[64] Osaka *et al.* investigated the influence of **TTz**-based dye geometry on the PCE of OSCs.[65,66] They specifically examined **TTz**-based copolymers with linear and branched alkyl substituents. Their findings indicated that polymers with branched side chains of similar lengths exhibited higher molecular aggregation through "face-on" π-π stacking, in contrast to the "edge-on" packing typically associated with linear side chains. This enhanced aggregation improved charge mobility, leading to superior device performance. Notably, the copolymer **PTzBT-BOHD** (**Figure 35**), when employed in an OSC, exhibited enhanced photocurrents, resulting in a PCE of 7.5%.

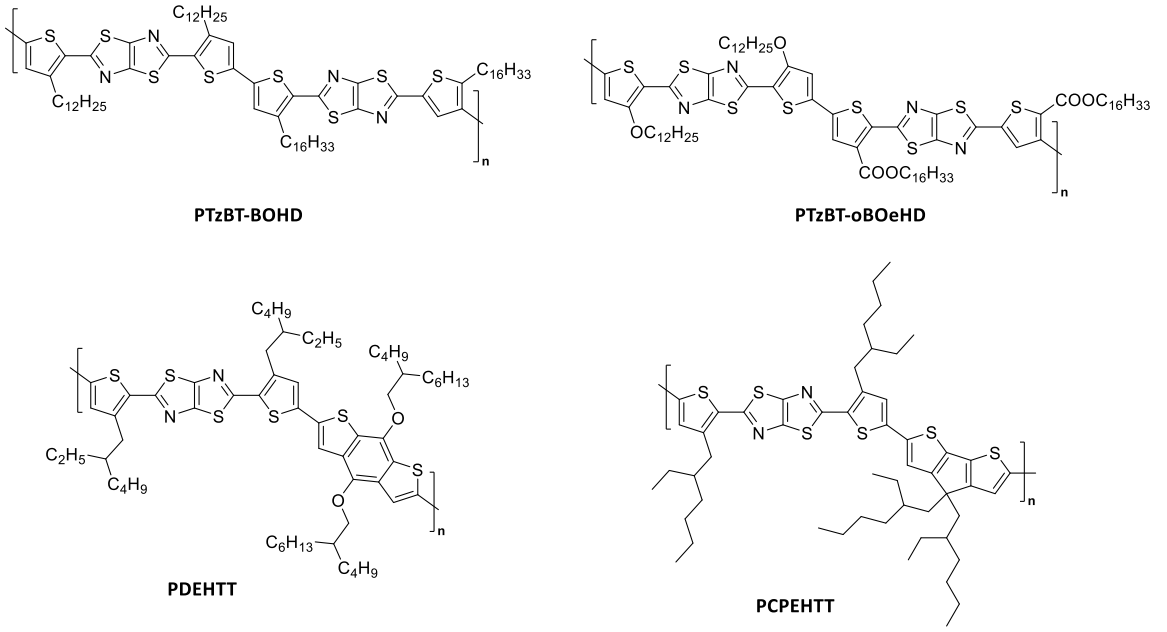

Figure 35. Structures of **TTz**-based copolymer used in OCSs.

In addition to alkyl chain branching, modifications involving electron-donating and electron-withdrawing ester groups on the polymer backbone were explored to reduce the HOMO-LUMO band gap, thereby inducing a red-shift in the absorption spectrum. Polymers such as **PTzBT-BOHD** and **PTzBT-oBOeHD** (**Figure 35**) demonstrated good performance due to their broad absorption spectra and the stabilization of the HOMO level attributed to the ester group, which contributed to the improved device efficiency.[60] Jenekhe and colleagues further expanded on the study of **TTz**-based copolymers by varying the donor and conjugated units.[67] Among the polymers investigated, **PDEHTT** (**Figure 35**), which incorporates a dithiophene unit, exhibited a high PCE of 5.71%. However, when the polymer backbone was modified to include a cyclopentadithiophene unit, resulting in **PCPEHTT** (**Figure 35**), the efficiency decreased significantly to 2.41%. These results underscore the impact of polymer structure on OSCs performance.

TTz-containing small molecules can also serve as donor materials in OSCs. These compounds typically feature a central electron-deficient **TTz** core flanked by conjugated chains terminated with electron-donating or electron-withdrawing units. Compared to polymers, small molecules offer advantages such as simpler and more reproducible synthesis, higher purity, and better solubility. However, **TTz**-based small molecules generally exhibit lower photovoltaic efficiencies than their polymer counterparts. The first example of a **TTz**-based small molecule was reported in 2012 by Zhan *et al.*,[68] who designed **TT-TTPA** (**Figure 36**), a molecule incorporating long alkyl chains. Although this molecule demonstrated a good photocurrent generation, its overall PCE was relatively low at 3.73%. Subsequent structural modifications were introduced to improve efficiency. For instance, two **TTz**-based molecules with shorter alkyl chains (**T0**) and an extended conjugated

backbone (**T2**) exhibited enhanced performance (**Figure 36**).[69] The **T2** molecule, with its extended conjugation, showed a red-shift in absorption and stronger light absorption, leading to an improved PCE of 4.05%.

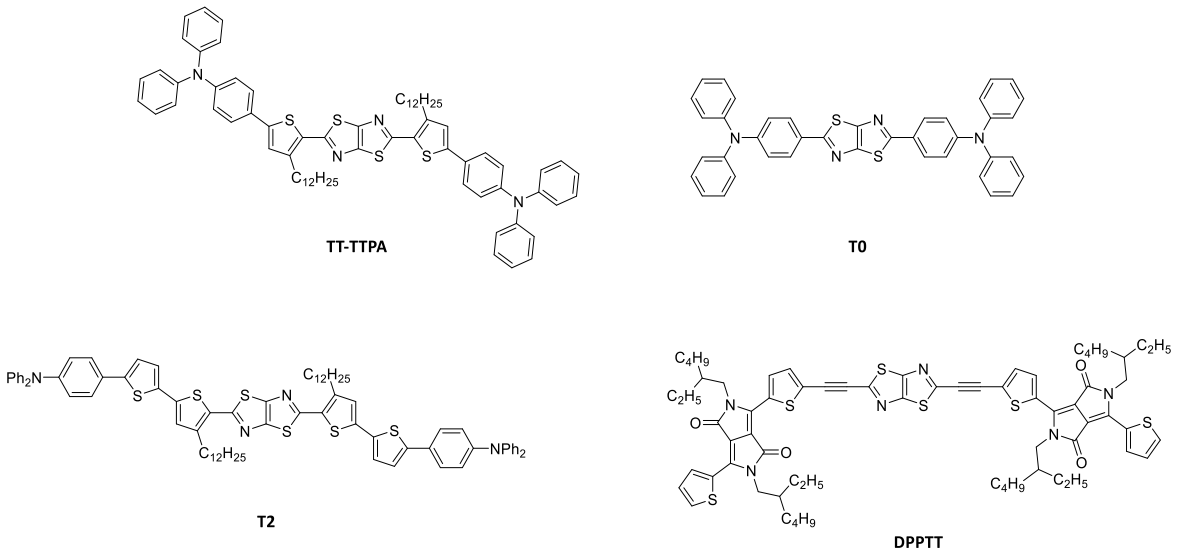

Figure 36. Structure of **TTz**-based small molecules for OSCs: **TT-TPA**, **T0**, **T2**, and **DPPTT**.

Another approach to tuning the energy levels of **TTz**-based materials and enhancing their light-absorbing properties is the incorporation of electron-withdrawing groups. In 2014, Zhang *et al*.[70] designed a diketopyrrole-based compound, **DPPTT** (**Figure 36**), where the central **TTz** ring system was connected to external functional groups *via* triple bonds. **DPPTT** exhibited a deep HOMO level, a red-shifted absorption maximum, and a high molar extinction coefficient, all of which contributed to improved the device performance, achieving a PCE of 4.18%.

Dye-sensitized solar cells (DSSCs). DSSCs share similarities with OSCs, but their operating principles and structure differ significantly. The working mechanism of DSSCs can be summarized in five key steps (**Figure 37**): (**1**) Photoexcitation: the absorption of sunlight induces the excitation of electrons from the dye's HOMO to its LUMO; (**2**) electron injection: the excited electron is injected from the dye's LUMO into the conduction band of the TiO_2 layer, which serves as an inorganic semiconductor. This is followed by the collection of charge at the electrode; (**3**) electron flow: the electron flows from the anode to the cathode, generating an electric current in the external circuit; (**4**) reduction at the cathode: at the cathode, which is typically platinum, the redox mediator is catalytically reduced; (**5**) dye regeneration: the dye is regenerated through electron transfer from the redox couple to its HOMO, completing the cycle and allowing the process to repeat. This sequence of events drives the generation of electrical energy in DSSCs.

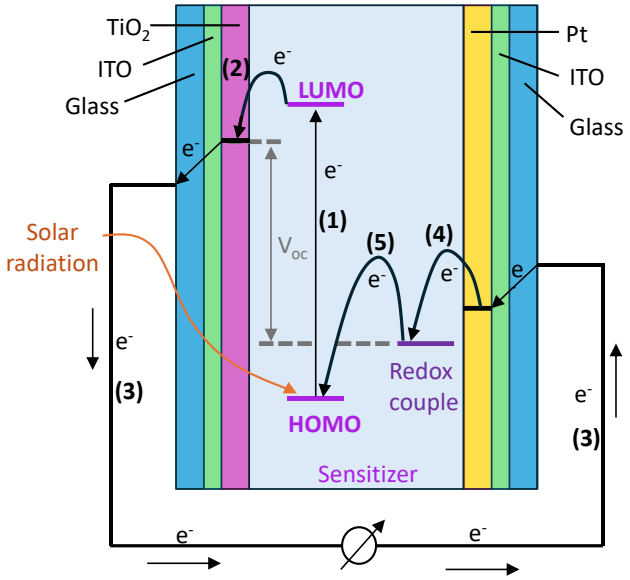

Figure 37. Working principle of a DSSC. The glass electrodes bear a transparent conductive oxide layer (indium-tin oxide, ITO). The first electrode is coated with a layer of inorganic semiconductor (nanocrystalline TiO_2), while the cathode is coated with a layer of platinum. The space between the two electrodes is filled with an electrolyte containing a redox couple.

The dye sensitizer plays a crucial role in both the light-harvesting and charge-separation processes in DSSCs. Commonly used dyes are characterized by a D-π-A architecture, making **TTz**-based dyes ideal candidates due to their high planarity, excellent electronic conductivity, and strong oxidative stability. The first use of **TTz**-based dyes in DSSCs was reported in 2013 by two research groups that synthesized and employed two **TTz**-based dyes: **FNE71-74**[71] and **TTZ1-2**[72] (**Figure 38**).

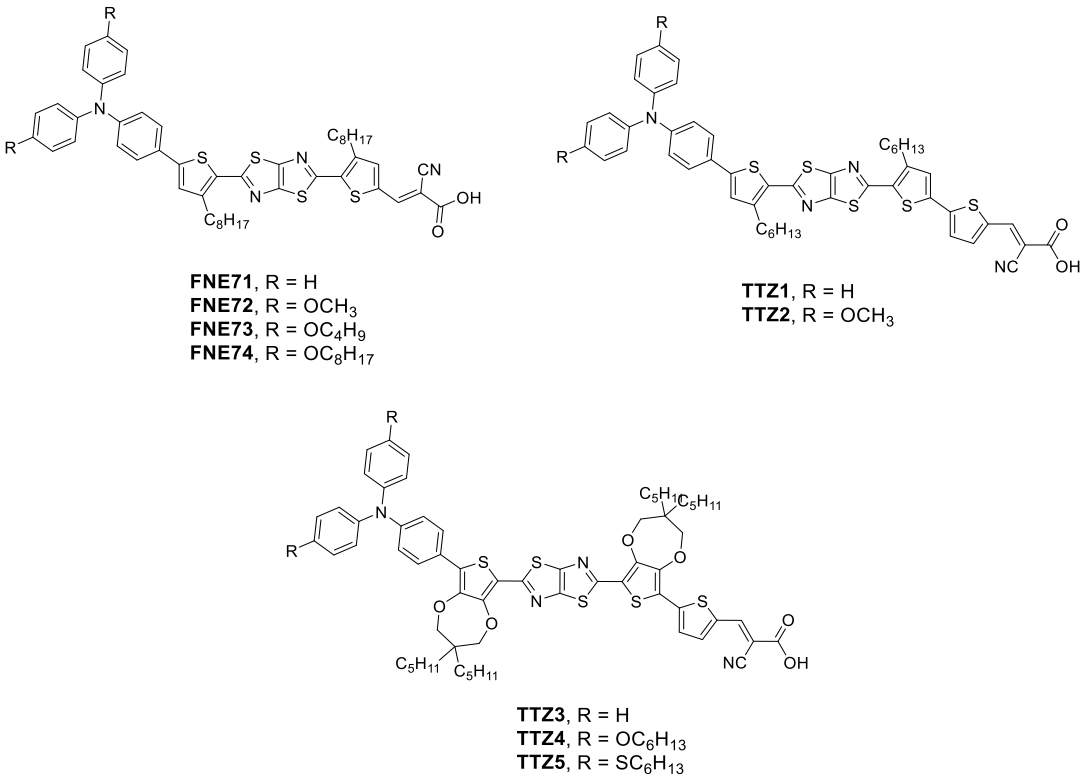

Figure 38. Structures of **TTz**-based dye for DSSCs.

Among the **FNE71-74** series, the dye **FNE74**, which featured the longest alkyl chain on the donor group, delivered the best performance, achieving a PCE of 5.10%. In contrast, within the **TTZ1**-**2** series, **TTZ1**, which lacked substituents on the donor unit, outperformed **TTZ2**, with a PCE of 3.53%. This series has been further expanded[72] by incorporating D-π-A dyes with dipentylpropylenedioxythiophene units in place of the simple thiophene ring, resulting in dyes **TTZ3**-**5** (**Figure 38**). These modified dyes exhibited red-shifted absorbance maxima compared to **TTZ1**-**2** and displayed higher molar extinction coefficients. Due to these enhanced optical properties, they are suitable for use in opaque thin-layer DSSCs. Under these conditions, these dyes showed superior performance relative to **TTZ1**-**2**, with **TTZ5** achieving the highest PCE value of 7.71%.

Calix[6]arene: A Supramolecular Macrocycle for Host-Guest Complexes

In supramolecular chemistry,[73] host-guest recognition[74] represents a fundamental concept. A host molecule is defined as a molecular entity with convergent binding sites, while a guest molecule is a species presenting complementary binding sites. The complementarity between the host and guest molecules, typically due to their size and shape, is often described using the lock-and-key model, where the host has binding sites correctly arranged in the space to bind a complementary guest. This complementarity is further reinforced by the formation of non-covalent intermolecular forces, commonly referred to as weak forces. These weak forces in supramolecular chemistry include electrostatic interactions (such as dipole-dipole or ion-dipole interactions), hydrogen bonding, halogen bonding, hydrophobic effects, π–π stacking, and London dispersion or Van der Waals forces. Due to the inherently weak nature of these non-covalent interactions compared to covalent bonds, cooperativity among multiple weak forces plays a crucial role in stabilizing the host-guest complex. When multiple weak interactions act synergistically, the overall binding strength is enhanced, often resulting in high binding constants. The association constant of a host-guest complex (K_{bind}) is defined by the equilibrium constant for the association between free host and guest molecules to form the complex, which is a thermodynamic process. Equation (**1**) represents the binding constant for a 1:1 host: guest system.

$$H + G \rightleftarrows HG$$

$$K_{bind} = \frac{[H][G]}{[HG]} \quad (\mathbf{1})$$

Usually, K_{bind} is calculated through NMR, UV-Vis, fluorescence spectroscopy, or calorimetric titrations. A high binding constant indicates that the equilibrium is significantly shifted towards the complexed state, reflecting strong and stable host-guest interactions.

Mechanically interlocked molecules (MIMs)

Host-guest complexes can facilitate the formation of supramolecular structures such as pseudorotaxanes and rotaxanes (**Figure 39**). A pseudorotaxane consists of a supramolecular complex where a linear guest molecule, referred to as the "axial component", is threaded through a macrocyclic host, stabilized by non-covalent interactions. The thermodynamic stability of pseudorotaxane depends on the nature and strength of these non-covalent forces. A rotaxane species represents a more evolved form of a pseudorotaxane, in which bulky substituents, known as "stoppers," are attached to the ends of the axial component. These stoppers are larger than the internal diameter of the macrocycle, thereby preventing the linear molecule from dethreading and effectively trapping the axial component within the macrocyclic host. This structural modification imparts additional stability to the rotaxane assembly. Cartoon representations of the two supramolecular entities are reported in **Figure 39**. The grey balls represent the stopper groups.

Figure 39. Representation of [2]pseudorotaxane (left) and [2]rotaxane (right).

In recent years, more complex supramolecular structures have been realized, ranging from simple [2]rotaxanes to more advanced architectures such as daisy chains,[76] oligorotaxanes,[77] and polyrotaxanes (**Figure 40**).[78] These supramolecular species have garnered significant attention due not only to their interlocked configurations but also to their dynamic properties, particularly the mobility of the macrocycle along the axle component.[75] Pseudorotaxanes exhibit responsive behavior, enabling control/release and lock/key mechanisms, while rotaxanes demonstrate macrocycle movement, including rotation and/or shuttling along the axle. This molecular shuttling mechanism has been foundamental in the development of artificial molecular machines.[79]

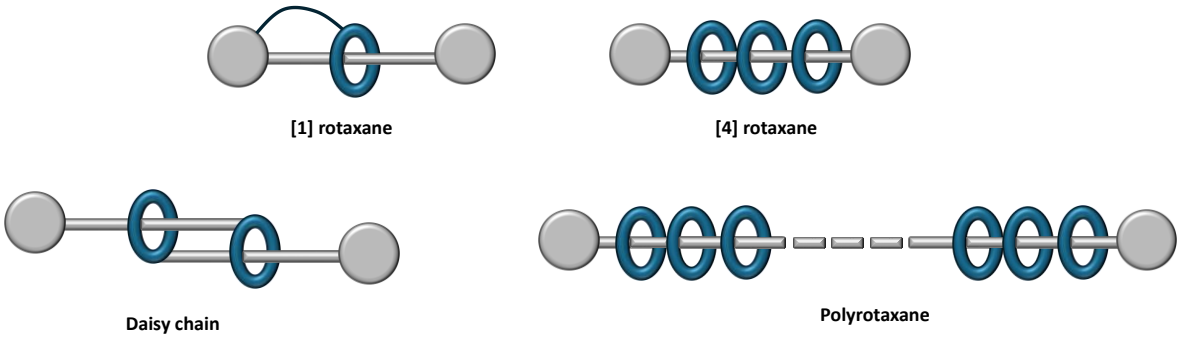

Figure 40. Representation of different types of rotaxanes.

Oriented rotaxane and pseudorotaxane species

The formation of pseudorotaxane and rotaxane species can yield different isomers, depending on the geometry of the macrocycle employed.[80] In supramolecular chemistry, macrocycles are typically classified into two main categories: planar and three-dimensional structures. Planar macrocycles include, for example, *crown ethers*, while three-dimensional structures include *calixarenes*, *cucurbiturils*, *cyclodextrins*, *resorcinarenes*, and *paracyclophanes*. Planar and symmetric 3D macrocycles exhibit a palindrome structure, meaning they present identical faces on both sides of the cavity. Consequently, an axial guest, whether symmetric or asymmetric, can pass through the cavity from either direction, yielding the same product (**Figure 41**, (***a***)). In contrast, when an asymmetric macrocycle is used, where the two sides of the cavity differ in size, shape, or chemical properties, the threading of an asymmetric axle component can lead to the formation of orientational pseudorotaxane isomers. These orientational pseudorotaxane isomers can subsequently be converted into rotaxane species by capping the ends of the asymmetric axle with bulky stoppers (**Figure 41**, (***b***)).

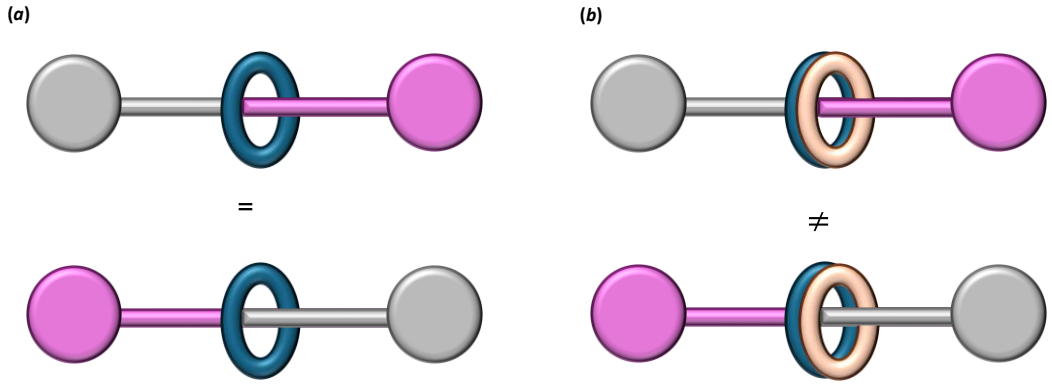

Figure 41. (***a***) Representation of rotaxane species in a palindrome wheel; (***b***) representation of orientational isomers of a non-symmetric axle inside a non-palindrome wheel.

Various macrocycles can be employed to synthesize pseudorotaxane and rotaxane species, including cyclodextrins, crown ethers, cucurbiturils, calixarenes, pillarenes, and paracyclophanes. In this thesis, calixarene macrocycles[81] will be specifically investigated. They are synthesized in good yields through condensation of *p*-tert-butylphenol and formaldehyde in basic conditions. The resulting macrocycle's size, i.e. the number of phenolic units, can be adjusted by suitably modifying the base employed and the nature of the solvent. Calix[4]arenes, characterized by a relatively small cavity, are generally unsuitable for complexing linear guest molecules and are thus rarely used in the formation of rotaxane species. In contrast, calix[6]arenes, with their larger cavity, facilitate the complexation of linear guests, enabling the formation of both pseudorotaxane and rotaxane species.[82,83] In 2000, Pochini and colleagues[84] reported the synthesis of [2]pseudorotaxane and

[2]rotaxane species utilizing triphenylureido calix[6]arene as the macrocycle and viologen salt derivatives as guest molecules in weakly polar media (**Figure 42**).

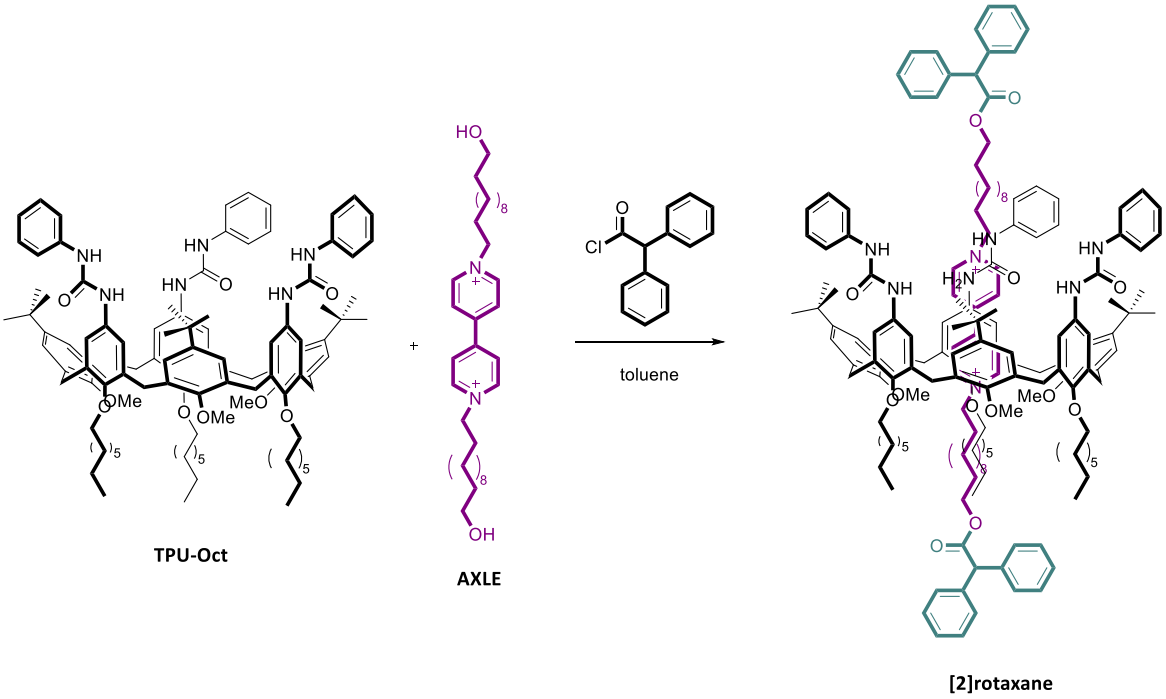

Figure 42. Synthesis of the [2]rotaxane species between triphenylureido calix[6]arene and dialkyl viologen salt through a clipping method.

The interaction between dialkyl viologen salts and the calix[6]arene macrocycle is driven by the high affinity between the π-electron-rich cavity of the calixarene and the electron-deficient viologen guests. Additionally, X-ray diffraction (XRD) analysis revealed the presence of hydrogen bonds between the counterions and the phenylureido groups of the calix[6]arene, further contributing to the stability of the complex.[85] The complexation is also accompanied by the emergence of a charge transfer (CT) band, resulting from the proximity of the calixarene's aromatic rings and the aromatic portion of the viologen axle. This CT band serves as a useful indicator for determining the binding constant of the complexation process *via* UV-Visible spectroscopy. In 2004, our research group evaluated the binding affinity between the triphenylureido calix[6]arene with a dialkyl viologen salt using two different counterions: tosylate and hexafluorophosphate.[86] The results indicated a significantly higher binding constant in the presence of tosylate anions compared to hexafluorophosphate [$K_{bind}(TsO^-) = 1.7\times10^6\ M^{-1}$, $K_{bind}(PF_6^-) = 6.0\times10^3\ M^{-1}$]. These findings highlight the crucial role of the counterion in the complexation process, influencing both the thermodynamic stability of the pseudorotaxane and the kinetics of the threading and dethreading processes.

To gain a deeper understanding of the threading process of a guest molecule within calix[6]arene and to determine the factors influencing complexation, asymmetric dialkyl viologen salts were employed as model systems. Threading of the guest (or axle) through the calix[6]arene cavity can

occur either through the wider rim, functionalized with phenylureido groups, or the narrower rim, functionalized with ethoxy or octyl chains. To elucidate this mechanism, the use of asymmetric axles offers valuable insights into the selectivity of the threading process.

In a study conducted by our research group in 2003,[87] an asymmetric axle equipped with a pre-installed diphenylacetyl stopper was investigated. This axle was threaded into a triphenyl ureido calix[6]arene (**TPU**), which featured three ethyl ethoxy chains on the lower rim. NMR analysis revealed the exclusive formation of one isomer, referred to as the "Up" isomer (***U***), in which the stopper group was located at the wider rim of the macrocycle (**Figure 43**). Notably, the alternative "Down" isomer (***D***), where threading would occur through the narrower rim, was not observed. This finding indicates that the threading process proceeds selectively through the upper rim of the calix[6]arene, where the phenyl urea units are located.

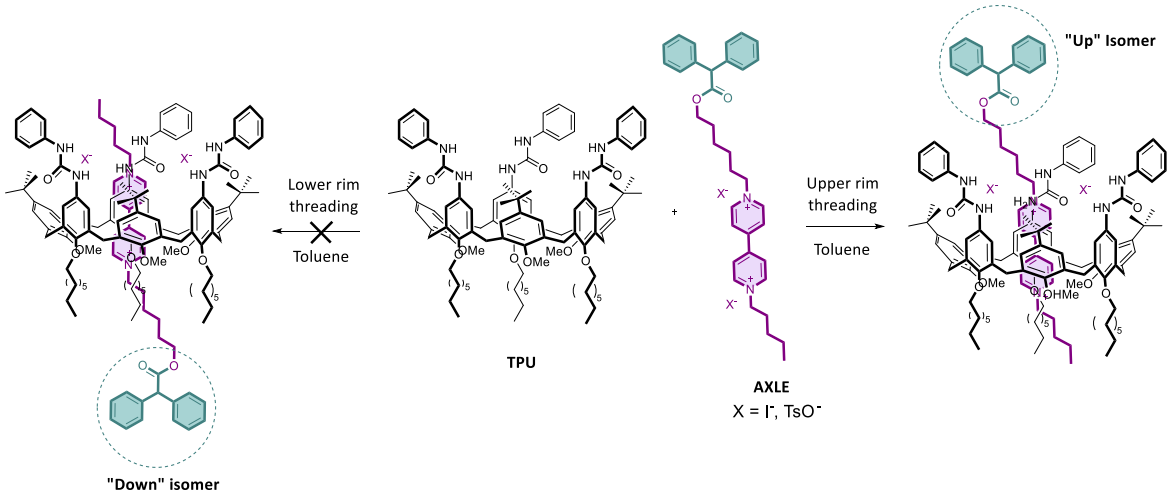

Figure 43. Complexation process between **TPU** and an asymmetric viologen axle leading to the selective formation of the ***U*** orientational isomer.

The selective threading of the axle through the upper rim of the calix[6]arene can be rationalized by considering some key factors. In low-polarity solvents, the methoxy groups within the calix[6]arene cavity are oriented inward, disfavoring guest access from the narrower rim. Additionally, the axle forms a tight ion pair with its associated anion in the solvent used. The separation of this ion pair is facilitated by the formation of hydrogen bonds with the phenylurea groups located on the wider rim of the calix[6]arene. Consequently, this hydrogen bonding interaction promotes selective threading through the upper rim of the macrocycle, where the phenylurea groups are positioned. The presence of a solvent capable of competing for hydrogen bonds formation is expected to reduce the formation of the ***U*** isomer. To investigate this, in 2005,[88] the complexation process was studied using a more polar solvent, such as acetonitrile. The increased polarity of acetonitrile influenced the binding interactions within the calix[6]arene, diminishing the role of the phenylureido groups in disrupting the axle-anion ion pair. As a result, it

was observed that axle **IV** threaded the **TPU** calix[6]arene wheel through both the upper and lower rims, leading to the formation of both the ***D*** and ***U*** isomers (**Figure 44**). This finding demonstrated that, in addition to the cavity size, the disruption of the guest ion pair plays a critical role in determining the threading pathway.

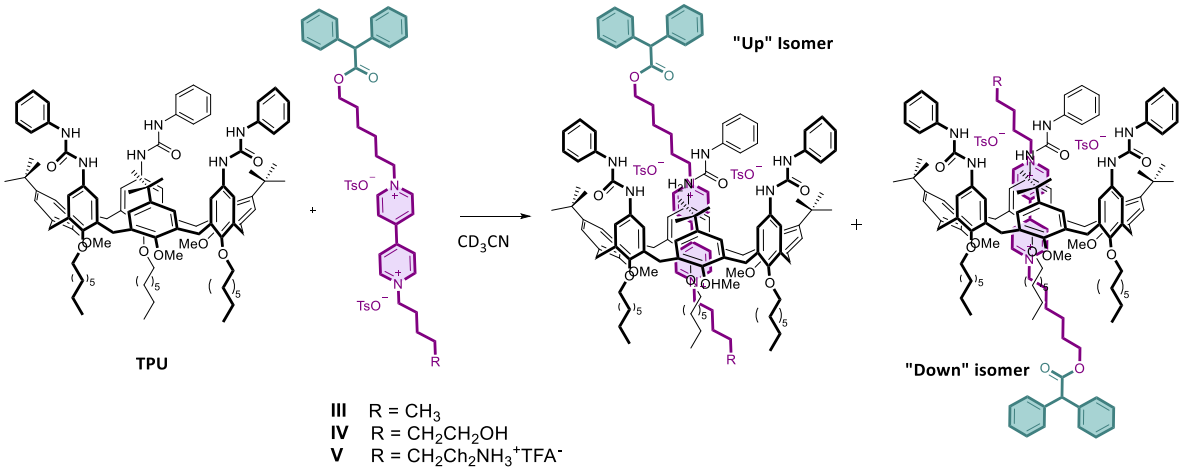

Figure 44. Formation of the two orientational pseudorotaxane isomers ***U*** and ***D*** in acetonitrile.

The thermodynamic and kinetic aspects of the threading process were investigated using a series of mono-stoppered viologen axles in benzene-d_6 as the solvent (**Figure 45**).[89] At room temperature, all axles threaded through the calix[6]arene from the upper rim. Upon heating, the threading process remained under kinetic control for axles **III** and **IV**, leading exclusively to the formation of the ***U*** isomer. In contrast, for axle **V**, which possesses an ammonium terminal group, the ***D*** isomer was preferentially formed under the same conditions.

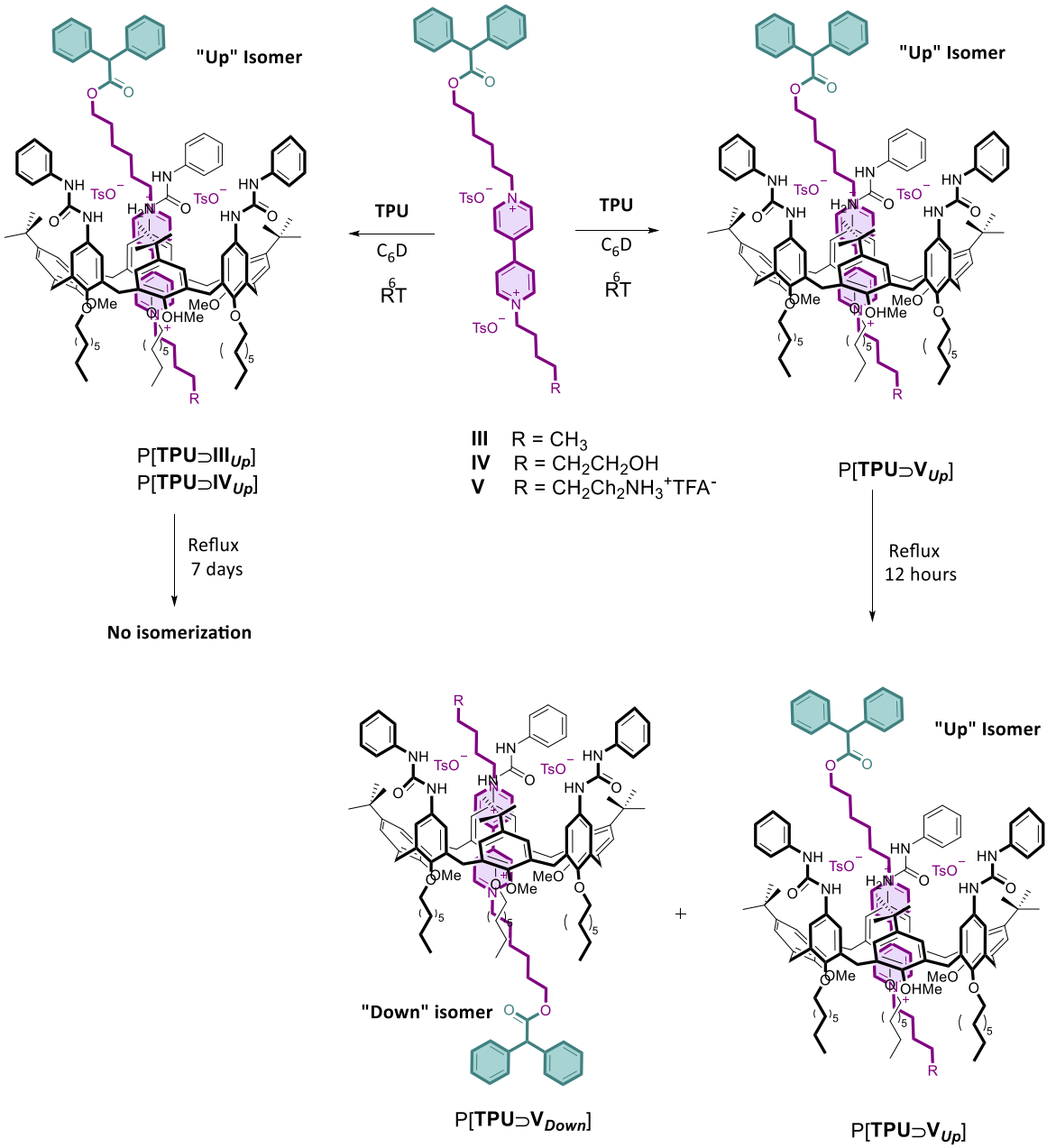

Figure 45. Thermodynamic and kinetic study of the formation of the two orientational isomers ***U*** and ***D*** in benzene-d_6 by varying the temperature.

Varying Guest Molecule Fluorescence with Macrocycles

The modulation of guest dye fluorescence upon complexation with macrocyclic hosts represents a significant area of study in supramolecular chemistry, with various applications, including stimuli-responsive systems, drug delivery, and molecular machines.[90-92] Macrocycles can induce fluorescence changes by offering a hydrophobic cavity that restricts the degrees of freedom of the encapsulated guest molecule.

In 2024, Choudhury *et al.*[93] reported the fluorescence enhancement of a styryl(pyridinium)-chromene hybrid dye (**DSP-C**) upon complexation with two *β*-cyclodextrin (***β*CD**) derivatives (**Figure 46**). The study focused on the impact of the elongated and deeper cavity of hydroxypropyl-*β*-

cyclodextrin (**HP*β*CD**) compared to native ***β*CD** on the dye's fluorescent properties. In **HP*β*CD**, the substitution of peripheral hydroxyl groups with 2-hydroxypropyl groups extends the cavity of the classical ***β*CD**. The results demonstrated that **HP*β*CD** exhibits a stronger binding affinity for the dye than ***β*CD**, leading to significantly enhanced fluorescence intensity and prolonged fluorescence lifetime.

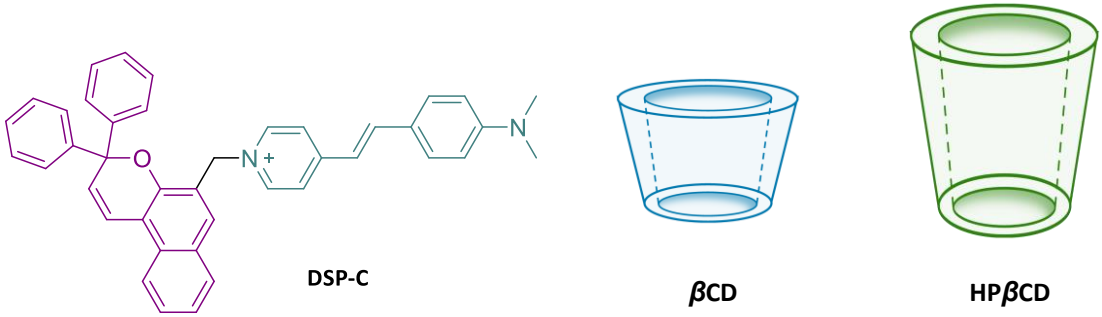

Figure 46. Structure of dye **DSP-C** and representation of native ***β*CD** and elongated **HP*β*CD**.

In 2022, Ge *et al*.[94] reported a study on the complexation of an organic dye within *β*-cyclodextrin. They developed a fluorescent probe, **PM-A**, specifically designed for cell membrane imaging and demonstrated that its inclusion within *β*-cyclodextrin significantly enhanced the fluorescence quantum yield, increasing it from 0% to 45% (**Figure 47**). Furthermore, this interaction with the macrocyclic host drastically lowered the concentration of **PM-A** required for effective cell staining, reducing it from 15 µM to 0.5 µM.

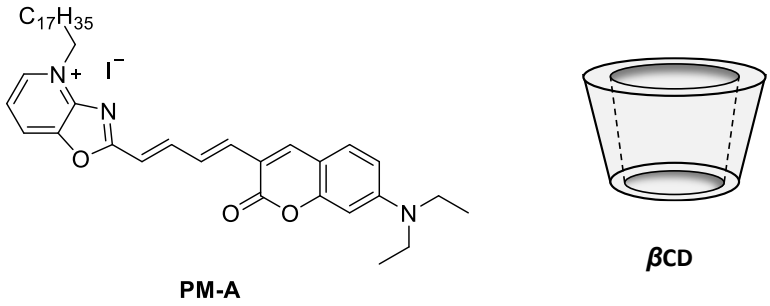

Solvent	$\lambda_{abs,\,max}$	$\lambda_{em,\,max}$	ε [$M^{-1}cm^{-1}$] ×10^4	Φ (%)
H_2O	508	ND	0.58	ND
β-CD (aqueous solution)	518	676	0.58	45

Figure 47. Structure of **PM-A** probe and representation of *β*-cyclodextrin. In the table, the optical properties of **PM-A** in both water and *β*-cyclodextrin aqueous solution are reported.

As seen in the previous example, the fluorescence of organic dyes is typically quenched in aqueous solutions. However, host-guest complexation can mitigate this quenching and enhance the fluorescence. In 2023,[95] the same research group showed that adamantane-modified dyes, upon

interacting with methylated *β*-cyclodextrin (**M-*β*-CD**), exhibited increased fluorescence (see data in **Figure 48**). Additionally, this interaction led to the formation of fluorescent supramolecular nanoparticles in aqueous solution.

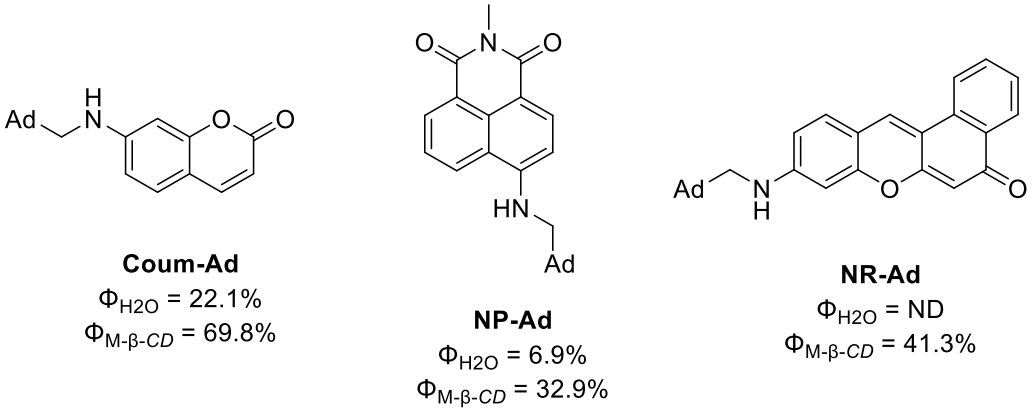

Figure 48. Structure of adamantane-based dyes and their fluorescence quantum yield in water solution with and without **M-*β*-CD**.

In 2023, Liu *et al*.[96] developed multilevel supramolecular assemblies that served as highly efficient platforms for a NIR dye, exhibiting significant signal amplification and multicolor luminescence information storage. The supramolecular system was constructed using a combination of tetraphenylethylene pyridinium dye (**TPE-Py**), cucurbit[8]uril (**CB[8]**), sulfobutylether-*β*-cyclodextrin (**SBE-*β*CD**), and sulfonated aluminum phthalocyanine (**AlPcS4**) through host-guest interactions, electrostatic forces, and π-π stacking (**Figure 49**). **TPE-Py** formed a host-guest complex with **CB[8]**, which then co-assembled with **SBE-*β*CD** into nanosheets, resulting in an approximately 20-fold enhancement in fluorescence. This supramolecular assembly functioned as an energy transfer platform, delivering energy to the **AlPcS4** acceptor dye with an efficiency of 75% and exhibiting an antenna effect of 29.3, leading to significant NIR amplification along with a bathochromic shift of approximately 10 nm.

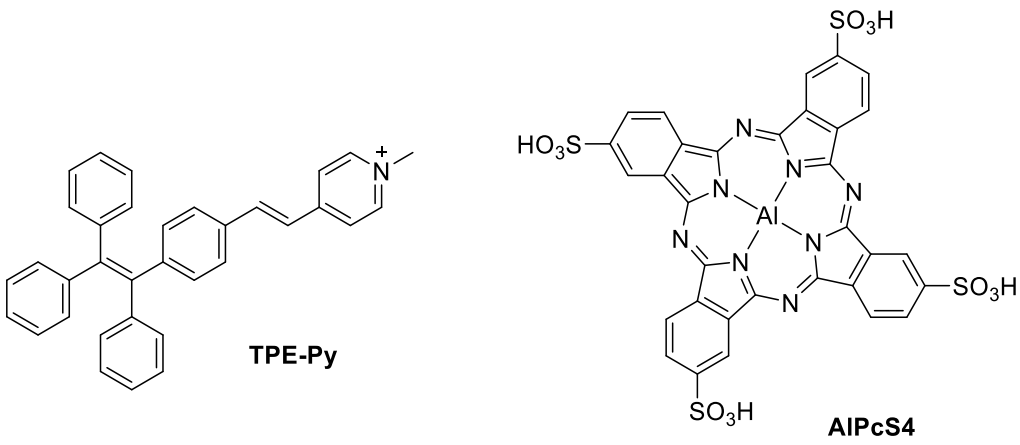

Figure 49. Structure of donor dye **TPE-Py** and acceptor dye **AlPcS4**.

An example of supramolecular complexation applied to microlasers was demonstrated by Huang *et al*. in 2018.[97] They developed solid-state organic microlasers by constructing host-guest complex microcrystals using the organic stilbazolium dye **DAST** and a pillarene-based host matrix, **P5** (**Figure 50**). The resulting host-guest complex microcrystals exhibited enhanced photoluminescence efficiency compared to the individual **DAST** microcrystals, highlighting the improved optical properties achieved through supramolecular assembly, which effectively reduced the aggregation caused-quenching (ACQ) effect.[98]

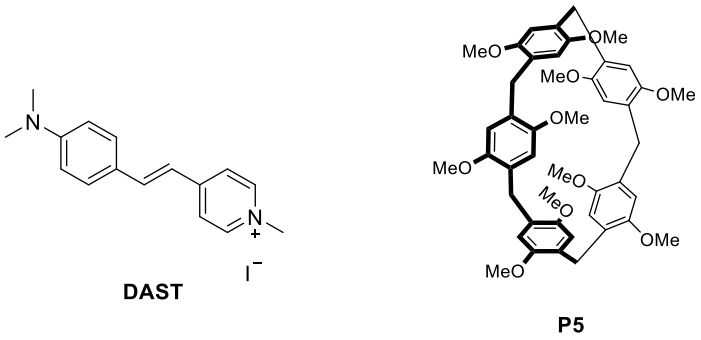

Figure 50. Structure of pillarene host **P5** and stilbazolium dye **DAST**.

A notable example of constructing tunable microlasers through supramolecular complexation was reported by Zhao *et al*. in 2016.[99] Typically, the ICT behavior of push-pull dyes can be modulated by temperature, which influences the population distribution between the locally excited (LE) state and the TICT state. However, the formation of the TICT state is often hindered by restricted excited-state molecular rotation caused by aggregation. In this study, the authors demonstrated that encapsulating an ICT compound within a cyclodextrin macrocycle promotes the transition from the LE to the TICT state, as the confined environment limits the non-radiative decay of the TICT state. Furthermore, the fluorescence of the system could be continuously modulated by adjusting the temperature, enabling the construction of microlasers with tunable emission across a wide wavelength range (**Figure 51**).

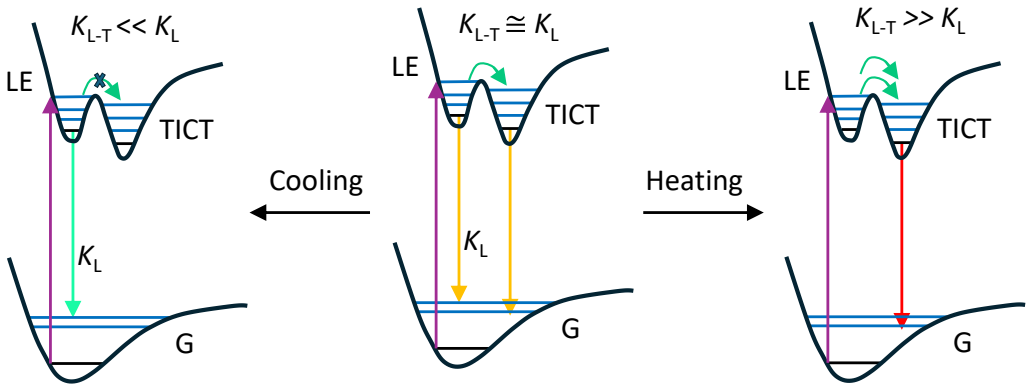

Figure 51. Temperature-controlled ICT process.

Due to the reversible nature of host-guest interactions, these fluorescence changes can be utilized for analyte detection *via* indicator displacement strategies, allowing for dynamic and reversible sensing mechanisms. An illustrative example of using a resorcin[4]arene macrocycle in an indicator displacement assay was reported by Kobuke *et al*. in 2004.[100] The authors developed an acetylcholine receptor that functions under physiological conditions. A tetracyanoresorcin[4]arene derivative was employed to selectively recognize acetylcholine, while a pyrene-modified pyridinium cation served as the fluorescent sensor. The mechanism involved the fluorescence quenching of the pyrene-modified dye upon complexation with the tetracyanoresorcin[4]arene derivative, followed by fluorescence regeneration of the pyrene-modified dye due to the competitive binding of acetylcholine, displacing the indicator. Another example of the indicator displacement technique utilizing cucurbiturils was reported by Nau *et al*. in 2008.[101] The authors demonstrated a method for monitoring and quantifying analyte binding to cucurbit[6]uril (**CB[6]**) using an indicator-displacement strategy (**Figure 52**). In this system, the affinity of the dye can be adjusted by modifying the structure of the anchor, as well as by altering the dye's charge, size, and hydrophobicity since the dye remains positioned outside of the **CB[6]** cavity. These tunable properties enable precise control over the binding interactions within the host-guest complex.

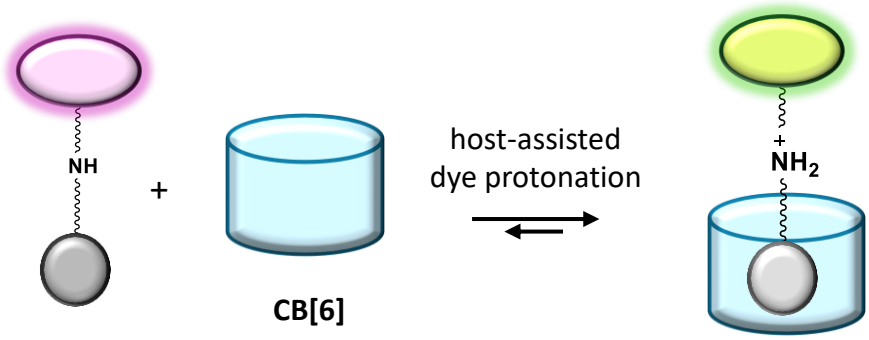

Figure 52. Schematic representation of the indicator displacement process.

A more recent study demonstrated an indicator displacement approach utilizing *p*-sulfonato-calix[4]arene (**SCX4**).[102] In this system, the acridine dye, in both its protonated (**AcH$^+$**) and neutral (**Ac**) forms, binds to **SCX4**, resulting in fluorescence quenching (**Figure 53**). Upon the introduction of the neurotransmitter acetylcholine (**AcCh**), which acts as a competitive binder, a significant fluorescence "turn-on" effect is observed. This system exhibits controlled binding and release of both the protonated (**AcH$^+$**) and neutral (**Ac**) forms of acetylcholine due to the competitive interaction with **AcCh**.

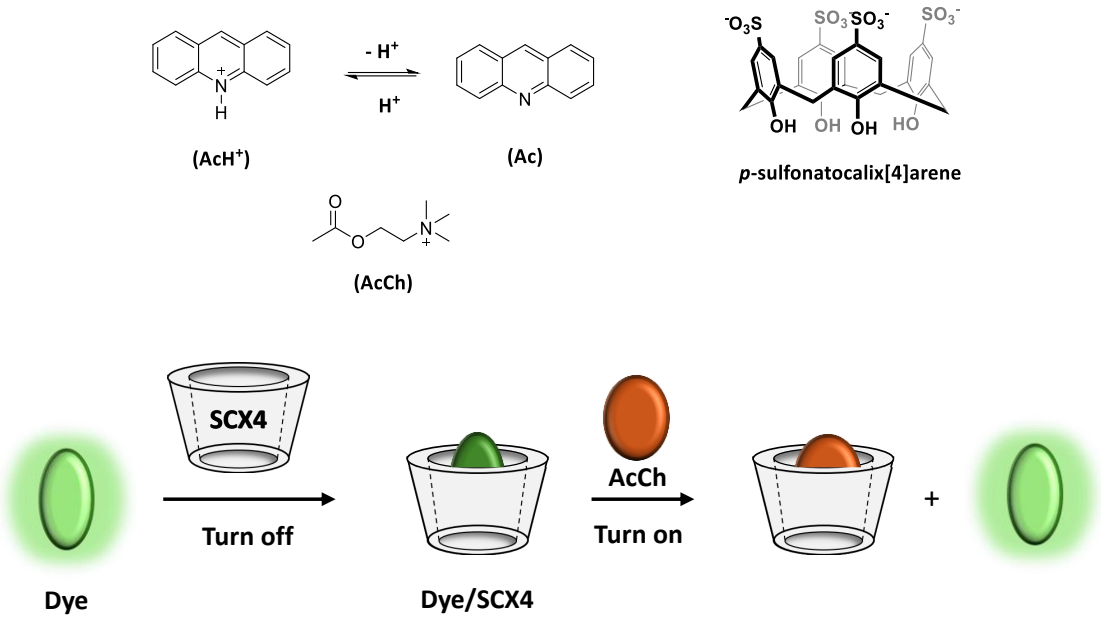

Figure 53. Top: chemical structures of the components used in the indicator displacement process; bottom: schematic representation of the indicator displacement process using acridine dye-**SCX4** as fluorescent sensor for the detection of acetylcholine.

Yu *et al.*[103] reported the synthesis of a guanidinium-functionalized calix[4]arene derivative (**GC5A**) designed for the detection and quantification of trimethylamine-*N*-oxide (**TMAO**), a metabolite associated with increased risk of cardiovascular metabolic diseases. The sensing mechanism relies on fluorescein (**FI**), whose fluorescence is quenched upon complexation with **GC5A** calix[4]arene (**Figure 54**). Upon the introduction of **TMAO**, fluorescein is displaced from the complex, leading to a restoration of fluorescence, thereby enabling the detection of **TMAO** *via* an increased fluorescence signal.

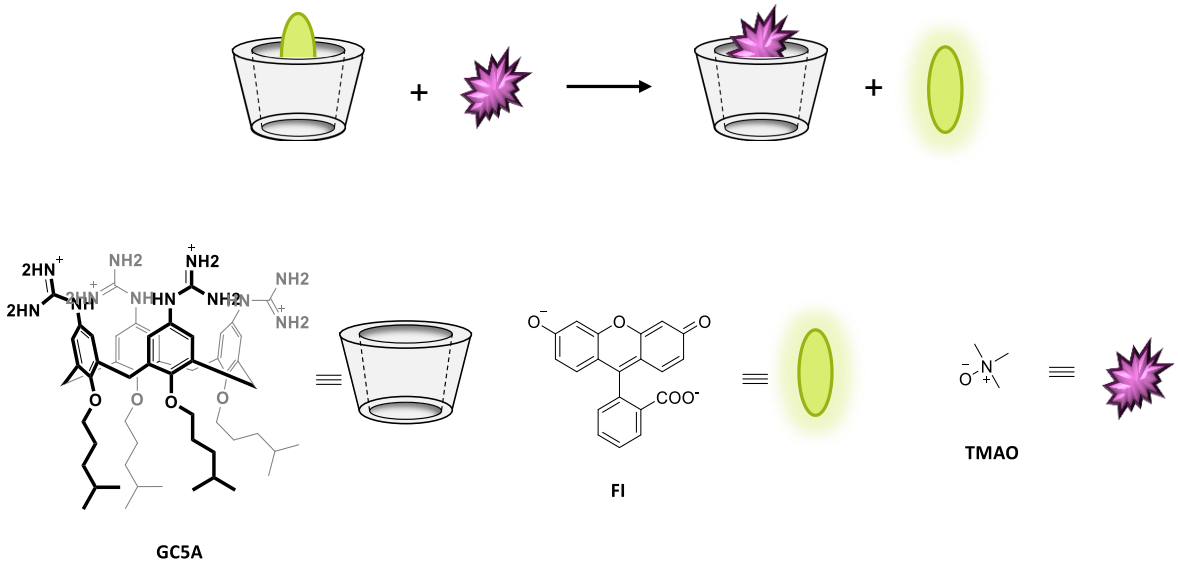

Figure 54. Schematic representation of the mechanism for fluorescence detection of **TMAO**.

Bibliography

(1) Medeiros, N. G.; Braga, C. A.; Câmara, V. S.; Duarte, R. C.; Rodembusch, F. S. Near-Infrared Fluorophores Based on Heptamethine Cyanine Dyes: From Their Synthesis and Photophysical Properties to Recent Optical Sensing and Bioimaging Applications. *Asian J. Org. Chem.* **2022**, *11* (6), e202200095. https://doi.org/10.1002/ajoc.202200095.

(2) Brooker, L. G. S. The Cyanine Dyes and Related Compounds. *J. Am. Chem. Soc.* **1965**, *87* (4), 937–938. https://doi.org/10.1021/ja01082a060.

(3) Chibisov, A. K.; Zakharova, G. V.; Görner, H. Effects of Substituents in the Polymethine Chain on the Photoprocesses in Indodicarbocyanine Dyes. *J. Chem. Soc. Faraday Trans* **1996**, *92* (24), 4917–4925. https://doi.org/10.1039/FT9969204917.

(4) Lee, H.; Berezin, M. Y.; Henary, M.; Strekowski, L.; Achilefu, S. Fluorescence Lifetime Properties of Near-Infrared Cyanine Dyes in Relation to Their Structures. *J. Photochem. Photobiol. Chem.* **2008**, *200* (2–3), 438–444. https://doi.org/10.1016/j.jphotochem.2008.09.008.

(5) Pascal, S.; Haefele, A.; Monnereau, C.; Charaf-Eddin, A.; Jacquemin, D.; Le Guennic, B.; Andraud, C.; Maury, O. Expanding the Polymethine Paradigm: Evidence for the Contribution of a Bis-Dipolar Electronic Structure. *J. Phys. Chem. A* **2014**, *118* (23), 4038–4047. https://doi.org/10.1021/jp501358q

(6) Bardagí, J. I.; Vaillard, V. A.; Rossi, R. A. The $S_{RN}1$ Reaction. In *Encyclopedia of Radicals in Chemistry, Biology and Materials*; Chatgilialoglu, C., Studer, A., Eds.; Wiley, **2012**. https://doi.org/10.1002/9781119953678.rad026

(7) Flanagan, James H.; Owens, C. V.; Romero, S. E.; Waddell, E.; Kahn, S. H.; Hammer, R. P.; Soper, S. A. Near-Infrared Heavy-Atom-Modified Fluorescent Dyes for Base-Calling in DNA-Sequencing Applications Using Temporal Discrimination. *Anal. Chem.* **1998**, *70* (13), 2676–2684. https://doi.org/10.1021/ac980018g.

(8) Redmond, R. W.; Kochevar, I. E.; Krieg, M.; Smith, G.; McGimpsey, W. G. Excited State Relaxation in Cyanine Dyes: A Remarkably Efficient Reverse Intersystem Crossing from Upper Triplet Levels. *J. Phys. Chem. A* **1997**, *101* (15), 2773–2777. https://doi.org/10.1021/jp963001f.

(9) Kasatani, K.; Sato, H. Viscosity-Dependent Decay Dynamics of the S2 State of Cyanine Dyes with 3, 5, and 7 Methine Units by Picosecond Fluorescence Lifetime Measurements. *Bull. Chem. Soc. Jpn.* **1996**, *69* (12), 3455–3460. https://doi.org/10.1246/bcsj.69.3455.

(10) Freyria, F. S.; Cordero, J. M.; Caram, J. R.; Doria, S.; Dodin, A.; Chen, Y.; Willard, A. P.; Bawendi, M. G. Near-Infrared Quantum Dot Emission Enhanced by Stabilized Self-Assembled J-Aggregate Antennas. *Nano Lett.* **2017**, *17* (12), 7665–7674. https://doi.org/10.1021/acs.nanolett.7b03735.

(11) Seki, T.; Ichimura, K.; Ando, E. Stable J-Aggregate Formation of Photoinduced Merocyanine in Bilayer Membrane. *Langmuir* **1988**, *4* (4), 1068–1069. https://doi.org/10.1021/la00082a046.

(12) Liu, C.; Qi, F.; Wen, F.; Long, L.; Liu, A.; Yang, R. Fluorescence Detection of Glutathione and Oxidized Glutathione in Blood with a NIR-Excitable Cyanine Probe. *Methods Appl. Fluoresc.* **2018**, *6* (2), 024001. https://doi.org/10.1088/2050-6120/aa86b7.

(13) Lim, S.-Y.; Hong, K.-H.; Kim, D. I.; Kwon, H.; Kim, H.-J. Tunable Heptamethine–Azo Dye Conjugate as an NIR Fluorescent Probe for the Selective Detection of Mitochondrial Glutathione over Cysteine and Homocysteine. *J. Am. Chem. Soc.* **2014**, *136* (19), 7018–7025. https://doi.org/10.1021/ja500962u.

(14) Liu, C.; Qi, F.; Wen, F.; Long, L.; Liu, A.; Yang, R. Fluorescence Detection of Glutathione and Oxidized Glutathione in Blood with a NIR-Excitable Cyanine Probe. *Methods Appl. Fluoresc.* **2018**, *6* (2), 024001. https://doi.org/10.1088/2050-6120/aa86b7.

(15) Patel, N. J.; Manivannan, E.; Joshi, P.; Ohulchanskyy, T. J.; Nani, R. R.; Schnermann, M. J.; Pandey, R. K. Impact of Substituents in Tumor Uptake and Fluorescence Imaging Ability of Near-Infrared Cyanine-like Dyes. *Photochem. Photobiol.* **2015**, *91* (5), 1219–1230. https://doi.org/10.1111/php.12482.

(16) Wu, J. B.; Shi, C.; Chu, G. C.-Y.; Xu, Q.; Zhang, Y.; Li, Q.; Yu, J. S.; Zhau, H. E.; Chung, L. W. K. Near-Infrared Fluorescence Heptamethine Carbocyanine Dyes Mediate Imaging and Targeted Drug Delivery for Human Brain Tumor. *Biomaterials* **2015**, *67*, 1–10. https://doi.org/10.1016/j.biomaterials.2015.07.028.

(17) Choi, P. J.; Cooper, E.; Schweder, P.; Mee, E.; Faull, R.; Denny, W. A.; Dragunow, M.; Park, T. I.-H.; Jose, J. The Synthesis of a Novel Crizotinib Heptamethine Cyanine Dye Conjugate That Potentiates the Cytostatic and Cytotoxic Effects of Crizotinib in Patient-Derived Glioblastoma Cell Lines. *Bioorg. Med. Chem. Lett.* **2019**, *29* (18), 2617–2621. https://doi.org/10.1016/j.bmcl.2019.07.051.

(18) Lv, Q.; Yang, X.; Wang, M.; Yang, J.; Qin, Z.; Kan, Q.; Zhang, H.; Wang, Y.; Wang, D.; He, Z. Mitochondria-Targeted Prostate Cancer Therapy Using a near-Infrared Fluorescence Dye–Monoamine Oxidase A Inhibitor Conjugate. *J. Controlled Release* **2018**, *279*, 234–242. https://doi.org/10.1016/j.jconrel.2018.04.038.

(19) Li, D.-H.; Schreiber, C. L.; Smith, B. D. Sterically Shielded Heptamethine Cyanine Dyes for Bioconjugation and High Performance Near-Infrared Fluorescence Imaging. *Angew. Chem.* **2020**, *132* (29), 12252–12259. https://doi.org/10.1002/ange.202004449.

(20) Gao, D.; Luo, Z.; He, Y.; Yang, L.; Hu, D.; Liang, Y.; Zheng, H.; Liu, X.; Sheng, Z. Low-Dose NIR-II Preclinical Bioimaging Using Liposome-Encapsulated Cyanine Dyes. *Small* **2023**, *19* (17), 2206544. https://doi.org/10.1002/smll.202206544.

(21) Liu, T.; Chen, Y.; Wang, H.; Cui, M.; Zhang, J.; Zhang, W.; Wang, P. Phototheranostic Agents Based on Nonionic Heptamethine Cyanine for Realizing Synergistic Cancer Phototherapy. *Adv. Healthc. Mater.* **2023**, *12* (11), 2202817. https://doi.org/10.1002/adhm.202202817.

(22) Xu, Y.; Yu, J.; Hu, J.; Sun, K.; Lu, W.; Zeng, F.; Chen, J.; Liu, M.; Cai, Z.; He, X.; Wei, W.; Sun, B. Tumor-Targeting Near-Infrared Dimeric Heptamethine Cyanine Photosensitizers with an Aromatic Diphenol Linker for Imaging-Guided Cancer Phototherapy. *Adv. Healthc. Mater.* **2023**, *12* (15), 2203080. https://doi.org/10.1002/adhm.202203080.

(23) Kejík, Z.; Hajduch, J.; Abramenko, N.; Vellieux, F.; Veselá, K.; Fialová, J. L.; Petrláková, K.; Kučnirová, K.; Kaplánek, R.; Tatar, A.; Skaličková, M.; Masařík, M.; Babula, P.; Dytrych, P.; Hoskovec, D.; Martásek, P.; Jakubek, M. Cyanine Dyes in the Mitochondria-Targeting Photodynamic and Photothermal Therapy. *Commun. Chem.* **2024**, *7* (1), 180. https://doi.org/10.1038/s42004-024-01256-6.

(24) Thomas, A. P.; Palanikumar, L.; Jeena, M. T.; Kim, K.; Ryu, J.-H. Cancer-Mitochondria-Targeted Photodynamic Therapy with Supramolecular Assembly of HA and a Water Soluble NIR Cyanine Dye. *Chem. Sci.* **2017**, *8* (12), 8351–8356. https://doi.org/10.1039/C7SC03169F.

(23) Xu, F.; Li, H.; Yao, Q.; Ge, H.; Fan, J.; Sun, W.; Wang, J.; Peng, X. Hypoxia-Activated NIR Photosensitizer Anchoring in the Mitochondria for Photodynamic Therapy. *Chem. Sci.* **2019**, *10* (45), 10586–10594. https://doi.org/10.1039/C9SC03355F.

(25) Zou, Y.; Liu, W.; Sun, W.; Du, J.; Fan, J.; Peng, X. Highly Inoxidizable Heptamethine Cyanine–Glucose Oxidase Conjugate Nanoagent for Combination of Enhanced Photothermal Therapy and Tumor Starvation. *Adv. Funct. Mater.* **2022**, *32* (17), 2111853. https://doi.org/10.1002/adfm.202111853.

(26) Tian, Y.; Chen, Z.; Liu, S.; Wu, F.; Cao, W.; Pang, D.; Xiong, H. "Dual-Key-and-Lock" NIR-II NSCyanines Enable High-Contrast Activatable Phototheranostics in Extrahepatic Diseases. *Angew. Chem. Int. Ed.* **2023**, *62* (38), e202309768. https://doi.org/10.1002/anie.202309768.

(27) Bureš, F. Fundamental Aspects of Property Tuning in Push–Pull Molecules. *RSC Adv.* **2014**, *4* (102), 58826–58851. https://doi.org/10.1039/C4RA11264D

(28) Mandal, H.; Rao, J. L.; Kulhánek, J.; Bureš, F.; Bangal, P. R. Understanding of Intramolecular Charge Transfer Dynamics of a Push–Pull Dimethylamino-Phenylethynylphenyl-Dicyanoimidazole by Steady-State and Ultrafast Spectroscopic Studies. *J. Phys. Chem. C* **2023**, *127* (9), 4724–4740. https://doi.org/10.1021/acs.jpcc.2c08320.

(29) Karmakar, S.; Ambastha, A.; Jha, A.; Dharmadhikari, A.; Dharmadhikari, J.; Venkatramani, R.; Dasgupta, J. Transient Raman Snapshots of the Twisted Intramolecular Charge Transfer State in a

Stilbazolium Dye. *J. Phys. Chem. Lett.* **2020**, *11* (12), 4842–4848. https://doi.org/10.1021/acs.jpclett.0c01124.

(30) Kulhánek, J.; Bureš, F.; Pytela, O.; Mikysek, T.; Ludvík, J.; Růžička, A. Push-Pull Molecules with a Systematically Extended π-Conjugated System Featuring 4,5-Dicyanoimidazole. *Dyes Pigments* **2010**, *85* (1–2), 57–65. https://doi.org/10.1016/j.dyepig.2009.10.004.

(31) Kulhánek, J.; Bureš, F.; Kuznik, W.; Kityk, I. V.; Mikysek, T.; Růžička, A. Ferrocene-Donor and 4,5-Dicyanoimidazole-Acceptor Moieties in Charge-Transfer Chromophores with π Linkers Tailored for Second-Order Nonlinear Optics. *Chem. – Asian J.* **2013**, *8* (2), 465–475. https://doi.org/10.1002/asia.201200963.

(32) Cheng, L. T.; Tam, W.; Marder, S. R.; Stiegman, A. E.; Rikken, G.; Spangler, C. W. Experimental Investigations of Organic Molecular Non-linear Optical Polarizabilities. 2. A Study of Conjugation Dependences. *J. Phys. Chem.* **1991**, *95* (26), 10643–10652. https://doi.org/10.1021/j100179a027.

(33) Stiegman, A. E.; Graham, E.; Perry, K. J.; Khundkar, L. R.; Cheng, L. T.; Perry, J. W. The Electronic Structure and Second-Order Non-linear Optical Properties of Donor-Acceptor Acetylenes: A Detailed Investigation of Structure-Property Relationships. *J. Am. Chem. Soc.* **1991**, *113* (20), 7658–7666. https://doi.org/10.1021/ja00020a030.

(34) Genin, E.; Hugues, V.; Clermont, G.; Herbivo, C.; Castro, M. C. R.; Comel, A.; Raposo, M. M. M.; Blanchard-Desce, M. Fluorescence and Two-Photon Absorption of Push—Pull Aryl(Bi)Thiophenes: Structure—Property Relationships. *Photochem. Photobiol. Sci.* **2012**, *11* (11), 1756–1766. https://doi.org/10.1039/c2pp25258a.

(35) Kulhánek, J.; Bureš, F.; Opršal, J.; Kuznik, W.; Mikysek, T.; Růžička, A. 1,4-Phenylene and 2,5-Thienylene π-Linkers in Charge-Transfer Chromophores. *Asian J. Org. Chem.* **2013**, *2* (5), 422–431. https://doi.org/10.1002/ajoc.201300063.

(36) Li, R.; Lv, X.; Shi, D.; Zhou, D.; Cheng, Y.; Zhang, G.; Wang, P. Dye-Sensitized Solar Cells Based on Organic Sensitizers with Different Conjugated Linkers: Furan, Bifuran, Thiophene, Bithiophene, Selenophene, and Biselenophene. *J. Phys. Chem. C* **2009**, *113* (17), 7469–7479. https://doi.org/10.1021/jp900972v.

(37) Avhad, K.; Jadhav, A.; Sekar, N. Fluorescent Vinyl and Styryl Coumarins: A Comprehensive DFT Study of Structural, Electronic and NLO Properties. *J. Chem. Sci.* **2017**, *129* (12), 1829–1841. https://doi.org/10.1007/s12039-017-1392-1

(38) Rajeshirke, M.; Sekar, N. NLO Properties of Ester Containing Fluorescent Carbazole Based Styryl Dyes – Consolidated Spectroscopic and DFT Approach. *Opt. Mater.* **2018**, *76*, 191–209. https://doi.org/10.1016/j.optmat.2017.12.035

(39) Sharma, S. J.; Sekar, N. Impact of π-Spacer on Dye-Sensitized Solar Cells and Non-Linear Optical Performance: Styryl vs Imine vs Azo. *J. Photochem. Photobiol. Chem.* **2024**, *452*, 115543. https://doi.org/10.1016/j.jphotochem.2024.115543

(40) Supabowornsathit, K.; Faikhruea, K.; Ditmangklo, B.; Jaroenchuensiri, T.; Wongsuwan, S.; Junpra-ob, S.; Choopara, I.; Palaga, T.; Aonbangkhen, C.; Somboonna, N.; Taechalertpaisarn, J.; Vilaivan, T. Dicationic Styryl Dyes for Colorimetric and Fluorescent Detection of Nucleic Acids. *Sci. Rep.* **2022**, *12* (1), 14250. https://doi.org/10.1038/s41598-022-18460-w.

(41) Gebhard, J.; Hirsch, L.; Schwechheimer, C.; Wagenknecht, H.-A. Hybridization-Sensitive Fluorescent Probes for DNA and RNA by a Modular “Click” Approach. *Bioconjug. Chem.* **2022**, *33* (9), 1634–1642. https://doi.org/10.1021/acs.bioconjchem.2c00241.

(42) Wangngae, S.; Ngivprom, U.; Khrootkaew, T.; Worakaensai, S.; Lai, R.-Y.; Kamkaew, A. Cationic Styryl Dyes for DNA Labelling and Selectivity toward Cancer Cells and Gram-Negative Bacteria. *RSC Adv.* **2023**, *13* (3), 2115–2122. https://doi.org/10.1039/D2RA07601B.

(43) Wickramasinghe, N. I.; Corbin, B.; Kanakarathna, D. Y.; Pang, Y.; Abeywickrama, C. S.; Wijesinghe, K. J. Bright NIR-Emitting Styryl Pyridinium Dyes with Large Stokes’ Shift for Sensing Applications. *Biosensors* **2023**, *13* (8), 799. https://doi.org/10.3390/bios13080799.

(44) Sangsuwan, W.; Faikhruea, K.; Supabowornsathit, K.; Sangsopon, D.; Ingrungruanglert, P.; Chuntakaruk, H.; Nuntavanotayan, N.; Nakprasit, K.; Israsena, N.; Rungrotmongkol, T.; Chuawong, P.; Vilaivan, T.; Aonbangkhen, C. Design, Synthesis, and Characterization of Novel Styryl Dyes as Fluorescent Probes for Tau Aggregate Detection *in Vitro* and in Cells. *Chem. – Asian J.* **2024**, *19* (6), e202301081. https://doi.org/10.1002/asia.202301081.

(45) Ie, Y.; Sasada, S.; Karakawa, M.; Aso, Y. Pyradinodithiazole: An Electron-Accepting Monomer Unit for Hole-Transporting and Electron-Transporting Conjugated Copolymers. *Org. Lett.* **2015**, *17* (18), 4580–4583. https://doi.org/10.1021/acs.orglett.5b02306.

(46) Wang, L.; Zhang, X.; Zhang, J.; Tian, H.; Lu, Y.; Geng, Y.; Wang, F. Synthesis and Characterization of Oligo(2,5-Bis(3-Dodecylthiophen-2-Yl)Thieno[3,2-b]Thiophene)s: Effect of the Chain Length and End-Groups on Their Optical and Charge Transport Properties. *J. Mater. Chem. C* **2014**, *2* (46), 9978–9986. https://doi.org/10.1039/C4TC01899K.

(47) Peng, Q.; Peng, J.-B.; Kang, E. T.; Neoh, K. G.; Cao, Y. Synthesis and Electroluminescent Properties of Copolymers Based on Fluorene and 2,5-Di(2-Hexyloxyphenyl)Thiazolothiazole. *Macromolecules* **2005**, *38* (17), 7292–7298. https://doi.org/10.1021/ma050378n.

(48) Jouaiti, A.; Huang, D.-C.; Giuso, V.; Cebrián, C.; Mercandelli, P.; Wang, K.-H.; Chang, C.-H.; Mauro, M. True- to Sky-Blue Emitters Bearing the Thiazolo[5,4- *d*]Thiazole Electron Acceptor for Single and Tandem Organic Light-Emitting Diodes. *ACS Appl. Electron. Mater.* **2023**, *5* (5), 2781–2792. https://doi.org/10.1021/acsaelm.3c00234.

(49) Ando, S.; Nishida, J.; Inoue, Y.; Tokito, S.; Yamashita, Y. Synthesis, Physical Properties, and Field-Effect Transistors of Novel Thiophene/Thiazolothiazole Co-Oligomers. *J. Mater. Chem.* **2004**, *14* (12), 1787. https://doi.org/10.1039/b403699a.

(50) Osaka, I.; Sauvé, G.; Zhang, R.; Kowalewski, T.; McCullough, R. D. Novel Thiophene-Thiazolothiazole Copolymers for Organic Field-Effect Transistors. *Adv. Mater.* **2007**, *19* (23), 4160–4165. https://doi.org/10.1002/adma.200701058.

(51) Dabuliene, A.; Shi, Z.-E.; Leitonas, K.; Lung, C.-Y.; Volyniuk, D.; Kaur, K.; Matulis, V.; Lyakhov, D.; Michels, D.; Chen, C.-P.; Grazulevicius, J. V. Enhancement of Efficiency of Perovskite Solar Cells with Hole-Selective Layers of Rationally Designed Thiazolo[5,4- *d*]Thiazole Derivatives. *ACS Appl. Mater. Interfaces* **2024**, *16* (23), 30239–30254. https://doi.org/10.1021/acsami.4c04105.

(52) Ji, M.; Dong, C.; Guo, Q.; Du, M.; Guo, Q.; Sun, X.; Wang, E.; Zhou, E. Recent Advances in Organic Photovoltaic Materials Based on Thiazole-Containing Heterocycles. *Macromol. Rapid Commun.* **2023**, *44* (13), 2300102. https://doi.org/10.1002/marc.202300102.

(53) Olgun, U.; Gülfen, M.; Burcu Güneser, H.; Seçkin Arslan, B.; Öztürk, N.; Nebioğlu, M.; Şişman, İ.; Gülsah Akca, F.; Uzay Karakaya, E.; Gul Yaglioglu, H. Poly(Triphenylamine-Thiazolo[5,4-d]Thiazole) Copolymer Dyes with Different Anchoring End Groups: Synthesis, Dye-Sensitized Solar Cell (DSSC) Performance and Femtosecond Excited State Absorption Spectroscopy. *J. Photochem. Photobiol. Chem.* **2024**, *454*, 115698. https://doi.org/10.1016/j.jphotochem.2024.115698.

(54) Dessì, A.; Calamante, M.; Sinicropi, A.; Parisi, M. L.; Vesce, L.; Mariani, P.; Taheri, B.; Ciocca, M.; Di Carlo, A.; Zani, L.; Mordini, A.; Reginato, G. Thiazolo[5,4- *d*]Thiazole-Based Organic Sensitizers with Improved Spectral Properties for Application in Greenhouse-Integrated Dye-Sensitized Solar Cells. *Sustain. Energy Fuels* **2020**, *4* (5), 2309–2321. https://doi.org/10.1039/D0SE00124D.

(55) Ephraim, J. Ueber die Einwirkung von Aldehyden auf Thioamide I. *Berichte Dtsch. Chem. Ges.* **1891**, *24* (1), 1026–1031. https://doi.org/10.1002/cber.189102401188.

(56) Johnson, J. R.; Ketcham, R. Thiazolothiazoles. I. The Reaction of Aromatic Aldehydes with Dithioöxamide [1]. *J. Am. Chem. Soc.* **1960**, *82* (11), 2719–2724. https://doi.org/10.1021/ja01496a017.

(57) Deb, S. K.; Chopoorian, J. A. Optical Properties and Color-Center Formation in Thin Films of Molybdenum Trioxide. *J. Appl. Phys.* **1966**, *37* (13), 4818–4825. https://doi.org/10.1063/1.1708145.

(58) Goulle, V.; Harriman, A.; Lehn, J.-M. An Electro-Photoswitch: Redox Switching of the Luminescence of a Bipyridine Metal Complex. *J. Chem. Soc. Chem. Commun.* **1993**, No. 12, 1034. https://doi.org/10.1039/c39930001034.

(59) Halder, S.; Pal, S.; Sivasakthi, P.; Samanta, P. K.; Chakraborty, C. Thiazolothiazole-Containing Conjugated Polymer with Electrochromism and Electrofluorochromism-Based Dual Performance for a Flip-Flop Molecular Logic Gate. *Macromolecules* **2023**, *56* (6), 2319–2327. https://doi.org/10.1021/acs.macromol.2c01767.

(60) Li, P.; Guo, M.-Y.; Yin, X.-M.; Gao, L.; Yang, S.-L.; Bu, R.; Gong, T.; Gao, E.-Q. Interpenetration-Enabled Photochromism and Fluorescence Photomodulation in a Metal–Organic Framework with the Thiazolothiazole Extended Viologen Fluorophore. *Inorg. Chem.* **2019**, *58* (20), 14167–14174. https://doi.org/10.1021/acs.inorgchem.9b02220.

(61) Adams, T. J.; Brotherton, A. R.; Molai, J. A.; Parmar, N.; Palmer, J. R.; Sandor, K. A.; Walter, M. G. Obtaining Reversible, High Contrast Electrochromism, Electrofluorochromism, and Photochromism in an Aqueous Hydrogel Device Using Chromogenic Thiazolothiazoles. *Adv. Funct. Mater.* **2021**, *31* (36), 2103408. https://doi.org/10.1002/adfm.202103408

(62) For a survey of applications of organic materials and semiconductors, see e.g. Forrest, S. R. *Organic Electronics: Foundations to Applications*, OUP, Oxford (UK), **2020**. ISBN: 978-0-19-852972-9.

(63) Jung, I. H.; Yu, J.; Jeong, E.; Kim, J.; Kwon, S.; Kong, H.; Lee, K.; Woo, H. Y.; Shim, H. Synthesis and Photovoltaic Properties of Cyclopentadithiophene-Based Low-Bandgap Copolymers That Contain Electron-Withdrawing Thiazole Derivatives. *Chem. – Eur. J.* **2010**, *16* (12), 3743–3752. https://doi.org/10.1002/chem.200903064.

(64) Osaka, I.; Saito, M.; Koganezawa, T.; Takimiya, K. Thiophene–Thiazolothiazole Copolymers: Significant Impact of Side Chain Composition on Backbone Orientation and Solar Cell Performances. *Adv. Mater.* **2014**, *26* (2), 331–338. https://doi.org/10.1002/adma.201303059.

(65) Osaka, I.; Saito, M.; Mori, H.; Koganezawa, T.; Takimiya, K. Drastic Change of Molecular Orientation in a Thiazolothiazole Copolymer by Molecular-Weight Control and Blending with $PC_{61}BM$ Leads to High Efficiencies in Solar Cells. *Adv. Mater.* **2012**, *24* (3), 425–430. https://doi.org/10.1002/adma.201103065.

(66) Saito, M.; Osaka, I.; Koganezawa, T.; Takimiya, K. Effect of Oxygen-Containing Functional Side Chains on the Electronic Properties and Photovoltaic Performances in a Thiophene–Thiazolothiazole Copolymer System. *Heteroat. Chem.* **2014**, *25* (6), 556–564. https://doi.org/10.1002/hc.21196.

(67) Subramaniyan, S.; Xin, H.; Kim, F. S.; Murari, N. M.; Courtright, B. A. E.; Jenekhe, S. A. Thiazolothiazole Donor–Acceptor Conjugated Polymer Semiconductors for Photovoltaic Applications. *Macromolecules* **2014**, *47* (13), 4199–4209. https://doi.org/10.1021/ma500250j.

(68) Shi, Q.; Cheng, P.; Li, Y.; Zhan, X. A Solution Processable D-A-D Molecule Based on Thiazolothiazole for High Performance Organic Solar Cells. *Adv. Energy Mater.* **2012**, *2* (1), 63–67. https://doi.org/10.1002/aenm.201100505.

(69) Cheng, P.; Shi, Q.; Lin, Y.; Li, Y.; Zhan, X. Evolved Structure of Thiazolothiazole Based Small Molecules towards Enhanced Efficiency in Organic Solar Cells. *Org. Electron.* **2013**, *14* (2), 599–606. https://doi.org/10.1016/j.orgel.2012.11.026.

(70) Yu, C.; Liu, Z.; Yang, Y.; Yao, J.; Cai, Z.; Luo, H.; Zhang, G.; Zhang, D. New Dithienyl-Diketopyrrolopyrrole-Based Conjugated Molecules Entailing Electron Withdrawing Moieties for Organic Ambipolar Semiconductors and Photovoltaic Materials. *J. Mater. Chem. C* **2014**, *2* (47), 10101–10109. https://doi.org/10.1039/C4TC01872A.

(71) Zhang, W.; Feng, Q.; Wang, Z.; Zhou, G. Novel Thiazolo[5,4- *d*]thiazole-Based Organic Dyes for Quasi-Solid-State Dye-Sensitized Solar Cells. *Chem. – Asian J.* **2013**, *8* (5), 939–946. https://doi.org/10.1002/asia.201201202.

(72) Dessì, A.; Barozzino Consiglio, G.; Calamante, M.; Reginato, G.; Mordini, A.; Peruzzini, M.; Taddei, M.; Sinicropi, A.; Parisi, M. L.; Fabrizi De Biani, F.; Basosi, R.; Mori, R.; Spatola, M.; Bruzzi, M.; Zani, L.

Organic Chromophores Based on a Fused Bis-Thiazole Core and Their Application in Dye-Sensitized Solar Cells. *Eur. J. Org. Chem.* **2013**, *2013* (10), 1916–1928. https://doi.org/10.1002/ejoc.201201629.

(73) Kubik, S. *Supramolecular Chemistry: From Concepts to Applications*. Walter De Gruyter GmbH, Berlin (Germany), 2020, ISBN: 978-3-11-059560-4; Beer, P. D., Barendt, T. A., Lim, J. Y. C. *Supramolecular Chemistry: Fundamentals and Applications*. Oxford University Press, Oxford (UK), **2022**; ISBN: 978-0-19-883284-3.

(74) Wagner, B. D. *Host–Guest Chemistry: Supramolecular Inclusion in Solution.* Walter De Gruyter GmbH, Berlin (Germany), **2020**, ISBN: 978-3-11-056439-6.

(75) Bruns, C. J., Stoddart, J. F. *The Nature of the Mechanical Bond: From Molecules to Machines*, John Wiley & Sons, Hoboken (USA), **2016**, ISBN: 978-1-11-904400-0

(76) Cai, K.; Shi, Y.; Zhuang, G.-W.; Zhang, L.; Qiu, Y.; Shen, D.; Chen, H.; Jiao, Y.; Wu, H.; Cheng, C.; Stoddart, J. F. Molecular-Pump-Enabled Synthesis of a Daisy Chain Polymer. *J. Am. Chem. Soc.* **2020**, *142* (23), 10308–10313. https://doi.org/10.1021/jacs.0c04029.

(77) Belowich, M. E.; Valente, C.; Smaldone, R. A.; Friedman, D. C.; Thiel, J.; Cronin, L.; Stoddart, J. F. Positive Cooperativity in the Template-Directed Synthesis of Monodisperse Macromolecules. *J. Am. Chem. Soc.* **2012**, *134* (11), 5243–5261. https://doi.org/10.1021/ja2107564.

(78) Harada, A.; Hashidzume, A.; Yamaguchi, H.; Takashima, Y. Polymeric Rotaxanes. *Chem. Rev.* **2009**, *109* (11), 5974–6023. https://doi.org/10.1021/cr9000622.

(79) See e.g. Credi, A., Balzani, V. *Molecular Machines*, 1088press, Bologna (Italy), **2020**; ISBN: 978-8-86-923559-7.

(80) Forgan, R. S.; Sauvage, J.-P.; Stoddart, J. F. Chemical Topology: Complex Molecular Knots, Links, and Entanglements. *Chemical Reviews* **2011**, *111* (9), 5434–5464. https://doi.org/10.1021/cr200034u.

(81) Gutsche, C. D. Calixarenes: An Introduction; *Royal Society of Chemistry*, **2008**. https://doi.org/10.1039/9781847558190.

(82) Arduini, A.; Orlandini, G.; Secchi, A.; Credi, A.; Silvi, S.; Venturi, M. Calixarene Threading by Viologen-Based Axles. In Calixarenes and Beyond; Neri, P., Sessler, J. L., Wang, M.-X., Eds.; *Springer International Publishing: Cham*, **2016**; pp 761–781. https://doi.org/10.1007/978-3-319-31867-7.

(83) Cera, G.; Arduini, A.; Secchi, A.; Credi, A.; Silvi, S. Heteroditopic Calix[6]Arene Based Intervowen and Interlocked Molecular Devices. *The Chemical Record*, **2021**, *21*, 1161–1181. https://doi.org/10.1002/tcr.202100012.

(84) Arduini, A.; Ferdani, R.; Pochini, A.; Secchi, A.; Ugozzoli, F. Calix[6]Arene as a Wheel for Rotaxane Synthesis. *Angew. Chem.* **2000**, *39* (19), 3453–3456. https://doi.org/10.1002/1521-3773(20001002)39:19<3453::AID-ANIE3453>3.0.CO;2-I.

(85) Ugozzoli, F.; Massera, C.; Arduini, A.; Pochini, A.; Secchi, A. Calix[6]Arene-Based Pseudorotaxanes: A Solid State Structural Investigation. *CrystEngComm*, **2004**, 6 (39), 227–232. https://doi.org/10.1039/b406591c.

(86) Credi, A.; Dumas, S.; Silvi, S.; Venturi, M.; Arduini, A.; Pochini, A.; Secchi, A. Viologen-Calix[6]Arene Pseudorotaxanes. Ion-Pair Recognition and Threading/Dethreading Molecular Motions. *J. Org. Chem.* **2004**, *69* (18), 5881–5887. https://doi.org/10.1021/jo0494127.

(87) Arduini, A.; Calzavacca, F.; Pochini, A.; Secchi, A. Unidirectional Threading of Triphenylureidocalix[6]arene-Based Wheels: Oriented Pseudorotaxane Synthesis. *Chem. – Eur. J.* **2003**, *9* (3), 793–799. https://doi.org/10.1002/chem.200390089.

(88) Arduini, A.; Ciesa, F.; Fragassi, M.; Pochini, A.; Secchi, A. Selective Synthesis of Two Constitutionally Isomeric Oriented Calix[6]arene-Based Rotaxanes. *Angew. Chem. Int. Ed.* **2005**, *44* (2), 278–281. https://doi.org/10.1002/anie.200461336.

(89) Arduini, A.; Bussolati, R.; Credi, A.; Faimani, G.; Garaudée, S.; Pochini, A.; Secchi, A.; Semeraro, M.; Silvi, S.; Venturi, M. Towards Controlling the Threading Direction of a Calix[6]Arene Wheel by Using

Nonsymmetric Axles. *Chem. – Eur. J.* **2009**, *15* (13), 3230–3242. https://doi.org/10.1002/chem.200801926.

(90) Qi, Z.; Schalley, C. A. Exploring Macrocycles in Functional Supramolecular Gels: From Stimuli Responsiveness to Systems Chemistry. *Acc. Chem. Res.* **2014**, *47* (7), 2222–2233. https://doi.org/10.1021/ar500193z.

(91) Webber, M. J.; Langer, R. Drug Delivery by Supramolecular Design. *Chem. Soc. Rev.* **2017**, *46* (21), 6600–6620. https://doi.org/10.1039/C7CS00391A.

(92) Xue, M.; Yang, Y.; Chi, X.; Yan, X.; Huang, F. Development of Pseudorotaxanes and Rotaxanes: From Synthesis to Stimuli-Responsive Motions to Applications. *Chem. Rev.* **2015**, *115* (15), 7398–7501. https://doi.org/10.1021/cr5005869.

(93) Naik, T.; Berdnikova, D. V.; Sundararajan, M.; Dutta Choudhury, S. Manifold Fluorescence Enhancement of a Styryl(Pyridinium)-Chromene Hybrid Dye upon Binding with an Elongated β-Cyclodextrin Cavity. *J. Phys. Chem. B* **2024**, acs.jpcb.4c04608. https://doi.org/10.1021/acs.jpcb.4c04608.

(94) Yu, Q.; Zhang, G.; Wang, Y.-N.; Hao, H.-C.; Sun, R.; Xu, Y.-J.; Ge, J.-F. Fluorescence Enhancement of near Infrared Cell Membrane Probe by β-Cyclodextrin Supramolecular Interaction. *Dyes Pigments* **2022**, *207*, 110693. https://doi.org/10.1016/j.dyepig.2022.110693

(95) Liu, H.; Zhang, G.; Xu, Y.; Sun, R.; Ge, J. Fluorescence Enhancement of Adamantane-Modified Dyes in Aqueous Solution via Supramolecular Interaction with Methyl-β-cyclodextrin and Their Application in Cell Imaging. *Chem. – Eur. J.* **2023**, *29* (65), e202302782. https://doi.org/10.1002/chem.202302782

(96) Tian, M.; Wang, Z.; Yuan, X.; Zhang, H.; Liu, Z.; Liu, Y. Configurationally Confined Multilevel Supramolecular Assemblies for Modulating Multicolor Luminescence. *Adv. Funct. Mater.* **2023**, *33* (22), 2300779. https://doi.org/10.1002/adfm.202300779

(97) Hua, B.; Zhou, W.; Yang, Z.; Zhang, Z.; Shao, L.; Zhu, H.; Huang, F. Supramolecular Solid-State Microlaser Constructed from Pillar[5]Arene-Based Host–Guest Complex Microcrystals. *J. Am. Chem. Soc.* **2018**, *140* (46), 15651–15654. https://doi.org/10.1021/jacs.8b11156.

(98) Ma, X.; Sun, R.; Cheng, J.; Liu, J.; Gou, F.; Xiang, H.; Zhou, X. Fluorescence Aggregation-Caused Quenching versus Aggregation-Induced Emission: A Visual Teaching Technology for Undergraduate Chemistry Students. *J. Chem. Educ.* **2016**, *93* (2), 345–350. https://doi.org/10.1021/acs.jchemed.5b00483.

(99) Dong, H.; Wei, Y.; Zhang, W.; Wei, C.; Zhang, C.; Yao, J.; Zhao, Y. S. Broadband Tunable Microlasers Based on Controlled Intramolecular Charge-Transfer Process in Organic Supramolecular Microcrystals. *J. Am. Chem. Soc.* **2016**, *138* (4), 1118–1121. https://doi.org/10.1021/jacs.5b11525.

(100) Tan, S.-D.; Chen, W.-H.; Satake, A.; Wang, B.; Xu, Z.-L.; Kobuke, Y. Tetracyanoresorcin[4]Arene as a pH Dependent Artificial Acetylcholine Receptor. *Org. Biomol. Chem.* **2004**, *2* (19), 2719. https://doi.org/10.1039/b410296g.

(101) Praetorius, A.; Bailey, D. M.; Schwarzlose, T.; Nau, W. M. Design of a Fluorescent Dye for Indicator Displacement from Cucurbiturils: A Macrocycle-Responsive Fluorescent Switch Operating through a p K_a Shift. *Org. Lett.* **2008**, *10* (18), 4089–4092. https://doi.org/10.1021/ol8016275.

(102) Sayed, M.; Shinde, K.; Shah, R.; Pal, H. pH-Responsive Indicator Displacement Assay of Acetylcholine Based on Acridine– *p* -Sulfonatocalix[4]Arene Supramolecular System: Fluorescence Off/On Switching and Reversible pK_a Shift. *ChemistrySelect* **2016**, *1* (5), 989–999. https://doi.org/10.1002/slct.201600226.

(103) Yu, H.; Geng, W.-C.; Zheng, Z.; Gao, J.; Guo, D.-S.; Wang, Y. Facile Fluorescence Monitoring of Gut Microbial Metabolite Trimethylamine *N* -Oxide via Molecular Recognition of Guanidinium-Modified Calixarene. *Theranostics* **2019**, *9* (16), 4624–4632. https://doi.org/10.7150/thno.33459.

Chapter 1. Stilbazolium dyes encapsulation in solution and on the surface

1.I Introduction

As discussed in the introduction, stilbazolium dyes possess a push-pull electronic structure that makes them useful for nonlinear optics, fluorescent sensing, and microlaser fabrication. It is well established that the complexation of these dyes with supramolecular macrocycles can significantly influence their optical properties, often leading to enhanced fluorescence. For instance, in 2015, Bitter *et al*.[1] reported a study in which three stilbazolium dyes (**Figure 1.1**) were complexed with a carboxylate-functionalized pillar[5]arene. The spectroscopic properties of the dyes varied notably upon complexation, with the most striking result observed for dye **III** exhibiting a 28-fold increase in fluorescence intensity.

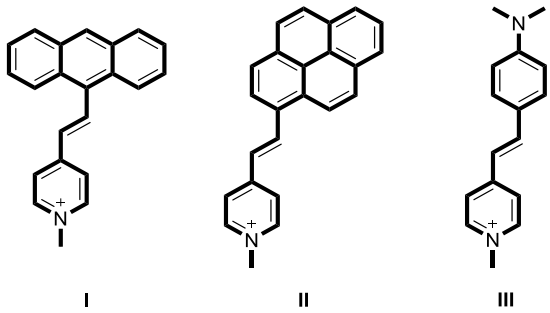

Figure 1.1. Structure of dyes **I**, **II**, and **III**.

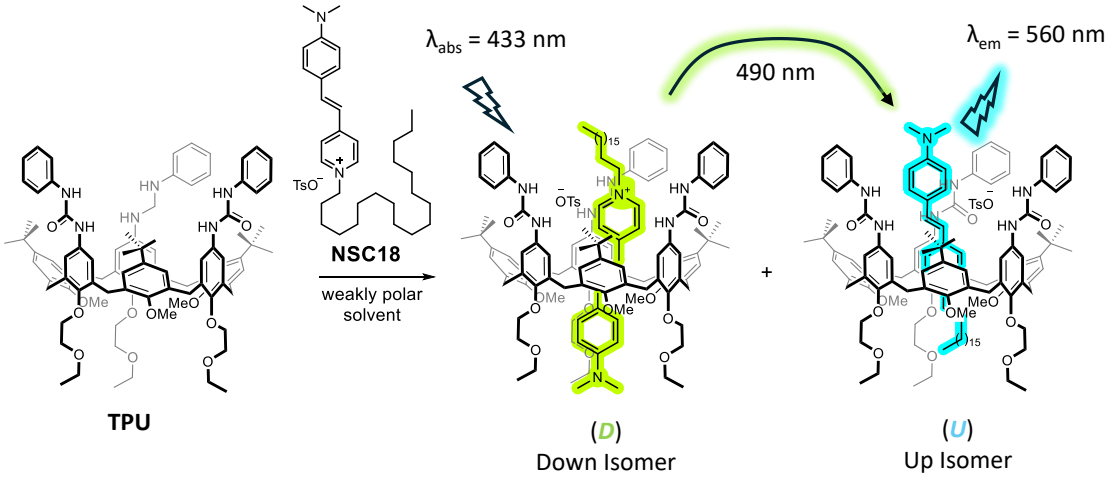

Scheme 1.1. Schematic representation of the formation of the two orientational pseudorotaxane isomers ***U*** and ***D***. Radiative excitation energy transfer process where the emission of the ***D*** isomer at 490 nm (λ_{exc} = 433 nm) is absorbed by the ***U*** isomer that emits at 560 nm.

Prompted by these results, in 2020, our research group initiated an investigation into the complexation of stilbazolium dyes with the tris(*N*-phenylureido)calix[6]arene derivative **TPU**.[2] Unlike the complexation of symmetric *N*,*N*-dialkyl viologen salts (see introduction), the inclusion of

these asymmetric dyes in the anisotropic cavity of **TPU** leads to the formation of two distinct orientational pseudorotaxane isomers, each exhibiting unique optical properties (**Scheme 1.1**).

A recent study published in 2023 provided a deeper insight into the complexation of stilbazolium dyes by **TPU**, specifically investigating the formation of [2]rotaxane species through the encapsulation of suitably functionalized stilbazolium dyes within the **TPU** macrocycle (**Figure 1.2**).[3] The photochemical properties of the two isolated rotaxane isomers, **R-Up** and **R-Down**, were examined separately, revealing distinct optical behaviors compared to both the free dye and each other, with a marked dependence on the dye's orientation. The **R-Up** isomer exhibited enhanced radiative decay, resulting in a high fluorescence quantum yield of 83%. In contrast, the **R-Down** isomer showed a lower quantum yield of 20% due to a competing photoisomerization process inside the host cavity that produced a non-optically active stilbazolium *Z* isomer. Additionally, the differing emission profiles of the two rotaxane orientational isomers, observed both in solution and in the solid state, enabled the precise determination of the dye's orientation within the macrocycle.

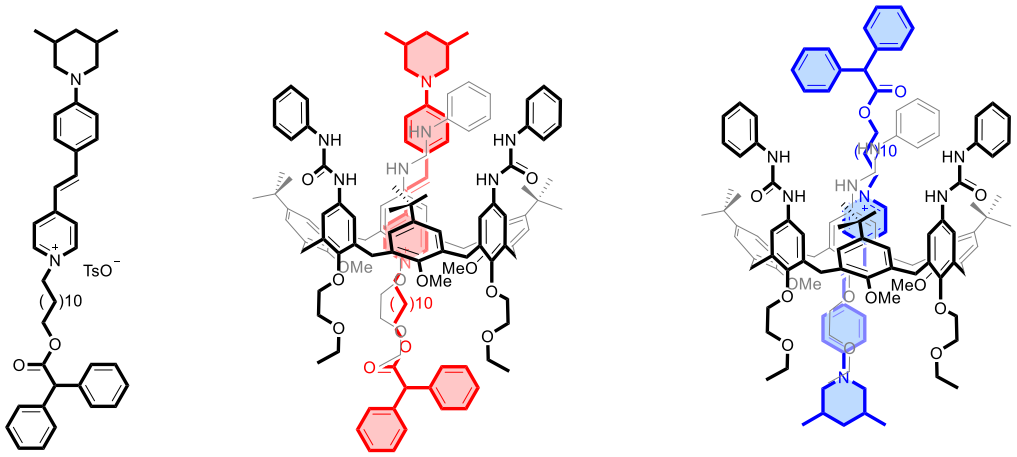

I	**R-Up**	**R-Down**
λ_{abs} = 450 nm	λ_{abs} = 469 nm	λ_{abs} = 425 nm
λ_{em} = 618 nm	λ_{em} = 561 nm	λ_{em} = 533 nm
Φ_f = 18%	Φ_f = 83%	Φ_f = 20%

Figure 1.2. Structures and photochemical properties of stilbazolium dye **I**, rotaxane **R-Up**, and rotaxane and **R-Down**.

I. Aim of the project

This chapter presents an in-depth investigation into the formation of orientational pseudorotaxane isomers from calix[6]arene **TPU** and a series of stilbazolium dyes. The investigation examines explicitly the threading behavior of stilbazolium dyes bearing an *N*,*N*-dimethylamino group on the electron-rich unit, which can enter the **TPU** cavity, and a bulky 3,5-dimethylpiperidine ring that hinders complete threading through the host cavity. To explore the impact of structural

modifications on the threading process, the dyes were further modified by varying the length and bulkiness of the alkyl chain attached to the electron-poor pyridinium ring. A combination of NMR spectroscopy, UV-Vis spectroscopy, fluorescence spectroscopy, and kinetic analysis was employed to characterize the resulting complexes. Notably, NMR measurements enabled the quantification of the isomeric ratio, showing that the length of the alkyl chain on the pyridinium ring significantly influences this ratio. Moreover, temperature variations, especially lower temperatures, were found to shift the equilibrium toward one isomer in some cases. UV-Vis titrations provided the binding constants for the complexation reactions, while fluorescence spectroscopy revealed that the complexation enhances the fluorescence quantum yield of the dyes. Finally, stopped-flow analysis was used to study the directionality of the threading process for some stilbazolium dyes, providing insights into the kinetic aspects of the threading mechanism. Overall, this study deepened the understanding of the threading dynamic of such dyes within the **TPU** macrocycle.

1.I Result and discussion

Two distinct series of stilbazolium salts were designed to understand the threading mechanism of such dyes inside the cavity of the **TPU** wheel. In the first series, the electron-rich aromatic ring of the dye is *para*-substituted with an *N*,*N*-dimethyl amino group, while the pyridinium ring is alkylated with alkyl chains of varying lengths (**NSCn**, with n = 1, 5, and 18). These dyes were synthesized by reacting the known styryl pyridine **NS** with the opportune alkyl tosylates in acetonitrile at reflux (**Scheme 1.2**). In the second series, the dyes bear a bulkier 3,5-dimethylpiperidine group in the electron-rich ring, with the pyridinium ring similarly alkylated with chains of different lengths (**PSCn**, with n = 1, 5, and 18). The bulky 3,5-dimethylpiperidine group was specifically chosen to influence the directionality of the threading process, ensuring that the stilbazolium dye threads exclusively *via* its pyridinium end.[3] Yet, the structure of this group does not significantly impact the electronic properties of the stilbazolium "push-pull" structure. **PSCn** dyes were synthesized by condensing benzaldehyde **1**, prepared according to a previously reported method,[3] with 4-methylpyridine in the presence of a base in DMF at 80 °C (**Scheme 1.2**). This reaction yielded the pyridyl precursor **PS** with an 85% yield. Subsequently, **PS** was alkylated using the appropriate alkyl chain, resulting in the formation of the stilbazolium salts **PSC1**, **PSC5**, and **PSC18** as red solids, with yields of 92%, 68%, and 82%, respectively.

To further elucidate the threading process, two additional stilbazolium dyes incorporating a diphenylacetyl stoppering group at the end of a C6 alkyl chain were synthesized (**NSC6(S)** and **PSC6(S)**, **Scheme 1.2**). **NSC6(S)** was designed to enter the cavity of **TPU** exclusively through its *N,N*-dimethylamino end, as the steric hindrance imposed by the stoppering group prevents passage

through the other end. In the case of **PSC6(S)**, entry into the **TPU** cavity was prevented due to the presence at both termini of bulky stoppering groups. [2,3]

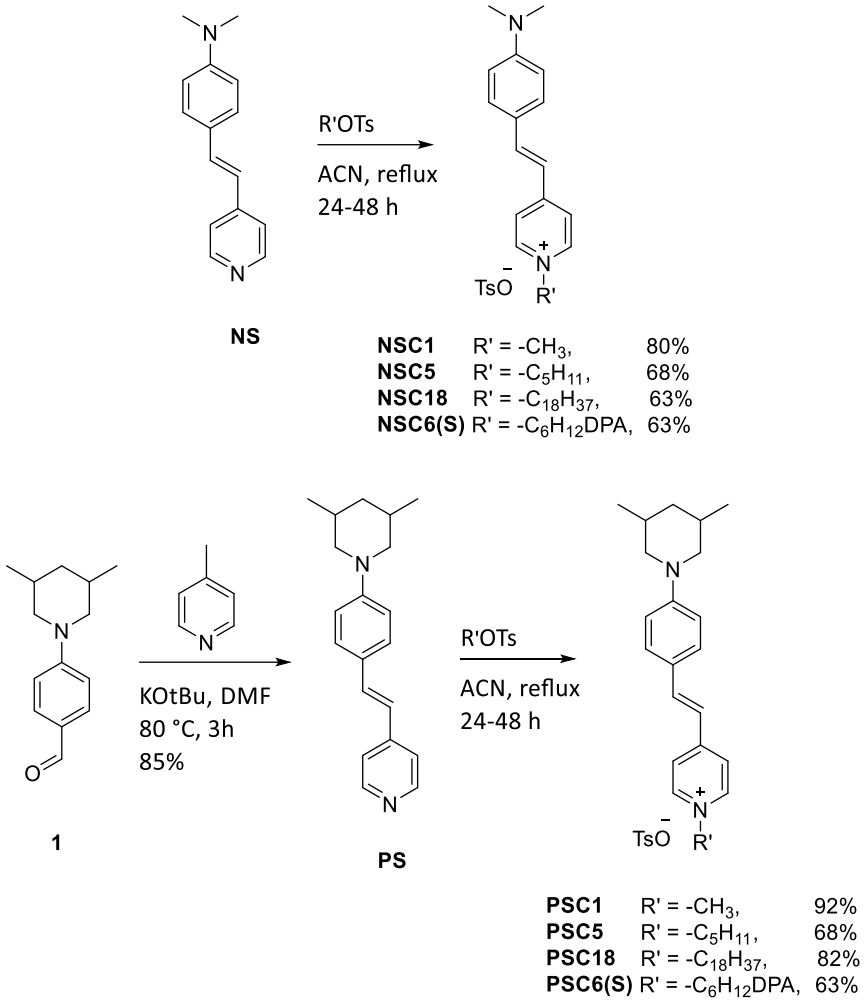

Scheme 1.2. Synthetic scheme for the synthesis of **NSCn** (top) and **PSCn** (bottom) salts.

The decision to vary the length and bulkiness of the alkyl chain on the dye's pyridinium ring was influenced by the observation that, due to their inherent asymmetry, stilbazolium salts can be encapsulated in the cavity of **TPU** in two distinct geometric arrangements (**Scheme 1.3**). The dye's π-deficient pyridinium ring is enclosed within the π-rich calix[6]arene cavity in both arrangements. However, in the orientational isomer ***U***, the dye *para*-substituted aromatic ring is encompassed by the host phenyl urea units, while in isomer ***D,*** this moiety protrudes from the calix[6]arene lower rim. Despite these differences, both [2]pseudorotaxane orientational isomers are stabilized through a host-guest charge transfer interaction between the host π-rich cavity and the guest's positively charged pyridinium ring. It is worth noting that in the ***D*** isomer, the guest retains a certain ion-pairing with the tosylate counteranion, keeping the pyridinium ring aligned with the phenyl urea groups at the macrocycle's wider rim, whereas in the ***U*** isomer, H-bonding between the host phenyl ureas and the guest's pyridinium prevents this ion-pairing. The geometries of these

[2]pseudorotaxane orientational isomers were inferred from the structures of the corresponding interlocked species **R-Up** and **R-Down**[3] and confirmed through NMR measurements and DFT calculations (vide infra).

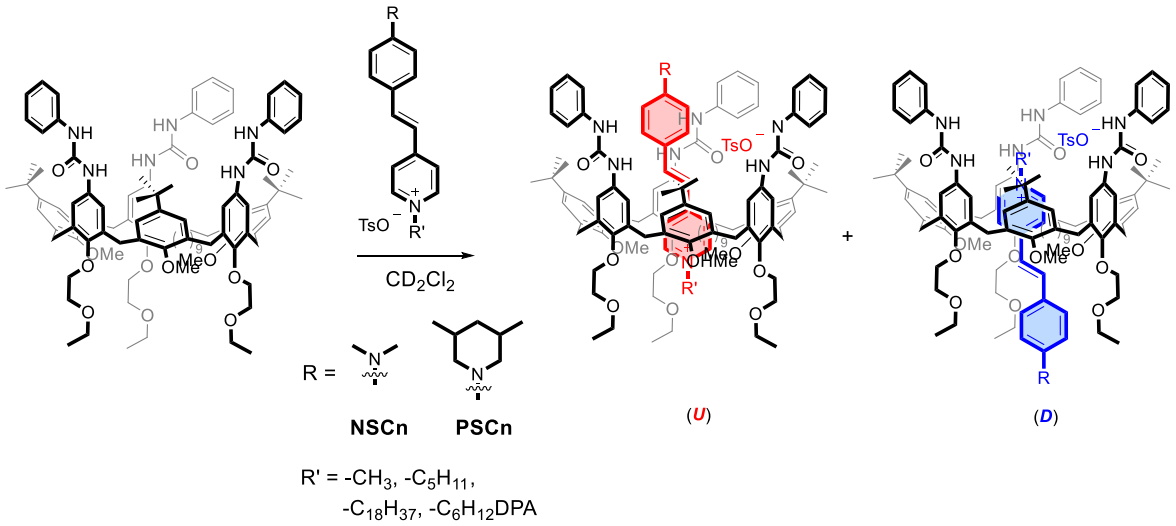

Scheme 1.3. Scheme of the formation of [2]pseudorotaxane orientational isomers: ***U*** isomer in red and ***D*** isomer in blue. DPA = diphenylacetyl.

The structural asymmetry of the interacting species affects the [2]pseudorotaxanes formation mechanism. For **NSCn** dyes, which lack a stoppering group, two orientational isomers can theoretically form through four possible threading pathways (**Figure 1.3**, top). These pathways involve the host threading with the guest's alkyl chain (R') entering either from the macrocycle's wider (upper) rim, resulting in the ***D*** isomer, or from the narrow (lower) rim, producing the ***U*** isomer. Alternatively, the threading can occur with the guest's dimethylamino group entering through the macrocycle's narrow rim (yielding the ***U*** isomer) or wider rim (yielding the ***D*** isomer) (**Figure 1.3**, top). For **PSCn**, since the bulky 3,5-dimethylpiperidine group cannot enter the calix[6]arene cavity, the threading process can only occur with the alkyl chain R', forming the ***U*** isomer from the upper rim, and the ***D*** isomer from the lower rim (**Figure 1.3**, bottom).

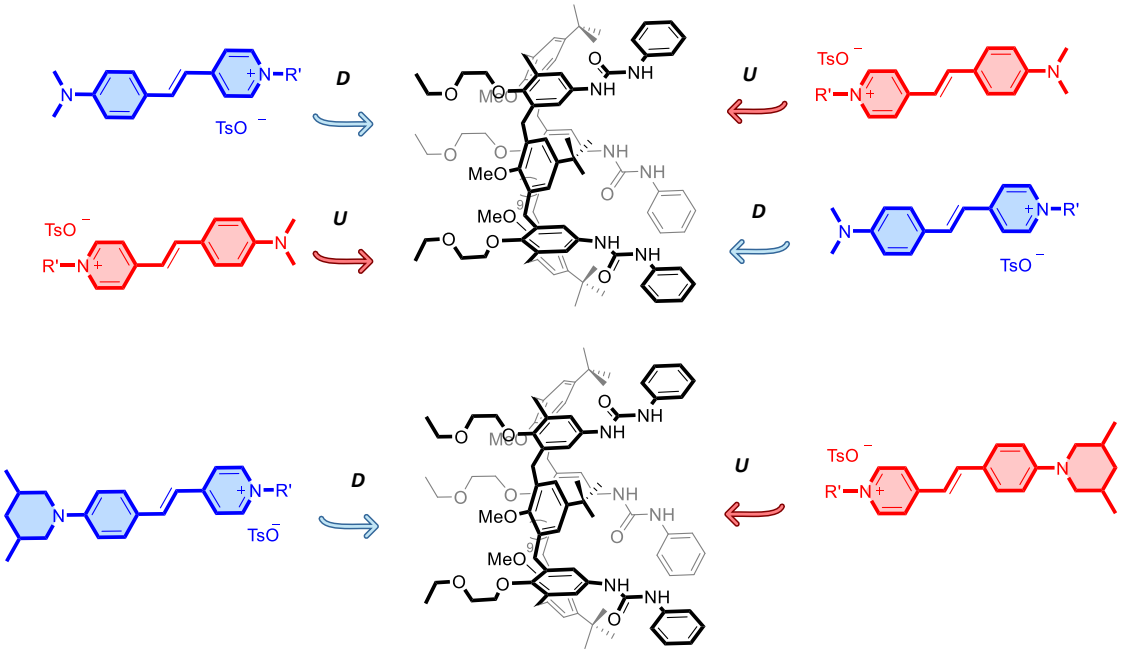

Figure 1.3. Schematic representation of the four (top) and two (down) threading processes yielding the [2]pseudorotaxane isomers ***U*** and ***D*** from **TPU** and, respectively, dyes **NSCn** (top) and **PSCn** (bottom).

I. NMR investigation

The formation of [2]pseudorotaxane complexes involving **NSCn** and **PSCn** with the **TPU** macrocycle was initially investigated by NMR spectroscopy. One-dimensional (1D) and two-dimensional (2D) NMR measurements were conducted on 1:1 mixtures of the appropriate dye and **TPU** in deuterated dichloromethane (CD_2Cl_2). This solvent was selected due to its low melting point (176 K), which allows the examination of inclusion complexes at low temperatures. Additionally, it facilitates a direct comparison between the NMR data and the results obtained from UV-Vis analyses (vide infra).

NMR investigation in CD_2Cl_2 of NSCn. **NSCn** salts were initially investigated through NMR analysis. ^{1}H NMR spectra of these compounds are characterized by the doublet signals from the pyridinium moiety at 8.55 and 7.99 ppm (protons *6* and *5*); the double bond resonates at 7.86 and 7.10 ppm (protons *4* and *3*), while the electron-rich aromatic unit gives rise to two peaks at 7.62 and 6.78 ppm (protons *2* and *1*). A singlet, observed at 3.08 ppm, integrating for 6 protons, corresponds to the methyl groups of the dimethyl amino group. Tosylate counterion is identified by two doublets at 7.70 and 7.22 ppm, attributed to aromatic protons, and a singlet at 2.38 ppm, corresponding to the methyl group. Each stilbazolium salt features a distinct alkyl chain, as delineated in **Figure 1.4**.

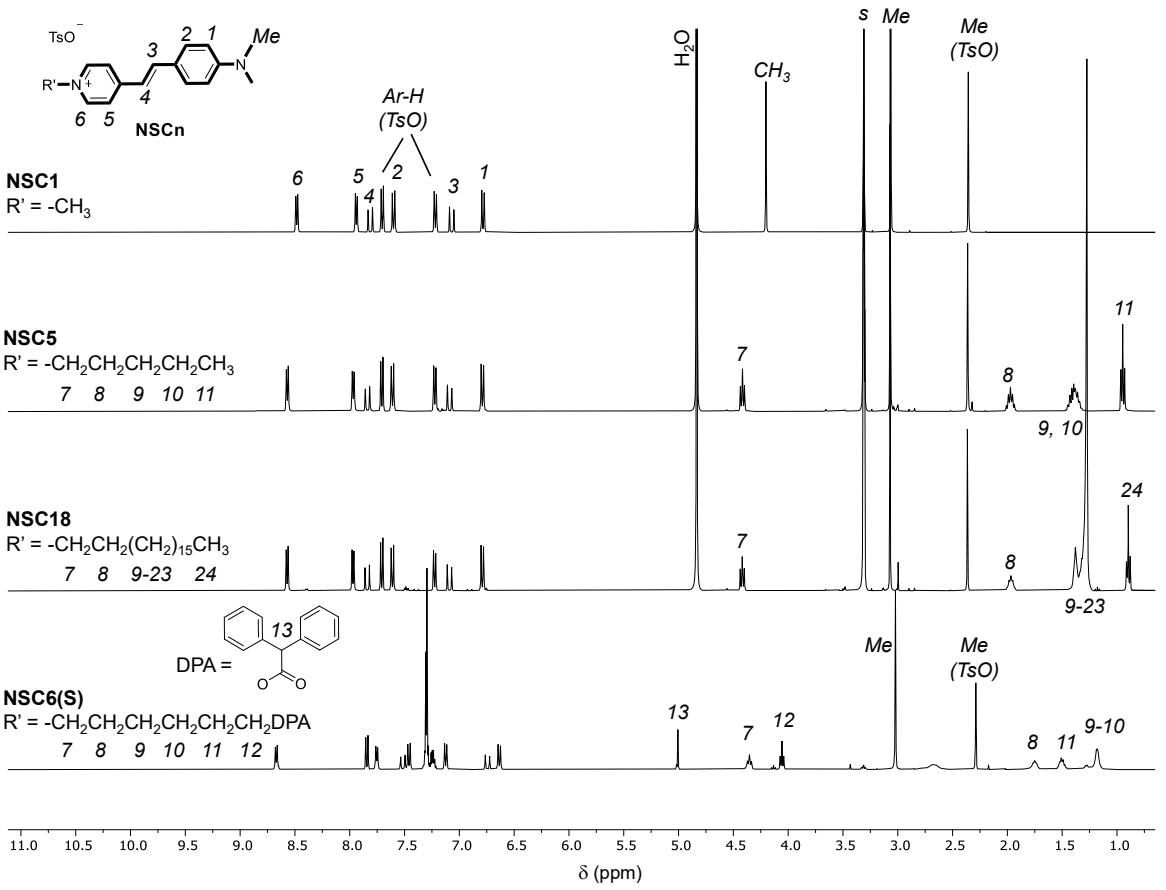

Figure 1.4. ^{1}H NMR spectra (CD_3OD, 400 MHz, 298 K) of stilbazolium dyes **NSC1**, **NSC5**, **NSC18** and **NSC6(S)**.

The formation of the complexes was achieved by mixing **TPU** and the appropriate **NSCn** salt in a 1:1 ratio directly in deuterated dichloromethane. The mixture was then sonicated for 10 minutes before the analysis. The formation of the two isomers, ***U*** and ***D***, was monitored by following the *N,N*-dimethylammino signal (δ = 3.08 ppm, *vide supra*), characteristic of all stilbazolium dyes. The ^{1}H NMR spectra of the 1:1 mixture of **NSC1**, **NSC5,** and **NSC18** with **TPU** are reported in **Figure 1.5**. For the stilbazolium dye with the longest alkyl chain, **NSC18** (**Figure 1.5**, bottom), two isomers in a 1:1 ratio were observed, indicating slow exchange conditions on the NMR timescale. The low-field signal (blue-rendered) at 3.11 ppm was attributed to the ***D*** isomer, in which the aromatic ring of the dye bearing the Me_2N group is positioned outside the calix[6]arene cavity. In contrast, the high-field signal (red-rendered) at 2.63 ppm was assigned to the ***U*** isomer, where the aromatic ring is inside the cavity. For the stilbazolium dyes with shorter alkyl chains, **NSC1** and **NSC5**, only a single broad signal (green-rendered) was detected: at 2.88 ppm for **NSC1** and 2.85 ppm for **NSC5**. This could indicate fast exchange conditions between the two orientational isomers, making them indistinguishable. To further investigate this behavior, variable-temperature (VT) NMR analyses were conducted.

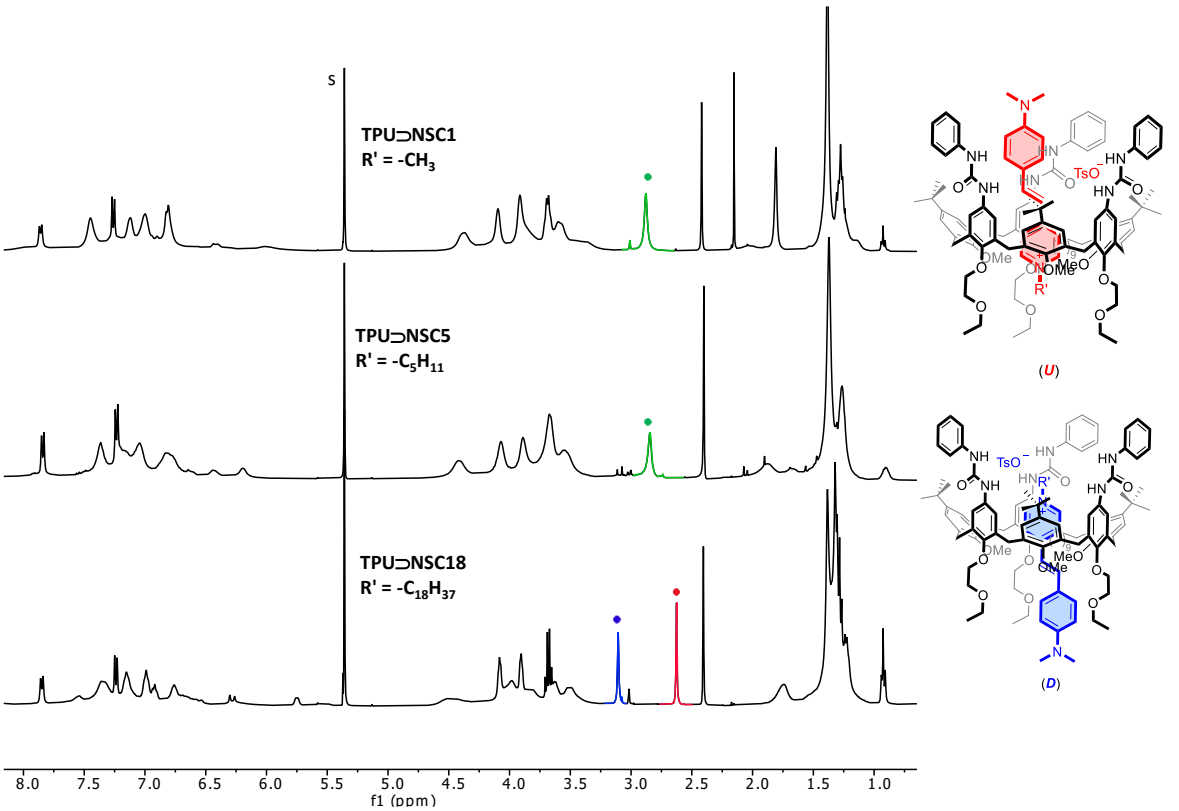

Figure 1.5. ^{1}H NMR stack plot (400 MHz, CD_2Cl_2, 298 K) of: (top) **TPU⊃NSC1** which shows the only presence of a broad signal at 2.88ppm; (middle) **TPU⊃NSC5** which shows the only presence of a broad signal at 2.84 ppm; (bottom) **TPU⊃NSC18** which shows the presence of the two isomers ***U***:***D*** in 50:50 ratio at 2.63 and 3.11 ppm, respectively.

The free stilbazolium dye **NSC1** was analyzed at temperatures ranging from 298 K to 203 K. The resulting ^{1}H NMR spectra are shown in **Figure 1.6**. Due to the limited solubility of the dye in deuterated dichloromethane, signal intensities were low at low temperatures. As the temperature decreased, all signals of **NSC1** exhibited broadening. An appreciable upfield drift was observed for the dye aromatic resonances with splitting, while the singlet of the dimethylamino group splits in two signals at 4.20 and 4.27 ppm at 203 K. These results suggest that such organic ion pair likely start to aggregate at very low temperatures.

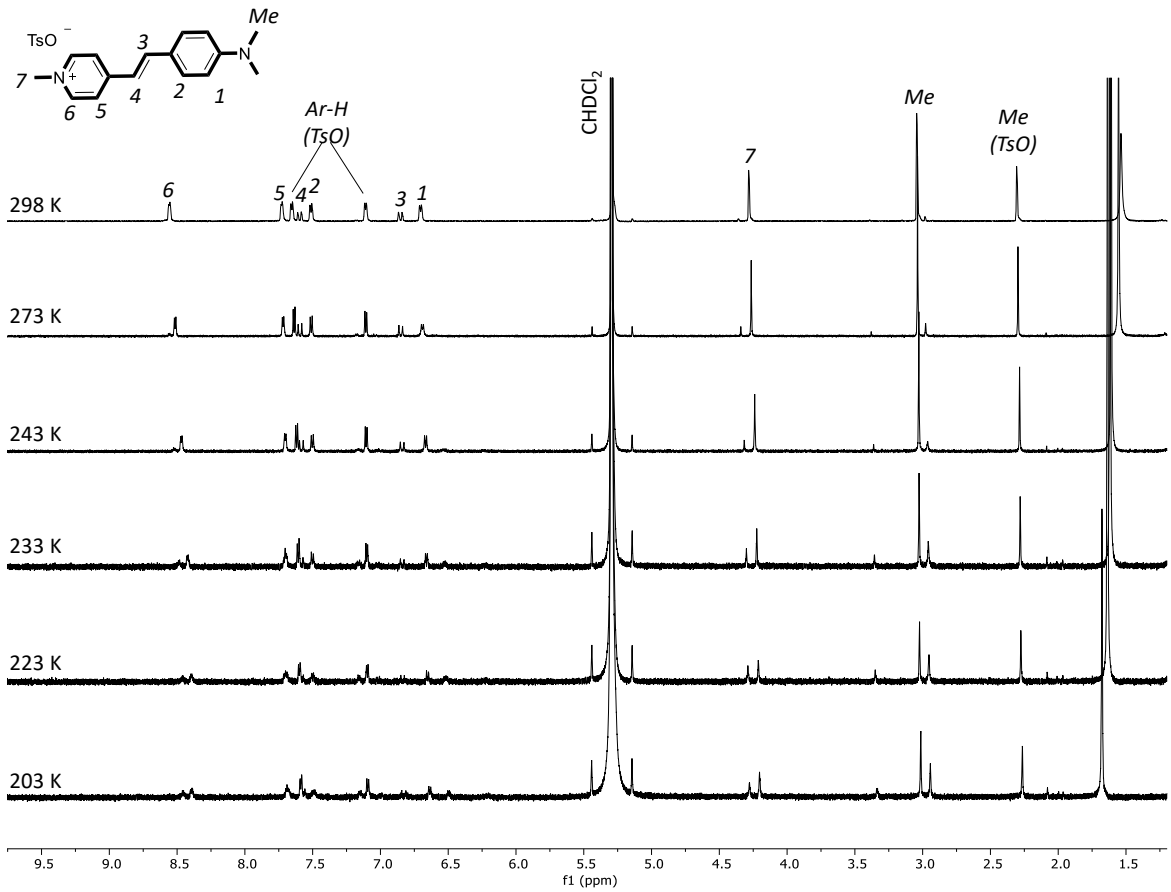

Figure 1.6. ^{1}H NMR stack plot spectra (600 MHz, CD_2Cl_2) of **NSC1** recorded at different temperatures: from 298 K to 203 K.

The corresponding 1:1 mixture with **TPU** was analyzed under similar conditions (**Figure 1.7**). The methyl signal at 2.80 ppm exhibited a decrease in intensity, and became broader as the temperature decreased, with coalescence disappearing below 243 K. Further temperature reductions made it challenging to accurately identify the signals of the two orientational isomers due to the appearance of multiple peaks, likely resulting from other conformations adopted by the calix[6]arene skeleton and the presence of adventitious water. Although attempts to record HSQC spectra at 203 K failed to return reliable results, two main signals could still be distinguished: one more intense but overlapped with other resonances at 2.95 ppm (***D*** isomer) and another at 2.65 ppm (***U*** isomer). Although these measurements were approximate ($\Delta\delta \approx 0.3$ ppm, thus $\Delta\nu = 180$ Hz, and $T_C \approx 243$ K), applying the Eyring equation for two isoenergetic states yielded an energy barrier ($\Delta G^{\ddagger}$) of approximately 11 kcal/mol for the isomer interconversion process. Considering correct the measured $\Delta\nu$, the rate constant (k_r) for the isomer interconversion process at the coalescence temperature becomes 4×10^2 s^{-1}.

In summary, at room temperature, the rate of exchange between the isomers of **NSC1** is too rapid on the NMR timescale, preventing the resolution of distinct signals for each isomer. This behavior is likely attributable to the shorter alkyl chain, which reduced the exchange time between the

isomers. This suggests that at room temperature, there is no inherent selectivity for the ***U*** isomer. Instead, the inability to distinguish between the two isomers is a consequence of the rapid exchange dynamics, preventing their differentiation in the NMR spectra.

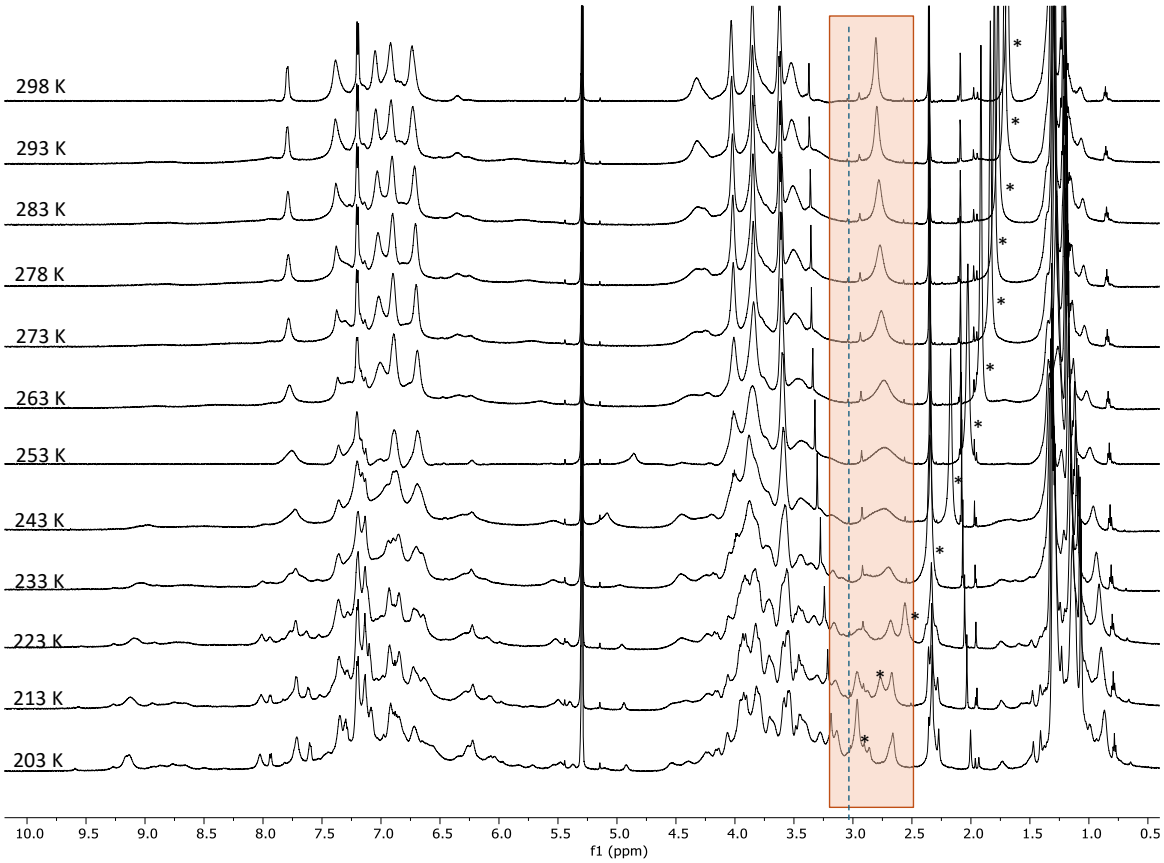

Figure 1.7. ^{1}H NMR stack plot spectra (600 MHz, CD_2Cl_2) of **TPU⊃NSC1** recorded at different temperatures: from 298 K to 203 K. The orange box highlights the spectral region where the orientational isomers' dimethylamino signals are found. *Signal of the water. The dashed line indicates the resonance (3.04 ppm) of the *Me*$_2$N group in the uncomplexed **NSC1**.

The VT NMR analysis was then carried out on the **TPU⊃NSC5** 1:1 complex to ascertain whether the single observed resonance at room temperature also results from a fast exchange process, similar to what was observed for **NSC1**. Initially, the free **NSC5** dye was examined over a temperature range from 298 K to 203 K. As shown in **Figure 1.8**, all the resonances broadened as the temperature decreased; however, unlike **NSC1**, no peak splitting was observed. Only a minor up-field shift in the *N,N*-dimethylamino chemical shift was noted, moving from 3.06 ppm at 298 K to 3.01 ppm at 203 K. Consequently, it was concluded that for this dye, temperature changes affect only the shape of the proton signals, not their chemical shift.

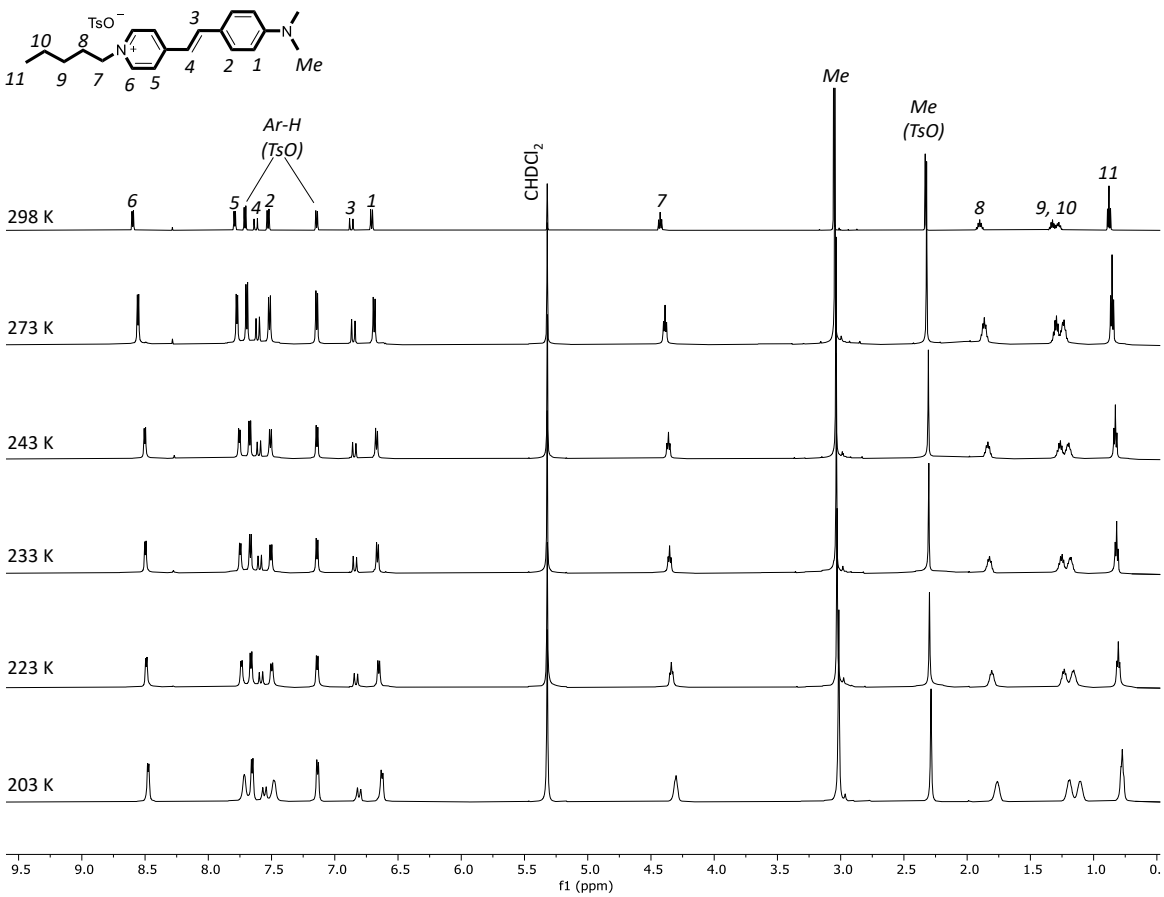

Figure 1.8. ^{1}H NMR stack plot spectra (600MHz, CD_2Cl_2) of **NSC5** recorded at different temperatures: from 298 K to 203 K.

The VT experiment carried out on the **TPU⊃NSC5** complex is shown in **Figure 1.9**. Upon decreasing the temperature, the peak belonging to the dimethylamino group, originally at 2.75 ppm, became broader as highlighted by the orange box, and new peaks emerged at both lower and higher chemical shifts. Notably, the peak at 2.75 ppm, then assigned to the ***U*** isomer, diminishes while a new peak, then assigned to the ***D*** isomer, appears at 3.05 ppm (see also the zoomed-in stack plot in **Figure 1.10**). Lowering the temperature also led to the appearance of new peaks between 0.7 and -1.0 ppm (green box), which were assigned to some protons of the **NSC5** pentyl chain. These significantly up-field-shifted peaks are consistent with the presence of the ***D*** isomer in solution. Indeed, in this configuration, the alkyl chain of the stilbazolium dye is deeply embedded within the **TPU** cavity, resulting in a pronounced shielding effect on these protons. Additionally, signals between 8.0 and 9.4 ppm (pink region) appear at temperatures below 248 K, which were assigned to the protons of the -NH- group of the phenyl ureido groups of the calix[6]arene host engaged in H-bonding with the tosylate.

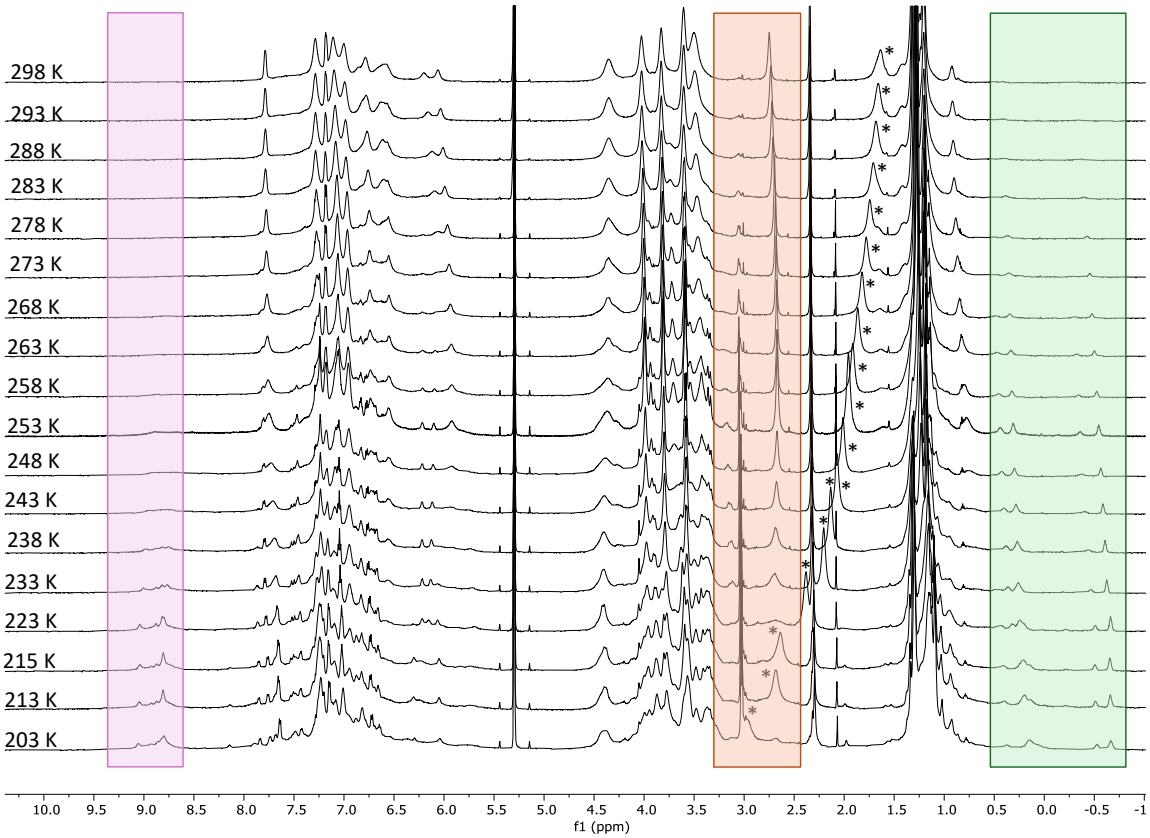

Figure 1.9. ^{1}H NMR stack plot spectra (600 MHz, CD_2Cl_2) of **TPU⊃NSC5** recorded at different temperatures: from 298 K to 203 K. The orange box highlights the spectral region where the orientational isomers' dimethylamino signals are found, the green box highlights the signal of the alkyl chain's protons in the ***D*** isomer, while the pink box highlights the signal of the amine of the phenylureido groups in the ***D*** isomer. *Signal of the water.

Figure 1.10 shows a detailed view of the 2.0 - 3.3 ppm region of the VT NMR stack plot of **TPU⊃NSC5**. At 278 K, a peak resonating to a chemical shift assignable to the ***D*** isomer begins to appear, becoming increasingly intense and shifting up-field as the temperature decreases. Conversely, the peak for the ***U*** isomer also shifts up-field but disappears completely by 223 K. Additionally, a nearby peak to the ***D*** isomer is observed. This peak was hypothesized to be associated with a partial cone (*p*C) conformation assumed by the calix[6]arene host. This conformation is characterized by the inversion of one of the three para-*tert*-butyl substituted aromatic rings of the macrocycle (**Figure 1.11**, top right) and was previously identified by our group in chlorinated solvent also with similar calix[4]arene hosts.[4] This hypothesis is supported by comparing the spectra of **NSC5** and **TPU⊃NSC5** at 203 K in CD_2Cl_2 (**Figure 1.11**). The signal of the dimethylamino group of the free **NSC5** does not coincide with the corresponding signal in the spectrum of the **TPU⊃NSC5** complex, leading to the conclusion that the adjacent signal is attributable to the *p*C conformation. This interpretation was further supported by the observation that the signal of the methyl group of the tosylate is split into two peaks: one corresponding to the cone conformer and the other to the partial cone conformer. In conclusion, this system exhibits a preferential formation of the ***U*** isomer at room temperature, whereas the ***D*** isomer is favored at

lower temperatures. Density functional theory (DFT) calculations are currently underway to further validate this isomerization process.

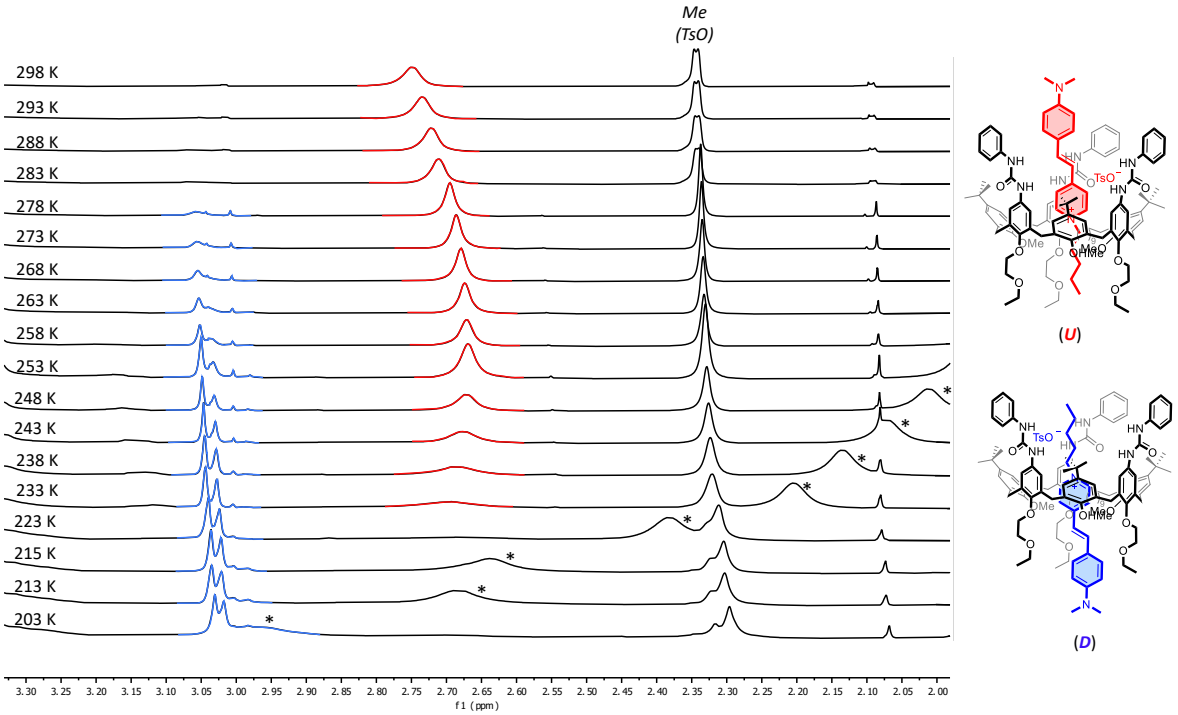

Figure 1.10. ^{1}H NMR zoom from 3.30 to 2.00 ppm of the stack plot of the spectra (600MHz, CD_2Cl_2) of **TPU⊃NSC5** recorded at different temperatures: from 298 K to 203 K. *N,N*-dimethyl amino protons of ***U*** isomer are evidenced in red, *N,N*-dimethyl amino protons of ***D*** isomer are evidenced in blue. *Signal of the water.

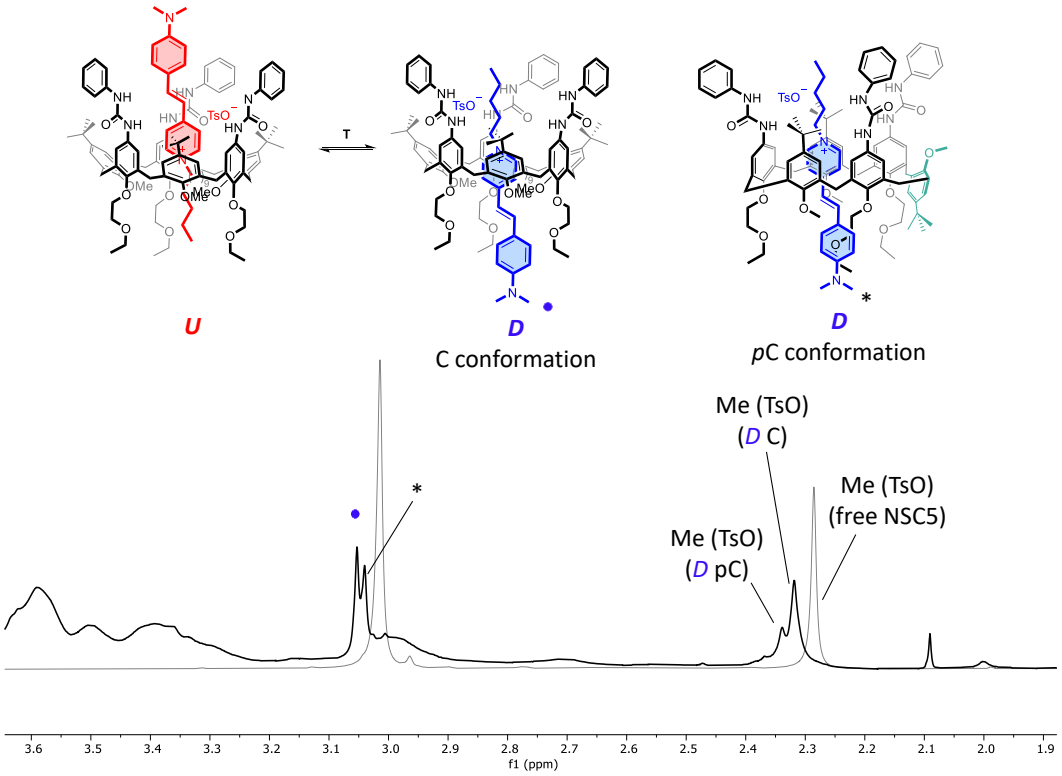

Figure 1.11. Superimposed ^{1}H NMR spectra (CD_2Cl_2, 600 MHz, 203 K) of **NSC5** (grey) and **TPU⊃NSC5** (black). Top: chemical structure of the possible conformations: ***U*** isomer, ***D*** isomer in cone (C) conformation and ***D*** isomer in partial cone (*p*C) conformation.

The last **NSCn** salt analyzed was **NSC6(S)**, which features a diphenylacetyl stoppering group at the end of its C6 alkyl chain. Due to the steric hindrance of this stoppering group, threading through the calix[6]arene cavity is inhibited. Consequently, the formation of the complex is expected to occur exclusively *via* the threading of the *N,N*-dimethyl amino group through either the upper or the lower rim, leading to the formation of the ***D*** and ***U*** isomers, as depicted in **Figure 1.12**.

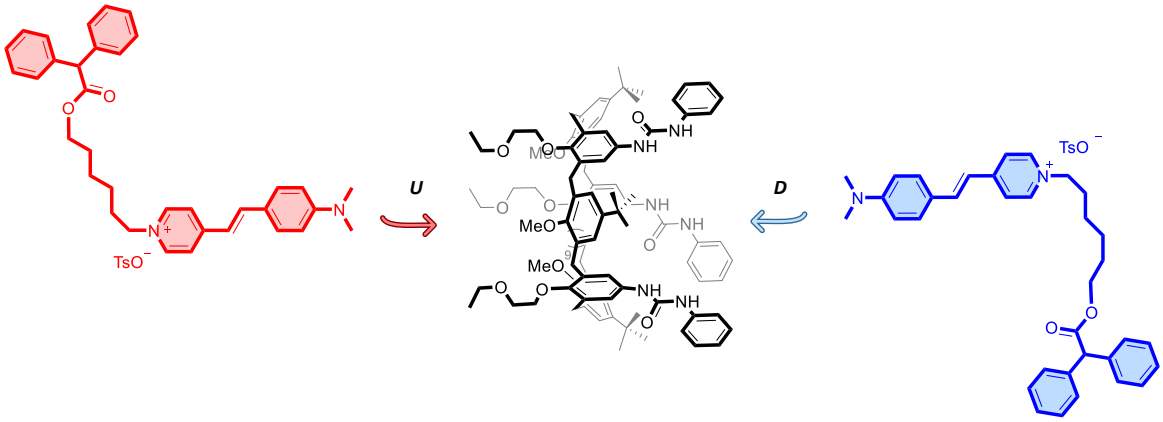

Figure 1.12. Formation of the two isomers ***U*** and ***D***: threading processes for **NSC6(S)** dye inside the calix[6]arene cavity.

The complexation experiment was performed in deuterated dichloromethane by mixing the **TPU** wheel and **NSC6(S)** in a 1:1 ratio. The resulting 2D HSQC experiment was reported in **Figure 1.13**. As observed in the previous cases, the formation of the complex is confirmed by the down-field shift of the signal of the methoxy group (3.94 ppm) and the up-field shift of the pyridinium aromatic protons. The spectrum analysis reveals the presence of the two isomers, ***U*** and ***D***, distinguished by the different chemical shifts of the *N,N*-dimethylamino group and the proton labeled as *13* of the diphenylacetyl group. Similarly to the case of **NSC18**, the system operates under slow exchange conditions, allowing the two isomers to be resolved on the NMR timescale. In particular, the Me_2N group resonates at 3.11 ppm in the ***D*** isomer and at 2.66 ppm in the ***U*** isomer, while proton *13* resonates at 5.09 ppm in the ***D*** isomer and at 4.97 ppm in the ***U*** isomer. Integration of the Me_2N signals reveals a ***D***:***U*** isomer ratio of 60:40, suggesting a preference for threading through the upper rim of **TPU**.

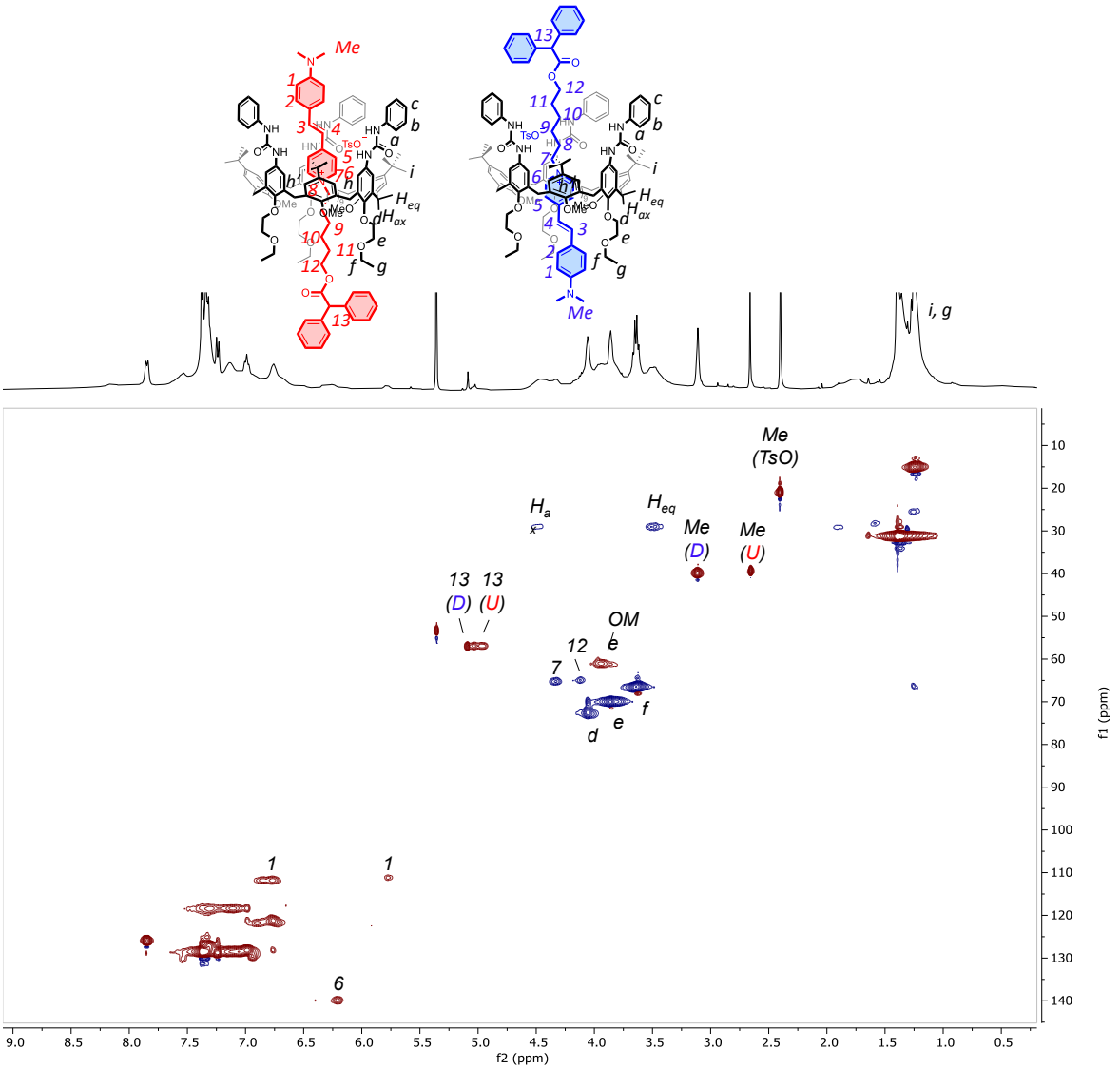

Figure 1.13. Edited HSQC (CD_2Cl_2, 400 MHz, 298 K) of **TPU⊃NSC6(S)**. Positive peaks (CH_3 and CH) are shown in red, while negative ones (CH_2) are in blue.

Table 1.1 presents the chemical shift data of all free **NSCn** dyes and their complexed forms with **TPU** wheel. Analysis at VT revealed that for **NSC1**, which has the shortest alkyl chain, a fast exchange regime is observed at room temperature. In contrast, **NSC5** predominantly forms the ***U*** isomer at RT (see previous NMR analysis at VT). For **NSCn** salts with longer chains, such as **NSC18** (C18 chain) and **NSC6(S)** (stoppered chain), a mixture of the two isomers was detected. Specifically, **NSC18** exhibits an equilibrium between the ***U*** and ***D*** isomers, while **NSC6(S)** shows a preference for the ***D*** isomer. In all the complexes, the occurrence of complexation was further evidenced by the up-field shifts of the signals corresponding to protons *1* and *6* of the stilbazolium aromatic rings (see **Figure 1.4** for protons assignment), as well as protons *7* of the methylene group adjacent to the positively charged nitrogen atom (see **Figure 1.4** for protons assignment), which is located deep within the **TPU** wheel cavity.

Table 1.1. Experimental chemical shifts for **NSCn** and **TPU⊃NSCn**. In the parenthesis is the ratio between the two isomers ***D***:***U***.

Entry	Compound	δ NMe_2 (ppm)	δ H_1 (ppm)	δ H_6 (ppm)	δ H_7 (ppm)
1	**NSC1**	3.06	6.78	8.48	4.28
2	**NSC5**	3.07	6.79	8.57	4.42
3	**NSC18**	3.09	6.81	8.59	4.44
4	**NSC6(S)**	3.02	6.64	8.67	4.35
5	**TPU⊃NSC1**	2.88 (*fast exchange*)	6.01	6.41	3.61
6	**TPU⊃NSC5**	2.84 (***U***)	6.20	6.86	3.57
7	**TPU⊃NSC18**	3.10 (***D***) 2.62 (***U***) (50:50)	7.04/6.29	6.64	3.46
8	**TPU⊃NSC6(S)**	3.11 (***D***) 2.66 (***U***) (60:40)	6.77/5.77	6.21	4.33

NMR investigation in CD_2Cl_2 of PSCn. The ^{1}H NMR spectra of **PSCn** salts were recorded in $CDCl_3$ for **PSC5** and **PSC18**, and in CD_3OD for **PSC1** for solubility reasons (**Figure 1.14**). Compared to the **NSCn** series, the aromatic regions of these axles display nearly identical patterns of peaks, while significant differences arise in the high-field region of the spectra, attributable to the 3,5-dimethylpiperidine group. This group generates several distinct peaks: the methyl groups, labeled *β*, resonate as a doublet at 0.98 ppm in CD_3OD and 0.94 ppm in $CDCl_3$, while the *γ* protons appear as a multiplet at 1.74 ppm in both solvents. The diastereotopic protons *α* and *δ* produce two distinct signals each: *α* gives rise to a doublet of doublets centered at 3.90 ppm in CD_3OD and 3.78 ppm in $CDCl_3$, alongside a triplet at 2.38 ppm in CD_3OD and 2.36 ppm in $CDCl_3$. Meanwhile, *δ* generates a multiplet at 1.87 ppm and a quadruplet at 0.83 ppm in CD_3OD, and at 1.84 ppm and 0.78 ppm in $CDCl_3$.

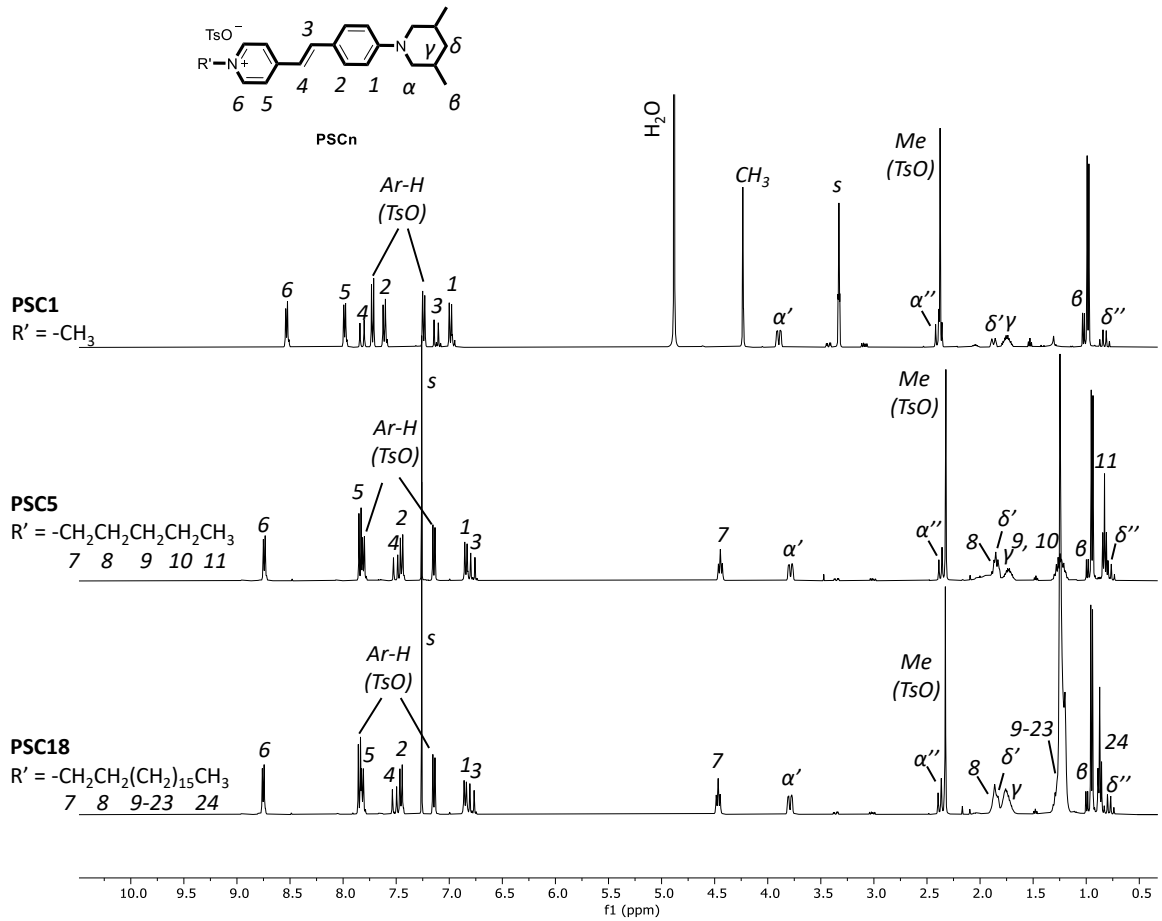

Figure 1.14. ^{1}H NMR spectra of stilbazolium dyes **PSC1** (CD_3OD, 400 MHz, 298 K), **PSC5** and **PSC18** ($CDCl_3$, 400MHz, 298 K).

For **TPU⊃PSCn**, evidence of complexation similar to **TPU⊃NSCn** can be observed (**Figure 1.15**). The calix[6]arene signals become sharper, indicating reduced fluxionality upon complexation. Because of the threading of the axle, the methoxy (OMe) groups on the calix[6]arene lower rim exhibit a downfield shift from 2.9 ppm to 3.8 ppm, while the axle pyridinium protons experience significant shielding by the calix[6]arene cavity, resonating at very high fields. The identification of orientational isomers for these complexes was challenging because of the complexity (signals crowding) of the resulting spectra. To distinguish between ***U*** and ***D*** isomers, the two double-doublet peaks relative to the diasterotopic protons *α*′ and α′′ of the 3,5-dimethylpiperidine stoppering group were selected and integrated using 2D NMR spectroscopy. The ^{1}H NMR stack plot of the 1:1 complexes **TPU⊃PSC1, TPU⊃PSC5** and **TPU⊃PSC18** is reported in **Figure 1.15**. The alkyl chain length significantly influences the ratio between the two isomers, similar to the behavior seen with **NSCn** dyes. Indeed, the dyes with longer alkyl chains, **PSC5** and **PSC18**, exhibited a slow exchange regime, allowing for the distinct observation of both isomers. In contrast, **PSC1**, which has a shorter methyl chain, displayed a fast exchange regime that precluded the differentiation of the two isomers. For **TPU⊃PSC5**, a ***U***:***D*** isomer ratio of 60:40 ratio was observed, with the proton *α*′ resonating at 3.86 ppm (***D***) and 3.45 ppm (***U***), and the *α*′′ protons at 2.42 ppm (***D***) and 2.11 ppm (***U***). The **TPU⊃PSC18**

complex shows a higher preference for the ***U*** isomer (***U***:***D*** isomer ratio of 70:30). The α′ protons resonated at 3.87 ppm (***D***) and 3.23 ppm (***U***), while those α′′ appeared at 2.43 ppm (***D***) and 1.92 ppm (***U***). The slightly different distribution of the isomers in **TPU⊃PSC5** and **TPU⊃PSC18** is likely due to the different length of the alkyl chains, which is pivotal in the formation of the two structures. For **PSC5** a preferential formation towards the ***U*** isomer is detected, which is consistent with the result found for **NSC5**, where the ***U*** isomer is the favoured one at room temperature. Thus, **PSC5** prefers to thread the calix[6]arene cavity with the alkyl chain from the upper rim. Similarly, **PSC18** demonstrated a preferential formation of the ***U*** isomer. This observation aligns with the expectation that the long alkyl chain favors insertion through the upper rim of the calix[6]arene. **Figure 1.16** presents the 2D HSQC spectrum of **TPU⊃PSC18**, serving as an example to illustrate the signal assignment of the system.

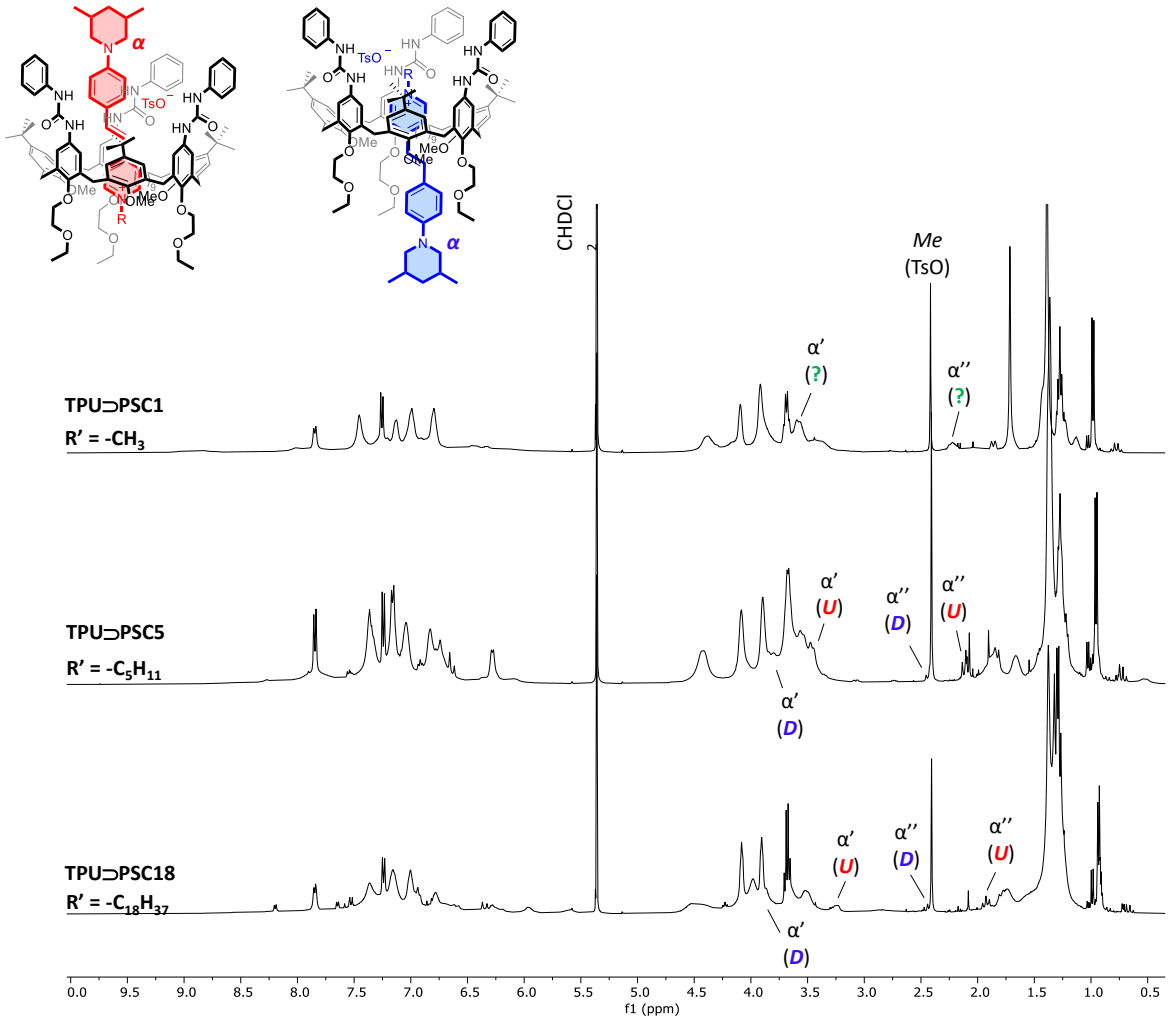

Figure 1.15. ^{1}H NMR stack plot (400 MHz, CD_2Cl_2, 298 K) of: (top) **TPU⊃PSC1** which shows the only presence of one peak (protons signals of α′ at 3.55 and α′′ at 2.23 ppm) indicative of a fast exchange situation; (middle) **TPU⊃PSC5** which shows the presence of the two isomers ***U***:***D*** in 2:1 ratio (protons signals of α′(***D***) at 3.86 ppm, of α′(***U***) at 3.45 ppm, of α′′(***D***) at 2.42 ppm and of α′′(***U***) at 2.11 ppm; (bottom) **TPU⊃PSC18** which shows the presence of the two isomers ***U***:***D*** in 1:2 ratio (protons signals of α′(***D***) at 3.87 ppm, of α′(***U***) at 3.23 ppm, of α′′(***D***) at 2.43 ppm and of α′′(***U***) at 1.92 ppm).

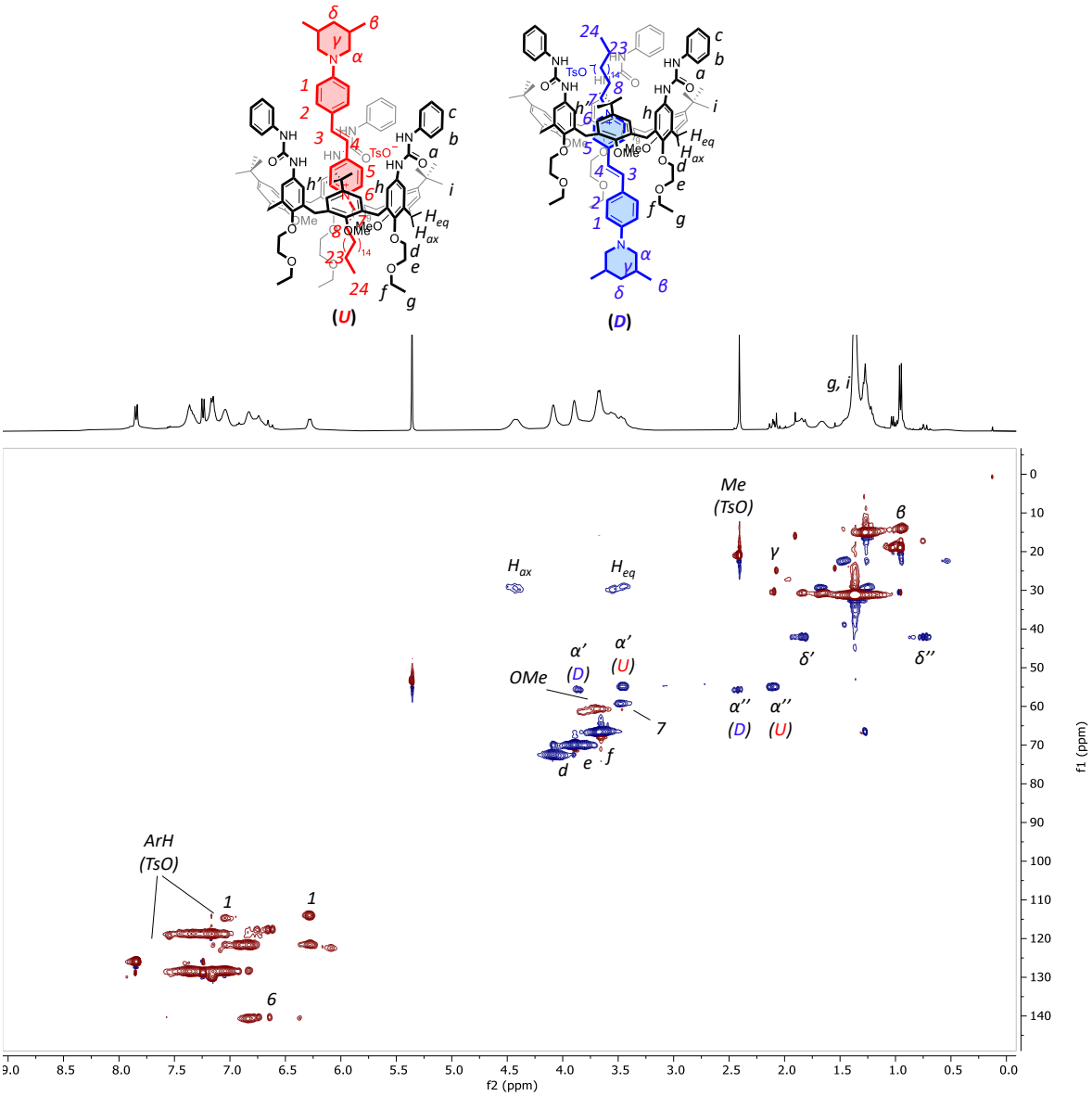

Figure 1.16. Edited HSQC (CD_2Cl_2, 400 MHz, 298 K) of **TPU⊃PSC18**. Positive peaks (CH_3 and CH) are shown in red, while negative ones (CH_2) are in blue.

Table 1.2 illustrates the variation in chemical shift for **PSCn** salts and their complexes with **TPU**. Similar to **NSC1**, **PSC1** displayed a single broad signal, indicative of a fast exchange process. In the case of **PSC5**, two isomers were observed, with a ***D***:***U*** ratio of 40:60, while **PSC18** exhibited a ***D***:***U*** ratio of 30:70, suggesting that the ***U*** isomer is favored over the ***D*** one in both cases. While, as expected, **PSC6(S)** showed no evidence of complexation with the **TPU** wheel. For **PSCn** salts (n = 1, 5, 18), protons *1* and *6* of the stilbazolium aromatic rings (see **Figure 1.14** for protons assignment) exhibited up-field shifts due to interactions with the aromatic cavity of the **TPU** wheel. Additionally, protons *7*, corresponding to the methylene group adjacent to the charged nitrogen(see **Figure 1.14** for protons assignment), also experienced up-field shifts as a result of complexation.

Table 1.2. Experimental NMR chemical shifts for **PSCn** and **TPU⊃PSCn**. In the parenthesis is the ratio between the two isomers ***D***:***U***.

Entry	Compound	δ $H_{\alpha'/\alpha''}$ (ppm)	δ H_1 (ppm)	δ H_6 (ppm)	δ H_7 (ppm)
1	**PSC1**	3.89/2.39	6.98	8.53	4.23
2	**PSC5**	3.78/2.36	6.84	8.74	4.44
3	**PSC18**	3.79/2.36	6.84	8.75	4.47
4	**PSC6(S)**	3.88/2.37	6.97	8.54	4.34
5	**TPU⊃PSC1**	3.55/2.22 (*fast exchange*)	6.42	6.91	3.55
6	**TPU⊃PSC5**	3.85/2.42 (***D***) 3.45/2.11 (***U***) (40:60)	6.29	6.38	3.46
7	**TPU⊃PSC18**	3.87/2.41 (***D***) 3.42/1.90 (***U***) (30:70)	6.93/5.95	6.26	4.24
8	**TPU⊃PSC6(S)**	3.88/2.37	6.97	8.54	4.34

I. UV-Visible investigation

UV-Visible spectroscopy was employed to investigate the binding interaction between **TPU** and the previously synthesized stilbazolium dyes (**NSCn** and **PSCn**) and to gain further insights into their threading mechanism in the calix[6]arene cavity. The study initially focused on **NSC5** that, as the NMR experiments have shown, selectively forms the ***U*** isomer at room temperature, making it an ideal candidate for a detailed analysis. Given that previous studies[5] on **TPU** have shown that, in weakly polar solvents, the binding of this host with viologen salts is greatly dependent on the guest's ion-pairing, an investigation was undertaken to assess the ion pairing of **NSC5**$^+$ cation with its tosylate counteranion in dichloromethane. The assumption was that, under very diluted conditions (approximately 10^{-5}/10^{-6} M), these organic salts behave as solvent-separated ion pairs (ss ip) whose optical properties differ significantly from their tight ion-pair form typically observed at higher concentrations such as those used in NMR experiments.

Figure 1.17 (bottom right) presents the UV-Vis spectrophotometric titration of a 2.0×10^{-6} M solution of **NSC5** in dichloromethane with a 5.0×10^{-3} M solution of tetrabutylammonium tosylate (TBATsO) used as a source of TsO^-. The spectra revealed that ion pairing induces a blue shift in the dye's absorption maximum from 525 nm ($\varepsilon = 4.8\times10^4$ $M^{-1}cm^{-1}$) to 490 nm ($\varepsilon = 3.8\times10^4$ $M^{-1}cm^{-1}$). This shift is further illustrated by the plot of the absorbance measured at 525 nm versus the TBATsO equivalents, as shown in the inset of **Figure 1.17**. An ion-pairing constant logK_{ip} = 4.8 was

determined through non-linear fitting of the absorption variations at this wavelength based on the following 1:1 ion-pairing equilibrium model:

$$\mathbf{NSC5}^{+}_{(DCM)} + \mathrm{TsO}^{-}_{(DCM)} \overset{K_{ip}}{\rightleftharpoons} \mathbf{NSC5}$$

The fluorescence properties of **NSC5** in dichloromethane were also characterized before and after the addition of TBATsO (**Figure 1.19**, right and **Table 1.3**). Before association, the dye showed an emission maximum centered at 612 nm and a fluorescence quantum yield of 23%. The interaction with TBATsO induced a blue shift to 605 nm, reducing the fluorescence quantum yield to 12%.

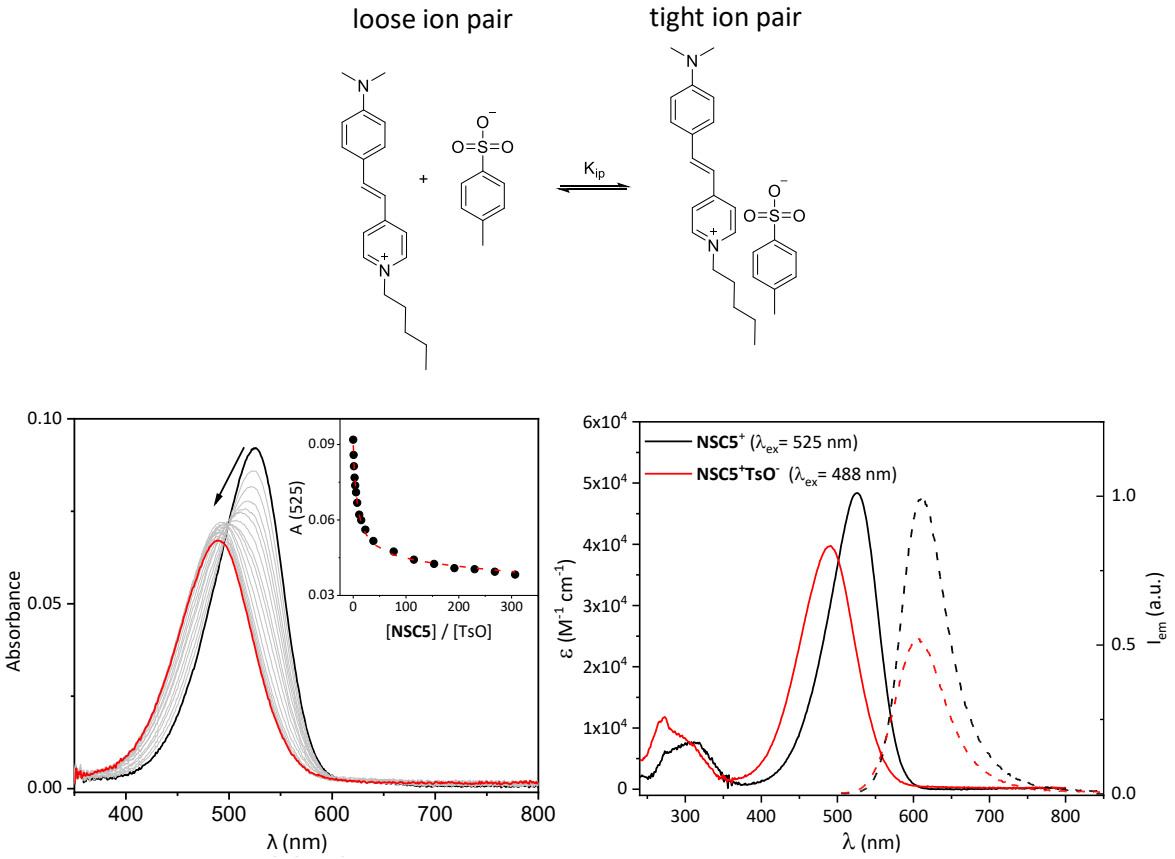

Figure 1.17. Top: scheme of the ion pair tightening between **NSC5** and **TsO**$^{-}$; bottom left: collection of absorbance spectra taken during the titration of **NSC5** solution in CH_2Cl_2 (c = 2.0×10^{-6} M) with a solution of TBATsO in CH_2Cl_2 (c = 5.0×10^{-3} M) at 298 K. Inset: absorption changes at 525 nm; right bottom: absorption (continuous lines) and emission (dashed lines) spectra of **NSC5** (black lines) and **NSC5-TsO** (red lines) in dichloromethane at 298 K. Excitation wavelength for **NSC5** 525 nm, excitation wavelength for **NSC5-TsO** 488 nm.

The same analyses were performed for **NSC1** and **NSC18**, with the results presented in **Table 1.3**. These results demonstrate that their behavior closely mirrors that observed for **NSC5**, suggesting that interaction with the tosylate anion induces similar optical changes in all three dyes. In each case, the formation of a tight ion pair between the axle and the tosylate anion led to a blue shift in both the absorbance and emission maxima, along with a decrease in the quantum yield and molar absorption coefficient. The ion-pair constant for **NSC1** was found to be slightly higher than those

for **NSC5** and **NSC18**, indicating a stronger influence of the tosylate anion on the complexation process.

Table 1.3. Spectroscopic data for **NSCn** dyes and **NSCn-TBATsO** (100-fold excess of TBATsO).

Entry	Compound	λ_{max}^{abs} (nm)	ε ($M^{-1}cm^{-1}$)×10^{-4}	Log K	λ_{max}^{em} (nm) (λ^{exc} / nm)	Φ_{em}
1	**NSC1**	527	4.7	-	612 (500)	0.14
2	**NSC1+TBATsO**	490	3.7	5.2	590 (500)	0.08
3	**NSC5**	525	4.8	-	612 (525)	0.23
4	**NSC5+TBATsO**	490	3.8	4.8	605 (488)	0.12
5	**NSC18**	524	5.4	-	509 (524)	0.17
6	**NSC18+TBATsO**	489	5.1	4.7	501 (489)	0.09

After assessing the dependence of the optical properties of **NSCn** dyes on the ion pairing, the association of calix[6]arene **TPU** with the tosylate anion was subsequently investigated, given that the tosylate anion interacts with the phenylureido units on the upper rim of the calix[6]arene. A UV-Vis titration in dichloromethane was performed by adding several aliquots of a 10 mM solution of TBATsO to a solution of the **TPU** (c = 1.0×10^{-5} M) up to reach a 100-fold excess of TBATsO (**Figure 1.18**). The analysis revealed the formation of two distinct complexes with **TPU** and tosylate anion, exhibiting 1:1 and 1:2 stoichiometries, respectively. The association constants were determined to be logK_1 = 4.7 and logK_2 = 3.2.

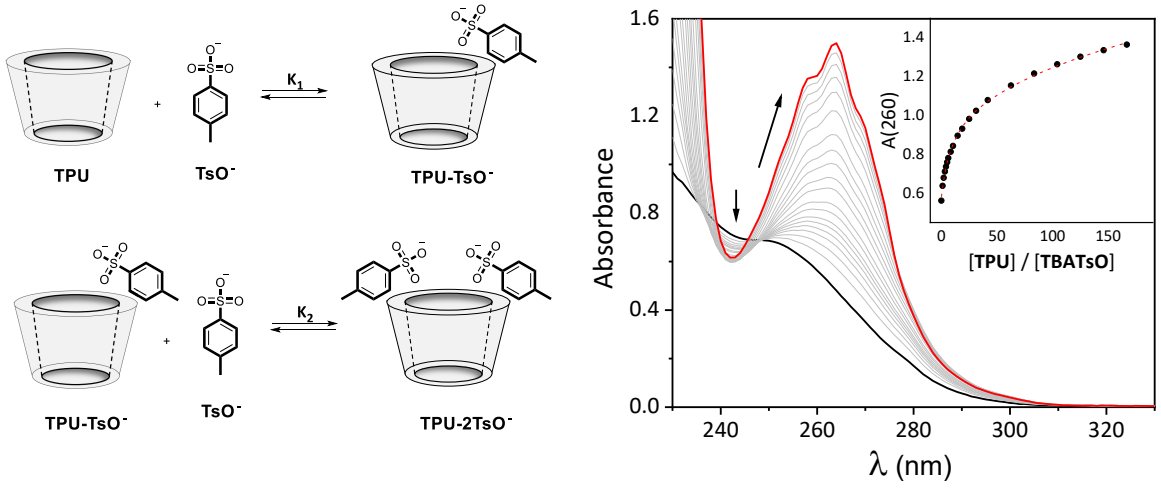

Figure 1.18. Left: scheme of the reaction complexation between **TPU** and **TsO⁻**; right: collection of absorbance spectra taken during the titration of **TPU** solution in CH_2Cl_2 (c = 1.0×10^{-5} M) with a solution of TBATsO in CH_2Cl_2 (c = 10×10^{-3} M) at 298 K. Inset: absorption changes at 260 nm.

The consequence of the above results is that the presence of a stoichiometric excess of tosylate in solution may significantly influence the binding properties of **TPU** toward **NSCn**. To verify this

hypothesis, the complexation between **TPU** and **NSC5** axle was initially assessed by comparing simultaneously the spectrum of the free species, referred to as the "sum" spectrum, with the spectrum of a 1:1 mixture of both components, referred to as the "mixture" spectrum. For this experiment, a specialized cuvette with a central septum was utilized: **TPU** was placed in one compartment, while **NSC5** was placed in the other. This setup allows for the recording of a spectrum that represents the mathematical sum of the two separate spectra. After shaking the cuvette to mix the solutions, the spectrum of the resulting mixture was recorded. If rapid interaction occurs between the host and guest, the "sum" and "mixture" spectra should differ. Any observed differences between these spectra are attributed to the formation of the complex.

As shown on the left of **Figure 1.19**, the experiment carried out without any stoichiometric excess of tosylate, the "mixture" spectrum (red line) exhibits a hypochromic effect along with a red-shift in the maximum absorption compared to the "sum" spectrum (black line). The same experiment repeated with the excess of tosylate (100 equivalents of TBAOTs, see **Figure 1.19**, right) shows instead a blue shift in the absorbance maximum.

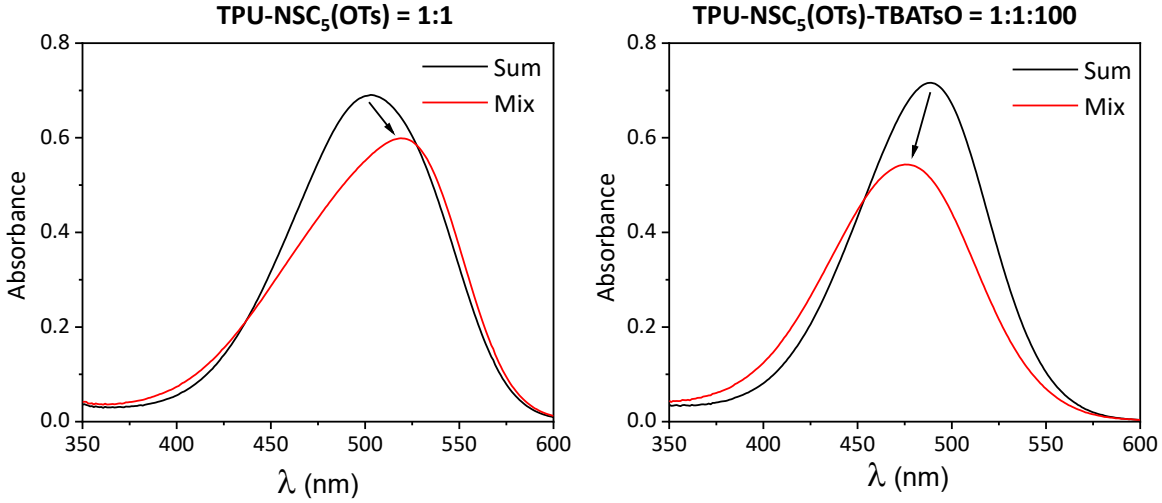

Figure 1.19. Left: sum of the absorption spectra of **TPU** (c = 0.5×10^{-3} M) and **NSC5** (c = 2.00×10^{-5} M) without excess of TBATsO (black line) and the absorption spectrum of the mixture of **TPU** and **NSC5** (red line) (CH_2Cl_2, 298 K); right: sum of the absorption spectra of **TPU** (c = 0.5×10^{-3} M) and **NSC5** (c = 2.00×10^{-5} M) with excess of TBATsO (c = 2.00×10^{-3} M) (black line) and the absorption spectrum of the mixture of **TPU** and **NSC5** with excess of **TsO**$^-$ (red line) (CH_2Cl_2, 298 K).

Based on these results, the association constant between **NSC5** and **TPU** was calculated in dichloromethane *via* UV-Vis spectroscopy in the presence of a 100-fold stoichiometric excess of tosylate. The UV-Vis titration spectra are reported in **Figure 1.20**. The data fit smoothly when the ion-pairing constant between **NSC5** and **TsO**$^-$ was fixed at logK_{ip} = 4.8, yielding an association constant of logK_{NSC5} = 5.6 (**Table 1.4**). The absorbance spectrum of the **TPU⊃NSC5** 1:1 complex, obtained from the data fitting, was compared with those of ***U*** and ***D*** rotaxanes used as model systems,[3] reasonably confirming the selective formation of the ***U*** isomer (**Figure 1.20**, bottom right).

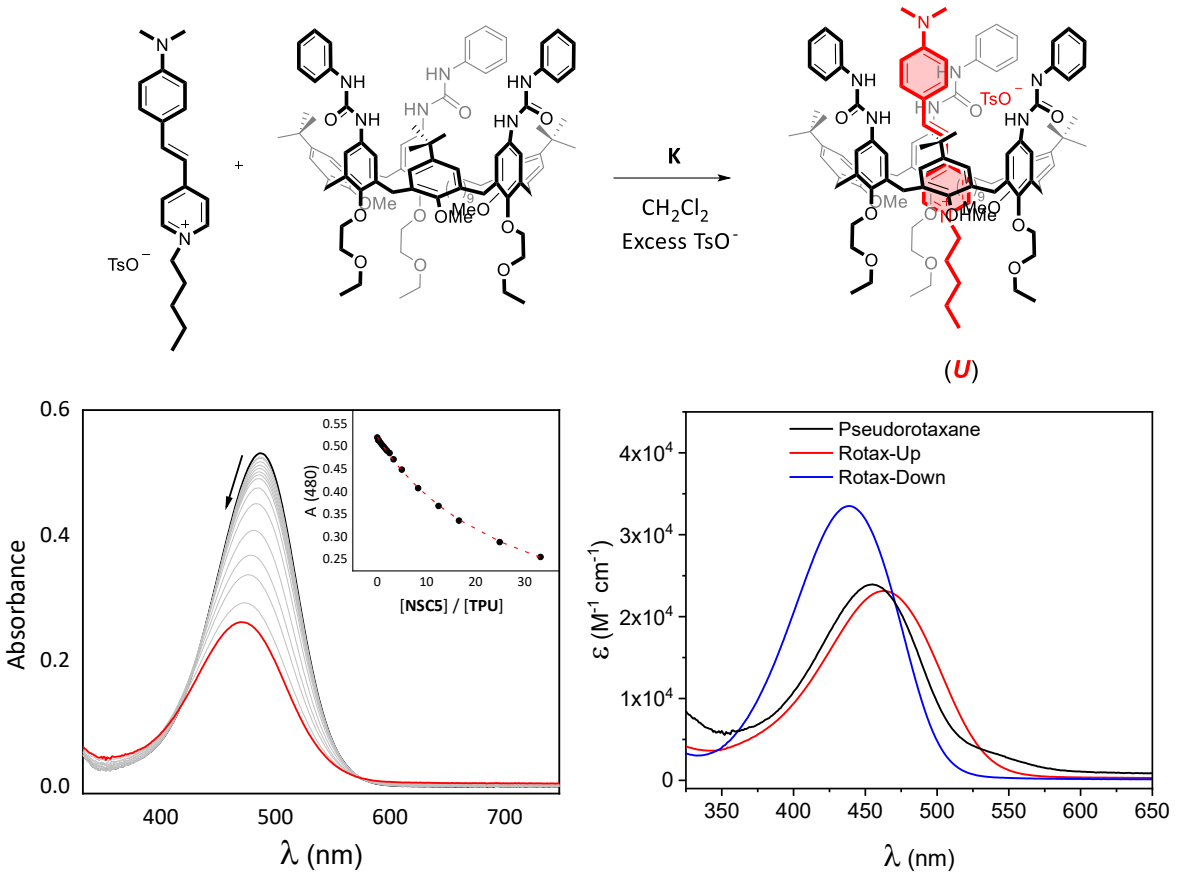

Figure 1.20. Top: Scheme of the reaction complexation between **NSC5** and **TPU**; bottom left: collection of absorbance spectra taken during the titration of **NSC5** solution in CH_2Cl_2 (c = 7.0 × 10^{-5} M) with a solution of **TPU** in CH_2Cl_2 (c = 5.0 × 10^{-3} M) in the presence of an excess of TBATsO (c = 7.0 × 10^{-3} M) at 298 K. Inset: absorption changes at 480 nm; bottom right: comparison of the absorbance spectra of ***U*** rotaxane (red line), ***D*** rotaxane (blue line), and pseudorotaxane spectrum (black line).

The system was further investigated using fluorescence analysis. The emission of the dye was monitored during the incremental addition of the **TPU** solution. **Figure 1.21** displays the collection of emission spectra recorded throughout the titration. An increase in fluorescence intensity was observed with the addition of the **TPU** wheel, indicating that the complexation of the dye significantly affects its fluorescence properties. Additionally, a blue shift in the emission wavelength was observed upon adding **TPU** (**Table 1.4**, entry 4). By comparing the predicted emission spectrum of the pseudorotaxane, derived from data fitting, with the emission spectra of the isolated ***U*** and ***D*** rotaxane isomers,[3] it becomes evident that only the ***U*** isomer is formed. Another significant change in the fluorescence properties of **NSC5** upon complexation is the increase in fluorescence quantum yield (**Table 1.4**, entry 4). Free **NSC5** exhibits a fluorescence quantum yield of 23%, which rises to 81% after encapsulation within the **TPU** cavity.

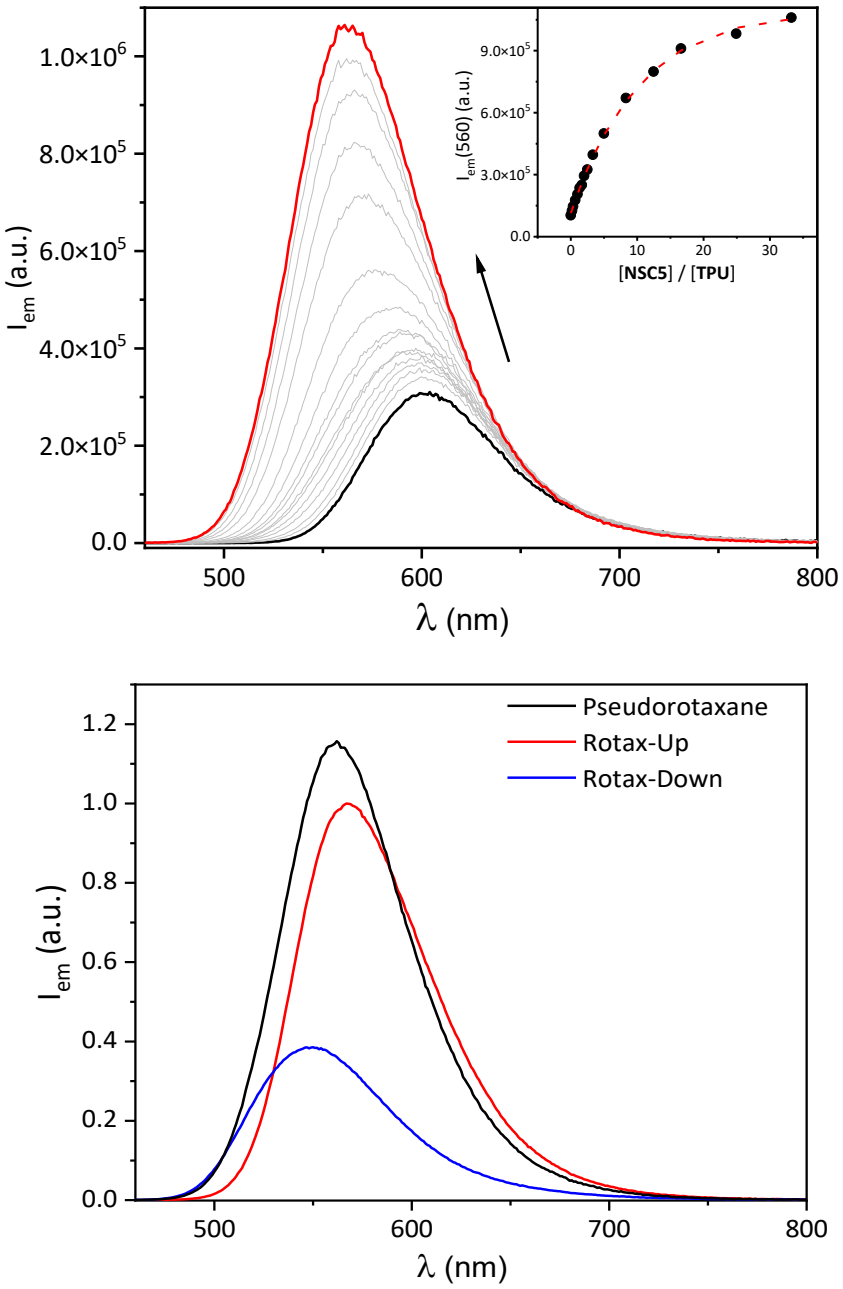

Figure 1.21. Top: collection of emission spectra taken during the titration of **NSC5** solution in CH_2Cl_2 (c = 7.0 × 10^{-5} M, λ_{max}^{ex} = 450 nm) with a solution of **TPU** in CH_2Cl_2 (c = 5.0 × 10^{-3} M) in the presence of an excess of TBATsO (c = 7.0 × 10^{-3} M) at 298 K. Inset: emission intensity changes at 560 nm; bottom: comparison of emission spectra of ***U*** rotaxane (red line), ***D*** rotaxane (blue line) and predicted pseudorotaxane spectrum (black line).

Similarly, binding constants were determined for the complexes between **TPU** and axles **NSC1** and **NSC18** (**Table 1.4**, entries 2 and 6). **NSC18** exhibited an association constant of $\log K_{NSC18}$ = 5.3, which is comparable to that of **NSC5** ($\log K_{NSC5}$ = 5.6). The binding constant between **TPU** and **NSC1** was calculated to be $\log K_{NSC1}$= 8.1, indicating a stronger interaction compared to the **TPU⊃NSC5** complex. This value is consistent with previously reported binding constants for the complexation

of **DOV** with the **TPU** macrocycle.[4] In all cases, complexation induced a slight blue shift in both the absorbance maximum (ca. 20 nm) and emission maximum (ca. 40-50 nm) (**Table 1.4**).

Table 1.4. Spectroscopic data and binding constants for **NSCn-TBATsO** and **TPU⊃ NSCn**.

Entry	Compound	λ_{max}^{abs} (nm)	Log K	λ_{max}^{em} (nm)
1	**NSC1+TBATsO**	490	5.2	590
2	**NSC1+TPU**	475	8.1	563
3	**NSC5+TBATsO**	490	4.8	605
4	**NSC5+TPU**	471	5.6	561
5	**NSC18+TBATsO**	489	4.7	601
6	**NSC18+TPU**	470	5.3	553

A significant change in the fluorescence properties of **NSC1** was observed upon complexation, with its quantum yield increasing from 14% in the free state to 55% upon binding with **TPU**. These alterations in **NSC1** dye's optical properties upon complexation align with those previously reported for the **NSC5** dye. This enhancement can be attributed to the increased rigidity of the dye upon complexation, which restricts its molecular motions. More importantly, the calix[6]arene in the complex reduces dye aggregation, thereby minimizing the aggregation-caused quenching (ACQ) effect.

I. Kinetic study

The threading process was further investigated to gain deeper insight into the formation of orientational isomers. For the **NSC1** salt, the threading kinetics were too rapid to be monitored using stopped-flow analysis, necessitating the consideration of longer axles. Specifically, axle **NSC5** was selected for investigation, as the threading kinetics of **NSC18** were too slow to be observed within a reasonable timeframe.

To investigate the directionality of the threading process of **NSC5**, two additional stilbazolium dyes, **PSC5** and **NSC6(S)**, were selected as model compounds (**Figure 1.22**). Both dyes incorporate sterically demanding groups that avoid interactions with the calix[6]arene cavity. Specifically, **PSC5** contains a 3,5-dimethylpiperidine ring, while **NSC6(S)** possesses a diphenylacetate moiety at the terminus of the alkyl chain, both of which prevent threading within the **TPU** cavity.

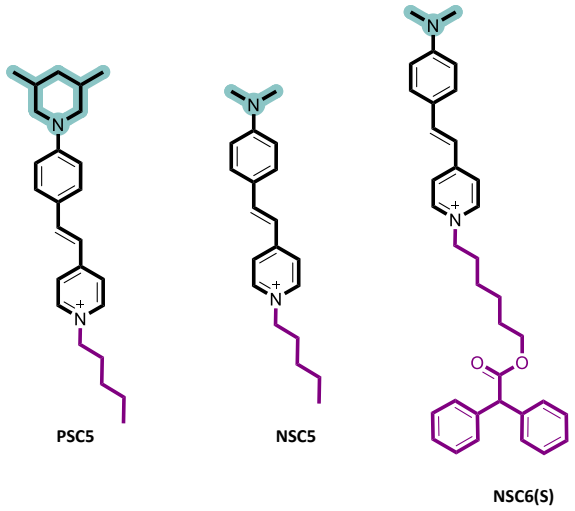

Figure 1.22. Structure of stilbazolium dyes used for the threading kinetic study.

Despite the presence of these stopper groups, the photophysical properties of the stilbazolium dyes remain unaffected. Specifically, the absorbance and emission maxima for all three dyes are comparable (as shown in **Tables 1.5**), as are the fluorescence quantum yields and association constants.

Table 1.5. Spectroscopic values and binding constants for **NSC5**, **NSC6(S)**, and **PSC5**. *K is the ion-pair constant for **dye-TsO**$^-$ and association constant for **TPU⊃dye**.

CH_2Cl_2	State	λ_{abs} (nm)	ε (M^{-1} cm^{-1}) ×10^4	λ_{em} (nm)	Stokes Shift(eV)	Φ_{fluo}	logK*
	NSC5	526	4.8	612	0.33	23%	\
NSC5	**NSC5-TsO**$^-$	490	3.8	605	0.48	12%	4.9
	TPU⊃NSC5	461	2.3	562	0.48	81%	5.5
	NSC6(S)	529	3.9	612	0.31	16%	\
NSC6(S)	**NSC6(S)-TsO**$^-$	490	3.4	600	0.46	10%	4.9
	TPU⊃NSC6(S)	456	2.6	561	0.51	71%	5.4
	PSC5	532	2.7	627	0.35	12%	\
PSC5	**PSC5-TsO**$^-$	489	2.3	616	0.52	9%	4.9
	TPU⊃PSC5	460	2.2	565	0.50	71%	5.7

The UV-Visible titrations of both **PSC5** and **NSC6(S)** indicate the sole presence of the ***U*** isomer. However, NMR analysis of both stilbazolium dyes confirms the formation of both isomers. The apparent selectivity for the ***U*** isomer observed in the UV-Visible analysis may be misleading.

Probably, the formation of the ***D*** isomer occurs so rapidly that it remains undetectable by UV-Vis techniques. Nevertheless, for the purposes of this study, the UV-Vis trace is assumed to represent the ***U*** isomer exclusively. Due to bulky groups that prevent complexation with the calix[6]arene cavity, the ***U*** isomer formation for both dyes can occur through only one possible pathway. In the case of **PSC5**, the ***U*** isomer is formed exclusively by the threading of the alkyl chain through the upper rim of the calix[6]arene (**Figure 1.23**, bottom left). For **NSC6(S)**, the ***U*** isomer formation occurs solely through the threading of the *N,N*-dimethylamino group from the lower rim of the calix[6]arene (**Figure 1.23**, bottom right).

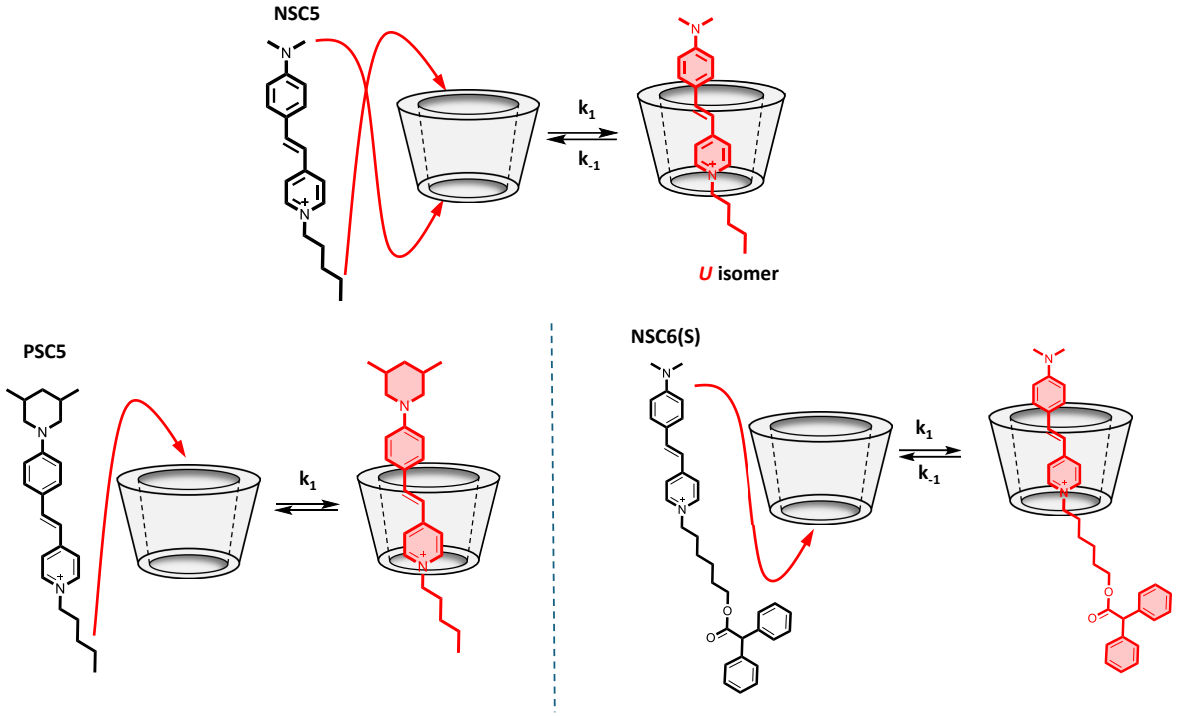

Figure 1.23. Representation of the threading process for **NSC5** (top), **PSC5** (left bottom), and **NSC6(S)** (right bottom).

A kinetic study utilizing a stopped-flow apparatus was conducted to elucidate the directionality of the threading process. **Figure 1.24** illustrates the kinetic profiles of the association process for **PSC5**, **NSC6(S)**, and **NSC5** with the **TPU** wheel. For all dyes, the threading process with calix[6]arene wheel follows second-order kinetics, with distinct rate constants: **PSC5** exhibits a rate constant of $k_1 = 2.2 \pm 0.1 \times 10^2\ s^{-1}M^{-1}$, **NSC6(S)** of $k_1 = 1.11 \pm 0.08 \times 10^5\ s^{-1}M^{-1}$, and **NSC5** of $k_1 = 0.97 \pm 0.06 \times 10^5\ s^{-1}M^{-1}$. When these values are compared with the rate constants for the dethreading process, which follows a first-order kinetics, (for **PSC5** $k_{-1} = 4.4 \pm 0.2 \times 10^{-4}\ s^{-1}$, for **NSC6(S)** $k_{-1} = 0.44 \pm 0.03\ s^{-1}$, and **NSC5** $k_{-1} = 0.31 \pm 0026\ s^{-1}$), it is evident that the threading process is kinetically favored.

Entry	Compound	K_1 [$s^{-1}M^{-1}$]	K_{-1} [s^{-1}]
1	**PSC5**	2.2 ± 0.1	4.4 ± 0.2
2	**NSC6(S)**	1.11 ± 0.08	0.44 ± 0.03
3	**NSC5**	0.97 ± 0.06	0.31 ± 0.03

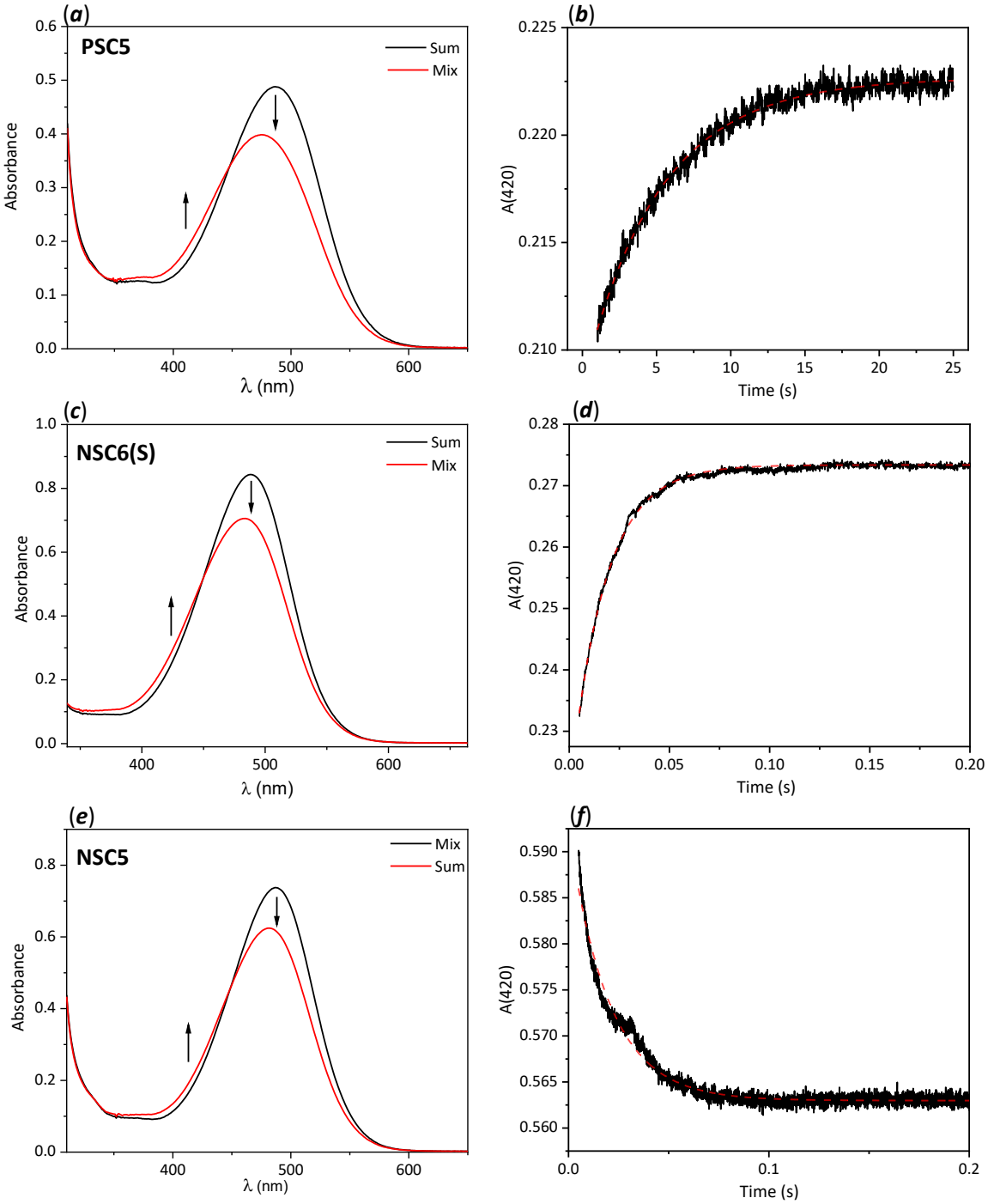

Figure 1.24. Top: Experimental values of threading (k_1) and dethreading (k_{-1}) constants; (***a***) Sum of the absorption spectra of a solution of **TPU** (c = 0.5×10^{-3} M) with an excess of TBATsO (c = 2.5×10^{-3} M) and **PSC5** (c = 2.5×10^{-5} M) (black line) and the absorption spectrum of the mixture of **TPU** and **PSC5** (red line) (CH_2Cl_2, 293 K);); (***b***) absorption changes at 420 nm (black dots) together with the fitting of the data (red dashed line)

for **TPU⊃PSC5** mixture; (***c***) sum of the absorption spectra of a solution of **TPU** (c = 0.5×10^{-3} M) with an excess of TBATsO (c = 2.5×10^{-3} M) and **NSC6(S)** (c = 2.5×10^{-5} M) (black line) and the absorption spectrum of the mixture of **TPU** and **NSC6(S)** (red line) (CH_2Cl_2, 293 K); (***d***) absorption changes at 420 nm (black dots) together with the fitting of the data (red dashed line) for **TPU⊃NSC6(S)** mixture; (***e***) sum of the absorption spectra of a solution of **TPU** (c = 0.5×10^{-3} M) with an excess of TBATsO (c = 2.5×10^{-3} M) and **NSC5** (c = 2.5×10^{-5} M) (black line) and the absorption spectrum of the mixture of **TPU** and **NSC5** (red line) (CH_2Cl_2, 293 K); (***f***) absorption changes at 420 nm (black dots) together with the fitting of the data (red dashed line) for **TPU⊃NSC5** mixture.

To investigate the directionality of the **NSC5** threading process with **TPU**, its kinetic constant was compared with those of **PSC5** and **NSC6(S)**. The kinetic constant for **PSC5** threading (**Figure 1.24**, (***a***)) was found to be three orders of magnitude lower than that of **NSC6(S)** (**Figure 1.24**, (***b***)), while the threading constant for **NSC5** (**Figure 1.24**, (***c***)) was nearly identical to that of **NSC6(S)**. Based on these data, it can be concluded that the threading mechanism of **NSC5** dye closely resembles that of **NSC6(S)**, suggesting that threading occurs with the *N,N*-dimethylamino group entering from the lower rim of the calix[6]arene. The observed selectivity from the lower rim of the calix[6]arene can be attributed to two primary factors. First, for the alkyl chain to enter the cavity, it must undergo desolvation and rigidification, which likely incurs a higher energetic cost compared to the entrance of the more rigid *N,N*-dimethylamino group. Second, since **NSC5** is soluble in dichloromethane, it is hypothesized that the ionic pair is already partially dissociated, reducing the significance of the phenylurea groups in disrupting the ionic pair and thereby diminishing the preference for complexation from the upper rim. DFT calculations and metadynamic studies are currently in progress to validate these hypotheses.

1.I Conclusions

This chapter presents an investigation into the formation of [2]pseudorotaxane isomers involving stilbazolium dyes and **TPU** calix[6]arene wheel. Two classes of stilbazolium dyes were examined: one containing an *N,N*-dimethylamino group on the aromatic ring of the stilbazolium core (**NSCn**), which facilitates complexation with the calix[6]arene, and another featuring a 3,5-dimethylpiperidine group (**PSCn**), which, due to its steric bulkiness, prevents complexation with the cavity. These stilbazolium dyes were subsequently alkylated at the pyridinium termini with varying alkyl chains to explore the effect of chain length on the threading process. The investigation was conducted using NMR, UV-Visible, and fluorescence spectroscopy. NMR analyses specifically highlighted the influence of alkyl chain length on the threading process. For stilbazolium dyes with long alkyl chains (**NSC18**, **PSC18**, **NSCS(6)**, and **PSC5**), the formation of both isomers at room temperature was detectable, indicating a slow exchange condition between the two orientational isomers. This slow interconversion is attributed to the long chains, which slow the isomerization process. In contrast, for stilbazolium dyes with methyl chains (**NSC1** and **PSC1**) the shorter chain promotes rapid interconversion between the two isomers, resulting in a fast exchange dynamic that

prevents the detection of both isomers on the NMR timescale. Variable-temperature NMR measurements for **NSC1** revealed that coalescence occurs at approximately 243 K, demonstrating that only at lower temperatures, where the interconversion process is sufficiently slowed, the two isomers can be distinguished. **NSC5** represents a unique case where the ***U*** isomer predominates at room temperature, but at lower temperatures, the ***D*** isomer becomes more prevalent. Variable-temperature NMR confirmed the isomerization process, showing the transition from the ***U*** to the ***D*** isomer as temperature decreases. These findings were further complemented by UV-Visible and fluorescence studies. A fast exchange regime was confirmed for stilbazolium dyes **NSC1** and **PSC1**; however, the kinetic analysis failed to capture the threading process due to its rapid nature. The binding constants determined for these dyes were comparable to those previously reported for di-alkyl viologen salts, indicating a strong association between the dye and the calix[6]arene. In contrast, the binding constants for **NSC18** and **PSC18** were determined to be three orders of magnitude lower than those for the methyl-substituted stilbazolium dyes. UV-Vis analysis of the **NSC5** dye confirmed the selective formation of the ***U*** isomer at room temperature, with an association constant of the same order of magnitude as that observed for **NSC18** and **PSC18** dyes. Stopped-flow kinetic analysis of **NSC5** threading, based on comparisons with the kinetics of stoppered stilbazolium dyes (**PSC5** and **NSC6(S)**), revealed a preferential directionality of the threading. Specifically, it was found that **NSC5** preferentially enters the calix[6]arene cavity *via* the *N,N*-dimethylamino group through the lower rim. In all cases, a significant enhancement in fluorescence quantum yield was observed, confirming that the interaction between the dyes and calix[6]arene can tune and enhance the fluorescence properties of the dyes.

1.I Experimental Section

General Methods

All solvents were dried using standard procedures; all other reagents were of reagent-grade quality obtained from commercial suppliers and used without further purification. Melting points are uncorrected. NMR spectra were recorded at 400 MHz for ^{1}H and 100 MHz for ^{13}C. Chemical shifts are expressed in ppm using the residual solvent signal as an internal reference (7.26 ppm for $CHCl_3$, 7.16 ppm for C_6D_5H, 5.32 for $CHDCl_2$, and 3.31 ppm for CD_2HOD). The terms m, s, d, t and q represent multiplet, singlet, doublet, triplet and quadruplet, respectively; "br. s" means a broad signal. Mass spectra were recorded in the ESI mode. Melting points were measured with a Gallenkamp melting-point apparatus and are uncorrected. UV–Vis spectra were recorded on a UV-Visible Cary 300 (Agilent). Fluorescence spectra were recorded on an Edinburgh Instrument FS5. Compounds **NS**[6], **C_5H_{11}OTs**[16], **$C_{18}H_{37}$OTs**[17], **DPAC_6H_{12}OTs**[18], **TPU**[19] and **1**[7] were synthesized according to published procedures.

Synthetic Procedure and Analytical Data

PS: under a nitrogen atmosphere, in a 100 mL round bottom flask, **1** (2.00 g, 9.2 mmol, 1.0 eq.) and *N*-methyl pyridine (0.86 g, 9.2 mmol, 1.0 eq.) were dissolved in dimethylformamide (40 mL). Then potassium *tert*-butoxide (1.24 g, 11.0 mmol, 1.8 eq.) was added. The reaction mixture was heated at 80 °C for 3 hours. After being cooled at room temperature, 200 mL of dichloromethane were added. The solution was washed with 200 mL of ice water and then three times with 200 mL of aqueous potassium hydroxide (1M). The organic phase was dried over sodium sulfate and then evaporated. The crude product was recrystallized from a 1:1 mixture of toluene/hexane to give **PS** (2.30 g) as an orange solid in 85% yield.

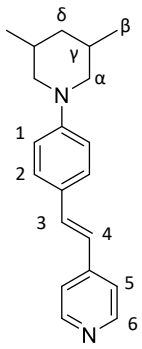

m.p. = 219-221 °C; **^{1}H NMR** ($CDCl_3$, 400 MHz): δ = 8.52 (d, 2H, J = 6.2 Hz, H_6), 7.42 (d, 2H, J = 8.8 Hz, H_5), 7.32 (d, 2H, J = 6.2 Hz, H_2), 7.23 (d, 1H, J = 16.3 Hz, H_4), 6.91 (d, 2H, J = 8.8 Hz, H_1), 6.82 (d, 1H, J = 16.3 Hz, H_3), 3.70 (m, 2H, $H_{\alpha'}$), 2.28 (t, 2H, J = 11.8 Hz, $H_{\alpha''}$), 1.81 (m, 3H, $H_{\delta'\text{-}\gamma}$), 0.94 (d, 6H, J = 6.5 Hz, H_β), 0.74 (q, 1H, J = 12.0 Hz, $H_{\delta''}$) ppm; **^{13}C NMR** ($CDCl_3$, 101 MHz): δ = 151.8, 149.1, 146.6, 134.2, 128.6, 126.0, 121.7, 120.7, 115.5, 56.3, 42.3, 30.8, 19.5. **ESI-MS (+):** calculated for $C_{20}H_{25}N_2^+$: m/z (z = 1): 293.2; found: 293.4.

General procedure for the synthesis of the stilbazolium salts.

In a 100 mL round bottom flask, **NS** or **PS** (1.3 mmol, 1.0 eq.) and the appropriate alkylating agent (1.7 mmol, 1.3 eq.) were dissolved in dry acetonitrile (40 mL). The reaction mixture was refluxed under vigorous stirring for 24 hours. Afterward, the solution was evaporated to dryness under reduced pressure.

NSC1: alkylation of **NS** with methyltosylate. The purification through column chromatography on silica gel (eluent: CH_2Cl_2/CH_3OH = 65/35) yields **NSC1** as a red solid in 80% yield.

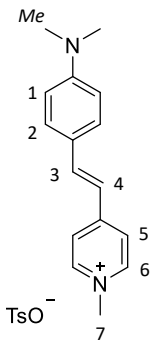

m.p. = 239-241 °C; **^{1}H NMR** (CD_3OD, 400 MHz): δ = 8.50 (d, 2H, *J* = 6.8 Hz, H_6), 7.96 (d, 2H, *J* = 6.8 Hz, H_5), 7.83 (d, 1H, *J* = 16 Hz, H_4), 7.72 (d, 2H, *J* = 8.1 Hz, $H_{Ar\text{-}H(TsO)}$), 7.62 (d, 2H, *J* = 8.9 Hz, H_2), 7.24 (d, 2H, *J* = 8.0 Hz, $H_{Ar\text{-}H(TsO)}$), 7.09 (d, 1H, *J* = 16.0 Hz, H_3), 6.80 (d, 2H, *J* = 8.9 Hz, H_1), 4.22 (s, 3H, H_7), 3.08 (s, 6H, H_{Me}), 2.37 (s, 3H, $H_{Me(TsO)}$) ppm; **^{13}C NMR** (CD_3OD, 101 MHz): δ = 154.7, 125.6, 143.8, 142.9, 142.2, 140.2, 130.1, 128.4, 125.6, 122.7, 122.1, 116.3, 111.7, 45.7, 38.8, 19.9. **ESI-MS (+):** calculated for $C_{16}H_{19}N_2^+$: m/z (z = 1): 239.2; found: 239.2.

NSC5: alkylation of **NS** with 1-pentyltosylate. Precipitation of the crude mixture from ethyl acetate yields **NSC5** as a red solid in 68%.

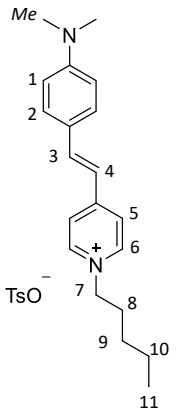

m.p. = 209-211 °C; **^{1}H NMR** (CD_3OD, 400 MHz): δ = 8.59 (d, 2H, *J* = 6.7 Hz, H_6), 7.99 (d, 2H, *J* = 6.6 Hz, H_5), 7.86 (d, 1H, *J* = 16.0 Hz, H_4), 7.73 (d, 2H, *J* = 8.1 Hz, $H_{Ar\text{-}H(TsO)}$), 7.63 (d, 2H, *J* = 8.9 Hz, H_2), 7.24 (d, 2H, *J* = 8.0 Hz, $H_{Ar\text{-}H(TsO)}$), 7.11 (d, 1H, *J* = 16.0 Hz, H_3), 6.81 (d, 2H, *J* = 8.9 Hz, H_1), 4.44 (t, 2H, *J* = 7.5 Hz, H_7), 3.09 (s, 6H, H_{Me}), 2.38 (s, 3H, $H_{Me(TsO)}$), 1.99 (m, 2H, H_8), 1.42 (m, 4H, $H_{9\text{-}10}$), 0.97 (t, 3H, *J* = 7.0 Hz, H_{11}) ppm; **^{13}C NMR** (CD_3OD, 101 MHz): δ = 155.0, 152.6, 143.1, 142.9, 142.3, 140.2, 130.2, 128.4, 125.9, 122.7, 122.3, 116.3, 111.7, 59.9, 38.8, 30.5, 27.9, 21.8, 19.9, 12.7. **ESI-MS (+):** calculated for $C_{19}H_{25}N_2^+$: m/z (z = 1): 281.2; found: 281.3.

NSC18: alkylation of **NS** with 1-octadecyltosylate. Precipitation of the crude mixture from ethyl acetate yields **NSC18** as a red solid in 63%.

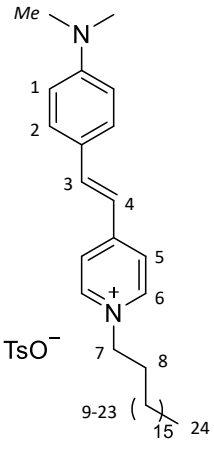

m.p. = 161 - 163 °C; **^{1}H NMR** (CD_3OD, 400 MHz): δ = 8.59 (d, 2H, *J* = 7.0 Hz, H_6), 7.99 (d, 2H, *J* = 6.6 Hz, H_5), 7.86 (d, 1H, *J* = 16.0 Hz, H_4), 7.73 (d, 2H, *J* = 8.2 Hz, $H_{Ar\text{-}H(TsO)}$), 7.63 (d, 2H, *J* = 8.9 Hz, H_2), 7.24 (d, 2H, *J* = 7.9 Hz, $H_{Ar\text{-}H(TsO)}$), 7.11 (d, 1H, *J* = 16.0 Hz, H_3), 6.81 (d, 2H, *J* = 9.0 Hz, H_1), 4.44 (t, 2H, *J* = 7.4 Hz, H_7), 3.09 (s, 6H, H_{Me}), 2.38 (s, 3H, $H_{Me(TsO)}$), 1.99 (m, 2H, H_8), 1.42-1.25 (m, 32H, $H_{9\text{-}23}$), 0.91 (t, 3H, *J* = 7.0 Hz, H24) ppm; **^{13}C NMR** (CD_3OD, 101 MHz): δ = 155.0, 152.6, 143.1, 142.9, 142.3, 140.2, 130.2, 128.4, 125.6, 122.7, 122.3, 116.3, 111.7, 59.9, 38.8, 31.7, 30.8, 29.4, 29.3, 29.2, 29.1, 28.7, 25.8, 22.3, 19.9, 13.0**. ESI-MS (+):** calculated for $C_{33}H_{53}N_2^+$: m/z (z = 1): 477.4; found: 477.4.

NSC6(S): alkylation of **NS** with 6-(tosyloxy)hexyl 2,2-diphenylacetate. The purification through column chromatography on silica gel (eluent: CH_2Cl_2/CH_3OH 90:10) yields **NSC6(S)** as a red solid in 63% yield.

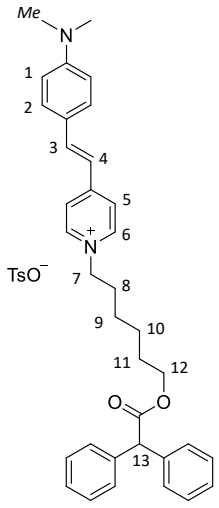

m.p. = 144-146 °C; **^{1}H NMR** ($CDCl_3$, 300 MHz): δ = 8.67 (d, 2H, *J* = 6.9 Hz, H_6), 7.84 (d, 2H, *J* = 8.1 Hz, H_5), 7.75 (d, 2H, *J* = 6.6 Hz, $H_{Ar\text{-}H(TsO)}$), 7.46 (d, 1H, *J* = 15.9 Hz, H_4), 7.31 (d, 2H, *J* = 9.0 Hz, H_2), 7.29 (m, 10H, $H_{Ar\text{-}H(DPA)}$), 7.12 (d, 2H, *J* = 8.1 Hz, $H_{Ar\text{-}H(TsO)}$), 6.74 (d, 1H, *J* = 15.9 Hz, H_3), 6.63 (d, 2H, *J* = 9.0 Hz, H_1), 5.01 (s, 1H, H_{13}), 4.35 (t, 2H, *J* = 5.4 Hz, H_7), 4.06 (t, 2H, *J* = 5.1 Hz, H_{12}), 3.02 (s, 6H, H_{Me}), 2.29 (s, 3H, $H_{Me(TsO)}$), 1.75 (m, 2H, H_8), 1.51 (m, 2H, H_{11}), 1.18 (m, 4H, $H_{9\text{-}10}$) ppm; **^{13}C NMR** ($CDCl_3$, 101 MHz): δ = 172.5, 153.9, 152.1, 144.2, 143.5, 142.5, 139.1, 138.7, 130.5, 128.7, 128.6, 127.2, 126.0, 122.8, 122.5, 116.6, 111.9, 65.0, 59.8, 57.1, 40.1, 31.4, 28.4, 25.5, 25.2, 21.3; **ESI-MS (+):** calculated for $C_{35}H_{39}N_2O_2^+$: m/z (z = 1): 519.3; found: 519.2.

PSC1: alkylation of **PS** with methyltosylate. Precipitation of the crude mixture from ethyl acetate yields **PSC1** as a yellow solid in 92%.

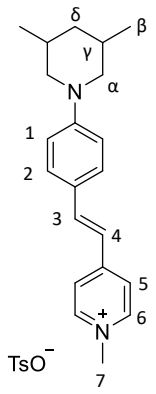

m.p. = 233-235 °C; **^{1}H NMR** (CD_3OD, 400 MHz): δ = 8.53 (d, 2H, *J* = 6.9 Hz, H_6), 7.99 (d, 2H, *J* = 7.0 Hz, H_5), 7.82 (d, 1H, *J* = 16.1 Hz, H_4), 7.72 (d, 2H, *J* = 8.2 Hz, $H_{Ar\text{-}H(TsO)}$), 7.61 (d, 2H, *J* = 8.9 Hz, H_2), 7.24 (d, 2H, *J* = 8.0 Hz, H $H_{Ar\text{-}H(TsO)}$), 7.12 (d, 1H, *J* = 16.0 Hz, H_3), 6.99 (d, 2H, *J* = 8.9 Hz, H_1), 4.23 (s, 3H, H_7), 3.90 (m, 2H, $H_{\alpha'}$), 2.39 (m, 5H, $H_{Me(TsO),\,\alpha''}$), 1.87 (m, 1H, $H_{\delta'}$), 1.75 (m, 2H, H_γ), 0.98 (d, 6H, *J* = 6.6 Hz, H_β), 0.83 (q, 1H, *J* = 12.1 Hz, $H_{\delta''}$) ppm; **^{13}C NMR** (CD_3OD, 101 MHz): δ = 154.6, 152.9, 143.9, 142.4, 142.2, 140.3, 130.1, 128.4, 125.6, 122.3, 117.2, 114.3, 55.0, 45.8, 42.1, 30.4, 19.9, 18.1. **ESI-MS (+):** calculated for $C_{21}H_{27}N_2^+$: m/z (z = 1): 307.2; found: 307.3.

PSC5: alkylation of **PS** with 1-pentyltosylate. Precipitation of the crude mixture from ethyl acetate yields **PSC5** as a red solid in 68%.

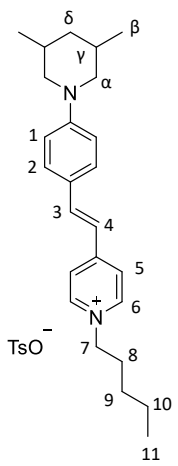

m.p. = 190-192 °C; **^{1}H NMR** ($CDCl_3$, 400 MHz): δ = 8.74 (d, 2H, *J* = 6.8 Hz, H_6), 7.84 (d, 2H, *J* = 8.2 Hz, $H_{Ar\text{-}H(TsO)}$), 7.81 (d, 2H, *J* = 6.7 Hz, H_5), 7.50 (d, 1H, *J* = 16.0 Hz, H_4), 7.45 (d, 2H, *J* = 9.0 Hz, H_2), 7.15 (d, 2H, *J* = 8.1 Hz, $H_{Ar\text{-}H(TsO)}$), 6.84 (d, 2H, *J* = 8.9 Hz, H_1), 6.78 (d, 1H, *J* = 16.1 Hz, H_3), 4.45 (t, 2H, *J* = 7.4 Hz, H_7), 3.78 (m, 2H, $H_{\alpha'}$), 2.36 (t, 2H, *J* = 12.0 Hz, $H_{\alpha''}$), 2.32 (s, 3H, H_{Me}), 1.85 (m, 3H, $H_{\delta'\text{-}8}$), 1.74 (m, 2H, H_γ), 1.25 (m, 4H, $H_{9\text{-}10}$), 0.94 (d, 6H, *J* = 6.6 Hz, H_β) 0.83 (t, 3H, *J* = 7.0 Hz, H_{11}), 0.78 (q, 1H, *J* = 12.0 Hz, $H_{\delta''}$) ppm; **^{13}C NMR** ($CDCl_3$, 101 MHz): δ = 153.8, 152.6, 144.0, 143.7, 142.2, 139.1, 130.5, 128.6, 126.1, 123.0, 117.3, 114.4, 60.4, 55.2, 42.2, 31.2, 30.6, 28.1, 22.1, 21.3, 19.3, 13.8; **ESI-MS (+):** calculated for $C_{25}H_{35}N_2^+$: m/z (z = 1): 363.3; found: 363.4.

PSC18: alkylation of **PS** with 1-octadecyltosylate. Precipitation of the crude mixture from ethyl acetate yields **PSC18** as a red solid in 82%.

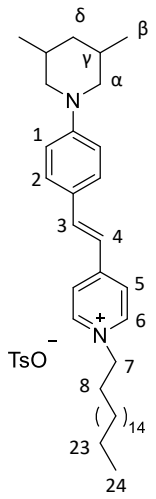

m.p. = 158-160 °C; **^{1}H NMR** ($CDCl_3$, 400 MHz): δ = 8.75 (d, 2H, *J* = 6.7 Hz, H_6), 7.85 (d, 2H, *J* = 8.2 Hz, $H_{Ar\text{-}H(TsO)}$), 7.82 (d, 2H, *J* = 6.9 Hz, H_5), 7.52 (d, 1H, *J* = 16.0 Hz, H_4), 7.45 (d, 2H, *J* = 8.9 Hz, H_2), 7.15 (d, 2H, *J* = 7.9 Hz, $H_{Ar\text{-}H(TsO)}$), 6.85 (d, 2H, *J* = 8.7 Hz, H_1), 6.79 (d, 1H, *J* = 16.1 Hz, H_3), 4.47 (t, 2H, *J* = 7.4 Hz, H_7), 3.78 (m, 2H, $H_{\alpha'}$), 2.36 (t, 2H, *J* = 12.0 Hz, $H_{\alpha''}$), 2.33 (s, 3H, H_{Me}), 1.85 (m, 3H, $H_{\delta'\text{-}8}$), 1.76 (m, 2H, H_γ), 1.25 (m, 30H, $H_{9\text{-}23}$), 0.95 (d, 6H, *J* = 6.6 Hz, H_β) 0.87 (t, 3H, *J* = 6.8 Hz, H_{24}), 0.79 (q, 1H, *J* = 12.1 Hz, $H_{\delta''}$) ppm; **^{13}C NMR** ($CDCl_3$, 101 MHz): δ = 154.0, 152.8, 144.3, 143.8, 142.4, 139.1, 130.7, 128.7, 126.2, 123.2, 117.4, 114.6, 60.6, 55.4, 42.4, 32.1, 31.7, 30.8, 29.9, 29.8, 29.8, 29.7, 29.5, 29.5, 29.2, 26.3, 22.8, 21.5, 19.4, 14.3; **ESI-MS (+):** calculated for $C_{38}H_{61}N_2^+$: m/z (z = 1): 545.5; found: 545.6.

PSC6(S): alkylation of **PS** with 6-(tosyloxy)hexyl 2,2-diphenylacetate. The purification through column chromatography on silica gel (eluent: CH_2Cl_2/CH_3OH 90:10) yields **PSC6(S)** as a red solid in 55% yield.

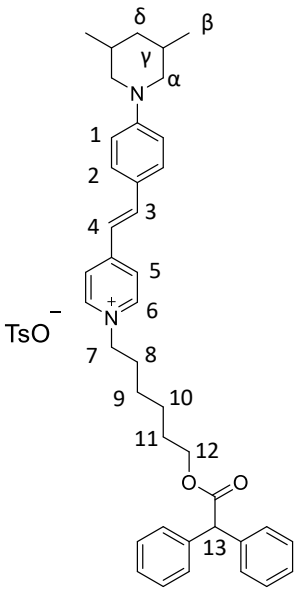

m.p. = 149-151 °C; **^{1}H NMR** (CD_3OD, 400 MHz): δ = 8.54 (d, 2H, *J* = 6.6 Hz, H_6), 7.96 (d, 2H, *J* = 6.7 Hz, H_5), 7.81 (d, 1H, *J* = 16.0 Hz, H_4), 7.71 (d, 2H, *J* = 8.2 Hz, $H_{Ar\text{-}H(TsO)}$), 7.60 (d, 2H, *J* = 9.0 Hz, H_2), 7.33-7.22 (m, 10H, $H_{Ar\text{-}H(DPA)}$), 7.10 (d, 1H, *J* = 16.0 Hz, H_3), 6.97 (d, 2H, *J* = 8.9 Hz, H_1), 5.06, (s, 1H, H_{13}), 4.35 (t, 2H, *J* = 7.4 Hz, H_7), 4.15 (t, 2H, *J* = 6.4 Hz, H_{12}), 3.88 (m, 2H, $H_{\alpha'}$), 2.37 (t, 2H, *J* = 12.0 Hz, $H_{\alpha''}$), 2.33 (s, 3H, H_{Me}), 1.86 (m, 3H, $H_{\delta'\text{-}8}$), 1.71 (m, 2H, H_γ), 1.62 (m, 2H, H_9), 1.25 (m, 4H, $H_{10\text{-}11}$), 0.96 (d, 6H, *J* = 6.6 Hz, H_β) 0.80 (q, 1H, *J* = 12.1 Hz, $H_{\delta''}$) ppm; **^{13}C NMR** ($CDCl_3$, 101 MHz): δ = 174.2, 156.2, 154.3, 144.0,141.6, 140.3, 131.6, 129.8, 129.7, 129.6, 128.3, 127.0, 125.5, 124.0, 118.6, 115.7, 65.9, 61.1, 58.3, 56.3, 43.5, 32.0, 31.8, 29.3, 26.5, 26.2, 21.3, 19.5; **ESI-MS (+):** calculated for $C_{40}H_{47}N_2O_2^+$: m/z (z = 1): 587.4; found: 587.6.

1.II Stilbazolium dyes on gold nanoparticles

1.II Introduction

In the previous section, the formation of oriented [2]pseudorotaxane species was examined. NMR analyses revealed that the ratio between the two oriented [2]pseudorotaxane isomers was influenced by the length of the alkyl chain attached to the stilbazolium core. Notably, the study demonstrated that the complexation of stilbazolium dyes within the **TPU** calix[6]arene macrocycle leads to an enhancement in the fluorescence of the dyes, likely attributable to a rigidification of their molecular structure. Based on these findings, we aimed to examine the effect of complexation on the fluorescence characteristics of the dyes, with the aim of developing a fluorescence-based "switch off-on" system. This system was designed to leverage the unique optical properties of gold nanostructures, which are known to modulate the fluorescence of nearby dye molecules. As mentioned in the introduction of the first section, in the literature a few examples on the encapsulation of stilbazolium dyes have been reported. However, while the modification of dye properties through macrocycle complexation has been extensively explored, particularly in the context of calixarenes, cucurbiturils, and cyclodextrins (see general Introduction), the investigation of this phenomenon on metal surfaces, especially gold, remains limited in the current scientific literature. Gold nanoparticles (AuNPs) are particularly intriguing due to their distinct optical and electronic properties, including plasmonic resonance and ultrahigh molar extinction coefficients. Of particular interest is the localized surface plasmon resonance (LSPR), which offers a range of exploitable properties. A key focus of our research is the quenching/enhancement of fluorescence of dyes in proximity to the gold surface. As discussed in Chapter 4, the fluorescence of dyes on the surface of AuNPs can be either enhanced or diminished, depending on the distance between the dye and the gold nanoparticle, and the spectral overlap between plasmon absorption and dye's emission.[20] In general, at short distances from the Au surface, the non-radiative energy transfer from the excited state of the dye to the metal predominates, favoring the quenching of the fluorescence. While the enhancement of the fluorescence is favored at long distances. The interaction between the plasmonic properties of gold nanomaterials and the supramolecular complexation of fluorescent guests represents a field that deserves further exploration.

In this section, we explore the complexation of stilbazolium-based dyes within the calix[6]arene macrocycle immobilized on the surface of AuNPs. Specifically, we synthesized two novel stilbazolium dyes, **NSC12OLip** and **PSC12OLip**, both featuring a terminal disulfide group crucial for anchoring to the gold surface (**Figure 1.25**). The choice of these dyes is driven by their "push-pull" and electron-poor molecular structure, which complements the electron-rich triphenylureido (**TPU**) calix[6]arene cavity. This recognition is also facilitated by the interaction of the tosylate anion with

the phenyl ureido groups, as previously demonstrated by our research group.[3] The complexation of these dyes on the gold surface with calix[6]arene macrocycle was investigated using fluorescence spectroscopy. The emission properties of such a system were evaluated both before and after the complexation to develop a "switch on-off" hybrid system. By investigating the behavior of these novel stilbazolium-based dyes on gold nanoparticles, we aim to deepen our understanding of supramolecular complexation of fluorophores on metal surfaces, thereby contributing valuable insights to the broader knowledge in this scientific domain.

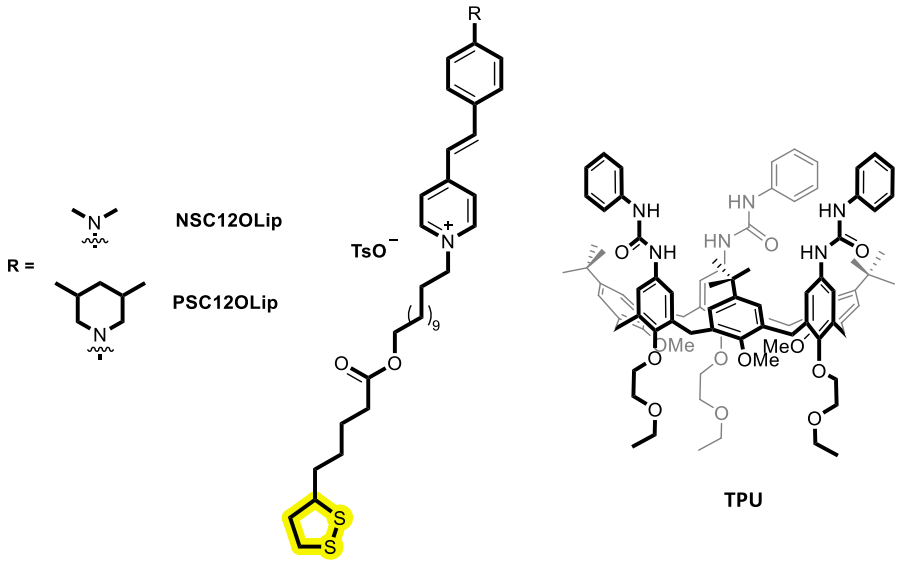

Figure 1.25 Structure of novel stilbazolium dyes **NSC12OLip** and **PSC12OLip**, and **TPU** wheel.

1.II Results and Discussion

II. Synthesis, NMR and optical characterization of lipoic-based stilbazolium dyes

To functionalize the surface of AuNPs, we synthetized two novel stilbazolium dyes, each distinguished by different terminal functionalization on the aromatic ring. The target compounds were obtained *via* a two-step synthesis, starting from known styryl pyridines para-substituted on their benzene ring with either an *N,N*-dimethylamino (**NS**), or 3,5-dimethylpiperidine (**PS**) group (**Scheme 1.4**). In the first step, the pyridine was alkylated with an ω-hydroxy dodecyl chain. In the second step, the resulting alkylated stilbazolium dyes **NSC12OH** and **PSC12OH** underwent a coupling reaction with lipoic acid using EDC·HCl as the coupling reagent, affording **NSC12OLip** and **PSC12OLip** as red solid compounds with yields of 73% and 89%, respectively.

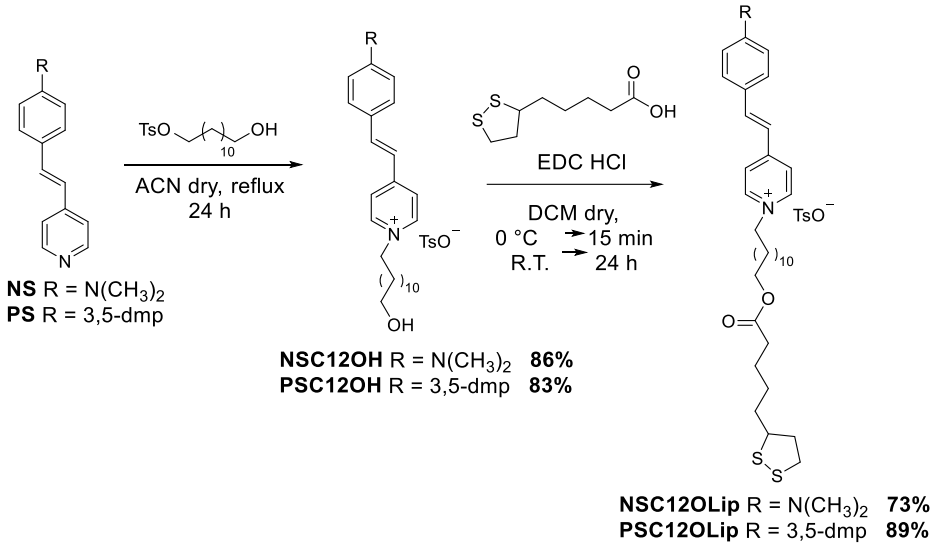

Scheme 1.4 Synthetic scheme of the synthesis of **NSC12OLip** and **PSC12OLip**.

The target products were characterized by NMR spectroscopy and ESI-MS measurements. The full peaks' assignment was achieved by performing several 2D NMR measurements, particularly HSQC experiments (see **Figure 1.27**). ^{1}H NMR spectra of these compounds (**Figure 1.26**) were characterized by the signals from the pyridinium ring at 8.58 and 7.97 ppm (protons labeled as *6* and *5*); the double bond resonates at 7.85 and 7.10 ppm (3 and *4*), while the electron-rich aromatic unit gives rise to two peaks at 7.61 and 6.79 ppm (*2* and *1*). Tosylate counterion resonates as two doublets at 7.71 and 7.23 ppm and as a singlet at 2.38 ppm relative to the methyl group. The triplet relative to the methylene group adjacent to the protonated nitrogen (*7*) resonates at 4.42 ppm, while the triplet at 4.06 ppm is associated with the methylene group near the ester moiety (*18*).

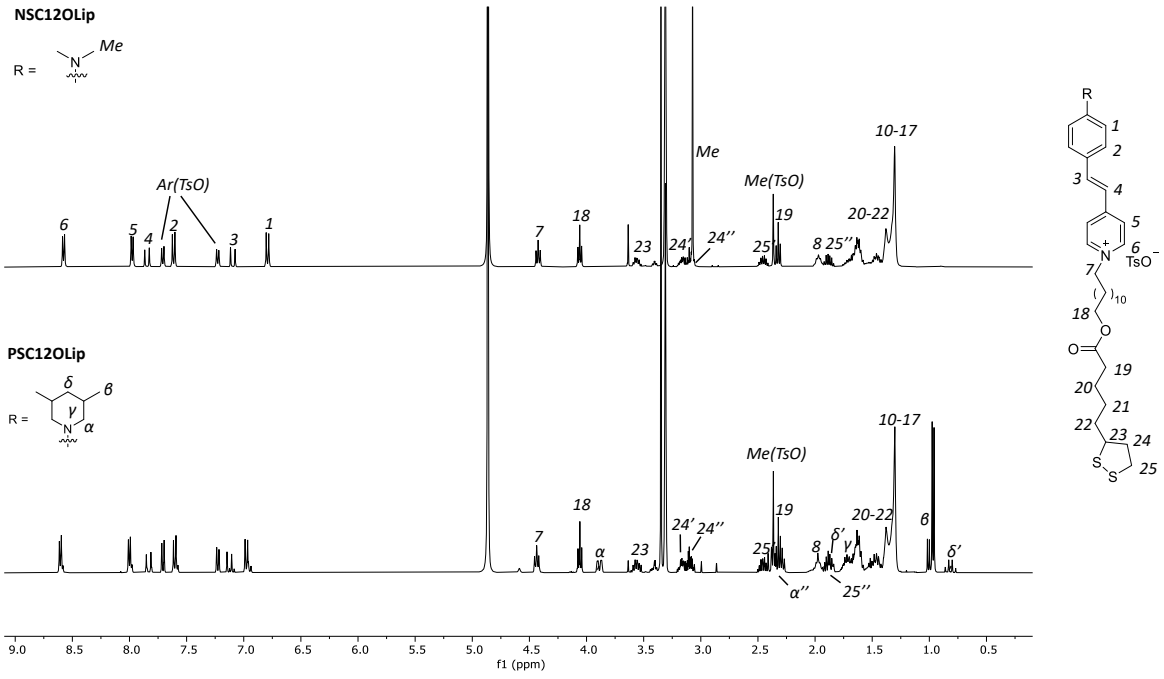

Figure 1.26. ^{1}H NMR spectra (CD_3OD, 400 MHz, 298 K) of **NSC12OLip** (top) and **PSC12OLip** (bottom).

The high field region is particularly crowded, notably for **PSC12OLip**, where both the lipoic acid residue and 3,5-dimehtylpiperidine moiety contribute to the splitting of various proton signals due to diasterotopic protons. In both **NSC12OLip** and **PSC12OLip**, protons labeled as *24* and *25* exhibit two distinct signals due to their diasterotopic nature: multiplets between 3.0-3.2 ppm correspond to protons labeled as *24'* and *24''*, while multiplets centered at 2.4 ppm and 1.9 ppm correspond to protons labeled as *25'* and *25''*. In the spectrum of **NSC12OLip**, the singlet at 3.09 ppm is attributed to the methylene group of the *N,N*-dimethyl amino group, while the spectrum of **PSC12OLip** exhibits several other peaks due to the presence of 3,5-dimethylpiperidine group: the methyl groups, labeled *β*, resonate as a doublet at 0.99 ppm, and the proton *γ* corresponds to the multiplet centered at 1.75 ppm. Diastereotopic protons *α* and *δ* generate two distinct signals each: the multiplet centered at 3.90 ppm and the one at 2.39 ppm relative to protons labeled as *α'* and *α''*, the multiplet centered at 1.88 ppm corresponding to proton labeled as *δ'* and the quadruplet at 0.83 ppm correspond to proton labeled as *δ''*. The 2D HSQC spectrum of **PSC12OLip** (see **Figure 1.27**), recorded in deuterated methanol, is reported as an example of the comprehensive peaks assignment. In the high-field region of the spectrum, it is possible to distinguish all the signals corresponding to the protons of the alkyl chain, the lipoic acid residue, and the 3,5-dimethylpiperidine group.

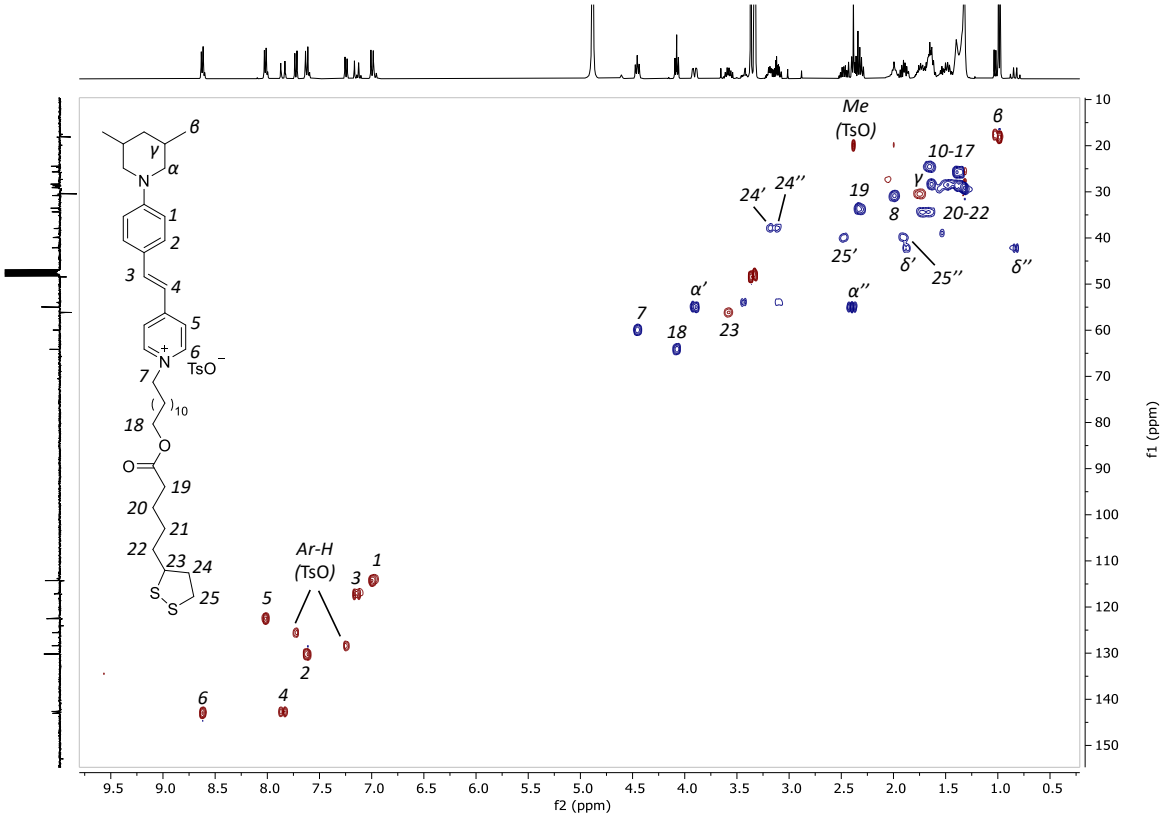

Figure 1.27. Edited HSQC NMR spectrum (400 MHz, CD_3OD, 298 K) of **PSC12OLip**. Positive peaks (CH_3 and CH) are shown in red, while negative ones (CH_2) are in blue.

The two dyes were also characterized using UV-Visible and fluorescence spectroscopy. The UV-Vis spectra and emission profiles of both **NSC12OLip** and **PSC12OLip** in toluene were nearly identical (**Figure 1.28**). For **NSC12OLip**, the maximum absorption (c = 5.85×10^{-5} M, λ_{max}^{abs} = 469 nm) and emission (c = 1.05×10^{-5} M, λ_{max}^{em} = 589 nm) result in a significant Stokes shift (ΔSt = 120 nm, 4344 cm^{-1}), with no fine structure observed in the fluorescence spectrum. Similarly, for **PSC12OLip** the maximum absorption (c = 3.88×10^{-5} M, λ_{max}^{abs} = 463 nm) and emission (c = 4.09×10^{-6} M, λ_{max}^{em} = 599 nm) result in a significant Stokes shift (ΔSt = 136 nm, 4904 cm^{-1}). The large Stokes shift observed is crucial for minimizing self-quenching of the fluorescence emission through self-absorption.

	λ_{max}^{abs} [nm]	λ_{max}^{em} [nm]	Stoke Shift [nm, cm^{-1}]	ε [mol^{-1}cm^{-1} L]
NSC12OLip	469	589	120, 4344	12058
PSC12OLip	463	599	136, 4904	15180

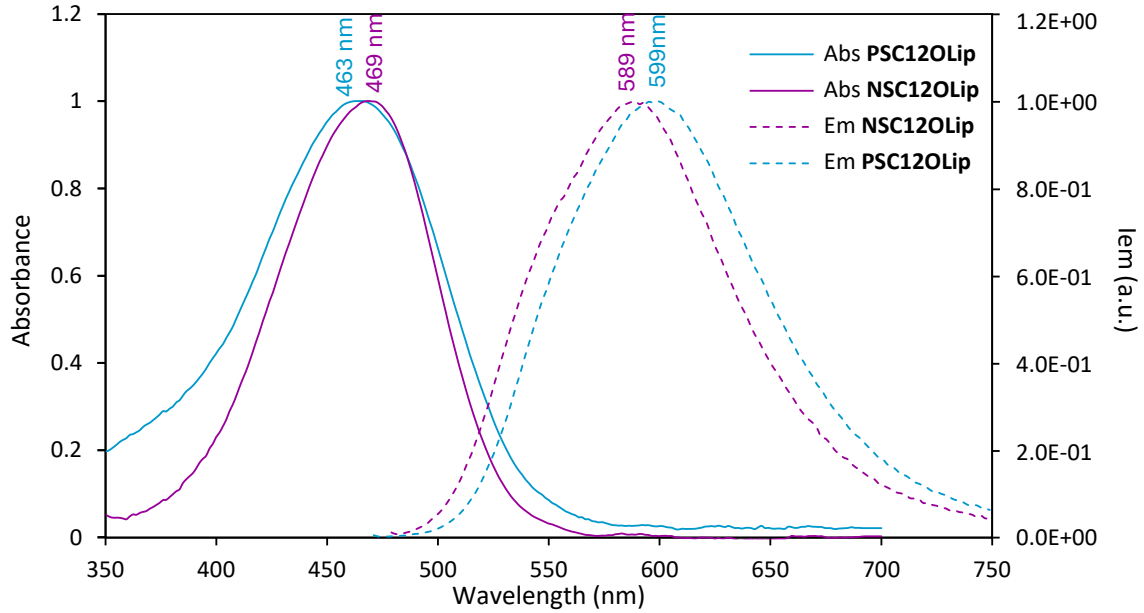

Figure 1.28. Normalized absorption (continuous lines) and emission (dashed lines) spectra of **NSC12OLip** (violet lines) and **PSC12OLip** (blue lines) in toluene at 298 K. Excitation wavelength for **NSC12OLip** is 474 nm and for **PSC12OLip** is 466 nm.

II. NMR complexation study in solution

An initial evaluation of the affinity between **TPU** and the newly synthesized **NSC12OLip** or **PSC12OLip** dyes was conducted in deuterated chloroform. It was indeed crucial to determine whether the lipoic unit attached to the stilbazolium core would hinder the threading of these dyes into the calix[6]arene cavity, leading to the formation of [2]pseudorotaxanes **TPU⊃NSC12OLip** and **TPU⊃PSC12OLip**. Additionally, it was important to assess how this bulky substituent might affect the distribution of the corresponding orientational isomers up (***U***) and down (***D***) (see **Scheme 1.5**). The formation of [2]pseudorotaxane orientational isomers mixture was analyzed as usual through

NMR measurements and UV-Vis analyses. 1D and 2D NMR spectra were taken in deuterated chloroform using an equimolar (1:1) mixture **NSC12OLip** or **PSC12OLip** with **TPU**. ^{1}H NMR spectra of the resulting mixtures were notably intricate, necessitating HSQC measurements for a thorough analysis.

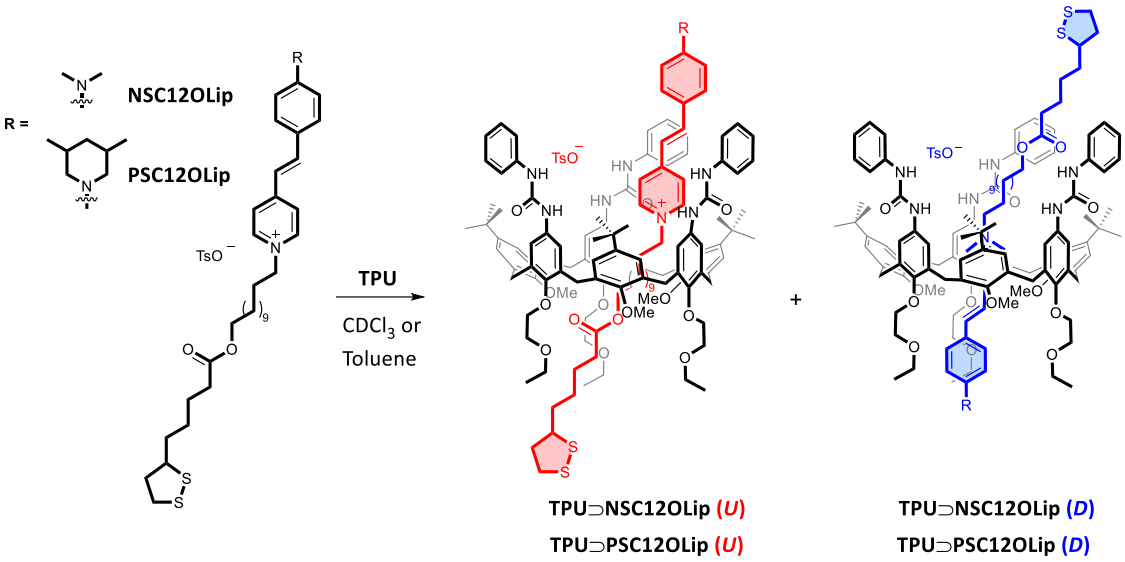

Scheme 1.5. Synthetic scheme of the complexation of **NSC12OLip** and **PSC12OLip** with **TPU** wheel. Representation of the two possible [2]pseudorotaxane: up isomer (***U***) in red and down isomer (***D***) in blue.

Figure 1.29 illustrates the ^{1}H NMR stack plot of **NSC12OLip** (bottom), recorded in CD_3OD for solubility reasons, alongside its 1:1 mixture with **TPU** (top) in $CDCl_3$. In the **TPU⊃NSC12OLip** spectrum, the upfield shifts of the stilbazolium aromatic protons - from 6.81 to 5.71 ppm for proton *1* (see dashed pink lines) and from 8.58 ppm to 6.17 ppm for proton *6* (see dashed pink line) - along with their splitting, provided clear evidence of complexation of the dye stilbazolium core within the electron-rich cavity of **TPU**. Interestingly, the signals related to the lipoic acid residue remain largely unchanged, indicating that this segment is not encapsulated within the cavity. Similar to the behavior observed with the dyes discussed in the previous section, the splitting of the aromatic signals arises from the presence of the two orientational isomers. This observation is further supported by the distinct signals of the *N,N*-dimethyl amino group protons: the resonance at 3.11 ppm corresponds to the ***D*** isomer (in blue), while the one at 2.63 ppm is attributed to the ***U*** isomer (in red). Integration of these signals indicates a 50:50 distribution between the two isomers. When compared to the result for **NSC18** and **NSC6(S)** (see **Table 1.1**, previous section), it appears that for para-dimethylamino substituted stilbazolium dyes, the nature of the alkyl chain attached to the stilbazolium core does not significantly impact the stability of the orientational isomers in chloroform solution at room temperature, indicating that the two orientations of the stilbazolium core into the cavity are nearly energetically degenerate.

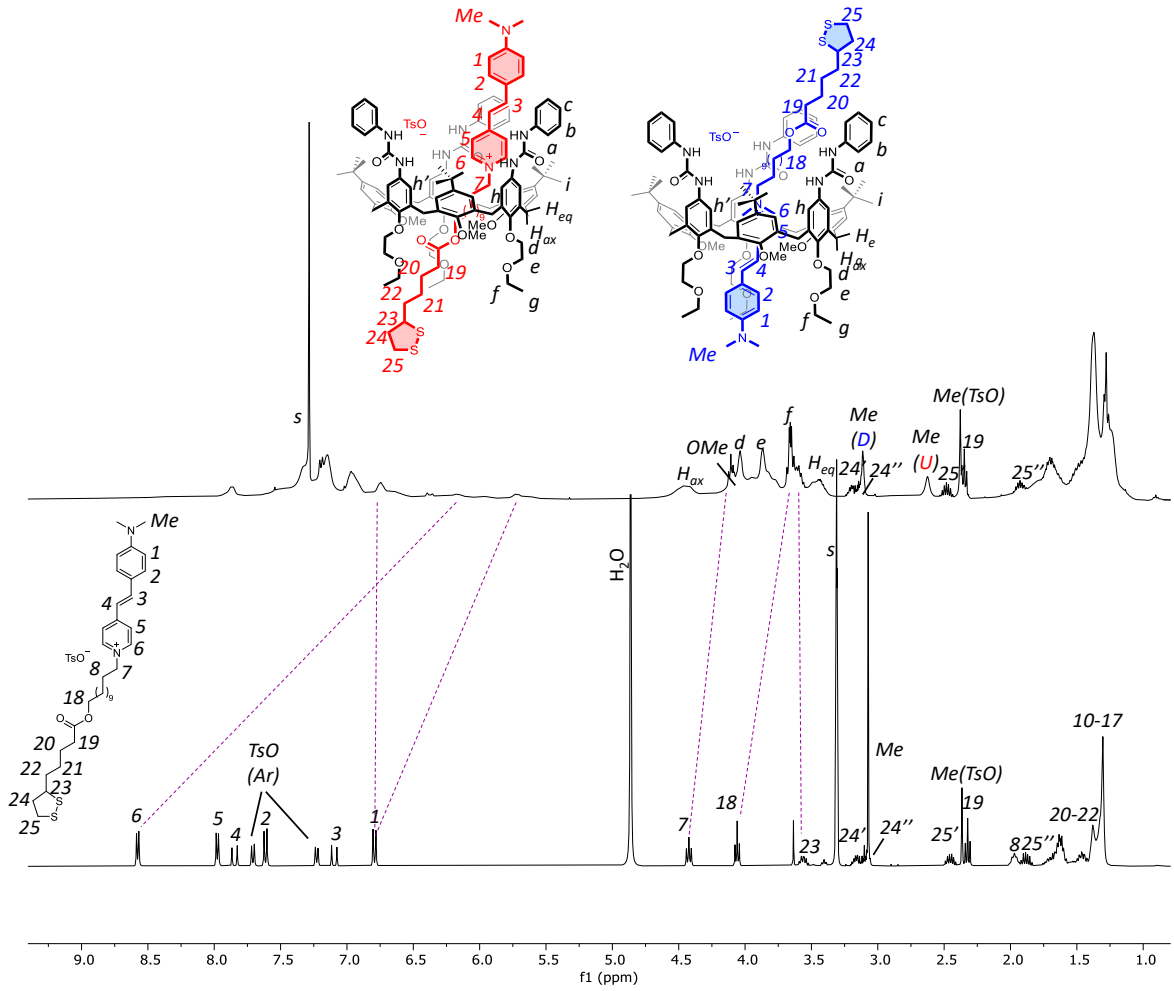

Figure 1.29. ^{1}H NMR stack plot of the 1:1 mixture of **TPU** and **NSC12OLip** in $CDCl_3$ (top) and of **NSC12OLip** in CD_3OD (bottom).

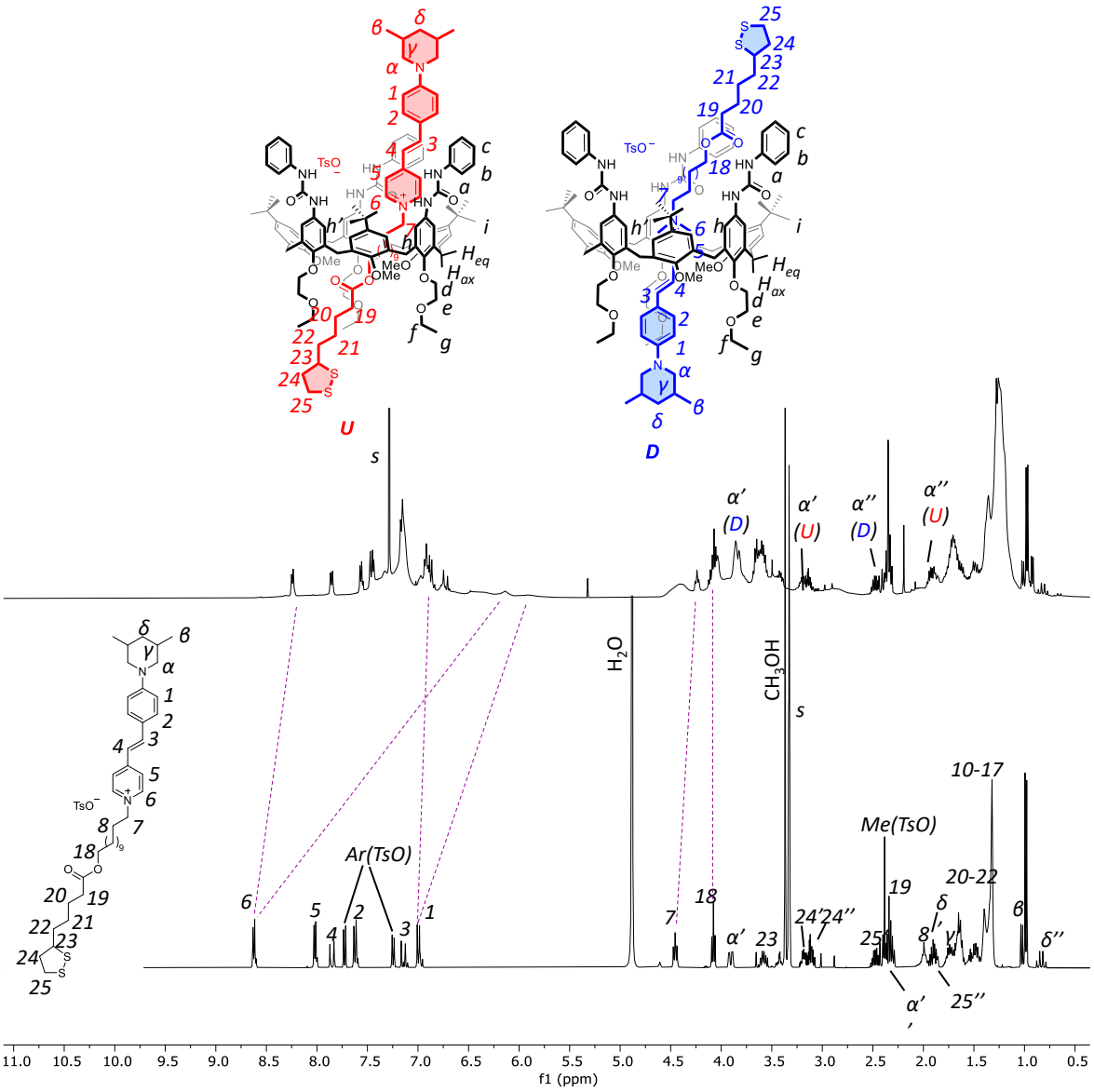

Figure 1.30. ^{1}H NMR stack plot (400 MHz, 298 K) of the 1:1 mixture of **TPU** and **PSC12OLip** in $CDCl_3$ (top) and of the **PSC12OLip** in CD_3OD (bottom).

Similarly, complexation between **PSC12OLip** and **TPU** in deuterated chloroform was evidenced by the shifts of the aromatic protons in **PSC12OLip** (**Figure 1.30**). Protons *6*, initially resonating at 8.62 ppm, shifted and split into two signals at 8.24 and 6.14 ppm (see dashed pink line), while protons *1* shifted and split from 6.98 to 6.87 and 5.90 ppm (see dashed pink line). As with **NSC12OLip**, this splitting is attributed to the presence of the two orientational isomers, while the lipoic acid residue resonances remain almost unchanged. The formation of these isomers was confirmed *via* 2D NMR spectroscopy. Specifically, in the HSQC spectrum (**Figure 1.31**), the ***U*** and ***D*** isomers were identified by the splitting of the diasterotopic protons *α′* and *α″*, each giving rise to two distinct signals: in the ***D*** isomer, *α′* was observed by the cross-peak at *F*1,*F*2 =55,3.84 ppm and *α″* at *F*1,*F*2 =55,2.41 ppm, whereas for the ***U*** isomer, *α′* appeared at *F*1,*F*2 =55,3.24 ppm and *α″* at *F*1,*F*2 =55,1.93 ppm. Approximate quantification of the isomers distribution, based on the integration of the *α′* and *α″*

cross-peaks, revealed a ***U***:***D*** ratio of 30:70. This suggests that the lipoic acid residue can interact with the **TPU** cavity from both the upper and lower rims since the 3,5-dimethylpiperidine group cannot enter the cavity. The unbalanced isomer ratio suggests a higher stability for the ***D*** isomer. (cf also **Table 1.2**, previous section).

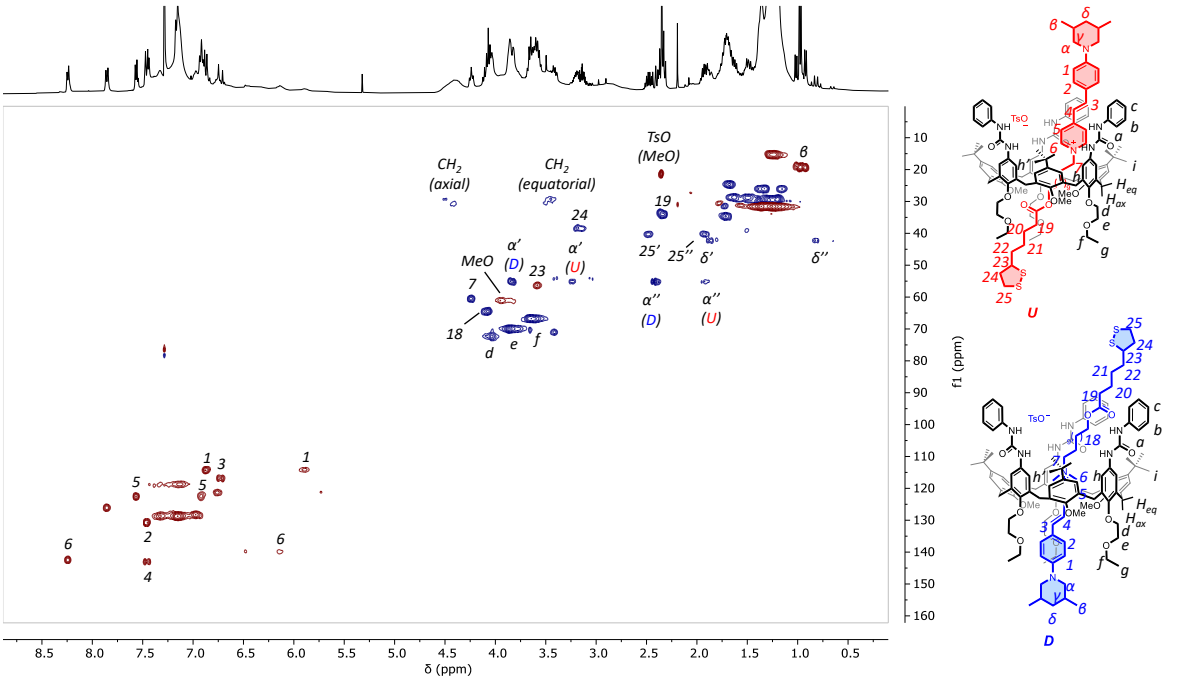

Figure 1.31. Edited HSQC NMR spectrum (400 MHz, $CDCl_3$, 298 K) of a 1:1 mixture of **TPU** and **PSC12OLip**. Positive peaks (CH_3 and CH) are shown in red, while negative ones (CH_2) are in blue.

II. UV-Visible complexation study

The formation of the [2]pseudorotaxane orientational isomers was also studied using UV-Visible spectroscopy. Specifically, UV-Vis titrations were conducted in toluene by monitoring the absorbance spectrum of a solution containing the appropriate stilbazolium dye while incrementally adding a **TPU** solution. Toluene was chosen as the solvent because it was employed in the synthesis of the gold nanoparticles (see next). **Figure 1.32** shows the results of **NSC12OLip** and **PSC12OLip** titrations with **TPU**. For **NSC12OLip** (**Figure 1.32**, left), the addition of the **TPU** led to a gradual blue shift of the absorbance maximum (from 468 nm to 432 nm), accompanied by the appearance of a fluorescent yellow hue in the solution. In contrast, **PSC12OLip** (**Figure 1.32**, right) exhibited a progressive red shift of the absorbance maximum (from 458 nm to 480 nm) and the development of a fluorescent orange coloration. The absorption changes were fitted with a 1:1 complexation model, yielding an apparent association constant of log$K$ = 4.30±0.09 for **NSC12OLip**, and of log$K$ = 4.60±0.07 for **PSC12OLip**.

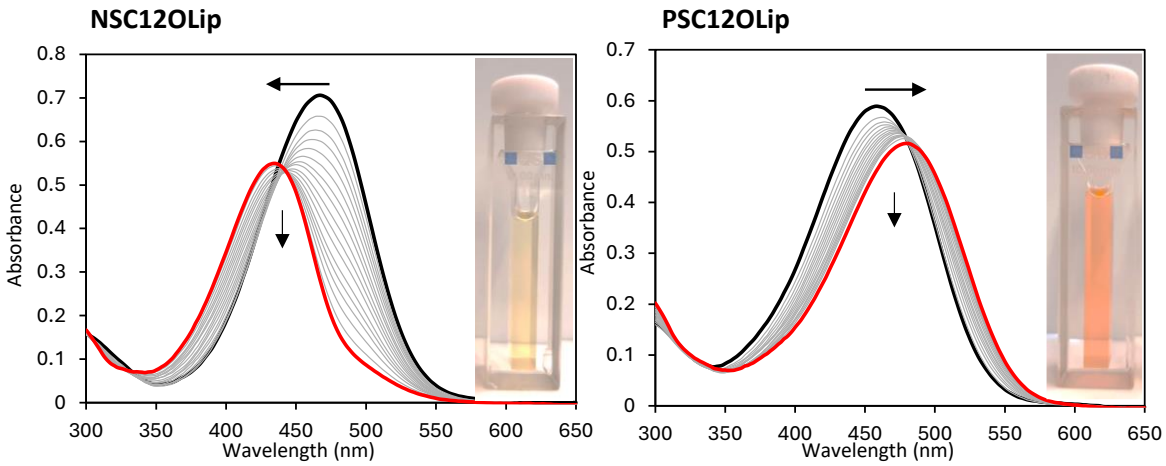

Figure 1.32. Left: Collection of UV-Vis absorption spectra (toluene, 298 K) taken during the titration of **NSC12OLip** (c = 5.85×10^{-5} M) with **TPU** (c = 1.23×10^{-4} M). A progressive blue-shift of the **NSC12OLip** band was observed together with a decrease in absorbance; right: Collection of UV-Vis absorption spectra (toluene, 298 K) taken during the titration of **PSC12OLip** (c = 3.88×10^{-5} M) with **TPU** (c = 1.23×10^{-4} M). A progressive red-shift of the **PSC12OLip** band was observed together with a decrease in absorbance. The arrows indicate the titration evolution.

To correlate the absorption band shifts with the distribution of the orientational isomers in solution, the results were compared with those previously reported for the [2]rotaxane orientational isomers **R-*Up*** and **R-*Down***.[3] For the former rotaxane, the maximum absorbance was found at 468 nm, while for the latter it was at 425 nm.[3] Interestingly, the final absorbance maximum for **TPU⊃PSC12OLip** (480 nm) resembled the one of **R-*Up*** rotaxane, whereas **TPU⊃NSC12OLip** (432 nm) aligned more closely with that of **R-*Down*** rotaxane. This latter result would not be, however, directly comparable since in **TPU⊃NSC12OLip** the para substituent (Me_2N) of the stilbazolium core is not identical to that of the two rotaxanes.

The above findings do not match the NMR analyses, which indicated ***U*:*D*** isomers ratio of 50:50 and 30:70 for **TPU⊃NSC12OLip** and **TPU⊃PSC12OLip**, respectively. Instead, the UV-Vis results suggest a preferential formation of the ***U*** isomer for **TPU⊃PSC12OLip** and the ***D*** isomer for **TPU⊃NSC12OLip**. It is important to note that the UV-Vis titrations were performed at lower concentrations (c ~ 10^{-5}M) compared to the NMR measurements (c ~ 10^{-3} M), which may account for the difference in the ***U*:*D*** isomers ratios (see previous section).

Further UV-Vis analysis was conducted to investigate the behavior of the two orientational isomers as a function of the temperature, using toluene as the solvent. The UV-Vis spectra of **TPU⊃NSC12OLip** and **TPU⊃PSC12OLip** were recorded at temperatures ranging from 298 to 343 K. For **TPU⊃NSC12OLip**, a new low energy shoulder band emerged at high temperatures, with an isosbestic point at 456 nm (**Figure 1.33**, left). This behavior suggests that the initially favored ***D*** isomer becomes less stable at high temperatures, allowing the ***U*** isomer to emerge. For **TPU⊃PSC12OLip**, the changes were less pronounced, with only a small blue-shift of the absorbance

maximum and an isosbestic point at 390 nm was detected (**Figure 1.33**, right). In this case, it thus seems that the temperature increment does not significantly affect the ***D***:***U*** isomers ratio, but there is a small indication that the ***U*** isomer could be more favored at high temperatures.

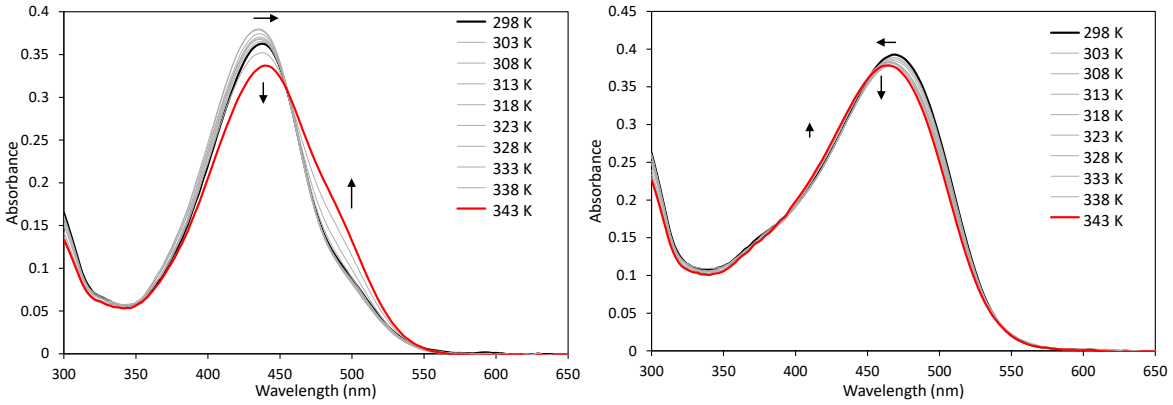

Figure 1.33. Collection of UV-Vis absorption spectra of **TPU⊃NSC12OLip** (left) and **TPU⊃PSC12OLip** (right) taken a variable temperature from 298 K to 343 K in toluene.

II. Nanomaterial Synthesis and Studies

The investigation of the **TPU** and **NSC12OLip**/**PSC12OLip** system in solution using NMR and UV-Vis spectroscopy revealed a strong host-guest interaction between the two components, resulting in the formation of two distinct isomers. Once the formation of the [2]pseudorotaxanes was evaluated, we proceeded with the organic hybridization of gold nanoparticles and conducted fluorescence studies. The strategy employed was based on a "switch off-on" fluorescence mechanism, leveraging both the plasmonic resonances of gold nanoparticles and the complexation capabilities of the calix[6]arene cavity. Specifically, the initial fluorescence of the dye was quenched upon functionalization with the gold nanoparticles, and fluorescence was subsequently restored upon complexation with the calix[6]arene wheel. To investigate this phenomenon, we used **NSC12OLip**, which can complex with the calix[6]arene cavity *via* its *N,N*-dimethylamino group, and **PSC12OLip**, which, due to the presence of the 3,5-dimethylpiperidine ring, is unable to form such a complex by this termini. In the case of **NSC12OLip**, an increase in fluorescence should be observed, while for **PSC12OLip**, fluorescence should remain unchanged due to the impossibility of threading the calix[6]arene wheel.

II. Synthesis of functionalized AuNPs. The synthesis of hybrid nanomaterials was accomplished through the covalent functionalization of gold nanoparticles with **NSC12OLip** and **PSC12OLip**. The ~5 nm AuNPs employed in this study were synthesized using the well-established Schiffrin procedure,[21] yielding toluene-soluble AuNPs stabilized electrostatically with tetraoctylammonium bromide (**AuNPs-TOABr**). Therefore, the synthesis of functionalized **AuNPs-NSC12OLip** and **AuNPs-**

PSC12OLip was achieved by exchanging the electrostatic stabilizer with the terminal disulfide group of the two dyes (**Scheme 1.6**).

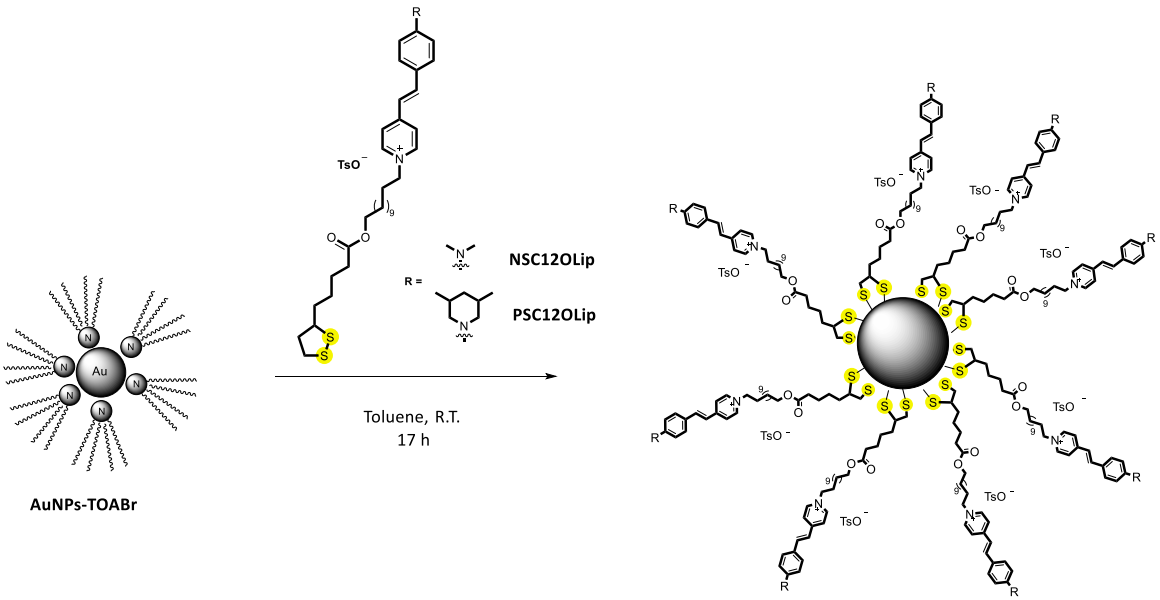

Scheme 1.6. Synthetic scheme for the synthesis of **AuNPs-NSC12OLip** and **AuNPs-PSC12OLip**.

The exchange involved stirring a 2 mL toluene solution of **NSC12OLip** (c = 7.15×10^{-4}M) or **PSC12OLip** (c = 6.81×10^{-4}M) with a freshly prepared solution of **AuNPs-TOABr** (c = 4.5×10^{-3}M, 6 mL) in toluene for 17 hours. The driving force behind this process is the enhanced stability of the Au-S bonding compared to the electrostatic stabilization between the positively charged gold surface and the bromide anions of TOABr. The resultant functionalized **AuNPs-NSC12OLip** and **AuNPs-PSC12OLip** were purified by three 10-minute-long centrifugation cycles 9,000 r.p.m. and redispersed in dichloromethane (3 mL).

AuNPs decorated with the [2]pseudorotaxanes **TPU⊃NSC12OLip** and **TPU⊃PSC12OLip** were prepared in a similar manner (**Scheme 1.7**). The pseudorotaxane species were initially prepared in toluene solution by mixing **TPU** and **XSC12OLip** in 1:1 ratio (c = 9.01×10^{-4}M for **NSC12OLip** and c = 8.97×10^{-4}M for **PSC12OLip**). After standing for 1 hour under stirring to ensure the formation of the [2]pseudorotaxanes, a solution of **AuNPs-TOABr** (c = 4.5×10^{-3}M) in toluene was added, and the resulting mixture was stirred for further 17 hours. The resulting **AuNPs-TPU⊃NSC12OLip** and **AuNPs-TPU⊃PSC12OLip** nanoparticles were purified through three 10-minute-long centrifugation cycles 9,000 r.p.m. and redispersed in dichloromethane (3 mL).

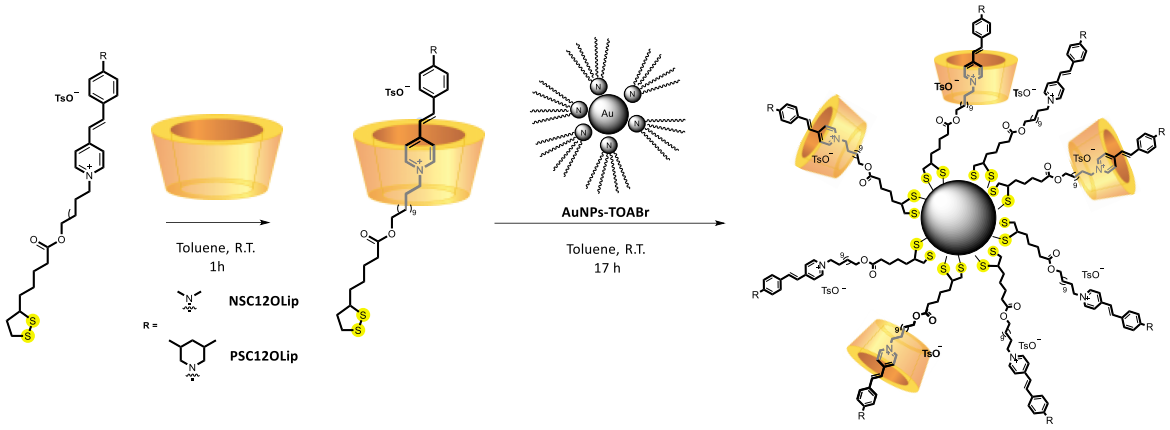

Scheme 1.7. Synthetic scheme of the synthesis of **AuNPs-TPU⊃NSC12OLip** and **AuNPs-TPU⊃PSC12OLip**.

*II. Characterization of the functionalized AuNPs***.** The functionalized AuNPs were characterized through UV-Vis spectroscopy and X-ray Photoelectron Spectroscopy (XPS) measurements. **Figure 1.34** shows the stacking of the UV-Vis spectra of the free stilbazolium dyes, the unfunctionalized **AuNPs-TOABr**, the resultant dyes-hybridized nanoparticles, and the pseudorotaxane-functionalized nanoparticles. The absorbing band of both dyes (red and pink lines in **Figure 1.34**) presents a good overlap with the plasmonic band of the tetrabutylammonium-stabilized nanoparticles **AuNPs-TOABr** (λ_{max} = 525 nm, **Figure 1.34**, black line), particularly with the high-energy interband portion of the nanoparticles spectrum. Upon hybridization with the dyes, the resulting nanoparticles, **AuNPs-NSC12OLip** (**Figure 1.34**, top, green line) and **AuNPs-PSC12OLip** (**Figure 1.34**, bottom, blue line), afford spectra characterized by a broad absorbance band having a maximum centered at 521 and 526 nm, respectively, slightly shifted from the original **AuNPs-TOABr** band. Direct hybridization with the pseudorotaxanes **TPU⊃NSC12OLip** and **TPU⊃PSC12OLip** results in UV-Vis spectra displaying maxima at 526 nm for **AuNPs-TPU⊃NSC12OLip** (**Figure 1.34**, top, green dashed line) and at 532 nm for **AuNPs-TPU⊃PSC12OLip** (**Figure 1.34,** bottom, blue dashed line). The relatively narrower broadening of these bands, compared to **AuNPs-NSC12OLip** and **AuNPs-PSC12OLip**, suggests reduced nanoparticle aggregation, likely because the stilbazolium cores of **NSC12OLip** and **PSC12OLip** are encapsulated into the **TPU** molecules.

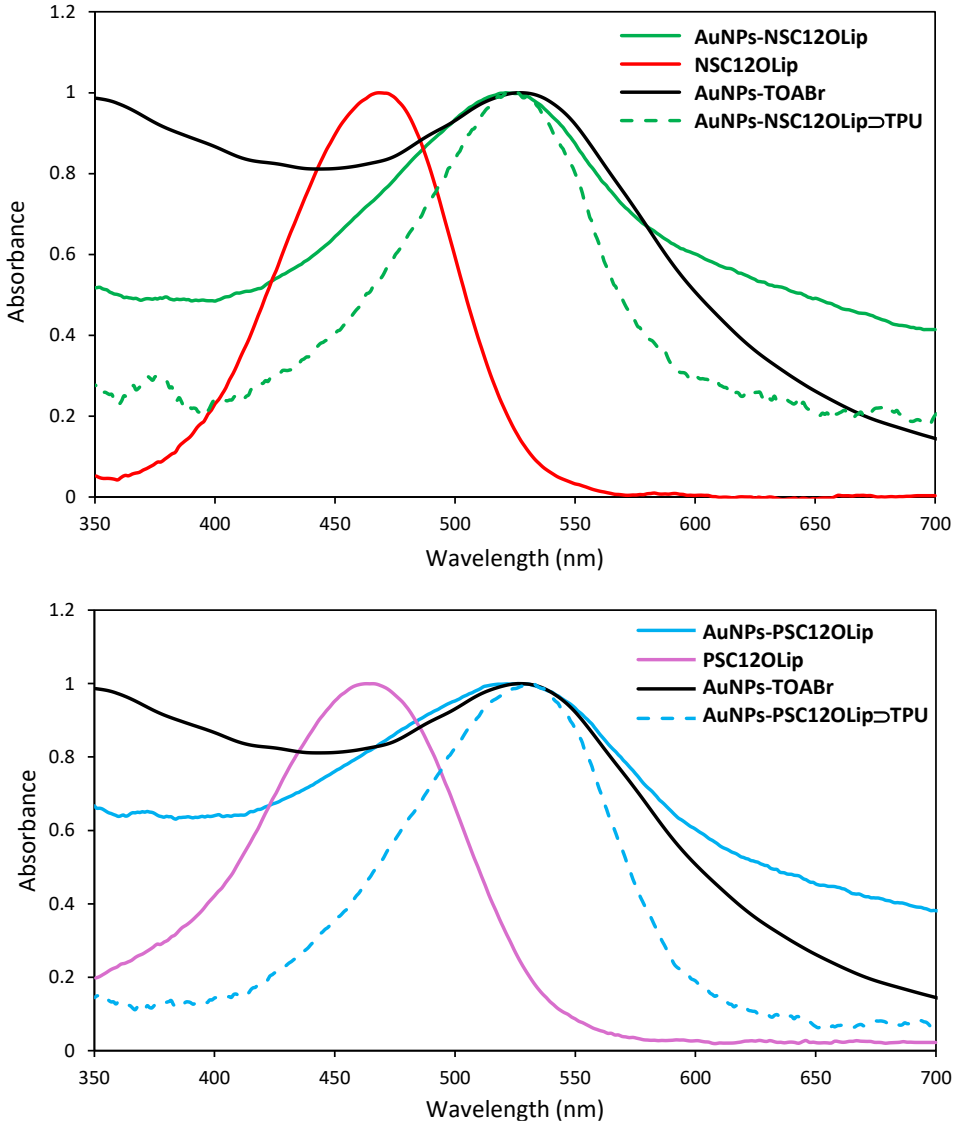

Figure 1.34. Top: normalized absorption spectra of the plasmonic band of **AuNPs-TOABr** (black line), **NSC12OLip** (red line), **AuNPs-NSC12OLip** (green line) and **AuNPs-TPU⊃NSC12OLip** (green dashed line); bottom: normalized absorption spectra of the plasmonic band of **AuNPs-TOABr** (black line), **PSC12OLip** (pink line), **AuNPs-PSC12OLip** (blue line) and **AuNPs-TPU⊃PSC12OLip** (blue dashed line).

XPS analyses of free stilbazolium dyes, **TPU** and functionalized AuNPs were conducted in collaboration with Andrea Marrani of the University of Roma "La Sapienza". The free stilbazolium dyes were analyzed using a monochromatized source (Al Kα 1486,7 eV). The samples were prepared by drop casting a dichloromethane solution of **NSC12OLip** and **PSC12OLip** on a graphite grid. As expected, the XPS spectra revealed both nitrogen N1s and sulfur S2p peaks were detected (**Figure 1.35**). For sulfur, two distinct signals were observed: a lower binding energy peak attributed to the sulfur of the lipoic acid residue (**Figure 1.35**, dark green line), and a higher binding energy peak associated with the sulfur in the tosylate anion (**Figure 1.35**, pink line). The N1s spectra show two signals in both dyes: one at lower binding energy (**Figure 1.35**, red line), corresponding to the neutral amine nitrogen from the dimethylamino or the piperidine group, and another at higher

energy values (**Figure 1.35**, green line) associated with the positively charged pyridinium nitrogen. This indicates that the positive charge is localized exclusively on the aromatic nitrogen in both cases. Furthermore, the measured N/S, S/S_{ox}, and N^+/N ratios were consistent with the theoretical values (**Figure 1.35**, table). Similarly, the XPS analysis of **TPU** yielded N/C and N/O ratios closely matching the expected values based on the carbon and oxygen content of this calix[6]arene (**Figure 1.36**).

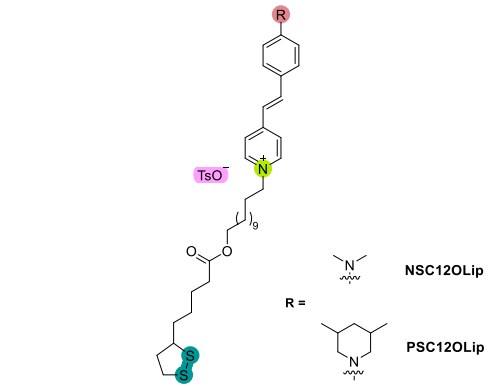

	N/S (theo.)	S/S_{ox} (theo.)	N^+/N (theo)
NSC12OLip	0.78 (0.67)	2.2 (2)	0.70 (1)
PSC12OLip	0.85 (0.67)	2.6 (2)	0.60 (1)

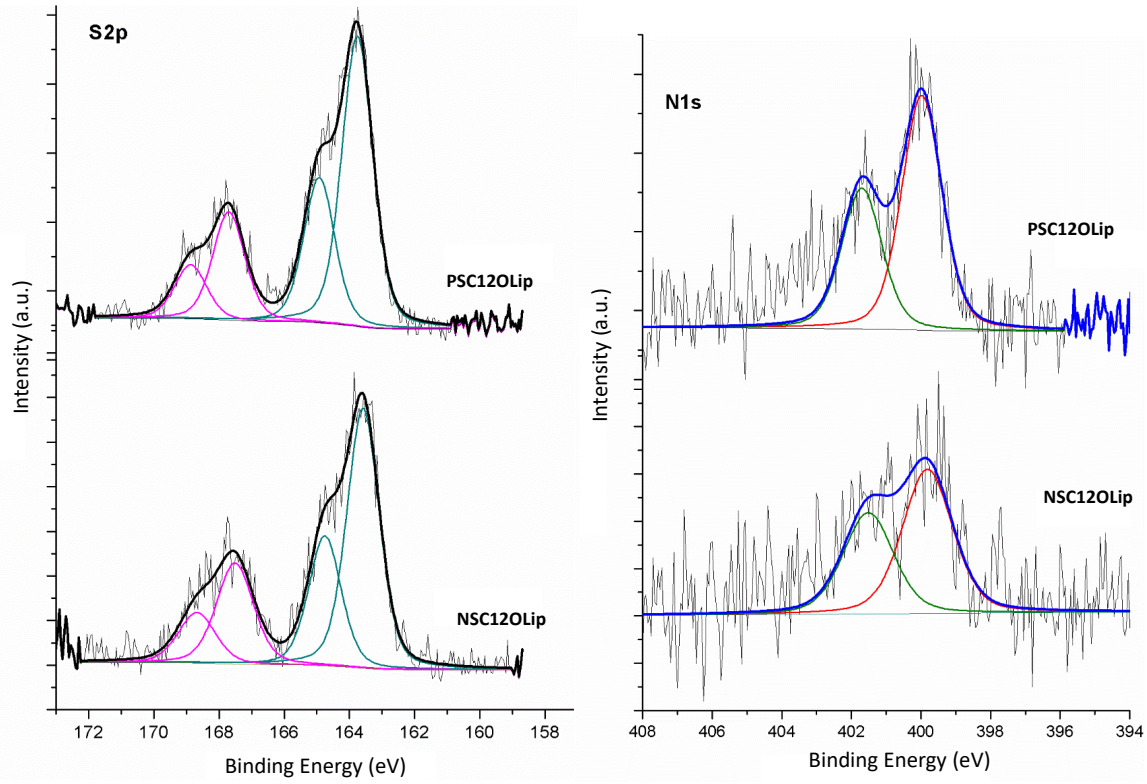

Figure 1.35. XPS analysis of **NSC12OLip** and **PSC12OLip**. Left: narrow scan spectrum of S 2p, S signal due to the contribution of the lipoic residue (dark green line) and the tosylate (pink line); right: narrow scan spectrum of N 1s, N signal due to the contribution of the aromatic nitrogen (green line) and the nitrogen of the R residue (red line); Table: XPS relative quantitative ratios for **NSC12OLip** and **PSC12OLip**.

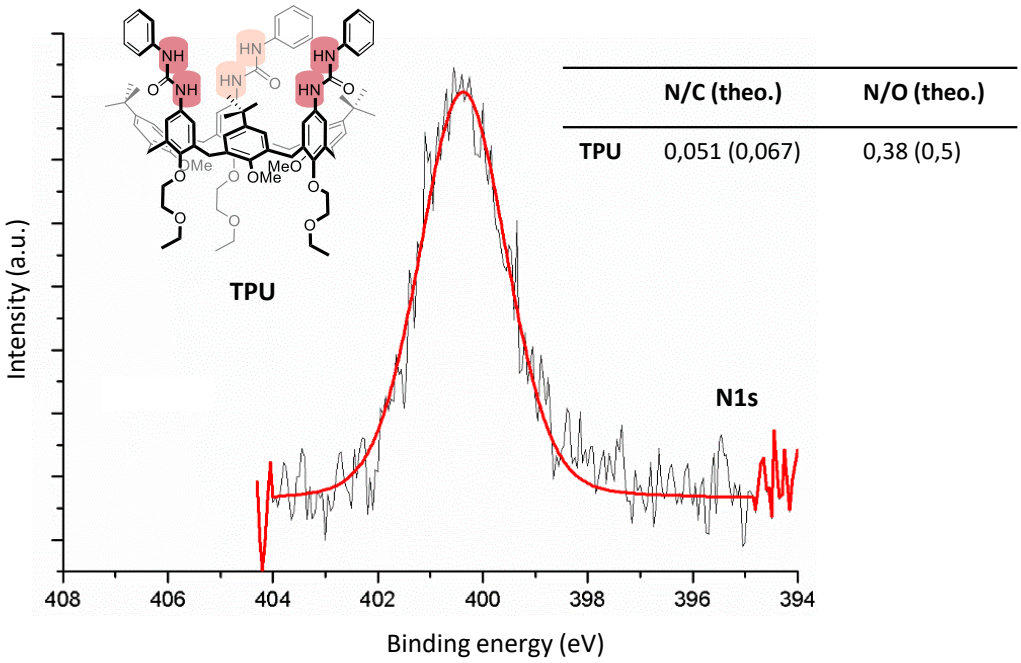

	N/C (theo.)	N/O (theo.)
TPU	0,051 (0,067)	0,38 (0,5)

Figure 1.36. XPS analysis of **TPU**: narrow scan spectrum of N 1s, N signal due to the sole contribution of the ureidic nitrogen (red line); right: XPS relative quantitative ratios for **TPU**.

XPS measurements were also performed for the dye- and pseudorotaxane-functionalized AuNPs using a non-monochromatized source, which resulted in broader signal peaks for both N1s and S2p regions. Despite this, similar observations were made across all samples: for sulfur (S2p), two signals were distinctively observed: the higher binding energy signal corresponds to the tosylate anion, while the one at lower binding energy was associated with the newly formed S-Au bond. The shift to a lower binding energy compared to the S-S signal in the free stilbazolium dye confirmed the formation of the S-Au bond. For nitrogen (N1s), two peaks were identified after the band deconvolution: the higher energy signal (**Figure 1.37**, green line) was attributed to the positively charged nitrogen, while the lower energy signal (**Figure 1.37**, red line) was associated with the neutral nitrogen. In samples containing [2]pseudorotaxanes on the surface, **AuNPs-TPU⊃NSC12OLip** and **AuNPs-TPU⊃PSC12OLip**, the intensity of the red component, relative to neutral nitrogen, was significantly higher compared to the green one. This increase indicates the presence of nitrogen from the phenyl urea groups in **TPU**, confirming the stability of the complex on the nanoparticle surface, which remained intact without dissociation.

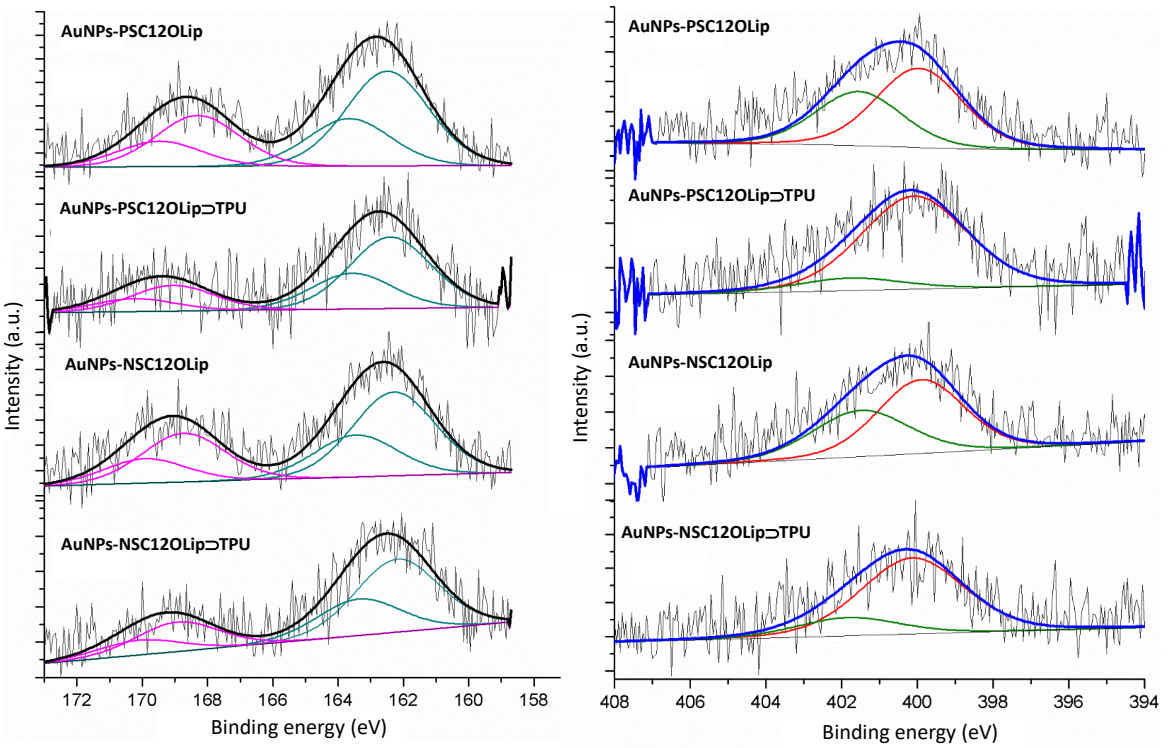

Figure 1.37. XPS analysis of **AuNPs-NSC12OLip, AuNPs-PSC12OLip, AuNPs-TPU⊃NSC12OLip** and **AuNPs-TPU⊃PSC12OLip**. Left: narrow scan spectrum of S 2p, S signal due to the contribution of the lipoic residue (dark green line) and the tosylate (pink line); right: narrow scan spectrum of N 1s, N signal due to the contribution of the positive charged nitrogen (green line) and the neutral nitrogen (red line).

Quantitative analysis revealed deviations between the experimental and theoretical values (**Table 1.6**). For both **AuNPs-NSC12OLip** and **AuNPs-PSC12OLip**, the measured N/S ratio was higher than the theoretical one, indicating a lower sulfur content than the predicted one. This discrepancy can be attributed to the positioning of the sulfur atoms in the dyes, which are in contact with the nanoparticle surface and located beneath the organic layer. As a result, signal attenuation occurs, leading to reduced sulfur detection and, consequently, lower sulfur values than those expected.

Table 1.6. XPS relative quantitative ratios for **AuNPs-NSC12OLip, AuNPs-PSC12OLip, AuNPs-TPU⊃NSC12OLip** and **AuNPs-TPU⊃PSC12OLip**.

	Au (%)	S (%)	N (%)	N/S (theo.)	S/S_{ox} (theo.)	S/Au
AuNPs-NSC12OLip	67.8	16.2	16.0	0.99 (0.66)	1.72 (2)	0.24
AuNPs-PSC12OLip	60.7	19.0	20.3	1.07 (0.66)	1.85 (2)	0.31
TPU⊃AuNPs-NSC12OLip	64.1	11.7	24.2	2.10 (2.7)	2.50 (2)	0.18
TPU⊃AuNPs-PSC12OLip	68.4	12.9	18.7	1.45 (2.7)	2.70 (2)	0.19

The XPS analysis of **AuNPs-TPU⊃NSC12OLip** and **AuNPs-TPU⊃PSC12OLip** revealed that the experimental N/S values were lower than the theoretical ones. These values suggest only a partial

complexation of the dyes on the surface of the nanoparticles. This result is not entirely unexpected and suggests two potential scenarios: (a) partial decomplexation of the dye from **TPU** before its grafting onto the AuNPs surface, or (b) decomplexation occurring during the AuNPs purification steps. On the other hand, the lower N/S value determined for **AuNPs-TPU⊃PSC12OLip** compared to **AuNPs-TPU⊃NSC12OLip** (1.45 vs. 2.10) does not support the latter hypothesis (b). If decomplexation occurred during the purification steps, we would expect the experimental N/S value for **AuNPs-TPU⊃NSC12OLip** to be lower than that for **AuNPs-TPU⊃PSC12OLip** because of the nature of the latter species. Indeed, once the **TPU⊃PSC12OLip** pseudorotaxane is linked to the surface, it is converted into a [2]rotaxane, with the gold surface of the nanoparticles acting as the second stopper. In these conditions, the calix[6]arene macrocycle becomes fully confined along the thread near the gold surface. It cannot be released into the bulk even in successive purification steps. Instead, hypothesis (a) seems more plausible, supported by the observation that the S/Au ratio is lower in samples containing the calix[6]arene macrocycle. The steric hindrance of **TPU** likely inhibits effective surface packing, suggesting that partial release of **TPU** may occur before dye grafting on the surface, allowing for better surface covering. Overall, XPS data confirmed the successful covalent functionalization of AuNPs with both the stilbazolium dyes and the [2]pseudorotaxane complexes.

II. Fluorescence study. An investigation into the fluorescence properties of the system was undertaken with the aim to develop a hybrid system capable of exhibiting “switch on-off” fluorescence emission. Firstly, the fluorescence behavior of stilbazolium dyes interfaced with **AuNPs-TOABr** surface was studied. To elucidate the impact of AuNPs plasmonic resonance on the emission properties of stilbazolium dyes **NSC12OLip** and **PSC12OLip**, fluorescence titrations were performed. This involved tracking the changes in fluorescence emission as incremental additions of an **AuNPs-TOABr** solution were added to a stilbazolium dye solution, as illustrated in **Scheme 1.8**. To this aim, a solution of each stilbazolium dye was prepared in toluene with an absorbance below 0.1 to minimize self-absorption effects. The experiment began by introducing a fixed volume (2.2 mL) of the dye solution into a cuvette. The fluorescence emission spectrum was measured using the excitation wavelength corresponding to the dye’s maximum absorbance: λ_{exc} = 474 nm for **NSC12OLip** and λ_{exc} = 466 nm for **PSC12OLip**. Sequential additions of the **AuNPs-TOABr** solution in toluene were performed, and after each addition, the fluorescence emission spectrum was recorded under the same experimental conditions.

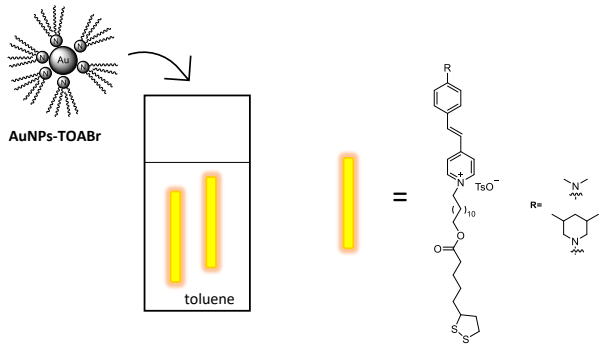

	Concentration (M)	λ^{ex} [nm]	λ^{em}_{max} [nm]
NSC12OLip	2.81×10^{-6}	474	589
PSC12OLip	4.09×10^{-6}	466	599

Scheme 1.8. Scheme of the fluorescence experiments for **NSC12OLip** and **PSC12OLip** with **AuNPs-TOABr** in toluene at 298 K.

This experimental approach provided valuable insights into the fluorescence alterations of the dye induced by the plasmonic resonance of the gold nanoparticles. For both dyes, the emission maximum exhibited a noticeable red-shift with the progressive addition of the **AuNPs-TOABr** solution, indicating interaction between the dyes and the nanoparticle surface (**Figure 1.38**). Specifically, a red-shift of 24 nm (664 cm^{-1}) was observed for **NSC12OLip** (from 589 nm to 613 nm), while **PSC12OLip** showed a 18 nm (487 cm^{-1}) shift (from 599 nm to 617 nm). Most importantly, both titrations showed the quenching of the dye's fluorescence emission upon interaction with **AuNPs-TOABr**, as illustrated in **Figure 1.38**. This quenching effect is attributed to the proximity of the dye to the gold surface and the good spectral overlap between the dye fluorescence and the plasmonic absorbance of the nanoparticles. The energy transfer mechanism involved, known as Förster Resonance Energy Transfer (FRET), where the dye functions as a donor and the gold nanoparticle as an acceptor, predominantly favors the non-radiative decay over radiative one, leading to fluorescence quenching.

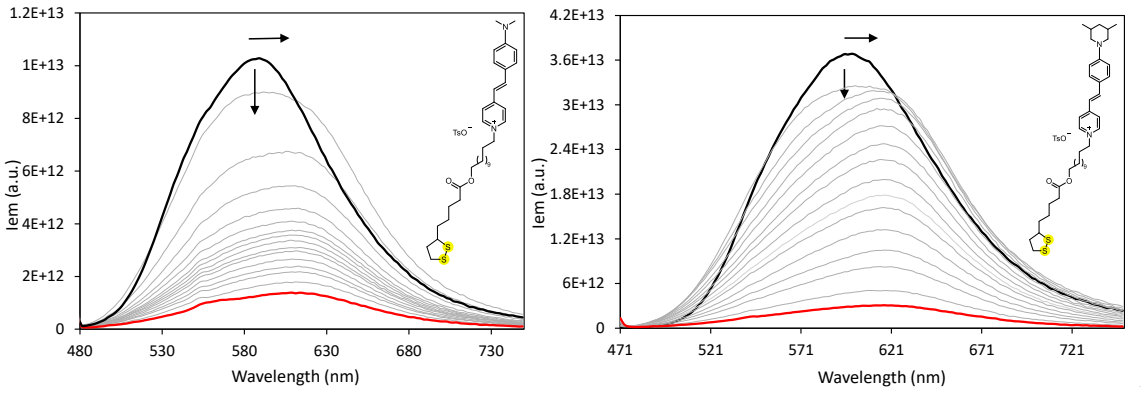

Figure 1.38. Left: collection of emission spectra of **NSC12OLip** titration (c = 2.81×10^{-6} M, excitation wavelength 474 nm) with **AuNPs-TOABr** in toluene at 298 K; right: collection of emission spectra of **PSC11OLip** titration (c = 4.09×10^{-6} M, excitation wavelength 466 nm) with **AuNPs-TOABr** in toluene at 298 K.

Having established that the interaction between stilbazolium salts and gold nanoparticles induces fluorescence quenching, the focus of the investigation shifted to exploring the effect of complexing the functionalized nanoparticles, **AuNPs-NSC12OLip** and **AuNPs-PSC12OLip**, with **TPU**. The hypothesis was that the complexation of the stilbazolium dye on the nanoparticle surface by **TPU** could interrupt the energy transfer mechanism responsible for the fluorescence quenching. Consequently, this would restore or "switch on" the dye fluorescence. It is noteworthy that this fluorescence restoration effect should be exclusive for **AuNPs-NSC12OLip** nanoparticles, where the dyes *N,N*-dimethyl amino group allow the interaction of the stilbazolium core with the **TPU** wheel (**Scheme 1.9**, top). In contrast, in **AuNPs-PSC12OLip**, the 3,5-dimethylpiperidine stopper group occupies the surface, precluding the interaction with the **TPU** macrocycle and thereby hindering its complexation (**Scheme 1.9**, bottom).

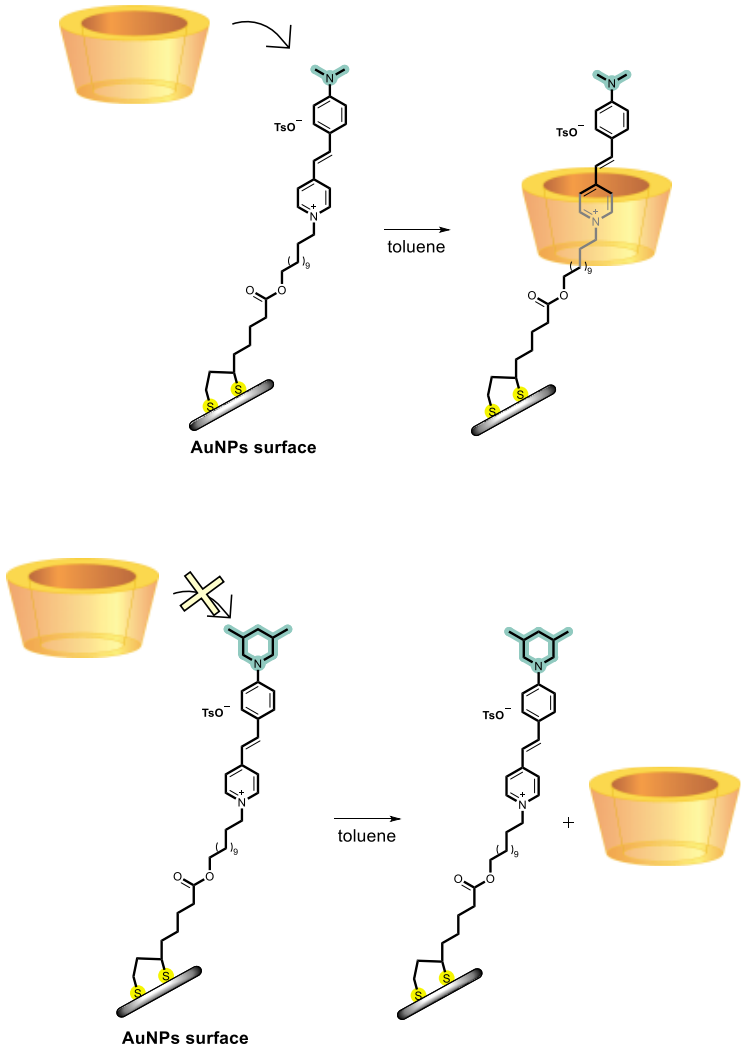

Scheme 1.9. Top: Complexation of *N,N*-dimethyl amino group on the surface of **AuNPs-NSC12OLip** with **TPU**; bottom: hindered complexation of 3,5-dimethylpiperidine group on the surface of **AuNPs-PSC12OLip** with **TPU**.

To investigate the effect of the complexation on the gold surface, the weak fluorescence emission of **AuNPs-NSC12OLip** and **AuNPs-PSC12OLip** was systematically monitored during the incremental addition of a **TPU** solution in toluene. **Figure 1.39** (left) illustrates the titration of **AuNPs-NSC12OLip** where the black line corresponds to the initial emission of the system, and the red line denotes the endpoint of the titration. Upon the addition of **TPU**, the emission spectra exhibited a gradual fluorescence enhancement accompanied by a blue shift of the emission band (λ_{em} from 605 to 569 nm), indicative of a successful complex formation. In contrast, an opposite trend was observed in the analogous experiment with **AuNPs-PSC12OLip** (**Figure 1.39**, right), wherein a decline in fluorescence emission transpired, likely due to a dilution effect contributing to the reduction in emission.

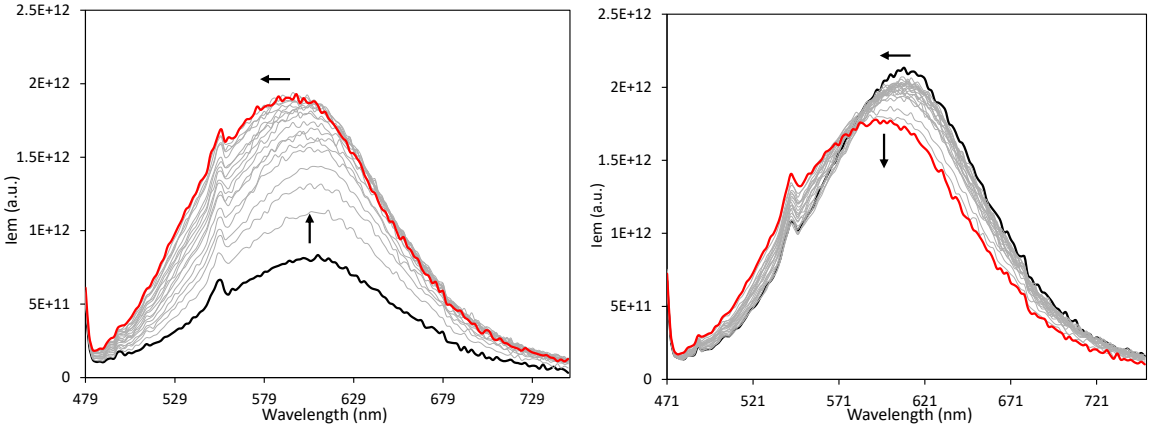

Figure 1.39. Left: collection of emission spectra of **AuNPs-NSC12OLip** titration (excitation wavelength 474 nm) with **TPU** in toluene at 298 K; right: collection of emission spectra of **AuNPs-PSC12OLip** titration (excitation wavelength 466 nm) with **TPU** in toluene at 298 K. Start point: black line; finish point: red line. The arrows indicate the titration evolution.

To quantify the fluorescence enhancement, the normalized fluorescence intensity of the **AuNPs-NSC12OLip** and **AuNPs-PSC12OLip** solutions was plotted against the volume of the added **TPU** solution. As illustrated in **Figure 1.40**, the fluorescence of **AuNPs-PSC12OLip** (violet circles) remained relatively constant, indicating null or minimal interaction with the **TPU** macrocycle. In contrast, a pronounced increase in fluorescence emission was observed for **AuNPs-NSC12OLip** (blue squares), demonstrating a significant fluorescent enhancement (switch on) resulting from the complexation of the dyes on the nanoparticle surface with **TPU**. This high contrast in fluorescence behavior further supports the hypothesis that the interaction between the **TPU** macrocycle and the stilbazolium core of **NSC12OLip** prevents the energy transfer mechanism between the fluorophore and the plasmonic nanostructure, effectively restoring the fluorescence emission.

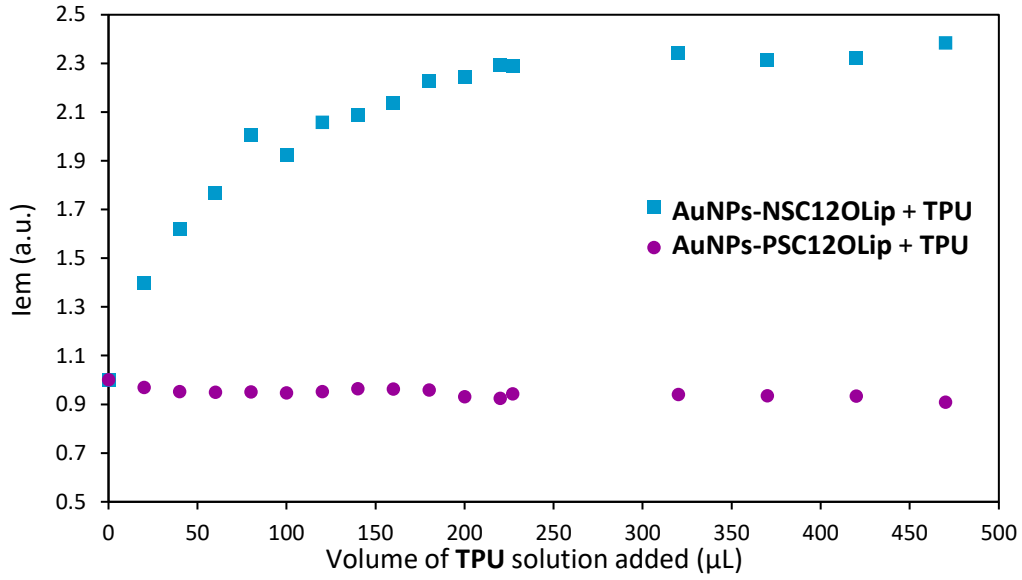

Figure 1.40. Graphic of the variation of fluorescence intensity for **AuNPs-NSC12OLip** and **AuNPs-PSC12OLip** upon the addition of **TPU** solution.

1.II. Conclusion

In this section, a "switch on-off" system based on the supramolecular complexation of stilbazolium dyes with a calix[6]arene macrocycle on the surface of gold nanoparticles was developed. Two novel stilbazolium dyes with terminal disulfide groups were synthesized: **NSC12OLip**, featuring an *N,N*-dimethylamino group, and **PSC12OLip**, containing a 3,5-dimethylpiperidine group. Both dyes exhibited absorbance bands overlapping with the plasmonic band of ~ 5 nm tetrabutylammonium-stabilized gold nanoparticles, promoting efficient coupling between the two systems. The complexation between the **TPU** calix[6]arene macrocycle and the synthesized dyes was initially investigated in solution using NMR and UV-Vis spectroscopy. The formation of two orientational isomers, designated as ***U*** and ***D***, was observed for both dyes, and the binding constants were determined through UV-Visible titrations. Hybrid gold nanoparticles conjugated with the stilbazolium dyes were prepared *via* an exchange reaction between **AuNPs-TOABr** and the respective dye. These nanoparticles were thoroughly characterized using UV-visible and XPS. The influence of the plasmonic gold nanoparticles on the stilbazolium dyes was assessed through fluorescence titrations, which revealed a notable fluorescence quenching effect. This quenching is attributed to the FRET effect, arising from the proximity of the dye to the gold surface and the favorable spectral overlap between the plasmonic absorbance of the nanoparticles and the dye's emission, which promotes non-radiative decay pathways. Further analysis of the on-surface complexation between the stilbazolium dyes and the **TPU** calix[6]arene macrocycle was conducted *via* fluorescence measurements. In the **AuNPs-NSC12OLip** system, complexation within the **TPU** macrocycle led to enhanced fluorescence emission, suggesting that the calix[6]arene acts as a

protective shield, mitigating quenching effects due to the dye's proximity to the gold surface. Conversely, for **AuNPs-PSC12OLip**, only a dilution effect was observed due to the hindered complexation caused by the steric bulk of the substituent groups on the dye. This study demonstrates the potential to manipulate the fluorescent properties of dyes on the surface of gold nanomaterials through controlled complexation, paving the way for the design of novel functional materials with tunable optical properties and enabling the development of switchable fluorescent systems.

1.I-II Acknowledgments

Thanks to Dr. Leonardo Andreoni (University of Bologna) for UV-Visible, fluorescence and electrochemical measurements in the first section. Thanks to Prof. Andrea Marrani (University "La Sapienza" of Roma) for XPS analyses.

1.II Experimental Section

General Methods

All solvents were dried using standard procedures; all other reagents were of reagent-grade quality obtained from commercial suppliers and used without further purification. Melting points are uncorrected. NMR spectra were recorded at 400 MHz for ^{1}H and 100 MHz for ^{13}C. Chemical shifts are expressed in ppm using the residual solvent signal as an internal reference (7.26 ppm for $CHCl_3$, 7.16 ppm for C_6D_5H, 5.32 for $CHDCl_2$, and 3.31 ppm for CD_2HOD). The terms m, s, d, t and q represent multiplet, singlet, doublet, triplet and quadruplet, respectively; "br. s" means a broad signal. Mass spectra were recorded in the ESI mode. Melting points were measured with a Gallenkamp melting-point apparatus and are uncorrected. UV–Vis spectra were recorded on a UV-Visible Cary 300 (Agilent). Fluorescence spectra were recorded on an Edinburgh Instrument FS5. Compounds **NS**[6], **PS**[3] and **PSC12OH**[3] were synthesized according to published procedures.

Synthesis of NSC12OH

In a two-necked round-bottomed flask, **NS** (0.15 g, 0.67 mmol, 1.0 eq.) and 1,12-dodecanediol monotosylate (0.26 g, 0.74 mmol, 1.1 eq.) were dissolved in 15 mL of dry acetonitrile under inert atmosphere. The reaction mixture was refluxed for two days. Afterwards, the solution was evaporated to dryness under reduced pressure. The solid residue was recrystallised from ethyl acetate to afford 0.32 g of **NSC12OH** as a red solid (82%).

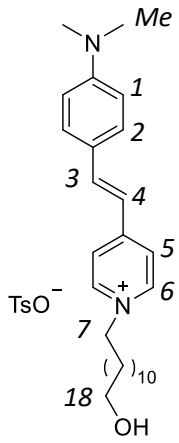

m.p.: 158-160 °C. **^{1}H NMR** (400 MHz, CD_3OD) δ = 8.53 (d, *J* = 6.9 Hz, 2H, H_6), 7.94 (d, *J* = 6.9 Hz, 2H, H_5), 7.88 (d, *J* = 16.0 Hz, 1H, H_4), 7.67 (d, *J* = 8.0 Hz, 2H, $H_{Ar\text{-}H(TsO)}$), 7.58 (d, *J* = 8.9 Hz, 2H, H_2), 7.21 (d, *J* = 7.8 Hz, 2H, $H_{Ar\text{-}H(TsO)}$), 7.13 (d, *J* = 16.0 Hz, 1H, H_3), 6.79 (d, *J* = 8.9 Hz, 2H, H_1), 4.45 (t, *J* = 7.4 Hz, 2H, H_7), 4.03 (t, *J* = 6.6 Hz, 2H, H_{18}), 3.04 (s, 6H, H_{Me}), 2.34 (s, 3H, $H_{Me(TsO)}$), 1.6-1.2 (m, 20H, $H_{8\text{-}17}$) ppm. **^{13}C NMR** (100 MHz, CD_3OD): δ = 156.4, 154.0, 144.5, 144.3, 131.6, 129.8, 126.9, 123.7, 117.7, 113.1, 65.5, 61.3, 41.3, 35.7, 34.9, 30.6, 30.6, 30.5, 30.3, 30.1, 27.1, 27.0, 25.9 ppm. **ESI-MS (+)**: calculated for $C_{27}H_{41}N_2O^+$: m/z (z = 1): 409.3; found: 409.3.

General procedure for the synthesis of the lipoic-based stilbazolium salts

In a two-neck round-bottom flask under nitrogen, the appropriate stilbazolium dye **NSC12OH** or **PSC12OH** (1.0 eq.) and 5-(1,2-dithiolan-3-yl)pentanoic acid (1.3 eq.) were dissolved in anhydrous DCM (10 mL), and the resulting solution was cooled down to 0 °C. After 15 minutes, EDC·HCl (1.3 eq.) and DMAP (cat.) were added. The resulting solution was stirred at this temperature for 15 minutes and then at room temperature for 24 hours. The mixture was then washed with water (3x10 mL). The organic layer was dried over Na_2SO_4, filtered, and evaporated under reduced pressure. The crude product was purified by column chromatography to give the pure product.

(*E*)-1-(12-((5-(1,2-dithiolan-3-yl)pentanoyl)oxy)dodecyl)-4-(4-(dimethylamino)styryl)pyridin-1-ium 4-methylbenzenesulfonate (**NSC12OLip**) was synthesized from **NSC12OH** (0.101 g, 0.174 mmol, 1 eq.) according to the general procedure described above, using 5-(1,2-dithiolan-3-yl)pentanoic acid (0.047 g, 0.256 mmol, 1.3 eq.) and 3-(((ethylimino)methylene)amino)-*N*,*N*-dimethylpropan-1-amine hydrochloride (0.043 g, 0.256 mmol, 1.3 eq.). The compound was purified by column chromatography (SiO_2, elution gradient CH_2Cl_2/MeOH 95:5 → 90:10) to give pure product **NSC12OLip** as red solid in 70 % yield.

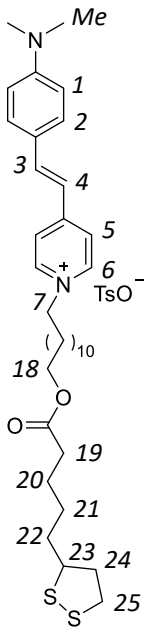

m.p.: 227-231 °C. **^{1}H NMR** (400 MHz, CD_3OD) δ = 8.58 (d, *J* = 6.9 Hz, 2H, H_6), 7.97 (d, *J* = 6.9 Hz, 2H, H_5), 7.85 (d, *J* = 16.0 Hz, 1H, H_4), 7.71 (d, *J* = 8.0 Hz, 2H, $H_{Ar\text{-}H(TsO)}$), 7.61 (d, *J* = 8.9 Hz, 2H, H_2), 7.23 (d, *J* = 7.8 Hz, 2H, $H_{Ar\text{-}H(TsO)}$), 7.10 (d, *J* = 16.0 Hz, 1H, H_3), 6.79 (d, *J* = 8.9 Hz, 2H, H_1), 4.42 (t, *J* = 7.4 Hz, 2H, H_7), 4.06 (t, *J* = 6.6 Hz, 2H, H_{18}), 3.6-3.5 (m, 1H, H_{23}), 3.2-3.1 (m, 2H, $H_{24',24''}$), 3.07 (s, 6H, H_{Me}), 2.5-2.4 (m, 1H, $H_{25'}$), 2.38 (s, 3H, $H_{Me(TsO)}$), 2.34 (t, *J* = 7.2 Hz, 2H, H_{19}), 1.97 (br. t, *J* = 7.2 Hz, 2H, H_8), 1.88 (m, 1H, $H_{25''}$), 1.7-1.2 (m, 22H, $H_{10\text{-}17,\ 20\text{-}22}$) ppm. **^{13}C NMR** (100 MHz, CD_3OD): δ = 156.4, 154.0, 144.5, 144.3, 131.6, 129.8, 126.9, 123.7, 117.7, 113.1, 65.5, 61.3, 57.6, 41.3, 40.2, 39.4, 35.7, 34.9, 32.2, 30.6, 30.6, 30.5, 30.4, 30.3, 30.1, 29.8, 29.7, 27.1, 27.0, 25.9 ppm. **ESI-MS (+)**: calculated for $C_{40}H_{61}N_2O_2S_2^+$: m/z (z = 1): 665.4; found: 665.5.

(*E*)-1-(12-((5-(1,2-dithiolan-3-yl)pentanoyl)oxy)dodecyl)-4-(4-(3,5-dimethylpiperidin-1-yl)styryl)-1,4-pyridin-2-ylium4-methylbenzenesulfonate (**PSC12OLip**) was synthesized from **PSC12OH** (0.13 g, 0.201 mmol, 1.0 eq.) according to the general procedure described above, using 5-(1,2-dithiolan-3-yl)pentanoic acid (0.054 g, 0.261 mmol, 1.3 eq.) and 3-(((ethylimino)methylene)amino)-*N,N*-dimethylpropan-1-amine hydrochloride (0.050 g, 0.261 mmol, 1.3 eq.). The compound was purified by column chromatography (SiO_2, elution gradient CH_2Cl_2/MeOH 95:5 → 90:10) to give pure product **PSC12OLip** as red solid in 89 % yield.

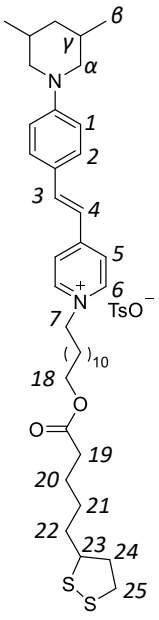

m.p.: 220-223 °C. **^{1}H NMR** (CD_3OD, 400 MHz): δ = 8.62 (d, *J* = 6.7 Hz, 2H, H_6), 8.02 (d, *J* = 7.0 Hz, 2H, H_5), 7.85 (dd, *J* = 16.0, 3.0 Hz, 1H, H_4), 7.73 (d, *J* = 8.2 Hz, 2H, $H_{Ar\text{-}H(TsO)}$), 7.62 (d, *J* = 9.0 Hz, 2H, H_2), 7.25 (d, *J* = 8.0 Hz, 2H, $H_{Ar\text{-}H(TsO)}$), 7.15 (d, *J* = 16.0 Hz, 1H, H_3), 7.00 (d, *J* = 9.0 Hz, 2H, H_1), 4.46 (t, *J* = 7.4 Hz, 2H, H_7), 4.08 (t, *J* = 6.5 Hz, 2H, H_{18}), 3.9 (m, 2H, $H_{\alpha'}$), 3.6-3.5 (m, 2H, H_{23}), 3.2-3.1 (m, 2H, $H_{24',24''}$), 2.5-2.3 (m, s, 7H, $H_{25',\ 19,\ \alpha'',\ Me(TsO)}$), 2.1-1.3 (m, 27H, $H_{8,\ 10\text{-}17,\ 20\text{-}22,\ \delta',\ 25'',\ \gamma}$), 1.01 (m, 6H, H_β), 0.83 (q, *J* = 11.9 Hz, 1H, $H_{\delta''}$) ppm. **^{13}C NMR** (CD_3OD, 100 MHz): δ = 154.9, 152.9, 143.0, 142.6, 130.2, 128.4, 125.6, 122.5, 122.4, 117.2, 114.3, 64.1, 59.9, 56.1, 54.9, 53.9, 42.1, 39.9, 39.8, 38.0, 37.9, 34.4, 34.3, 33.5, 30.8, 30.4, 29.2, 29.1, 29.1, 29.0, 28.9, 28.7, 28.5, 28.4, 28.3, 25.7, 25.6, 24.5, 18.1 ppm. **ESI-MS (+):** calculated for $C_{35}H_{53}N_2O_2S_2^+$: m/z (z = 1): 597.3; found: 597.3.

General synthesis of AuNPs decorated with XSC12OLip and TPU⊃XSC12OLip

In a 25 mL round bottom flask, 2 mL of a solution of **XSC12OLip** or **TPU⊃XSC12OLip** in toluene (c = 10^{-4}) was inserted. While stirring, 6 mL of a freshly prepared solution of **AuNPs-TOABr** in toluene was added.[17] The mixture was stirred at room temperature for 17 hours. The **AuNPs-XSC12OLip** or **AuNPs-TPU⊃XSC12OLip** were purified using three 10-minute-long centrifugation cycles at 9,000 r.p.m. (Hettich, Universal 320R). At the end of each centrifugation cycle, the supernatant was removed and the precipitated **AuNPs-XSC12OLip** or **AuNPs-TPU⊃XSC12OLip** were redispersed in CH_2Cl_2.

AuNPs-NSC12OLip: synthesized from **NSC12OLip** (C = 7.15×10^{-4} M) according to the general procedure. UV-Vis (CH_2Cl_2): λ_{max} = 521 nm.

AuNPs-PSC12OLip: synthesized from **PSC12OLip** (C = 6.81×10^{-4} M) according to the general procedure. UV-Vis (CH_2Cl_2): λ_{max} = 526 nm.

AuNPs-TPU⊃NSC12OLip: synthesized from **TPU⊃NSC12OLip** (C = 9.0×10^{-4} M) according to the general procedure. UV-Vis (CH_2Cl_2): λ_{max} = 526 nm.

AuNPs-TPU⊃PSC12OLip: synthesized from **TPU⊃PSC12OLip** (C = 8.97×10^{-4} M) according to the general procedure. UV-Vis (CH_2Cl_2): λmax = 532 nm.

1. Bibliography

(1) Bojtár, M.; Szakács, Z.; Hessz, D.; Kubinyi, M.; Bitter, I. Optical Spectroscopic Studies on the Complexation of Stilbazolium Dyes with a Water Soluble Pillar[5]Arene. *RSC Adv.* **2015**, *5* (34), 26504–26508. https://doi.org/10.1039/C4RA14809F.

(2) Bazzoni, M.; Terenziani, F.; Secchi, A.; Cera, G.; Jabin, I.; De Leener, G.; Luhmer, M.; Arduini, A. Tuning the Fluorescence Through Reorientation of the Axle in Calix[6]Arene-Based Pseudorotaxanes. *Chem. – Eur. J.* **2020**, *26* (14), 3022–3025. https://doi.org/10.1002/chem.201905500.

(3) Andreoni, L.; Bonati, F. C.; Groppi, J.; Balestri, D.; Cera, G.; Credi, A.; Secchi, A.; Silvi, S. Selective Enhancement of Organic Dye Properties through Encapsulation in Rotaxane Orientational Isomers. *Chem. Commun.* **2023**, *59* (33), 4970–4973. https://doi.org/10.1039/D3CC01135F.

(4) Cera, G.; Arduini, A.; Secchi, A.; Credi, A.; Silvi, S. Heteroditopic Calix[6]Arene Based Intervowen and Interlocked Molecular Devices. *Chem. Rec.* **2021**, *21* (5), 1161–1181. https://doi.org/10.1002/tcr.202100012.

(5) Arduini, A.; Orlandini, G.; Secchi, A.; Credi, A.; Silvi, S.; Venturi, M. Calix-Based Molecular Machines and Devices. In *Reference Module in Chemistry, Molecular Sciences and Chemical Engineering*; Elsevier, **2014**; p B9780124095472108261. https://doi.org/10.1016/B978-0-12-409547-2.10826-1.

(6) Brasselet, S.; Cherioux, F.; Audebert, P.; Zyss, J. New Octupolar Star-Shaped Strucures for Quadratic Nonlinear Optics. *Chem. Mater.* **1999**, *11* (7), 1915–1920. https://doi.org/10.1021/cm990093n.

(7) Osmaniye, D.; Kaya Cavusoglu, B.; Saglik, B.; Levent, S.; Acar Cevik, U.; Atli, O.; Ozkay, Y.; Kaplancikli, Z. Synthesis and Anticandidal Activity of New Imidazole-Chalcones. *Molecules* **2018**, *23* (4), 831. https://doi.org/10.3390/molecules23040831.

(8) Lin, Q.; Zhong, K.-P.; Zhu, J.-H.; Ding, L.; Su, J.-X.; Yao, H.; Wei, T.-B.; Zhang, Y.-M. Iodine Controlled Pillar[5]Arene-Based Multiresponsive Supramolecular Polymer for Fluorescence Detection of Cyanide, Mercury, and Cysteine. *Macromolecules* **2017**, *50* (20), 7863–7871. https://doi.org/10.1021/acs.macromol.7b01835.

(9) Chen, J.-F.; Lin, Q.; Yao, H.; Zhang, Y.-M.; Wei, T.-B. Pillar[5]Arene-Based Multifunctional Supramolecular Hydrogel: Multistimuli Responsiveness, Self-Healing, Fluorescence Sensing, and Conductivity. *Mater. Chem. Front.* **2018**, *2* (5), 999–1003. https://doi.org/10.1039/C8QM00065D.

(10) Dutta Choudhury, S. Multiple Effects of an Anionic Cyclodextrin Macrocycle on the Reversible Isomerization of a Photoactive Guest Dye. *Langmuir* **2022**, *38* (48), 14819–14826. https://doi.org/10.1021/acs.langmuir.2c02470.

(11) Herbert, F. C.; Brohlin, O. R.; Galbraith, T.; Benjamin, C.; Reyes, C. A.; Luzuriaga, M. A.; Shahrivarkevishahi, A.; Gassensmith, J. J. Supramolecular Encapsulation of Small-Ultrared Fluorescent Proteins in Virus-Like Nanoparticles for Noninvasive In Vivo Imaging Agents. *Bioconjug. Chem.* **2020**, *31* (5), 1529–1536. https://doi.org/10.1021/acs.bioconjchem.0c00190.

(12) Nie, H.; Wei, Z.; Ni, X.-L.; Liu, Y. Assembly and Applications of Macrocyclic-Confinement-Derived Supramolecular Organic Luminescent Emissions from Cucurbiturils. *Chem. Rev.* **2022**, *122* (9), 9032–9077. https://doi.org/10.1021/acs.chemrev.1c01050.

(13) Sayed, M.; Tom, D. M.; Pal, H. Multimode Binding and Stimuli Responsive Displacement of Acridine Orange Dye Complexed with *p* -Sulfonatocalix[4/6]Arene Macrocycles. *Phys. Chem. Chem. Phys.* **2020**, *22* (23), 13306–13319. https://doi.org/10.1039/D0CP00030B.

(14) Kadam, V.; Kakatkar, A. S.; Barooah, N.; Chatterjee, S.; Bhasikuttan, A. C.; Mohanty, J. Supramolecular Interaction of Sanguinarine Dye with Sulfobutylether-β-Cyclodextrin: Modulation of the Photophysical Properties and Antibacterial Activity. *RSC Adv.* **2020**, *10* (42), 25370–25378. https://doi.org/10.1039/D0RA03823G.

(15) Li, M.; Yang, Y.; Liu, R.; Wang, Y.; Shao, L.; Hua, B.; Liu, X.; Huang, F. Pillar[5]Arene-Based Ion-Pair Recognition for Encapsulation of a Stilbazolium-Type Dye with Enhanced Photophysical Properties and Nonlinear Optical Activity. *Chem. – Eur. J.* **2024**. https://doi.org/10.1002/chem.202402345.

(16) Dapeng Z.; Elena N.; Juncheng L; Devendra S.; Qi X.; Matthew L.; Jasper A.; Nathan O.; Erin K. R.; Houping N.; Drew W.; Virgil P. The Unexpected Importance of the Primary Structure of the Hydrophobic Part of One-Component Ionizable Amphiphilic Janus Dendrimers in Targeted mRNA Delivery Activity. *J. Am. Chem. Soc.* **2022**, 144, 11, 4746–4753. https://doi.org/10.1021/jacs.2c00273.

(17) A. Arduini, F. Ciesa, M. Fragassi, A. Pochini, A. Secchi, Heteroditopic Calix[6]arene Based Intervowen and Interlocked Molecular Devices. *Angew. Chem.* **2005**, 117, 282–285. https://doi.org/10.1002/anie.201813125

(18) J. J. González, R. Ferdani, E. Albertini, J. M. Blasco, A. Arduini, A. Pochini, P. Prados, J. De Mendoza, Directional Threading and Sliding of a Dissymmetrical Foldamer Helix on Dissymmetrical Axles. *Chem. Eur. J.* **2000**, 6, 73–80. DOI: 10.1002/tcr.202100012

(20) Peng, B.; Zhang, Q.; Liu, X.; Ji, Y.; Demir, H. V.; Huan, C. H. A.; Sum, T. C.; Xiong, Q. Fluorophore-Doped Core–Multishell Spherical Plasmonic Nanocavities: Resonant Energy Transfer toward a Loss Compensation. *ACS Nano* **2012**, *6* (7), 6250–6259. https://doi.org/10.1021/nn301716q.

(21) Fink, J.; Kiely, C. J.; Bethell, D.; Schiffrin, D. J. Self-Organization of Nanosized Gold Particles. *Chem. Mater.* **1998**, *10* (3), 922–926. https://doi.org/10.1021/cm970702w.

Chapter 2. Calix[6]arene encapsulation of thiazolo[5,4-*d*]thiazole dyes

2 Introduction

Thiazo[5,4-*d*]thiazole (**TTz**) dyes are extensively utilized in organic optoelectronics due to their advantageous properties, such as a planar, rigid structure and an extended π-conjugated electronic system, which confer high thermo-oxidative and photochemical stability (see Introduction). Common **TTz**-based dyes typically exhibit a symmetric structure, with identical functional groups attached to both sides of the central ring system. These dyes are characterized by high fluorescence quantum yields and long fluorescence lifetimes. Walter *et al.*[1] demonstrated the potential of **TTz**-based dyes for various applications, including optoelectronics, sensing, and photochemistry (**Figure 2.1**, left). Additionally, the reversible "turn-off" of fluorescence through electrochemical reduction allows these dyes to be employed in sensing applications, particularly in monitoring photoinduced electron transfer processes.[1]

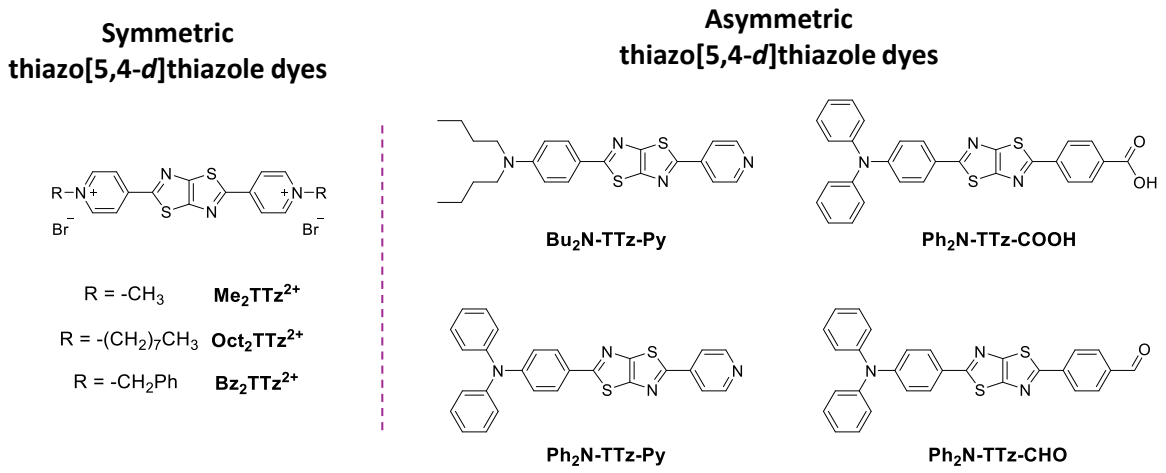

Figure 2.1 Left: structure of symmetric thiazo[5,4-*d*]thiazole dyes; right: structures of asymmetric thizo[5,4-*d*]thiazole dyes.[2]

Asymmetric **TTz**-based dyes have garnered significant interest due to their unique optical properties derived from their push-pull structure. Combined with the high fluorescence and electron-deficient nature of the **TTz** ring system, these dyes are especially appealing for advanced applications. In 2019, Walter *et al.*[2] developed novel asymmetric thiazo[5,4-*d*]thiazole dyes that exhibited high molar absorption coefficients, high fluorescence quantum yields, substantial Stokes shifts, red-shifted absorption and emission spectra, and strong intramolecular charge transfer (ICT) characteristics (**Figure 2.1**, right). These properties make them highly promising for sensing applications.

It is well established that the photophysical properties of organic dyes can be modulated through complexation with supramolecular macrocycles. However, the impact of such complexation on

thiazo[5,4-*d*]thiazole dyes has been relatively underexplored. In 2019,[3] Zhang and co-workers reported the formation of a supramolecular radical dimer between cucurbit[8]uril and a symmetric **TTz**-based dye (**Figure 2.2**). This supramolecular dimer exhibited enhanced intramolecular charge transfer, resulting in strong absorption in the NIR-II region of the spectrum. This study demonstrated how supramolecular complexation can significantly improve the optical properties of **TTz**-based dyes, expanding their potential for future applications.

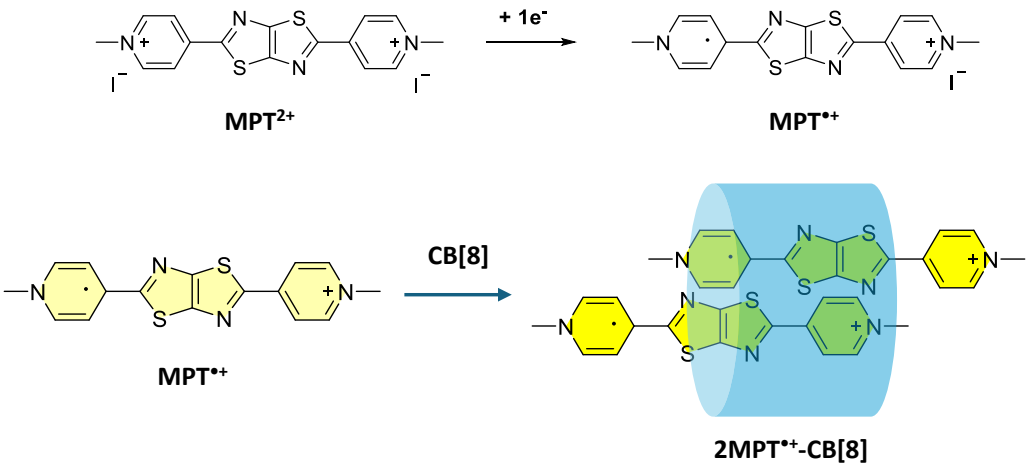

Figure 2.2. Top: generation of **MPT•+** upon reduction of **MPT2+**; bottom: schematic representation of the formation of supramolecular radical dimer **2MPT•+-CB[8]**.

Aim of the project

In this chapter, novel thiazo[5,4-*d*]thiazole dyes were synthesized, and their optical properties were systematically studied. Both symmetric and asymmetric dyes were explored (**Figure 2.3**, top). The challenging synthesis of the asymmetric dyes was successfully achieved *via* a one-pot reaction, which was tailored according to the reactants employed. The optical properties of symmetric and asymmetric dyes differed significantly, particularly in terms of maximum absorbance/emission wavelengths, which are red-shifted in the case of asymmetric dyes, and Stokes shift values, which are larger for asymmetric dyes with respect to the symmetric ones. Following the characterization of the individual dyes, their complexation within the cavity of triphenylureido calix[6]arene (**TPU**) was investigated using NMR, UV-Visible spectroscopy, fluorescence, and electrochemical analysis (**Figure 2.3**, bottom). Distinct behaviors were observed for symmetric and asymmetric dyes. NMR analysis revealed the formation of a 1:1 complex for the asymmetric dyes, while symmetric dyes showed the formation of high order adduct species. Fluorescence studies indicated a change in the emission properties of the dyes upon complexation, particularly leading to fluorescence quenching. Electrochemical analysis revealed behavior similar to that of di-alkyl viologen salts, where under reducing conditions, the formation of the radical-cationic dye resulted in its dethreading from the

calix[6]arene cavity. This comprehensive investigation provides the first insight into the complexation behavior of thiazo[5,4-*d*]thiazole dyes with calix[6]arene derivatives.

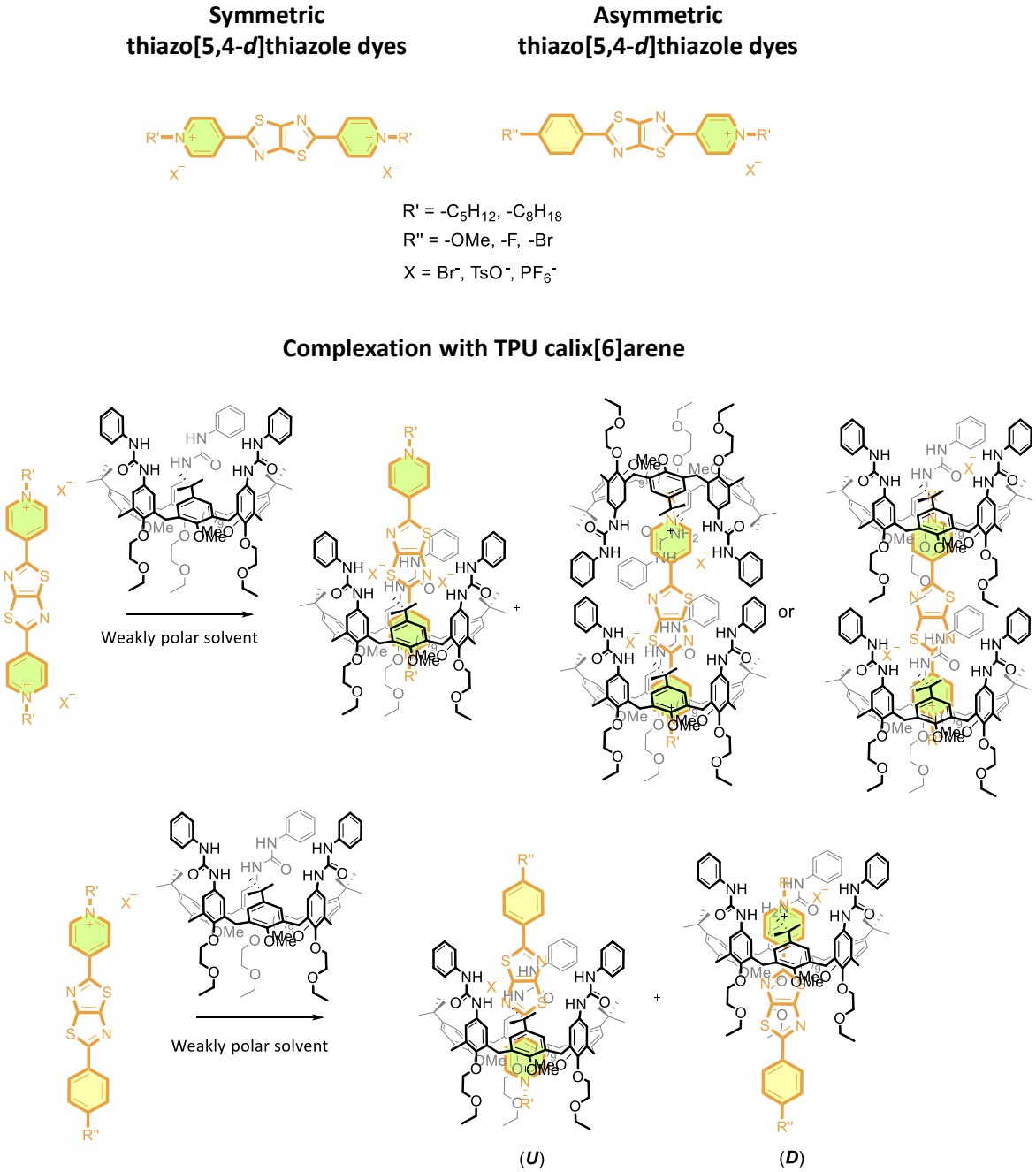

Figure 2.3. Top: structure of thiazo[5,4-*d*]thiazole dyes investigated; bottom: representation of the complexation within **TPU** calix[6]arene.

2 Result and discussion

Synthesis and NMR characterization of thiazo[5,4-d]thiazole dyes

To investigate the interaction between thiazo[5,4-*d*]thiazole (**TTz**) dyes and calix[6]arene **TPU** wheel, novel target dyes were synthesized. Both symmetric and asymmetric thiazolo[5,4-*d*]thiazole dyes were designed. Symmetric **TTz**-based dyes are well-known in the literature for their notable optical properties (see Introduction) and facile synthesis. Indeed, the symmetric **TTz** scaffold, featuring two pyridine groups at the end of the bicyclic heterocycle, is obtained in a single-step process involving two sequential condensations followed by a dehydrogenation (**Scheme 2.1**). The mechanism reported in **Scheme 2.1** is derived from the work of Johnson and Ketcham (1960),[4] which elucidates the precise nature of the condensation product.

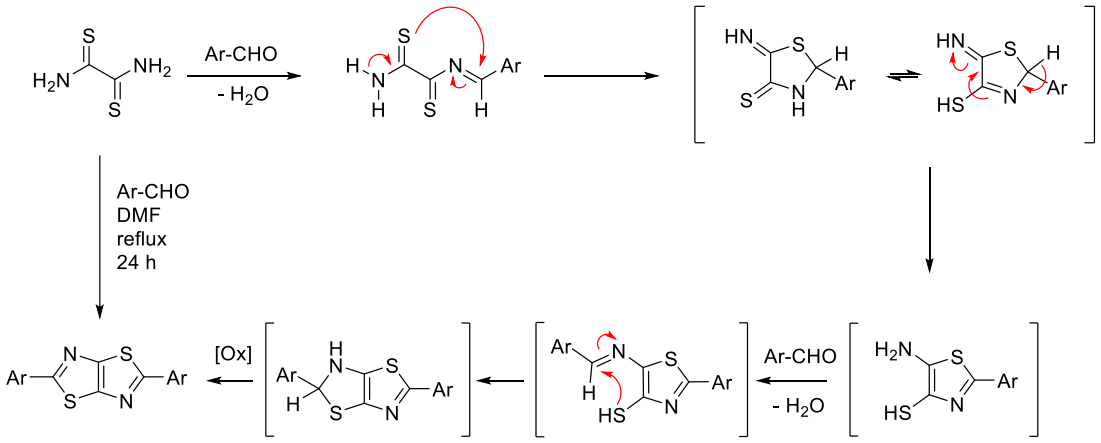

Scheme 2.1. Mechanism of the formation of symmetric **TTz** scaffold.

The symmetric **Py$_2$TTz** was synthesized by reacting 2 equivalents of 4-pyridine carboxaldehyde with 1 equivalent of dithiooxamide in dimethylformamide (DMF) under reflux for 24 hours[1] (**Scheme 2.2**, **i)**).

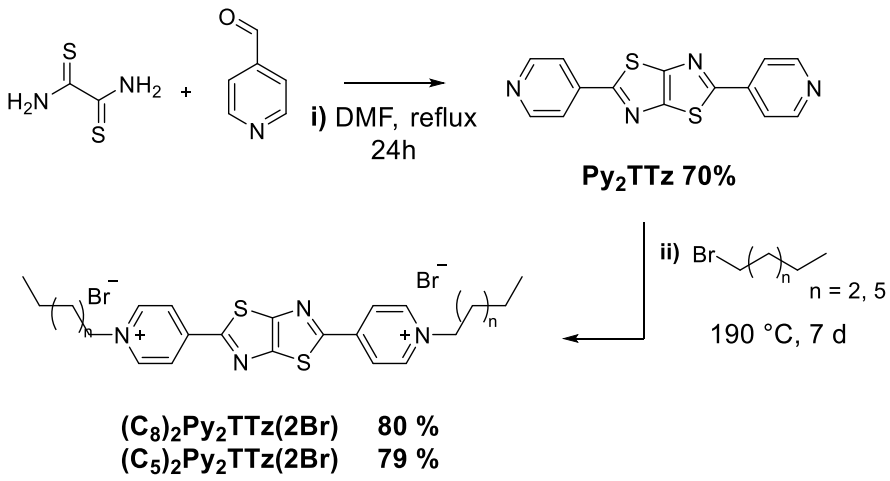

Scheme 2.2 i) Synthesis of the symmetric thiazolo[5,4-*d*]thiazole scaffold **Py$_2$TTz**; **ii)** synthesis of symmetric thiazolo[5,4-*d*]thiazole dyes **(C$_8$)$_2$Py$_2$TTz(2Br)** and **(C$_5$)$_2$Py$_2$TTz(2Br)**.

The synthesis of asymmetric **TTz**-based dyes has been historically challenging due to the simultaneous occurrence of two condensation reactions in the typical reaction pathway (**Scheme 2.1**), making the isolation of the single condensed intermediate unfeasible. In the literature, there are a few examples of asymmetric **TTz**-based dyes, all of which achieved asymmetry *via* post-synthetic derivatization of initially symmetric **TTz**-based dyes.[5–7] Our aim was to synthesize asymmetric **TTz**-based dyes through a single-step reaction. In 2019, G. Walter *et al.*[2] reported the synthesis of novel **TTz**-based derivatives using a single-step reaction. Their synthetic strategy involved the reaction between two aromatic aldehydes and the dithiooxiamide, yielding one asymmetric and two symmetric **TTz**-based dyes. Inspired by their approach, we designed three different asymmetric **TTz**-based scaffolds by reacting 4-pyridine carboxaldehyde with various *para*-substituted benzaldehydes: 4-bromobenzaldehyde, 4-fluorobenzaldehyde, and 4-methoxybenzaldehyde. As previously observed, three distinct products were obtained: two symmetric **TTz**-based dyes, resulting from the reaction of identical aromatic aldehydes with dithiooximaide, and the desired asymmetric **TTz**-based dye, obtained from the reaction of the two distinct aromatic aldehydes with dithiooxiamide (**Scheme 2.3**).

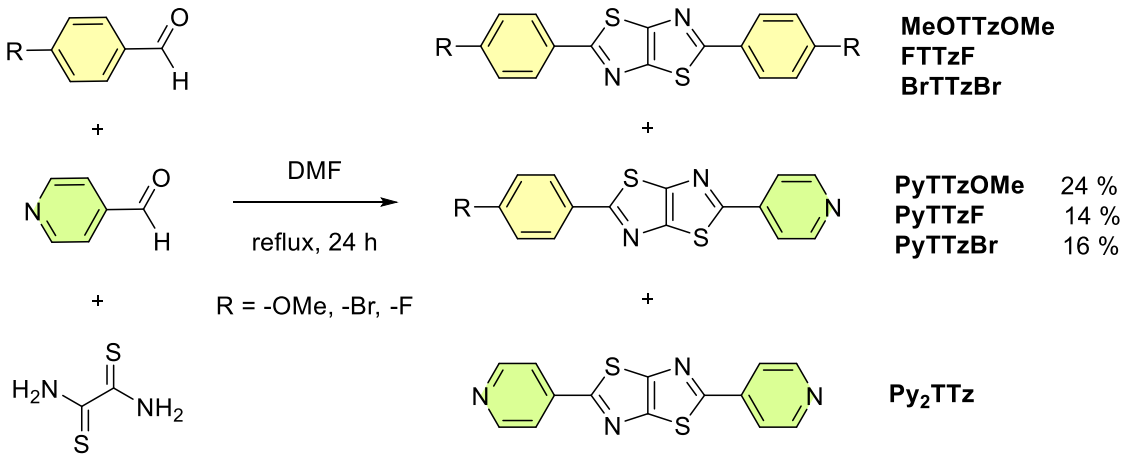

Scheme 2.3 Single-step synthetic reaction for the formation of asymmetric **TTz**-based dyes: three potential products are generated during the reaction.

The molar ratios of the two aromatic aldehydes were adjusted based on the electrophicity of their carbonyl groups. Several attempts were made to synthesize the asymmetric **TTz** dye with the methoxy group (**PyTTzOMe**) by varying the ratio of 4-methoxy benzaldehyde to 4-pyridine carboxaldehyde since the strong electron-donating nature of the methoxy group of the first reactant greatly reduces the reactivity of the aldehyde compared to the 4-pyridine carboxaldehyde. Consequently, to favor the formation of the asymmetric product over the symmetric ones, 7 equivalents of 4-methoxybenzaldehyde were necessary. After purification *via* column chromatography, **PyTTzOMe** was obtained in 24% yield.

For the bromide- and fluoride-substituted asymmetric **TTz** dyes, a lower excess of the respective aldehyde derivatives was sufficient due to their electronic-withdrawing nature: **PyTTzBr** was synthesized in 16% yield by using 2 equivalents of 4-bromobenzaldehyde in respect to 4-pyridine carboxaldehyde, while the same reaction using 1.3 equivalents of 4-fluorobenzaldehyde resulted in a 14% yield of **PyTTzF** (**Scheme 2.4**). In general, using mixtures of CH_2Cl_2 and MeOH, it was possible to separate the asymmetric products **PyTTzF** and **PyTTzBr**, exhibiting a yellow fluorescence, from the symmetric dyes **BrTTzBr** and **FTTzF**, exhibiting a blue fluorescence.

The second step of the synthetic strategy involved the alkylation of the pyridine ring in the appropriate scaffold. Two alkyl chains, differing in length (C5 and C8), were selected to investigate their ability to thread the calix[6]arene cavity of **TPU** (see next). The synthesis was achieved by heating the reaction mixture at reflux with 1-bromooctane or 1-bromopentane, which served both as the solvent and the reagent (**Schemes 2.2** and **2.4**). This procedure leads to the formation of the desired symmetric **TTz**-based dyes **$(C_8)_2Py_2TTz(2Br)$** and **$(C_5)_2Py_2TTz(2Br)$** (**Scheme 2.2**, **ii)**), and asymmetric **TTz**-based dyes **(C_8)PyTTzX(Br)** and **(C_5)PyTTzOMe(Br)** (**Scheme 2.4**) in high yields.

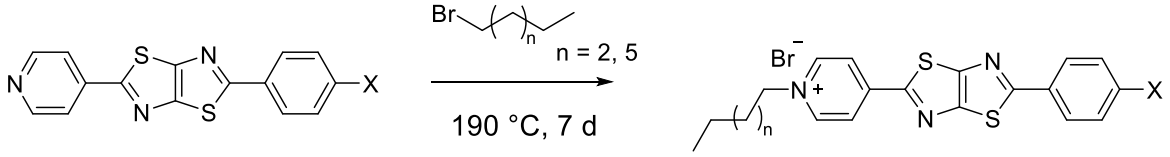

PyTTzOMe
PyTTzF
PyTTzBr

(C_8)PyTTzOMe(Br)	**74 %**
(C_5)PyTTzOMe(Br)	**98 %**
(C_8)PyTTzF(Br)	**91 %**
(C_8)PyTTzBr(Br)	**94 %**

Scheme 2.4 Synthesis of asymmetric thiazolo[5,4-*d*]thiazole dyes **(C_8)PyTTzOMe(Br)**, **(C_5)PyTTzOMe(Br)**, **(C_8)PyTTzF(Br)**, and **(C_8)PyTTzBr(Br)**.

The obtained products were fully characterized using ESI-MS spectrometry and NMR measurements. The ^{1}H NMR spectra of the asymmetric dyes were gathered in **Figure 2.4**. Their asymmetric **TTz** scaffolds display four distinct signals in the aromatic region of the spectra. For **PyTTzBr** (**Figure 2.4**, top), the *α* protons appear as a doublet integrating for 2 protons at 8.76 ppm. The *β* and *γ* protons are observed as a multiplet between 7.9-7.8 ppm, and the *δ* protons resonate as a doublet at 7.64 ppm. Similarly, for **PyTTzF** (**Figure 2.4**, middle), the low-field doublet at 8.76 ppm, integrating for 2 protons, was assigned to the *α* protons. Another doublet at 7.86 ppm, also integrating for 2 protons, was attributed to the *β* protons. The *para*-fluoro substituted aromatic ring gives rise to a triplet and a multiplet due to the coupling with the fluorine atom: the multiplet centered at 8.0 ppm corresponds to the *γ* protons, while the triplet at 7.20 ppm was associated with the *δ* protons. For **PyTTzOMe** (**Figure 2.4**, bottom), the aromatic region shows four doublets: the doublet at 8.74 ppm correspond to *α* protons, the doublet at 7.96 ppm to the *β* protons, the

doublet at 7.84 ppm to the *γ* protons and the doublet at 7.01 ppm to the *δ* protons. Additionally, the singlet at 3.89 ppm was attributed to the methoxy group.

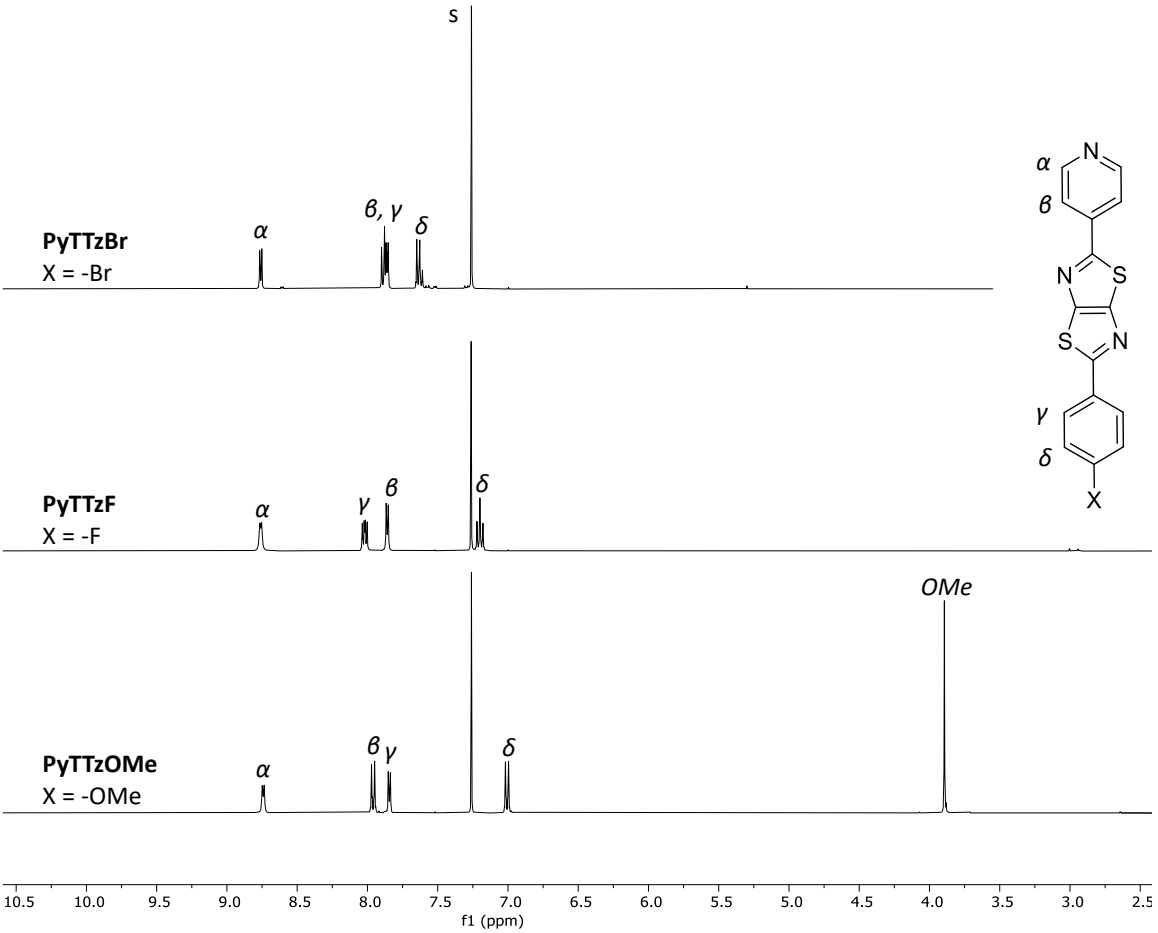

Figure 2.4. ^{1}H NMR stack plot spectra ($CDCl_3$, 400 MHz, 298 K) of **PyTTzBr** (top), **PyTTzF** (middle) and **PyTTzOMe** (bottom).

To evaluate the effect of the anion on the complexation of the **TTz** dyes with **TPU**, the bromide anion in both the symmetric and asymmetric dyes was exchanged with tosylate and hexafluorophosphate anions. This anion exchange reaction was performed in CH_3OH using silver salts of the respective anions, yielding the desired products in quantitative yield (**Scheme 2.5**). The resulting compounds were fully characterized, and the success of the anion exchange was particularly confirmed *via* NMR analysis.

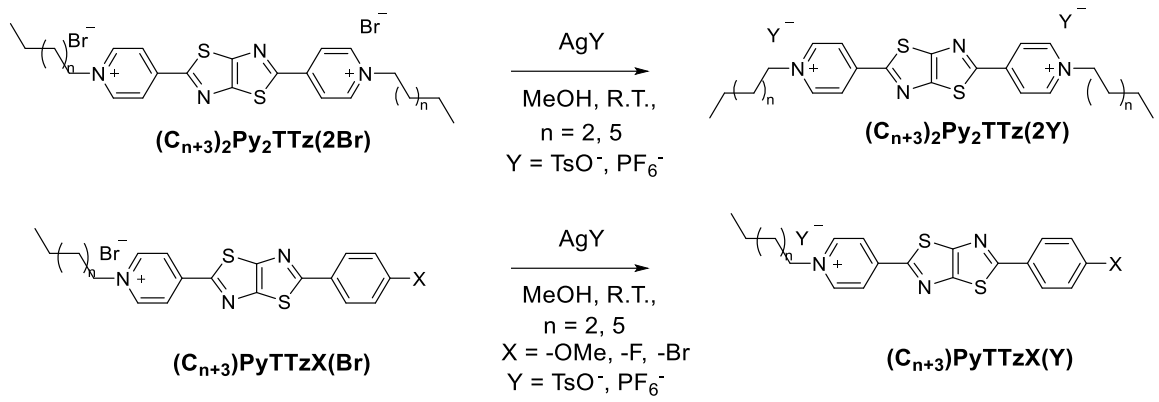

Scheme 2.5 Synthetic scheme for the anion exchange reaction carried out on **TTz**-based dyes having bromide (Br^-) as counterion with tosylate (TsO^-) and hexafluorophosphate (PF_6^-) anions.

Figure 2.5 presents the stacked plot of the ^{1}H NMR spectra of the symmetric **$(C_8)_2Py_2TTz$** with the three different anions. In the low-field region (8.5-9.5 ppm), two doublets from the pyridine protons (*α* and *β*, see **Figure 2.5** for labeling) are observed: for **$(C_8)_2Py_2TTz(2Br)$** protons *α* resonate at 9.18 ppm and protons *β* at 8.76 ppm; for **$(C_8)_2Py_2TTz(2PF_6)$** and **$(C_8)_2Py_2TTz(2TsO)$**, the protons *α* resonate at 9.12 ppm and protons *β* at 8.74 ppm. **$(C_8)_2Py_2TTz(2TsO)$** also displays two doublets at 7.69 and 7.21 ppm, each integrating for 2 protons, and one singlet at 2.35 ppm, integrating for three protons. These signals correspond to the tosylate anion. The triplet at 4.71 ppm for **$(C_8)_2Py_2TTz(2Br)$** and at 4.67 ppm for **$(C_8)_2Py_2TTz(2PF_6)$** and **$(C_8)_2Py_2TTz(2TsO)$** corresponds to the protons, labeled as *8*, of the methylene groups linked to the pyridinium rings. In the high-field region of the spectrum are observed several multiplets related to the two alkyl chains: the multiplet at 2.1-2.0 ppm corresponds to protons labeled as *7*, while the multiplet at 1.5-1.3 ppm corresponds to the other protons of the internal methylene groups of the chain. Finally, the triplet at 0.91 ppm was attributed to the terminal methyl group labeled as *1*.

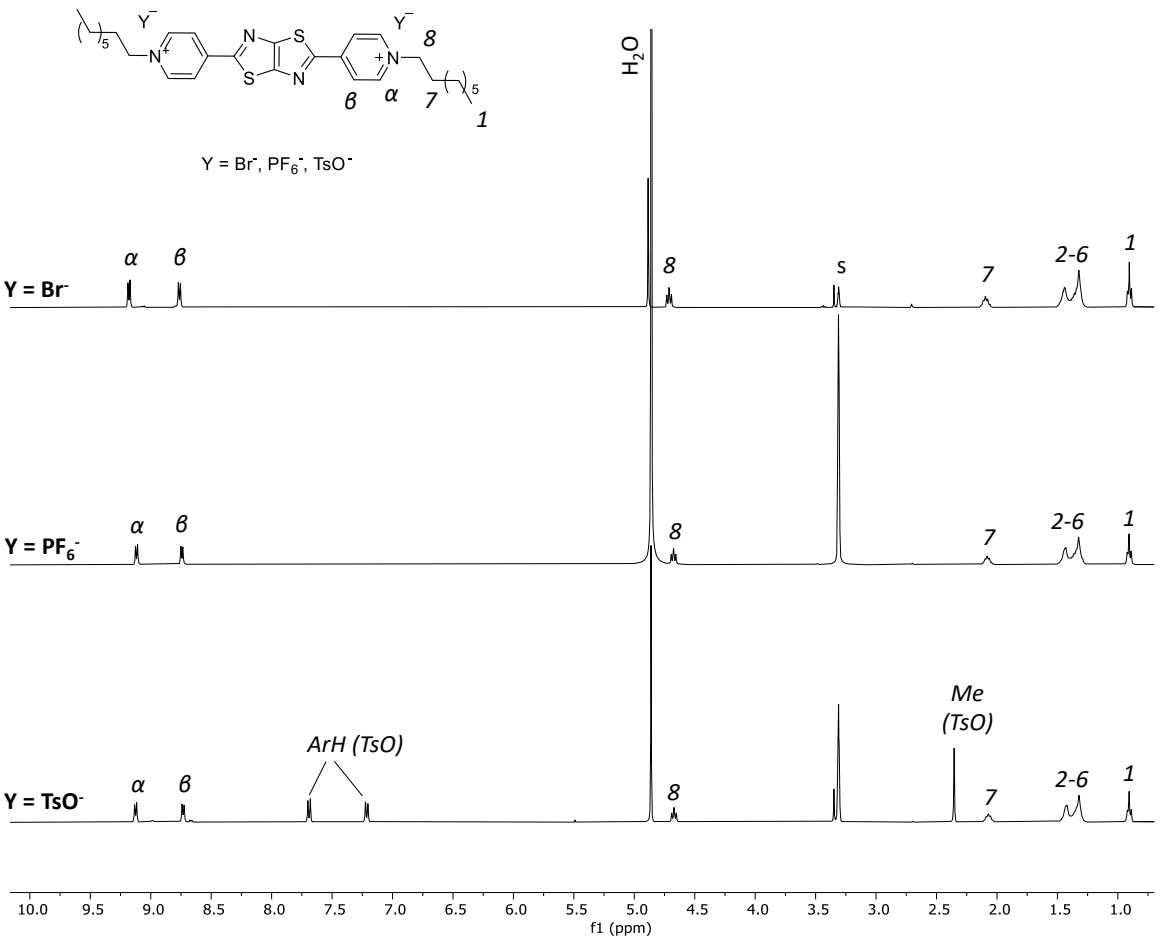

Figure 2.5 ^{1}H NMR spectra (CD_3OD, 400 MHz, 298 K) of **$(C_8)_2Py_2TTz(2Br)$** (top), **$(C_8)_2Py_2TTz(2PF_6)$** (middle) and **$(C_8)_2Py_2TTz(2TsO)$** (bottom).

Similarly, NMR analyses were conducted for the asymmetric thiazolo[5,4-*d*]thiazole dyes. **Figure 2.6** reports the stacked plot of ^{1}H NMR spectra of **(C_8)PyTTzOMe** with the three different anions. The asymmetry of the molecule generates, in all cases, four different doublets in the low-field region of the NMR spectrum, each integrating for two protons and corresponding to the aromatic protons of the dyes. For **(C_8)PyTTzOMe(Br)**, the *α* protons adjacent to the positively charged nitrogen resonate at 9.48 ppm, the *β* protons at 8.42 ppm, the *γ* protons at 7.93 ppm, and *δ* protons at 6.99 ppm. In **(C_8)PyTTzOMe(PF_6)** protons *α* are upfield-shifted at 8.95 ppm, while protons *β* resonate at 8.47 ppm, *γ* at 7.99 ppm and *δ* at 7.03 ppm. In **(C_8)PyTTzOMe(TsO)**, 6 distinct doublets are observed due to the presence of the tosylate anion: protons *α* resonate at 9.26 ppm, *β* at 8.39 ppm, the *γ* protons resonate together with the aromatic protons of the tosylate, forming a multiplet centered at 7.8 ppm. Protons *δ* resonate at 6.95 ppm, and an additional doublet corresponding to the aromatic protons of tosylate appears at 7.19 ppm. In the middle region of the spectra, the triplet related to the protons labeled as *8* was observed: for **(C_8)PyTTzOMe(Br)** it appears at 5.00 ppm, for **(C_8)PyTTzOMe(PF_6)** at 4.72 ppm, and for **(C_8)PyTTzOMe(TsO)** at 4.84 ppm. The singlet of the methoxy group appears around 3.9 ppm in all cases. For **(C_8)PyTTzOMe(TsO)**, the singlet for the

protons of the methyl group of the tosylate anion resonates at 2.37 ppm. Finally, in the high-field region, multiplets corresponding to the protons of the alkyl chain are present, along with the triplet at 0.89 ppm corresponding to the terminal methyl group labeled as *1*.

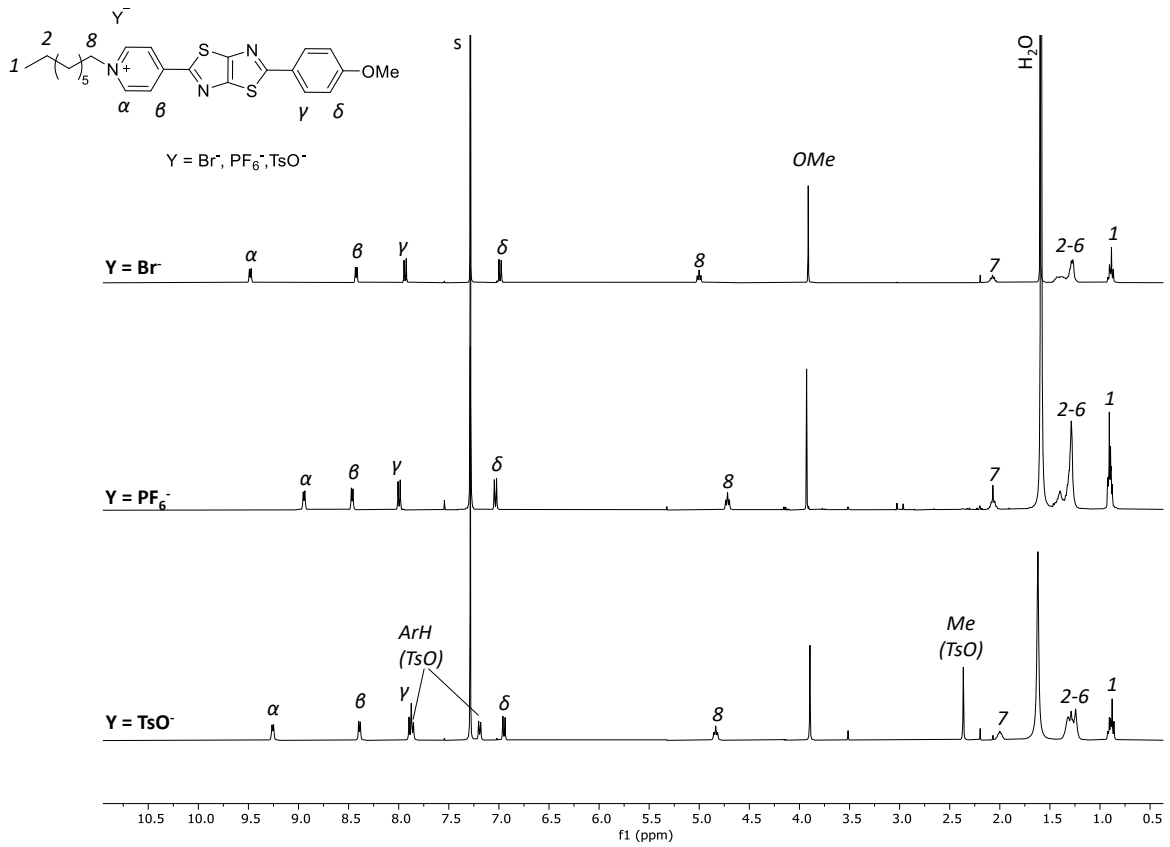

Figure 2.6 ^{1}H NMR spectra ($CDCl_3$, 400 MHz, 298 K) of **(C_8)PyTTzOMe(Br)** (top), **(C_8)PyTTzOMe(PF_6)** (middle) and **(C_8)PyTTzOMe(TsO)** (bottom).

Spectroscopic characterization of TTz-based dyes

The target dyes were further characterized using UV-visible and fluorescence spectroscopy. All analyses were carried out with methanol as the solvent for solubility reasons. Fluorescence spectra were recorded from dye solutions with absorbance values below 0.1 to prevent self-absorption artifacts. **Table 2.1** summarizes the collected spectroscopic data.

When comparing **TTz**-based dyes with the same chain lengths but different anions (cf. entries 1-3, 4-6, 7-9, 10-12, and 13-15), no significant variation was observed in their maximum absorbance and emission wavelengths, or fluorescence lifetime (τ). Similarly, an analogous conclusion can be drawn when comparing **TTz**-based dyes having the same counterion but different chain lengths (C8 and C5, cf. entries 1 and 4, 2 and 5, 3 and 6, 7 and 10, etc.). However, significant differences emerged when comparing the symmetric and asymmetric **TTz**-based dyes. Specifically, all symmetric dyes (entries 1-6) exhibit a mean absorption maximum at 395 nm, a mean emission maximum at 465

nm, and Stokes Shift values ranging from 3,600 to 4,000 cm^{-1}. In contrast, asymmetric dyes exhibited both absorption and emission bands shifted to lower energy values. For **(C_n)PyTTzOMe(Y)** dyes (entries 7-12), the absorption maximum is at ca. 428 nm and the emission at 579-580 nm, with Stokes Shifts larger than 6,000 cm^{-1}(**Figure 2.7**, left). Asymmetric halogenated dyes **(C_n)PyTTzBr** and **(C_n)PyTTzF** (entries 13-16) exhibit a mean absorption maximum at 404 nm and emission around 500 nm, with Stokes Shifts approximatively ranging from 4,500 to 5,000 cm^{-1} (**Figure 2.7**, right). The distinct optical properties of symmetric and asymmetric **TTz**-based dyes can be attributed to the specific nature of the aromatic units attached to the thiazolo[5,4-*d*]thiazole core. In particular, the substitution of a pyridinium ring with a para-substituted benzene, whether the para-substituent is electron-withdrawing (Br, F) or electro-donating (OMe), induces a red shift in both absorption and emission spectra. This substitution also increases the Stokes shift and extends the fluorescence lifetime. DFT studies are in due course to rationalize the substituents' electronic effect.

Table 2.1 Experimental spectroscopic properties in MeOH at 298 K of symmetric and asymmetric thiazolo[5,4-*d*]thiazole dyes. The sample concentrations for UV-Visible analysis ranged from 1.00 to 1.27 × 10^{-5} M, while for fluorescence analysis, concentrations varied from 1.00 to 1.27 × 10^{-6} M. The excitation wavelength used for fluorescence was at the absorbance maximum of each dye.

Entry	Compound	λ_{max}^{abs} [nm]	λ_{max}^{em} [nm]	Stokes Shift [nm, cm^{-1}]	ε [mol^{-1} L cm^{-1}] ×10^4	τ [ns]
1	**(C_8)$_2$Py$_2$TTz(2Br)**	397	465	68, 3684	6.85	1.73
2	**(C_8)$_2$Py$_2$TTz(2TsO)**	393	465	72, 3940	4.16	1.85
3	**(C_8)$_2$Py$_2$TTz(2PF_6)**	394	465	71, 3876	6.00	1.91
4	**(C_5)$_2$Py$_2$TTz(2Br)**	394	465	71, 3876	7.70	1.92
5	**(C_5)$_2$Py$_2$TTz(2TsO)**	392	465	73, 4005	6.35	1.73
6	**(C_5)$_2$Py$_2$TTz(2PF_6)**	395	465	70, 3811	5.64	1.93
7	**(C_8)PyTTzOMe(Br)**	428	580	152, 6123	8.70	3.13
8	**(C_8)PyTTzOMe(TsO)**	428	579	150, 6039	4.80	3.13
9	**(C_8)PyTTzOMe(PF_6)**	428	579	151, 6093	5.70	3.13
10	**(C_5)PyTTzOMe(Br)**	428	579	151, 6093	8.50	3.13
11	**(C_5)PyTTzOMe(TsO)**	427	580	153, 6178	3.55	3.05
12	**(C_5)PyTTzOMe(PF_6)**	428	580	152, 6123	3.96	3.01
13	**(C_8)PyTTzBr(Br)**	406	498	92, 4550	3.20	2.37
14	**(C_8)PyTTzBr(TsO)**	404	505	102, 4973	2.70	2.37
15	**(C_8)PyTTzBr(PF_6)**	404	504	100, 4911	2.50	2.46
16	**(C_8)PyTTzF(Br)**	404	502	98, 4832	2.90	2.67

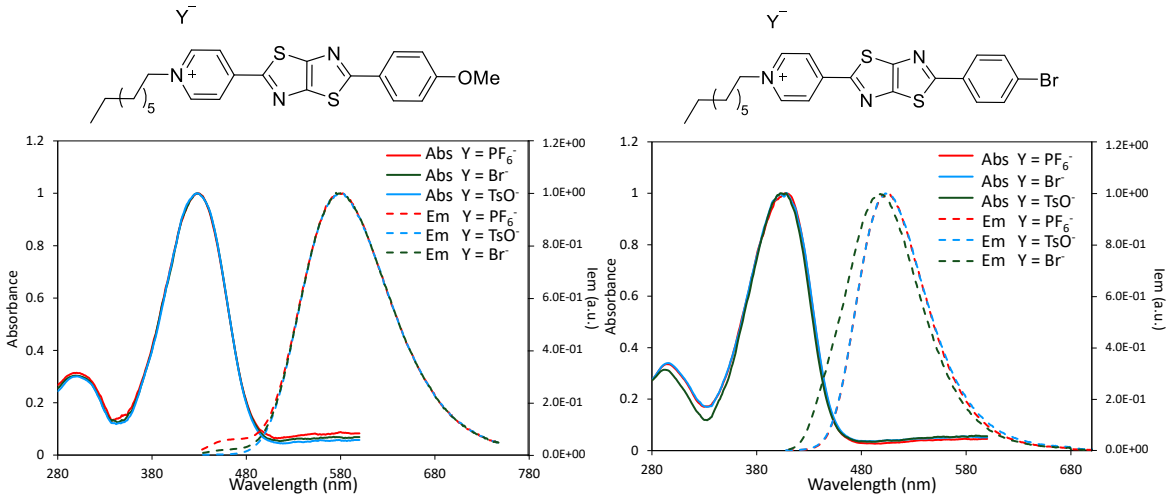

Figure 2.7. Left: normalized absorbance and emission spectra of **(C_8)PyTTzOMe(Y)** dyes (c = 1.00×10^{-5} M for UV-Vis analyses, c = 1.00×10^{-6} M for fluorescence analyses, MeOH); right: normalized absorbance and emission spectra of **(C_8)PyTTzBr(Y)** dyes (c = 1.00×10^{-5} M for UV-Vis analyses, c = 1.00×10^{-6} M for fluorescence analyses, MeOH). Y = Br^-, TsO^-, and PF_6^-.

The solvatochromic behavior of **(C_8)PyTTzBr(TsO)** and **(C_8)PyTTzOMe(TsO)** dyes was investigated through both absorbance and emission studies across five different solvents: methanol (MeOH), acetone, dichloromethane (DCM), tetrahydrofuran (THF), and toluene (**Figure 2.8**). For **(C_8)PyTTzBr(TsO)**, the maximum absorption wavelength ranged from 425 nm in DCM to 367 nm in toluene, while for **(C_8)PyTTzOMe(TsO)**, it red-shifted from 450 nm in DCM to 422 nm in THF. The solubility in toluene of the two dyes was particularly challenging, and the absorbance spectrum is likely to be affected by the formation of *H*-aggregates in the solution.[8]

The range in the emission spectra maxima was broader: for **(C_8)PyTTzBr(TsO)**, the maximum emission wavelength was at 582 nm in MeOH, and the minimum at 482 nm in toluene. Similarly, for **(C_8)PyTTzOMe(TsO)**, the emission blue-shifted from 580 nm in MeOH to 437 nm in toluene. The emission maximum wavelength of 582 nm recorded for **(C_8)PyTTzBr(TsO)** in MeOH was significantly red-shifted compared to other solvents (see **Figure 2.8**, *c*). In contrast, **(C_8)PyTTzOMe(TsO)** showed a maximum emission wavelength at ca. 580 nm in MeOH, acetone, and DCM, with a pronounced blue shift in solvents such as THF and toluene (ca. 440 nm) (see **Figure 2.8**, *d*).

The Stokes shift values were calculated for both dyes (**Table 2.2**). Both exhibited the largest Stokes shift in MeOH (7,570 vs. 6,123 cm^{-1}), but overall, **(C_8)PyTTzBr(TsO)** demonstrated lower Stokes shift values compared to **(C_8)PyTTzOMe(TsO)**.

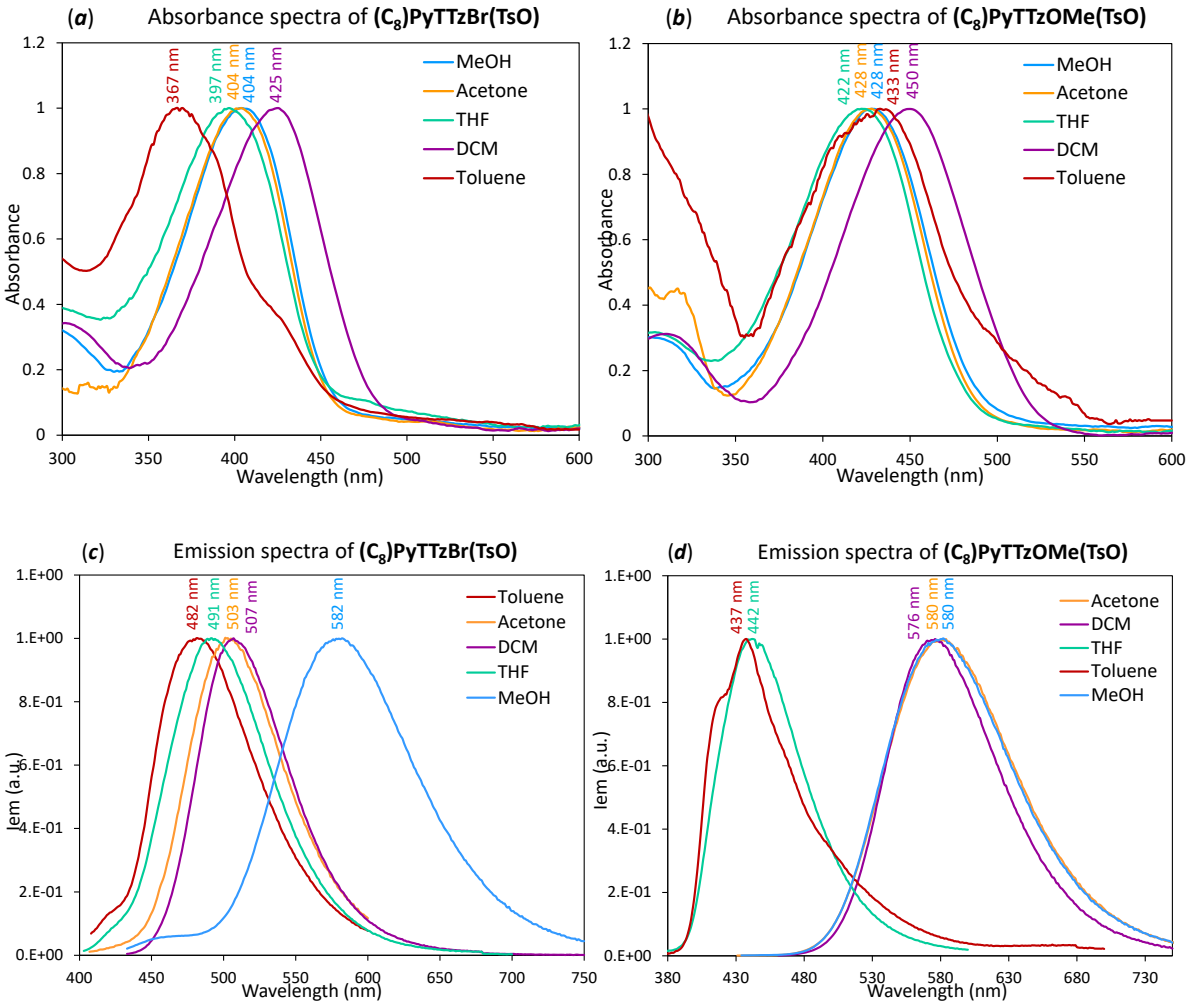

Figure 2.8. (***a***) Normalized absorbance spectra of **C8PyTTzBr(TsO)** (c = 1×10^{-5} M) in different solvents at 298 K; (***b***) normalized absorbance spectra of **C8PyTTzOMe(TsO)** (c = 1×10^{-5} M) in different solvents at 298 K; (***c***) normalized emission spectra of **C8PyTTzBrTsO)** (c = 1×10^{-6} M) in different solvents at 298 K; (***d***) normalized emission spectra of **C8PyTTzOMe(TsO)** (c = 1×10^{-6} M) in different solvents at 298 K.

Table 2.2. Stokes Shift values of **(C8)PyTTzBr(TsO)** and **(C8)PyTTzOMe(TsO)** in different solvents.

	(C_8)PyTTzBr(TsO) nm (cm^{-1})	**(C_8)PyTTzOMe(TsO)** nm (cm^{-1})
MeOH	178 (7,570)	152 (6,123)
Acetone	82 (3,805)	152 (6,123)
DCM	99 (4,871)	156 (6,241)
THF	94 (4,823)	20 (1,073)
Toluene	115 (6,501)	aggregate species in solution

Complexation study with NMR spectroscopy

The complexation of the symmetric and asymmetric **TTz** dyes with the calix[6]arene **TPU** was initially investigated through NMR spectroscopy. As with the stilbazolium dyes discussed in Chapter 1, a detailed structural interpretation of the formed complexes required both 1D and 2D NMR measurements. The complexation experiments were conducted in deuterated chloroform, where **TPU** and the opportune **TTz**-based dye were mixed in a 1:1 ratio. The **TTz**-based dyes themselves were insoluble in this chlorinated solvent at the concentration needed for the NMR measurements (c = 10^{-2} to 10^{-3} M). However, upon complexation with **TPU**, they became soluble. For these NMR measurements, **TTz**-based dyes with the tosylate as a counterion were used.

NMR investigation of asymmetric TTz-based dyes

Scheme 2.6 shows the scheme of the complexation of **(C_8)PyTTzOMe(TsO)** and **(C_5)PyTTzOMe(TsO)** with the **TPU** macrocycle. As for the complexation observed with the stilbazolium dyes described in Chapter 1, two orientational isomers can form. In the first, referred to as the *upper* isomer (***U***), the dye's methoxy group is positioned near the macrocycle phenylurea groups. In the second, named *down* isomer (***D***), the dye's methoxy group protrudes from the lower rim, while the alkyl chain is inside the aromatic cavity. **Figure 2.9** shows a ^{1}H NMR stack plot comparing the spectra of the free **TPU** (**A**), the potential mixture of the [2]pseudorotaxane orientational isomers ***U*** and ***D*** for **TPU⊃(C_5)PyTTzOMe(TsO)** (**B**) and **TPU⊃(C_8)PyTTzOMe(TsO)** (**C**), and the free dye **(C_8)PyTTzOMe(TsO)** (**D**). Notably, the spectrum of **TPU⊃(C_5)PyTTzOMe(TsO)** (**B**) appears broader than that of **TPU⊃(C_8)PyTTzOMe(TsO)** (**C**), in particular in the low- and mid-field region. This may be attributed to a different distribution of the orientational isomers or to a kinetic effect of the longer C8 alkyl chain that could reduce the kinetic of the complexation reaction.

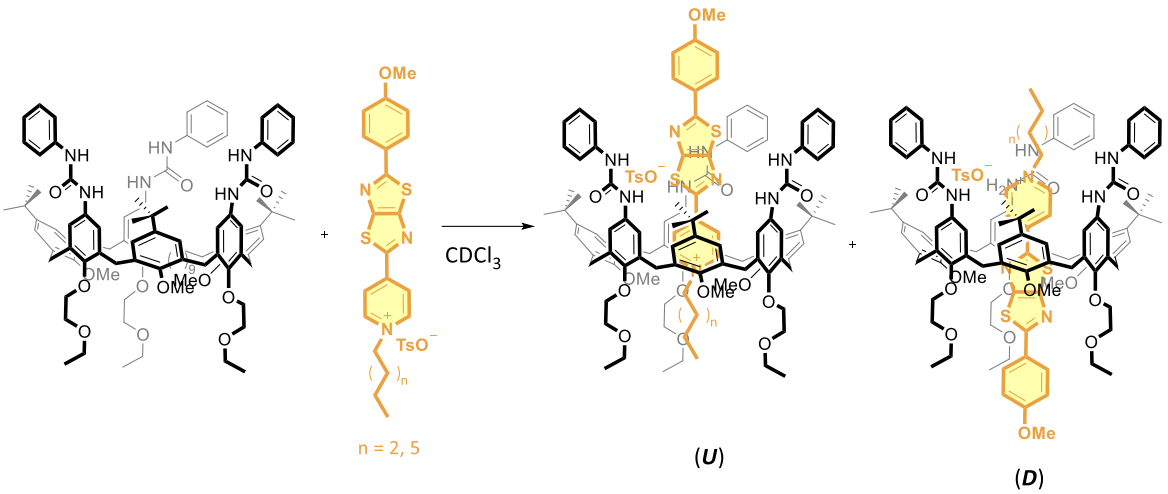

Scheme 2.6 Formation of [2]pseudorotaxane orientational isomers **[TPU⊃(C_{n+3})PyTTzOMe(TsO)]$_{Up}$** and **[TPU⊃(C_{n+3})PyTTzOMe(TsO)]$_{Down}$**.

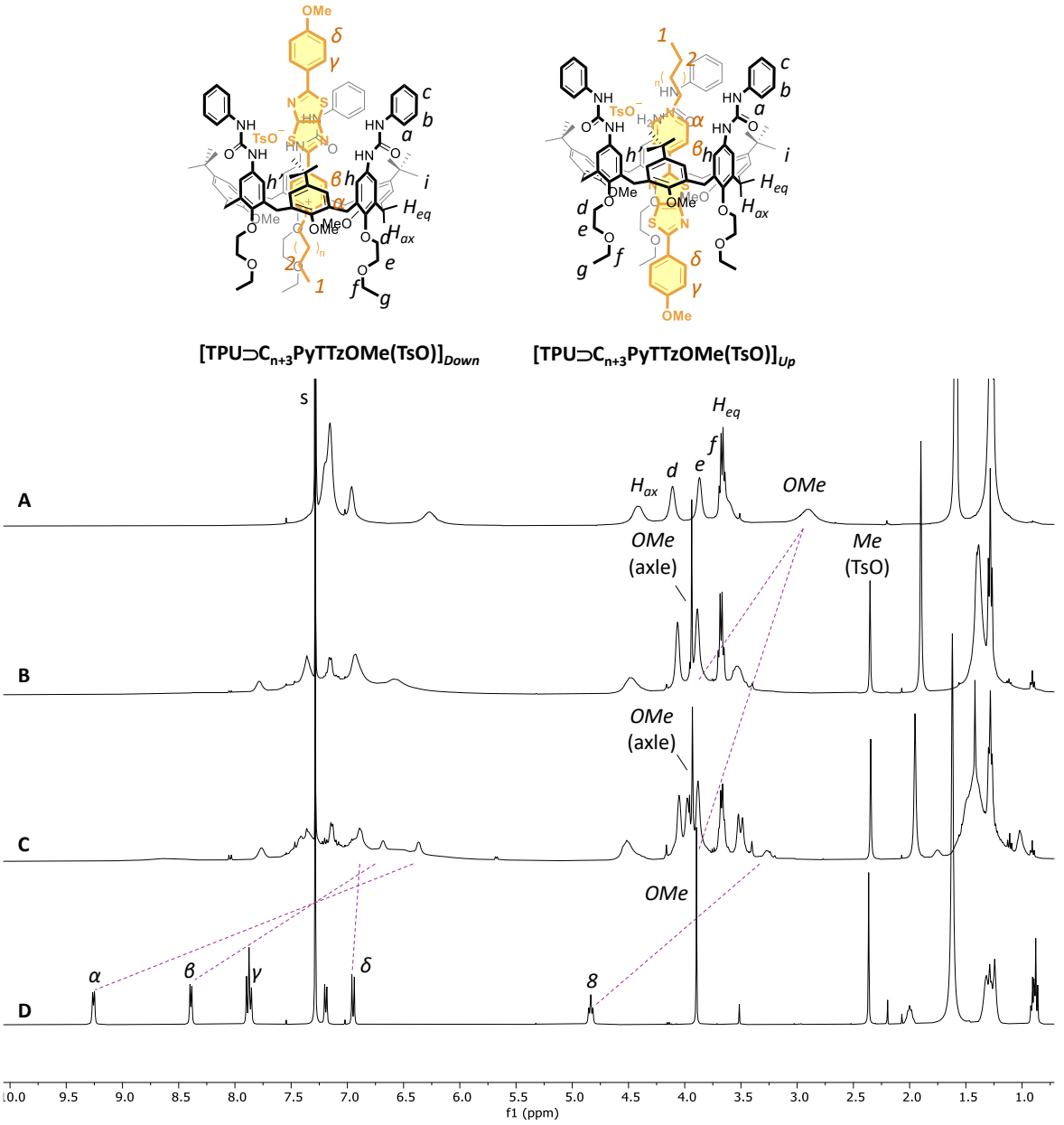

Figure 2.9. ^{1}H NMR stack plot ($CDCl_3$, 400 MHz, 298 K) of **TPU** (**A**), 1:1 mixture of **TPU** and **(C_5)PyTTzOMe(TsO)** (**B**), 1:1 mixture of **TPU** and **(C_8)PyTTzOMe(TsO)** (**C**), and **(C_8)PyTTzOMe(TsO)** (**D**).

To assign peaks in the ^{1}H NMR spectrum of **TPU⊃(C_8)PyTTzOMe(TsO)**, a 2D HSQC experiment was recorded (**Figure 2.10**). The characteristic signals corresponding to the formation of a [2]pseudorotaxane complex were observed: the signal of the calix[6]arene methoxy groups downfield shifted to 3.98 ppm.[9] The aromatic protons of the pyridinium moiety, deeply engulfed within the cavity, experienced significant up-field shifts. The *α* protons shifted from 9.26 ppm in the free dye to 6.38 ppm in the complex, the *β* protons shifted from 8.39 ppm to 6.68 ppm, and the *δ* protons from 6.95 ppm to 6.89 ppm. However, the *γ* protons were overlapped with other signals, making their identification challenging. The formation of the two possible orientational isomers was identified by looking at the signal of the dye methoxy group. In the ^{13}C spectrum of the free dye,

the methoxy group is observed at 55.4 ppm. In the HSCQ spectrum of the 1:1 mixture with **TPU**, a unique signal at the same chemical ^{13}C shift suggests the presence of only one isomer.

Additionally, the formation of the *partial cone* conformation (*p*C) (**Figure 2.10**) of the calix[6]arene was observed: the low-intensity signal visible at *F*1,*F*2 = 34.8,3.9 ppm, in the center of the spectrum (see green circle in **Figure 2.10**), was attributed to the macrocycle bridging methylene groups (*) (see the inset sketch) adjacent to a flipped p-*tert*-butyl anisole ring (green colored in the inset sketch) of the *p*C conformation. This flipped ring determines the splitting of several signals, such as, for example, the *α* signal of **(C$_8$)PyTTzOMe(TsO)** splits into two peaks, one more intense at 6.38 ppm corresponding to the cone (*C*) conformation, and another less intense at 5.67 ppm corresponding to *p*C conformation. This phenomenon has been commonly observed in previous studies of threaded species involving calix[6]arene **TPU** and similar calix[6]arene derivatives with charged guests in chlorinated solvents.[9]

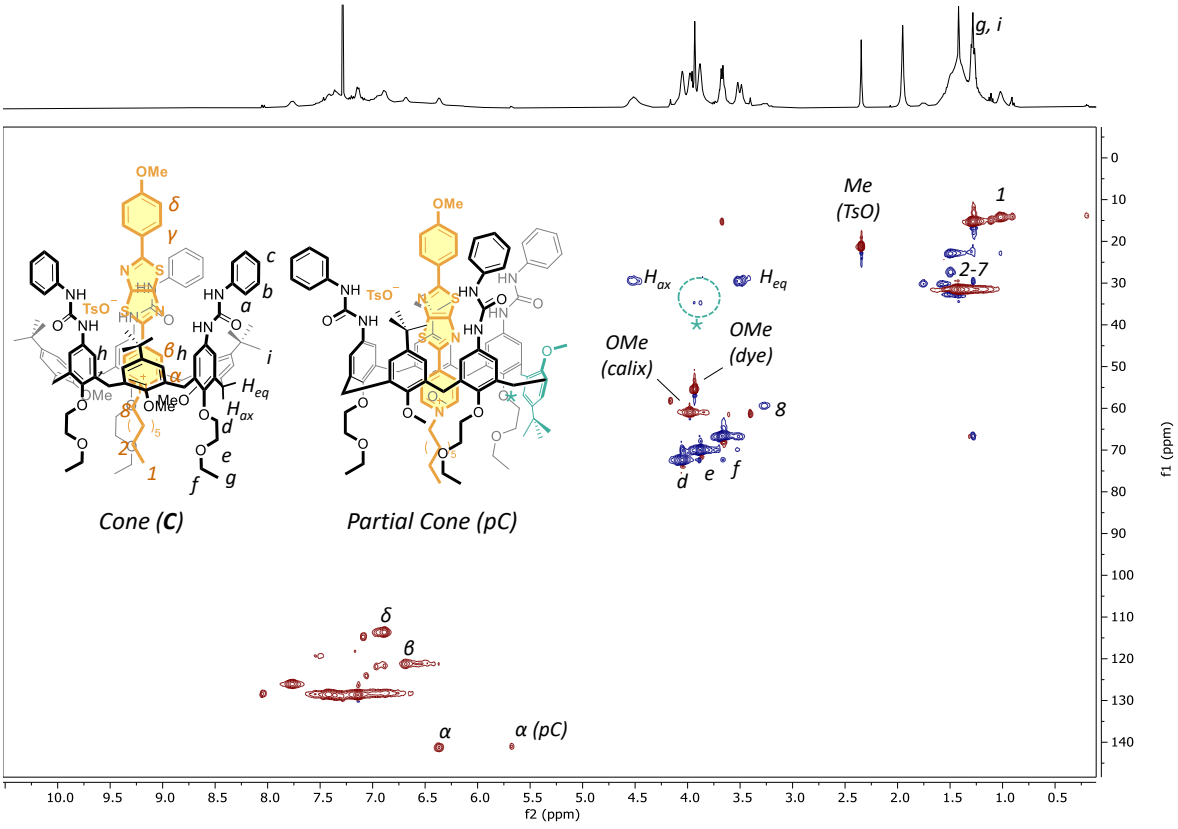

Figure 2.10. 2D Edited HSQC ($CDCl_3$, 400 MHz, 298 K) of **TPU⊃(C$_8$)PyTTzOMe(TsO)**. Positive peaks (CH_3 and CH) are shown in red, while negative ones (CH_2) are in blue. Methylene proton signals (*) of **TPU** in *p*C conformation have been highlighted with a dashed green circle.

The selective formation of a single isomer, tentatively identified as the ***U*** isomer, was further supported through a selective ROESY NMR experiment. The 1D ROESY spectrum (**Figure 2.11**) revealed spatial correlations between the dye's methoxy group, whose signal resonates at 3.93 ppm, and the protons *a* and *b* of the phenyl urea moieties at the macrocycle's upper rim, as well as

with its *δ* protons, as indicated by the red dashed lines in **Figure 2.11**. However, the signal of the dye methoxy group was challenging to select due to partial overlap with other resonances at 3.93 ppm. Nevertheless, the ROE correlations suggest a predominant formation of the ***U*** orientational isomer. The absence of detectable ***D*** isomer signals in the NMR spectrum does not necessarily imply that this orientational isomer is not formed, but rather suggests that its population in solution may be too low to be detectable by this technique. It is likely that the ***U*** isomer represents the thermodynamically more stable form, while ***D***, though kinetically favored, forms and interconverts too rapidly to be observed by NMR (as also discussed in Chapter 1 for stilbazolium dyes). Kinetic studies are planned to further investigate and demonstrate this hypothesis.

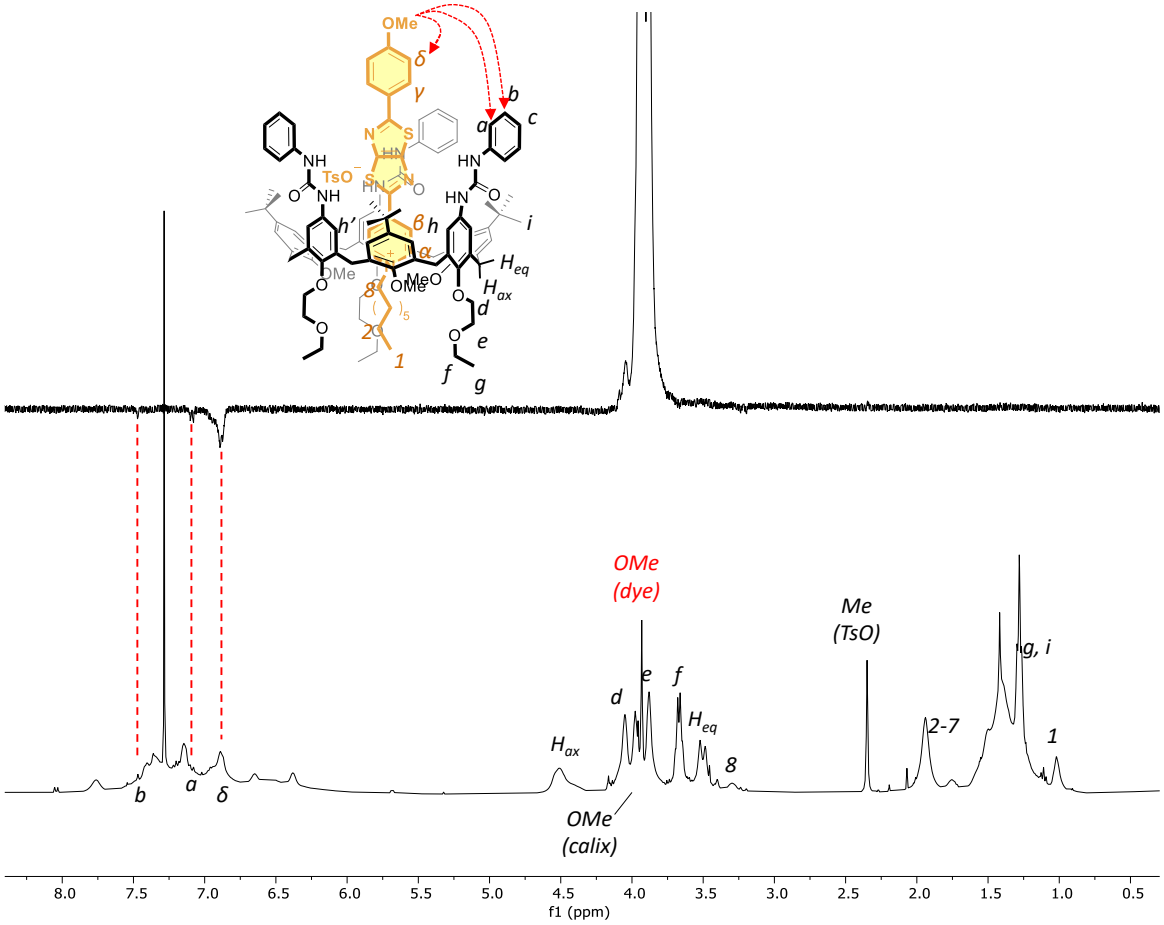

Figure 2.11. Stack plot of (top) 1D ROESY (Spin-lock = 200 ms) and (bottom) ^{1}H NMR of the 1:1 mixture of **TPU** and **(C$_8$)PyTTzOMe(TsO)** ($CDCl_3$, 400 MHz, 298 K). The red dashed lines show the spatial proximity between *OMe* protons of **(C$_8$)PyTTzOMe(TsO)** and protons *a* and *b* of **TPU**.

The complexation of asymmetric **(C$_8$)PyTTzBr(TsO)** with **TPU** was also investigated through NMR spectroscopy. As before, the formation of two isomers must be considered: the ***U*** isomer, where the bromide atom is close to the phenyl urea groups on the upper rim of the cavity, and the ***D*** isomer, where the bromide atom is located near the lower rim of the cavity (**Scheme 2.7**).

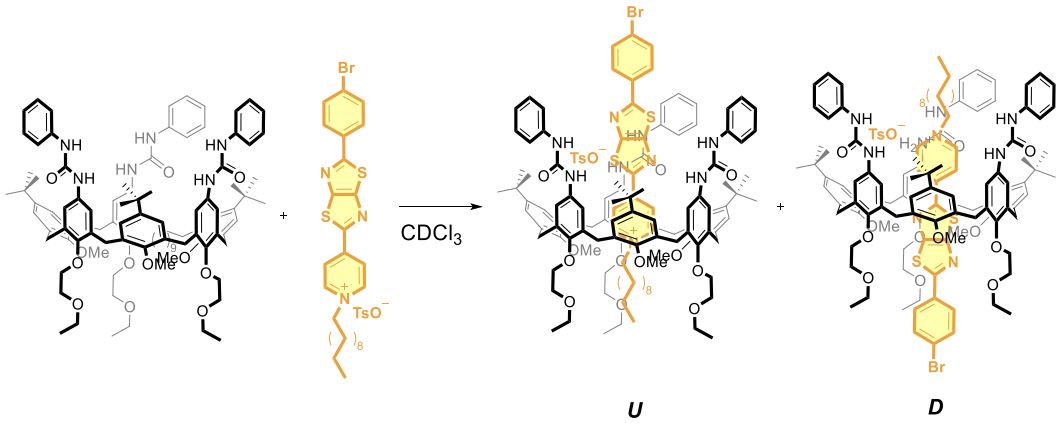

Scheme 2.7 Scheme of the formation of [2]pseudorotaxane ***U*** and ***D*** isomers of **TPU⊃(C$_8$)PyTTzBr(TsO)**.

The ^{1}H NMR stack plot of **Figure 2.12** displays the spectra of **TPU** (top), **(C$_8$)PyTTzBr(TsO)** (bottom), and their 1:1 mixture (middle) in deuterated chloroform. Based on the results obtained for the complexation of **(C$_8$)PyTTzOMe(TsO) (Figure 2.9**), also in this case, the ***U*** isomer is the sole orientational isomer that can be detected with NMR techniques.

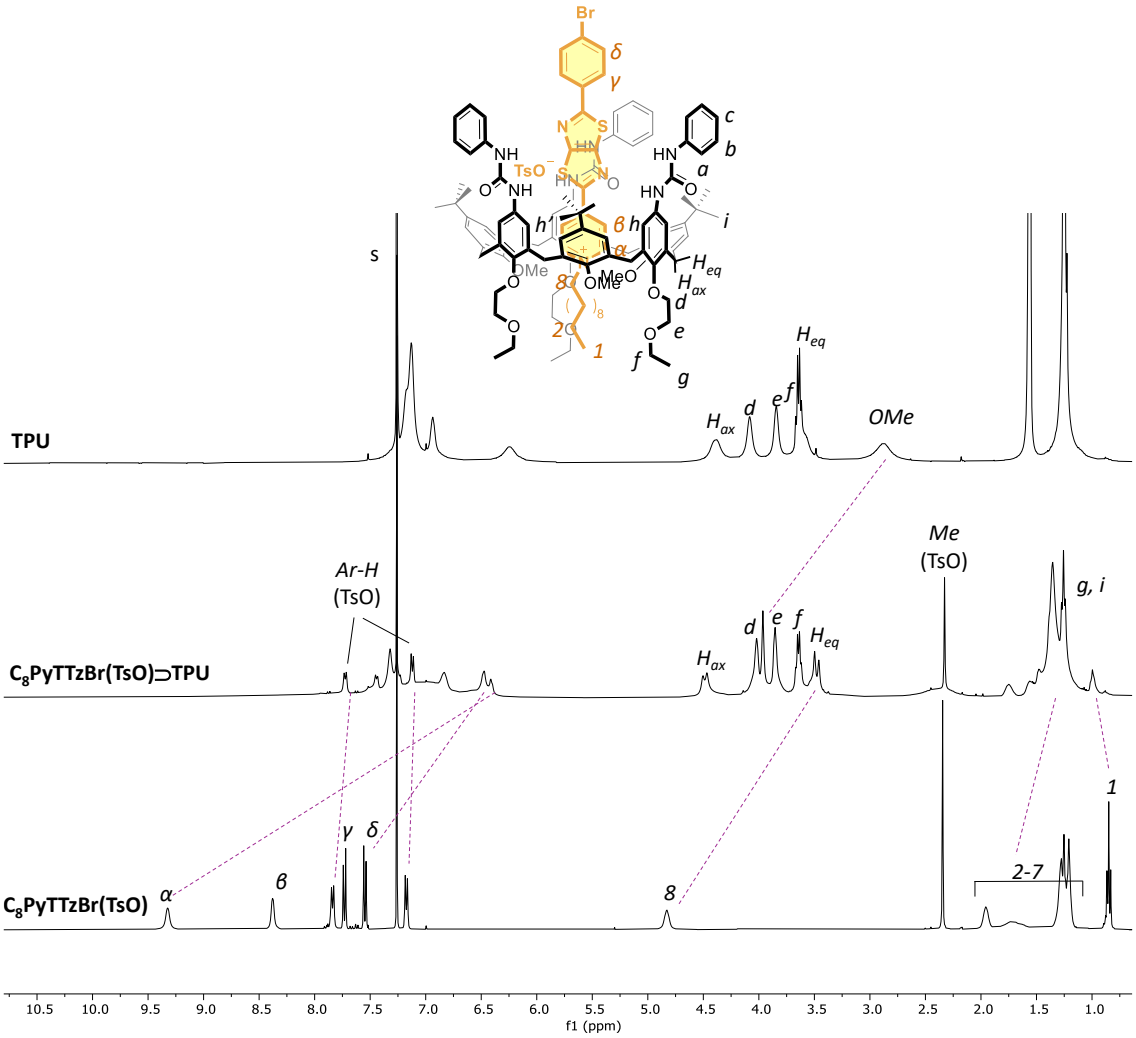

Figure 2.12 ^{1}H NMR stack plot (CDCl$_3$, 400 MHz, 298 K) of **TPU** (top), 1:1 mixture of **TPU** and **C$_8$PyTTzBr(TsO)** (middle), and **C$_8$PyTTzBr(TsO)** (bottom).

NMR investigation of symmetric TTz-based dyes

The complexation of symmetric **TTz**-based dyes, featuring tosylates as counterions, with **TPU**, was facilitated by the symmetry of the dyes, which excluded the formation of orientational isomers. The interaction between the dyes and **TPU** was investigated using ^{1}H NMR spectroscopy in deuterated chloroform by mixing the calix[6]arene with either **$(C_8)_2Py_2TTz(2TsO)$** or **$(C_5)_2Py_2TTz(2TsO)$** in a 1:1 molar ratio (**Scheme 2.8**).

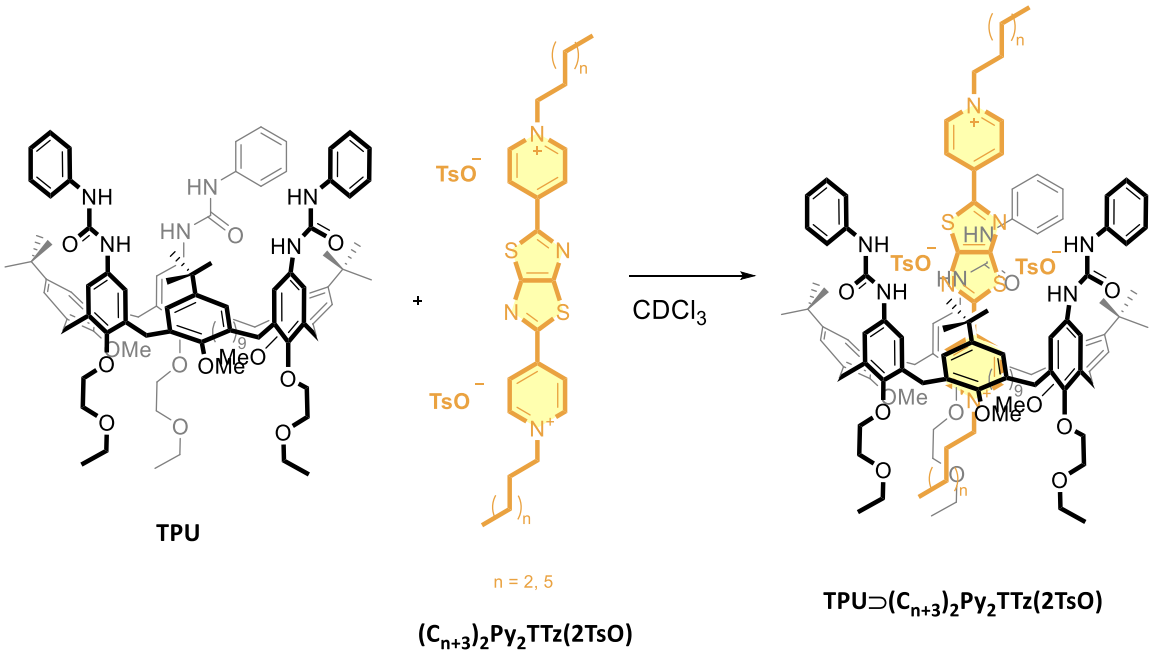

Scheme 2.8 Formation of [2]pseudorotaxanes **TPU⊃$(C_5)_2Py_2TTz(2TsO)$** and **TPU⊃$(C_8)Py_2TTz(2TsO)$**.

As previously observed for the asymmetric dyes (**Figure 2.9**), the formation of [2]pseudorotaxane complexes was witnessed by the downfield shift of the signal of the **TPU** methoxy group from 2.88 to 4.00 ppm in the resulting mixtures. For example, **Figure 2.13** shows the ^{1}H NMR stack plot of the 1:1 mixture, along with the free reactants **TPU** and **$(C_8)_2Py_2TTz(2TsO)$**. Besides the methoxy groups signal shift, the increased signal sharpness observed in the 1:1 mixture relative to free **TPU** serves as further evidence of the formation of the pseudorotaxane complex **TPU⊃$(C_8)_2Py_2TTz(2TsO)$**. Converesely, the spectrum for the complex with the dye having the shorter C5 alkyl chains, **TPU⊃$(C_5)_2Py_2TTz(2TsO)$** (not reported), was broader and exhibited less well-defined peaks compared to that of **TPU⊃$(C_8)_2Py_2TTz(2TsO)$**, similarly to what observed before for asymmetric **TTz**-base dyes.

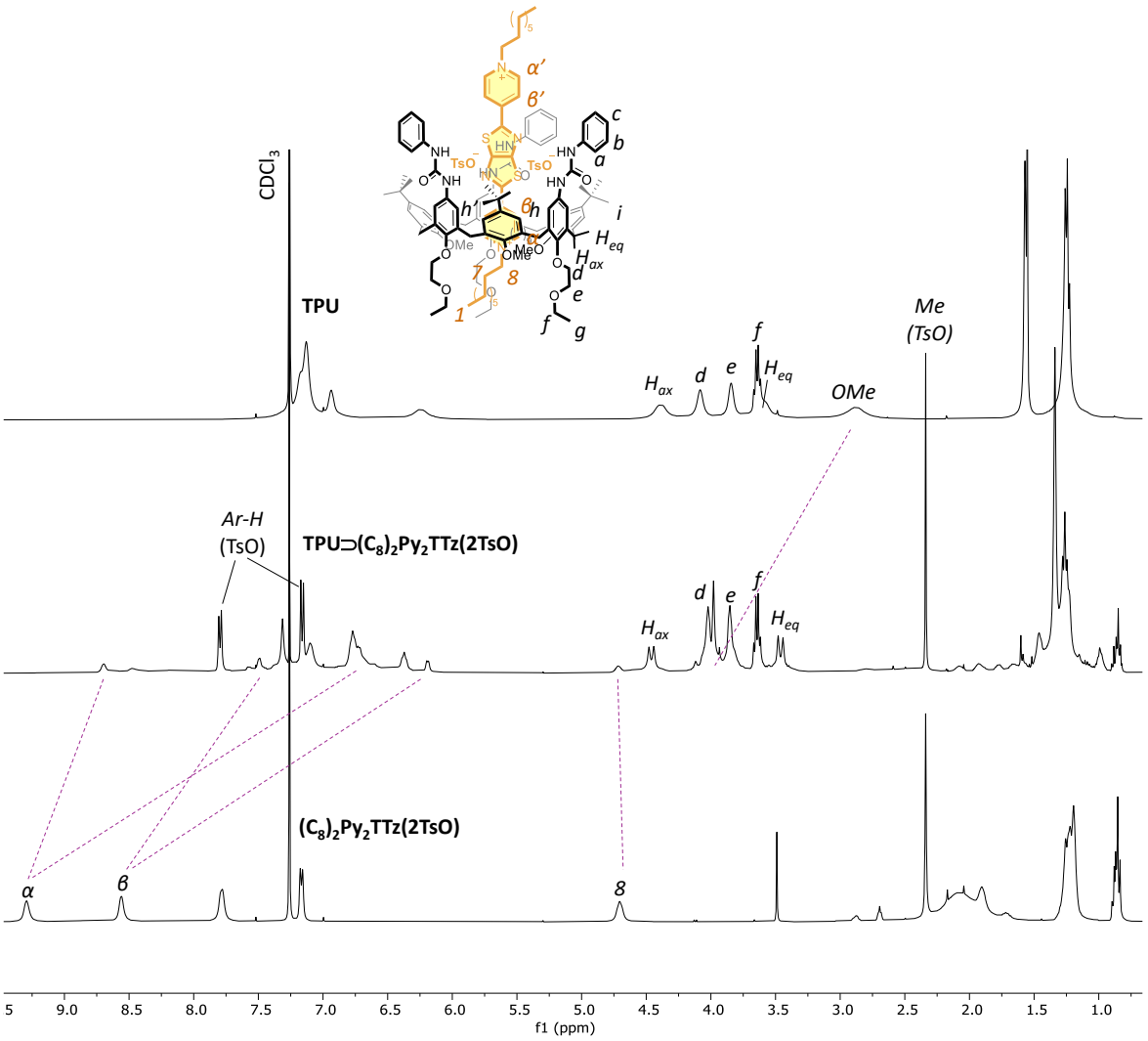

Figure 2.13 ^{1}H NMR stack plot ($CDCl_3$, 400 MHz, 298 K) of **TPU** (top), of **TPU⊃$(C_8)_2Py_2TTz(2TsO)$** (middle), and **$(C_8)_2Py_2TTz(2TsO)$** (bottom).

A detailed analysis of the 2D HSQC NMR spectrum (**Figure 2.14**) shows the splitting of the cross-peak relative to protons *δ* of the dye into two cross-peaks: one intense at *F*1,*F*2 = 61.5,4.75 ppm and one a less intense at *F*1,*F*2 = 61.5,4.63 ppm. Similarly, two cross-peaks can be identified for the methoxy group of **TPU**: a more intense signal at *F*1,*F*2 = 61.2,4.00 ppm and a less intense one at *F*1,*F*2 = 61.2,3.83 ppm. Additionally, the *α* protons of the pyridine moiety, which give a unique signal at 9.23 ppm in the proton spectrum of the free dye (**Figure 2.13**), split into four cross-peaks: the *α'* protons inside the cavity resonated at a higher field due to the cavity's effect with a more intense signal at *F*1,*F*2 = 141.8,6.74 ppm and one less intense at *F*1,*F*2 = 141.8,6.52 ppm, while the *α''* protons, which are external the cavity, give rise to an intense signal at *F*1,*F*2 = 143.7,8.74 ppm and one less intense at *F*1,*F*2 = 143.7,8.51 ppm. Similarly, *β* protons of the pyridine moiety, which in the free dyes resonate as a broad signal at 8.56 ppm, originated two intense signals at *F*1,*F*2 = 123.1,7.53 and *F*1,*F*2 = 121.9,6.22 ppm and one less intense at *F*1,*F*2 = 123.1,7.36 ppm. The HSCQ spectrum also displays two unexpected cross-peaks at unusual fields: a methyl group at *F*1,*F*2 =

15.3,3.67 ppm, and a methylene one at *F*1,*F*2 = 66.7,1.29 ppm, which were of challenging assignation.

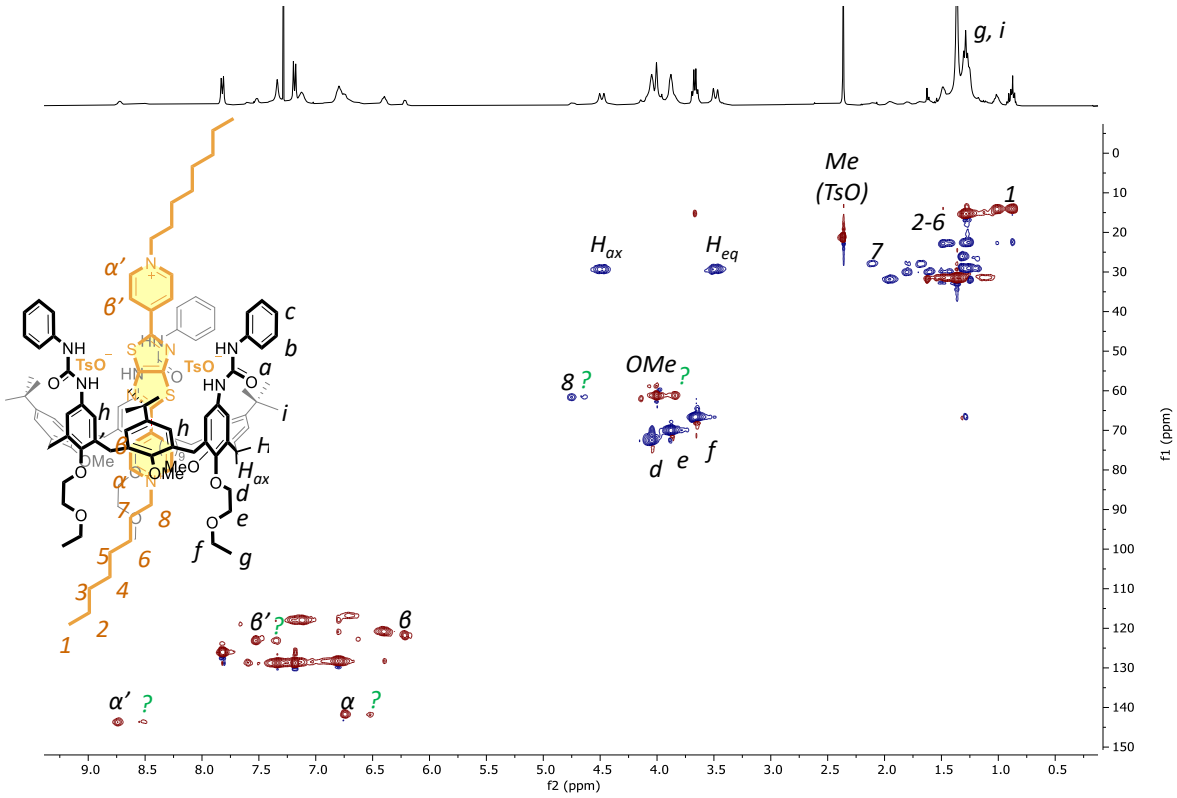

Figure 2.14 Edited HSQC ($CDCl_3$, 400 MHz, 298 K) of pseudorotaxane **TPU⊃$(C_8)_2Py_2TTz(2TsO)$**. Positive peaks (CH_3 and CH) are shown in red, while negative ones (CH_2) are in blue.

The duplication of peaks from the central core of the **TTz** dye (pyridinium protons *α* and *β*, and methylene protons *8*) was an unexpected finding that could be tentatively explained by also considering the formation of higher-order adducts with stoichiometry beyond 1:1 (**Figure 2.15**).

To investigate this hypothesis, a second equivalent of **TPU** was added to the 1:1 mixture. The ^{1}H NMR spectrum of the 1:2 mixture (**Figure 2.15**, top) appeared broader than the 1:1 mixture. Reasonably, this signal broadness could arise either by the presence in solution of an excess of free **TPU** or by the formation of a 1:2 complex in which each of the two pyridine units of dye interacts with **TPU** affording the **2TPU⊃$(C_8)_2Py_2TTz(2TsO)$** [3]pseudorotaxane. By comparing the HSQC spectra of the 1:1 and 1:2 mixtures (cf. **Figures 2.14** and **2.16**), it is possible to note that the dye signals splitting seen for the former are no longer observable in the latter. As a result, the aromatic protons in ortho to the positively charged pyridine nitrogens give rise only to two distinct signals at *F*1,*F*2 = 143.6,8.63 ppm (*α′*) and *F*1,*F*2 = 141.6,6.73 ppm (*α″*) instead of the previous four. The disappearance of the minor "twin" cross-peaks seems to support the formation of adduct species involving two calix[6]arene macrocycles. The asymmetrical magnetic environment experienced by the protons belonging to the dye core (protons *α* split in *α′* and *α″*) suggests the formation of a *upper-to-lower* rims [3]pseudorotaxane arrangement rather than a symmetric *upper-to-upper* rims

configuration, which would only yield a single signal. However, further analyses are required to fully elucidate the exact geometry of the adduct formed.

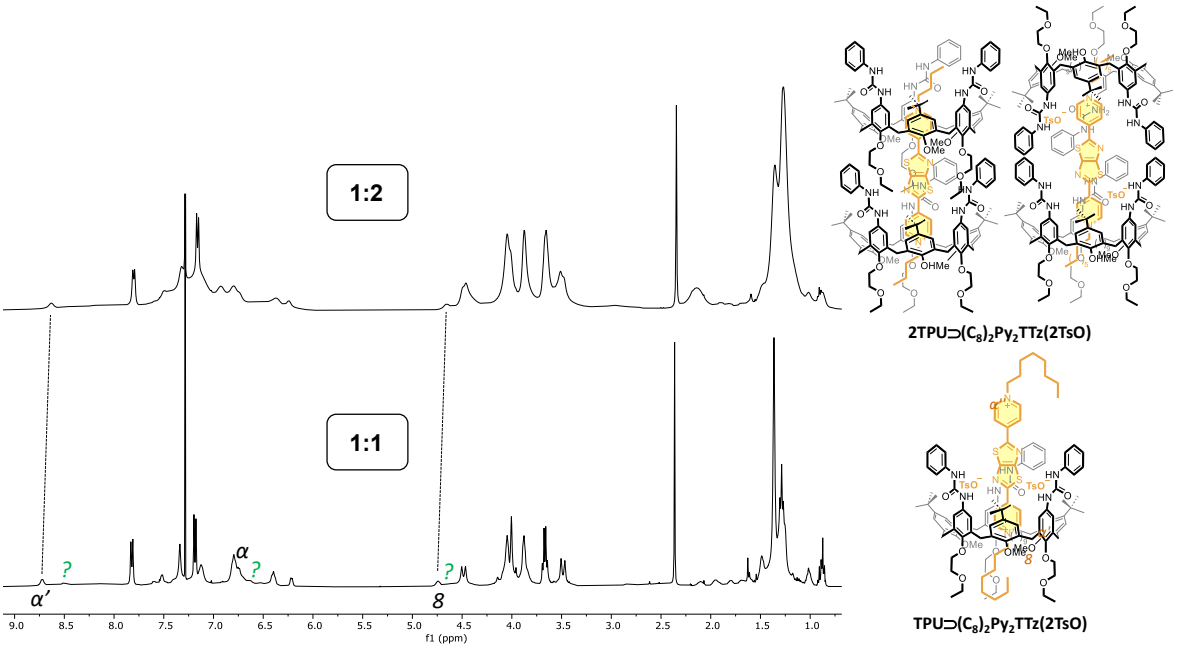

Figure 2.15 ^{1}H NMR stack plot ($CDCl_3$, 400 MHz, 298 K) of the 1:1 and 1:2 mixtures of **$(C_8)_2Py_2TTz(2TsO)$** and **TPU**.

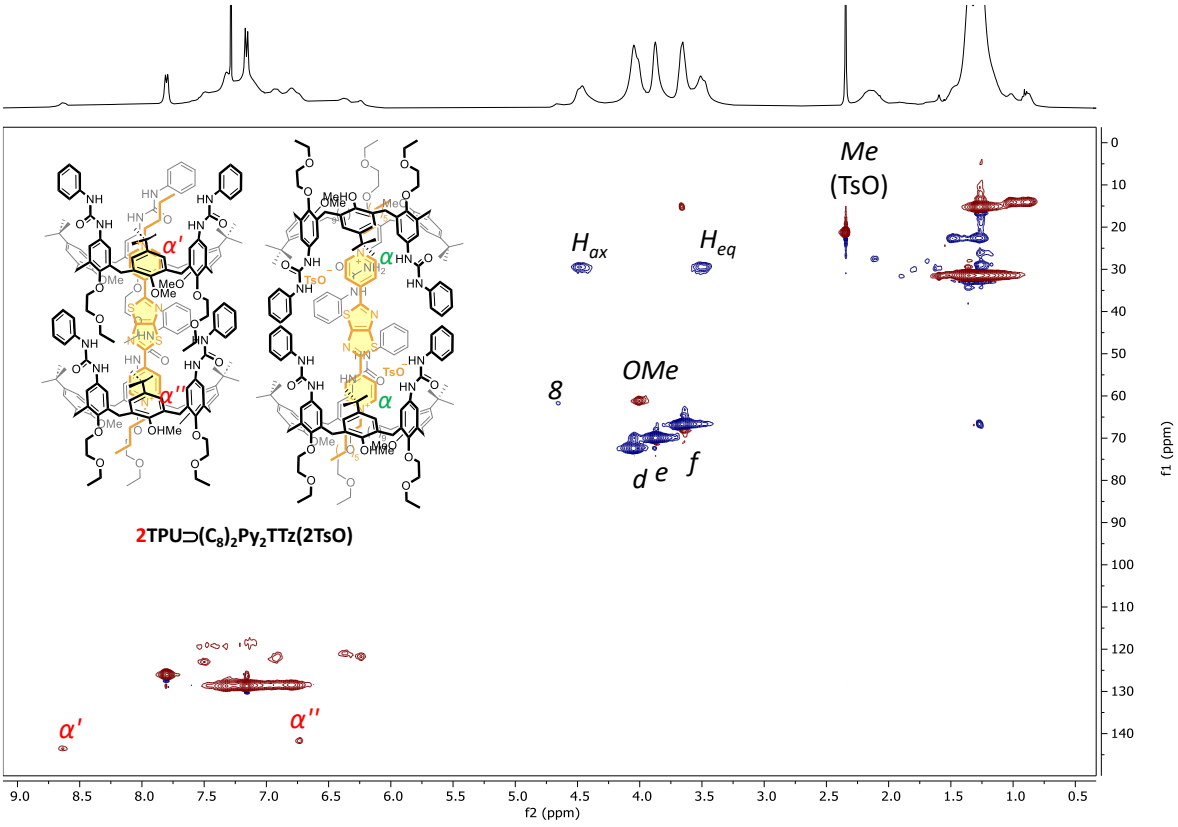

Figure 2.16 Edited HSQC ($CDCl_3$, 400 MHz, 298 K) of the 1:2 mixture of **$(C_8)_2PyTTz(2TsO)$** and **TPU**. Positive peaks (CH_3 and CH) are shown in red, while negative ones (CH_2) are in blue.

A DOSY NMR experiment was then conducted on the 1:2 mixture and the individual components **$(C_8)_2Py_2TTz(2TsO)$** and **TPU**. The diffusion coefficient *D*, which provides insight into how quickly a molecule diffuses through a medium, with higher values indicating species diffusing fast, was used to estimate the molecular weight of the 1:1 and 1:2 adducts. Based on molecular weights, the free dye should exhibit a higher diffusion coefficient compared to **TPU**. In turn, it is expected that the 1:2 adduct, i.e., the [3]pseudorotaxane, will have a lower *D* than the 1:1 adduct ([2]psuedorotaxane) and **TPU**.[10] The fitting of the experimental data allowed us to calculate a diffusion coefficient for **TPU** of $D = 5.25\times10^{-10}$ m²/s and for the free **$(C_8)_2Py_2TTz(2TsO)$** of $D = 3.40\times10^{-9}$m²/s. As expected, the diffusion coefficient calculated for the 1:2 mixture ($D = 3.46\times10^{-10}$ m²/s) was much lower than that of the free **TPU**. Independently of the geometrical arrangement of the two **TPU** units around the dye, the theoretic diffusion coefficient for the [3]pseudorotaxane adduct was calculated using the following formula:[10]

$$\frac{D_{\mathrm{TPU}}}{D_{\mathrm{Dye}}} = \sqrt[3]{\frac{M_{\mathrm{Dye}}}{M_{\mathrm{TPU}}}}$$

which yields a diffusion coefficient of 3.82×10^{-10} m²/s. This value is slightly larger than the value determined experimentally ($D = 3.46\times10^{-10}$ m²/s). Although this result provides evidence supporting the formation of the 1:2 adduct, the exact geometric arrangement of the **TPU** macrocycles around the symmetrical **TTz** dye remains unclear. Further studies will be necessary to confirm the precise structure of the proposed [3]pseudorotaxane.

The NMR characterization of the **$(C_5)_2Py_2TTz(2TsO)$** and **TPU** wheel mixture presented greater challenges compared to the analogous system involving **$(C_8)_2Py_2TTz(2TsO)$**, which was already inherently complex. Despite efforts with 2D NMR techniques, the high mobility of the system remained unresolved, ultimately making DOSY NMR analysis impractical for such mixture.

UV-Visible, fluorescence, and electrochemical investigation of symmetric $(C_8)_2Py_2TTz(2PF_6)$

The symmetric dye **$(C_8)_2Py_2TTz(2PF_6)$** was selected as a model compound to investigate the photophysical properties of **TTz**-based dyes in dichloromethane. **Figure 2.17** presents the absorbance and emission spectra of **$(C_8)_2Py_2TTz(2PF_6)$** at a concentration of 3 µM. The dye shows an absorption maximum of 405 nm, while the emission maximum is red-shifted to 465 nm, resulting in a Stokes Shift of 60 nm (3,186 cm^{-1}). The molar extinction coefficient (ε) was determined as 4×10^4 $M^{-1}cm^{-1}$, and the fluorescence quantum yield (Φ_{fluo}) was remarkably high at 99%.

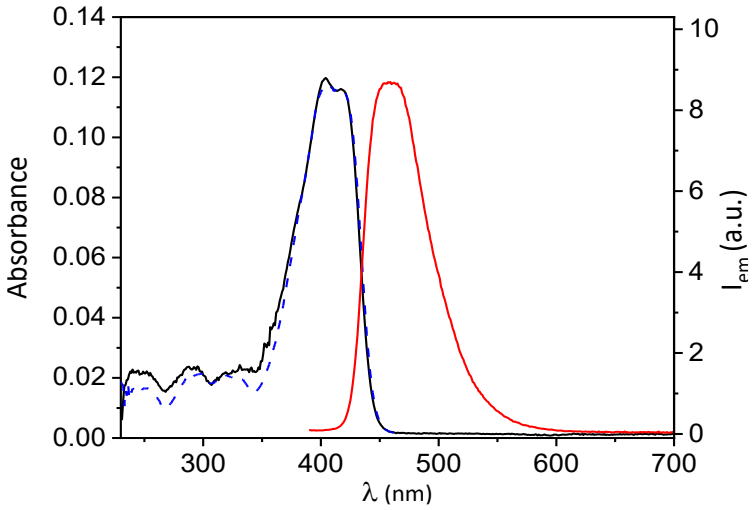

Figure 2.17 Absorbance and emission spectra of **$(C_8)_2Py_2TTz(2PF_6)$** (c = 3 µM) in dichloromethane at 298 K. Excitation wavelength 402 nm.

The interaction between the dye and **TPU** calix[6]arene was further explored using UV-Visible titrations. Unlike NMR measurements, which were conducted at higher concentrations (10^{-2} to 10^{-3} M), UV-Vis analyses require significantly lower concentrations, typically around 10^{-5} M, making direct comparison between the two techniques not feasible.

To investigate the complexation of **$(C_8)_2Py_2TTz(2PF_6)$** with **TPU**, the variation of the absorbance of the dye, at a concentration of 5×10^{-5} M, was monitored upon incremental additions of a solution of **TPU** in dichloromethane (c = 0.3×10^{-3} M). **Figure 2.18** presents the resulting collection of UV-Vis spectra. Upon the addition of **TPU**, a new absorption band emerged around 500 nm, indicative of a CT interaction generated by the dye complexation. Analysis of the titration data with a 1:1 binding model yielded an association constant of log*K* = 4.1, which is comparatively much weaker than the association constant observed for dioctyl viologen salt **$DOV(2PF_6)$** (log*K* = 5.9).[11]

The significant advantage of this system lies in the dye's strong emission, which facilitates the study of complexation and its effects on fluorescence. The variation of the dye's emission (c = 5×10^{-5} M) was monitored upon addition of incremental amounts of a **TPU** solution (c = 0.3×10^{-3} M). The fluorescence variation, presented in **Figure 2.19**, demonstrates that the dye's emission was quenched upon complexation with **TPU**. This phenomenon is attributed to the formation of a CT interaction band between the calix[6]arene and the **TTz**-based dye. The CT excited state, energetically lower than the excited state of the **TTz**-based dye, leads to a non-radiative state relaxation resulting in fluorescence quenching. Thus, a competitive interaction arises between the CT process and the intrinsic emission of the dye.

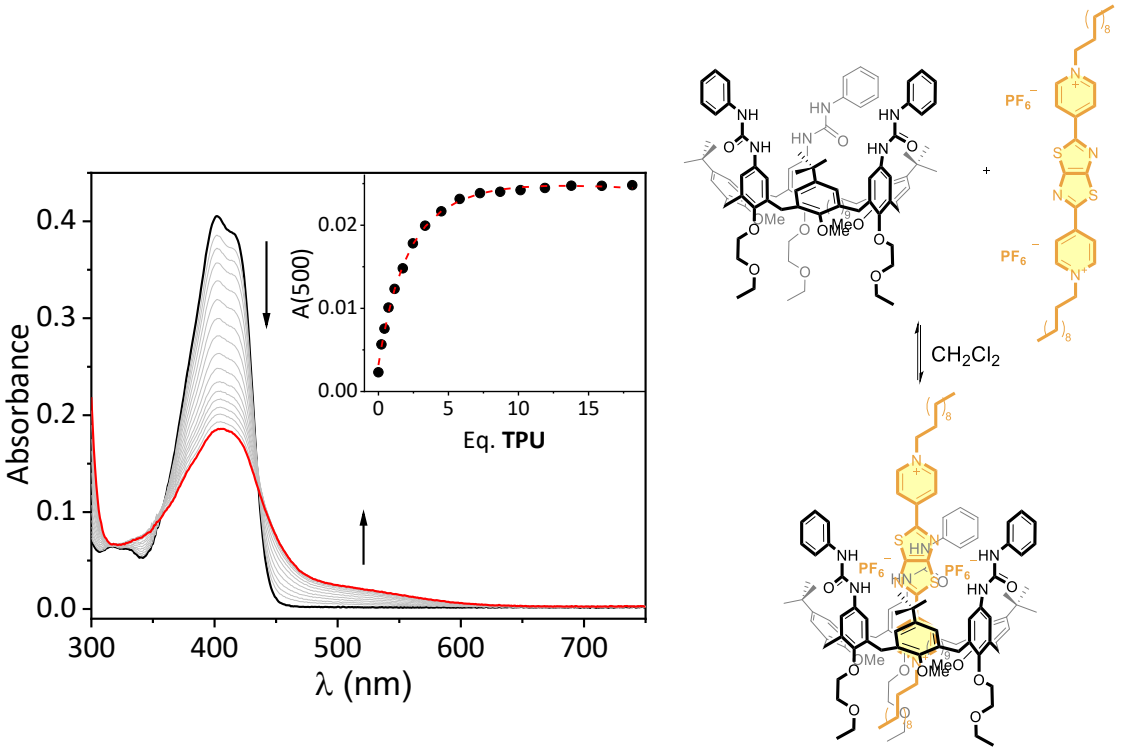

Figure 2.18 Left: collection of absorbance spectra taken during the titration of **$(C_8)_2Py_2TTz(2PF_6)$** solution in CH_2Cl_2 (c = 5×10^{-5} M) with a solution of **TPU** in CH_2Cl_2 (c = 0.3×10^{-3} M) at 298 K; right: schematic representation of the complexation between **$(C_8)_2Py_2TTz(2PF_6)$** and **TPU**.

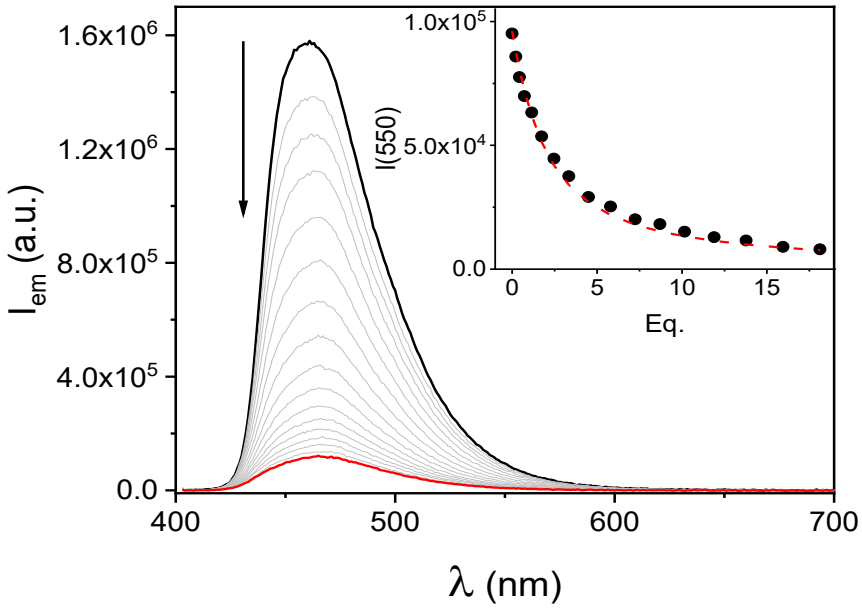

Figure 2.19 Collection of emission spectra taken during the titration of **$(C_8)_2Py_2TTz(2PF_6)$** solution in CH_2Cl_2 (c = 5×10^{-5} M, λ_{max}^{ex} = 402 nm) with a solution of **TPU** in CH_2Cl_2 (c = 0.3×10^{-3} M) at 298 K.

The kinetic of the complex formation was subsequently examined using the stopped-flow technique. The threading and dethreading processes were monitored at 405 nm and 445 nm, respectively (**Figure 2.20**). The kinetic rate constant for the threading process was determined to be k_{th} = 2.7×10^3 $M^{-1}s^{-1}$, while the rate constant for the dethreading process was k_{deth} = 0.27 s^{-1}. These

values indicate that the threading kinetics are comparable to those observed for **DOV(2PF$_6$)**, which has a threading rate constant of $k_{th, DOV}$ = 6.0×10^3 M^{-1}s^{-1}.

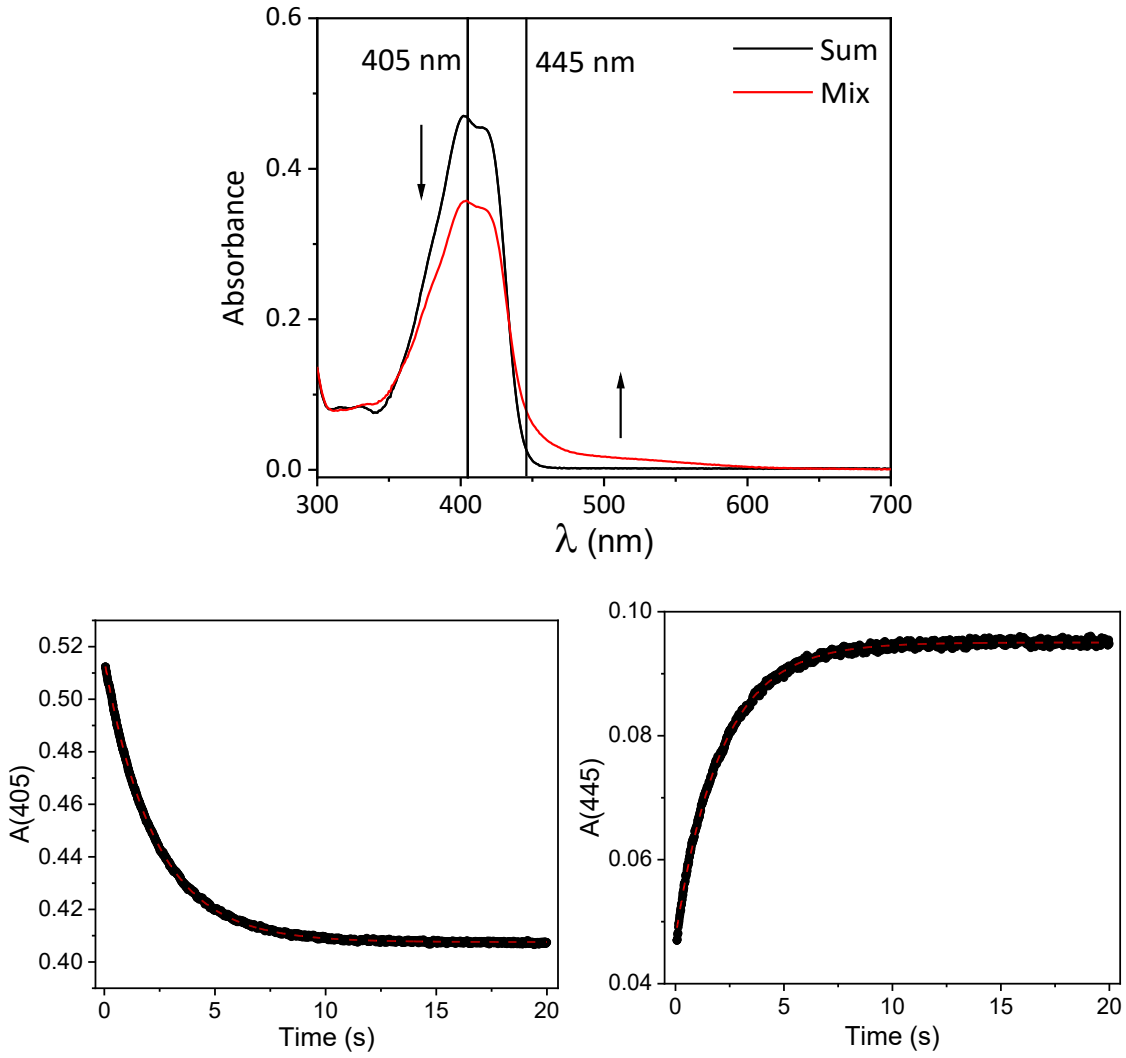

Figure 2.20 Top: Sum of the absorption spectra of **TPU** and **(C$_8$)$_2$Py$_2$TTz(2PF$_6$)** (black line) and the absorption spectrum of the mixture of **TPU** and **(C$_8$)$_2$Py$_2$TTz(2PF$_6$)** (red line) (CH_2Cl_2, 298 K, λ = 300-700 nm region); bottom: absorption changes at 405 nm (left) and 445 nm (right) upon mixing **(C$_8$)$_2$Py$_2$TTz(2PF$_6$)** and **TPU**.

The electrochemical properties of **(C$_8$)$_2$Py$_2$TTz(2PF$_6$)** and its complex with **TPU** were also examined through cyclic voltammetry (CV). The CV of **(C$_8$)$_2$Py$_2$TTz(2PF$_6$)** exhibits characteristic redox behavior typical of di-alkyl viologen salts. **Figure 2.21** compares the CV spectra of **DOV·(2PF$_6$)** (red line) and **(C$_8$)$_2$Py$_2$TTz(2PF$_6$)** (black line). Both spectra display two reversible redox processes. The first reduction occurs at a lower potential for **DOV·(2PF$_6$)** (-0.29 V) compared to **(C$_8$)$_2$Py$_2$TTz(2PF$_6$)**, where the reduction potential is slightly shifted to -0.35 V. Conversely, the second reduction event occurs at a higher potential for **(C$_8$)$_2$Py$_2$TTz(2PF$_6$)** (-0.56 V) than for **DOV·(2PF$_6$)** (-0.81 V), indicating that the second reduction is more easily achieved in **(C$_8$)$_2$Py$_2$TTz(2PF$_6$)**. In both cases, two reversible redox processes happen.

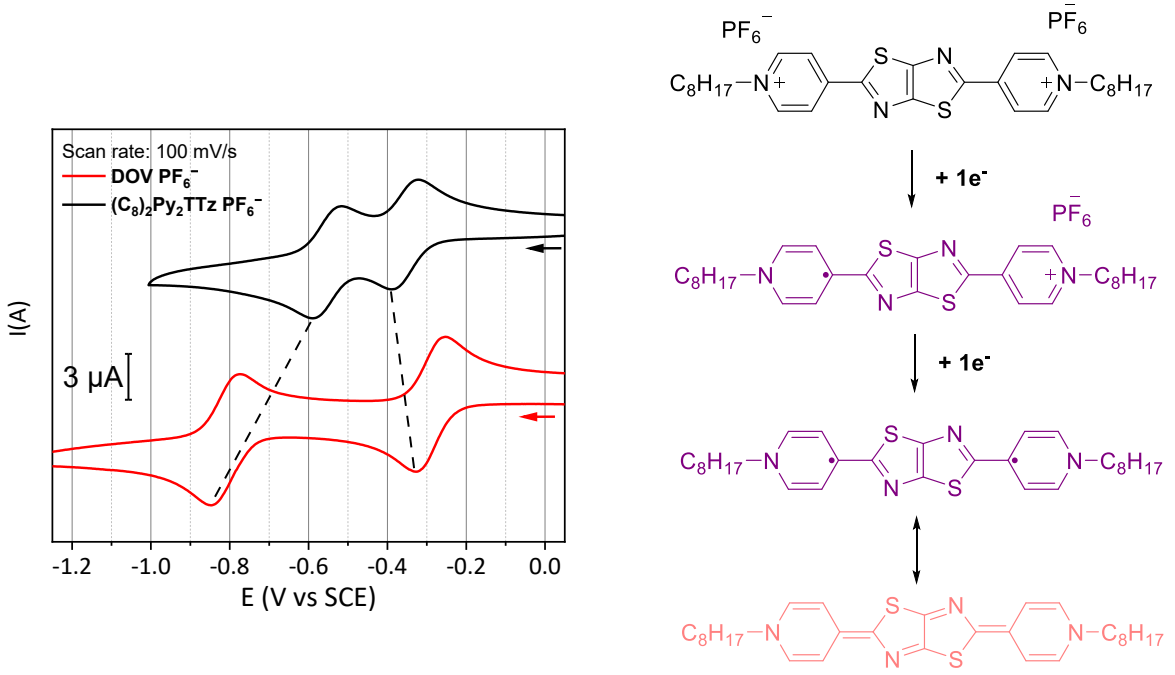

Figure 2.21 Right: cyclic voltammograms (v = 0.1 V·s^{-1}) of **DOV(2PF$_6$)** (black line) and **(C$_8$)$_2$Py$_2$TTz(2PF$_6$)** (red line) in dry DCM (100 mM TEAPF$_6$); left: redox process for **(C$_8$)$_2$Py$_2$TTz(2PF$_6$)**.

Following the evaluation of the electrochemical behavior of **(C$_8$)$_2$Py$_2$TTz(2PF$_6$)**, its interaction with the **TPU** macrocycle was further investigated. A mixture of the dye at a concentration of 2.0×10^{-4} M with an excess of **TPU** (3 equivalents, c = 6.0×10^{-4} M) was analyzed using cyclic voltammetry (CV) and differential pulse voltammetry (DPV) in dichloromethane. **Figure 2.22** presents the CV and DPV spectra for both the free **(C$_8$)$_2$Py$_2$TTz(2PF$_6$)** and its mixture with **TPU**. In both spectra, it is apparent that the two reversible reduction peaks observed in the free **(C$_8$)$_2$Py$_2$TTz(2PF$_6$)** (black line) merge into a single peak in the **TTz**-based dye-**TPU** complex (red line). This suggests that in the mixture, most of the dye exists as a complex with **TPU**, making the reduction process more challenging. Consequently, the first reduction potential shifts from -0.35 V in the free dye to -0.56 V in the complex (**Figure 2.22**). After the initial reduction, the radical-cation species exhibits decreased affinity for the electron-rich cavity of the calix[6]arene, leading to the dethreading of the dye (**Scheme 2.9**). In the oxidation process, the presence of two peaks indicates the restoration of the typical behavior of the free **TTz**-based dye. This suggests that upon oxidation, the positive charge is reinstated, promoting the threading of the dye into the calix[6]arene cavity due to attractive Coulombic interactions. Thus, a threading/dethreading process promoted by external electrochemical stimulus is obtained.

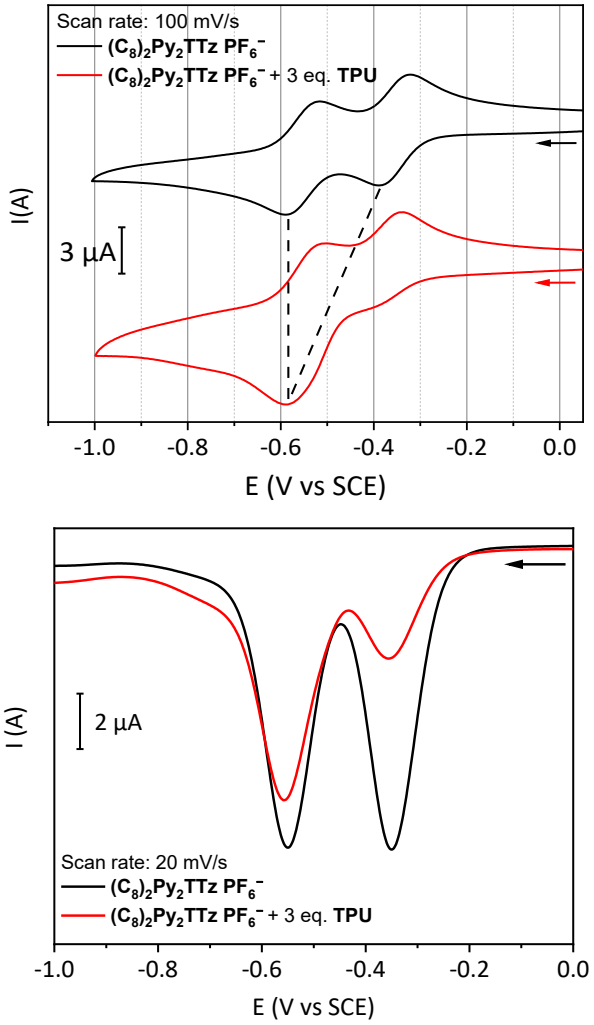

Figure 2.22 Left: Cyclic voltammograms (v = 0.1 V·s^{-1}) of **$(C_8)_2Py_2TTz(2PF_6)$** (black line) and the 1:3 mixture of **$(C_8)_2Py_2TTz(2PF_6)$** and **TPU** (red line) in dry DCM (100 mM $TEAPF_6$); right: DPV in oxidation direction (v = 0.02 V·s^{-1}) of **$(C_8)_2Py_2TTz(2PF_6)$** (black line) and the 1:3 mixture of **$(C_8)_2Py_2TTz(2PF_6)$** and **TPU** (red line) in dry DCM (100 mM $TEAPF_6$).

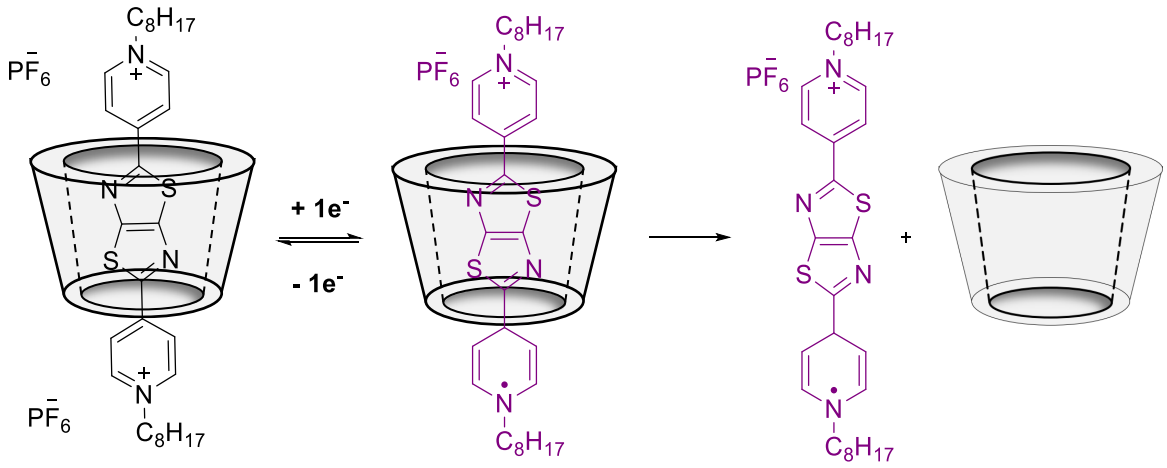

Scheme 2.9 Redox process for the mixture of **$(C_8)_2Py_2TTz(2PF_6)$** and **TPU**.

2 Conclusions

In this chapter, we detailed the synthesis of novel symmetric and asymmetric thiazolo[5,4-*d*]thiazole dyes, followed by their characterization using NMR spectroscopy and optical analysis. Both symmetric and asymmetric **TTz**-based dyes were synthesized *via* a one-pot reaction. For the asymmetric dye, the reaction conditions were specifically optimized based on the nature of the reactants used. The effects of counterion type and alkyl chain length were investigated using UV-Vis and fluorescence spectroscopy. No significant variations were observed with respect to different counterions or chain lengths. However, notable differences in absorption/emission maxima and Stokes shift values were identified between symmetric and asymmetric dyes. Thus, the incorporation of various functional groups (e.g., methoxy, bromide, and fluoride) in the asymmetric **TTz**-based dyes led to distinct changes in their optical properties. The interaction of these dyes with the calix[6]arene macrocycle **TPU** was extensively studied through NMR spectroscopy, UV-Vis and fluorescence spectroscopy, and electrochemical methods. The dyes exhibited electroactivity and a high fluorescence quantum yield, properties that are advantageous to study their complexation with macrocycles. Asymmetric **TTz**-based dyes, owing to their asymmetric structure, have the potential to form two orientational isomers with calix[6]arene. However, only the formation of the ***U*** isomer was observed. This does not imply that only one isomer is produced, but rather that only the ***U*** isomer is detectable at the NMR timescale. The NMR analysis of symmetric **TTz**-based dyes presented interpretative challenges, indicating the potential formation of higher-order adduct species. However, further analyses are required to precisely determine the structure of these dimeric species. UV-Visible measurements indicated a 1:1 stoichiometry, while fluorescence analysis revealed a decrease in the dye's emission intensity upon the addition of the **TPU** wheel. This reduction in fluorescence is attributed to the formation of a charge-transfer band, which is responsible for quenching the dye's emission. Electrochemical analysis revealed that the free **TTz**-based dye exhibits two reversible redox processes. However, when complexed with the **TPU** wheel, the formation of radical-cationic species leads to the dethreading of the dye from the cavity due to the lack of interactions. In conclusion, these novel dyes demonstrate effective performance as guests for the calix[6]arene macrocycle, exhibiting interesting properties with respect to di-alkyl viologen salts. Although the association constant is somewhat lower, the ability to monitor the complexation process through fluorescence analysis adds a significant advantage, enhancing their potential for diverse applications. These dyes hold promise not only as guests for simple calix[6]arene macrocycles but also for more complex systems, as discussed in Chapter 5.

2. Acknowledgments

Thanks to Dr. Leonardo Andreoni (University of Bologna) for UV-Visible, fluorescence and electrochemical measurements. Thanks to Dr. Sara Anzellotti for the help with dye's synthesis.

2. Experimental Section

General Methods

All solvents were dried using standard procedures; all other reagents were of reagent-grade quality obtained from commercial suppliers and used without further purification. Column chromatography was carried out on 230–400 mesh silica gel (Aldrich) unless otherwise stated. NMR spectra were recorded at 400 MHz for ^{1}H and 100 MHz for ^{13}C. Chemical shifts are expressed in ppm (δ) using the residual solvent signal as an internal reference (7.26 ppm for $CHCl_3$, 5.32 for $CHDCl_2$ and 3.31 ppm for CD_2HOD). Coupling constants (J) are given in Hz and the following abbreviations have been used to describe the signals: singlet (s); broad singlet (br. s); doublet (d); triplet (t); quadruplet (q); multiplet (m). Mass spectra were recorded in the ESI mode. Melting points were measured with a Gallenkamp melting-point apparatus and are uncorrected. UV–Vis spectra were recorded on a UV-Visible Cary 300 (Agilent). Fluorescence spectra were recorded on an Edinburgh Instrument FS5. Compounds 2,5-di(pyridin-4-yl)thiazolo[5,4-*d*]thiazole[1] was synthesised according to published procedures.

Synthesis of novel compounds

PyTTzOMe: 4-Pyridinecarboxaldehyde (240 µL, 3.12 mmol, 1.0 eq.), 4-methoxybenzaldehyde (2.65 mL, 21.8 mmol, 7.0 eq.) and dithiooxamide (0.300 g, 2.50 mmol, 1.0 eq.) were refluxed in 10 mL anhydrous DMF for 17 hours under aerobic conditions. The reaction mixture was allowed to sit for 40 minutes, and the precipitated product was collected by filtration and rinsed with DMF. The crude solid was dissolved in MeOH, adsorbed onto silica, and purified by column chromatography (SiO_2, CH_2Cl_2/MeOH 99:1) to afford **PyTTzOMe** as a yellow solid in 24 % yield (0.19 g, 0.06 mmol).

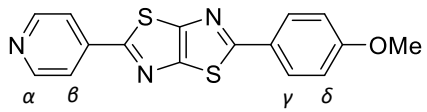

m.p.: 279-282 °C. **^{1}H NMR** (400 MHz, $CDCl_3$) δ = 8.77 (d, *J* = 6.2 Hz, 2H, H_α), 7.98 (d, *J* = 8.8 Hz, 2H, H_β), 7.87 (d, *J* = 6.2 Hz, 2H, H_γ), 7.03 (d, *J* = 8.9 Hz, 2H, H_δ), 3.92 (s, 3H, H_{OMe}) ppm. **^{13}C NMR** (101 MHz, $CDCl_3$) δ = 150.8, 140.8, 128.2, 126.6, 119.9, 114.6, 55.5 ppm. **ESI-MS (+):** calculated for $C_{16}H_{12}N_3OS_2$: m/z (z = 1): 326.03, found: 326.26.

Synthesis of PyTTzF: 4-Pyridinecarboxaldehyde (0.27 g, 2.50 mmol, 1.0 eq.), 4-fluorobenzaldehyde (0.40 g, 3.24 mmol, 1.3 eq.) and dithiooxamide (0.30 g, 2.50 mmol, 1.0 eq) were refluxed in 15 mL anhydrous DMF for 24 hours under aerobic conditions. The reaction mixture was allowed to sit for 40 minutes, and the precipitated product was collected by filtration and rinsed with DMF. The crude solid was dissolved in MeOH, adsorbed onto silica, and purified by column chromatography (SiO_2, CH_2Cl_2/MeOH 99:1) to afford **PyTTzF** as a yellow solid in 14 % yield (0.08 g, 0.26 mmol).

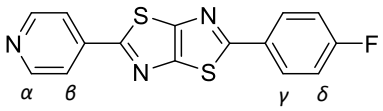

m.p.: 280-282 °C. **^{1}H NMR** (400 MHz, $CDCl_3$) δ = 8.78 (d, *J* = 5.6 Hz, 2H, H_α), 8.1-8.0 (m, 2H, H_γ), 7.88 (d, *J* = 6.2 Hz, 2H, H_β), 7.22 (t, *J* = 8.6 Hz, 2H, H_δ) ppm. **^{13}C NMR** (101 MHz, $CDCl_3$) δ = 150.8, 128.7, 119.9, 116.6, 116.3 ppm. **ESI-MS (+):** calculated for $C_{15}H_8FN_3S_2$: m/z (z = 1): 314.38, found: 314.24.

Synthesis of PyTTzBr: 4-Pyridinecarboxaldehyde (0.27 g, 2.50 mmol, 1.0 eq.), 4-bromobenzaldehyde (0.92 g, 4.99 mmol, 2.0 eq.) and dithiooxamide (0.30 g, 2.50 mmol, 1.0 eq) were refluxed in 15 mL anhydrous DMF for 24 hours under aerobic conditions. The reaction mixture was allowed to sit for 40 minutes, and the precipitated product was collected by filtration and rinsed with DMF. The crude product was purified by column chromatography (SiO_2, CH_2Cl_2/MeOH 99:1) to afford **PyTTzBr** as a yellow solid in 16 % yield (0.14 g, 0.04 mmol).

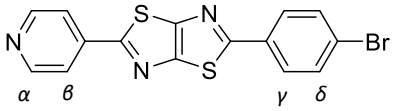

m.p.: 286-290 °C. **^{1}H NMR** (400 MHz, $CDCl_3$) δ = 8.8-8.7 (m, 2H, H_α), 7.9-7.8 (m, 4H, $H_{\beta,\gamma}$), 7.7-7.6 (m, 2H, H_δ) ppm. **^{13}C NMR** (101 MHz, $CDCl_3$) δ = 150.8, 127.9, 127.8, 119.9 ppm. **ESI-MS (+):** calculated for $C_{15}H_8BrN_3S_2$: m/z (z = 1): 374.27, found: 374.32.

General procedure for the synthesis of alkylated thiazo[5,4-d]thiazole (A):

In a dry Schlenk tube, 2,5-di(pyridin-4-yl)-3a,6a-dihydrothiazolo[5,4-d]thiazole **(Py_2TTz)** was heated to 190 °C for 7 days in 8 mL of the appropriate bromooctane under nitrogen atmosphere. After that, the medium was diluted with methanol and hexane was added. The layers were separated, and the methanol layer was washed with hexane (3×15 mL). Methanol was removed under reduced pressure to afford the pure product.

$(C_8)_2Py_2TTz(Br)$: was synthesized from **Py_2TTz** (0.5 g, 1.69 mmol, 1.0 eq.) according to the general procedure using 8 mL of 8-bromooctane. The pure product **$(C_8)_2Py_2TTz(Br)$** was obtained as a green solid in 80 % (0.92 g, 1.35 mmol).

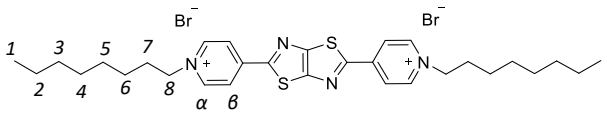

m.p.: 277-280 °C. **^{1}H NMR** (400 MHz, CD_3OD) δ = 9.18 (d, *J* = 7.0 Hz, 4H, H_α), 8.76 (d, *J* = 6.9 Hz, 4H, H_β), 4.71 (t, *J* = 7.6 Hz, 4H, H_8), 2.1-2.0 (m, 4H, H_7), 1.5-1.2 (m, 18H, $H_{2\text{-}6}$), 0.90 (t, *J* = 6.6 Hz, 6H, H_1) ppm. **^{13}C NMR** (101 MHz, CD_3OD) δ = 165.2, 155.8, 147.2, 145.6, 124.2, 61.6, 31.5, 31.1, 28.8, 28.7, 25.9, 22.3, 13.2 ppm. **ESI-MS (+):**

calculated for $C_{30}H_{42}N_4S_2^{2+}$: m/z (z = 2): 261.14, found: 261.27. **UV-Vis** (CH_3OH): λ_{max} (ε)= 397 nm (68503 $mol^{-1}dm^3cm^{-1}$), 291 nm (15748 $mol^{-1}dm^3cm^{-1}$). **Fluorescence** (CH_3OH): λ_{ex} = 397 nm, λ_{em} = 465 nm.

$(C_5)_2Py_2TTz(Br)$: was synthetized from **Py_2TTz** (1.0 g, 3.37 mmol, 1.0 eq.) according to the general procedure using 8 mL of 5-bromooctane. The pure product **$(C_5)_2Py_2TTz(Br)$** was obtained as a green solid in 79 % (1.60 g, 2.67 mmol).

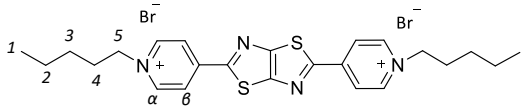

m.p.: 281-283 °C. **^{1}H NMR** (400 MHz, CD_3OD) δ = 9.16 (d, *J* = 7.1 Hz, 4H, H_α), 8.76 (d, *J* = 6.9 Hz, 4H, H_β), 4.70 (t, *J* = 7.6 Hz, 4H, H_5), 2.1-2.0 (m, 4H, H_4), 1.5-1.4 (m, 6H, $H_{2,3}$), 0.97 (t, *J* = 6.9 Hz, 6H, H_1) ppm. **^{13}C NMR** (101 MHz, CD_3OD) δ = 165.2, 147.3, 145.5, 61.6, 30.8, 27.9, 21.8, 12.7 ppm. **ESI-MS (+):** calculated for $C_{24}H_{30}N_4S_2^{2+}$: m/z (z = 2): 219.09, found: 219.32. **UV-Vis** (CH_3OH): λ_{max} (ε)= 394 nm (77000 $mol^{-1}dm^3cm^{-1}$), 293 nm (23000 $mol^{-1}dm^3cm^{-1}$). **Fluorescence** (CH_3OH): λ_{ex} = 394 nm, λ_{em} = 465 nm.

General procedure for the synthesis of thiazo[5,4-d]thiazole (B):

In a dry Schlenk tube, the appropriate thiazothiazole (**PyTTzOMe**, **PyTTzF**, **PyTTzBr**) was heated to 190 °C for 7 days in 8 mL of the proper bromooctane under nitrogen atmosphere. After that, the medium was diluted with methanol and hexane was added. The layers were separated, and the methanol layer was washed with hexane (3×15 mL). Methanol was removed under reduced pressure. The crude solid was dissolved in CH_2Cl_2, adsorbed onto silica, and purified by column chromatography (SiO_2, CH_2Cl_2/MeOH gradient from 95:5 to 90:10).

(C_8)PyTTzOMe(Br): was synthesized from **PyTTzOMe** (0.034 g, 0.10 mmol, 1.0 eq.) according to the general procedure using 8 mL of 8-bromooctane. The pure product **(C_8)PyTTzOMe(Br)** was obtained as a yellow solid in 74 % (0.040 g, 0.077 mmol).

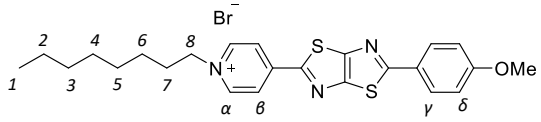

m.p.: 250-253 °C. **^{1}H NMR** (400 MHz, $CDCl_3$) δ = 9.48 (d, *J* = 6.5 Hz, 2H, H_α), 8.42 (d, *J* = 6.4 Hz, 2H, H_β), 7.93 (d, *J* = 8.8 Hz, 2H, H_γ), 6.98 (d, *J* = 8.9 Hz, 2H, H_δ), 5.00 (t, *J* = 7.4 Hz, 2H, H_8), 3.91 (s, 3H, H_{OMe}), 2.1-2.0 (m, 2H, H_7), 1.5-1.2 (m, 10H, H_{2-6}), 0.88 (t, *J* = 8.2 Hz, 3H, H_1) ppm. **^{13}C NMR** (101 MHz, $CDCl_3$) δ = 145.5, 128.8, 122.8, 114.7, 61.8, 55.6, 31.9, 31.6, 29.0, 26.1, 22.6, 14.0 ppm. **ESI-MS (+):** calculated for $C_{24}H_{28}N_3OS^{2+}$: m/z (z = 2): 438.63, found:

438.52. **UV-Vis** (CH_3OH): λ_{max} (ε)= 428 nm (87000 $mol^{-1}dm^3cm^{-1}$), 298 nm (26000 $mol^{-1}dm^3cm^{-1}$). **Fluorescence** (CH_3OH): λ_{ex} = 428 nm, λ_{em} = 580 nm.

(C_5)PyTTzOMe(Br): was synthesized from **PyTTzOMe** (0.035 g, 0.11 mmol, 1.0 eq.) according to the general procedure using 8 mL of 5-bromooctane. The pure product **(C_5)PyTTzOMe(Br)** was obtained as a yellow solid in 98 % (0.050 g, 0.10 mmol).

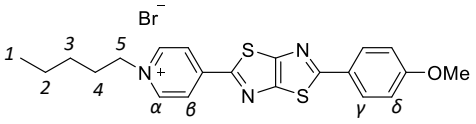

m.p.: > 400 °C.**^{1}H NMR** (400 MHz, CD_3OD) δ = 9.04 (d, *J* = 7.1 Hz, 2H, H_α), 8.64 (d, *J* = 7.0 Hz, 2H, H_β), 8.08 (d, *J* = 8.9 Hz, 2H, H_γ), 7.13 (d, *J* = 8.9 Hz, 2H, H_δ), 4.65 (t, *J* = 7.4 Hz, 2H, H_5), 3.93 (s, 3H, H_{OMe}), 2.1-2.0 (m, 2H, H_4), 1.5-1.4 (m, 4H, $H_{2,3}$), 0.99 (t, *J* = 6.6 Hz, 3H, H_1) ppm. **^{13}C NMR** (101 MHz, CD_3OD) δ = 145.0, 128.4, 123.1, 114.5, 61.2, 54.8, 30.7, 27.9, 21.8, 12.7 ppm. **ESI-MS (+):** calculated for $C_{21}H_{22}N_3OS^{2+}$: m/z (z = 2): 396.12, found: 396.28. **UV-Vis** (CH_3OH): λ_{max} (ε)= 428 nm (85000 $mol^{-1}dm^3cm^{-1}$), 299 nm (26000 $mol^{-1}dm^3cm^{-1}$). **Fluorescence** (CH_3OH): λ_{ex} = 428 nm, λ_{em} = 579 nm.

(C_8)PyTTzF(Br): was synthetized from **PyTTzF** (0.023 g, 0.07 mmol, 1.0 eq.) according to the general procedure using 8 mL of 8-bromooctane. The pure product **(C_8)PyTTzF(Br)** was obtained as a yellow solid in 94 % (0.015 g, 0.03 mmol).

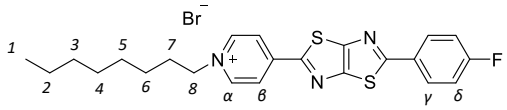

m.p.: 215-218 °C. **^{1}H NMR** (400 MHz, $CDCl_3$) δ = 9.54 (d, *J* = 6.4 Hz, 2H, H_α), 8.46 (d, *J* = 6.0 Hz, 2H, H_β), 7.97 (m, 2H, H_γ), 7.17 (t, *J* = 8.4 Hz, 2H, H_δ), 5.03 (t, *J* = 7.4 Hz, 2H, H_8), 2.1-2.0 (m, 2H, H_7), 1.5-1.2 (m, 10H, H_{2-6}), 0.87 (t, J = 6.4 Hz, 3H, H_1) ppm. **^{13}C NMR** (101 MHz, $CDCl_3$) δ = 172.2, 161.0, 148.2, 146.1, 132.9, 132.4, 128.1, 126.1, 122.2, 61.0, 31.8, 32.0, 28.9, 27.7, 25.6, 22.3, 12.6 ppm. **ESI-MS (+):** calculated for $C_{23}H_{25}FN_3S_2^+$: m/z (z = 1): 426.59, found: 426.43.

(C_8)PyTTzBr(Br): was synthetized from **PyTTzBr** (0.060 g, 0.16 mmol, 1.0 eq.) according to the general procedure using 8 mL of 8-bromooctane. The pure product **(C_8)PyTTzBr(Br)** was obtained as a yellow solid in 91 % (0.083 g, 0.15 mmol).

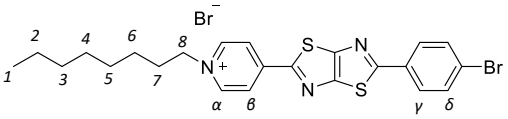

m.p.: 213-217 °C. **^{1}H NMR** (400 MHz, CD_3OD) δ = 9.06 (d, *J* = 7.0 Hz, 2H, H_α), 8.64 (d, *J* = 6.9 Hz, 2H, H_β), 8.01 (d, *J* = 8.6 Hz, 2H, H_γ), 7.71 (d, *J* = 8.6 Hz, 2H, H_δ), 4.65 (t, *J* = 7.6 Hz, 2H, H_8), 2.07 (m, 2H, H_7), 1.5-1.2 (m, 10H, H_{2-6}), 0.90 (t, *J* = 6.6 Hz, 3H, H_1) ppm. **^{13}C**

NMR (101 MHz, CD_3OD) δ = 172.6, 160.8, 147.7, 145.2, 132.4, 132.1, 128.1, 125.9, 123.4, 61.4, 31.5, 31.1, 28.8, 28.7, 25.9, 22.3, 13.0 ppm. **ESI-MS (+):** calculated for $C_{23}H_{25}BrN_3S_2^+$: m/z (z = 1): 486.07, found: 486.36.

General procedure for anion exchange (C):

The appropriate alkylated thiazo[5,4-*d*]thiazole (1.00 eq.) was dissolved in methanol. Then AgX (X = TsO^-; PF_6^-) (1.99 eq.) was added and the mixture was sonicated for 2 minutes. The exchange was allowed to proceed until the solution became clear. In the case of exchange with $AgPF_6$, the tube was wrapped in foil to prevent light exposure. Then, the AgBr precipitated was filtered off and the methanol was removed in vacuo.

$(C_8)_2Py_2TTz(TsO)$:

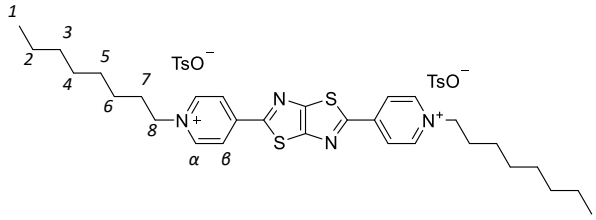

m.p.: 240-243 °C. **^{1}H NMR** (400 MHz, CD_3OD) δ = 9.15 (d, *J* = 7.4 Hz, 4H, $H_α$), 8.75 (d, *J* = 6.7 Hz, 4H, $H_β$), 7.71 (d, *J* = 7.9 Hz, 4H, $H_{Ar\text{-}H(TsO)}$), 7.21 (d, *J* = 7.9 Hz, 4H, $H_{Ar\text{-}H(TsO)}$), 4.67 (t, *J* = 7.6 Hz, 4H, H_8), 2.35 (s, 6H, $H_{Me(TsO)}$), 2.1-2.0 (m, 4H, H_7), 1.5-1.2 (m, 20H, $H_{2\text{-}6}$), 0.91 (t, *J* = 6.6 Hz, 6H, H_1) ppm. **^{13}C NMR** (101 MHz, CD_3OD) δ = 145.5, 128.4, 125.6, 124.2, 61.7, 31.4, 31.1, 28.8, 28.7, 25.9, 22.3, 20.2, 13.1 ppm. **ESI-MS (+):** calculated for $C_{30}H_{42}N_4S_2^{2+}$: m/z (z = 2): 261.14, found : 261.39. **UV-Vis** (CH_3OH): $λ_{max}$ (ε)= 393 nm (41592 $mol^{-1}dm^3cm^{-1}$), 282 nm (29203 $mol^{-1}dm^3cm^{-1}$). **Fluorescence** (CH_3OH): $λ_{ex}$ = 393 nm, $λ_{em}$ = 465 nm.

$(C_8)_2Py_2TTz(PF_6)$:

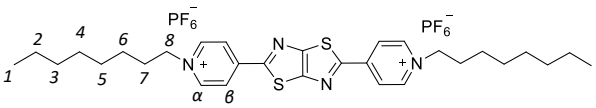

m.p.: 261-264 °C. **^{1}H NMR** (400 MHz, CD_3OD) δ = 9.14 (d, *J* = 6.6 Hz, 4H, $H_α$), 8.76 (d, *J* = 6.5 Hz, 4H, $H_β$), 4.70 (t, *J* = 7.6 Hz, 4H, H_8), 2.1-2.0 (m, 4H, H_7), 1.6-1.2 (m, 20H, $H_{2\text{-}6}$), 0.93 (t, *J* = 6.7 Hz, 6H, H_1) ppm. **^{13}C NMR** (101 MHz, CD_3OD) δ = 145.5, 124.2, 61.6, 31.5, 31.1, 28.8, 28.7, 25.8, 22.3, 13.0 ppm. **ESI-MS (+):** calculated for $C_{30}H_{42}N_4S_2^{2+}$: m/z (z = 2): 261.14, found : 261.39. **UV-Vis** (CH_3OH): $λ_{max}$ (ε)= 394 nm (60000 $mol^{-1}dm^3cm^{-1}$), 291 nm (17000 $mol^{-1}dm^3cm^{-1}$). **Fluorescence** (CH_3OH): $λ_{ex}$ = 394 nm, $λ_{em}$ = 465 nm.

$(C_5)_2Py_2TTz(TsO)$:

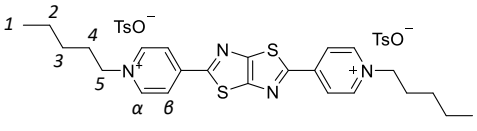

m.p.: 285-288 °C. **^{1}H NMR** (400 MHz, CD_3OD) δ = 9.12 (d, *J* = 7.1 Hz, 4H, $H_α$), 8.73 (d, *J* = 7.5 Hz, 4H, $H_β$), 7.68 (d, *J* = 8.0 Hz, 4H, $H_{Ar\text{-}H(TsO)}$), 7.21 (d, *J* = 8.0 Hz, 4H, $H_{Ar\text{-}H(TsO)}$),

4.67 (t, *J* = 7.6 Hz, 4H, H_5), 2.35 (s, 6H, $H_{Me(TsO)}$), 2.1-2.0 (m, 4H, H_4), 1.5-1.4 (m, 8H, $H_{2,3}$), 0.97 (t, *J* = 6.7 Hz, 6H, H_1) ppm. **^{13}C NMR** (101 MHz, CD_3OD) δ = 145.5, 128.4, 126.4, 125.6, 125.5, 124.2, 61.6, 30.8, 27.9, 21.81, 19.9, 12.8 ppm. **m.p.:** 285-288 °C. **ESI-MS (+):** calculated for $C_{24}H_{30}N_4S_2^{2+}$: m/z (z = 2): 219.09, found : 219.34. **UV-Vis** (CH_3OH): λ_{max} (ε)= 392 nm (63478 $mol^{-1}dm^3cm^{-1}$), 293 nm (12173 $mol^{-1}dm^3cm^{-1}$). **Fluorescence** (CH_3OH): λ_{ex} = 392 nm, λ_{em} = 465 nm.

$(C_5)_2Py_2TTz(PF_6)$:

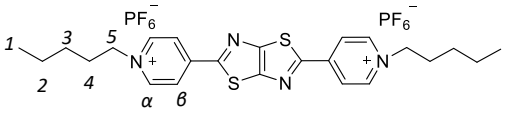

m.p.: 250-253 °C. **^{1}H NMR** (400 MHz, CD_3OD) δ = 9.11 (d, *J* = 6.8 Hz, 4H, H_α), 8.74 (d, *J* = 6.7 Hz, 4H, H_β), 4.67 (t, *J* = 7.5 Hz, 4H, H_5), 2.2-2.0 (m, 4H, H_4), 1.5-1.4 (m, 8H, $H_{2,3}$), 0.97 (t, *J* = 6.6 Hz, 6H, H_1) ppm. **^{13}C NMR** (101 MHz, CD_3OD) δ = 149.4, 128.1, 65.6, 34.7, 31.8, 25.7, 16.7 ppm. **ESI-MS (+):** calculated for $C_{24}H_{30}N_4S_2^{2+}$: m/z (z = 2): 219.09, found : 219.34. **UV-Vis** (CH_3OH): λ_{max} (ε)= 395 nm (56363 $mol^{-1}dm^3cm^{-1}$), 293 nm (11818 $mol^{-1}dm^3cm^{-1}$). **Fluorescence** (CH_3OH): λ_{ex} = 395 nm, λ_{em} = 465 nm.

(C_5)PyTTzOMe(TsO):

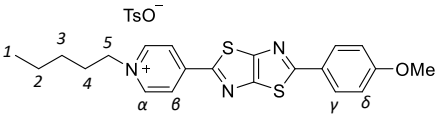

m.p.: 118-220 °C. **^{1}H NMR** (400 MHz, CD_3OD) δ = 9.01 (d, *J* = 7.0 Hz, 2H, H_α), 8.61 (d, *J* = 6.9 Hz, 2H, H_β), 8.07 (d, *J* = 8.9 Hz, 2H, H_γ), 7.70 (d, *J* = 8.3 Hz, 2H, $H_{Ar\text{-}H(TsO)}$), 7.23 (d, *J* = 7.9 Hz, 2H, $H_{Ar\text{-}H(TsO)}$), 7.11 (d, *J* = 8.9 Hz, 2H, H_δ), 4.62 (t, *J* = 8.1 Hz 2H, H_5), 3.91 (s, 3H, H_{OMe}), 2.37 (s, 3H, $H_{Me(TsO)}$), 2.1-2.0 (m, 2H, H_4), 1.5-1.3 (m, 4H, $H_{2,3}$), 0.97 (t, *J* = 6.8 Hz, 3H, H_1) ppm. **^{13}C NMR** (101 MHz, CD_3OD) δ = 128.4, 124.3, 125.6, 123.1, 114.5, 61.2, 54.8, 30.7, 27.9, 21.8, 19.9, 12.7 ppm. **ESI-MS (+):** calculated for $C_{21}H_{22}N_3OS^{2+}$: m/z (z = 2): 396.55, found: 396.40. **UV-Vis** (CH_3OH): λ_{max} (ε)= 427 nm (35488 $mol^{-1}dm^3cm^{-1}$), 282 nm (27602 $mol^{-1}dm^3cm^{-1}$). **Fluorescence** (CH_3OH): λ_{ex} = 427 nm, λ_{em} = 580 nm.

(C_5)PyTTzOMe(PF_6):

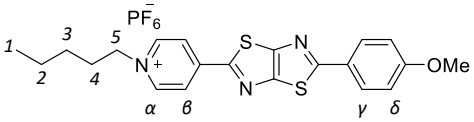

m.p.: 248-250 °C. **^{1}H NMR** (400 MHz, CD_3OD) δ = 9.04 (d, *J* = 7.1 Hz, 2H, H_α), 8.64 (d, *J* = 7.0 Hz, 2H, H_β), 8.08 (d, *J* = 8.9 Hz, 2H, H_γ), 7.13 (d, *J* = 8.9 Hz, 2H, H_δ), 4.65 (t, *J* = 7.4 Hz, 2H, H_5), 3.93 (s, 3H, H_{OMe}), 2.1-2.0 (m, 2H, H_4), 1.5-1.4 (m, 4H, $H_{2,3}$), 0.99 (t, *J* = 6.6 Hz, 3H, H_1) ppm. **^{13}C NMR** (101 MHz, CD_3OD) δ = 145.0, 128.4, 123.1, 114.5, 61.2, 54.8, 30.7, 27.9, 21.8, 12.7 ppm. **ESI-MS (+):** calculated for $C_{21}H_{22}N_3OS^{2+}$: m/z (z = 2): 396.55, found: 396.40. **UV-Vis** (CH_3OH): λ_{max} (ε)= 428 nm (39583 $mol^{-1}dm^3cm^{-1}$), 300 nm (8333 $mol^{-1}dm^3cm^{-1}$). **Fluorescence** (CH_3OH): λ_{ex} = 428 nm, λ_{em} = 580 nm.

(C_8)PyTTzOMe(TsO):

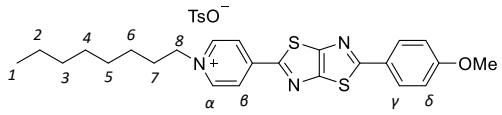

m.p.: 229-231 °C. **^{1}H NMR** (400 MHz, $CDCl_3$) δ = 9.26 (d, *J* = 6.3 Hz, 2H, H_α), 8.39 (d, *J* = 6.4 Hz, 2H, H_β), 7.9-7.8 (m, 4H, $H_{\gamma+Ar\text{-}H(TsO)}$), 7.19 (d, *J* = 7.7 Hz, 2H, $H_{Ar\text{-}H(TsO)}$), 6.95 (d, *J* = 10.1 Hz, 2H, H_δ), 4.84 (t, *J* = 7.5 Hz, 2H, H_8), 3.90 (s, 3H, H_{OMe}), 2.36 (s, 3H, $H_{Me(TsO)}$), 2.0-1.9 (m, 2H, H_7), 1.4-1.2 (m, 10H, $H_{2\text{-}6}$), 0.89 (t, *J* = 6.7 Hz, 2H, H_1) ppm. **^{13}C NMR** (101 MHz, $CDCl_3$) δ = 145.8, 128.7, 126.0, 123.0, 114.7, 61.7, 55.5, 31.8, 31.7, 29.0, 26.1, 22.6, 21.3, 14.0 ppm. **ESI-MS (+):** calculated for $C_{24}H_{28}N_3OS^{2+}$: m/z (z = 2): 438.63, found: 438.46. **UV-Vis** (CH_3OH): λ_{max} (ε)= 429 nm (48000 $mol^{-1}dm^3cm^{-1}$), 298 nm (16000 $mol^{-1}dm^3cm^{-1}$). **Fluorescence** (CH_3OH): λ_{ex} = 429 nm, λ_{em} = 465579 nm.

(C_8)PyTTzOMe(PF_6):

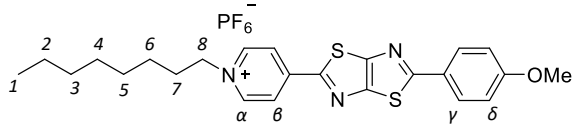

m.p.: 269-271 °C.**^{1}H NMR** (400 MHz, $CDCl_3$) δ = 8.94 (d, *J* = 6.3 Hz, 2H, H_α), 8.46 (d, *J* = 6.3 Hz, 2H, H_β), 8.00 (d, *J* = 8.7 Hz, 2H, H_γ), 7.03 (d, *J* = 8.8 Hz, 2H, H_δ), 4.72 (t, *J* = 7.5 Hz, 2H, H_8), 3.93 (s, 3H, H_{OMe}), 2.1-2.0 (m, 2H, H_7), 1.5-1.2 (m, 10H, $H_{2\text{-}6}$), 0.91 (t, *J* = 6.6 Hz, 3H, H_1) ppm.**^{13}C NMR** (101 MHz, $CDCl_3$) δ = 145.5, 128.8, 122.8, 114.7, 61.8, 55.6, 31.9, 31.6, 29.0, 26.1, 22.6, 14.0 ppm. **ESI-MS (+):** calculated for $C_{24}H_{28}N_3OS^{2+}$: m/z (z = 2): 438.63, found: 438.52. **UV-Vis** (CH_3OH): λ_{max} (ε)= 428 nm (57000 $mol^{-1}dm^3cm^{-1}$), 297 nm (18000 $mol^{-1}dm^3cm^{-1}$). **Fluorescence** (CH_3OH): λ_{ex} = 428 nm, λ_{em} = 579 nm.

(C_8)PyTTzBr(TsO):

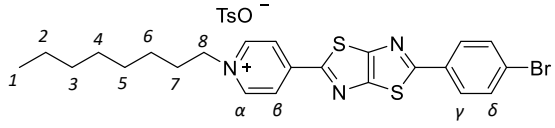

m.p.: 229-231 °C.**^{1}H NMR** (400 MHz, $CDCl_3$) δ = 9.32 (br. s, 2H, H_α), 8.38 (br. s, 2H, H_β), 7.84 (d, *J* = 7.7 Hz, 2H, H_γ), 7.73 (d, *J* = 8.5 Hz, 2H, $H_{Ar\text{-}H(TsO)}$), 7.55 (d, *J* = 8.5 Hz, 2H, $H_{Ar\text{-}H(TsO)}$), 7.17 (d, *J* = 7.6 Hz, 2H, H_δ), 4.83 (br. s, 2H, H_8), 2.35 (s, 3H, $_{Me(TsO)}$), 1.96 (m, 2H, H_7), 1.3-1.2 (m, 10H, $H_{2\text{-}6}$), 0.85 (t, *J* = 6.8 Hz, 3H, H_1) ppm. **^{13}C NMR** (101 MHz, $CDCl_3$) δ = 159.8, 146.2, 132.6, 131.7, 128.7, 128.0, 126.7, 126.0, 123.2, 61.8, 31.8, 31.7, 29.0, 28.9, 26.1, 22.6, 21.3, 14.0 ppm. **ESI-MS (+):** calculated for $C_{23}H_{25}BrN_3S_2^+$: m/z (z = 1): 486.07, found: 486.36.

(C_8)PyTTzBr(PF_6):

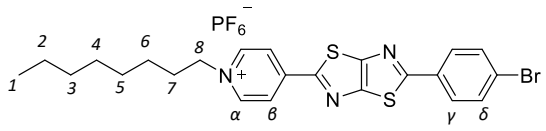

m.p.: 225-228 °C. **^{1}H NMR** (400 MHz, $CDCl_3$) δ = 8.83 (d, *J* = 6.3 Hz, 2H, H_α), 8.49 (d, *J* = 6.0 Hz, 2H, H_β), 7.91 (d, *J* = 8.6 Hz, 2H, H_γ), 7.68 (d, *J* = 8.6 Hz, 2H, H_δ), 4.68 (t, *J* = 7.8 Hz, 2H, H_8), 2.1-2.0 (m, 2H, H_7), 1.5-1.2 (m, 10H, $H_{2\text{-}6}$), 0.89 (t, *J* = 5.5 Hz, 3H, H_1) ppm. **^{13}C NMR** (101 MHz, CD_3OD) δ = 172.6, 160.8, 147.7, 145.2, 132.4, 132.1, 128.1, 125.9, 123.4, 61.4, 31.5, 31.1, 28.8, 28.7, 25.9, 22.3, 13.0 ppm. **ESI-MS (+):** calculated for $C_{23}H_{25}BrN_3S_2^+$: m/z (z = 1): 486.07, found: 486.36.

DOSY NMR:

DOSY experiments were carried out in $CDCl_3$ at 400 MHz on a Bruker Avance 400 Spectrometer using a stimulated echo sequence with bipolar gradients (STEbp).[10] The diffusion coefficient *D* of the species present in solution was determined by monitoring the intensity decay of at least six resonances present in the NMR spectrum of the sample as a function of gradient strength applied to the sample. The fitting of the attenuation profiles was carried out using the equation:

$$I = I_0 \exp\left(-D\gamma^2 g^2 \delta^2 \left(\Delta - \frac{\delta}{3} - \frac{\tau}{2}\right)\right)$$

Table with experimental DOSY NMR data of the diffusion coefficients for free **TPU**, free **(C_8)$_2$Py$_2$TTz(2TsO)**, and their 2:1 mixture.

TPU		**(C_8)$_2$Py$_2$TTz(TsO$^-$)**		**2TPU⊃ (C_8)$_2$Py$_2$TTz(TsO$^-$)**	
Area [ppm]	Diff. Con (10^{-10}) [m^2/s]	Area [ppm]	Diff. Con (10^{-9}) [m^2/s]	Area [ppm]	Diff. Con (10^{-10}) [m^2/s]
7.337 to 7.255	9.387	8.659 to 8.462	3.147	7.888 to 7.745	3.358
7.262 to 7.106	4.638	7.902 to 7.676	3.037	7.242 to 7.083	3.325
7.039 to 6.890	4.630	7.361 to 7.224	4.697	4.585 to 4.317	3.527
4.541 to 4.302	4.660	7.224 to 7.076	3.013	4.216 to 3.973	3.441
3.959 to 3.788	4.621	4.875 to 4.570	2.807	3.931 to 3.797	3.474
3.743 to 3.520	4.632	2.418 to 2.280	3.115	3.772 to 3.604	3.460
2.162 to 1.991	0.5184	0.993 to 0.717	3.142	3.588 to 3.370	3.816
1.700 to 1.536	0.4918	0.148 to -0.078	4.328	2.422 to 2.288	3.316
1.499 to 0.992	4.662	Diff. Coeff. = 3.40×10^{-9} m^2/s		1.442 to 1.140	3.424
Diff. Coeff. = 5.25×10^{-10} m^2/s				Diff. Coeff. = 3.46×10^{-10} m^2/s	

2. Bibliography

(1) Woodward, A. N.; Kolesar, J. M.; Hall, S. R.; Saleh, N.-A.; Jones, D. S.; Walter, M. G. Thiazolothiazole Fluorophores Exhibiting Strong Fluorescence and Viologen-Like Reversible Electrochromism. *J. Am. Chem. Soc.* **2017**, *139* (25), 8467–8473. https://doi.org/10.1021/jacs.7b01005.

(2) Sayresmith, N. A.; Saminathan, A.; Sailer, J. K.; Patberg, S. M.; Sandor, K.; Krishnan, Y.; Walter, M. G. Photostable Voltage-Sensitive Dyes Based on Simple, Solvatofluorochromic, Asymmetric Thiazolothiazoles. *J. Am. Chem. Soc.* **2019**, *141* (47), 18780–18790. https://doi.org/10.1021/jacs.9b08959.

(3) Tang, B.; Li, W.; Chang, Y.; Yuan, B.; Wu, Y.; Zhang, M.; Xu, J.; Li, J.; Zhang, X. A Supramolecular Radical Dimer: High-Efficiency NIR-II Photothermal Conversion and Therapy. *Angew. Chem. Int. Ed.* **2019**, *58* (43), 15526–15531. https://doi.org/10.1002/anie.201910257.

(4) Johnson, J. R.; Ketcham, R. Thiazolothiazoles. I. The Reaction of Aromatic Aldehydes with Dithioöxamide [1]. *J. Am. Chem. Soc.* **1960**, *82* (11), 2719–2724. https://doi.org/10.1021/ja01496a017.

(5) Ziessel, R.; Nano, A.; Heyer, E.; Bura, T.; Retailleau, P. Rational Design of New Thiazolo□Thiazole Dyes as Input Energy Units in Molecular Dyads. *Chem. – Eur. J.* **2013**, *19* (8), 2582–2588. https://doi.org/10.1002/chem.201203121.

(6) Kudrjasova, J.; Herckens, R.; Penxten, H.; Adriaensens, P.; Lutsen, L.; Vanderzande, D.; Maes, W. Direct Arylation as a Versatile Tool towards Thiazolo[5,4-d]Thiazole-Based Semiconducting Materials. *Org. Biomol. Chem.* **2014**, *12* (26), 4663–4672. https://doi.org/10.1039/C4OB00360H.

(7) Kudrjasova, J.; Kesters, J.; Verstappen, P.; Brebels, J.; Vangerven, T.; Cardinaletti, I.; Drijkoningen, J.; Penxten, H.; Manca, J.; Lutsen, L.; Vanderzande, D.; Maes, W. A Direct Arylation Approach towards Efficient Small Molecule Organic Solar Cells. *J. Mater. Chem. A* **2016**, *4* (3), 791–795. https://doi.org/10.1039/C5TA09023G.

(8) Klymchenko, A. S. Emerging Field of Self-Assembled Fluorescent Organic Dye Nanoparticles, *J. Nanosci. Lett.*, 3, 21, **2013**.

(9) Cera, G.; Arduini, A.; Secchi, A.; Credi, A.; Silvi, S. Heteroditopic Calix[6]Arene Based Intervowen and Interlocked Molecular Devices. *Chem. Rec.* **2021**, *21* (5), 1161–1181. https://doi.org/10.1002/tcr.202100012.

(10) Cohen, Y.; Avram, L.; Frish, L. Diffusion NMR Spectroscopy in Supramolecular and Combinatorial Chemistry: An Old Parameter—New Insights. *Angew. Chem. Int. Ed.* **2005**, *44* (4), 520–554. https://doi.org/10.1002/anie.200300637.

(11) Credi, A.; Dumas, S.; Silvi, S.; Venturi, M.; Arduini, A.; Pochini, A.; Secchi, A. Viologen-Calix[6]Arene Pseudorotaxanes. Ion-Pair Recognition and Threading/Dethreading Molecular Motions. *J. Org. Chem.* **2004**, *69* (18), 5881–5887. https://doi.org/10.1021/jo0494127.

Chapter 3. Complexation of cyanine-viologen hybrids in calix[6]arene hosts

3 Introduction

As discussed in previous chapters, the complexation of organic dyes within calix[6]arene can significantly alter their photophysical properties, often resulting in enhanced fluorescence emission. Cyanine dyes are limited by poor photostability and are prone to aggregation in solution, leading to fluorescence quenching. Several strategies can be employed to improve their fluorescence and/or photostability. One approach is their inclusion within supramolecular macrocycles, where the host cavity protects the dye, thereby increasing its photostability and tuning its optical properties. Another strategy involves interaction with noble metal nanomaterials, which can induce plasmon-enhanced fluorescence (PEF).

The encapsulation of dyes within supramolecular macrocycles is extensively documented in the literature. One of the earliest examples dates back to 1997,[1] when Reddington *et al.* demonstrated the complexation of a cyanine dye derivative within *β*-cyclodextrin conjugates, resulting in a photostable labeling reagent (**Figure 3.1**). Typically, the photobleaching of cyanine dyes in aqueous solution arises from the reaction of singlet oxygen $^1O_2$ with the polymethine chain of the dye. However, as shown in this study, the presence of cyclodextrin conjugates can prevent this reactivity, thereby enhancing the photostability of the cyanine dye.

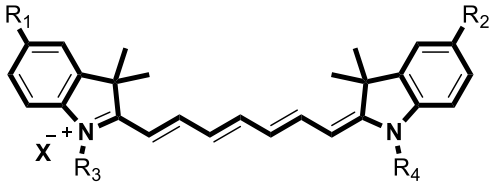

$R_1 = R_2 = H$, $R_3 = Me$, $R_4 = (CH_2)_2CO_2H$
$R_1 = R_2 = H$, $R_3 = Me$, $R_4 = (CH_2)_5CO_2H$
$R_1 = R_2 = H$, $R_3 = Me$, $R_4 = (CH_2)_{10}CO_2H$
$R_1 = R_2 = H$, $R_3 = CH_2CHMe_2$, $R_4 = (CH_2)_2CO_2H$
$R_1 = R_2 = SO_3^-$, $R_3 = Et$, $R_4 = (CH_2)_5CO_2H$

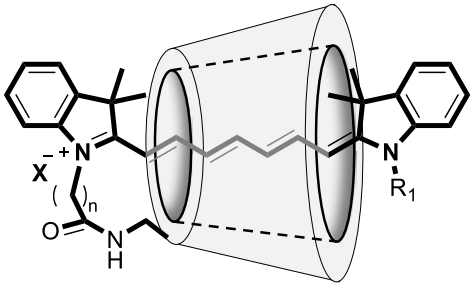

$R_1 = Me$, n = 2
$R_1 = Me$, n = 5
$R_1 = Me$, n = 10
$R_1 = CH_2CHMe_2$, n = 2

Figure 3.1. Cyanine-based dyes studied in ref. 1 and cyanine dye-*β*-cyclodextrin conjugates.

In 2016, Klymchenko *et al.*[2] reported the synthesis of micelles formed from amphiphilic calix[4]arenes (**CX8TP**), which possess four alkyne groups at their polar head regions covalently linked to PEGylated corona cyanine-based dye (**Figure 3.2**). These micelles exhibited a fluorescence that was two times brighter than that of quantum dots (QD-585), demonstrated high stability in

both aqueous and organic solvents, and readily entered cells. This system represents a promising platform for the development of protein-sized nanoparticles for bioimaging applications.

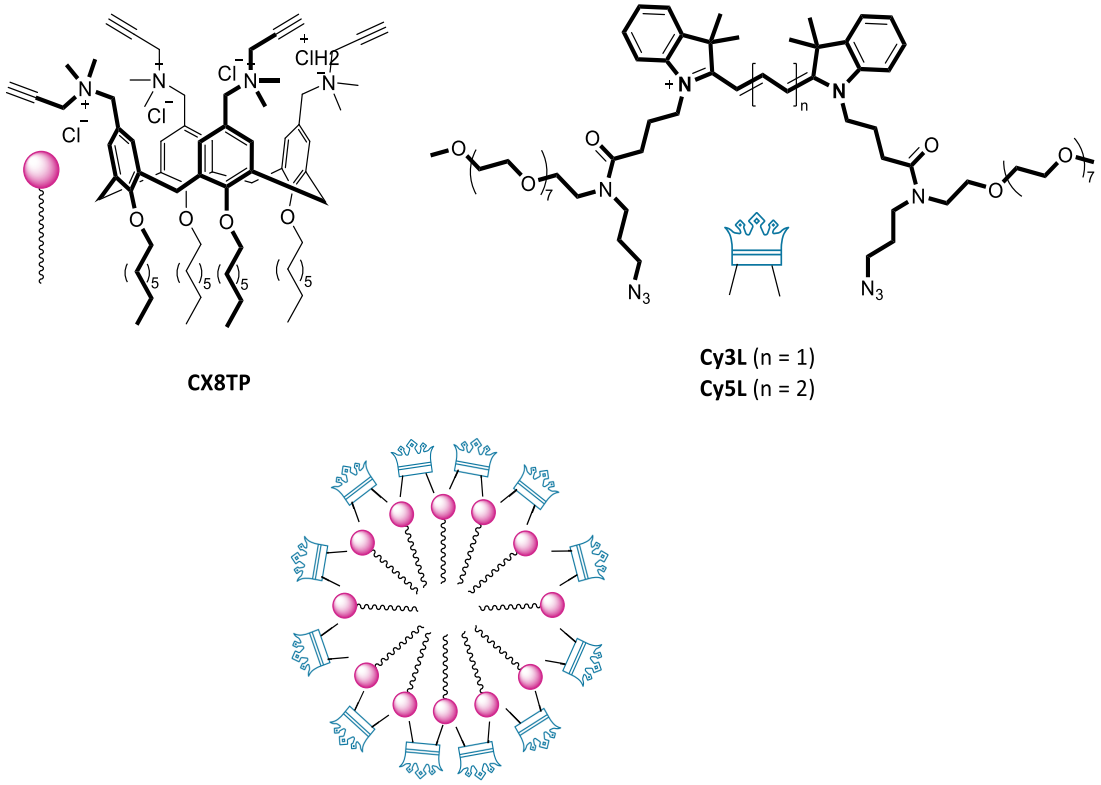

Figure 3.2. Top: structures of calix[4]arene **CX8TP** and cyanine corona dyes **Cy3L** and **Cy5L**;bottom: representation of calix[4]arene-based micelles with cyanine corona.

In 2022, Soavi *et al.* investigated the aggregation behavior of cyanine dyes in aqueous environments.[3] Their study demonstrated that the complexation of cyanine-based dye **Cy3** with cucurbit[8]uril (**CB[8]**) effectively disrupted cyanine dye aggregates in water. Later that year, Smith and colleagues published a separate study focused on the complexation of cationic cyanine dyes with cucurbit[7]uril (**CB[7]**).[4] Their findings showed that this complexation altered the π-electron distribution of the cyanine dyes, providing a potential strategy to overcome the "cyanine limit," a phenomenon characterized by broad absorption spectra and low fluorescence caused by asymmetric π-electron density distribution (**Figure 3.3**).

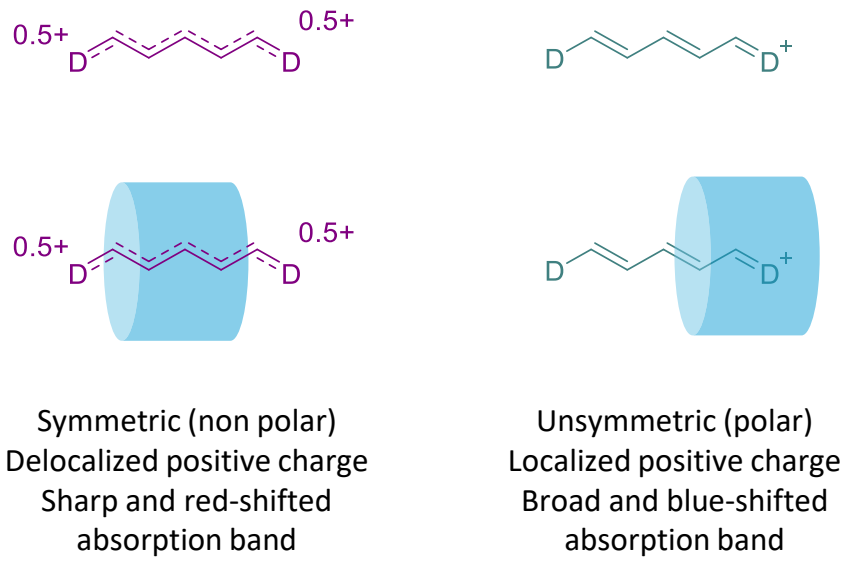

Figure 3.3. Representation of a cyanine dye and its complex with curcubit[7]uril **CB[7]** in a non-polar (left) and polar (right) state.

As previously said, the fluorescence properties of cyanine-based dyes can also be enhanced by exploiting the PEF effect. To achieve fluorescence enhancement, it is essential to keep in mind that the fluorophore must be positioned at an optimal distance from the gold surface (see Chapter 4). If the dye is too close to the surface, the non-radiative decay process dominates over the radiative one, leading to fluorescence quenching. For instance, in 2014, Sarkar *et al.*[5] conducted a systematic study on the fluorescence quenching of cyanine dyes in the presence of gold nanoclusters. They observed that the primary deactivation mechanism was an electron transfer process occurring between the gold nanoclusters and the cyanine dyes. An example of utilizing the PEF effect to enhance cyanine dye fluorescence was demonstrated by Huang *et al.*[6] in 2021. In their study, a fluorescent probe based on the PEF effect was developed to activate the detection of lipopolysaccharides (LPS). This PEF-based approach improved the photostability, fluorescence signal, and biocompatibility of the cyanine dye. In 2018, Xu *et al.*[7] harnessed the PEF phenomenon to develop a DNA-based nano assembly that functions as a turn-on platform for the highly sensitive and selective detection of specific DNA sequences (**Figure 3.4**). Initially, the fluorescence of the **Cy5** dye was quenched by its attachment to the surface of gold nanoparticles (**AuNSs**) *via* single-stranded DNA (ssDNA). This fluorescence was subsequently restored upon the formation of a nano assembly with DNA hybridized to various enhancing substrates, including **AuNSs**, gold nanorods (**AuNRs**), and silver-coated gold nanostars (**Au@AgNSs**). Among these nanomaterials, **Au@AgNSs** exhibited the most significant fluorescence enhancement, yielding an increase of up to 100-fold compared to the quenching effect observed with **Cy5-AuNSs**.

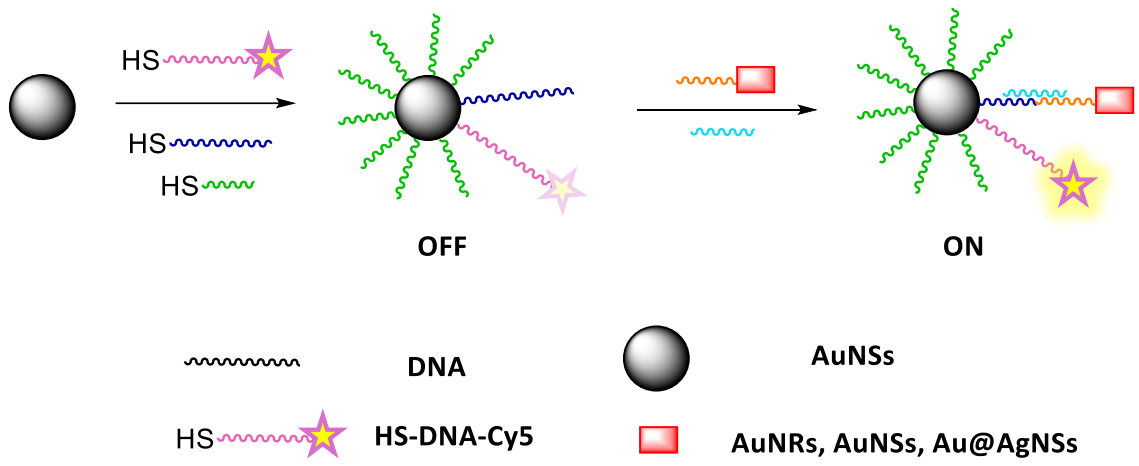

Figure 3.4. Schematic representation of the DNA-based nano assembly based on the PEF effect.

In 2019, Ouyang *et al.*[8] introduced the first example of an aggregation-induced emission (AIE)-based PEF sensor. This sensor, constructed using a water-soluble sulfonated anthracene derivative (BSNVA), was engineered to detect conformational changes in proteins, employing prion protein (PrP) as a model system. The sensor displayed non-emissive behavior when complexed with the normal cellular prion protein (PrP^{C}), while it exhibited significant fluorescence upon binding to the disease-associated prion protein (PrP^{Sc}). This differential emission response enables the sensor to effectively distinguish between the two prion protein states.

Aim of the project

In this chapter, we present the design of a system in which the optical properties of a near-infrared (NIR) cyanine-based dye (**Cy7-Bpy**) are enhanced through complexation with a calix[6]arene derivative. Near-infrared (NIR) cyanine dyes are distinguished by their absorbance and emission characteristics within the biological window, specifically in the ranges of 700 nm to 950 nm (NIR-I) and 1000 nm to 1350 nm (NIR-II). These properties render them highly suitable for various biological applications (see Introduction). However, a significant limitation of NIR cyanine dyes is their inherently low fluorescence intensity and poor photostability. To address these challenges, we aimed to enhance both the fluorescence intensity and photostability of these dyes through the complexation with calix[6]arene derivatives and their interaction with plasmonic nanomaterials. The NIR cyanine-based dye used in this chapter was specifically designed to promote complexation within the calix[6]arene by incorporating a viologen unit, which facilitates the threading into the cavity (**Figure 3.5**, top). Two calix[6]arene derivatives were employed: triphenylureido (**TPU-SH**) and trisulfonamido (**TSA-SH**) calix[6]arenes, which serve as functional monolayers on the surface of plasmonic nanostructures (**Figure 3.5**, top). These calix[6]arene derivatives can be covalently attached to the metallic surface *via* their ω-alkyl thiolate chains, while their heteroditopic, π-rich

aromatic cavities are capable of reversibly recognizing the cyanine-based dye functionalized with the di-alkyl viologen anchoring unit (**Figure 3.5**, bottom).

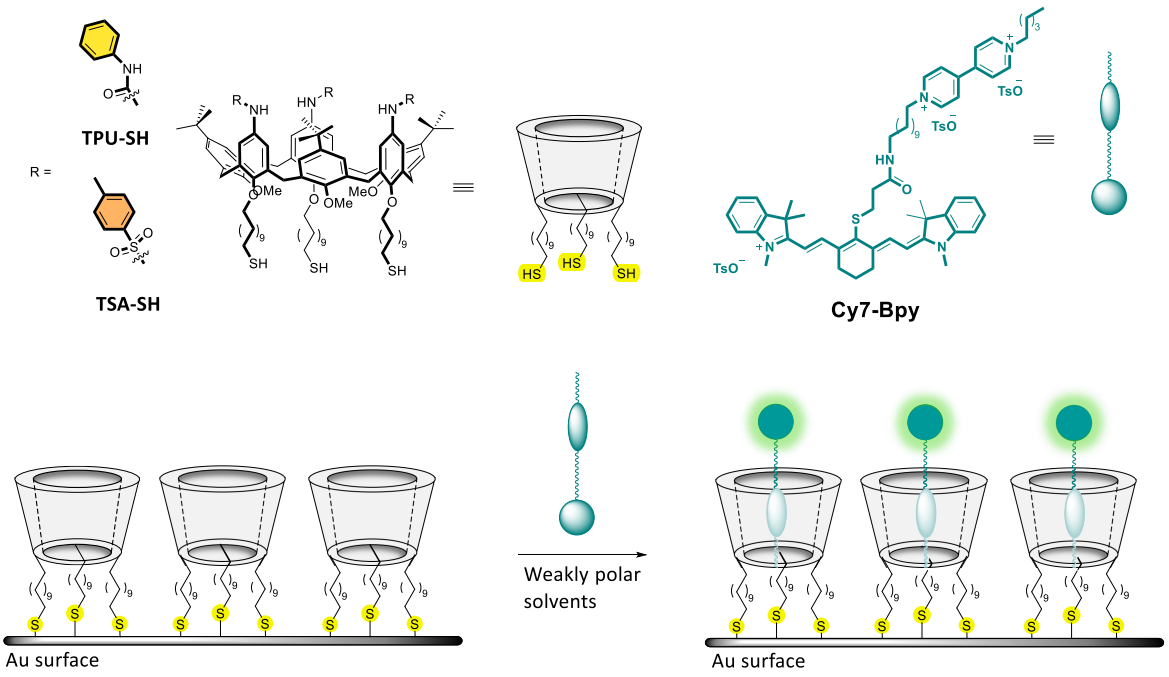

Figure 3.5. Top: structure of calix[6]arene derivatives **TPU-SH** and **TSA-SH**, and cyanine-based dye **Cy7-Bpy**; bottom: schematic representation of the functionalized monolayer on a gold surface with calix[6]arene and complexation with **Cy7-Bpy**.

Here, we report the synthesis and characterization of the designed target molecules. An initial investigation using NMR and UV-Visible spectroscopy was conducted to assess the complexation between the NIR cyanine-based dye and the calix[6]arene derivative. The results indicated a high binding affinity between the viologen unit and the calix[6]arene cavity. Furthermore, the fluorescence quantum yield of the cyanine dye increased upon complexation. Future studies will focus on evaluating the complexation on gold nanomaterial surfaces to examine the influence of plasmonic effects on the optical properties of the cyanine dye.

3 Results and Discussion

Synthesis of the ω-alkyl thiolate calix[6]arene derivatives

As calix[6]arene targets, we designed two derivatives featuring alkyl chains at the narrow rim, each terminated with thiol groups to enable anchoring onto the gold nanoparticles surface. The upper rim was functionalized in two distinct manners: with phenylureido (**TPU-SH**) and sulfonamido (**TSA-SH**) groups. It is known that both functional groups lead to the complexation of di-alkyl viologen salts.[9] The synthesis of these derivatives follows a common pathway for the first two steps, with the final upper functionalization achieved using isocyanate in one case (**TPU-SH**), and tosyl chloride in the other (**TSA-SH**). Due to the propensity of terminal thiol groups to oxidize and form disulfide

(S-S) bonds and their nucleophilicity, a protecting group was necessary for their incorporation into the hosts. Thioacetate was selected as the protecting group because it can be removed without interfering with the other functional groups in the molecule.

The first step in synthesizing the thiolated hosts involved the alkylation of tri-methoxy tri-nitro calix[6]arene (**TN**) with *S*-(11-bromoundecyl) ethanethioate (**Scheme 3.1**). This reaction required long reaction times and resulted in a relatively low yield of **TN-SCOCH$_3$** (30%). Subsequently, the challenging step was the reduction of the nitro groups at the upper rim of **TN-SCOCH$_3$**. While the reduction of nitro groups is typically performed on **TN** derivatives using hydrazine as the reducing agent and palladium on carbon (Pd/C) as the catalyst in refluxing methanol, this method was unsuitable due to the presence of the thioacetate protecting group that could react with hydrazine. Therefore, stannous chloride ($SnCl_2 \cdot 4H_2O$) was selected as the reducing agent, successfully yielding the desired product **TA-SCOCH$_3$**, albeit in modest yields, which was used directly in the subsequent steps without any purification. Following the reduction, the resulting amino groups were reacted with phenyl isocyanate to produce **TPU-SCOCH$_3$** in a 34% yield and with tosyl chloride to form **TSA-SCOCH$_3$**, also in a 25% yield.

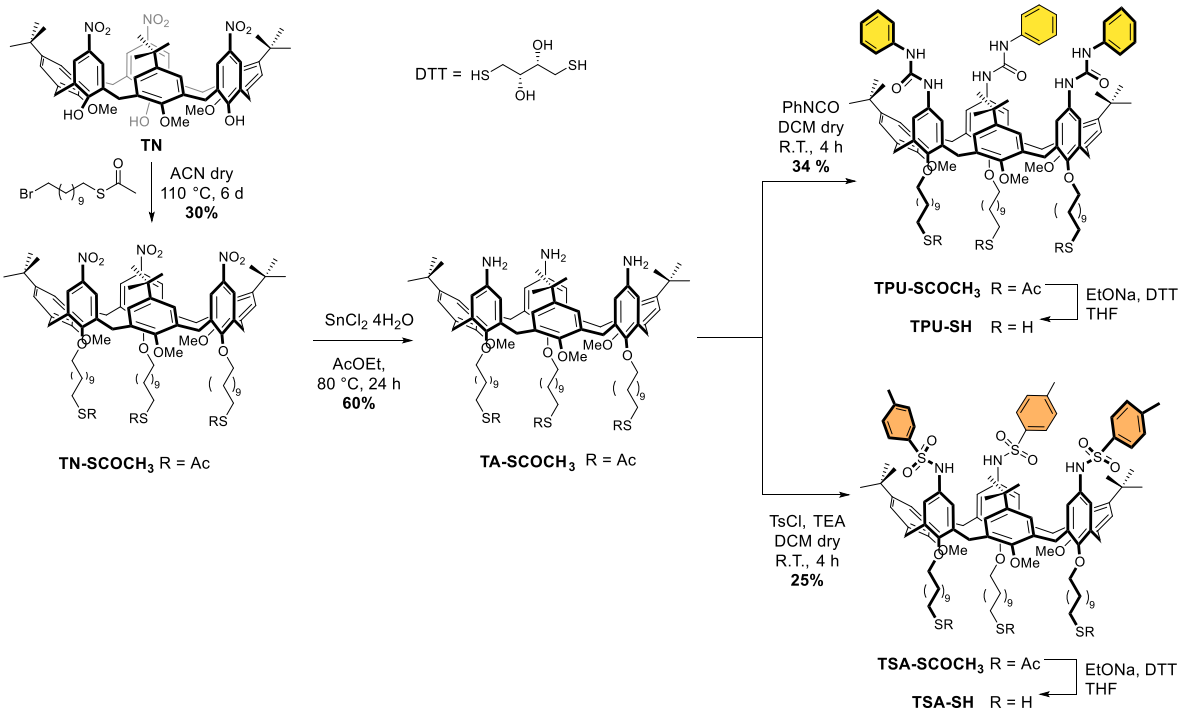

Scheme 3.1. Synthetic scheme of the synthesis of **TPU-SH** and **TSA-SH** calix[6]arene derivatives.

The final step to obtain the desired target products was the removal of the thioacetate protecting group. To find the opportune conditions for its removal, calix[6]arene **TSA-SCOCH$_3$** was chosen as a model compound. The several conditions employed for the PG removal are reported in **Table 3.1**.

Table 3.1. Experimental conditions of the attempts carried out for the removal of thioacetate protecting group of **TSA-SCOCH$_3$**.

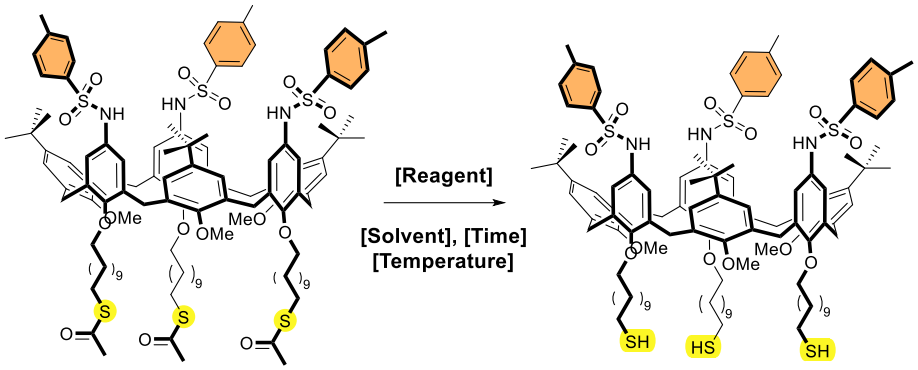

Entry	Reagent	Solvent	Time	Temperature (°C)	Yield (%)
1	NH_3 (30%) (15 eq.)	THF/MeOH 50:50	3 d	R.T.	-
2	NH_3 (30%) (large excess)	THF/MeOH 50:50	2 d	50	Degradation
3	Acetyl chloride (large excess)	DCM/MeOH 50:50	1 d	R.T.	Traces
4	Acetyl chloride (large excess)	Toluene/EtOH 50:50	1 d	80	Traces
5	*p*-toluensulfonic acid monohydrate (15 eq.)	DCM	1 d	R.T. → 60	-
6	*p*-toluensulfonic acid monohydrate (15 eq.)	DCM/MeOH	1 d	R.T.	-
7	EtONa, DTT	EtOH/THF 50:50	20 min	R.T.	100

Initially, basic hydrolysis was attempted using a 30% aqueous ammonia solution as the hydrolyzing reagent. Ammonia is a well-established basic hydrolyzing agent. Its employment is well-documented in the literature and often yields high product conversions.[10–14] While methanol is commonly employed as the solvent in such reactions, a 1:1 mixture of tetrahydrofuran (THF) and methanol was selected to enhance the solubility of the calix[6]arene derivative. Two attempts were conducted at different temperatures with a large excess of ammonia solution (**Table 3.1,** entries 1 and 2); however, both attempts proved unsuccessful in yielding the desired product. Subsequently, acetyl chloride in methanol was tested as a deprotecting agent in two additional trials, where the solvent and temperature were varied (**Table 3.1,** entries 3 and 4). Despite these efforts, only trace amounts of the target product were detected in both cases. Another acidic hydrolysis was then explored using *p*-toluenesulfonic acid monohydrate in dichloromethane and a dichloromethane/methanol mixture. However, no product formation was observed in these attempts either (**Table 3.1,** entries 5 and 6). The complete thiol deprotection was successfully achieved using sodium ethoxide (EtONa) as the hydrolyzing agent in combination with dithiothreitol

(DTT), which acted as a sacrificial reducing agent (**Table 3.1,** entry 7). DTT is known for reducing disulfide bonds, and upon oxidation, it forms a stable six-membered ring, facilitating the release of free thiol groups on the calix[6]arene scaffold.[15,16]

The obtained product was fully characterized using NMR and mass spectrometry. **Figure 3.6** shows the ^{1}H NMR stacked plot comparing the spectra of **TSA-SCOCH$_3$** (top) and **TSA-SH** (bottom). Full peak assignment was achieved thanks to 2D NMR techniques. Both spectra displayed close similarities, except for slightly sharper peaks in **TSA-SH**. In particular, in the low-field region of the two spectra, two doublets are observed at 7.57 and 7.20 ppm, each integrating for six protons, which were assigned to the aryl protons labeled *a* and *b*. These resonances belong to the three 4-methylbenzensulfonamide units attached to the calix[6]arene upper rim. Two singlets at 7.14 and 6.22 ppm were identified as the macrocycle scaffold aromatic protons *e* and *e'*, respectively. In the mid-field region, the two doublets at 4.39 and 3.41 ppm, displaying geminal coupling, were assigned respectively to the axial and equatorial protons of the macrocycle methylene bridges. A triplet at 3.87 ppm corresponds to the six methylene protons (*f*) of the three C11 thiolated alkyl chains at the macrocycle lower rim. In the **TSA-SCOCH$_3$**, the triplet at 2.87 ppm was assigned to the *r* protons, while the two broad singlets at 2.52 ppm and 2.41 ppm corresponded to the methoxy protons and methyl protons *c* of the tosyl groups, respectively. The sharp singlet at 2.33 ppm was attributed to the methyl protons *s* of the thioacetate-protecting units. These peaks served as key indicators for monitoring the deprotection reaction. Indeed, in the **TSA-SH** spectrum, the signal for the *r* protons shifted from 2.87 ppm to 2.54 ppm and converted into a quadruplet because of the coupling with the SH proton. However, this diagnostic multiplicity was partially compromised by the overlap of the C*H*$_2$SH signal with that of the methoxy group, which resonated at the same chemical shift. The chemical shift of the methyl protons (*c*) of the sulfonamido groups remained unchanged, while the singlet relative to the acetyl protons *s* (at 2.30 ppm in **TSA-SCOCH$_3$**) disappeared, confirming the successful removal of the thioacetate group. In the high-field region, both spectra exhibited multiplets corresponding to the alkyl chain protons (*g*-*q*) and the protons *d* of the tert-butyl groups. The same deprotection procedure was applied to **TPU-SCOCH$_3$**, and the successful removal of the thioacetate-protecting group was also confirmed in this case (see Experimental).

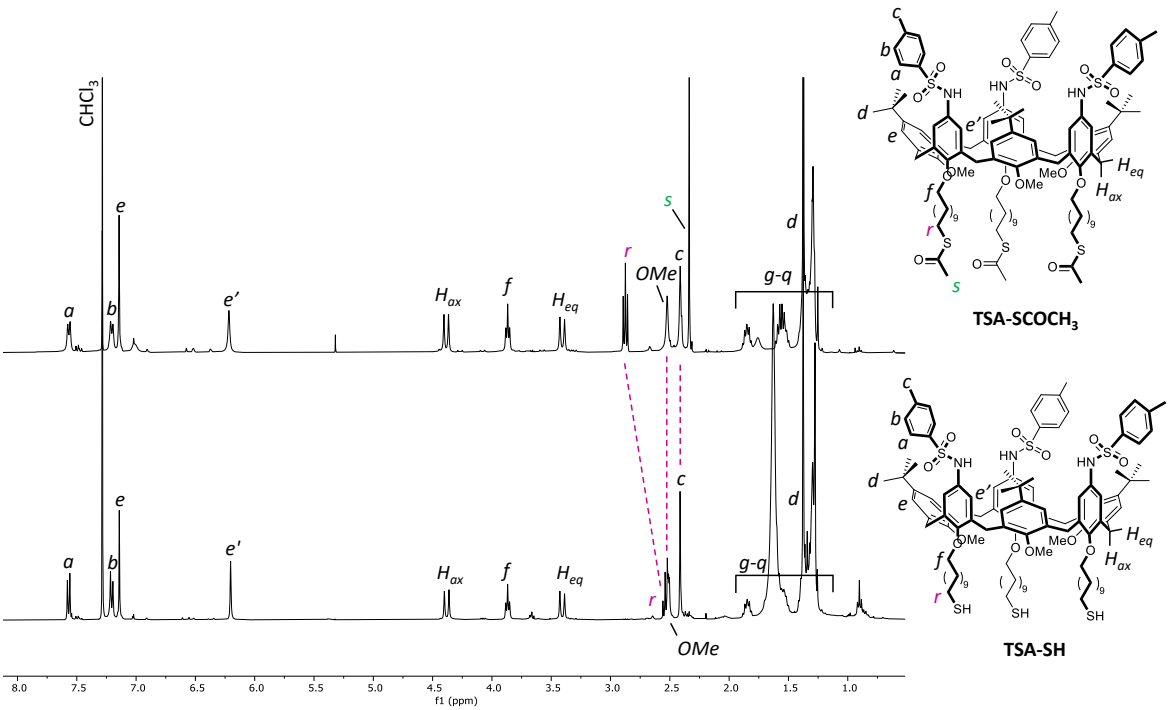

Figure 3.6. ^{1}H NMR stack plot spectra ($CDCl_3$, 400 MHz, 298 K) of **TSA-SCOCH₃** (top), and **TSA-SH** (bottom).

Synthesis of the NIR cyanine-based guest

To explore how the optical properties of a guest molecule change when complexed near the gold surface of a plasmonic nanostructure, the NIR cyanine-based dye **Cy7-Bpy** (**Figure 3.7**) was chosen as the candidate guest. This dye, a heptamethine cyanine, is covalently linked to a viologen unit *via* an amide bond, resulting in a tricationic species. The dye also possesses three tosylate counterions, which are expected to promote complexation within the cavity of the calix[6]arene derivatives **TPU-SH** or **TSA-SH**.

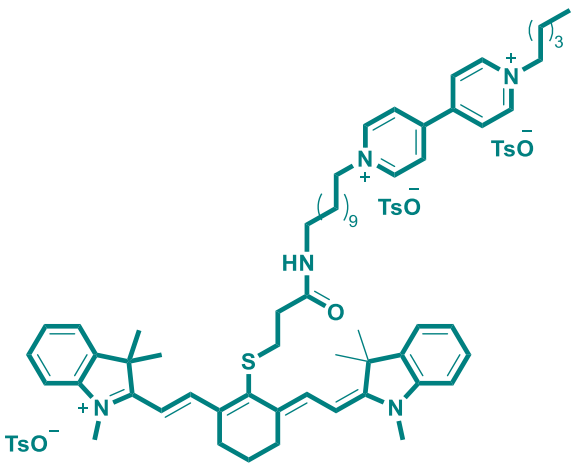

Cy7-Bpy

Figure 3.7. Structure of cyanine-based guest **Cy7-Bpy**.

A convergent synthetic approach was employed to obtain the target guest molecule through a multi-step process. Initially, the cyanine and viologen salt components were synthesized separately, followed by their coupling *via* the formation of a stable amide bond. To this aim, the cyanine derivative was functionalized in the meso position with a thiolated carboxylic acid, while the viologen salt was modified with an amino terminus.

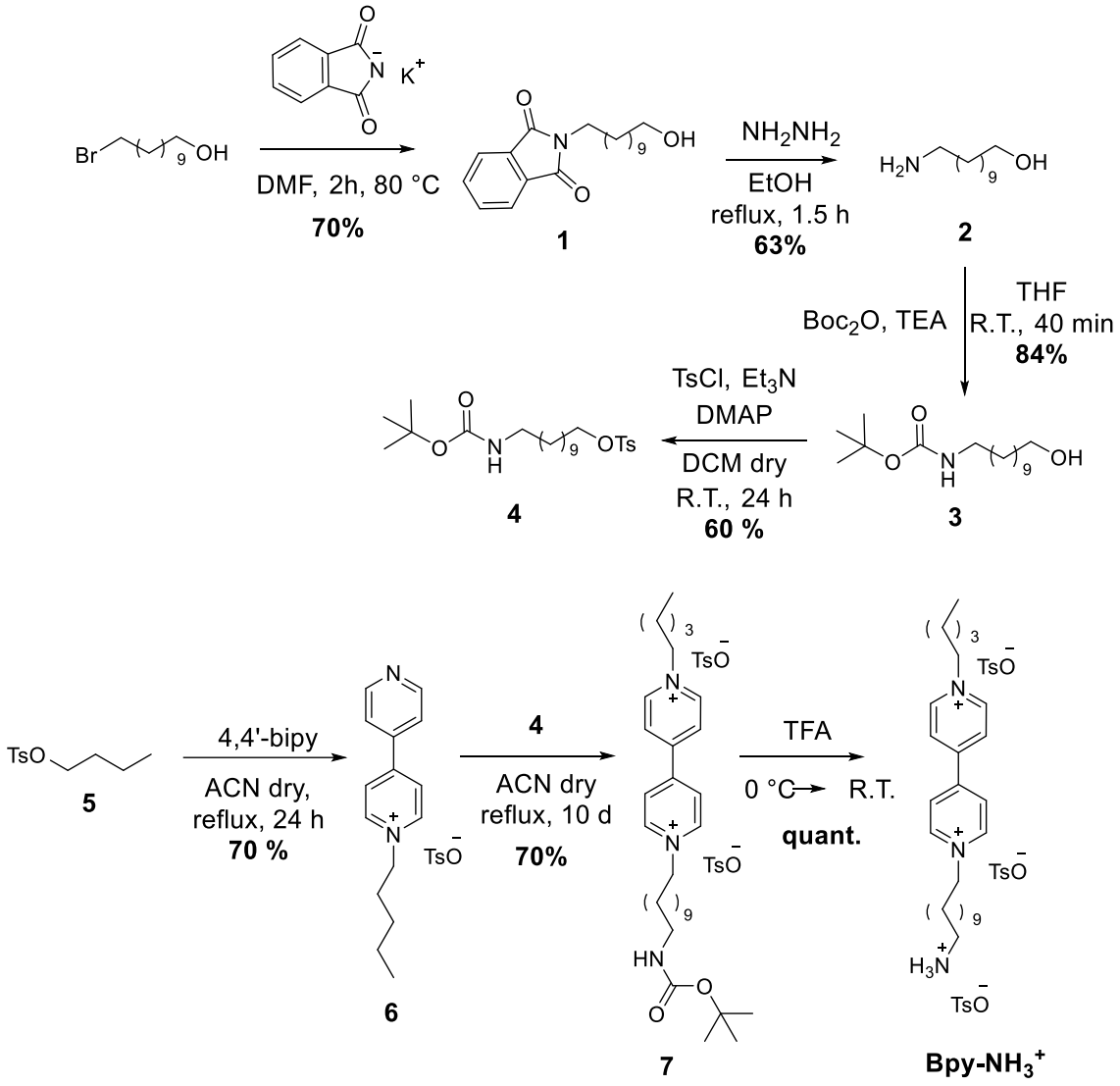

Scheme 3.2. Synthetic scheme for the synthesis of **Bpy-NH_3^+**.

The synthesis of the viologen salt (**Bpy-NH_3^+**), depicted in **Scheme 3.2**, was accomplished in seven steps. The amino functionality was first introduced as a phthalimide group on the commercial 11-bromoundecanol, following a reported procedure.[17] The resulting phtalimido derivative **1** underwent hydrazinolysis yielding the 11-aminoundecanol **2** (63%).[17] The deprotected amino group of **2** was reprotected with a Boc group to give **3** in good yields. This protecting group replacement was necessary because the deprotection of a phthalimido group requires basic conditions in which alkylated viologen salts are unstable. In contrast, the Boc group can be quantitatively deprotected

using triflic acid (TFA), ensuring compatibility with the viologen structure. The OH group of **3** was then activated toward the nucleophilic substitutions by converting it into the tosylate **4**.[18] The known pentyl tosylate **5** was reacted with a two-fold stoichiometric excess of 4,4′-bipyridine (4,4′-bipy) to yield the monoalkylated pyridyl pyridinium tosylate **6** in good yields.[19] Subsequent reaction of the latter with **4** gave the desired *N*,*N*′-dilakylated viologen **7**, and the final deprotection of the undecanylamino group was achieved quantitively to afford the target synthon **Bpy-NH$_3^+$** with an overall yield of 11%.

The synthesis of the carboxylic acid-terminating cyanine involved substituting the chloride atom at the meso position with an appropriate thiolated alkyl chain bearing a terminal carboxylic acid group. To achieve this, two thiol-containing linkers were used as nucleophiles: the 3-mercaptopropionic acid (MPA) and 11-mercaptoundecanoic acid (MUA). These linkers differ in the length of their alkyl chain: one contains a three-carbon (C3) chain, while the other features an eleven-carbon (C11) chain. The goal was to test the impact of different chain lengths to study the effect of the distance of the dye from the gold surface of the nanomaterial. The synthesis of **Cy7-SC2COOH** and **Cy7-SC10COOH** involved a nucleophilic substitution reaction, utilizing triethylamine as the base and the appropriate thiol as the nucleophile in anhydrous DMF (**Scheme 3.3**). Due to the low reaction yield (36%) observed in the synthesis of **Cy7-SC10COOH**, we opted to proceed with only **Cy7-SC2COOH** for the further synthetic steps leading to our viologen-cyanine target.

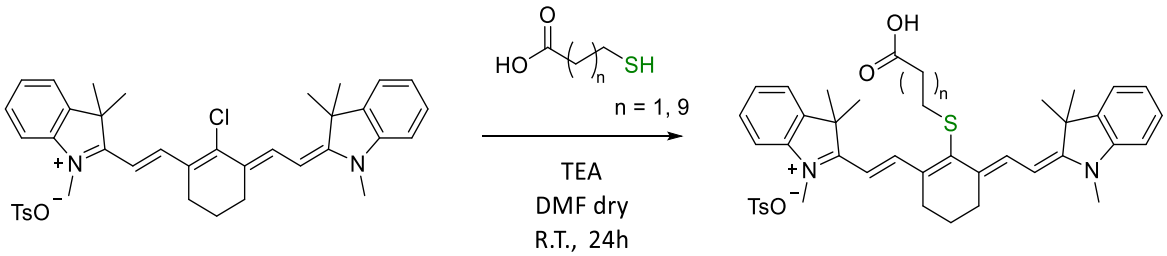

Cy7-Cl

Cy7-SC2COOH, n = 1, 80%

Cy7-SC10COOH, n = 9, 36%

Scheme 3.3. Synthetic scheme for the synthesis of **Cy7-SC2COOH** and **Cy7-SC10COOH**.

To facilitate the formation of the amide bond between the cyanine derivative and the viologen salt (**Bpy-NH$_3^+$**), we chose to activate the carboxylic acid group of **Cy7-SC2COOH** using *N*-hydroxysuccinimide (NHS) to generate an activated ester (**Cy7-SC2COSu**). The latter compound should readily react with the amine group of **Bpy-NH$_3^+$** in the presence of a base to form the desired amide bond. **Table 3.2** summarizes various attempts to activate **Cy7-SC2COOH** with NHS, using several coupling reagents such as carbonyldiimidazole (CDI), *N*-(3-dimethylaminopropyl)-*N*′-ethylcarbodiimide hydrochloride (EDC·HCl), *N*,*N*′-dicyclohexylcarbodiimide (DCC), and *N*,*N*′-diisopropylcarbodiimide (DIC). While all attempts using EDC·HCl showed no conversion (**Table 3.2**,

entries 2 and 3), those using CDI and DCC resulted in partial conversion (**Table 3.2**, entries 1 and 4). The optimal result was achieved using an excess of DIC (2.6 equivalents) and NHS (2.8 equivalents) in dichloromethane at room temperature over 48 hours (**Table 3.2**, entry 6), which led to complete conversion. The resulting product was utilized directly without further purification.

Table 3.2. Experimental conditions for the activation of **Cy7-SC2COOH** with NHS.

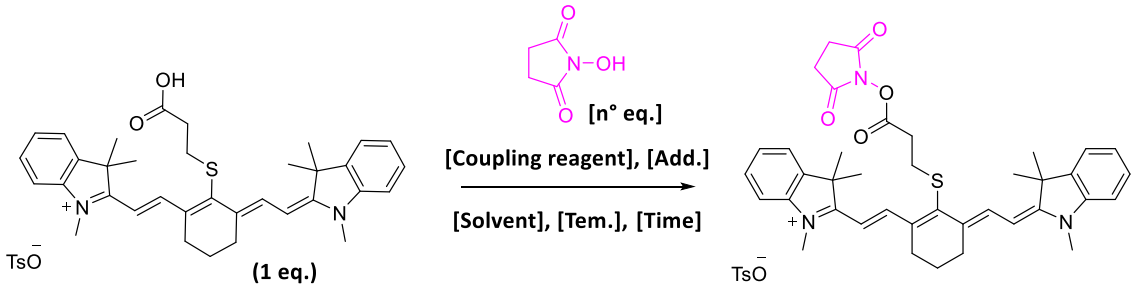

Entry[a]	Eq. HOSu	Coupling reagent (eq.)	Additive (eq.)	Solvent	Temperature	Time	Conversion
1	-	CDI (2.8)	-	DCM dry	R.T.	30 h	Not complete
2	1.5	EDC·HCl (1.3)	-	DCM dry	R.T.	6 h	No conversion
3	2.9	EDC·HCl (3.6)	TsOH (0.5)	DCM dry	R.T.	30 h	No conversion
4	1.5	DCC (1.3)	-	DCM dry	R.T.	2 d	Not complete
5	1.5	DIC (1.3)	-	DCM dry	R.T.	2 d	Not complete
6	2.8	DIC (2.6)	-	DCM dry	R.T.	2 d	Complete

[a]Because of the high reactivity of the resulting activated ester, the reactions could only be monitored by TLC (see Experimental part).

Before reacting the activated ester **Cy7-SC2COSu** with the amino derivative viologen salt **Bpy-NH$_3^+$**, the reaction was first tested with the commercially available dodecylamine (**Scheme 3.4**). The reaction was conducted in dichloromethane (DCM) at room temperature over two days using diisopropylethylamine (DIPEA) as the base. After purification by column chromatography, **Cy7-SC2CONHC12** was obtained with a yield of 56%.

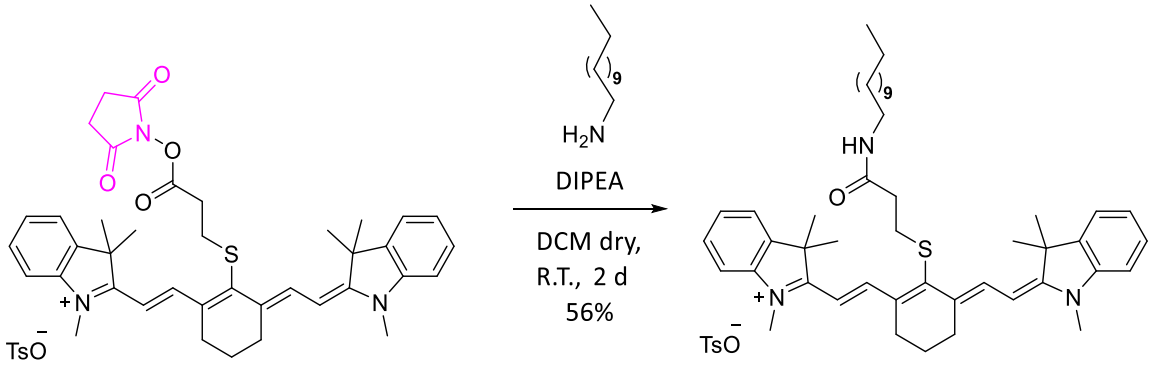

Scheme 3.4. Synthesis of **Cy7-SC2CONHC12**.

The formation of the amide bond was confirmed through ^{1}H NMR and mass spectrometric analysis. **Figure 3.8** presents the ^{1}H NMR spectrum of **Cy7-SC2CONHC12** recorded in deuterated methanol.

The evidence for amide bond formation is indicated by the appearance of resonances assigned to the dodecylamine chain in the high-fields region of the spectrum. In particular, a triplet at 0.90 ppm corresponding to the terminal methyl group of the dodecyl chain and a triplet at 3.14 ppm corresponding to methylene protons (labeled as *9* in **Figure 3.8**) near the amide group, are diagnostic for the successful synthesis of **Cy7-SC2CONHC12**.

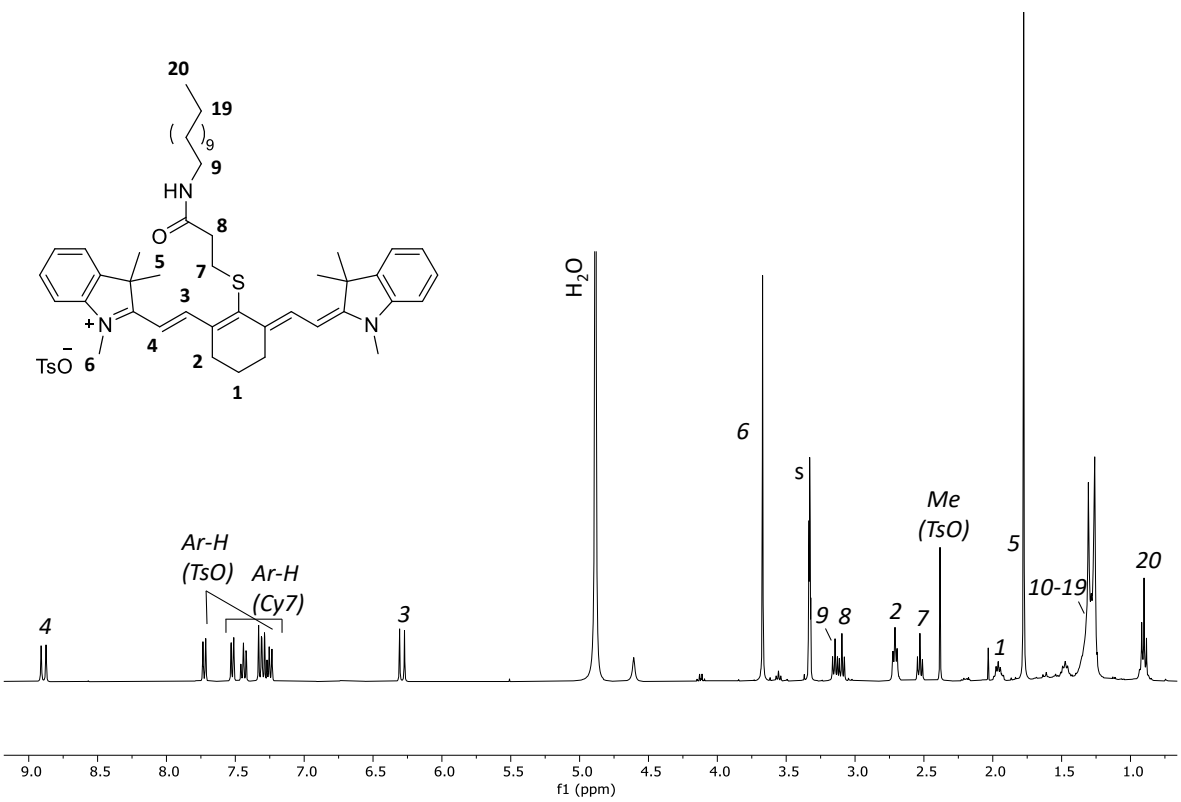

Figure 3.8. ^{1}H NMR spectrum (CD_3OD, 400 MHz, 298 K) of **Cy7-SC2CONHC12**.

The absorbance properties of **Cy7-SC2CONHC12** were compared to those of **Cy7-Cl** to assess whether the sulfur substituent in the meso position affects the absorbance maximum of the cyanine. **Figure 3.9** displays the absorbance spectra of both dyes: **Cy7-Cl** (blue line) shows a maximum absorbance at 787 nm, while **Cy7-SC2CONHC12** (pink line) shows a maximum slightly red-shifted at 793 nm. As expected, this substitution did not significantly alter the dye's optical properties, with an absorption maximum remaining in the NIR region.

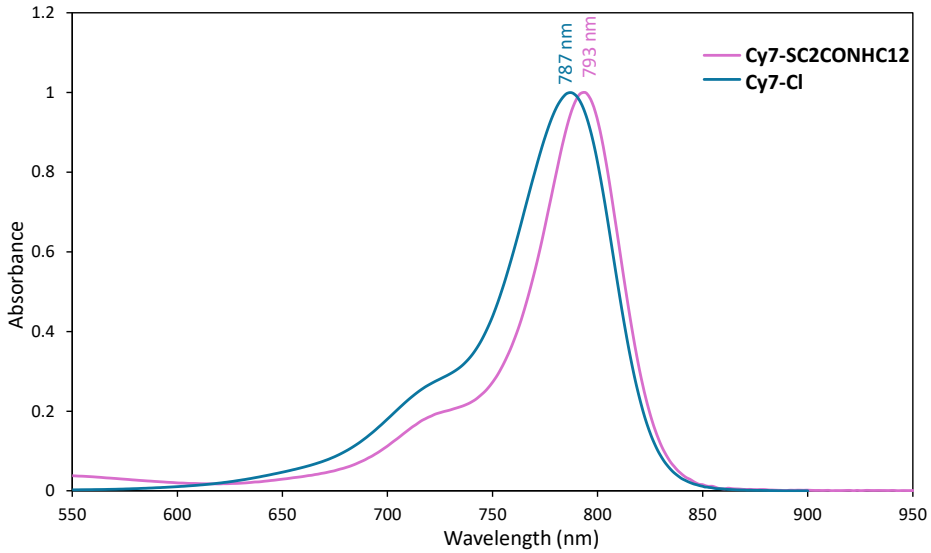

Figure 3.9. Normalized absorbance spectra of **Cy7-Cl** (blue line, c = 5.2×10^{-6} M) and **Cy7-SC2CONHC12** (pink line, c = 4.3×10^{-6} M) in dichloromethane at 298 K.

After confirming the feasibility of the amide bond formation, the same protocol was applied to the reaction with the **Bpy-NH$_3^+$** salt. In this case, careful control over the reaction stoichiometry was crucial, as the final product, **Cy7-Bpy**, is tri cationic, making it difficult to separate from unreacted **Bpy-NH$_3^+$**. To ensure complete reaction, a slight stoichiometric defect of **Bpy-NH$_3^+$** (0.9 equivalents) was used (**Scheme 3.5**), while DIPEA was added in slight excess (1.5 equivalents) to facilitate the deprotonation of the amine group. Dimethylformamide (DMF) was selected as the solvent due to its favorable solubility properties. The target purification was the most challenging step due to its highly ionic nature, which precluded the use of direct phase chromatographic methods. After several trials, the target product was successfully isolated in a 37% yield by precipitation, first with diethyl ether and then ethyl acetate.

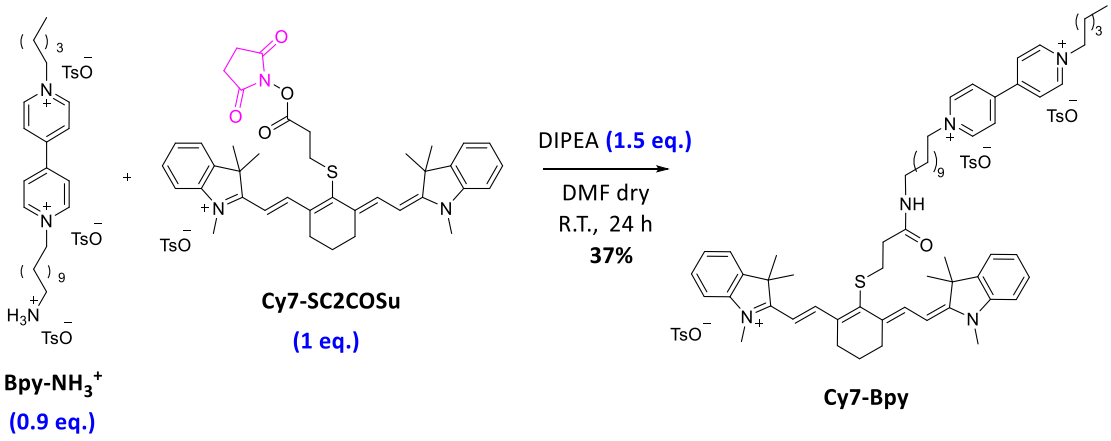

Scheme 3.5. Synthetic scheme of the synthesis of **Cy7-Bpy**.

The formation of the product was confirmed through NMR spectroscopy and mass spectrometric analysis. Complete peaks assignment was achieved using both 1D (**Figure 3.10**) and 2D NMR experiments. NMR spectra were recorded in deuterated methanol (CD_3OD) for solubility reasons.

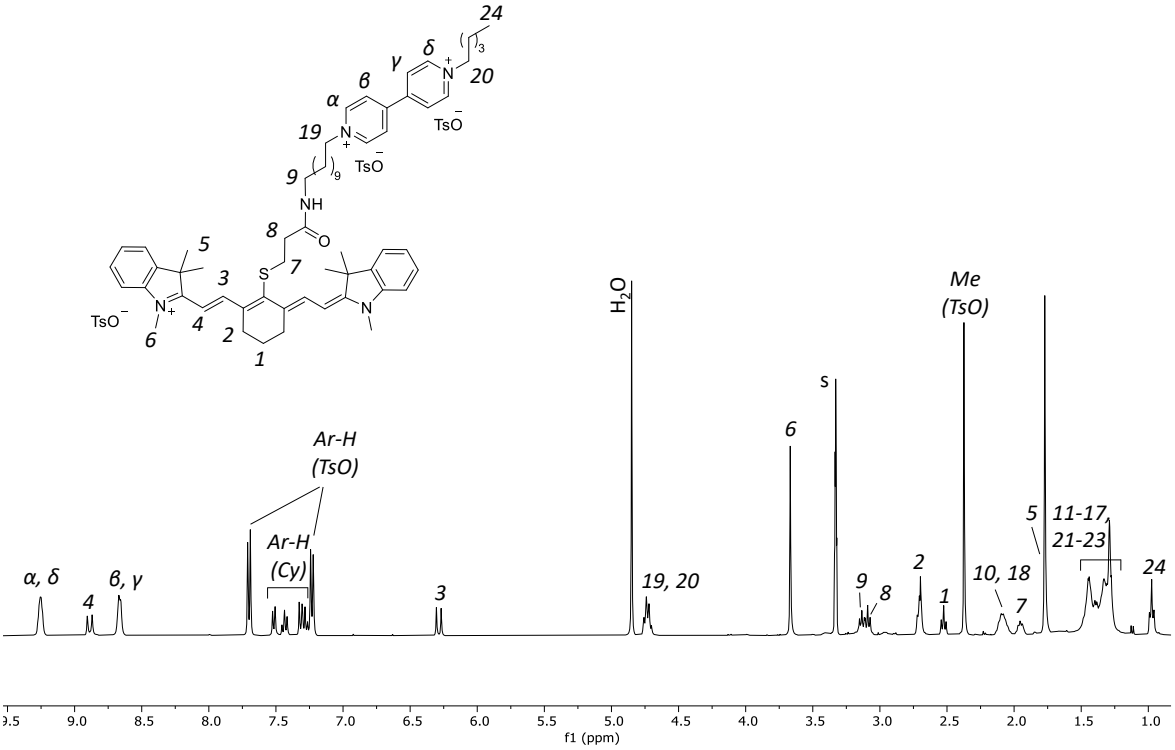

Figure 3.10. ^{1}H NMR spectrum (CD_3OD, 400 MHz, 298 K) of **Cy7-BPy**.

In the downfield region, the alkene protons labeled as *4* and *3* were observed as doublets at 8.88 and 6.28 ppm, respectively. The viologen protons were detected as two broad doublets, with protons *α* and *δ* resonating at 9.25 ppm, and protons *β* and *γ* at 8.66 ppm. The downfield shift of protons *α* and *δ* is attributed to their proximity to the positively charged pyridinium nitrogen. Between 7.1-7.8 ppm, signals corresponding to the aromatic protons of the cyanine core and the tosylate anion were observed, with the tosylate yielding two doublets at 7.70 ppm and 7.23 ppm. A multiplet centered at 4.7 ppm was assigned to the methylene protons labeled as *19* and *20*, which are directly linked to the pyridinium rings of the viologen unit. In the high-field region, three singlets were observed: one at 3.67 ppm corresponding to methyl protons labeled as *6*, deshelded by the adjacent positively charged nitrogen atom; one at 2.37 ppm assigned to the methyl protons of the tosylate anion; and one at 1.77 ppm attributed to the two methyl groups of the cyanine moieties labeled as *5*. Two adjacent triplets at 3.13 ppm and 3.09 ppm were assigned to methylene protons near the amide group, labeled as *9* and *8*, respectively. The protons of the cyclohexenyl ring within the cyanine core exhibited two resonances: a multiplet between 2.6-2.7 ppm (protons *2*) and a triplet at 2.52 ppm (protons *1*). The remaining alkyl chain protons were assigned as follows: a multiplet at 2.1-2.0 ppm for protons labeled as *10* and *18*, a multiplet at 1.9-2.0 ppm for protons

labeled as *7*, and a broader multiplet between 1.2-1.5 ppm corresponding to protons *11-17* and *21-23*. Lastly, a triplet at 0.97 ppm was assigned to the protons of the terminal methyl group labeled as *24*.

NMR analysis of Cy7-Bpy interaction with calix[6]arene derivative in solution

Before exploring the system on the surface of gold nanomaterials, the complexation behavior in solution was thoroughly examined using both NMR spectroscopy and UV-Visible analysis. A model calix[6]arene derivative was selected for this study. To mimic the behavior of **TSA-SH** and **TPU-SH**, which contain undecyl thiol-terminated chains at the lower rim, a calix[6]arene derivative (**TPU-Oct**) functionalized with octyl chains at the lower rim and with phenylureido groups at the upper rim was utilized. The synthesis of this calix[6]arene derivative is well-established in our laboratories and has already been reported in the literature.[9] **TPU-Oct** and **Cy7-Bpy** were mixed in a 1:1 ratio in deuterated dichloromethane and several NMR experiments were carried out to elucidate the structure of the resulting supramolecular complex (**Scheme 3.6**). **Figure 3.11** presents a stacked plot of the ^{1}H NMR spectra for free **TPU-Oct** (**A**), free **Cy7-Bpy** (**C**), and their 1:1 mixture (**B**). Peak assignment was successfully achieved through a 2D HSQC experiment (**Figure 3.12**).

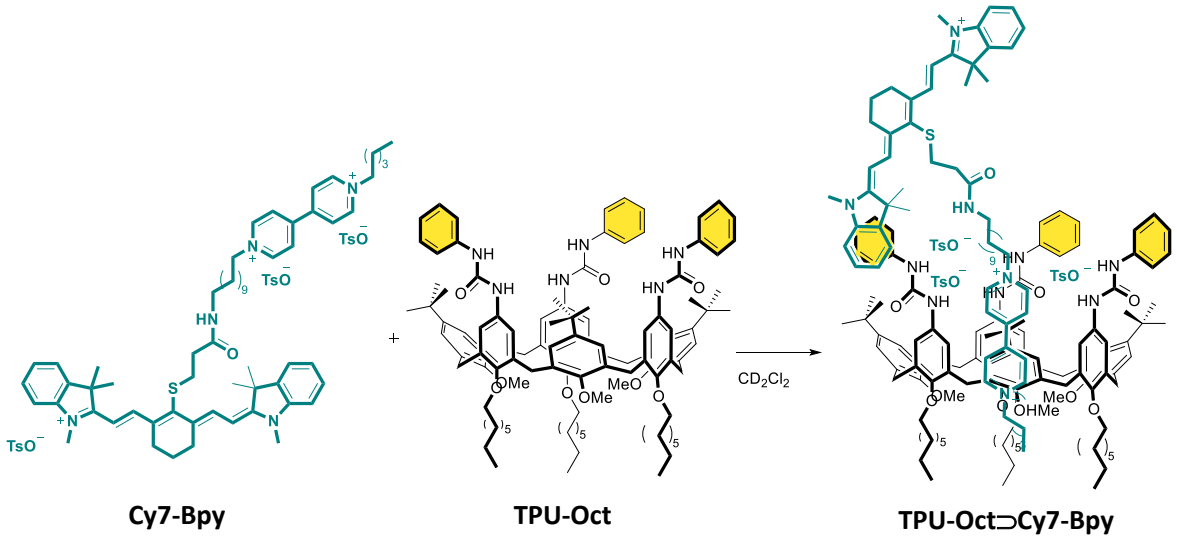

Scheme 3.6. Scheme for the NMR complexation experiment between **Cy7-Bpy** and **TPU-Oct**.

The formation of a [2]pseudorotaxane complex (**TPU-Oct⊃Cy7-Bpy**) with the viologen unit threading the calix[6]arene cavity was supported by several key signals. As reported in previous studies involving the complexation of simpler *N*,*N*'-dialkylviologen salts, the downfield shift of the signal of **TPU-Oct** methoxy groups from 2.83 to 3.99 ppm suggests the successful complexation of the bispyridinium moiety within the calix[6]arene cavity. Indeed, this shift reflects the displacement of the methoxy groups from the cavity due to the threading of the guest viologen unit into the cavity.[21] Additionally, the up-field shift of the viologen unit protons to higher fields confirms the

interaction of this electron-deficient moiety with the electron-rich cavity of the calix[6]arene. Notably, the *α* and *δ* protons, which appear as a broad doublet at 9.25 ppm in the free dye, undergo splitting and shift to 7.91 ppm for the *α* protons and 6.99 ppm for the *δ* protons in the complex. The more pronounced shift observed for the *δ* protons indicates their deeper positioning within the calix[6]arene cavity. Similarly, the *β* and *γ* protons also show splitting and shift to 7.42 ppm for the *β* protons and 5.78 ppm for the *γ* protons, with the latter experiencing a notable 2.89 ppm shielding effect, consistent with their deeper location within the calix[6]arene cavity. Notably, the signals associated with the cyanine core remain unshifted, indicating that while the viologen unit interacts within the calix[6]arene cavity, the cyanine moiety remains external to the macrocycle.

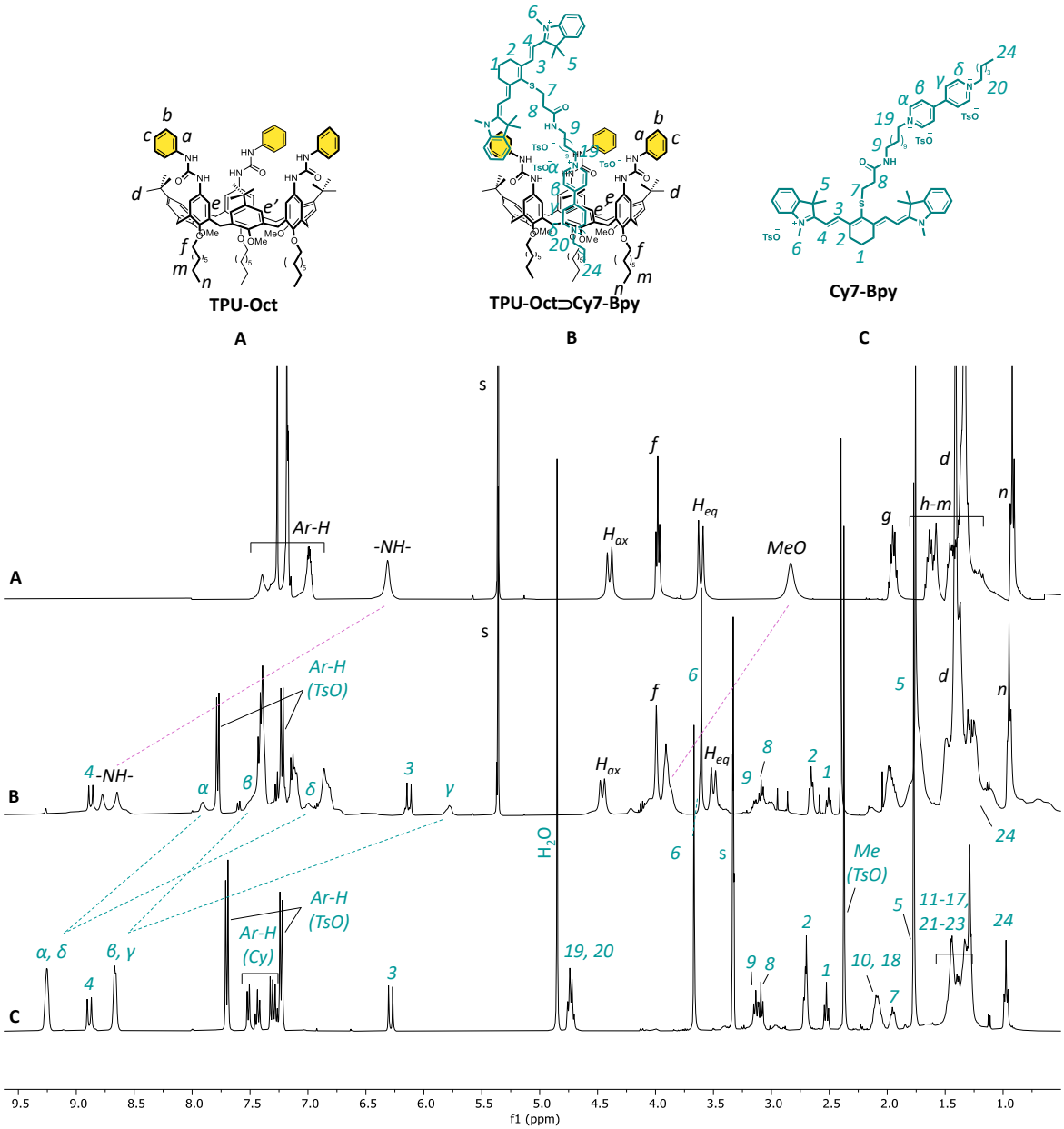

Figure 3.11. ^{1}H NMR stack plot spectra (400 MHz, 298 K) of free **TPU-Oct** (**A**, CD_2Cl_2), free **Cy7-Bpy** (**B**, CD_3OD), and of the resulting [2]pseudorotaxane complex **TPU-Oct⊃Cy7-Bpy** (**C**, CD_2Cl_2).

The peak assignments for the [2]pseudorotaxane complex were further confirmed through the analysis of the 2D HSQC spectrum, which played a crucial role, especially in identifying the pyridinium protons labeled *α*, *β*, *γ*, and *δ* (**Figure 3.12**). These protons are usually challenging to distinguish in 1D ^{1}H NMR spectra of calix[6]arene-based rotaxanes and pseudorotaxanes due to their large up-field shifts, placing them in a crowded region of the spectrum where most of the aromatic signals of these supramolecular species resonate. However, in HSQC spectra, their ^{13}C chemical shifts are less affected by the anisotropic effect exerted by the calix[6]arene cavity, making them easier to identify. The pyridinium *α* and *δ* protons give rise to distinguishable cross-peaks at approximately 142 ppm on the indirect ^{13}C dimension (axis), while the *β* and *γ* protons have cross-peaks near 123 ppm.

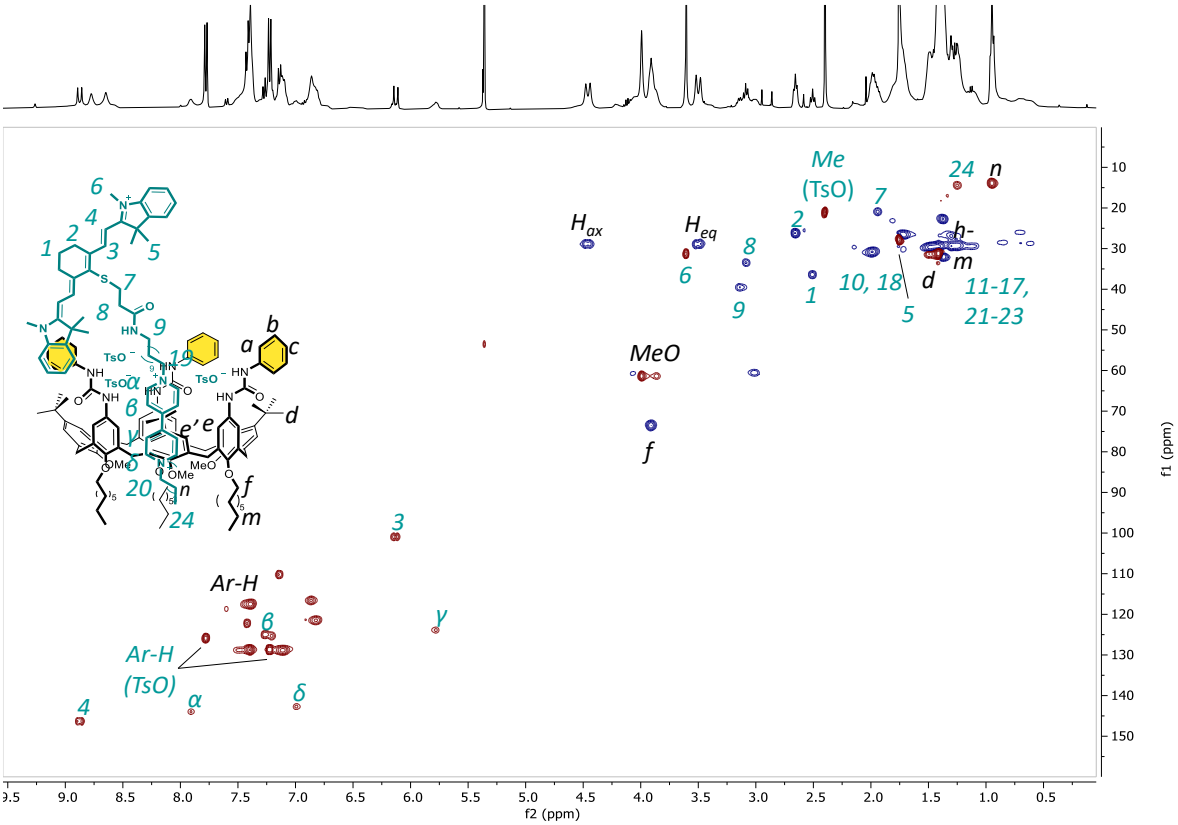

Figure 3.12. Edited HSQC (CD_2Cl_2, 400 MHz, 298 K) of [2]pseudorotaxane complex **TPU-Oct⊃Cy7-Bpy**. Positive peaks (CH_3 and CH) are shown in red, while negative ones (CH_2) are in blue.

An additional NMR study was conducted to verify that the interaction occurs exclusively *via* the viologen unit and not through the cyanine core. In this study, the calix[6]arene **TPU-Oct** was used as the host, while **Cy7-Cl,** which lacks the viologen unit functionalization, served as the guest (**Scheme 3.7**).

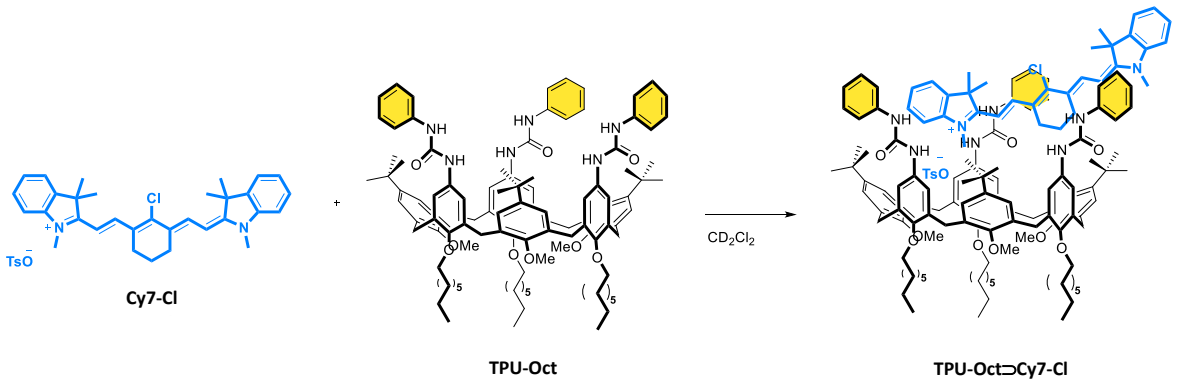

Scheme 3.7. Scheme for the NMR complexation experiment between **Cy7-Cl** and **TPU-Oct**.

The NMR experiment was repeated in deuterated dichloromethane under the previously specified conditions employed for **Cy7-Bpy**. **Figure 3.13** shows the stacked ^{1}H NMR spectra of free **TPU-Oct** (top), free **Cy7-Cl** (bottom), and their 1:1 mixture (middle). While a minor interaction between the cyanine and calix[6]arene can be inferred, there is no evidence of significant complexation. Notably, the signal of the methoxy group remains unchanged, indicating that the calix[6]arene cavity remains unoccupied by the guest. Additionally, no substantial shifts in the cyanine signals were detected, apart from minor, insignificant changes. This experiment confirms that the viologen unit is essential for effective complexation within the calix[6]arene cavity.

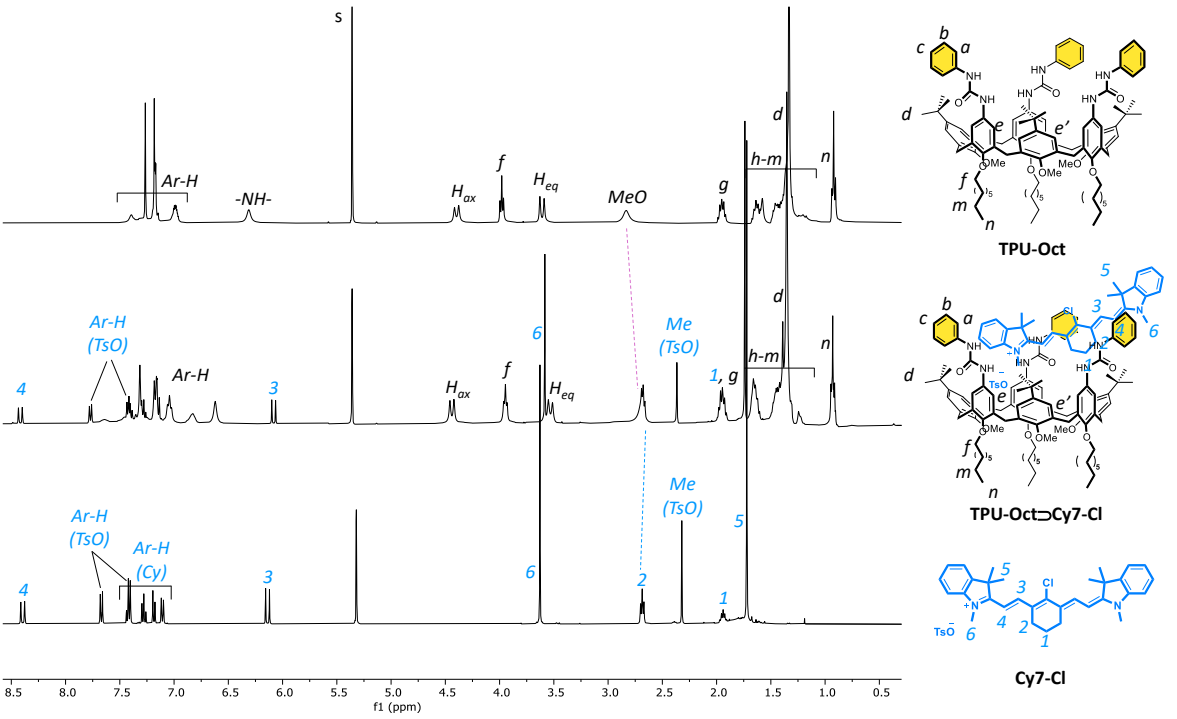

Figure 3.13. ^{1}H NMR stack plot spectra (CD_2Cl_2, 400 MHz, 298 K) of free **TPU-Oct** (top), free **Cy7-Cl** (bottom), and their 1:1 mixture (middle).

Optical characterization of Cy7-Bpy and its [2]pseudorotaxane complex with TPU-Oct

The absorbance and emission spectra of **Cy7-Bpy** were measured and compared with those of **Cy7-Cl** (**Figure 3.14**). **Cy7-Bpy** shows a narrow and intense absorbance band centered at 785 nm (black continuous line) with an emission peak at 802 nm (black dashed line), whereas **Cy7-Cl** exhibited an absorbance maximum at 788 nm (red continuous line) and an emission maximum at 810 nm (red dashed line). The fluorescence quantum yield (Φ) for **Cy7-Cl** was calculated at 27%, while that of **Cy7-Bpy** was significantly lower, at just 14%. The observed decrease in fluorescence quantum yield passing from **Cy7-Cl** to **Cy7-Bpy** can be attributed to the presence of the di-alkyl viologen moiety in **Cy7-Bpy**, which forms a charge transfer (CT) band upon complexation with the **TPU** calix[6]arene (see Chapter 2). The CT excited state has a lower energy than the excited state of the cyanine-based dye. As a result, upon excitation, the system transitions from the cyanine dye's excited state to the lower-energy CT excited state. Since this CT excited state undergoes non-radiative relaxation, fluorescence emission is consequently reduced.

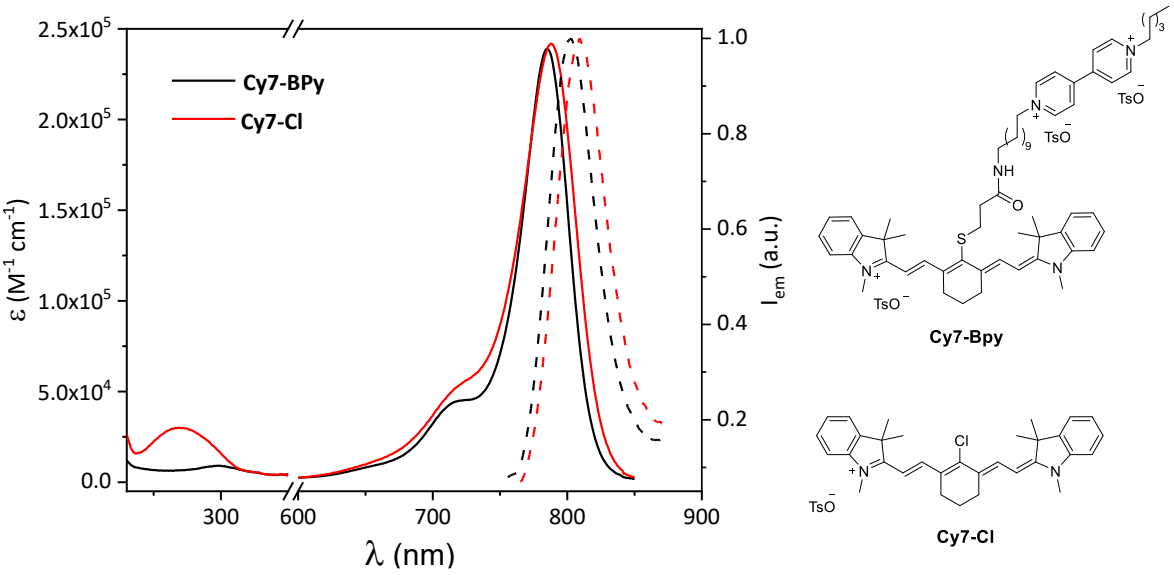

Figure 3.14. Left: Absorbance (continuous lines) and emission (dashed lines) spectra of **Cy7-Cl** (red lines), and **Cy7-Bpy** (black lines); right: structure of cyanine dyes.

Subsequently, a 1:1 mixture of **Cy7-Bpy** and **TPU-Oct** was analyzed using a two-chamber quartz cuvette, as detailed in Chapter 1. This setup allows simultaneous recording of the absorbance spectra of the individual components (the "sum" spectrum) and, after rapid mixing, the spectrum of the mixture (the "mix" spectrum) (**Figure 3.15**). A distinct difference in the spectra was observed around 280 nm, suggesting an effective supramolecular interaction between the two components, resulting in the formation of a [2]pseudorotaxane complex, denoted as **TPU-Oct⊃Cy7-Bpy**.

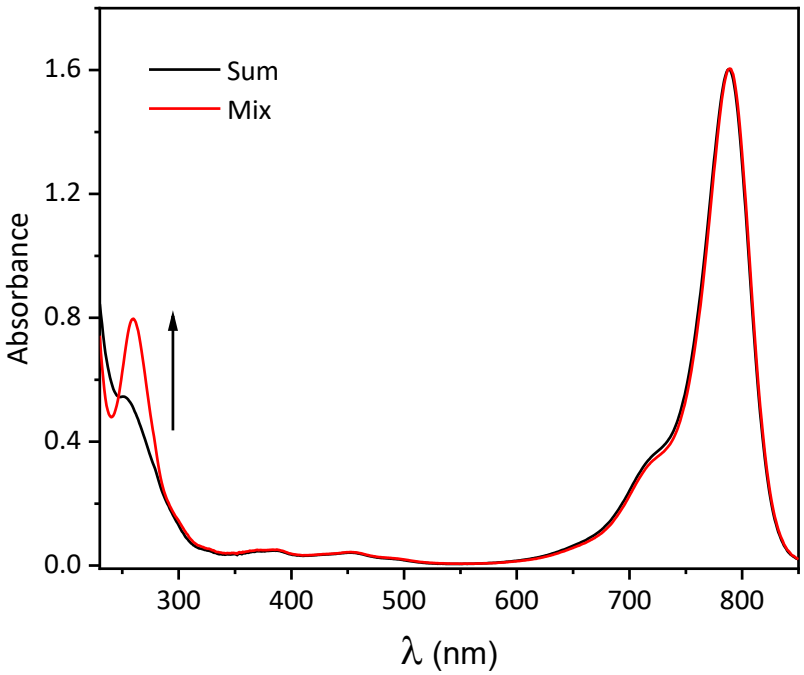

Figure 3.15. Sum of the absorption spectra of **Cy7-Bpy** (c = 1.3×10^{-5} M) and **TPU-Oct** (c = 1.3×10^{-5} M) (black line) and the absorption spectrum of the mixture of **Cy7-Bpy** and **TPU-Oct** (red line) (CH_2Cl_2, 298 K, λ = 225-850 nm region).

Subsequently, UV-Vis and fluorescence titrations were performed to determine the binding constant of the **TPU-Oct⊃Cy7-Bpy** complex. **Figure 3.16** presents, on the top left, the UV-Vis titration tracking the dye's absorbance variations upon incremental addition of a **TPU-Oct** solution, while, in the top right, the fluorescence titration. In the bottom, the emission intensity at 808 nm was plotted as a function of **TPU-Oct** equivalents added. This plot reveals an increase in the dye fluorescence upon complexation. The corresponding slope change occurring at 1.0 equivalent of **TPU-Oct** added confirms the hypothesized 1:1 stoichiometry of the binding event. Data fitting yielded a binding constant with a log*K* value of 8.3. The elevated association constant can be attributed to the presence of three tosylate anions, which facilitate the formation of more hydrogen bonds, thereby enhancing the stability of the complex.

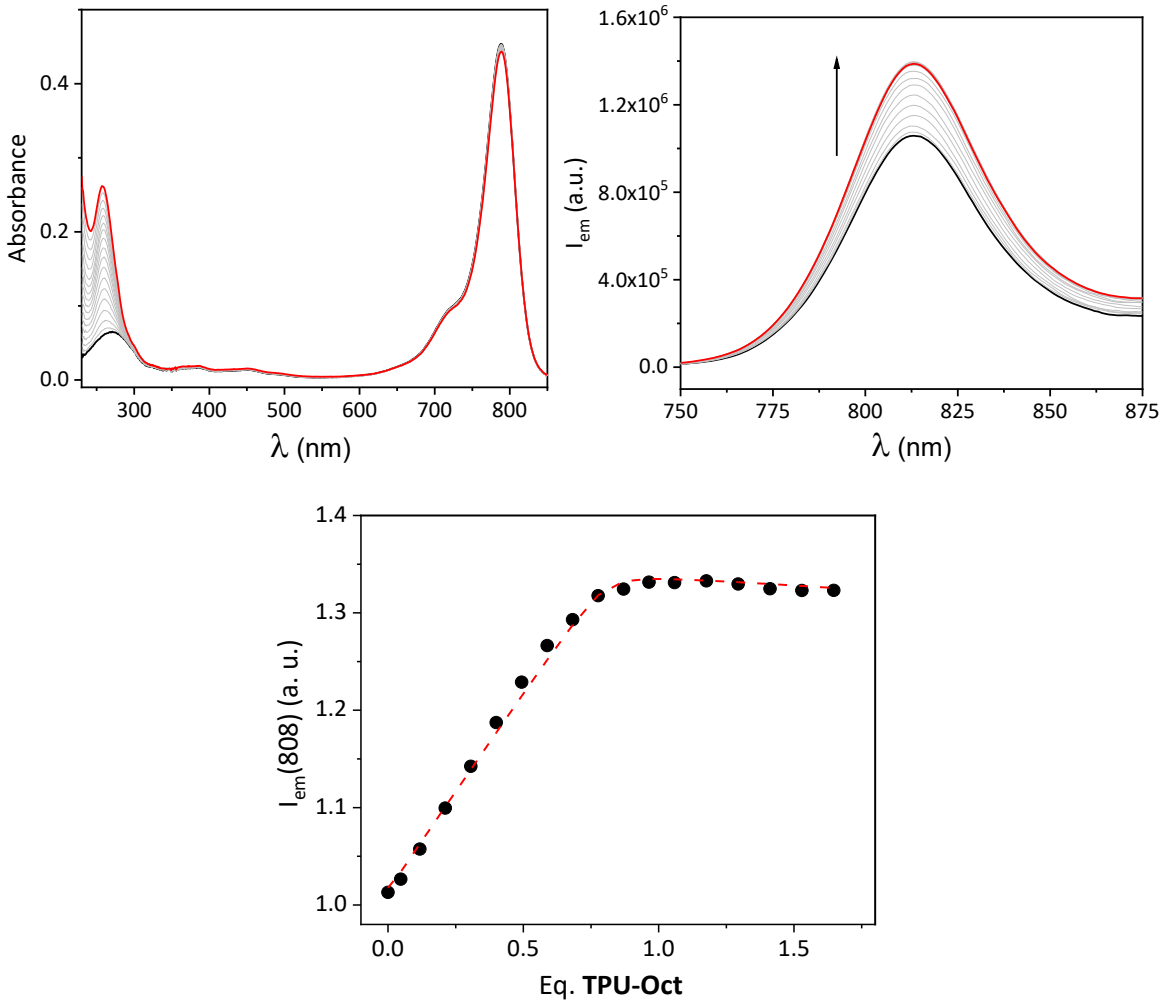

Figure 3.16. Top left: collection of absorbance spectra taken during the titration of a **Cy7-Bpy** solution in CH_2Cl_2 (C = 2×10^{-6} M) with a solution of **TPU-Oct** in CH_2Cl_2 (c = 1.5×10^{-4} M) at 298 K; top right: collection of emission spectra taken during the titration of a **Cy7-Bpy** solution in CH_2Cl_2 (c = 2×10^{-6} M, λ_{max}^{ex} = 730 nm) with a solution of **TPU-Oct** in CH_2Cl_2 (c = 1.5×10^{-4} M) at 298 K; bottom: binding isotherm (λ = 808 nm) for the complexation of **Cy7-Bpy** with **TPU-Oct**. Black dots: experimental points; continuous red line: fitting.

Additionally, fluorescence quantum yield measurements revealed an increase from 14% for unbound **Cy7-Bpy** to 20% after complexation. This enhancement suggests that the fluorescence properties of the cyanine core are modulated by the interaction of the viologen unit within the cavity of **TPU-Oct**.

3 Conclusion

This chapter presents the synthesis and characterization of two *ω*-thiolated calix[6]arene derivatives, **TPU-SH** and **TSA-SH**, along with a NIR cyanine-based dye **Cy7-Bpy**. The cyanine dye was specifically designed to include a viologen unit to facilitate, enabling its efficient complexation within the calix[6]arene cavity. The interaction between the cyanine dye and calix[6]arene derivatives was initially investigated in solution using a model calix[6]arene derivative (**TPU-Oct**) featuring phenyl ureido groups at the upper rim and octyl chains at the lower rim. NMR analysis of the 1:1 mixture of **TPU-Oct** and **Cy7-Bpy** revealed that the covalent attachment of the viologen unit

to the cyanine core is essential for efficient complexation. A similar analysis with a cyanine dye lacking the viologen unit (**Cy7-Cl**) demonstrated minimal complexation with **TPU-Oct**, underscoring the importance of the viologen moiety for effective binding. Subsequently, UV-Visible titrations were employed to determine the binding constant between **TPU-Oct** and **Cy7-Bpy**. The calculated log*K* was found to be slightly higher than that of simple *N*,*N*-dialkyl viologen salts. Fluorescence studies indicated an enhancement in the dye's quantum yield upon complexation with the calix[6]arene derivative. These encouraging results represent an initial step toward exploring these systems on the surface of gold nanostructures. The next phase will involve the synthesis of either gold nanoparticles or nanorods functionalized with the *ω*-thiolated calix[6]arenes **TPU-SH** and **TSA-SH**, followed by an investigation into the interaction between **Cy7-Bpy** and the calix[6]arene cavity on the nanostructures surface. This approach aims to couple the plasmonic properties of gold nanomaterials with the enhanced fluorescence of the cyanine dye. Additionally, the ability to regulate the threading/dethreading process of the cyanine from the calix[6]arene cavity *via* redox stimuli or by varying solvent conditions offers a promising avenue for developing functional responsive materials.

3 Acknowledgments

Thanks to Dr. Leonardo Andreoni (University of Bologna) for UV-Visible and fluorescence measurements.

3 Experimental Section

General Methods

All solvents were dried using standard procedures; all other reagents were of reagent-grade quality obtained from commercial suppliers and used without further purification. Column chromatography was carried out on 230–400 mesh silica gel (Aldrich) unless otherwise stated. NMR spectra were recorded at 400 MHz for ^{1}H and 100 MHz for ^{13}C. Chemical shifts are expressed in ppm (δ) using the residual solvent signal as an internal reference (7.26 ppm for $CHCl_3$, 5.32 for $CHDCl_2$ and 3.31 ppm for CD_2HOD). Coupling constants (*J*) are given in Hz and the following abbreviations have been used to describe the signals: singlet (s); broad singlet (br. s); doublet (d); triplet (t); quadruplet (q); multiplet (m). Mass spectra were recorded in the ESI mode. Melting points were measured with a Gallenkamp melting-point apparatus and are uncorrected. UV–Vis spectra were recorded on a UV-Visible Cary 300 (Agilent). Fluorescence spectra were recorded on an Edinburgh Instrument FS5. Compounds **1**,[17] **2**,[17] **3**,[22] **4**,[18] and **6**[19] were synthesised according to published procedures.

Synthesis of novel compounds

7: In a Schlenk tube, under nitrogen atmosphere, pentyl-4-methylbenzenesulfonate **5** (0.103 g, 0.424 mol, 1.3 eq.) and 1-(3-((tert-butoxycarbonyl)amino)propyl)-1'-propyl-[4,4'-bipyridine]-1,1'-diium 4-methylbenzenesulfonate **6** (0.195 g, 0.326 mol, 1.0 eq.) were suspended in dry ACN (2 mL). The reaction mixture was refluxed in a sealed Schlenk tube for 10 days. After completion, the reaction mixture was cooled down and the solvent was removed under reduced pressure. The crude product was dissolved in methanol/ethyl acetate 1:3 and the precipitated solid was decanted (3 times). Finally, the pure product **7** was obtained as white solid in 40 % yield (0.118 g, 0.13 mol).

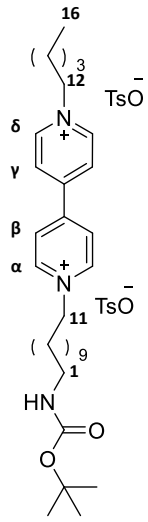

m.p.: 103-105 °C. **^{1}H NMR** (400 MHz, CD_3OD) δ = 9.25 (d, *J* = 6.1 Hz, 4H, $H_{\alpha,\,\delta}$), 8.66 (d, *J* = 6.1 Hz, 4H, $H_{\beta,\,\gamma}$), 7.70 (d, *J* = 8.2 Hz, 4H, $H_{Ar\text{-}H(TsO)}$), 7.24 (d, *J* = 7.8 Hz, 4H, $H_{Ar\text{-}H(TsO)}$), 4.73 (t, *J* = 7.6 Hz, 4H, $H_{11,\,12}$), 3.03 (t, *J* = 7.1 Hz, 2H, H_1), 2.38 (s, 6H, $H_{Me(TsO)}$), 2.09 (m, 4H, $H_{10,\,13}$), 1.7-1.2 (m, 27H, $H_{2\text{-}9,\,14,\,15,\,t\text{-}Bu}$), 0.97 (m, 3H, H_{16}). **^{13}C NMR** (CD_3OD, 101 MHz): 149.9, 145.6, 140.3, 128.5, 126.9, 125.5, 61.9, 39.9, 39.4, 31.2, 30.8, 29.6, 29.2, 29.2, 29.1, 29.0, 28.7, 27.9, 27.4, 26.5, 25.8, 21.8, 19.9, 12.7. **ESI-MS (+):** calculated for $C_{38}H_{58}N_3O_5S^+$: m/z (z = 1): 668.96, found: 668.70.

Bpy-NH$_3^+$: In a 25 mL round-bottom flask, under nitrogen atmosphere, compound **7** (0.050 g, 0.060 mmol, 1.0 eq.) was dissolved in trifluoroacetic acid (2 mL). The reaction mixture was stirred at room temperature for 15 minutes. After completion, the trifluoroacetic acid was removed under reduced pressure. The pure product **Bpy-NH$_3^+$** was obtained as brown sticky solid in quantitative yield (0.054 g, 0.060 mmol) without further purification.

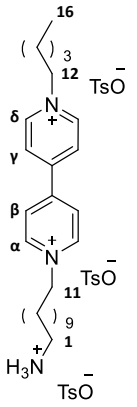

^{1}H NMR (400 MHz, CD_3OD) δ = 9.25 (d, *J* = 6.9 Hz, 4H, $H_{\alpha,\delta}$), 8.66 (d, *J* = 6.3 Hz, 4H, $H_{\beta,\gamma}$), 7.70 (d, *J* = 8.2 Hz, 6H, $H_{Ar\text{-}H(TsO)}$), 7.24 (d, *J* = 7.9 Hz, 6H, $H_{Ar\text{-}H(TsO)}$), 4.73 (t, *J* = 7.6 Hz, 4H, $H_{11,12}$), 2.92 (t, *J* = 7.7 Hz, 2H, H_1), 2.38 (s, 9H, $H_{Me(TsO)}$), 2.2-2.0 (m, 4H, $H_{10,13}$), 1.7-1.6 (m, 2H, H_2), 1.5-1.3 (m, 18H, $H_{2\text{-}9,14,15}$), 0.98 (t, *J* = 6.9 Hz, 3H, H_{16}) ppm. **^{13}C NMR** (CD_3OD, 101 MHz): δ = 145.7, 128.5, 126.8, 125.7, 61.9, 39.3, 30.9, 29.2, 28.2, 27.1, 26.1, 25.8, 22.8, 21.8, 19.9, 12.6 ppm. **ESI-MS (+):** calculated for $C_{33}H_{51}N_3O_3S^{2+}$: m/z (z = 2): 284.68, found: 284.85; calculated for $C_{28}H_{44}F_3N_3O_2^{2+}$: m/z (z = 2): 255.67, found: 255.86; calculated for $C_{35}H_{51}F_3N_3O_5S^{2+}$: m/z (z = 2): 682.35, found: 682.36.

Cy7-SC2COOH: In a 25 mL two-necked round-bottom flask, under nitrogen atmosphere, **Cy7-Cl** (0.332 g, 0.507 mmol, 1.0 eq.) was dissolved in dry DMF (3 mL). Then 3-mercaptoundecanoic acid (0.064 g, 53 µL, 0.608 mmol, 1.2 eq.) and triethylamine (0.062 g, 85 µL, 0.608 mmol, 1.2 eq.) were added to the reactor. The reaction mixture was stirred at room temperature for 20 hours. The reaction was recovered with dichloromethane and the organic layer was washed with a sat. solution of LiCl (3 × 10 mL), water (2 × 10 mL), and finally with brine. The organic layer was dried over Na_2SO_4, filtered and the solvent was removed under reduced pressure. The crude product was purified by crystallization from 2-propanol to give pure **Cy7-SC2COOH** as a dark green sticky solid in 80 % yield (0.294 g, 507 µmol).

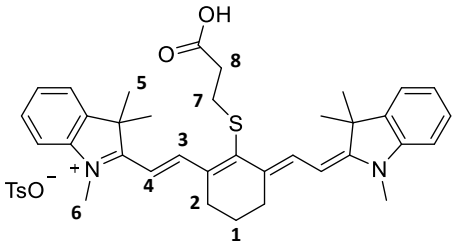

^{1}H NMR (400 MHz, CD_3OD) δ = 8.90 (d, *J* = 14.2 Hz, 2H, H_4), 7.8-7.2 (m, 12H, $H_{Ar\text{-}H(TsO + Cy)}$), 6.29 (d, *J* = 14.2 Hz, 2H, H_3), 3.67 (s, 6H, H_6), 3.09 (t, *J* = 6.9 Hz, 2H, H_7), 2.71 (t, *J* = 6.3 Hz, 4H, H_2), 2.60 (t, *J* = 6.9 Hz, 2H, H_8), 2.38 (s, 3H, $H_{Me(TsO)}$), 1.95 (q, *J* = 6.2 Hz, 2H, H_1), 1.78 (s, 12H, H_5). **^{13}C NMR** (CD_3OD, 101 MHz) δ =173.2, 145.8, 143.0, 140.9, 133.3, 128.4, 125.6, 124.8, 121.9, 110.3, 100.8, 49.0, 34.8, 32.7, 30.2, 26.8, 25.8, 20.8. **ESI-MS (+):** calculated for $C_{35}H_{41}N_2O_2S^+$: m/z (z = 1): 553.78, found: 553.62.

Cy7-SC10COOH: In a 25 mL two-necked round-bottom flask, under argon atmosphere, dry DMF (6 mL) was inserted and degassed by bubbling argon for 10 minutes. Then 11-mercaptoundecanoic

acid (0.058 g, 0.266 mmol, 1.5 eq.) and sodium hydride 60% (0.013 g, 0.531 mmol, 3.0 eq.) were added to the reactor. After 30 minutes **Cy7-Cl** (0.116 g, 0.177 mmol, 1.0 eq.) was added to the reactor and the reaction was stirred at 60 °C for 7 hours. After that, the reaction mixture was cooled down to room temperature. The organic layer was washed with a sat. solution of LiCl (3 × 10 mL), brine, and with acidic water by TsOH. The organic layer was dried over Na_2SO_4, filtered and the solvent was removed under reduced pressure. The crude product was dissolved in CH_2Cl_2, adsorbed onto silica, and purified by column chromatography (SiO_2, CH_2Cl_2/MeOH gradient from 95:5 to 90:10) to give pure **Cy7-SC10COOH** as a green sticky solid in 36 % yield (0.034 g, 41 µmol).

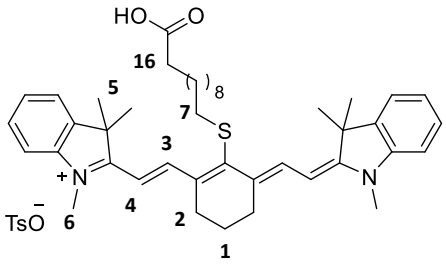

^{1}H NMR (400 MHz, CD_3OD) δ = 8.94 (d, *J* = 14.2 Hz, 2H, H_4), 7.72 (d, *J* = 8.2 Hz, 2H, $H_{Ar\text{-}H(TsO)}$), 7.53 (d, *J* = 7.6, 2H, $H_{Ar\text{-}H(TsO)}$), 7.44 (td, *J* = 7.7, 1.2 Hz, 2H, $H_{Ar\text{-}H(Cy)}$), 7.3-7.2 (m, 6H, $H_{Ar\text{-}H(Cy)}$), 6.29 (d, *J* = 14.2 Hz, 2H, H_3), 3.67 (s, 6H, H_6), 2.86 (t, *J* = 7.3 Hz, 2H, H_7), 2.71 (t, *J* = 6.2 Hz, 4H, H_2), 2.39 (s, 3H, $H_{Me(TsO)}$), 2.23 (t, *J* = 7.4 Hz, 2H, H_{16}), 1.94 (q, *J* = 6.2 Hz, 2H, H_1), 1.78 (s, 12H, H_5), 1.7-1.2 (m, 16H, $H_{8\text{-}15}$) ppm. **^{13}C NMR** (CD_3OD, 101 MHz) δ = 173.0, 157.7, 145.8, 143.04, 140.9, 133.2, 128.4, 124.8, 121.9, 110.4, 100.7, 42.5i, 38.4, 37.6, 34.9, 30.2, 30.1, 29.2, 29.1, 29.0, 29.0, 29.0, 28.8, 28.7, 28.4, 26.9, 25.8, 25.2, 20.92 ppm. **ESI-MS (+):** calculated for $C_{43}H_{57}N_2O_2S^+$: m/z (z = 1): 665.41, found: 665.61.

Cy7-SC2CONHC12: In a 25 mL two-necked round-bottom flask, under nitrogen atmosphere, **Cy7-SC2COOH** (0.04 g, 0.055 mmol, 1.0 eq.) was dissolved in dry CH_2Cl_2 (3 mL). Then NHS (0.018 g, 0.154 mmol, 2.8 eq.) and DIC (0.018 g, 0.143 mmol, 2.6 eq.) were added to the reaction mixture. The reaction was stirred at room temperature for 2 days. After completion, the solvent was washed with water (3 × 5 mL). The organic layer was dried over Na_2SO_4, filtered and the solvent removed under reduced pressure to give the crude product as green solid. The crude product was dissolved in dry CH_2Cl_2, then DIPEA (0.014 mL, 0.0823 mmol, 1.5 eq.) and dodecan-1-amine (0.010 g, 0.055 mmol, 1.0 eq.) were added. The reaction mixture was stirred at room temperature for 2 days. After completion of the reaction, the solvent was washed with water (3 × 5 mL). The organic layer was dried over Na_2SO_4, filtered and the solvent removed under reduced pressure. The crude product was dissolved in CH_2Cl_2, adsorbed onto silica, and purified by column chromatography (SiO_2, CH_2Cl_2/MeOH gradient from 95:5 to 90:10) to give pure **Cy7-SC2CONHC12** as a green sticky solid in 70 % yield (0.032 g, 0.039 mmol).

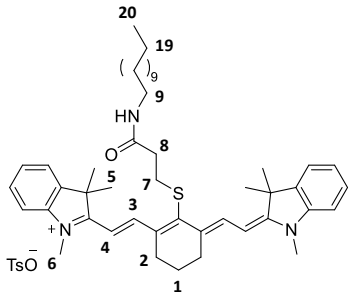

^{1}H NMR (400 MHz, CD_3OD) δ = 8.89 (d, *J* = 14.2 Hz, 2H, H_4), 7.72 (d, *J* = 8.3 Hz, 2H, $H_{Ar\text{-}H(TsO)}$), 7.52 (dd, *J* = 7.5, 1.2 Hz, 2H, $H_{Ar\text{-}H(Cy)}$), 7.44 (td, *J* = 8.5, 1.2 Hz, 2H, $H_{Ar\text{-}H(Cy)}$), 7.3-7.2 (m, 6H, $H_{Ar\text{-}H(TsO)+ Ar\text{-}H(Cy)}$), 6.29 (d, *J* = 14.2 Hz, 2H, H_3), 3.67 (s, 6H, H_6), 3.12 (dt, *J* = 20.0, 7.2 Hz, 4H, $H_{8,9}$), 2.71 (t, *J* = 6.2 Hz, 4H, H_2), 2.53 (t, *J* = 7.2 Hz, 2H, H_7), 2.38 (s, 3H, $H_{Me(TsO)}$), 2.0-1.9 (m, 2H, H_1), 1.78 (s, 12H, H_5), 1.5-1.2 (m, 20H, $H_{10\text{-}19}$), 0.90 (t, *J* = 6.9 Hz, 3H, H_{20}) ppm. **^{13}C NMR** (CD_3OD, 101 MHz) δ = 173.1, 171.4, 156.6, 145.7, 143.0, 140.9, 133.4, 128.4, 128.4, 125.6, 124.8, 121.9, 110.4, 100.8, 49.0, 39.2, 35.8, 33.1, 31.7, 30.2, 29.3, 29.3, 28.9, 26.9, 26.6, 25.8, 22.3, 20.8, 13.0 ppm. **ESI-MS (+):** calculated for $C_{47}H_{66}N_3OS^+$: m/z (z = 1): 720.49, found: 720.68.

Cy7-Bpy: In a 25 mL two-necked round-bottom flask, under nitrogen atmosphere, **Cy7-SC2COOH** (0.040 g, 0.055 mmol, 1.0 eq.) was dissolved in dry CH_2Cl_2 (3 mL). Then, NHS (0.018 g, 0.153 mmol, 2.8 eq.) and DIC (0.018 g, 0.142 mmol, 2.6 eq.) were added to the reaction mixture. The reaction was stirred at room temperature for 2 days. After completion, the solvent was washed with water (3 × 5 mL). The organic layer was dried over Na_2SO_4, filtered and the solvent removed under reduced pressure to give the crude product as green solid. The crude product was dissolved in dry DMF (2 mL), then a solution of **Bpy-NH$_3^+$** (0.010 g, 0.055 mmol, 1.0 eq.) in dry DMF (1 mL) was added. DIPEA (0.014 mL, 0.082 mmol, 1.5 eq.) was added dropwise, and the reaction mixture was stirred at room temperature for 24 hours. To the reaction mixture, diethyl ether was added in large excess (~10 mL). The mixture was left to sit for 1 hour and then the solid was filtered off. The liquid phase was concentrated and then precipitated from ethyl acetate. The solids obtained were combined. The pure product **Cy7-Bpy** was obtained as a green sticky solid in 37 % yield (0.029 g, 0.02 mmol).

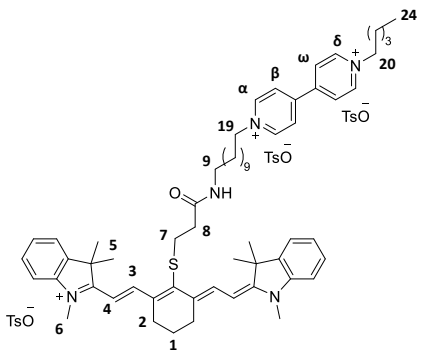

^{1}H NMR (400 MHz, CD_3OD) δ = 9.24 (br. d, 4H, $H_{\alpha,\delta}$), 8.87 (d, *J* = 14.2 Hz, 2H, H_4), 8.65 (br. d, 4H, $H_{\beta,\omega}$), 7.67 (d, *J* = 8.2 Hz, 4H, $H_{Ar\text{-}H(TsO)}$), 7.5-7.2 (m, 8H, $H_{Ar\text{-}H(Cy)}$), 7.2 (d, *J* = 7.9 Hz, 4H, $H_{Ar\text{-}H(TsO)}$), 6.27 (d, *J* = 14.2 Hz, 2H, H_3), 4.71 (m, 4H, $H_{19,20}$), 3.65 (s, 6H, H_6), 3.12 (t, *J* = 7.2 Hz, 2H, H_9), 3.07 (t, *J* = 7.2 Hz, 2H, H_8), 2.7-2.6 (m, 4H, H_2), 2.51 (t, *J* = 7.3 Hz, 2H, H_1), 2.35 (s, 9H, $H_{Me(TsO)}$), 2.06 (m, 4H, $H_{10,18}$), 1.93 (m, 2H, H_7), 1.75 (s, 12H, H_5), 1.5-1.2 (m, 18H, $H_{21\text{-}23,11\text{-}17}$), 0.95 (t, *J* = 6.7 Hz, 3H, H_{24}) ppm. **^{13}C NMR** (CD_3OD, 101 MHz) δ = 173.1, 171.4, 149.9, 145.7, 143.0, 142.3, 140.9, 140.2, 133.4, 128.4, 126.9, 125.5, 124.8, 121.9, 110.4, 100.8, 61.9, 49.0, 39.2, 35.8, 33.1, 31.2, 30.8, 30.3, 29.3, 29.2, 29.1, 29.0, 28.7, 27.9, 26.9, 26.7, 26.2, 25.8, 24.8, 21.8, 20.8, 19.9, 12.7 ppm. **HR-MS (ORBITRAP LQ)** calculated for

$C_{61}H_{82}N_5O_1S_1^{3+}$: m/z (z = 3): 310.87412, 311.20857, 311.54302, 311.87748; found: 310.87473, 311.20872, 311.54254, 311.87727; Calculated for $C_{68}H_{89}N_5O_4S_2^{2+}$: m/z (z = 2): 551.81725, 552.31893, 552.82061, 553.31683; found: 551.81781, 552.31936, 552.82007, 553.32102.

TPU-SCOCH3: In a 25 mL two-necked round-bottom flask, under nitrogen atmosphere, calix[6]arene tri-ammino tri-undecylthiol (0.050 g, 0.032 mmol, 1.0 eq.) and phenyl isocyanate (0.015 g, 0.014 mL, 0.127 mmol, 4.0 eq.) were dissolved in dry dichloromethane (10 mL). The reaction mixture was stirred at room temperature for 4 hours. After completion of the reaction, the organic layers were washed with water (3 × 10 mL), dried over Na_2SO_4, filtered and the solvent was concentrated under reduced pressure. The crude solid was dissolved in CH_2Cl_2, adsorbed onto silica, and purified by column chromatography (SiO_2, elution gradient hexane/ethyl acetate from 80:20 to 75:15) to give pure **TPU-SCOCH3** as a yellow solid in 34 % yield (0.021 g, 0.031 mmol).

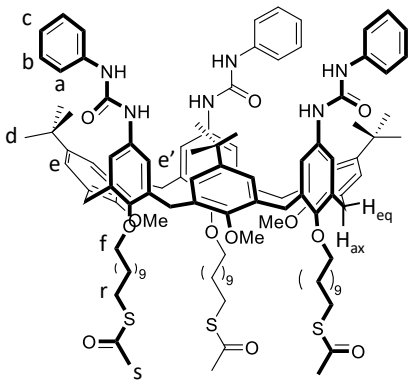

m.p.: 118-121 °C. **^{1}H NMR** ($CDCl_3$, 400 MHz) δ = 7.21 (br.s, 9H, H_{ArH}), 7.2-6.9 (m, 18H, H_{ArH}), 6.27 (br. s, 6H, $H_{\text{-}NH\text{-}}$), 4.40 (d, *J* = 15.7 Hz, 6H, H_{ax}), 3.93 (t, *J* = 6.5 Hz, 6H, H_f), 3.57 (d, *J* = 15.7 Hz, 6H, H_{eq}), 2.88 (t, *J* = 7.3 Hz, 6H, H_r), 2.79 (br. s, 9H, H_{OMe}), 2.34 (s, 9H, H_s), 1.9-1.1 (m, 60H, $H_{d,\ g\text{-}q}$) ppm. **^{13}C NMR** ($CDCl_3$, 101 MHz) δ = 152.4, 146.7, 138.2, 135.8, 133.1, 132.3, 128.9, 123.5, 123.3, 120.6, 34.2, 31.9, 30.6, 29.6, 29.6, 29.6, 29.5, 29.5, 29.2, 29.1, 28.8, 26.3. **ESI-MS (+):** calculated for $C_{117}H_{157}N_6O_{12}S_3^+$: m/z (z = 1): 1934.74, found: 1934.79.

TSA-SCOCH3: In a 50 mL two-necked round-bottom flask, under nitrogen atmosphere, calix[6]arene tri-ammino tri-undecyl thiol (0.303 g, 0.92 mmol, 1.0 eq.) and triethylamine (0.64 mL, 4.6 mmol, 5.0 eq.) were dissolved in dry dichloromethane (20 mL). Subsequently, tosyl chloride (0.7 g, 3.7 mmol, 4.0 eq.) was added at 0 °C to the reaction mixture. The reaction was stirred at room temperature for 4 hours. After completion of the reaction, a solution of sat. NH_4Cl (10 mL) was added and the mixture was extracted with dichloromethane (3×20 mL). The organic layers were dried over Na_2SO_4, filtered and the solvent was concentrated under reduced pressure. The crude solid was dissolved in CH_2Cl_2, adsorbed onto silica, and purified by column chromatography (SiO_2, hexane/ethyl acetate 95:5) to give pure **TPU-SCOCH3** as a yellow solid in 25 % yield (0.47 g, 0.23 mmol).

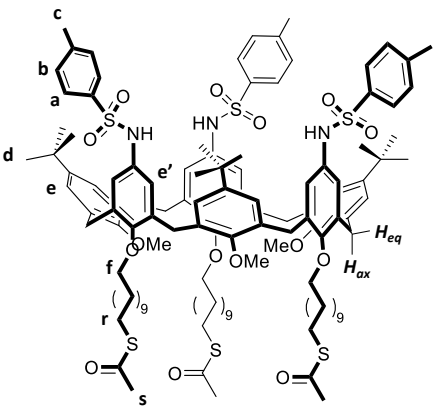

m.p.: 120-122 °C. **^{1}H NMR** ($CDCl_3$, 400 MHz) δ = 7.57 (d, *J* = 7.9 Hz, 6H, H_a), 7.21 (d, *J* = 8.0 Hz, 6H, H_b), 7.14 (s, 6H, H_e), 6.22 (s, 6H, $H_{e'}$), 4.39 (d, *J* = 15.6 Hz, 6H, H_{ax}), 3.87 (t, *J* = 6.5 Hz, 6H, H_f), 3.41 (d, *J* = 15.6 Hz, 6H, H_{eq}), 2.87 (t, *J* = 7.4 Hz, 6H, H_r), 2.52 (br. s, 9H, H_{OMe}), 2.41 (br. s, *J* = 5.4 Hz, 9H, H_c), 2.34 (s, 9H, H_s), 1.9-1.2 (m, 60H, $H_{d,\ g\text{-}q}$) ppm. **^{13}C NMR** ($CDCl_3$, 101 MHz) δ = 196.2, 154.7, 151.9, 146.5, 143.2, 136.7, 135.7, 132.9, 132.0, 129.4, 129.4, 127.9, 127.6, 120.7, 73.0, 60.1, 34.3, 31.6, 30.8, 30.7, 30.6, 29.7, 29.6, 29.6, 29.6, 29.5, 29.3, 29.2, 28.9, 26.4, 21.7 ppm. **HR-MS (ORBITRAP LQ)** calculated for $C_{117}H_{160}N_3O_{15}S_6^+$: m/z (z = 1): 2039.01682; found: 2039.01692. Calculated for $C_{117}H_{163}N_4O_{15}S_6^+$: m/z (z = 1): 2056.04337; found: 2056.04339. Calculated for $C_{117}H_{159}N_3O_{15}Na_1S_6^+$: m/z (z = 1): 2060.99877; found: 2060.99050. Calculated for $C_{117}H_{159}N_3O_{15}KS_6^+$: m/z (z = 1): 2076.97270; found: 2076.97097.

TPU-SH: In a 25 mL two-necked round-bottom flask, under argon atmosphere, calix[6]arene **TPU-SCOCH3** (0.015 g, 0.008 mmol, 1.0 eq.) and dithiothreitol DTT (0.007 g, 0.048 mmol, 6.0 eq.) were dissolved in a 50:50 mixture of THF:EtOH. Subsequently, sodium ethoxide (0.008 g, 0.12 mmol, 15.0 eq.) was added at room temperature to the reaction mixture. The reaction was stirred at room temperature for 15 minutes. After completion, the solvents were removed under reduced pressure, the crude was dissolved in CH_2Cl_2 and washed with water (3 × 5 mL). The organic layer was dried over Na_2SO_4, filtered and the solvent was concentrated under reduced pressure. The pure product **TPU-SH** was obtained as a yellow solid in a quantitative yield without further purification.

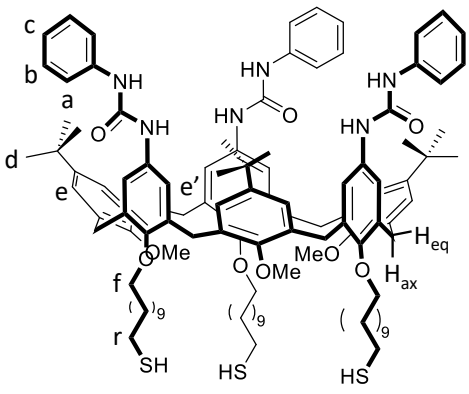

m.p.: 115-117 °C. **^{1}H NMR** (400 MHz, $CDCl_3$) δ = 7.57 (d, *J* = 7.9 Hz, 6H, H_a), 7.21 (d, *J* = 8.0 Hz, 9H, $H_{b,\ c}$), 7.14 (br. s, 6H, H_e), 6.22 (br. s, 6H, $H_{e'}$), 4.39 (d, *J* = 15.6 Hz, 6H, H_{ax}), 3.87 (t, *J* = 6.5 Hz, 6H, H_f), 3.41 (d, *J* = 15.6 Hz, 6H, H_{eq}), 2.87 (t, *J* = 7.4 Hz, 6H, H_r), 1.9-1.2 (m, 60H, $H_{d,\ g\text{-}q}$) ppm. **^{13}C NMR** ($CDCl_3$, 101 MHz) δ = 153.1, 151.8, 146.8, 144.6, 136.0, 133.3, 129.7, 129.5, 128.2, 127.9, 127.7, 127.5, 122.2, 73.4, 60.3, 35.0, 34.8, 33.5, 31.7, 30.9, 30.1, 29.9, 29.5, 28.8, 26.7, 25.1, 14.6 ppm. **ESI-MS (+):** calcd. for $C_{111}H_{150}N_6O_9S_3^+$: m/z (z = 1): 1809.1; found: 1809.3.

TSA-SH: In a 25 mL two-necked round-bottom flask, under argon atmosphere, calix[6]arene **TSA-SCOCH3** (0.009 g, 0.004 mmol, 1.0 eq.) and dithiothreitol DTT (0.004 g, 0.025 mol, 6.0 eq.) were dissolved in a 50:50 mixture of THF:EtOH. Subsequently, sodium ethoxide (0.004 g, 0.063 mmol, 15.0 eq.) was added at room temperature to the reaction mixture. The reaction was stirred at room temperature for 15 minutes. After completion, the solvents were removed under reduced pressure, the crude was dissolved in CH_2Cl_2 and washed with water (3 × 5 mL). The organic layer was dried over Na_2SO_4, filtered and the solvent was concentrated under reduced pressure. The pure product **TSA-SH** was obtained as a yellow solid in a quantitative yield without further purification.

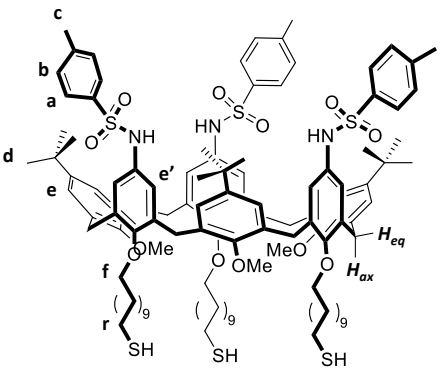

m.p.: 115-117 °C. **^{1}H NMR** (400 MHz, $CDCl_3$) δ = 7.54 (d, *J* = 8.3 Hz, 6H, H_a), 7.15 (d, *J* = 29.7 Hz, 6H, H_b), 7.11 (s, 6H, H_e), 6.18 (s, 6H, $H_{e'}$), 4.36 (d, *J* = 15.6 Hz, 6H, H_{ax}), 3.84 (t, *J* = 6.5 Hz, 6H, H_f), 3.38 (d, *J* = 15.7 Hz, 6H, H_{eq}), 2.6-2.4 (q, s 15H, $H_{r,OMe}$), 2.39 (s, 9H, H_c), 1.9-1.8 (m, 6H, H_g), 1.7-1.1 (m, 54H, $H_{d,\ h\text{-}q}$) ppm. **^{13}C NMR** ($CDCl_3$, 101 MHz) δ = 155.1, 152.2, 146.8, 143.5, 136.0, 133.3, 129.7, 128.2, 127.9, 127.7, 127.6, 121.2, 73.3, 60.5, 34.6, 34.5, 32.0, 31.9, 30.9, 30.0, 29.9, 29.9, 29.5, 28.8, 26.7, 25.1, 22.0, 14.6 ppm. **ESI-MS (+):** calcd. for $C_{111}H_{153}N_3NaO_{12}S_6^+$: m/z (z = 1): 1935.9; found: 1935.9.

3 Bibliography

(1) Guether, R.; Reddington, M. V. Photostable Cyanine Dye β-Cyclodextrin Conjugates. *Tetrahedron Lett.* **1997**, *38* (35), 6167–6170. https://doi.org/10.1016/S0040-4039(97)01426-3.

(2) Shulov, I.; Rodik, R. V.; Arntz, Y.; Reisch, A.; Kalchenko, V. I.; Klymchenko, A. S. Protein-Sized Bright Fluorogenic Nanoparticles Based on Cross-Linked Calixarene Micelles with Cyanine Corona. *Angew. Chem. Int. Ed.* **2016**, *55* (51), 15884–15888. https://doi.org/10.1002/anie.201609138.

(3) Soavi, G.; Pedrini, A.; Devi Das, A.; Terenziani, F.; Pinalli, R.; Hickey, N.; Medagli, B.; Geremia, S.; Dalcanale, E. Encapsulation of Trimethine Cyanine in Cucurbit[8]Uril: Solution versus Solid-State Inclusion Behavior. *Chem. – Eur. J.* **2022**, *28* (23), e202200185. https://doi.org/10.1002/chem.202200185.

(4) Li, D.-H.; Smith, B. D. Supramolecular Mitigation of the Cyanine Limit Problem. *J. Org. Chem.* **2022**, *87* (9), 5893–5903. https://doi.org/10.1021/acs.joc.2c00179.

(5) Banerjee, C.; Kuchlyan, J.; Banik, D.; Kundu, N.; Roy, A.; Ghosh, S.; Sarkar, N. Interaction of Gold Nanoclusters with IR Light Emitting Cyanine Dyes: A Systematic Fluorescence Quenching Study. *Phys. Chem. Chem. Phys.* **2014**, *16* (32), 17272. https://doi.org/10.1039/C4CP02563F.

(6) Li, Y.; Yang, X.; Hou, F.; Chen, D.; Liu, Y.; Yu, D.; Ming, D.; Yang, Y.; Huang, H. Near-Infrared-Fluorescent Probe for Turn-On Lipopolysaccharide Analysis Based on PEG-Modified Gold Nanorods with Plasmon-Enhanced Fluorescence. *ACS Appl. Mater. Interfaces* **2021**, *13* (48), 57058–57066. https://doi.org/10.1021/acsami.1c19746.

(7) Zhu, Z.; Yuan, P.; Li, S.; Garai, M.; Hong, M.; Xu, Q.-H. Plasmon-Enhanced Fluorescence in Coupled Nanostructures and Applications in DNA Detection. *ACS Appl. Bio Mater.* **2018**, *1* (1), 118–124. https://doi.org/10.1021/acsabm.8b00032.

(8) Cui, Y.; Yuan, C.; Tan, H.; Zhang, Z.; Jia, Y.; Na, N.; Ouyang, J. Plasmon-Enhanced Fluorescent Sensor Based on Aggregation-Induced Emission for the Study of Protein Conformational Transformation. *Adv. Funct. Mater.* **2019**, *29* (10), 1807211. https://doi.org/10.1002/adfm.201807211.

(9) Cera, G.; Arduini, A.; Secchi, A.; Credi, A.; Silvi, S. Heteroditopic Calix[6]Arene Based Intervowen and Interlocked Molecular Devices. *Chem. Rec.* **2021**, *21* (5), 1161–1181. https://doi.org/10.1002/tcr.202100012.

(10) Pignot, M.; Pljevaljcic, G.; Weinhold, E. Efficient Synthesis ofS-Adenosyl-L-Homocysteine Natural Product Analogues and Their Use to Elucidate the Structural Determinant for Cofactor Binding of the DNA Methyltransferase M·HhaI. *Eur. J. Org. Chem.* **2000**, *2000* (3), 549–555. https://doi.org/10.1002/(SICI)1099-0690(200002)2000:3<549::AID-EJOC549>3.0.CO;2-7.

(11) Guillerm, G.; Guillerm, D.; Vandenplas-Vitkowski, C.; Glapski, C.; De Clercq, E. Inactivation of S-Adenosyl-l-Homocysteine Hydrolase with Novel 5'-Thioadenosine Derivatives. Antiviral Effects. *Bioorg. Med. Chem. Lett.* **2003**, *13* (10), 1649–1652. https://doi.org/10.1016/S0960-894X(03)00279-8.

(12) Petrelli, R.; Sham, Y. Y.; Chen, L.; Felczak, K.; Bennett, E.; Wilson, D.; Aldrich, C.; Yu, J. S.; Cappellacci, L.; Franchetti, P.; Grifantini, M.; Mazzola, F.; Di Stefano, M.; Magni, G.; Pankiewicz, K. W. Selective Inhibition of Nicotinamide Adenine Dinucleotide Kinases by Dinucleoside Disulfide Mimics of Nicotinamide Adenine Dinucleotide Analogues. *Bioorg. Med. Chem.* **2009**, *17* (15), 5656–5664. https://doi.org/10.1016/j.bmc.2009.06.013.

(13) Zhang, D.; Markoulides, M. S.; Stepanovs, D.; Rydzik, A. M.; El-Hussein, A.; Bon, C.; Kamps, J. J. A. G.; Umland, K.-D.; Collins, P. M.; Cahill, S. T.; Wang, D. Y.; Von Delft, F.; Brem, J.; McDonough, M. A.; Schofield, C. J. Structure Activity Relationship Studies on Rhodanines and Derived Enethiol Inhibitors of Metallo-β-Lactamases. *Bioorg. Med. Chem.* **2018**, *26* (11), 2928–2936. https://doi.org/10.1016/j.bmc.2018.02.043.

(14) Chernykh, A. V.; Kudryk, O. V.; Olifir, O. S.; Dobrydnev, A. V.; Rusanov, E.; Moskvina, V. S.; Volochnyuk, D. M.; Grygorenko, O. O. Expanding the Chemical Space of 1,2-Difunctionalized Cyclobutanes. *J. Org. Chem.* **2023**, *88* (5), 3109–3131. https://doi.org/10.1021/acs.joc.2c02892.

(15) Konigsberg, W. Reduction of Disulfide Bonds in Proteins with Dithiothreitol. In *Methods in Enzymology*; Elsevier, **1972**; Vol. 25, pp 185–188. https://doi.org/10.1016/S0076-6879(72)25015-7.

(16) Lukesh, J. C.; Palte, M. J.; Raines, R. T. A Potent, Versatile Disulfide-Reducing Agent from Aspartic Acid. *J. Am. Chem. Soc.* **2012**, *134* (9), 4057–4059. https://doi.org/10.1021/ja211931f.

(17) Jarboe, S. G.; Terrazas, M. S.; Beak, P. The Endocyclic Restriction Test: The Geometries of Nucleophilic Substitutions at Sulfur(VI) and Sulfur(II). *J. Org. Chem.* **2008**, *73* (24), 9627–9632. https://doi.org/10.1021/jo8016428.

(18) Zanichelli, V.; Bazzoni, M.; Arduini, A.; Franchi, P.; Lucarini, M.; Ragazzon, G.; Secchi, A.; Silvi, S. Redox-Switchable Calix[6]arene-Based Isomeric Rotaxanes. *Chem. – Eur. J.* **2018**, *24* (47), 12370–12382. https://doi.org/10.1002/chem.201800496.

(19) Boccia, A.; Lanzilotto, V.; Di Castro, V.; Zanoni, R.; Pescatori, L.; Arduini, A.; Secchi, A. Preparation, Reactivity and Controlled Release of SAMs of Calix[4,6]Arenes and Calix[6]Arene-Based Rotaxanes and Pseudorotaxanes Formed on Polycrystalline Cu. *Phys. Chem. Chem. Phys.* **2011**, *13* (10), 4452. https://doi.org/10.1039/c0cp01921f.

(20) Teng, L.; Han, X.; Liu, Y.; Lu, C.; Yin, B.; Huan, S.; Yin, X.; Zhang, X.; Song, G. Smart Nanozyme Platform with Activity-Correlated Ratiometric Molecular Imaging for Predicting Therapeutic Effects. *Angew. Chem. Int. Ed.* **2021**, *60* (50), 26142–26150. https://doi.org/10.1002/anie.202110427.

(21) Arduini, A.; Calzavacca, F.; Pochini, A.; Secchi, A. Unidirectional Threading of Triphenylureidocalix[6]arene-Based Wheels: Oriented Pseudorotaxane Synthesis. *Chem. – Eur. J.* **2003**, *9* (3), 793–799. https://doi.org/10.1002/chem.200390089.

(22) Belser, T.; Stöhr, M.; Pfaltz, A. Immobilization of Rhodium Complexes at Thiolate Monolayers on Gold Surfaces: Catalytic and Structural Studies. *J. Am. Chem. Soc.* **2005**, *127* (24), 8720–8731. https://doi.org/10.1021/ja0500714.

Chapter 4. Hybridization of plasmonic gold nanoparticles with cyanine dyes

4 Introduction

Cyanine dyes are a class of organic chromophores widely used thanks to their wide range of applications across various fields. Among the different families of cyanine dyes, this chapter focuses on heptamethine cyanine dyes.[1] These dyes are distinguished by their extensive conjugated system, which results in strong absorption and emission in the near-infrared (NIR) region. Their NIR fluorescence makes them particularly valuable in biomedical imaging, offering deep tissue penetration and minimal background interference (see Introduction).[2–7] Heptamethine cyanine dyes, like other organic fluorophores, are often coupled with noble metal nanostructures to exploit their plasmon resonance properties,[8] which can modify the dye's fluorescence properties.[9–12] Plasmon resonance is a characteristic feature of noble metal nanostructures and vary depending on the type of metal, as well as the shape and size of the nanostructure.[13] In this chapter, gold nanoparticles were used as the source of plasmon resonances.

Gold Nanoparticles (AuNPs):

Gold nanoparticles (AuNPs) have been widely employed in a range of fields, including microelectronics (transistors, sensors, solar cells) and biomedical applications[14] (imaging,[15] drug delivery, photoinduced therapeutics[16]). Their unique electronic properties, such as plasmonic resonances, have made them particularly attractive. Plasmonic resonances are intrinsic properties of noble metal nanostructures arising from the spatial confinement of free electrons. Gold nanoparticles exhibit localized surface plasmon resonances (LSPR) when subjected to an external electric field. To elucidate LSPR, let's consider a small spherical metallic nanoparticle (**Figure 4.1**).

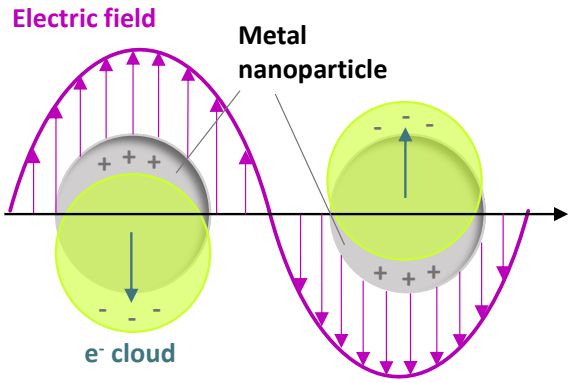

Figure 4.1. Schematic representation of the conduction of electrons within a metal nanoparticle under an external oscillating electric field. In green, the electron cloud, in grey, the metal nanoparticles, while the violet arrows indicate the oscillating electric field.

Upon irradiation by light, the oscillating electric field induces coherent oscillations of the conduction electrons. The displacement of the electron cloud relative to the nuclei generates a restoring force

due to the Coulomb attraction between the electrons and nuclei, resulting in the oscillation of the electron cloud relative to the nuclear framework.

A crucial outcome of plasmon oscillations is the amplification of the electric field at the surfaces of the metal particles. In the presence of a fluorophore near the gold surface, the electric field enhancement resulting from LSPR can influence the fluorophore's fluorescence. This fluorescence modulation, whether enhancement or quenching, strongly depends on two factors: the distance between the fluorophore and the metallic surface and the spectral overlap between the fluorophore's emission and the plasmonic absorbance of the nanostructure. When an enhancement in the fluorescence of the dye due to LSPR is observed, this phenomenon is referred to as plasmon-enhanced fluorescence (PEF). To better understand these phenomena, a simplified Jablonski diagram can be employed (**Figure 4.2**). When a fluorophore is excited by incident photons in the absence of plasmonic resonances, electrons pass from the ground state to an excited state (γ_0, green arrow). The electrons then return to the ground state through either a radiative decay (the fluorescence phenomenon, r_{rad}^0, violet arrow) or a non-radiative one, in which the system relaxation occurs without radiation emission (r_{nrad}^0, light blue arrow).

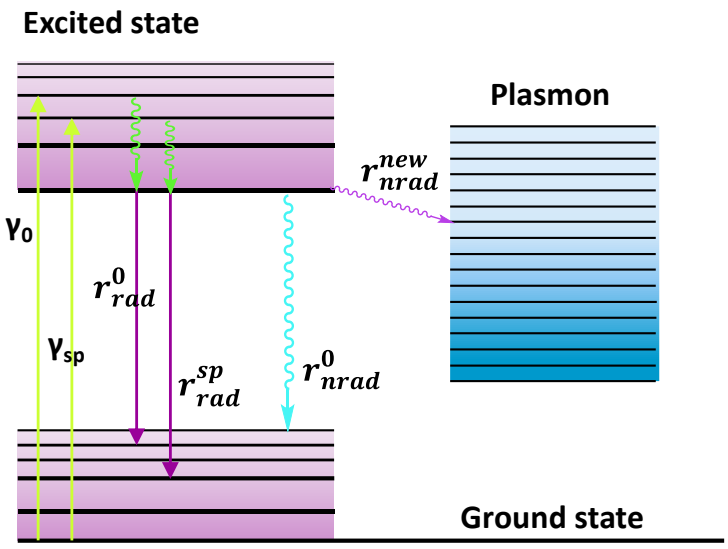

Figure 4.2. Jablonski diagram for fluorescence excitation and decay on a plasmonic system: direct photon excitation without plasmon (γ_0) (green arrow) and enhanced excitation due to plasmon (γ_{sp}) (green arrow), radiative model without plasmon (r_{rad}^0, violet arrow), radiative model with plasmon (r_{rad}^{sp}, violet arrow), non-radiative model without plasmon (r_{nrad}^0 light blue arrow), and new decay non-radiative model due to plasmon (r_{nrad}^{new}, pink arrow).

In the presence of plasmon resonances, the local electromagnetic field is enhanced, leading to an enhanced excitation rate, defined as $\gamma_{exc} = \gamma_0 + \gamma_{sp}$ where γ_{sp} represents the excitation rate contribution from plasmon resonance. Similarly, the radiative decay rate is a sum of contributions from both the intrinsic radiative decay r_{rad}^0 and the plasmon radiative decay r_{rad}^{sp} expressed as $r_{rad} = r_{rad}^o + r_{rad}^{sp}$. On the other hand, the non-radiative decay rate is also modified in the

presence of plasmons. A new non-radiative decay rate (r_{nrad}^{new}) is induced when metallic nanoparticles are proximate to the fluorophore due to Förster energy transfer (FRET) from exciton to lossy plasmon. This results in an accelerated non-radiative decay rate, denoted as $r_{nrad}^{sp} = r_{nrad}^{o} + r_{nrad}^{new}$, where r_{nrad}^{0} is the non-radiative decay rate without plasmon influence. This accelerated non-radiative decay transfers more energy to the plasmon, reducing the quantum yield of the fluorophore.

The excitation rate of the fluorophore is strongly influenced by its distance from the metallic surface. When the fluorophore is close to the metallic surface (≲10 nm), fluorescence quenching occurs *via* a FRET mechanism.[17] The non-radiative decay of the excited fluorophore is promoted by the metallic surface, facilitating energy transfer from the fluorophore's excited state to surface electrons. Contrarily, at long distances, the excitation rate surpasses the non-radiative decay rate, resulting in a strong enhancement of the fluorophore's fluorescence. In conclusion, the modulation of the distance between the chromophore and the metallic surface can result in either quenching or enhancement of the dye's fluorescence. Moreover, the spectral overlap between the plasmonic absorbance of metal nanostructure and the dye's emission can be exploited to amplify the effect of plasmon resonances.

In this chapter, novel heptamethine cyanine dyes were synthesized for their covalent attachment to the surface of gold nanoparticles. Fluorescence studies of the system were conducted to examine the effect of plasmon resonances on the cyanine dyes. Furthermore, the nature of the interactions between these dyes and the gold surface was investigated.

4 Result and discussion

Synthesis of organic dyes

To investigate the effect of hybridization of gold nanoparticles with cyanine dyes, we designed two different families of cyanine-based chromophores. The well-known chloro heptamethine cyanine dye (**Cy7-Cl**, **Figure 4.3**, left), obtained *via* a condensation reaction between a quaternary ammonium salt 4-methylbenzenesulfonate and a bisaldehyde reagent 2-chloro-3-(hydroxymethylene)-1-cyclohexene-1-carboxaldehyde, was selected as the initial compound for subsequent post-functionalization. The central cyclohexenyl ring in the dye enhances its photostability,[18] while the chlorine facilitates the *meso*-position functionalization. One family of cyanine dyes was specifically designed for covalent attachment to gold surfaces *via* a terminal disulfide group (**Figure 4.3**, middle). The second family, featuring a terminal methyl group, was intended for adsorption onto metal nanoparticle surface (**Figure 4.3**, right).

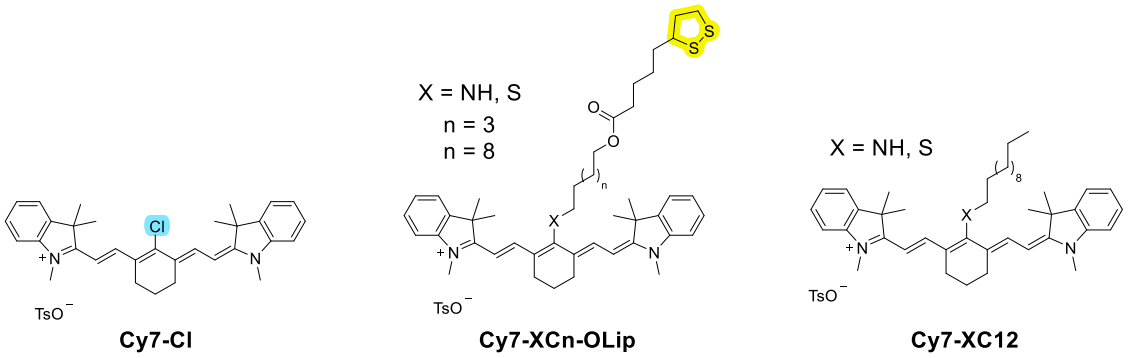

Figure 4.3. Structure of **Cy7-Cl** and the two families of cyanine-based dyes.

The synthetic route for novel cyanine dyes is depicted in **Scheme 4.1**. Starting with **Cy7-Cl** as the precursor, an initial nucleophilic substitution was conducted to *meso*-functionalize the chlorine atom with amine or thiol nucleophilic reagents through an $S_{RN}1$ mechanism. The $S_{NR}1$ mechanism is considered the most likely pathway, involving electron transfer from the nucleophilic to the cationic cyanine. The reaction was carried out in an aprotic polar solvent, DMF, to maintain constant the concentration of radical anions formed during the reaction.[2] In this case, either nitrogen or thiol alkyl chains terminated with a hydroxyl group were used, leading to cyanine dye intermediates **Cy7-XCn-OH**. Nitrogen and sulfur were selected as substituents to modulate the optical properties concerning absorbance and emission of the dyes. Additionally, to probe the impact of the fluorophore-metal distance, variations in the central chain length were introduced (C6 and C11). Through a coupling reaction with lipoic acid, using EDC·HCl as the coupling reagent, the hydroxyl group of **Cy7-XCn-OH** was converted to an ester, incorporating a terminal S-S functionality, giving rise to the desired heptamethine cyanine dyes (**Cy7-NHC6-OLip** obtained with 82% yield, **Cy7-NHC11-OLip** obtained with 86% yield, and **Cy7-SC11-OLip** obtained with 54% yield). The non-anchoring cyanine dyes **Cy7-NHC12** and **Cy7-SC12** were synthesized *via* nucleophilic substitution of the chloride atom employing commercially available chains: 1-dodecylamine for **Cy7-NHC12** and 1-dodecylthiol for **Cy7-SC12** (**Scheme 4.1**). The pure products **Cy7-NHC12** and **Cy7-SC12** were obtained after purification *via* column chromatography in 58% and 41% yield, respectively.

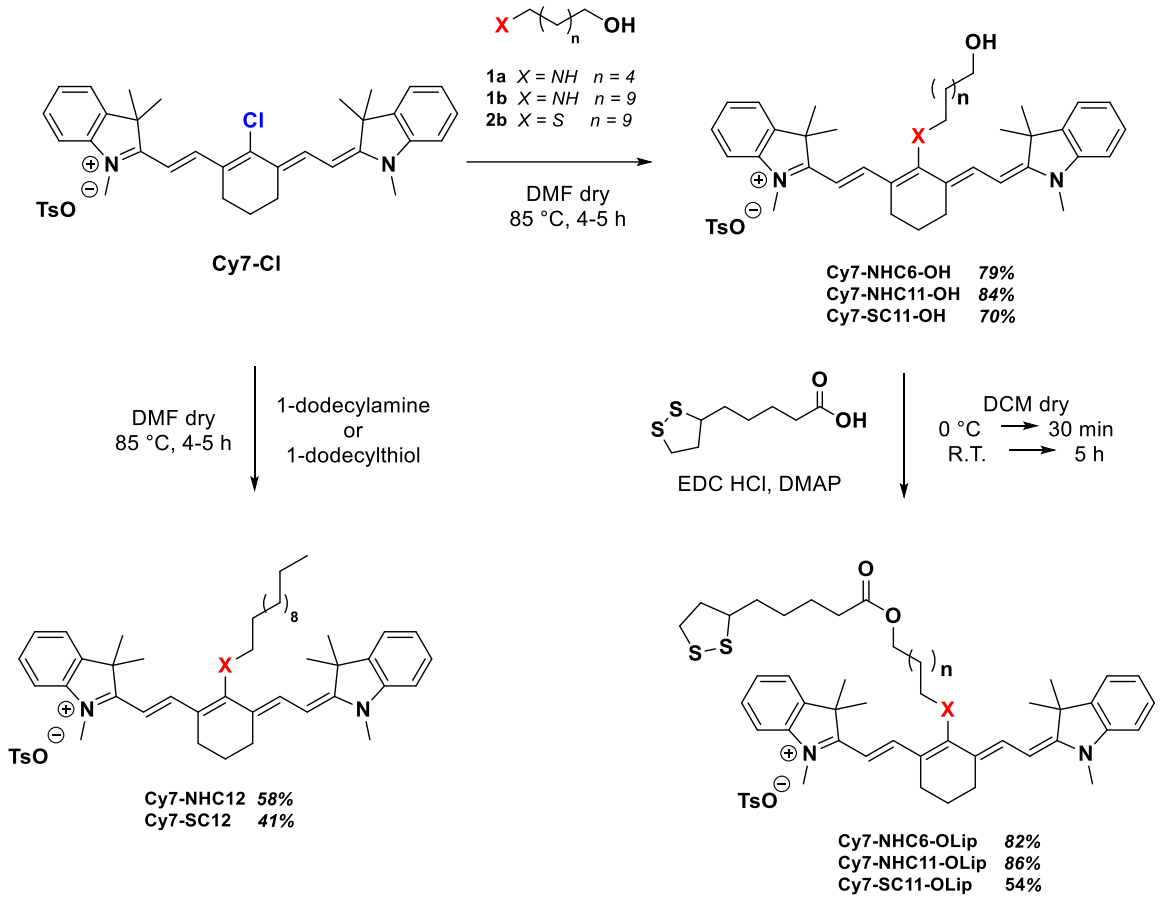

Scheme 4.1. Synthetic scheme of the synthesis of novel heptamethine cyanine-based dyes.

NMR characterization of cyanine-based dyes

The synthesized dyes were comprehensively characterized by NMR spectroscopy and ESI-MS measurements. ^{1}H NMR spectra of **Cy7-XCn-OLip** dyes (**Figure 4.4**) reveal the molecular symmetry of the dyes, showing characteristic signals for the alkene protons labeled as *4* and *3*, which appear at 7.79 and 5.80 ppm for **Cy7-NH** derivatives, and at 8.94 and 6.29 ppm for **Cy7-S** derivative. The aromatic proton signals of the cyanine and tosylate anions are observed in the 7.7-7.0 ppm region. Specifically, the aromatic protons of tosylate anions are at 7.73 and 7.24 ppm for **Cy7-NH** derivatives and 7.73 and 7.53 ppm for the **Cy7-S** derivative. The remaining signals correspond to the aromatic protons of the indolium terminal groups. In the high-field region, the spectra of **Cy7-NHC6-OLip** and **Cy7-NHC11-OLip** are identical, differing only for the integrals reflecting the different lengths of the carbon chains. The triplet at 4.10 ppm is attributed to the methylene group adjacent to the -NH- group in the *meso* position (labeled as *7*), while the triplet at 3.80 ppm is associated with the methylene group near to the oxygen of the ester group (proton labeled as *12* for **Cy7-NHC6-OLip** and as *17* for **Cy7-NHC11-OLip**). In the spectrum of **Cy7-SC11-OLip,** the triplet at 4.05 ppm is assigned to the methylene group adjacent to the oxygen atom (labeled as *17*), while the more shielded triplet at 2.86 ppm corresponds to the methylene group near the sulfur atom

(labeled as *7*). All three cyanine dyes display identical chemical shifts for the protons of the lipoic residue, where protons labeled as *β* and *γ* each generate two distinct signals due to their diasterotopic nature: multiplets between 3.2-3.0 ppm correspond to *γ* and *γ'*, while multiplets centered at 2.4 ppm and 1.9 ppm correspond to *β* and *β'* protons. The multiplet at 3.5 ppm corresponds to the *α* proton. The methyl protons of the tosylate anion resonate as a singlet at 2.38 ppm, while the methyl protons linked to the positively charged nitrogen atom are downfield shifted to 3.46 ppm for **Cy7-NH** derivatives and 3.67 ppm for the **Cy7-S** derivative. A triplet at 2.57 ppm for **Cy7-NH** derivatives and at 2.71 ppm for **Cy7-S** derivatives corresponds to protons of the cyclohexyl ring labeled as *2*. Finally, protons relative to the alkyl chain are detectable in the high-field region.

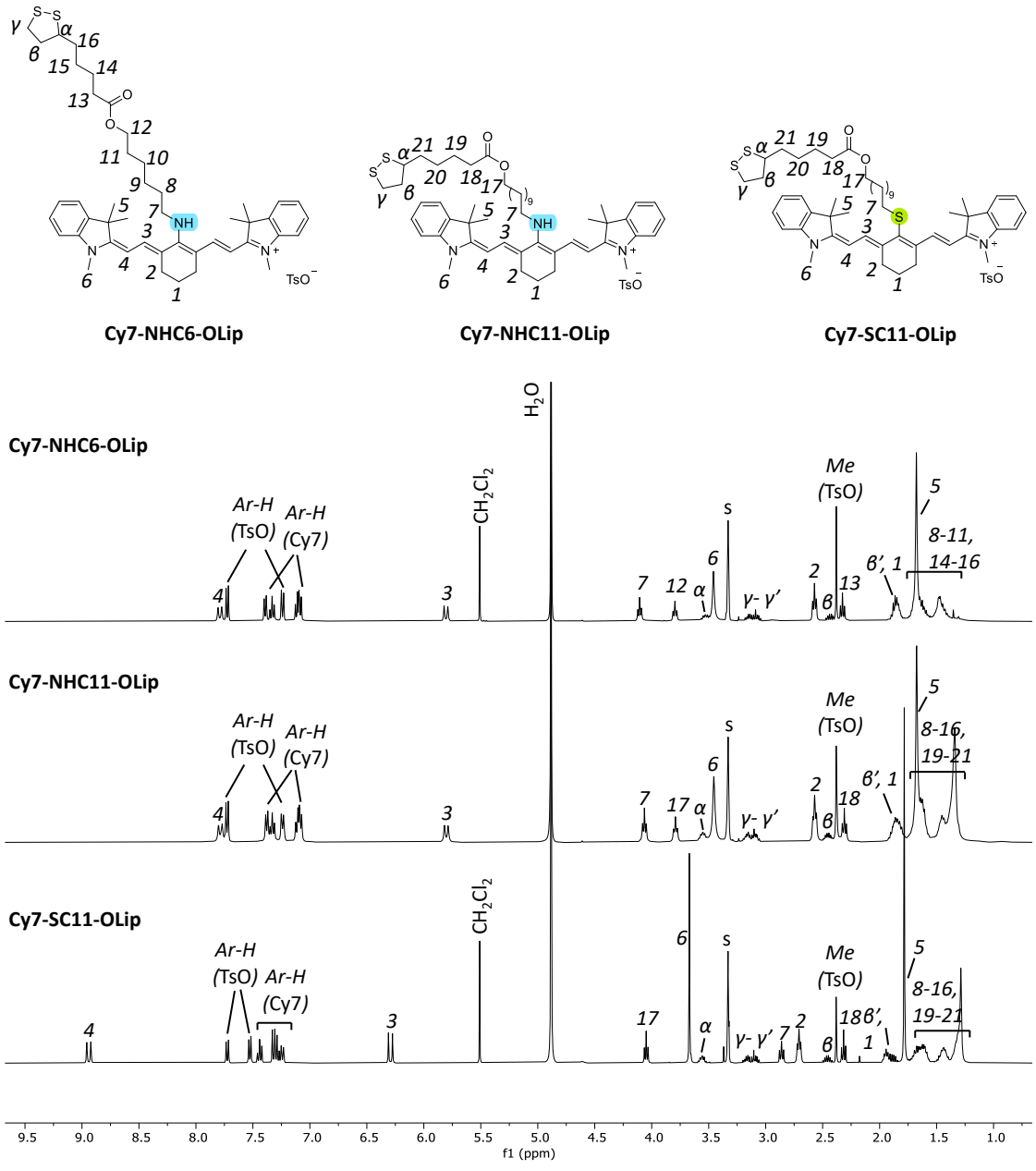

Figure 4.4. ^{1}H NMR spectra (CD_3OD, 400 MHz, 298 K) of **Cy7-NHC6-OLip** (top), **Cy7-NHC11-OLip** (middle) and **Cy7-SC11-OLip** (bottom).

The complete assignment of all peaks of the synthesized dyes was accomplished through a series of 2D NMR measurements, in particular thanks to 2D COSY, TOCSY, and edited HSQC experiments. **Figure 4.5** presents, for example, the edited HSQC spectrum of **Cy7-SC11-OLip**, in which all peaks have been assigned to the corresponding protons.

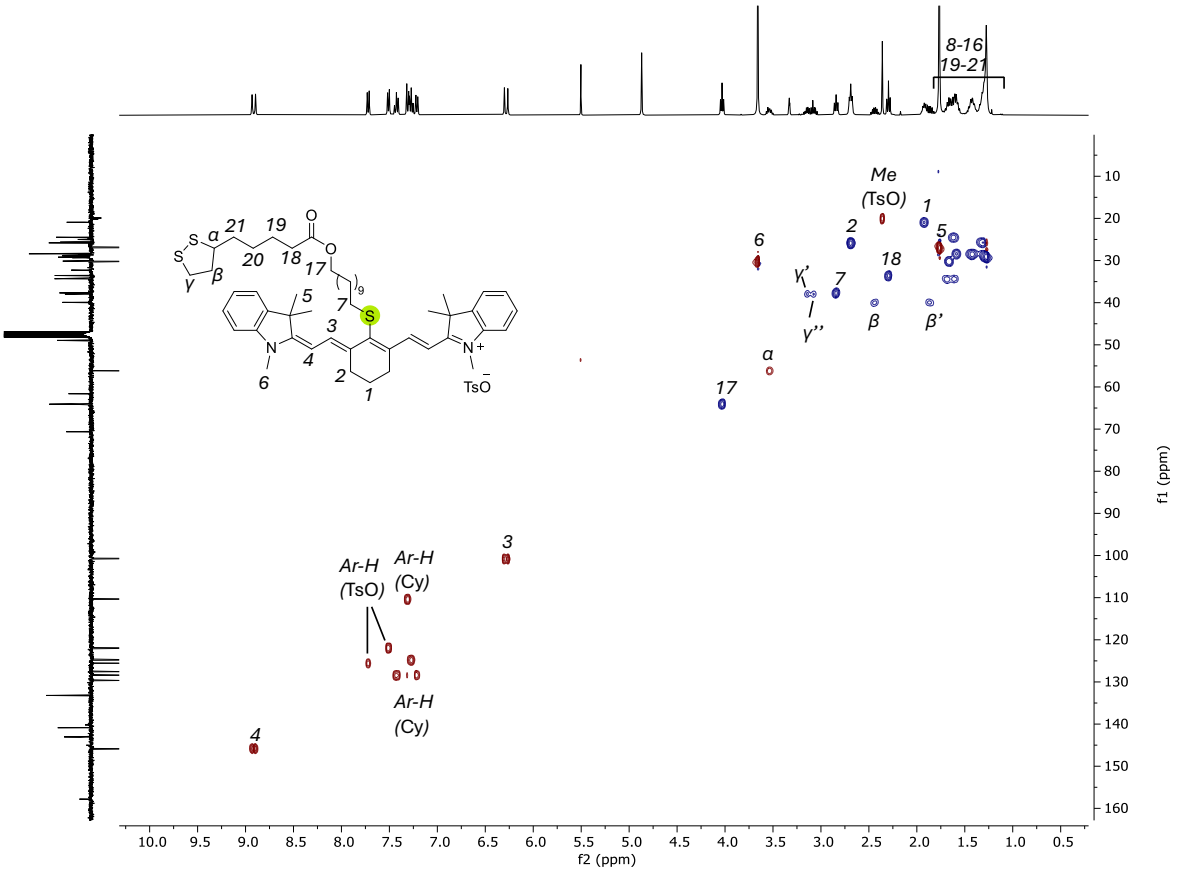

Figure 4.5. Edited HSQC NMR spectrum (400 MHz, CD_3OD, 298 K) of **Cy7-SC11-OLip**. Positive peaks (CH_3 and CH) are shown in red, while negative ones (CH_2) are in blue.

^{1}H NMR spectra of non-anchoring cyanine dyes are similar to those previously described but less complex due to the absence of the lipoic residue (**Figure 4.6**). The downfield region exhibits the same peaks as observed earlier. In the high-field region, the triplet at 0.89 ppm corresponds to the terminal protons of the methyl group labeled as *18*. As noted before for **Cy7-NHC12**, the triplet adjacent to the nitrogen atom is at 3.79 ppm (proton labeled as *7*), while for **Cy7-SC12** is shifted to a higher field at 2.86 ppm. The previously made considerations regarding the other signals also apply here (the full assignment is found in **Figure 4.6**).

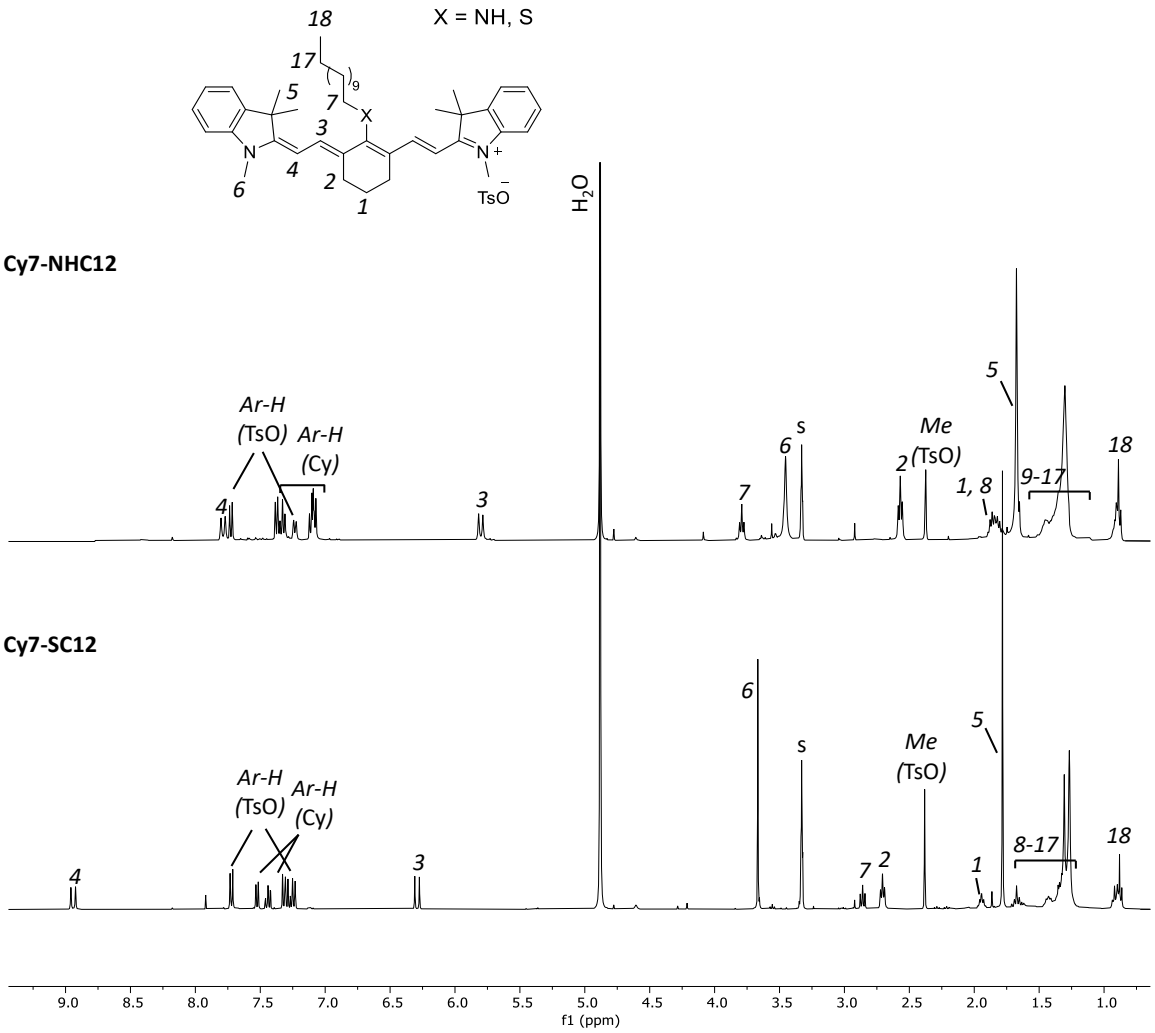

Figure 4.6. ^{1}H NMR spectra (CD_3OD, 400 MHz, 298 K) of **Cy7-NHC12** (top) and **Cy7-SC12** (bottom).

Optical characterization of cyanine-based dyes

The optical properties of cyanine dyes vary depending on the hetero-atom located at the *meso*-position of the cyanine structure. In general, cyanine dyes with an amino group in the central position exhibit a shortened absorption wavelength and a significant Stokes shift.[1] In contrast, thiol-substituted derivatives retain the absorption properties characteristic of the cyanine dye precursor (**Cy7-Cl**). Specifically, for our **Cy7-NH** derivatives, the maximum absorbance was observed at around 656 nm in CH_2Cl_2 (**Figure 4.7**), which falls in the red-visible region of the spectrum. In contrast, the **Cy7-S** derivatives exhibit a red-shifted maximum absorbance at 786 nm, positioned in the near-infrared (NIR) region of the spectrum. Despite these differences in absorbance, all cyanine dyes show maximum emission in the NIR region (as indicated by the dashed lines in **Figure 4.7** (**a**)).

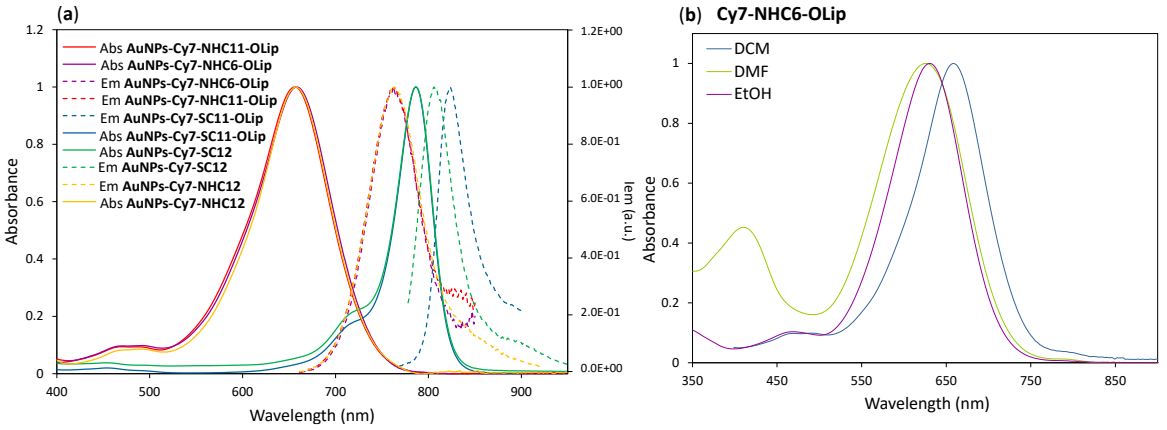

Figure 4.7. (**a**) Collection of absorbance and emission spectra of **Cy7-NH** and **Cy7-S** derivatives in CH_2Cl_2 at 298 K. Excitation wavelength for **Cy7-NHC6-OLip** is 658 nm, for **Cy7-NHC11-OLip** is 656 nm, for **Cy7-SC11-OLip** is 764 nm, for **Cy7-NHC12** is 622 nm and for **Cy7-SC12** is 792 nm; (**b**) collection of absorbance spectra of **Cy7-NHC6-OLip** collected in three different solvents DCM (blue line), DMF (green line), and EtOH (violet line).

As reported before, the literature indicates that thiol substituents typically induce a minor bathochromic shift relative to the parent dye (**Cy7-Cl**), whereas amino-cyanine derivatives often exhibit a pronounced blue shift.[1] In our study, the initial absorption of **Cy7-Cl** at 785 nm was blue-shifted to 656-658 nm in the presence of an amino substituent (**Table 4.1**, entries 1,2 and 4), representing a difference exceeding 100 nm. Moreover, for amino substituents, a substantial Stokes shift of approximately 2,000 cm^{-1} was observed, while for thiol derivatives a less significant Stokes shift was found (347 cm^{-1} for **Cy7-SC12** and 408 cm^{-1} for **Cy7-SC11-OLip**). In general, the changes observed for amino substituents can be understood as a perturbation of the conjugated system due to the interaction of the lone pair of nitrogen with the conjugated polymethine system. This seems related to a drastic change in the overall electronic structure, which resembles an imine-type bonding in the ground and shifts towards an amine bond in the photoexcited state.[19] Additionally, it has been recently proposed that symmetry breaking during photoexcitation contributes to the broad absorption bands and significant Stokes shifts observed.[20] Large Stokes shifts are usually desired as they minimize fluorescence self-quenching caused by molecular self-absorption.

Table 4.1. Experimental spectroscopic properties in CH_2Cl_2 at 298 K of **Cy7-NHC6-OLip**, **Cy7-NHC11-OLip**, **Cy7-SC11-OLip**, **Cy7-NHC12** and **Cy7-SC12**.

Entry	Compound (TsO)	λ_{max}^{abs}[nm]	λ_{max}^{em} [nm]	Stokes Shift [nm, cm^{-1}]	ε [mol^{-1} L cm^{-1}]	Φ
1	**Cy7-NH-C6-OLip**	658	763	105, 2091	$8.0 \cdot 10^3$	0.33
2	**Cy7-NH-C11-OLip**	656	764	108, 2155	$5.9 \cdot 10^4$	0.31
3	**Cy7-S-C11-OLip**	786	812	26, 408	$2.5 \cdot 10^4$	0.02
4	**Cy7-NH-C12**	657	764	107, 2132	$4.5 \cdot 10^4$	0.30
5	**Cy7-S-C12**	785	807	22, 347	$4.4 \cdot 10^4$	0.10

The quantum yields were determined using as a reference the cyanine known as HITC (1,1',3,3,3',3'-hexamethylindotricarbocyanine iodide), whose quantum yield (Φ) is 0.28. The quantum yield values for the **Cy7-S** derivatives (**Table 4.1**, entries 3 and 5) were lower than those observed for the **Cy7-NH** derivatives (**Table 4.1**, entries 1,2 and 4). This phenomenon can be attributed to the different properties conferred by different atoms in *meso*-position. Specifically, as we just observed, for **Cy7-S** derivatives, the Stokes shift is negligible (**Table 4.1**), leading to significant self-absorption and consequently to a low quantum yield. In contrast, the large Stokes shift exhibited by the **Cy7-NH** derivatives reduces the self-absorption and thus results in higher quantum yields.

The solvatochromic effect on dyes **Cy7-NHC6-OLip**, **Cy7-NHC11-OLip**, and **Cy7-SC11-OLip** was investigated using dichloromethane (CH_2Cl_2), dimethylformamide (DMF), and absolute ethanol (EtOH) as solvents. Due to solubility constraints, other solvents were not utilized. Despite the limited number of solvents evaluated, our study showed that the energy associated with the electronic transition of the dyes increases as the solvent polarity increases, leading to a decrease in the absorption maximum wavelength (see **Table 4.2** and **Figure 4.7** right).

Table 4.2. Experimental spectroscopic data for the study of solvatochromic effect and optical band gap of cyanine dyes **Cy7-NHC6-OLip**, **Cy7-NHC11-OLip** and **Cy7-SC11-OLip**. Analyses were also conducted in toluene and tetrahydrofuran (THF), but aggregation was observed due to the poor solubility of the dyes in these solvents.

Compound	Solvent	ε [mol^{-1} L cm^{-1}]	λ_{onset} [nm]	Optical band gap [eV]
Cy7-NH-C6-OLip	DCM	$8.0 \cdot 10^3$	738	1.680
	DMF	$1.4 \cdot 10^3$	720	1.723
	EtOH	$7.2 \cdot 10^3$	712	1.743
Cy7-NH-C11-OLip	DCM	$5.9 \cdot 10^4$	734	1.689
	DMF	$5.9 \cdot 10^2$	724	1.714
	EtOH	$7.2 \cdot 10^3$	710	1.747
Cy7-SC11-O-Lip	DCM	$2.5 \cdot 10^4$	820	1.512
	DMF	$1.4 \cdot 10^4$	835	1.486
	EtOH	$5.0 \cdot 10^3$	821	1.511

In other words, a higher stabilization of the dyes' ground state than the excited state is observed when the solvent's polarity increases. This phenomenon is also indicated as an *inverse* solvatochromic effect. The energy band gap between the excited and ground states of the different dyes was determined using the Planck's equation, $\mathrm{E} = {}^{h \cdot c}/_{\lambda_{onset}}$, where *h* is the Planck's constant, *c* is the speed of light in vacuum, and λ_{onset} can be extrapolated from the absorption spectrum as the x-intercept of a tangent line on the inflection point for the lowest energy absorption transition of the dye. The calculated energy band gap values are reported in **Table 4.2**,

corroborating an increase in the energy band gap as solvent polarity shifts from less polar to more polar, confirming the *inverse* solvatochromic effect.

Hybridization of AuNPs-TOABr with Cy7-XCn-OLip dyes

For the hybridization of the previously synthesized cyanine dyes with plasmonic nanomaterials, we chose to employ tetraoctylammonium bromide-stabilized gold nanoparticles (**AuNPs-TOABr**), which are soluble in toluene, and that can be easily prepared through the protocol developed by Schiffrin.[21] Specifically, the $AuCl_4^-$ ion, which is the gold nanoparticles source, undergoes a transfer from the aqueous phase to the organic phase (toluene) facilitated by tetraoctylammonium bromide (TOABr), which acts as a phase transfer catalyst. The reduction of Au (III) to Au (0) is achieved by the addition of sodium borohydride ($NaBH_4$), resulting in the formation of metal nanoparticles stabilized by electrostatic interactions with TOABr and having a mean diameter of the metallic core of ca. 4 nm.[21] The hydrodynamic radius of the obtained gold nanoparticles **AuNPs-TOABr**, determined *via* dynamic light scattering (DLS) measurements, was ca. 10 nm. The attractive characteristic of these AuNPs is that their organic monolayer of TOABr can be easily replaced by a thiolated ligand through an exchange reaction.[22,23] This process exploits the higher affinity of sulfur for gold compared to the electrostatic interaction mediated by TOABr.[24] Thus, the functionalization of these nanoparticles was accomplished through an exchange mechanism, exploiting the increased stability of covalent sulfur-gold bonds (S-Au) over the electrostatic interactions ($AuNPs^+Br^-TOABr^+$). To achieve this, 3 mL of a solution of the appropriate cyanine dye: **Cy7-NHC6-OLip** (c = 9.85×10^{-4} M), **Cy7-NHC11-OLip OLip** (c = 2.62×10^{-4} M), and **Cy7-SC11-OLip OLip** (c = 5.74×10^{-4} M) in CH_2Cl_2 were stirred in the dark with 4 mL of a freshly prepared solution of **AuNPs-TOABr** (c = 4.5×10^{-3} M) in toluene for 17 hours (**Scheme 4.2**). Subsequent purification *via* centrifugation removed all unattached dye molecules and yielded pure **AuNPs-Cy7-XCn-OLip** that were soluble in CH_2Cl_2.

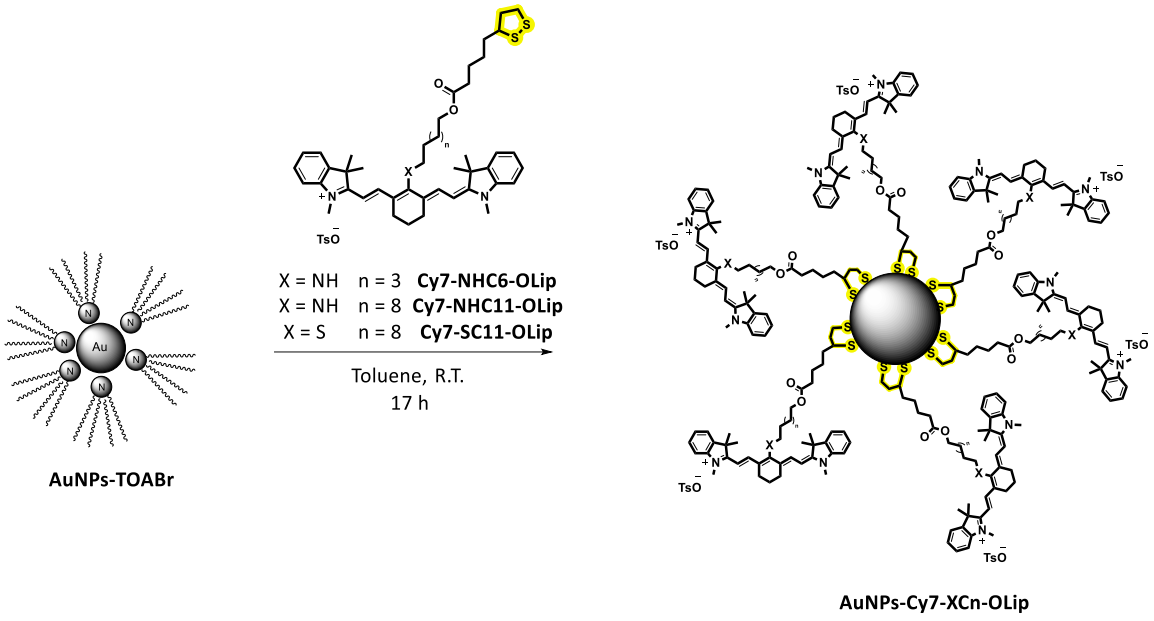

Scheme 4.2. Schematic representation of the synthesis of **AuNPs-Cy7-XCn-OLip**. The number of ligands on the surface of the nanoparticles does not represent their actual loading.

UV-Visible spectroscopy, transmission electron microscopy (TEM) and X-ray Photoelectron Spectroscopy (XPS) characterization

The batches of synthesized nanoparticles loaded with the different cyanine dyes were characterized by UV-Visible spectroscopy, transmission electron microscopy (TEM), and X-ray photoelectron spectroscopy (XPS). UV-Vis analyses of the novel functionalized gold nanoparticles were taken in CH_2Cl_2 and gathered in **Figure 4.8** (right). **AuNPs-Cy7-NHC6-OLip** exhibited a broad and flat absorption ranging from 560 to 650 nm (**Figure 4.8,** right (**a**), black line), likely due to the merging of the nanoparticles' plasmonic absorbance at 525 nm ((**a**), red line) with that of the cyanine dye at 658 nm ((**a**), dashed light blue line). The red-shift of the maximum of the plasmon resonance from 525 nm in **AuNPs-TOABr** to ca. 562 nm in **AuNPs-Cy7-NHC6-OLip** is consistent with a change of polarity near the nanoparticles' surface upon the replacement of TOABr with the fatty alkyl chain of **Cy7-NH6-OLip**. In contrast, the absorption spectrum of the **AuNPs-Cy7-NHC11-OLip** sample (**Figure 4.8**, right (**b**)) showed a less broad absorption with a maximum at 562 nm ((**b**), black line), positioned between the plasmonic absorption of **AuNPs-TOABr** at 525 nm ((**b**), red line) and the cyanine dye absorption at 656 nm ((**b**), dashed light blue line). The effect of **Cy7-NHC11-OLip** dye on the overall nanoparticles' absorption seems less pronounced than in the previous case. The **AuNPs-Cy7-SC11-OLip** sample (**Figure 4.8**, right (**c**)) gives rise to two distinct absorption peaks: one at 542 nm, attributed to the red-shifted plasmonic resonance (525 nm in **AuNPs-TOABr**, red line) that is less red-shifted and more damped with respect to the other two samples, and another, more sharp band due to the cyanine dye coating at 790 nm ((**c**), black line).

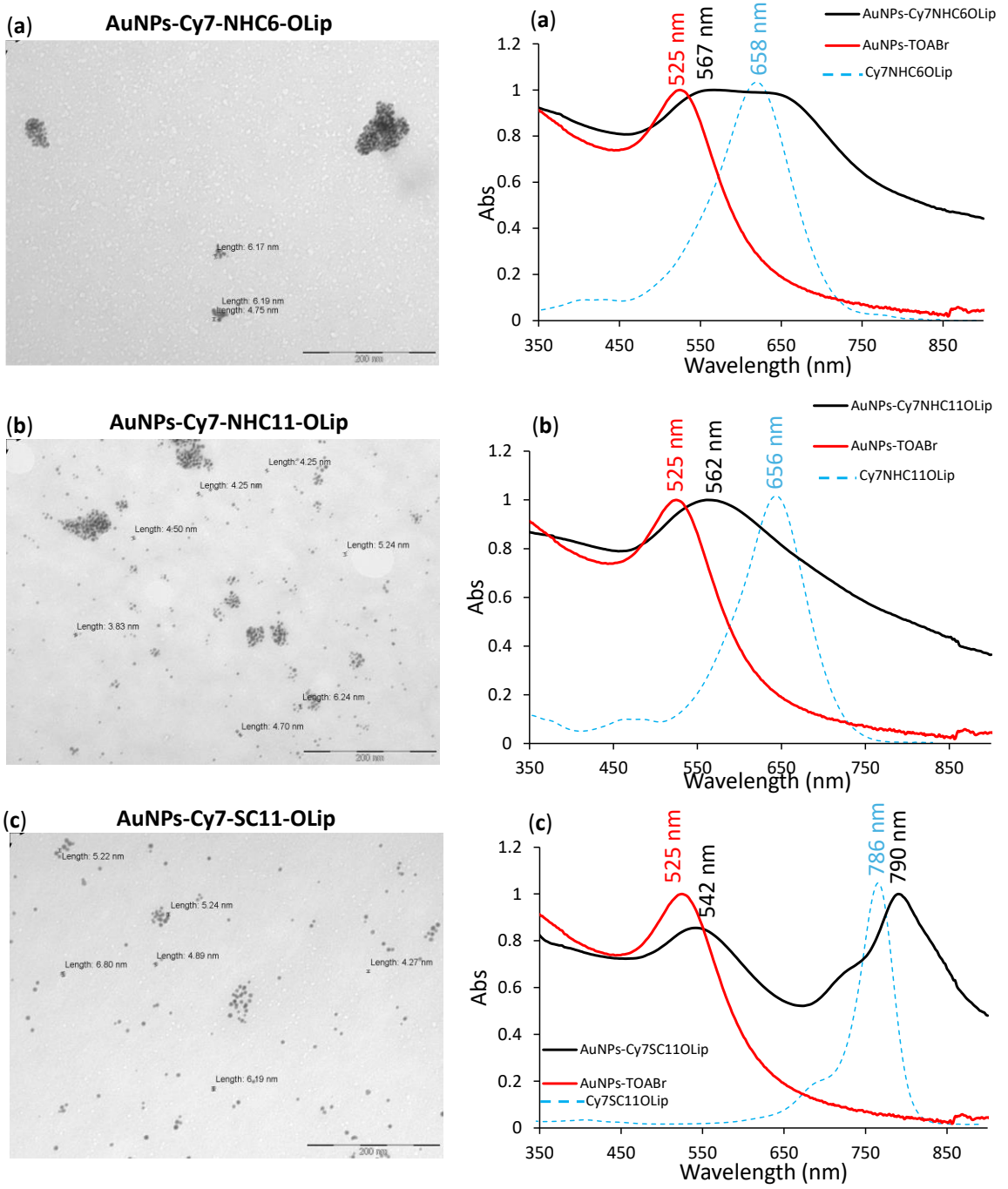

Figure 4.8. Left: TEM images (scale bar 200 nm) of **AuNPs-Cy7-NHC6-OLip** (**a**), **AuNPs-Cy7-NHC11-OLip** (**b**), and **AuNPs-Cy7-SC11-OLip** (**c**); right: normalized absorption spectra of (**a**) **AuNPs-Cy7-NHC6-OLip** (continuous black line), **AuNPs-TOABr** (continuous red line), and **Cy7-NHC6-OLip** (dashed light blue line), (**b**) **AuNPs-Cy7-NHC11-OLip** (continuous black line), **AuNPs-TOABr** (consinuous red line), and **Cy7-NHC11-OLip** (dashed light blue line), and (**c**) **AuNPs-Cy7-SC11-OLip** (continuous black line), **AuNPs-TOABr** (consinuous red line), and **Cy7-SC11-OLip** (dashed light blue line), in CH_2Cl_2 at 298 K.

TEM measurements were also carried out on the three samples of coated AuNPs. The snapshots gathered in **Figure 4.8** (left) show that in all three cases, the slow evaporation of the dichloromethane solvent on the TEM grid produces aggregates of nanoparticles, which were particularly extensive in the case of **AuNPs-Cy7-NHC6-OLip**. Nevertheless, size analysis on the portions of the images in which isolated nanoparticles were present, evidenced that the

introduction of the thiolated cyanine ligands on the gold surface did not change the mean diameter of the nanoparticles' metallic core appreciably (medium value of ca. 5.7 nm for **AuNPs-Cy7-NHC6-OLip**, 4.7 nm for **AuNPs-Cy7-NHC11-OLip**, and 5.4 nm for **AuNPs-Cy7-SC11-OLip**).

XPS analyses were performed. The relevant XPS regions for the investigated systems were those of Au 4f, S 2p, and N 1s, which were analyzed *via* curve-fitting procedures, and the relative quantitative ratios are presented in **Figure 4.9**.

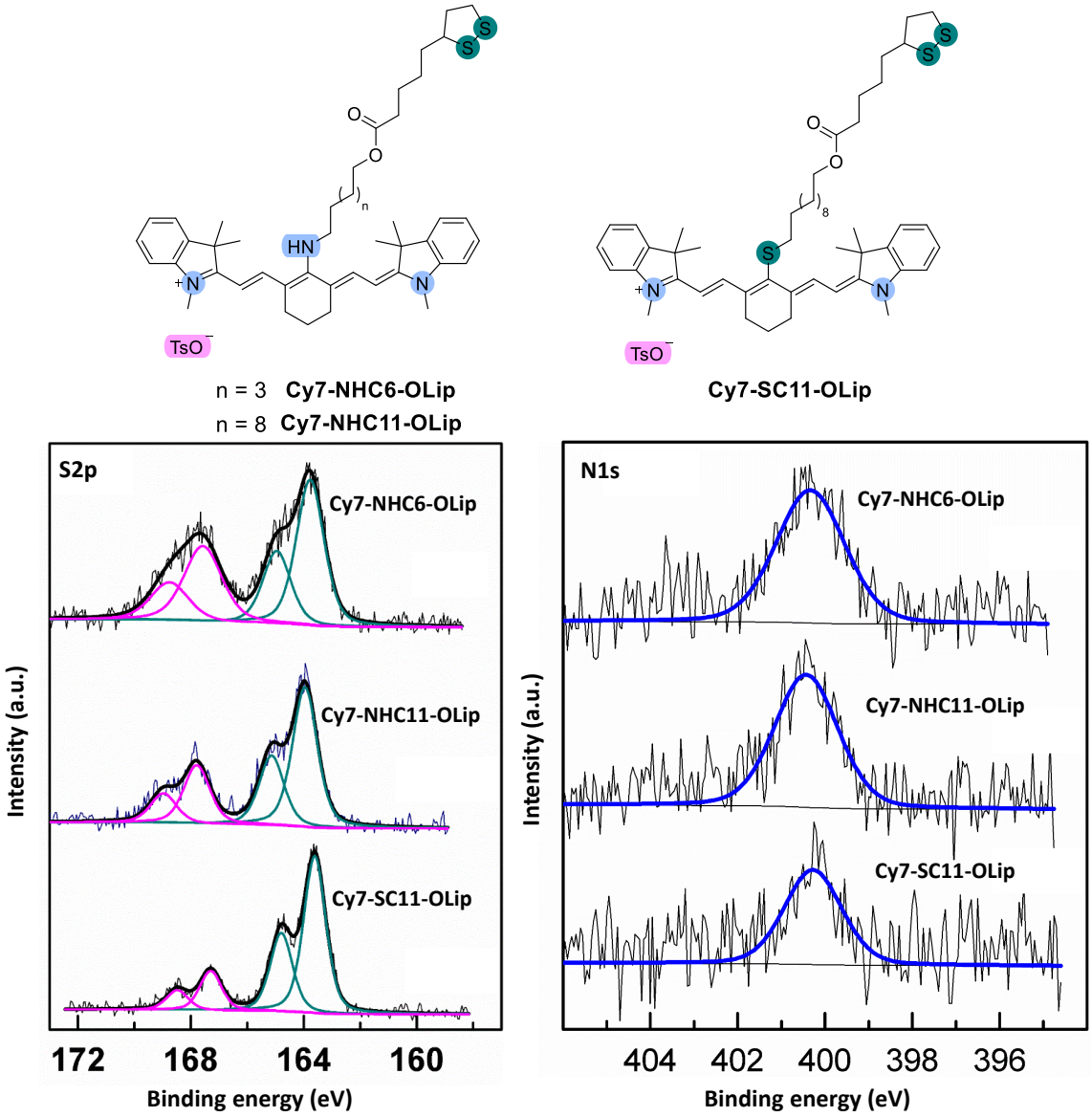

	N/S_{TOT} (theo.)	S_{low}/S_{ox} (theo.)
Cy7-NH-C6-OLip	1.1 (1)	1.4 (2)
Cy7-NH-C11-Olip	1.1 (1)	1.9 (2)
Cy7-S-C11-Olip	0.49 (0.5)	3.4 (3)

Figure 4.9. XPS relative quantitative atomic ratios for **Cy7-NHC6-OLip**, **Cy7-NHC11-OLip,** and **Cy7-SC11-OLip** with theoretical values in parentheses.

Initially, pure cyanine dyes **Cy7-NHC6-OLip**, **Cy7-NHC11-OLip,** and **Cy7-SC11-OLip** were investigated (**Figure 4.9**). The S 2p signal (constituted by spin-orbit (SO) split doublets with *j* = 3/2 and 1/2, separated by a ΔE_{SO} = 1.17 eV) was distinctly observed in all three samples, with contributions from the lipoic residue (**Figure 4.9**, dark green lines, $2p_{3/2}$ BE = 163.8 eV) and the tosylate anion (**Figure 4.9**, pink lines, $2p_{3/2}$ BE = 167.6). An additional contribution from the thiol ether group in the cyanine meso position was detected for **Cy7-SC11-Olip**, falling at the same BE of the lipoic residue. The N 1s signal was also clearly visible. Its BE is compatible with an amine-derived nitrogen with partial iminic character resulting from the high π-bond conjugation and positive charge delocalization (**Figure 4.9**, blue line, BE = 400.2 eV), as that typical of oxidized polyaniline derived materials. The N/S_{TOT} and S_{low}/S_{OX} ratios (S_{TOT} being the total S, S_{OX} that related to tosylate anion and S_{low} that related to lipoic and thiol ether groups) reported in the table in **Figure 4.9** perfectly agree with the theoretical values in all cases (reported in parentheses).

For the cyanine-coated AuNPs samples, the XPS analyses revealed slight differences with respect to the pure cyanines (see **Table 4.3** and **Figure 4.10**). The Au 4f signal is composed by convoluted spin-orbit split doublets (with *j* = 7/2 and 5/2, separated by a ΔE_{SO} = 3.68 eV), with a minor component associated to the Au(I) contribution ($4f_{7/2}$ BE = 84.65 eV) resulting from the bonding with the cyanine lipoic unit, detected in all samples (**Figure 4.10**, pink line). As expected for all the samples, this component is weak compared to the Au(0) component, which is associated with the bulk gold (**Figure 4.10**, blue line, $4f_{7/2}$ BE = 83.75 eV). This result is consistent with the mean diameter of approximately 5 nm for the exchanged AuNPs (*vide supra*). At this size, only about 30% of the gold atoms are on the surface[25] and available for linkage with the lipoic units. According to the photon energy of the X-ray source used (Al Kα, hν = 1486.6 eV), the XPS sampling depth in the Au 4f region is ~ 5.2 nm, which points at a full sampling of the bulk Au atoms in the AuNPs. A negligible trace of Au(III) (**Figure 4.10**, green line, $4f_{7/2}$ BE = 86.10 eV), likely residual from the nanoparticles' preparation, was also detected. Due to the overall lower concentration of the cyanines in AuNP samples compared to the pure substances, the S 2p and N 1s signals were weaker in this case. In the S 2p spectra, peak deconvolution revealed the contribution from the lipoic sulfur atoms bound to the gold surface as Au-S (**Figure 4.10**, green line) in the BE range 162.0 – 162.4 eV ($2p_{3/2}$) and from the oxidized sulfur (sulfate) of the tosylate group (**Figure 4.10**, pink line, $2p_{3/2}$ BE = 168.5 eV). Due to the low signal-to-noise ratio, in the **AuNPs-Cy7-SC11-OLip** sample the contribution from ethereal sulfur (-S-) was included within the predominant Au-S contribution, since the two features are very close in energy. Notably, the signals associated with the Au-S bond (S $2p_{3/2}$ BE in the range 162.0 – 162.4 eV) appear at lower BE than those of the S-S bond in the free cyanine dyes (S $2p_{3/2}$ BE = 163.8 eV),[26] strongly supporting the formation of a covalent bonding of the cyanine ligands to the gold surface of the AuNPs, and confirming the successful outcome of the exchange reaction. Finally,

as in the free cyanines, a single weak N 1s signal was observed across all three samples at BE of approximately 400 eV, consistent with amine/imine nitrogen.

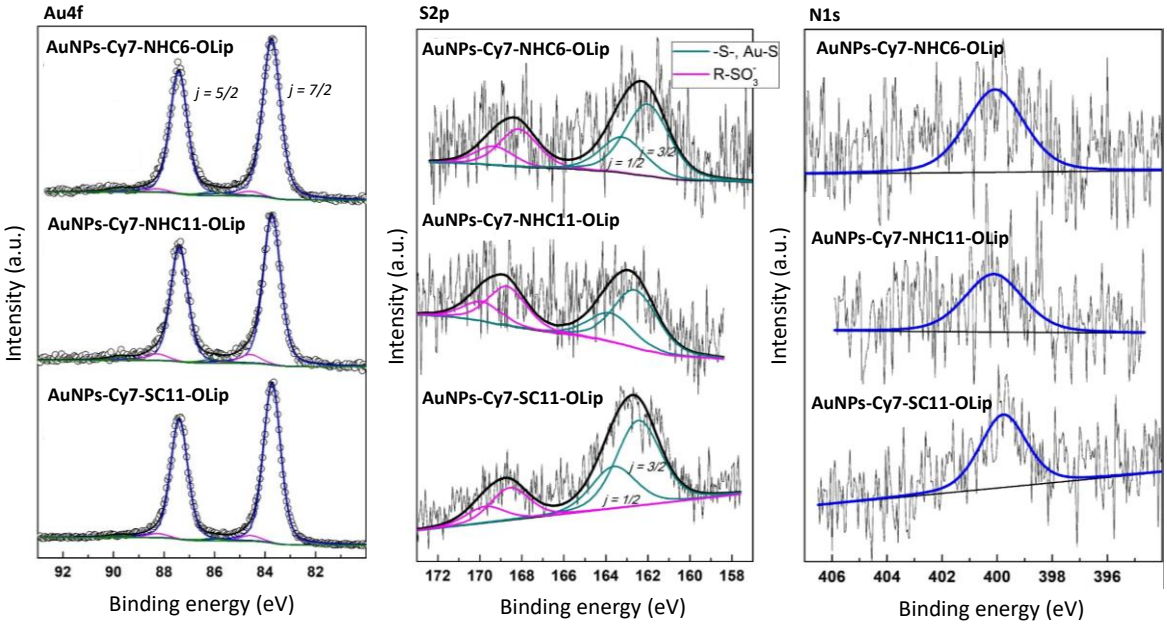

Figure 4.10. XPS analysis of **AuNPs-Cy7-NHC6-OLip**, **AuNPs-Cy7-NHC11-OLip** and **AuNPs-Cy7-SC11-OLip**. Left: narrow scan spectrum of Au 4f: Au(I) associated with S bonding in pink, Au(0) in blue and Au(III) in green; middle: narrow scan spectrum of S 2p, S signal due to the mixed contributions of the Au bonding of lipoic residue and S ethereal group (dark green lines) and the tosylate (pink lines); right: narrow scan spectrum of N 1s (blue line).

Quantitative XPS data for the **AuNPs-Cy7-XCn-OLip** nanoparticles are presented in **Table 4.3**. Since the spectra are rather noisy, the N/S_{TOT} ratios might inherently be hampered by a significant error. However, the substantial deviation from the expected theoretical value may also stem from the strong attenuation of the sulfur signal from Au-bound atoms, caused by the overlaying molecular structure, a common characteristic of XPS spectra of ordered surface bound molecular systems, such as self-assembled monolayers (SAM). As to the S 2p region, the ratio between the sulfur signal from the dye (S_{low}) and that from the tosylate counteranion (S_{ox}) was in excellent agreement with theoretical predictions.

For the **AuNPs-Cy7-NH-C11-OLip** nanoparticles, the Au 4f spectral intensity was particularly low (44.7%) resulting in a correspondingly high S/Au ratio (0.39 vs. 0.21 and 0.25 of the other two samples, see **Table 4.3**). This result might tentatively be ascribed to the lower dimensions of the **AuNPs-Cy7-NH-C11-OLip** nanoparticles compared to the others (4.7 nm vs. 5.7 and 5.4 nm, see TEM.), which points at a smaller portion of gold sampled by XPS. However, these results warrant further investigation to fully understand the underlying mechanisms of the nanoparticles' coating.

Table 4.3. XPS relative quantitative ratios for **Cy7-NHC6-OLip**, **Cy7-NHC11-OLip** and **Cy7-SC11-OLip**, theoretical value in parenthesis.

	Au (%)	S (%)	N (%)	S/Au	N/S_{TOT} (theo.)	S_{low}/S_{ox} (theo.)
Cy7-NH-C6-OLip	61.2	13.0	25.8	0.21	1.98 (1)	2.17 (2)
Cy7-NH-C11-Olip	44.7	17.4	37.9	0.39	2.17 (1)	1.67 (2)
Cy7-S-C11-Olip	68.3	17.2	14.5	0.25	0.84 (0.5)	2.96 (3)

XPS measurements of the valence band (VB) spectra of **AuNPs-Cy7-XCn-OLip** were conducted to gain deeper insights into the system's structural characteristics, with a particular focus on assessing the potential energy alignment between the VB of the underlying gold structure and highest molecular orbitals of the dye. **Figure 4.11** compares the VB spectra of **AuNPs-Cy7-XCn-OLip** (black) with those of free cyanine dye (blue), while the contribution from the graphite support (red) is also shown to account for its influence on the overall spectra. Close to the Fermi energy (0 eV), distinct contributions from gold (Au 5d and Au 6s bands) are clearly observable. A comparative analysis of the spectra of free cyanine dye (**Cy7-XCn-OLip**) and **AuNPs-Cy7-XCn-OLip** reveals that the molecular orbitals (MOs) of the free cyanine dyes contribute to the signals of **AuNPs-Cy7-XCn-OLip**, as highlighted by the green arrows in **Figure 4.11**. Although the intensity of the lower-energy signals in the 4-8 eV region from the cyanine dyes is very low due to the low photoionization cross-section of carbon-based MOs with X-ray photons instead of UV radiation, these signals perfectly overlap with the Au 5d bands observed in the **AuNPs-Cy7-XCn-OLip** samples. This observation confirms the successful functionalization of AuNPs with cyanine ligands and further suggests a partial electronic overlap between the Au nanoparticle bands and the MOs of the cyanine ligands.

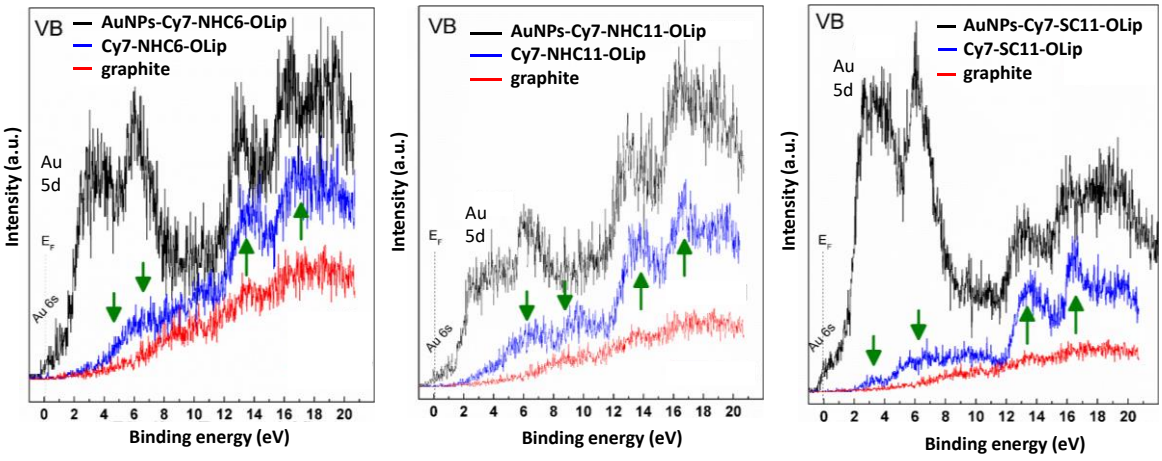

Figure 4.11. Spectra of the valence/MO region: (left) **AuNPs-Cy7-NHC6-OLip** (black line), **Cy7-NHC6-OLip** (blue line), graphite (red line); (middle) **AuNPs-Cy7-NHC11-OLip** (black line), **Cy7-NHC11-OLip** (blue line),

graphite (red line); (right) **AuNPs-Cy7-SC11-OLip** (black line), **Cy7-SC11-OLip** (blue line), graphite (red line). The green arrows indicate the signals of the cyanine dye.

Fluorescence study with gold nanoparticles

To investigate the fluorescence emission trends of dye-nanoparticle hybrid systems, we employed a titration method based on fluorescence detection. This approach involved monitoring the emission changes of a cyanine dye solution upon incremental additions of an **AuNPs-TOABr** solution (as depicted in **Scheme 4.3**). A cyanine dye solution in CH_2Cl_2 was prepared with an absorbance below 0.1 to avoid potential self-absorption effects. The experiment began by introducing a predetermined volume (2.2 mL) of the fluorophore solution in CH_2Cl_2 into a cuvette. The fluorescence emission spectrum was then recorded using the excitation wavelength corresponding to the dye's maximum absorption (λ_{max}). Sequential successive additions of the **AuNPs-TOABr** solution in toluene were made: eight aliquots of 50 µL each followed by two aliquots of 100 µL, totalling 600 µL. After each addition, the fluorescence emission spectrum was recorded under identical conditions. To account for dilution effects resulting from the nanoparticle additions, control experiments were conducted in parallel, where only toluene was added in the same aliquots employed in the titration. This allowed for the correction of fluorescence emission changes due to dye dilution. This procedure was carried out for the cyanine dyes **Cy7-NHC6-OLip**, **Cy7-NHC11-OLip**, and **Cy7-SC11-OLip**.

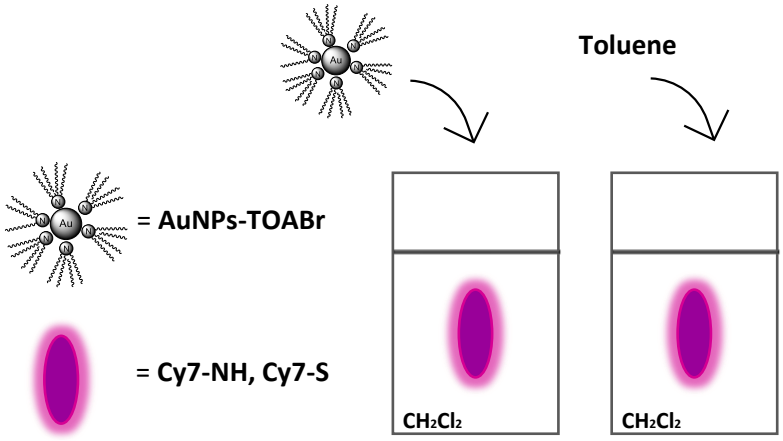

Scheme 4.3. Scheme of the fluorescence titrations: solution in CH_2Cl_2 of **Cy7-NH-C6-OLip** (c = 3×10^{-6} M, λ_{max}^{ex} = 658 nm, λ_{max}^{em} = 763 nm), **Cy7-NH-C11-OLip** (c = 9.6×10^{-6} M, λ_{max}^{ex} = 656 nm, λ_{max}^{em} = 764 nm), **Cy7-SC11-OLip** (c =2.9×10^{-6} M, λ_{max}^{ex} = 764 nm, λ_{max}^{em} = 812 nm), **Cy7-NHC12** (c = 3.7×10^{-5} M, λ_{max}^{ex} = 622 nm, λ_{max}^{em} = 764 nm) and **Cy7-SC12** (c = 2.5×10^{-7} M, λ_{max}^{ex} = 792 nm, λ_{max}^{em} = 807 nm).

A pronounced fluorescence quenching was observed in all three experiments following the addition of the **AuNPs-TOABr** solution (**Figure 4.12**). To assess the impact of the fluorophore-to-nanoparticle surface distance on fluorescence quenching, a comparative analysis was conducted between the cyanine dyes **Cy7-NHC6-OLip** and **Cy7-NHC11-OLip**, which differ only in spacer length. However, no significant difference in quenching trends was observed (cf. **Figure 4.12**, top-left and bottom-left).

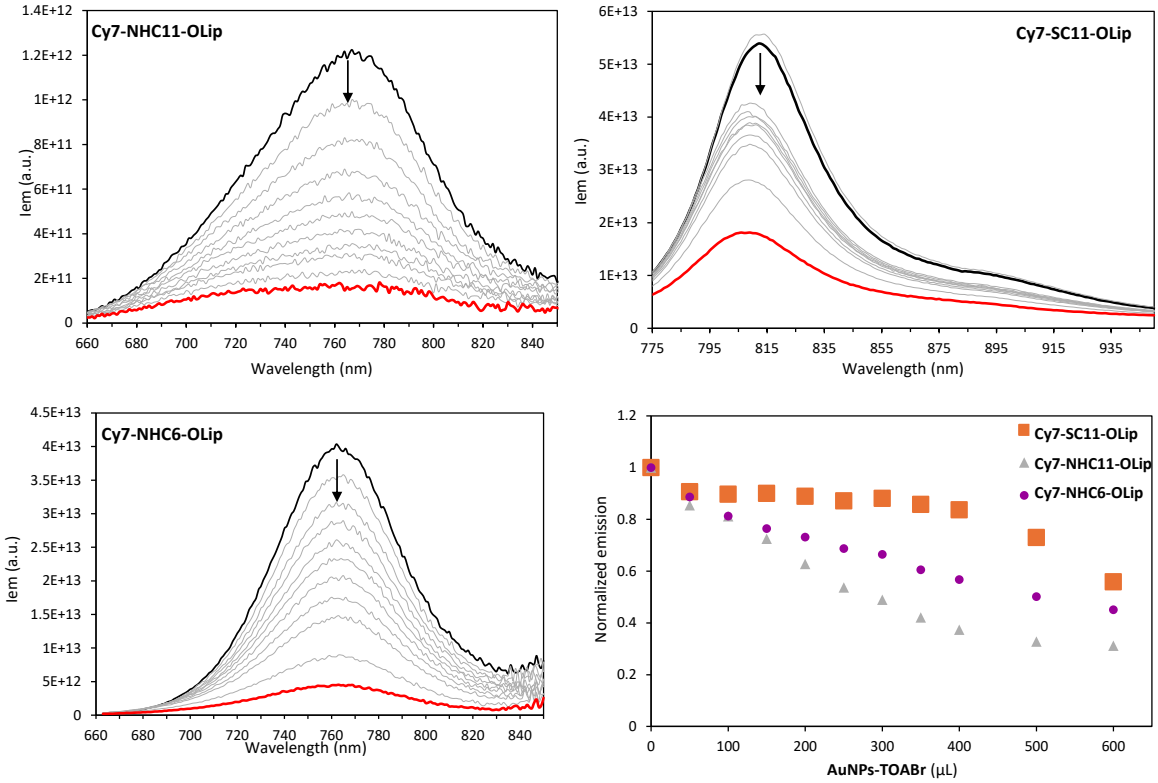

Figure 4.12. Collection of emission spectra taken during the titration of CH_2Cl_2 solutions of **Cy7-NHC11-OLip** (c = 9.6×10^{-6} M, λ_{max}^{ex} = 656 nm, top-left), **Cy7-SC11-OLip** (c = 2.9×10^{-6} M, λ_{max}^{ex} = 764 nm, top-right), and **Cy7-NHC6-OLip** (c = 3×10^{-6} M, λ_{max}^{ex} = 658 nm, bottom-left) with a solution of **AuNPs-TOABr** in toluene at 298 K; the normalized maximum emission intensity variations, corrected for the dilution effects, taken during the above titrations are gathered in the bottom-right graph: **Cy7-NHC6-OLip** (violet circles, λ_{em} = 761 nm), **Cy7-NHC11-OLip** (grey triangles, , λ_{em} = 761 nm) and **Cy7-SC11-OLip** (orange squares, , λ_{em} = 810 nm).

The most accurate interpretation of the quenching results emerged when dilution effects were considered as shown in the plot of **Figure 4.12**, bottom-right. After correcting the titration curves for dilution, insights into the interactions between nanoparticles and dyes in solution were revealed. Notably, the "longer" **Cy7-NHC11-OLip** (grey triangles) exhibited more efficient quenching than the "shorter" **Cy7-NHC6-OLip** (violet circles).

Unlike the other two cyanine dyes, **Cy7-SC11-OLip** is characterized by absorption and emission in the NIR region of the spectrum (see **Figure 4.7**), resulting in reduced spectral overlap with the plasmonic absorption band of **AuNPs-TOABr** (see **Figure 4.8**). This reduced overlap is expected to lower the fluorescence quenching efficiency of **Cy7-SC11-OLip**.[27] Experimental results revealed a decrease in fluorescence for **Cy7-SC11-OLip** (**Figure 4.12**, top-right), though with a different trend compared to **Cy7-NHC6-OLip** and **Cy7-NHC11-OLip**. Initially, a modest decrease in fluorescence intensity was observed, which became more pronounced with increasing the concentration of **AuNPs-TOABr**. Following the addition of the final aliquot of the **AuNPs-TOABr** solution, the fluorescence intensity remains higher than that of the **Cy7-NH** derivatives (see **Figure 4.12**, bottom-right, for the plot corrected for the dilution effects). Given the structural similarity between the **Cy7-NH** derivatives and **Cy7-SC11-OLip**, differences in dyes-to-nanoparticles anchoring kinetics can

be ruled out. This suggests that the greater spectral overlap between the **Cy7-NH** derivatives' emission and the **AuNPs-TOABr**' surface-plasmon band (SPB) facilitates more efficient energy transfer, resulting in pronounced fluorescence quenching. Conversely, for **Cy7-SC11-OLip**, whose emission spectrum does not overlap with the nanoparticles' SPB, the quenching effect is less pronounced, as illustrated in **Figure 4.12**. Therefore, fluorescence quenching in these dye-AuNP systems appears to be primarily driven by the degree of spectral overlap between cyanine dyes' emission and the gold nanoparticles' plasmonic absorption rather than by the distance between the fluorophore and nanoparticle surface.

Metal-dye interaction study

XPS analysis confirmed, as previously observed, the formation of covalent S-Au bonds between cyanine dyes and gold nanoparticles. However, additional interactions between the cyanine dye and the gold surface are also plausible (**Figure 4.13**). For example, electrostatic interactions between the ion-paired cyanine tosylates and the gold surface may promote layer-by-layer stabilization of the positively charged nanoparticle surface ($Au^{+}//TsO^{-}//Cy7^{+}$). Furthermore, dispersive interactions could drive interdigitation between the dyes and the alkyl chains of an organic monolayer present on the nanoparticles, i.e. tetraoctylammonium bromide (TOABr). To further investigate these interactions, a fluorescence study utilizing cyanine dyes both with and without the lipoic linker was conducted, aiming to explore the intrinsic interactions between the organic and inorganic components.

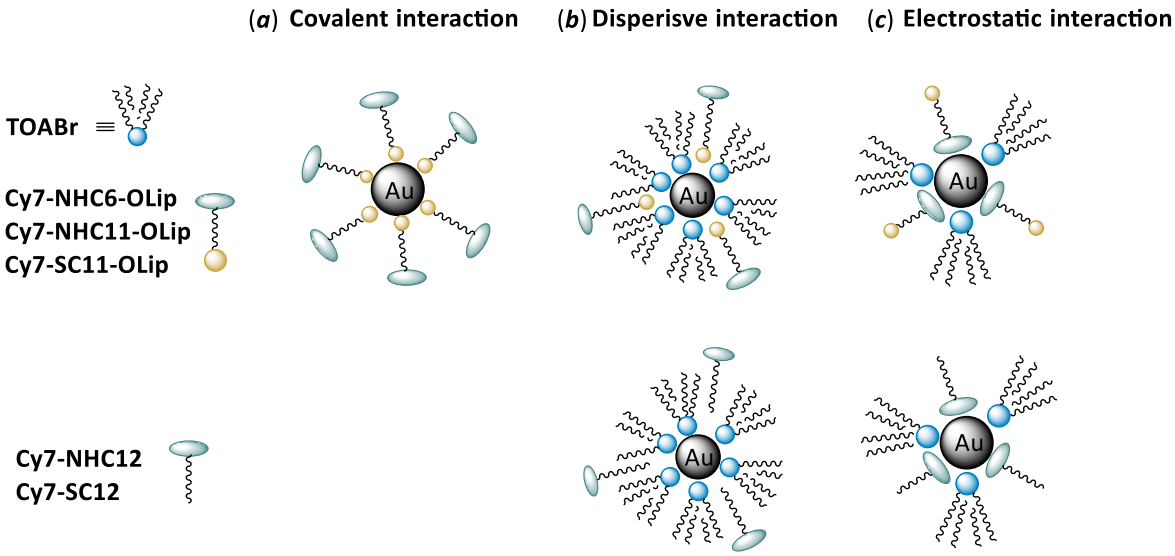

Figure 4.13. Scheme of the possible interactions of **Cy7-NH** and **Cy7-S** derivative dyes and gold surface nanoparticles.

For this purpose, two novel dyes, **Cy7-NHC12** and **Cy7-SC12**, featuring a dodecyl alkyl chain on the cyanine scaffold in place of the lipoic unit, were synthesized (see **Scheme 4.1**) and employed. These

dyes allow for the assessment of the influence of the other interactions, namely interdigitation and electrostatic interactions, on the modulation of the dye's initial fluorescence intensity. Fluorescence experiments were carried out following the previously described methodology (**Scheme 4.3**). Unexpectedly, even without gold-anchoring functionalities, interactions between **Cy7-NHC12** and **Cy7-SC12** and the metal nanoparticle surface were evident, as shown in **Figure 4.14**. Indeed, compared to solvent-only controls, fluorescence analyses conducted upon nanoparticles' addition revealed a fluorescence quenching for both **Cy7-NHC12** and **Cy7-SC12** (**Figure 4.14**), indicative of interactions between the organic and inorganic constituents. However, the fluorescence quenching was more pronounced for **Cy7-NHC12**, likely due to the better spectral overlap of its emission spectrum (maximum of emission at λ = 657 nm) with the plasmon absorption of **AuNPs-TOABr** (maximum of absorption at λ = 525 nm), compared to that of **Cy7-SC12** (maximum of emission at λ = 785 nm). The fluorescence behavior of **Cy7-NHC12** closely resembles that of **Cy7-NHC6-OLip** and **Cy7-NHC11-OLip**, whereas **Cy7-SC12** exhibits fluorescence characteristics similar to **Cy7-SC11-OLip** (see **Figure 4.12**). In summary, the outcomes of these experiments suggest that both **Cy7-NHC12** and **Cy7-SC12** interact with the metallic surface of **AuNPs-TOABr**. Thus, even non-covalent interactions can lead to fluorescence quenching when the dye comes into contact with the nanoparticle.

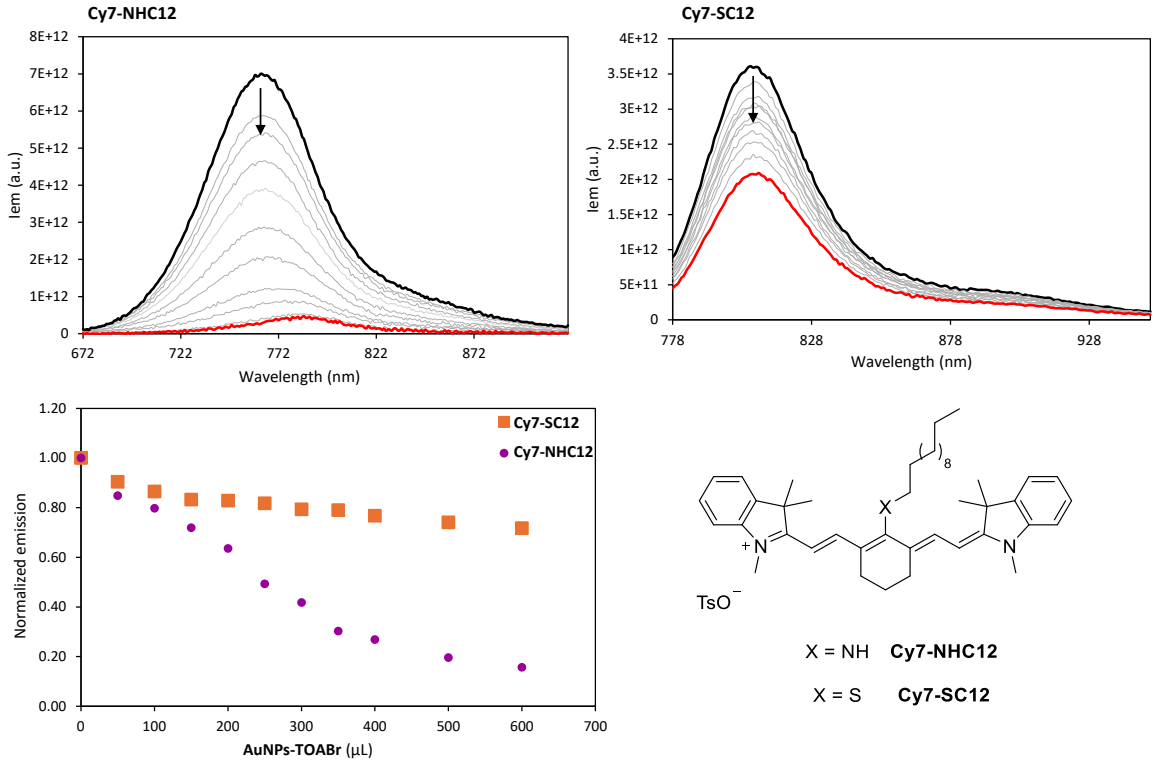

Figure 4.14. Collection of emission spectra taken during the titration of dichloromethane solutions of **Cy7-NHC12** (c = 3.7×10^{-5} M, λ_{max}^{ex} = 622 nm, top-left), **Cy7-SC12** (c = 2.5×10^{-7} M, λ_{max}^{ex} = 792 nm, top-right) with a solution of **AuNPs-TOABr** in toluene at 298 K; the normalized maximum emission intensity variations, corrected for the dilution effects, taken during the above titrations are gathered in the bottom-left plot: **Cy7-**

NH12 (violet circles, λ_{em} = 770 nm), **Cy7-SC12** (orange squares, , λ_{em} = 810 nm); bottom-right: structure of **Cy7-NHC12** and **Cy7-SC12**.

Kinetic study

To gain deeper insights into the mechanism of organic-inorganic hybridization of our thiolated cyanine dyes, ~4 nm octanethiol-stabilized gold nanoparticles, soluble in organic solvent and stabilized by covalent Au-S interactions, were employed. This strong stabilization was designed to prevent electrostatic interactions between the organic dye and the gold surface. The alkylthiol-protected gold nanoparticles were synthesized using the same method as **AuNPs-Cy7-XCn-OLip**, replacing the electrostatic stabilizer (TOABr) with 1-octanethiol (C_8SH). The exchange reaction, driven by the formation of a more stable thiol-gold bond, yielded nanoparticles **AuNPs-SC$_8$**, which were soluble in CH_2Cl_2.

Three cyanine derivatives were selected for this investigation: **Cy7-NHC11-OLip**, featuring a lipoic S-S bidentate anchoring point*;* **Cy7-NHC12**, lacking a gold surface anchoring point but retaining an alkyl chain on the Cy7 scaffold; and **Cy7-Cl**, which lacks both the anchoring point and the alkyl chain. This selection enabled the investigation of different interaction modes between the dyes and the gold nanoparticles. Indeed, **Cy7-NHC11-OLip** is expected to interact covalently with the surface, **Cy7-Cl** should interact solely through electrostatic interactions, and **Cy7-NHC12** could interact with both dispersive and electrostatic interactions.

As in the previous experiments, fluorescence measurements were used to investigate these systems by adding successive aliquots of **AuNPs-SC$_8$** to cyanine dye solutions (2.2 mL). No interaction was expected for **Cy7-Cl** as the electrostatic stabilization should be prevented by the dielectric effect of the organic monolayer. In contrast, emission quenching was anticipated for **Cy7-NHC11-OLip**, due to its covalent interaction with the gold surface, and **Cy7-NHC12** through interdigitation with the thiolated-protected layer.

Initially, the fluorescence emission spectra of the three cyanine solutions in CH_2Cl_2 were recorded. Next, three aliquots of 100 µL of **AuNPs-SC$_8$** in CH_2Cl_2 were sequentially added to each cyanine dye solution. After each addition, the emission spectrum was promptly recorded, and again after 30 minutes and 1 hour, using the excitation wavelength corresponding to each fluorophore's maximum absorption. Upon the addition of the nanoparticles' final aliquot (cumulative volume of 300 µL), the system underwent 15 minutes of sonication, and another emission spectrum was recorded to capture any alterations induced by the sonication process (**Scheme 4.4**). Parallel control experiments were also conducted by adding solvent (CH_2Cl_2) instead of the nanoparticles' solutions to the solution of each dye, establishing the relationship between fluorescence emission and dilution.

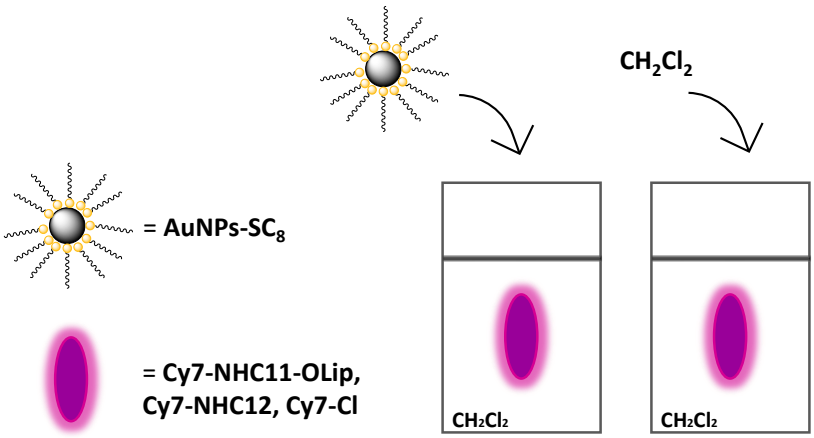

Scheme 4.4. Scheme of the fluorescence titrations: solution in CH_2Cl_2 of **Cy7-NH-C11-OLip** (c = 6×10^{-6} M, λ_{max}^{ex} = 657 nm, λ_{max}^{em} = 762 nm), of **Cy7-NH-C12** (c = 3.4×10^{-6} M, λ_{max}^{ex} = 657 nm, λ_{max}^{em} = 762 nm), and of **Cy7-Cl** (c = 9.0×10^{-7} M, λ_{max}^{ex} = 770 nm, λ_{max}^{em} = 806 nm).

The fluorescence emission variation of the three cyanine dye solutions upon the addition of the solution of **AuNPs-SC$_8$** is depicted in **Figure 4.15**. The emission spectrum was recorded following each successive addition, and a time-dependent analysis was conducted to assess potential kinetic effects. No significant temporal changes in the emission were observed, indicating that the interaction between the gold nanoparticles and the cyanine dye occurs rapidly. However, a consistent decrease in emission intensity was noted after each addition, attributed to the interaction of the dye molecules with the gold nanoparticle surface. Notably, the influence of sonication should be highlighted: for solutions containing **Cy7-NHC11-OLip** (**Figure 4.15** top-left) and **Cy7-NHC12** (**Figure 4.15** top-right), complete fluorescence quenching was reached, corroborating the strong interaction between the dye and the metal surface. In contrast, for the **Cy7-Cl** solution, sonication did not alter the fluorescence (**Figure 4.15** bottom), suggesting a weak interaction between the dye and the metal surface.

These findings suggest that the electrostatic interaction between the cyanine dye **Cy7-Cl** and the metal surface of the nanomaterial is not stable over time. Furthermore, the differences between the results obtained for **Cy7-Cl** and **Cy7-NHC12**, preclude the possibility of the latter interacting with the nanoparticles *via* electrostatic interactions. Instead, **Cy7-NHC12** likely interacts *via* intercalation of its alkyl chain with the thiolated layer on the nanoparticle surface.

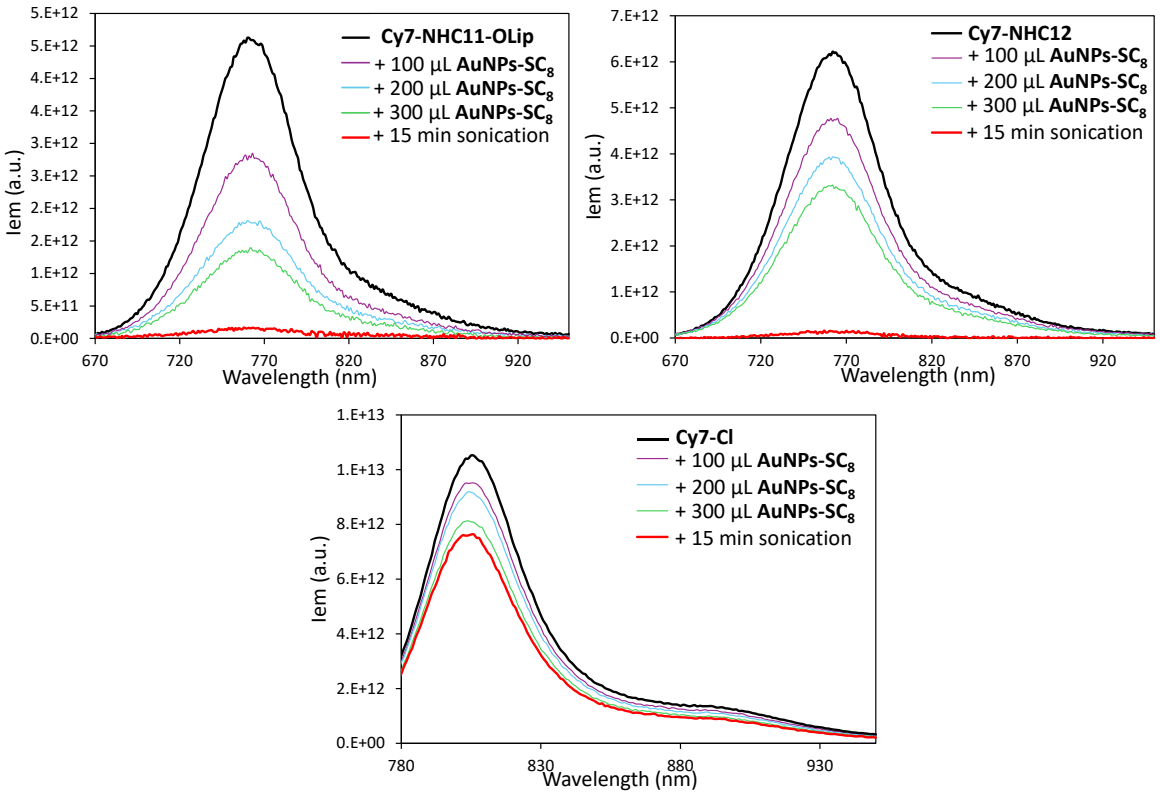

Figure 4.15. Temporal fluorescence emission variation during the titration of CH_2Cl_2 solutions of **Cy7-NHC11-OLip** (c = 6×10^{-6} M, λ_{max}^{ex} = 657 nm, top-left), **Cy7-NHC12** (c = 3.4×10^{-6} M, λ_{max}^{ex} = 657 nm, top-right) and **Cy7-Cl** (c = 9×10^{-7} M, λ_{max}^{ex} = 770 nm, bottom) with a CH_2Cl_2 solution of **AuNPs-SC$_8$**.

4 Conclusion

In this Chapter, novel heptamethine cyanine dyes were synthesized and comprehensively characterized using NMR, UV-Vis, and fluorescence spectroscopy. Gold nanoparticles conjugated with these designed cyanine dyes were also synthesized and fully characterized through UV-Vis spectroscopy, TEM imaging, XPS analysis, and DLS measurements. The influence of the gold nanoparticles' plasmon absorption on the fluorescence of cyanine dyes was investigated through a series of fluorescence titrations. It was confirmed that the fluorescence quenching of the dyes is primarily due to their proximity to the gold surface and the spectral overlap between the dye's emission and the plasmonic absorbance. Additionally, the nature of the interaction between cyanine dyes and gold nanoparticles was investigated by using fluorescence analyses. Cyanine dyes equipped with an anchoring group for the gold surface exhibited a strong interaction with the metallic surface. In contrast, cyanine dyes with only a terminal alkyl chain demonstrated weaker, unstable interactions due to interdigitation, and cyanine **Cy7-Cl**, which relies solely on electrostatic interactions, exhibited only a weak association with the gold surface. These findings highlight the importance of a robust anchoring point for the gold surface to achieve stable hybrid nanomaterials. Furthermore, the fluorescence studies confirmed the crucial role of spectral overlap between

plasmonic absorption and dye emission, as well as the significance of distance-dependent interactions between the dye and the gold surface.

4 Acknowledgments

Thanks to Prof. Andrea Giacomo Marrani (University of Roma "La Sapienza") for the XPS analyses and to Prof. Pier Sandro Pallavicini (University of Pavia) for the TEM images. Thanks to Dr. Alice Erbisti for the help with the synthesis of cyanine dyes and UV-Visible and fluorescence studies.

4 Experimental Section

General Methods

All solvents were dried using standard procedures; all other reagents were of reagent-grade quality obtained from commercial suppliers and used without further purification. Column chromatography was carried out on 230–400 mesh silica gel (Aldrich) unless otherwise stated. If not specifically stated, NMR spectra were recorded at 400 MHz for ^{1}H and 100 MHz for ^{13}C. Chemical shifts are expressed in ppm (δ) using the residual solvent signal as an internal reference (7.26 ppm for $CHCl_3$, 7.16 ppm for C_6D_5H, 5.32 for $CHDCl_2$, and 3.31 ppm for CD_2HOD). Coupling constants (*J*) are given in Hz, and the following abbreviations have been used to describe the signals: singlet (s); broad singlet (br. s); doublet (d); triplet (t); quadruplet (q); multiplet (m). Mass spectra were recorded in the ESI mode. Melting points were measured with a Gallenkamp melting-point apparatus and were uncorrected. High-resolution mass spectra (HR-MS) were performed with an LTQ ORBITRAP XL Thermo instrument. UV–Vis spectra were recorded on a UV-Visible Evolution 260 spectrophotometer (sh = shoulder, ε [$mol^{-1}dm^3cm^{-1}$] is reported in parentheses). Fluorescence spectra were recorded on an Edinburgh Instrument FLS1000, with a photomultiplier tube detector (PMTNIR). 1,3,3-trimethyl-3H-indol-1-ium 4-methylbenzenesulfonate[28] and 2-chloro-3-(hydroxymethylene)-1-cyclohexene-1-carboxaldehyde[29] were synthesized according to published procedures.

Synthesis of **Cy7-Cl**: In a 50 mL two-necked bottom flask, 1,3,3-trimethyl-3H-indol-1-ium 4-methylbenzenesulfonate (1.00 g, 2.9 mmol, 2.0 eq.), 2-chloro-3-(hydroxymethylene)-1-cyclohexene-1-carboxaldehyde (0.26 g, 1.5 mmol, 1.0 eq.) and sodium acetate (0.25 g, 3.0 mmol, 2.0 eq.) were dissolved in absolute EtOH (14 mL) under nitrogen atmosphere. The reaction was stirred at 85 °C for 1 hour. After this time, p-toluensulfonic acid (0.25 g, 0.23 mmol, 0.2 eq.) was added and the reaction was stirred at 85 °C for 20 minutes. After cooling to room temperature, the solvent was evaporated to dryness under reduced pressure. Then, the reaction mixture was recovered with dichloromethane and extracted with water (2 × 20 mL). The resulting organic layer was dried over Na_2SO_4, filtered, and evaporated to dryness under reduced pressure. The crude

product was purified by precipitation from a mixture of CH_2Cl_2/Et_2O =1/3 to give pure **Cy7-Cl** as green-red crystals in 85% yield (0.84 g, 1.3 mmol).

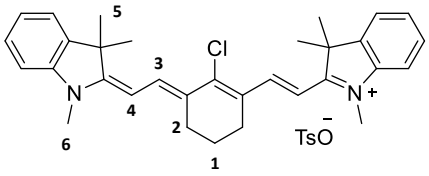

m.p.: 74-77 °C. **^{1}H NMR** (CD_3OD, 400 MHz) δ (ppm) = 8.47 (d, *J* = 14.2 Hz, 2H, H4), 7.72 (d, *J* = 6.4 Hz, 2H, $H_{Ar(TsO)}$), 7.54 (d, *J* = 7.4 Hz, 2H, $H_{Ar(Cy)}$), 7.46 (td, J_1 = 7.6 Hz, J_2 = 1.2 Hz, 2H, $H_{Ar(Cy)}$), 7.4-7.3 (m, 4H, $H_{Ar(Cy)}$), 7.25 (d, *J* = 7.8 Hz, 2H, $H_{Ar(TsO)}$), 6.29 (d, *J* = 14 Hz, 2H, H_3), 3.69 (s, 6H, H_6), 2.76 (t, *J* = 6.3 Hz, 4H, H_2), 2.39 (s, 3H, $H_{OMe(TsO)}$), 2.0-1.9 (m, 2H, H_1), 1.76 (s, 12H, H_5). **^{13}C-APT NMR** (CD_3OD, 101 MHz) δ (ppm) = 173.4, 149.5, 143.9, 142.9, 142.3, 141.1, 140.2, 128.5, 128.4, 126.6, 125.6, 125.1, 122.0, 110.7, 101.1, 49.1, 37.9, 30.4, 29.3, 26.8, 25.9, 24.7, 24.5, 22.8, 20.7, 20.0. **ESI-MS (+):** calculated for $C_{32}H_{36}ClN_2^+$: m/z (z = 1): 483.3, found: 483.5. **UV-Vis** (CH_2Cl_2): λ_{max} (ε)= 785 nm (30444 $mol^{-1}dm^3cm^{-1}$), 714 nm (sh, 14006 $mol^{-1}dm^3cm^{-1}$). **Fluorescence** (CH_2Cl_2): λ_{ex} = 774 nm, λ_{em} = 830 nm.

General procedure for the synthesis of Cy7-NHCn-OH derivatives

In a 25 mL two-necked round bottom flask kept under an inert atmosphere, a mixture of **Cy7-Cl** (0.16 mmol) and the appropriate α,ω-amino alcohol (0.30 mmol) in dry DMF (10 mL) was reacted at 85 °C for 4 hours under stirring. After cooling to room temperature, the solvent was evaporated to dryness under reduced pressure. The crude product was dissolved in CH_2Cl_2, adsorbed onto silica and purified by column chromatography on silica gel to isolate the desired **Cy7-NHCn-OH** product.

Cy7-NHC6-OH: the crude product was purified by column chromatography (SiO_2, CH_2Cl_2/MeOH 95:5). The pure product **Cy7-NHC6-OH** was obtained as a blue solid in 79 % (0.092 g, 0.13 mmol).

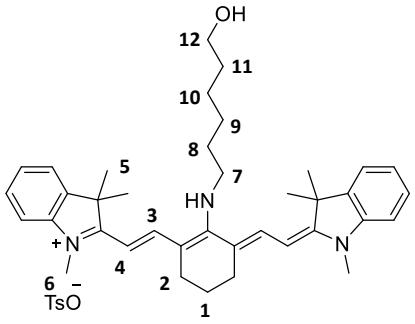

m.p.: 118-120 °C. **^{1}H NMR** (CD_3OD, 400 MHz) δ (ppm) =7.77 (d, *J* = 13.0 Hz, 2H, H_4), 7.71 (d, *J* = 8.2 Hz, 2H, $H_{Ar(TsO)}$), 7.36 (d, *J* = 7.4 Hz, 2H, $H_{Ar(Cy)}$), 7.31 (td, *J* = 7.7 Hz, *J* = 1.2 Hz, 2H, $H_{Ar(Cy)}$), 7.23 (d, *J* = 7.9 Hz, 2H, $H_{Ar(TsO)}$), 7.07 (m, 4H, $H_{Ar(Cy)}$), 5.78 (d, *J* = 13.0 Hz, 2H, H_3), 3.78 (t, *J* = 6.9 Hz, 2H, H_7), 3.55

(t, *J* = 6.4 Hz, 2H, H_{12}), 3.44 (s, 6H, H_6), 2.55 (t, *J* = 6.9 Hz, 4H, H_2), 2.37 (s, 3H, $H_{OMe(TsO)}$), 1.9-1.8 (m, 4H, $H_{1,8}$), 1.66 (s, 12H, H_5), 1.6-1.3 (m, 8H, $H_{9\text{-}11}$). **^{13}C NMR** (CD_3OD, 101 MHz) δ (ppm) = 128.4, 127.9, 125.6, 121.9, 121.5, 107.9, 61.4, 60.1, 56.9, 32.1, 31.3, 29.4, 27.6, 26.3, 25.3, 24.9, 22.3, 19.1, 16.9, 13.03. **ESI-MS (+):** calculated for $C_{38}H_{50}N_3O^+$: m/z (z = 1): 564.4, found: 564.4.

Cy7-NHC11-OH: the crude product was purified by column chromatography (SiO_2, CH_2Cl_2/MeOH 95:5). The pure product **Cy7-NHC11-OH** was obtained as a blue sticky solid in 70 % (0.085 g, 0.11 mmol).

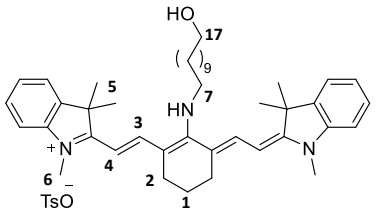

m.p.: 126-128°C. **^{1}H NMR** (CD_3OD, 400 MHz) δ (ppm) =7.76 (d, *J* = 13.0 Hz, 2H, H_4), 7.70 (d, *J* = 8.2 Hz, 2H, $H_{Ar(TsO)}$), 7.36 (d, *J* = 7.4 Hz, 2H, $H_{Ar(Cy)}$), 7.31 (td, J_1 = 7.7 Hz, J_2 = 1.2 Hz, 2H, $H_{Ar(Cy)}$), 7.23 (d, *J* = 7.9 Hz, 2H, $H_{Ar(TsO)}$), 7.1-7.0 (m, 4H, $H_{Ar(Cy)}$), 5.78 (d, *J* = 13.0 Hz, 2H, H_3), 3.77 (t, *J* = 6.8 Hz, 2H, H_7), 3.51 (t, *J* = 6.7 Hz, 2H, H_{17}), 3.4 (br. s, 6H, H_6), 2.55 (t, *J* = 6.4 Hz, 4H, H_2), 2.37 (s, 3H, $H_{OMe(TsO)}$), 1.9-1.8 (m, 4H, $H_{1,8}$), 1.66 (s, 12H, H_5), 1.5-1.2 (m, 20H, $H_{9\text{-}16}$). **^{13}C NMR** (CD_3OD, 101 MHz) δ (ppm) = 128.4, 127.9, 125.6, 121.9, 121.5, 107.9, 61.6, 56.9, 50.6, 32.3, 31.3, 29.3, 29.3, 29.2, 28.9, 27.6, 26.6, 25.6, 24.9, 22.3, 21.6, 16.9, 13.0. **ESI-MS (+):** calculated for $C_{43}H_{60}N_3O^+$: m/z (z = 1): 634.5, found: 634.4.

Synthesis of Cy7-SC11-OH derivative

In a 25 mL two-necked round bottom flask, **Cy7-Cl** (150.0 mg, 0.23 mmol, 1.0 eq.) and 11-mercapto-1-hexanol (94.0 mg, 0.46 mmol, 2.0 eq.) were solubilized in anhydrous DMF (10 mL) under nitrogen atmosphere. Then triethylamine (69.5 mg, 95 µL, 0.69 mmol, 3.0 eq.) was added to the mixture. The reaction mixture was stirred at 85 °C for 4 hours. After cooling down to room temperature, the solvent was evaporated to dryness under reduced pressure. The crude solid was dissolved in CH_2Cl_2, adsorbed onto silica, and purified by column chromatography (SiO_2, CH_2Cl_2/MeOH 96:4) to afford pure **Cy7-SC6-OH** as a dark-green sticky solid in 69% yield (129.7 mg, 0.16 mmol).

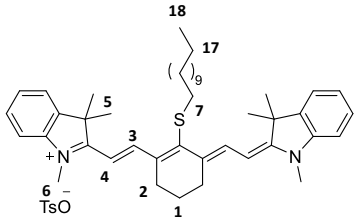

^{1}H NMR (CD_3OD, 400 MHz) δ (ppm) = 8.94 (d, *J* = 14.2 Hz, 2H, H_4), 7.72 (d, *J* = 8.3 Hz, 2H, $H_{Ar(TsO)}$), 7.52 (d, *J* = 7.5 Hz, 2H, $H_{Ar(Cy)}$), 7.44 (td, *J* = 7.5 Hz, *J* = 1.2 Hz, 2H, $H_{Ar(Cy)}$), 7.3-7.2 (m, 6H, $H_{Ar(Cy)+ Ar(TsO)}$), 6.29 (d, *J* = 14.3Hz, 2H, H_3), 3.67 (s, 6H, H_6), 3.52 (t, *J* = 6.6 Hz, 2H, H_7), 2.86 (t, *J* = 7.3 Hz, 2H, H_{17}), 2.71 (t, *J* = 6.2 Hz, 4H, H_2), 2.39 (s, 3H, H_{OMe}), 2.0-1.9 (m, 2H, H_1), 1.78 (s, 12H, H_5), 1.7-1.6 (m, 2H, H_8), 1.5-1.3 (m, 16H, H_{9-16}).**^{13}C NMR** (CD_3OD, 101 MHz) δ (ppm)= 173.1, 145.9, 143.0, 140.9, 133.2, 128.4, 125.6, 124.8, 121.9, 110.4, 100.7, 61.6, 37.7, 32.3, 30.2 (2 sn.), 29.4, 29.2, 29.1, 28.9, 28.5, 26.9, 25.8, 25.6, 21.0, 20.0. **ESI-MS (+):** calculated for $C_{43}H_{59}N_2OS^+$: m/z (z = 1): 651.4, found: 651.4.

General procedure for the synthesis of Cy7-XCn-OLip ligands

In a 50 mL two-necked round bottom flask kept under an inert atmosphere, a mixture of **Cy7-XCn-OH** (X = NH or S, n = 6 or 11) (0.29 mmol, 1.0 eq.) and (±)-α-Lipoic acid (0.38 mmol, 1.3 eq.) in dry CH_2Cl_2 (20 mL) was stirred at 0 °C for 15 minutes. Afterwards, EDC·HCl (0.07 g, 0.38 mmol, 1.3 eq.) and DMAP (catalytic) were added, and the resulting reaction mixture was stirred at room temperature for 24 hrs. The reaction mixture was then treated with a 10% w/v aqueous solution of $NaHCO_3$ (20 mL), separated and then washed with water up to neutrality (2 × 20 mL). Finally, the organic layer was dried over Na_2SO_4, filtered, and evaporated to dryness under reduced pressure. The crude product was dissolved in CH_2Cl_2, adsorbed onto silica, and purified by column chromatography on silica gel to isolate the desired **Cy7-XCn-OLip** product.

Cy7-NHC6-OLip: the crude product was purified by column chromatography (SiO_2, CH_2Cl_2/MeOH 95:5). The pure product **Cy7-NHC6-OLip** was obtained as a blue sticky solid in 80 % (0.23 g, 0.23 mmol).

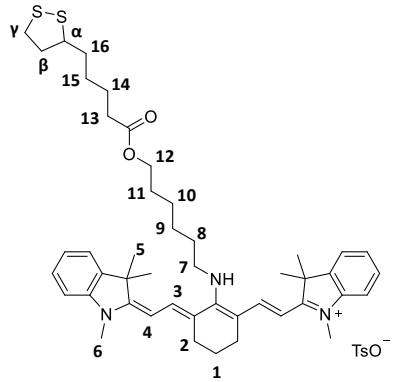

^{1}H NMR (CD_3OD, 400 MHz) δ (ppm) = 7.79 (d, *J* = 13.0 Hz, 2H, H_4), 7.72 (d, *J* = 8.0 Hz, 2H, $H_{Ar(TsO)}$), 7.39 (d, *J* = 7.4 Hz, 2H, $H_{Ar(Cy)}$), 7.33 (t, *J* = 7.7 Hz, 2H, $H_{Ar(Cy)}$), 7.24 (d, *J* = 7.9 Hz, 2H, $H_{Ar(TsO)}$), 7.15-7.05 (m, 4H, $H_{Ar(Cy)}$), 5.81 (d, *J* = 13.0 Hz, 2H, H_3), 4.11 (t, *J* = 6.5 Hz, 2H, H_7), 3.80 (t, *J* = 6.8 Hz, 2H, H_{12}), 3.6-3.5 (m, 2H, H_α), 3.5 (br. s, 6H, H_6), 3.2–3.04 (m, 2H, $H_{\gamma,\gamma'}$), 2.57 (t, *J* = 6.5 Hz, 4H, H_2), 2.5–2.4 (m, 2H, H_β), 2.38 (s, 3H, H_{OMe}), 2.33 (t, *J* = 7.2 Hz, 2H, H_{13}), 1.9–1.8 (m, 5H, $H_{\beta',1,8}$), 1.8–1.3 (m, 22H, $H_{5,9\text{-}11,14\text{-}16}$). **^{13}C NMR** ($CD_3OD$, 101 MHz) δ (ppm) = 173.9, 169.7, 168.5, 143.6, 142.2, 139.8, 138.8, 128.4, 128.4, 125.6, 122.5, 121.6, 120.3, 108.4, 94.12, 63.9, 56.2, 50.2, 39.9, 37.9, 34.30, 33.54, 31.07, 29.0, 28.4, 28.3, 27.7, 26.2, 25.4, 24.6, 24.4, 21.6, 19.9. **HR-MS** (ESI, Orbitrap LQ) calculated for $C_{46}H_{62}O_2N_3S_2^+$: m/z (z = 1): 752.42780, found: 752.42839. **UV-Vis** (CH_2Cl_2): λ_{max} (ε)= 658 nm (80000 $mol^{-1}dm^3cm^{-1}$). **Fluorescence** (CH_2Cl_2): λ_{ex} = 658 nm, λ_{em} = 763 nm.

Cy7-NHC11-OLip: the crude product was purified by column chromatography (SiO_2, CH_2Cl_2/MeOH 95:5). The pure product **Cy7-NHC11-OLip** was obtained as a blue sticky solid in 70 % (0.26 g, 0.20 mmol).

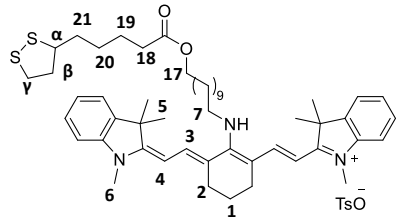

^{1}H NMR (CD_3OD, 400 MHz) δ (ppm) = 7.78 (d, *J* = 13.0 Hz, 2H, H_4), 7.73 (d, *J* = 8.1 Hz, 2H, $H_{Ar(TsO)}$), 7.4–7.3 (m, 4H, $H_{Ar(Cy)}$), 7.22 (d, *J* = 7.9 Hz, 2H, $H_{Ar(TsO)}$), 7.1–7.0 (m, 4H, $H_{Ar(Cy)}$), 5.79 (d, *J* = 13.0 Hz, 2H, H_3), 4.05 (t, *J* = 6.5 Hz, 2H, H_7), 3.79 (t, *J* = 6.8 Hz, 2H, H_{17}), 3.6-3.5 (m, 1H, H_α), 3.45 (s, 6H, H_6), 3.2-3.1 (m, 2H, $H_{\gamma,\gamma'}$), 2.56 (t, *J* = 6.4 Hz, 4H, H_2), 2.5-2.4 (m, 2H, H_β), 2.37 (s, 3H, H_{OMe}), 2.30 (t, *J* = 7.2 Hz, 2H, H_{18}), 1.9-1.8 (m, 5H, $H_{\beta',1,8}$), 1.7-1.3 and 1.66 (m, s, 34H, $H_{5,9\text{-}16,19\text{-}21}$). **^{13}C NMR** ($CD_3OD$, 101 MHz) δ (ppm) = 173.9, 169.7, 168.4, 143.6, 142.4, 140.1, 139.7, 138.7, 128.4, 128.0, 125.6, 122.5, 121.6, 120.3, 108.4, 94.2, 64.1, 56.2, 50.2, 39.9, 38.0, 34.3, 33.6, 31.1, 29.2, 29.2, 29.2, 29.1, 29.0, 28.9, 28.43, 28.4, 27.7, 26.6, 26.5, 25.7, 24.6, 24.5, 21.6, 20.0. **HR-MS** (ESI, Orbitrap LQ) calculated for $C_{51}H_{72}O_2N_3S_2$: m/z (z = 1): 822.50605, found: 822.50731. **UV-Vis** (CH_2Cl_2): λ_{max} (ε)= 656 nm (59100 $mol^{-1}dm^3cm^{-1}$). **Fluorescence** (CH_2Cl_2): λ_{ex} = 656 nm, λ_{em} = 765 nm.

Cy7-SC11-OLip: the crude product was purified by column chromatography (SiO_2, CH_2Cl_2/MeOH 95:5). The pure product **Cy7-SC11-OLip** was obtained as a green sticky solid in 60 % (0.061 g, 0.17 mmol).

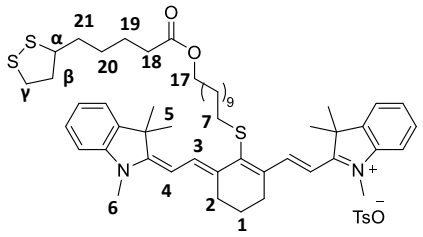

^{1}H NMR (CD_3OD, 400 MHz) δ (ppm) = 8.94 (d, *J* = 14.2 Hz, 2H, H_4), 7.72 (d, *J* = 8.3 Hz, 2H, $H_{Ar(TsO)}$), 7.52 (d, *J* = 7.8 Hz, 2H, $H_{Ar(Cy)}$), 7.44 (td, *J* = 7.7 Hz, *J* = 1.2 Hz, 2H, $H_{Ar(Cy)}$), 7.3-7.2 (m, 6H, $H_{Ar(Cy)+ Ar(TsO)}$), 6.29 (d, *J* = 14.2 Hz, 2H, H_3), 4.05 (t, *J* = 6.5 Hz, 2H, H_7), 3.67 (s, 6H, H_6), 3.6-3.5 (m, 1H, H_α), 3.2-3.0 (m, 2H, $H_{\gamma, \gamma'}$), 2.86 (t, *J* = 7.3 Hz, 2H, H_{17}), 2.70 (t, *J* = 6.2 Hz, 4H, H_2), 2.5-2.4 (m, 1H, H_β), 2.38 (s, 3H, H_{OMe}), 2.32 (t, *J* = 7.2 Hz, 2H, H_{18}), 2.0-1.9 (m, 2H, H_1), 1.9-1.8 (m, 1H, $H_{\beta'}$), 1.78 (s, 12H, H_5), 1.7-1.3 (m, 24H, $H_{8\text{-}16,\ 19\text{-}21}$).**^{13}C NMR** ($CD_3OD$, 101 MHz) δ (ppm)= 173.9, 173.0, 157.8, 145.9, 143.0, 140.9, 133.2, 129.6, 128.4 (2 sn.), 127.6, 125.6, 124.8, 121.9, 110.4, 100.7, 70.6, 64.1, 61.6, 56.2, 48.9, 39.9, 38.0, 37.7, 34.3, 33.5, 32.3, 30.2, 30.1, 29.3 (2 sn.), 29.2, 29.1 (3 sn.), 29.0, 28.9,28.8, 28.5, 28.4 (2 sn), 28.3, 26.9, 25.8, 25.6, 25.0, 24.5, 20.9, 19.9. **HR-MS** (ESI, Orbitrap LQ) calculated for $C_{51}H_{71}O_2N_2S_3$: m/z (z = 1): 839.46722, found: 839.46848. **UV-Vis** (CH_2Cl_2): λ_{max} (ε)= 785 nm (25000 $mol^{-1}dm^3cm^{-1}$), 719 nm (sh, 13908 $mol^{-1}dm^3cm^{-1}$). **Fluorescence** (CH_2Cl_2): λ_{ex} = 770 nm, λ_{em} = 816 nm.

General procedure for the synthesis of Cy7-XC12 derivatives

In a 25 mL two-necked round bottom flask kept under an inert atmosphere, a mixture of **Cy7-Cl** (0.175 mmol, 1.2 eq.), dodecylamine or dodecan-1-thiol (0.15 mmol, 1.0 eq.) and DIPEA (0.15 mmol, 1.2 eq.) in dry DMF (10 mL) was reacted at 85 °C for 4 hours under stirring. After cooling to room temperature, the solvent was evaporated to dryness under reduced pressure. The crude product was dissolved in CH_2Cl_2, adsorbed onto silica, and purified by column chromatography on silica gel to isolate the desired **Cy7-XC12** product.

Cy7-NHC12: the crude product was purified by column chromatography (SiO_2, CH_2Cl_2/MeOH 95:5). The pure product **Cy7-NHC12** was obtained as a blue sticky solid in 58 % (0.082 g, 0.09 mmol).

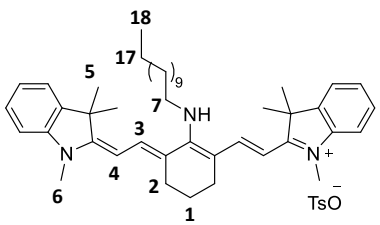

^{1}H NMR (CD_3OD, 400 MHz) δ (ppm) = 7.78 (d, *J* = 13.0 Hz, 2H, H_4), 7.72 (d, *J* = 8.2 Hz, 2H, $H_{Ar(TsO)}$), 7.4-7.2 (m, 4H, $H_{Ar(Cy)}$), 7.23 (d, *J* = 8.2 Hz, 2H, $H_{Ar(TsO)}$), 7.1-7.0 (m, 4H, $H_{Ar(Cy)}$), 5.80 (d, *J* = 16.0 Hz, 2H,

H_3), 3.79 (t, *J* = 8.0 Hz, 2H, H_7), 3.45 (s, 6H, H_6), 2.57 (t, *J* = 8.0 Hz, 4H, H_2), 2.37 (s, 3H, H_{OMe}), 1.9-1.7 (m, 6H, $H_{8\text{-}10}$), 1.67 (s, 12H, H_5), 1.5-1.3 (m, 14H, $H_{11\text{-}17}$), 0.89 (t, *J* = 6.9 Hz, 3H, H_{18}).**^{13}C NMR** (CD_3OD, 101 MHz) δ (ppm) = 138.3, 128.5, 127.9, 125.7, 122.4, 121.4, 108.4, 94.1, 50.4, 48.3, 48.0, 47.8, 47.6, 47.4, 47.2, 46.9, 31.7, 29.3, 29.0, 28.9, 27.6, 27.1, 26.5, 24.6, 22.3, 21.6, 19.9, 13.1. **ESI-MS (+)**: calculated for $C_{44}H_{62}N_3^+$: m/z (z = 1): 632.5, found: 632.6. **UV-Vis** (CH_2Cl_2): λ_{max} (ε) = 657 nm (4500 $mol^{-1}dm^3cm^{-1}$), 401 nm ($mol^{-1}dm^3cm^{-1}$). **Fluorescence** (CH_2Cl_2): λ_{ex} = 656 nm, λ_{em} = 763 nm.

Cy7-SC12: the crude product was purified by column chromatography (SiO_2, CH_2Cl_2/MeOH 95:5) to afford 0.059 g of a green sticky solid in 41% (0.059 g, 0.06 mmol).

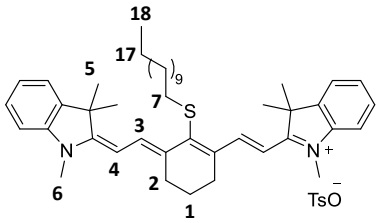

^{1}H NMR (CD_3OD, 400 MHz) δ (ppm) = 8.93 (d, *J* = 16.0 Hz, 2H, H_4), 7.72 (d, *J* = 12.0 Hz, 2H, $H_{Ar(TsO)}$), 7.52 (d, *J* = 7.9 Hz, 2H, $H_{Ar(Cy)}$), 7.4-7.2 (m, 2H, $H_{Ar(Cy)}$), 7.1-7.0 (m, 6H, $H_{Ar(Cy)+\ Ar(TsO)}$), 6.29 (d, *J* = 13.0 Hz, 2H, H_3), 3.66 (s, 6H, H_6), 2.85 (t, *J* = 8.0 Hz, 2H, H_7), 2.70 (t, *J* = 7.6, 4H, H_2), 2.37 (s, 3H, H_{OMe}), 2.0-1.9 (m, 2H, H_1), 1.70 (s, 12H, H_5), 1.7-1.6 (m, 2H, H_8), 1.4-1.2 (m, 18H, $H_{9\text{-}17}$), 0.89 (t, *J* = 9.8 Hz, 3H, H_{18}).**^{13}C NMR** (CD_3OD, 101 MHz) δ (ppm) = 173.0, 157.8, 145.9, 143.0, 140.9, 140.2, 133.2, 128.4, 125.6, 124.8, 121.9, 110.4, 100.7, 48.9, 47.4, 47.2, 46.9, 37.6, 31.6, 30.1, 29.3, 29.2, 29.1, 28.8, 28.4, 26.8, 25.8, 22.3, 20.9, 19.9, 13.0. **ESI-MS (+)**: calculated for $C_{44}H_{61}N_2S^+$: m/z (z = 1): 649.5, found: 649.6. **UV-Vis** (CH_2Cl_2): λ_{max} (ε) = 785 nm (44000 $mol^{-1}dm^3cm^{-1}$). **Fluorescence** (CH_2Cl_2): λ_{ex} = 425 nm, λ_{em} = 820 nm.

General synthesis of AuNPs decorated with Cy7-XCn-OLip

In a 25 mL round bottom flask 3 mL of a solution of **Cy7-XCn-OLip** in CH_2Cl_2 (C = 10^{-4} M) was inserted. While stirring 4 mL of a freshly prepared solution of **AuNPs-TOABr** in toluene was added. The mixture was stirred at room temperature for 17 hours. The **AuNPs-Cy7-XCn-OLip** was purified using three 10-minute-long centrifugation cycles at 9,000 r.p.m. (Hettich, Universal 320R). At the end of each centrifugation cycle, the supernatant was removed and the precipitated **AuNPs-Cy7-XCn-OLip** were redispersed in CH_2Cl_2.

AuNPs-Cy7-NHC6-OLip: synthesized from **Cy7-NHC6-OLip** (3 mL of a solution C = 9.85×10^{-4} M) according to the general procedure.

AuNPs-Cy7-NHC11-OLip: synthesized from **Cy7-NHC11-OLip** (3 mL of a solution C = 2.62×10^{-4} M) according to the general procedure.

AuNPs-Cy7-SC11-OLip: synthesized from **Cy7-SC11-OLip** (3 mL of a solution C = 5.74×10^{-4} M) according to the general procedure.

Experimental XPS

For the acquisition of XPS spectra, the pure cyanine samples were dissolved in ethanol, while the AuNP samples in a dichloromethane/methanol mixture (80:20, v/v) and ultrasonicated for 15 min. The specimens for XPS analisys were obtained *via* drop-casting of the sample solutions onto a graphite foil mounted on the XPS sample holder via a conductive tape. After solvent evaporation, samples were introduced into the UHV system of XPS spectrometer.

The experimental conditions were: excitation by monochromatic Al Kα photons (hν = 1486.7 eV) generated at 14 kV, 16 mA, take-off angle (ϑ) of 21° with respect to the sample surface normal. In the only case of N 1s and S 2p regions of the AuNP samples an a-chromatic Al Kα source was used in order to gain a higher intensity. All photoionization regions were acquired using an analyser pass energy of 20 eV. The binding energy (BE) of the C 1s line of the graphite support at 284.3 eV was used as an internal standard reference for BE scale (accuracy of ±0.05 eV). Experimental spectra were theoretically reconstructed by fitting the secondary electrons background to linear and Shirley functions and the elastic peaks to symmetric pseudo-Voigt functions. XPS atomic ratios between relevant core lines were estimated from experimentally determined area ratios (±10% associated error) corrected for the corresponding Scofield cross sections and for a square root dependence of the photoelectrons kinetic energies.

4 Bibliography

(1) Feng, L.; Chen, W.; Ma, X.; Liu, S. H.; Yin, J. Near-Infrared Heptamethine Cyanines (Cy7): From Structure, Property to Application. *Org. Biomol. Chem.* **2020**, *18* (46), 9385–9397. https://doi.org/10.1039/D0OB01962C.

(2) Medeiros, N. G.; Braga, C. A.; Câmara, V. S.; Duarte, R. C.; Rodembusch, F. S. Near-Infrared Fluorophores Based on Heptamethine Cyanine Dyes: From Their Synthesis and Photophysical Properties to Recent Optical Sensing and Bioimaging Applications. *Asian J. Org. Chem.* **2022**, *11* (6), e202200095. https://doi.org/10.1002/ajoc.202200095.

(3) Li, Y.; Tuttle, M. A.; Liu, Q.; Pang, Y. An NIR-Emitting Cyanine Dye with Pyridinium Groups: The Impact of Regio-Bond Connection on the Photophysical Properties. *Chem. Commun.* **2024**, *60* (16), 2208–2211. https://doi.org/10.1039/D3CC06189B.

(4) Hassan, M.; Su, Y. T.; Iqbal, S. Z.; Nawaz, R.; Wang, Y.; Jiang, W. Symmetrically Fluorinated D-π-A Structured Cyanine Dye for Highly Efficient NIR-II Imaging-Guided Cancer Phototheranostics. *Small* **2024**, 2401905. https://doi.org/10.1002/smll.202401905.

(5) Bricks, J. L.; Kachkovskii, A. D.; Slominskii, Y. L.; Gerasov, A. O.; Popov, S. V. Molecular Design of near Infrared Polymethine Dyes: A Review. *Dyes Pigments* **2015**, *121*, 238–255. https://doi.org/10.1016/j.dyepig.2015.05.016.

(6) Zhao, X.; Zhang, F.; Lei, Z. The Pursuit of Polymethine Fluorophores with NIR-II Emission and High Brightness for *in Vivo* Applications. *Chem. Sci.* **2022**, *13* (38), 11280–11293. https://doi.org/10.1039/D2SC03136A.

(7) Li, H.; Kim, H.; Xu, F.; Han, J.; Yao, Q.; Wang, J.; Pu, K.; Peng, X.; Yoon, J. Activity-Based NIR Fluorescent Probes Based on the Versatile Hemicyanine Scaffold: Design Strategy, Biomedical Applications, and Outlook. *Chem. Soc. Rev.* **2022**, *51* (5), 1795–1835. https://doi.org/10.1039/D1CS00307K.

(8) Marcelo, G. A.; Galhano, J.; Oliveira, E. Applications of Cyanine-Nanoparticle Systems in Science: Health and Environmental Perspectives. *Dyes Pigments* **2023**, *208*, 110756. https://doi.org/10.1016/j.dyepig.2022.110756.

(9) Tam, F.; Goodrich, G. P.; Johnson, B. R.; Halas, N. J. Plasmonic Enhancement of Molecular Fluorescence. *Nano Lett.* **2007**, *7* (2), 496–501. https://doi.org/10.1021/nl062901x.

(10) Chen, Y.; Munechika, K.; Ginger, D. S. Dependence of Fluorescence Intensity on the Spectral Overlap between Fluorophores and Plasmon Resonant Single Silver Nanoparticles. *Nano Lett.* **2007**, *7* (3), 690–696. https://doi.org/10.1021/nl062795z.

(11) Fu, Y.; Zhang, J.; Lakowicz, J. R. Plasmon-Enhanced Fluorescence from Single Fluorophores End-Linked to Gold Nanorods. *J. Am. Chem. Soc.* **2010**, *132* (16), 5540–5541. https://doi.org/10.1021/ja9096237.

(12) Ayala-Orozco, C.; Liu, J. G.; Knight, M. W.; Wang, Y.; Day, J. K.; Nordlander, P.; Halas, N. J. Fluorescence Enhancement of Molecules Inside a Gold Nanomatryoshka. *Nano Lett.* **2014**, *14* (5), 2926–2933. https://doi.org/10.1021/nl501027j.

(13) Li, J.-F.; Li, C.-Y.; Aroca, R. F. Plasmon-Enhanced Fluorescence Spectroscopy. *Chem. Soc. Rev.* **2017**, *46* (13), 3962–3979. https://doi.org/10.1039/C7CS00169J.

(14) Kucherenko, I. S.; Soldatkin, O. O.; Kucherenko, D. Yu.; Soldatkina, O. V.; Dzyadevych, S. V. Advances in Nanomaterial Application in Enzyme-Based Electrochemical Biosensors: A Review. *Nanoscale Adv.* **2019**, *1* (12), 4560–4577. https://doi.org/10.1039/C9NA00491B.

(15) Dykman, L.; Khlebtsov, N. Gold Nanoparticles in Biomedical Applications: Recent Advances and Perspectives. *Chem. Soc. Rev.* **2012**, *41* (6), 2256–2282. https://doi.org/10.1039/C1CS15166E.

(16) Ghobashy, M. M.; Alkhursani, Sh. A.; Alqahtani, H. A.; El-damhougy, T. K.; Madani, M. Gold Nanoparticles in Microelectronics Advancements and Biomedical Applications. *Mater. Sci. Eng. B* **2024**, *301*, 117191. https://doi.org/10.1016/j.mseb.2024.117191.

(17) Su, Q.; Jiang, C.; Gou, D.; Long, Y. Surface Plasmon-Assisted Fluorescence Enhancing and Quenching: From Theory to Application. *ACS Appl. Bio Mater.* **2021**, *4* (6), 4684–4705. https://doi.org/10.1021/acsabm.1c00320.

(18) St. Lorenz, A.; Buabeng, E. R.; Taratula, O.; Taratula, O.; Henary, M. Near-Infrared Heptamethine Cyanine Dyes for Nanoparticle-Based Photoacoustic Imaging and Photothermal Therapy. *J. Med. Chem.* **2021**, *64* (12), 8798–8805. https://doi.org/10.1021/acs.jmedchem.1c00771.

(19) Exner, R. M.; Cortezon-Tamarit, F.; Pascu, S. I. Explorations into the Effect of *Meso* -Substituents in Tricarbocyanine Dyes: A Path to Diverse Biomolecular Probes and Materials. *Angew. Chem. Int. Ed.* **2021**, *60* (12), 6230–6241. https://doi.org/10.1002/anie.202008075.

(20) Sissa, C.; Painelli, A.; Terenziani, F.; Trotta, M.; Ragni, R. About the Origin of the Large Stokes Shift in Aminoalkyl Substituted Heptamethine Cyanine Dyes. *Phys. Chem. Chem. Phys.* **2020**, *22* (1), 129–135. https://doi.org/10.1039/C9CP05473A.

(21) Fink, J.; Kiely, C. J.; Bethell, D.; Schiffrin, D. J. Self-Organization of Nanosized Gold Particles. *Chem. Mater.* **1998**, *10* (3), 922–926. https://doi.org/10.1021/cm970702w.

(22) Woehrle, G. H.; Brown, L. O.; Hutchison, J. E. Thiol-Functionalized, 1.5-Nm Gold Nanoparticles through Ligand Exchange Reactions: Scope and Mechanism of Ligand Exchange. *J. Am. Chem. Soc.* **2005**, *127* (7), 2172–2183. https://doi.org/10.1021/ja0457718.

(23) Dewi, M. R.; Laufersky, G.; Nann, T. A Highly Efficient Ligand Exchange Reaction on Gold Nanoparticles: Preserving Their Size, Shape and Colloidal Stability. *RSC Adv* **2014**, *4* (64), 34217–34220. https://doi.org/10.1039/C4RA05035E.

(24) Bürgi, T. Properties of the Gold–Sulphur Interface: From Self-Assembled Monolayers to Clusters. *Nanoscale* **2015**, *7* (38), 15553–15567. https://doi.org/10.1039/C5NR03497C.

(25) Poole, C. P.; Owens, F. J. *Introduction to Nanotechnology*; A John Wiley & Sons, Inc., publication; Wiley, **2003**.

(26) Munir, A.; Haq, T. ul; Qurashi, A.; Rehman, H. ur; Ul-Hamid, A.; Hussain, I. Ultrasmall Ni/NiO Nanoclusters on Thiol-Functionalized and -Exfoliated Graphene Oxide Nanosheets for Durable Oxygen Evolution Reaction. *ACS Appl. Energy Mater.* **2019**, *2* (1), 363–371. https://doi.org/10.1021/acsaem.8b01375.

(27) Peng, B.; Zhang, Q.; Liu, X.; Ji, Y.; Demir, H. V.; Huan, C. H. A.; Sum, T. C.; Xiong, Q. Fluorophore-Doped Core–Multishell Spherical Plasmonic Nanocavities: Resonant Energy Transfer toward a Loss Compensation. *ACS Nano* **2012**, *6* (7), 6250–6259. https://doi.org/10.1021/nn301716q.

(28) Klochko, O. P.; Fedyunyayeva, I. A.; Khabuseva, S. U.; Semenova, O. M.; Terpetschnig, E. A.; Patsenker, L. D. Benzodipyrrolenine-Based Biscyanine Dyes: Synthesis, Molecular Structure and Spectroscopic Characterization. *Dyes Pigments* **2010**, *85* (1–2), 7–15. https://doi.org/10.1016/j.dyepig.2009.09.007.

(29) Prousis, K. C.; Canton-Vitoria, R.; Pagona, G.; Goulielmaki, M.; Zoumpourlis, V.; Tagmatarchis, N.; Calogeropoulou, T. New Cationic Heptamethinecyanine-Graphene Hybrid Materials. *Dyes Pigments* **2020**, *175*, 108047. https://doi.org/10.1016/j.dyepig.2019.108047.

Chapter 5. Encapsulation of organic dyes in calix[6]arene-based cages

5 Introduction

According to the IUPAC definition, a cage molecule is a "*polycyclic compound with the shape of a cage*."[1] Various types of cages are documented in the literature, ranging from coordination and inorganic cages[2–4] to organic and supramolecular cages.[5] Molecular cages provide precisely tailored cavities that facilitate the encapsulation of guest molecules through a series of non-covalent interactions.[6] The selective encapsulation of guests is governed by the complementary size, shape, and functionalization of the host's cavity. This process isolates the guest molecules within the three-dimensional host structure, shielding them from the external environment and endowing the encapsulated species with distinct physicochemical properties due to the constrained environment within the host. In this context, numerous supramolecular research groups have concentrated on the synthesis of molecular cages with tailored cavities designed for a range of applications, including molecular recognition, separation,[7] reactive species stabilization,[8] and catalysis,[9,10] among others.[11,12]

This chapter focuses on the study of organic cages. Typically, an organic cage is an organic molecule where the structure forming the cage consists of carbon-carbon bonds, often incorporating functional groups commonly found in organic molecules. The synthesis of covalent cages involves the convergent assembly of components to form a robust central cavity. The design of the building blocks is critical to the success of this process, with key factors including the molecular shape, spatial conformation, and the functional groups involved in the covalent linkage. One of the earliest examples of an organic cage compound (from now on, simply "cage") was introduced by Jean-Marie Lehn,[13] who extended crown ethers into three-dimensional molecules known as *cryptands*, which, according to the IUPAC definition, qualify as cage compounds. Later, in 1984, Fritz Vogtle's group synthesized a cage compound, marking the first artificial cage compound with a specific function, which served as a ligand for Fe^{3+}.[14] These initial examples of cages were constructed using irreversible covalent bonds. Indeed, the synthesis of organic cages can be approached through the formation of either reversible or irreversible bonds. Irreversible bonds have seen limited use in molecular cage synthesis due to their tendency to produce low yields, undesired oligomerization by-products, and generally required multistep synthesis. Additionally, the inflexibility of irreversible bonds, where errors during cage formation cannot be corrected, further reduces the overall yield as the number of required reactions increases. However, these bonds do offer the advantage of greater stability. In recent years, the utilization of reversible bond formation has become increasingly prevalent. This approach, known as "dynamic covalent bond formation," involves reversible processes of bond formation and cleavage, which continue until a thermodynamically

stable product is achieved. The major advantage of this method lies in its ability to construct complex structures from simple building blocks in a single reaction, often yielding high efficiency. This technique is a key aspect of dynamic covalent chemistry (DCC), a concept introduced by Jean-Marie Lehn[16], which exploits the formation of reversible bonds to reach the most thermodynamically stable product. Among the most widely used motifs in DCC is imine bond formation. In 1991, Cram and colleagues pioneered the use of reversible imine bond formation, involving the reaction between amines and aldehydes, to synthesize a hemicarcerand cage in high yield.[15] Since then, reversible bonds have been extensively utilized in the synthesis of cages. In 2008, Mastalerz *et al*.[17,18] investigated the influence of functional group positioning, specifically hydroxyl substituents, on cage formation. Their study demonstrated that the condensation of triptycene triamine (**I**) with salicyldialdehyde (**II**) yielded an *endo*-functionalized [4+6] cage compound (**IV**), whereas the use of dialdehyde (**III**) featuring hydroxyl groups at the 4,6-positions, resulted in the formation of *exo*-functionalized [4+6] cage (**V**) (**Figure 5.1**, (***a***)).

The same research group further explored the impact of linker rigidity on cage formation.[29] They examined two bis(salicylaldehyde) precursors (**VI** and **VII** in **Figure 5.1**, (***b***)) and found that the more flexible linker (**VII**) produced lower yields compared to the more rigid one (**VI**), leading to the conclusion that a predefined geometry of the reaction linkers is advantageous for cage formation.

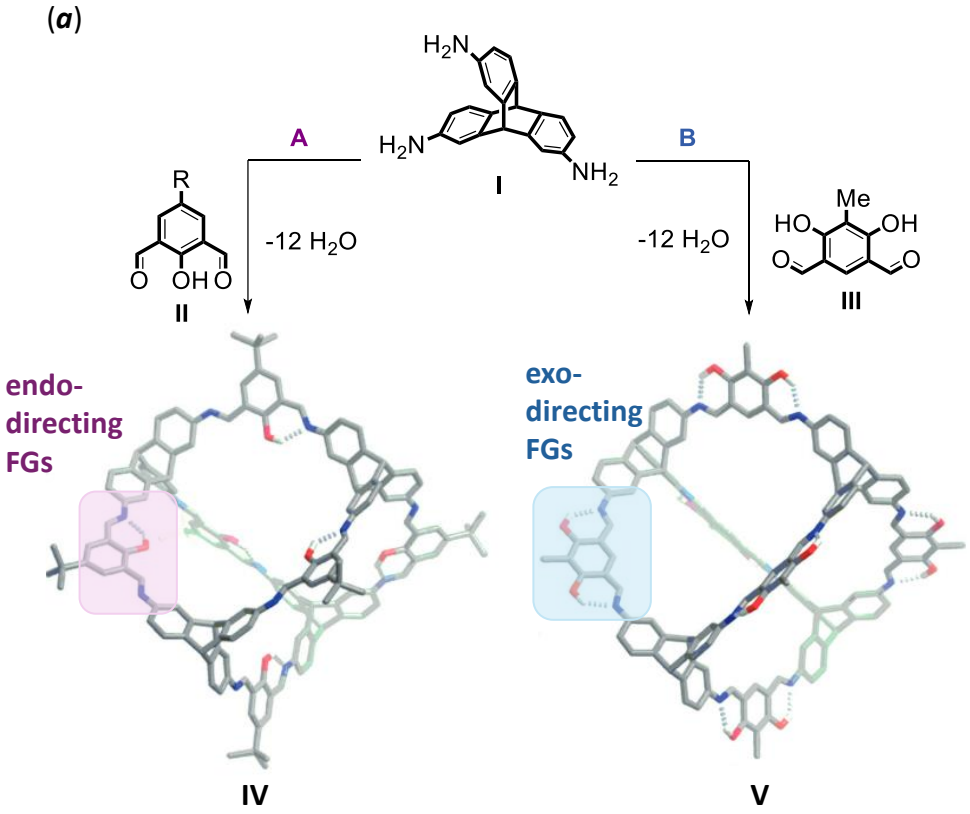

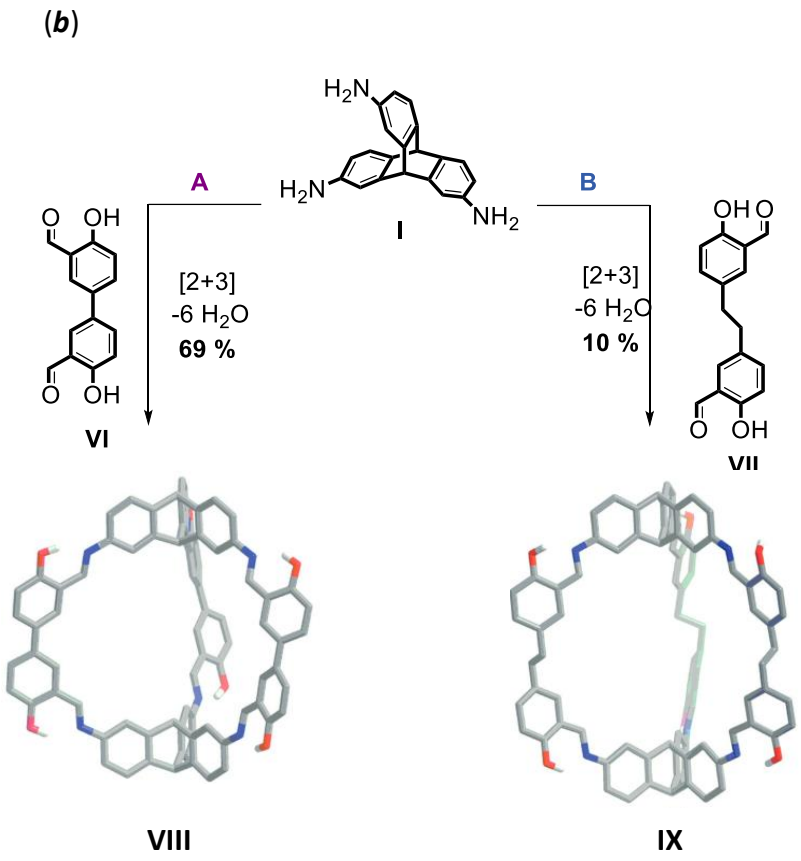

Figure 5.1. (***a***): Formation of *endo*- (**IV**) and *exo*- (**V**) cages. The structure of **IV** represents a single crystal X-ray structure, while the structure of **V** is based on an AM1-model. Partially adapted from ref. 18, © copyright *Chem. Commun.* **2012**; (***b***): formation of cages **VIII** and **IX** with rigid and flexible linkers. The structures of the cages represent single X-ray crystal structures. Partially adapted from ref. 19, © copyright *Chem. – Eur. J.* **2012**.

Additionally, it was observed that the solvent choice significantly influences the shape of the resulting molecular cages. Warmuth *et al*., in 2006,[20] investigated the formation of cavitand-based cages and demonstrated that the cage geometry is influenced by the solvent used during the synthesis. Specifically, the use of $CHCl_3$ resulted in an octahedral structure, THF produced a tetrahedral structure, and CH_2Cl_2 led to the formation of a square-antiprismatic cage. Moreover, other factors can also affect cage formation, such as the presence or absence of specific reactants. For instance, Hasell *et al*.[21] found that the reaction of a tri-aldehyde with a diamine produced different outcomes depending on the presence of trifluoroacetic acid (TFA). In the absence of TFA, a monomeric cage **X** was formed, whereas the presence of TFA under identical conditions resulted in an interpenetrated cage catenate **XI** (**Figure 5.2**).

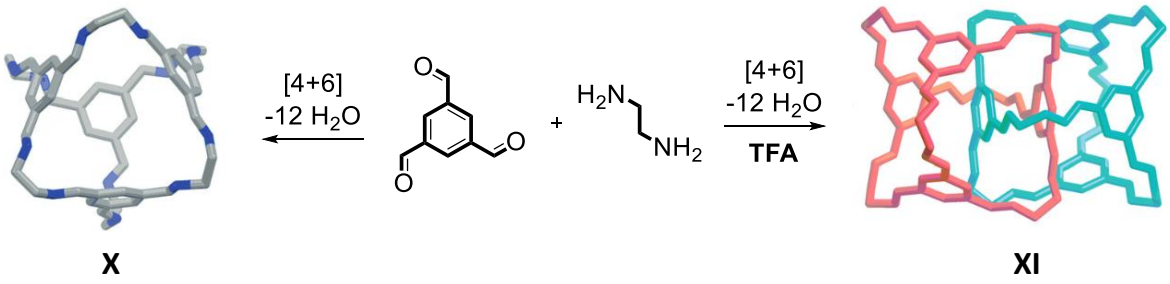

Figure 5.2. Formation of the monomeric cage **X** and interlocked structure **XI** in absence and presence of TFA, respectively. Partially adapted from ref. 21, © copyright *Nat. Chem.* **2010**.

Mukherjee *et al*.[22] investigated the concept of adaptive chemistry by reacting two isostructurally similar dialdehydes with two triamines that primarily differed in their structural rigidity (**Figure 5.3**). When these four components were mixed, only the formation of two distinct cages (**XVI** and **XVII**), each containing one flexible (**XII** or **XIII**) and one rigid unit (**XIV** or **XV**), was observed. This outcome demonstrated high fidelity in self-recognition during the assembly process.

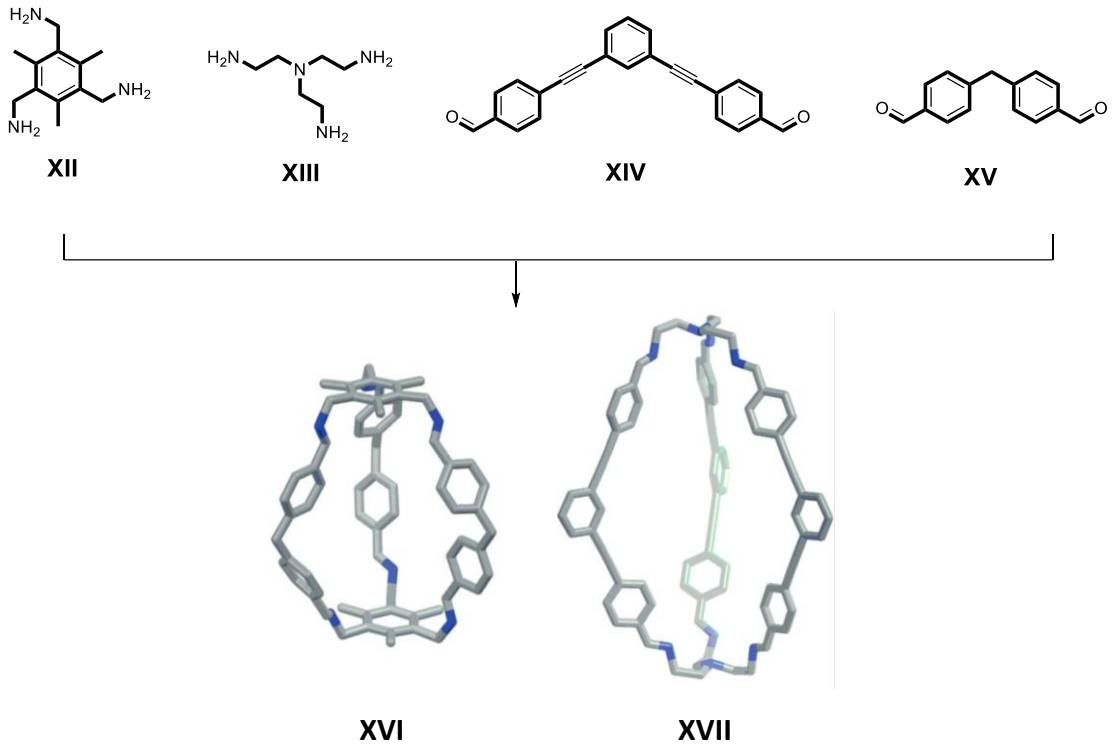

Figure 5.3. Selective formation of cages **XVI** and **XVII**. Partially adapted from ref. 22, © copyright *J. Am. Chem. Soc.* **2013**.

A less commonly utilized type of reversible bond formation is the dynamic boronic ester formation between boronic acids and diols, which is less prevalent in the literature compared to imine bond formation. One of the few examples was reported by Kubo *et al*.[23] in 2007, where a covalent cage was synthesized *via* the condensation of a rigid cyclotricatechylene (CTC) and a flexible hexahomotrocalix[3]arene trisboronic acid. This reaction was notably enhanced by the addition of

$Et_4N^+OAc^-$, with the cation acting as a template through cation-π interactions. In 2008, Kobayashi and Nishimura described the synthesis of a large molecular cage (**XVIII**) by reacting a tetraboronic acid cavitand with a flexible tetraol (**Figure 5.4**).[24] The resulting cage was capable of encapsulating various diaryl and anthracene derivatives.

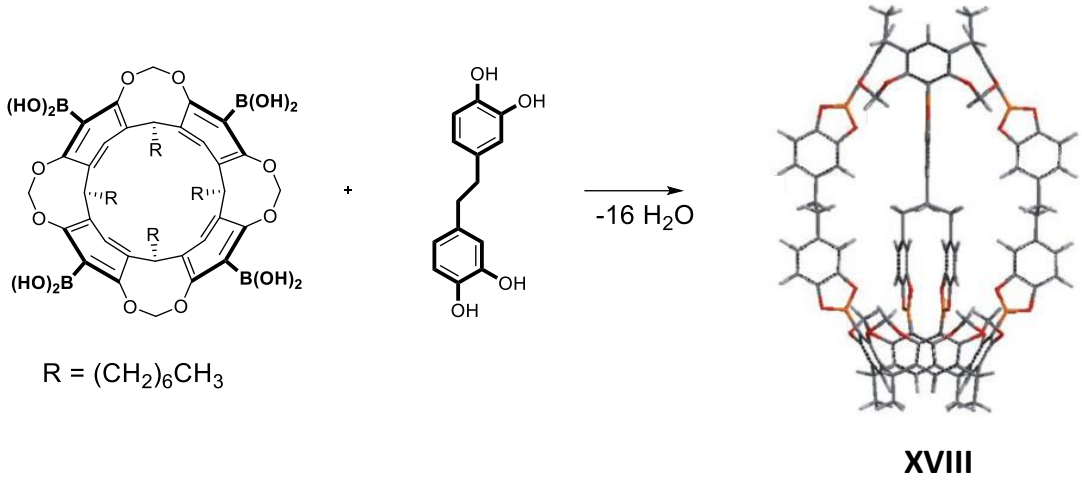

Figure 5.4. [4+2] Condensation of tetaboronic cavitand and a flexible tetraol. The structure of cage **XVIII** is based on Spartan '06 calculations. Partially adapted from ref. 24, © copyright *Angew. Chem.* **2008**.

The formation of boronic esters in conjunction with imine bond formation has also been employed. However, a significant drawback of this combination is the potential catalysis of imine bond hydrolysis by boronic acids. Despite this challenge, the combination of these two types of reversible bonds can be harnessed for the construction of molecular cages. In 2007, Kay *et al.*[25,26] demonstrated the simultaneous use of imine and boronic ester bond formation to construct large macrocycles. When both imine and boronic ester moieties are present within the same molecule, B-N interactions can occur, stabilizing the system.

Additionally, another dynamic covalent bond formation, albeit with limited examples, is alkyne metathesis. Wei Zhang and colleagues reported a successful instance in which a porphyrin-based molecular cage (**COP-5**) was synthesized *via* alkyne metathesis, exhibiting high selectivity in binding C_{70} over C_{60}.[27] Furthermore, the combination of olefin metathesis and imine bond formation has been explored. Okochi *et al.* reported an example where the orthogonal nature of these two reactions was utilized in a one-pot synthesis.[28] The formation of cage **XIX** (**Figure 5.5**) was achieved through the initial condensation of an amine with an aldehyde, followed by direct olefin metathesis, yielding the cage **XIX** with a 51% yield.

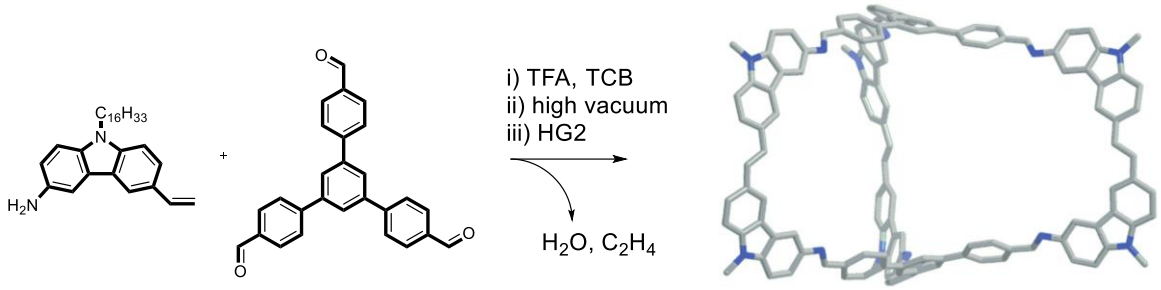

XIX

Figure 5.5. Synthesis of cage **XIX** *via* imine bond formation and olefin metathesis. Partially adapted from ref. 28, © copyright *Org. Lett.* **2013**.

Despite the suitable geometry and the preorganization of the building blocks, synthesizing molecular capsules remains challenging. To overcome this obstacle, various research groups found an appealing alternative to use template-assisted approaches. The template molecule has the role of spatially arranging the building blocks and stabilizing the intermediates that lead to the formation of the cage. Following this method, Ballester and co-workers recently prepared chiral polyimine capsules (**XX**) through a template-assisted assembly.[29] In this work, a bispyridyl-*N*-oxide was used as a template, which was demonstrated to form hydrogen interactions with two tetra-aldehyde calix[4]pyrrole units simultaneously (**Figure 5.6**). In such a manner, two monomers were brought in proximity, promoting the capsule formation through condensation with suitable diamines as linkers. When no template was added, the result was the formation of insoluble oligomerization products.

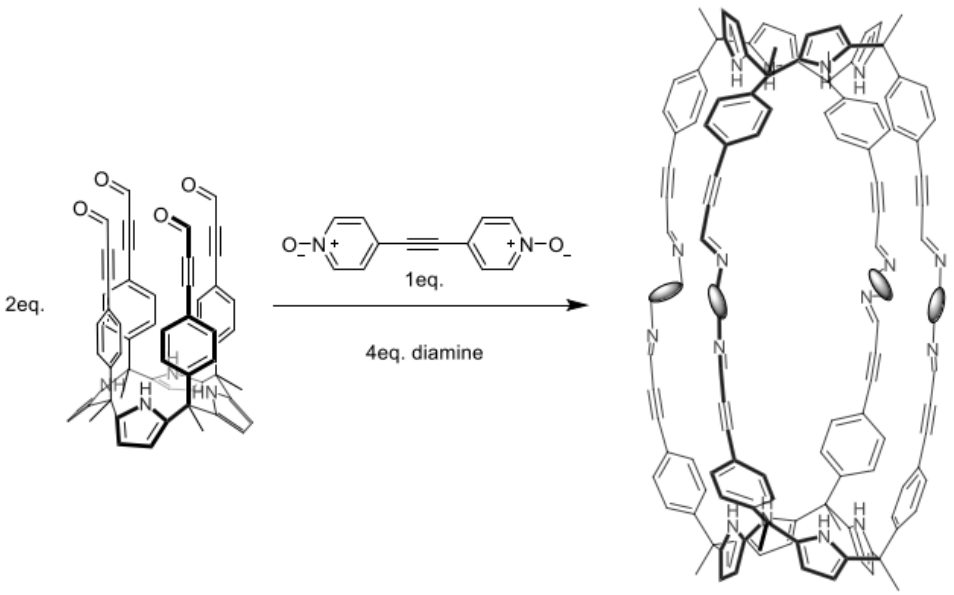

XX

FIgure 5.6. Template assembly of polyimine capsule **XX** from tetraaldehyde calix[4]pyrrole in the presence of bispyridyl-N-oxide.

There are relatively few examples in the literature concerning calix[6]arenes. Notably, Jabin's group reported the synthesis of several tail-to-tail calix[6]arene tubes designed to encapsulate organic ions (**Figure 5.7**).[30,31] One such example, calix[6]azatube (**XXIII**), was synthesized with yields ranging from 34-42% through the condensation of calix[6]arene (**XXI**), which was functionalized with three tosylate groups on its lower rim, with the *N*-protected triamino calix[6]arene derivative (**XXII**) (**Figure 5.7**, top). The success and favorable yields of this reaction were attributed to the dual role of cesium carbonate: used as a base in combination with K_2CO_3, the cesium cation also acted as a template during the synthesis. Additionally, the reaction between calix[6]arene tri-isocyanate (**XXIV**) and calix[6]arene tri-amine (**XXV**), conducted under high-dilution conditions, produced calix[6]tube (**XXVI**) with a 26% yield, along with a cross-linked by-product (**XXVII**) (**Figure 5.7**, bottom).

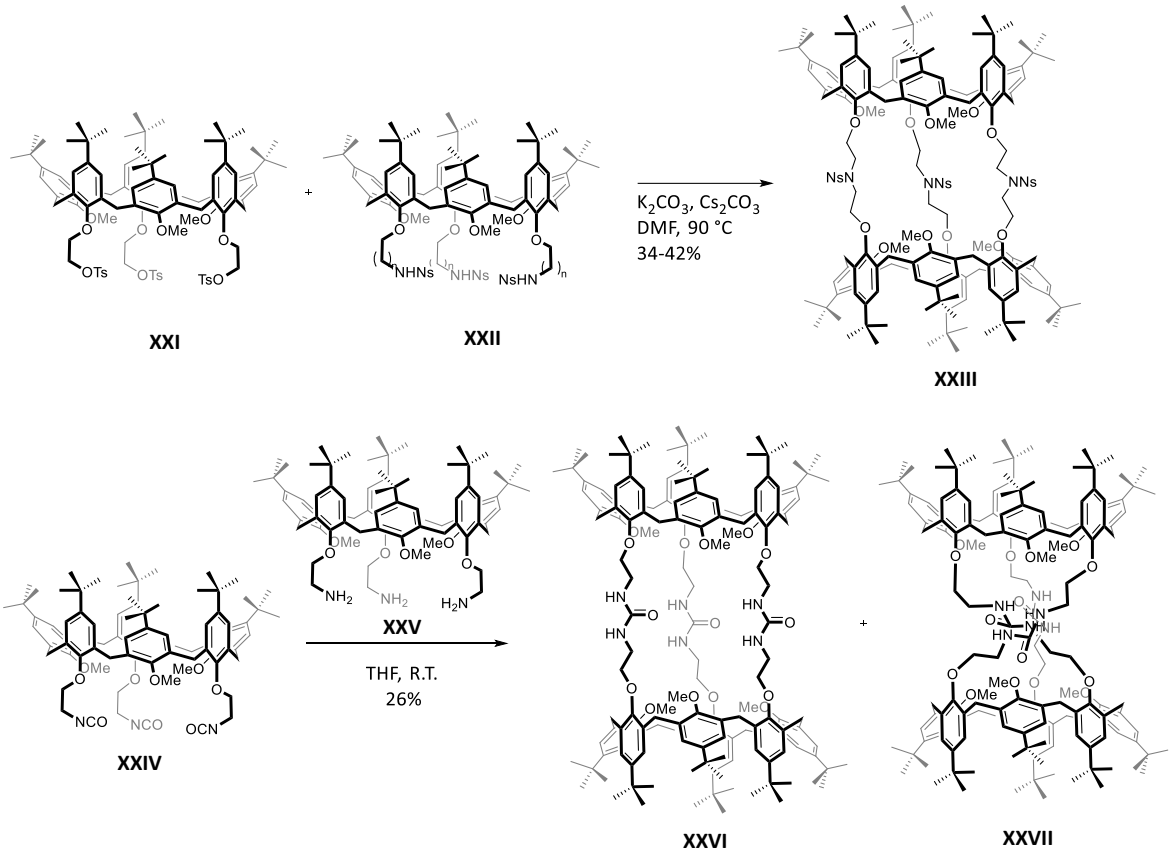

Figure 5.7. Synthesis of tail-to-tail calix[6]arene tubes **XXIII**, **XXVI** and **XXVII**.[30]

In 2000, our group reported the synthesis and complexation properties of covalently-linked double calix[6]arenes featuring imino and 1,4-phenylenediimino bridges (**Figure 5.8**).[32] The reaction between a trialdehyde calix[6]arene derivative and a triamino calix[6]arene yielded the three-point-grafted double calix[6]arene (**XXVIII**) with a 26% yield. Alternatively, the larger dimer (**XXIX**) was synthesized with a 50% yield by condensing two trialdehyde calix[6]arene monomers with 1,4-

diaminobenzene as the linker. However, these bis-calix[6]arenes exhibited limited complexation properties.

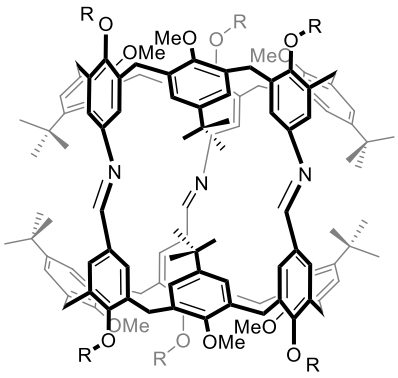

XXVIII

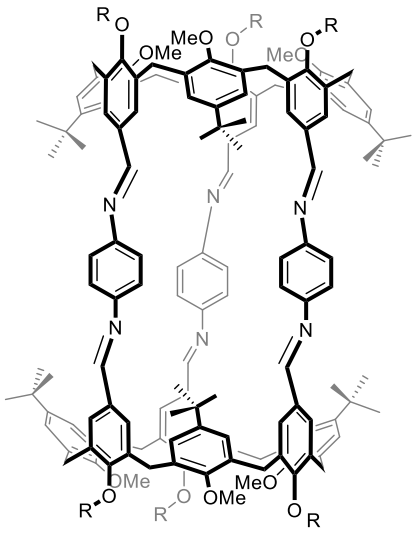

XXIX

Figure 5.8. Polyimino calix[6]arene cages **XXVIII** and **XXIX**.

Aim of the project

In this chapter, the synthesis and characterization of novel head-to-head calix[6]arene-based cages are presented. The cavities of these cages are defined by *N*-phenylureido groups, which are designed to interact with potential guest molecules. Calix[6]arene derivatives with strategically chosen functional groups on the upper rim were selected to construct head-to-head cages through the formation of either ureido or imine bonds, depending on the chosen linker molecule. Thus, both irreversible and reversible approaches were employed: ureido bonds provided strong, covalent, irreversible connections, while imine bonds were utilized for their reversible nature. In certain cases, a template-directed synthesis approach was utilized, with bis-viologen salts serving as templates due to their ability to interact with the *N*-phenylureido moieties of the calix[6]arene. The presence of a template molecule preorganized the calix[6]arene macrocycles into an optimal geometry, facilitating the subsequent formation of the cage upon adding a linker molecule. In other instances, the template approach was not required; instead, two distinct calix[6]arene units, bearing complementary functionalities on their upper rims, were directly reacted to form the cages without needing a linker molecule. The resulting supramolecular cages were subjected to complexation experiments with various organic guests. The interactions between the cages and guests were assessed using NMR spectroscopy, while association constants were determined where possible through UV-Visible and fluorescence spectroscopy.

5 Results and Discussion

Cages synthesis

In our research group, we previously synthesized three calix[6]arene-based cages (**Figure 5.9**) utilizing a template-assisted strategy.[33] The approach leveraged *N*-phenylureido moieties on the upper rim of calix[6]arene macrocycles to promote hydrogen bonding interactions with a template molecule, thereby facilitating the formation of the cages (**Scheme 5.1**). The template molecules used in this approach consisted of bis-viologen salts characterized by an alkyl spacer between the two bispyridinium units of different lengths. Initially, a [3]pseudorotaxane complex was formed by reacting the template with 2 equivalents of a suitably functionalized calix[6]arene derivative (**Scheme 5.1**, 1). Then, the addition of 3 equivalents of a linker molecule afforded the formation of three-arm bridged calix[6]arene cages through a clipping reaction (**Scheme 5.1**, 2). Thanks to chromatographic purification, the template was dethreaded, yielding an empty calix[6]arene-based cage (**Scheme 5.1**, 3). The *N*-phenylurea groups decorating the cavity of these cages enable the complexation of organic guests, making these structures effective as supramolecular containers.

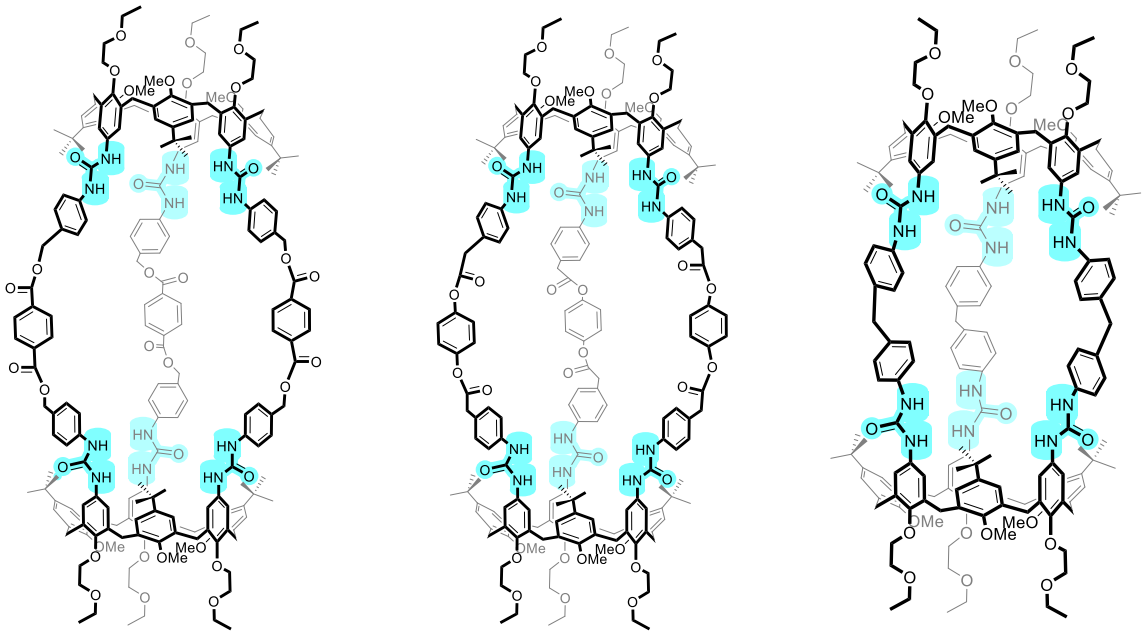

XXX **XXXI** **XXXII**

Figure 5.9. Structure of previously synthesized calix[6]arene-based cages.

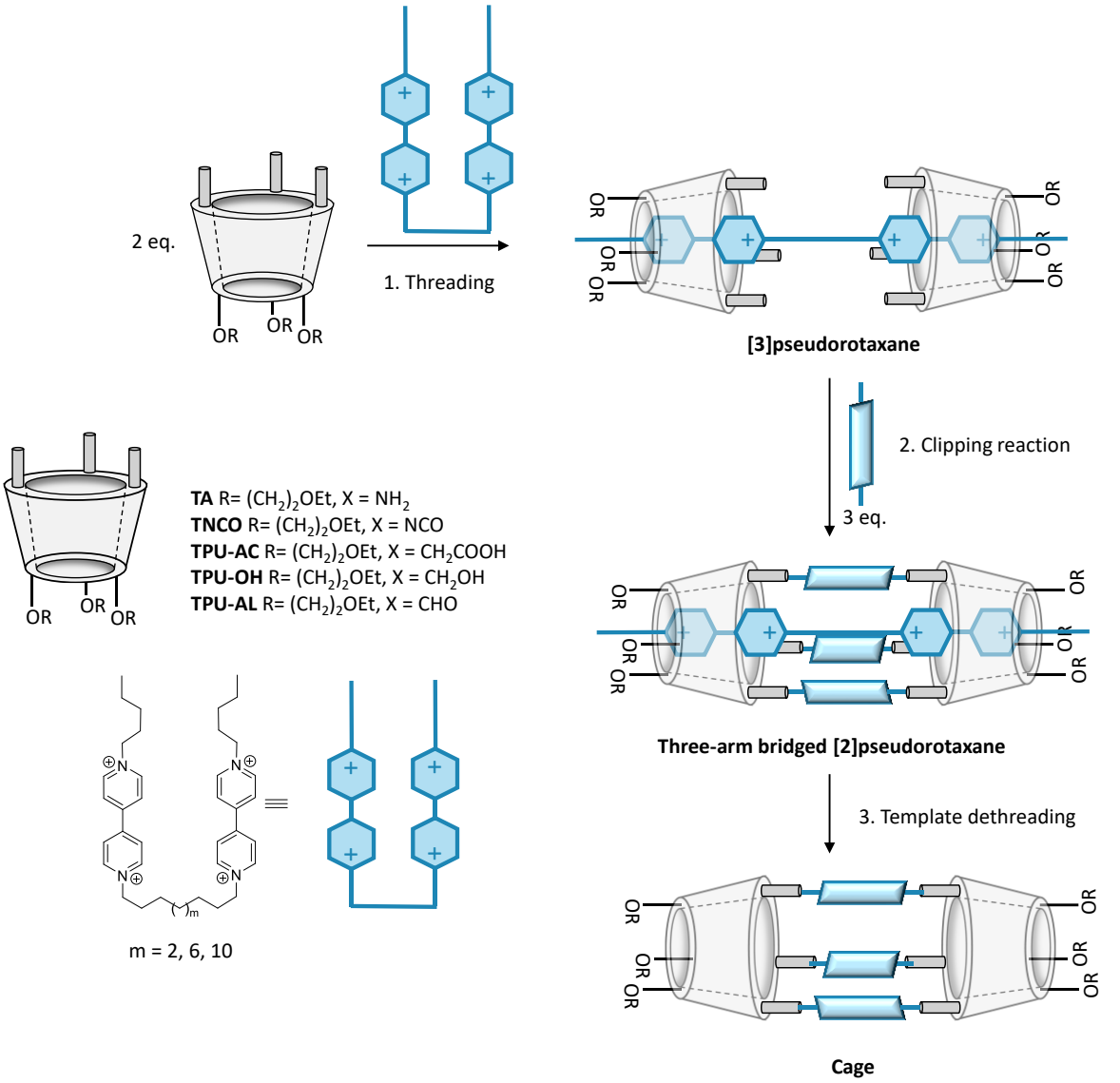

Scheme 5.1. Template-assisted strategy for the synthesis of calix[6]arene-based cages. The counterions of the template axle were not shown for clarity.

Based on this approach, we designed new cages with varying dimensions and shapes (**Figure 5.10**). The aim was to obtain cages with smaller and more rigid cavities to enhance the selective complexation of organic guests. The first two cages, **Cage 1** and **Cage 2**, were characterized by *N*-phenylurea bonds, while **Cage 3** featured imine bonds. Finally, **Cage 4** combined both imine and urea groups, resulting in an asymmetric cage structure.

Synthesizing these new cages posed a challenge due to the distinct properties of the starting calix[6]arene macrocycles and linkers used. The synthesis of **Cage 1** and **Cage 3** was accomplished by using two equivalents of the appropriate calix[6]arene and three equivalents of a suitable linker molecule, which led to three bridges connecting the two macrocycles. For **Cage 2** and **Cage 4**, two complementary calix[6]arene macrocycles were used to form three arms without the use of a linker molecule.

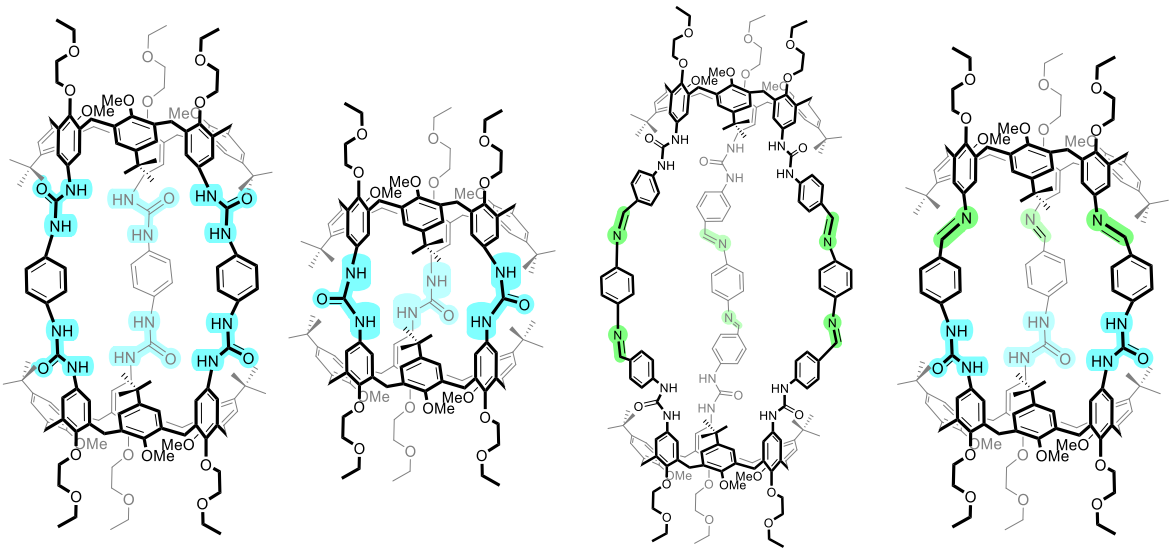

Figure 5.10. Structure of new supramolecular calix[6]arene-based cages. *N*-phenylurea groups highlighted in clear-blue, imine bonds highlighted in green.

Synthesis and Characterization of Cage 1

The synthesis of **Cage 1** was achieved using the well-known calix[6]arene tri-ammino (**TA**) as starting material. This calix[6]arene features three ammino groups on the upper rim and three ethoxy chains on the lower rim. We exploited a well-established organic reaction in which an amino group reacts with an isocyanate to form a urea derivative. Thus, **Cage 1** was synthesized from **TA**[3] using 1,4-phenylene diisocyanate as the linker (**Scheme 5.3**). This linker, characterized by limited rotational freedom, was intended to create a stiffer and smaller cavity. The reaction was conducted under high-dilution conditions ($c = 10^{-4}$ M) to prevent the formation of oligomers. The reaction was tested both with and without the templating effect. As previously specified, the templating effect refers to using a bis-viologen salt capable of guiding the cage assembly by properly orienting, through complexation, two calix[6]arene macrocycles.

Thus, the template effect was evaluated using three different bis-viologen templates, which differ for the length of their internal chain: $\mathbf{3}_8$ having 8 carbon atoms in the central chain, $\mathbf{3}_{12}$ with 12 carbon atoms, and $\mathbf{3}_{16}$ with 16 carbon atoms. The variation in chain length allowed for the study of how the distance between the two bis-pyridinium units affects the interaction between the two calix[6]arene moieties. These bis-viologen salts were prepared in good yields by reacting pentylpyridylpiridinium tosylate (**1**) with the corresponding ditosylate chain ($\mathbf{2}_m$) in refluxing acetonitrile for ten days (**Scheme 5.2**). The identity of the synthesized bis-viologen axles ($\mathbf{3}_m$) was confirmed through NMR spectroscopy and ESI-MS measurements.

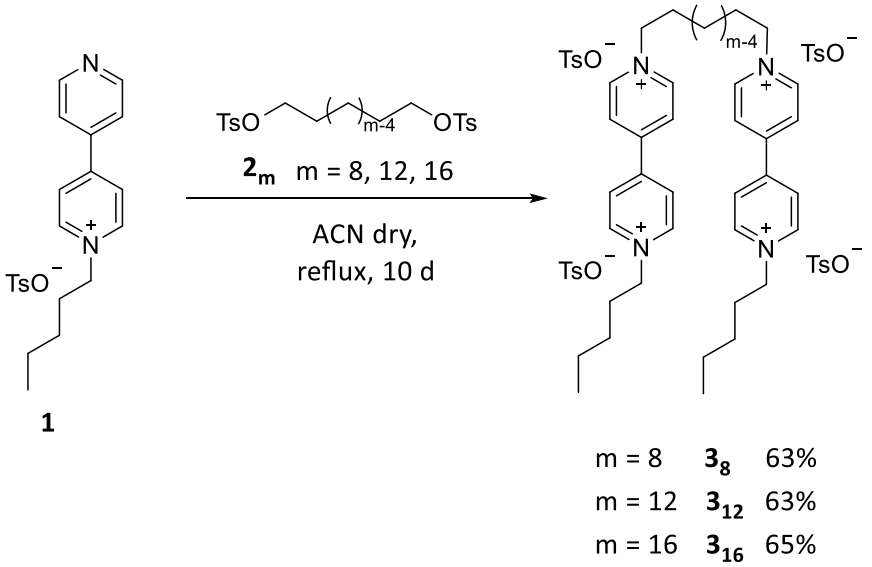

Scheme 5.2. Synthesis of axles $\mathbf{3}_m$.

The templating effect became apparent only upon the formation of the first ureido bond between **TA** and the linker, as shown in **Scheme 5.3**. Initially, **TA** could not interact with the viologen units of the template, as evidenced by the lack of color change of the solution when the template and **TA** were mixed in dichloromethane: the solution remained colorless, and the template did not dissolve, indicating no complexation. However, upon the dropwise addition of the linker, the solution immediately turned red. This color change was a clear evidence of complexation, as calix[6]arene-viologen complexes typically exhibit a red color due to the formation of a CT band. As more linker was added, the solution's red hue intensified, further indicating the progressive formation of the complex. After completing the reaction, chromatographic separation was used to purify and decomplex the system, yielding the free cage. In all cases, including the reaction without the axle, **Cage 1** was detected in the reaction mixtures. The yields for the reactions with $\mathbf{3}_{12}$, $\mathbf{3}_{16}$, and without axle were 60%, 48%, and 58%, respectively, whereas a lower 27% yield was observed with axle $\mathbf{3}_8$. The formation of **Cage 1** in all cases suggests that **TA** does not interact strongly with the templates, indicating that the presence or absence of a template had a minimal impact on the reaction outcome. The low yield with axle $\mathbf{3}_8$ is likely due to its shorter chain length, which may be insufficient to promote the formation of the [3]pseudorotaxane, thereby hindering the formation of the cage.

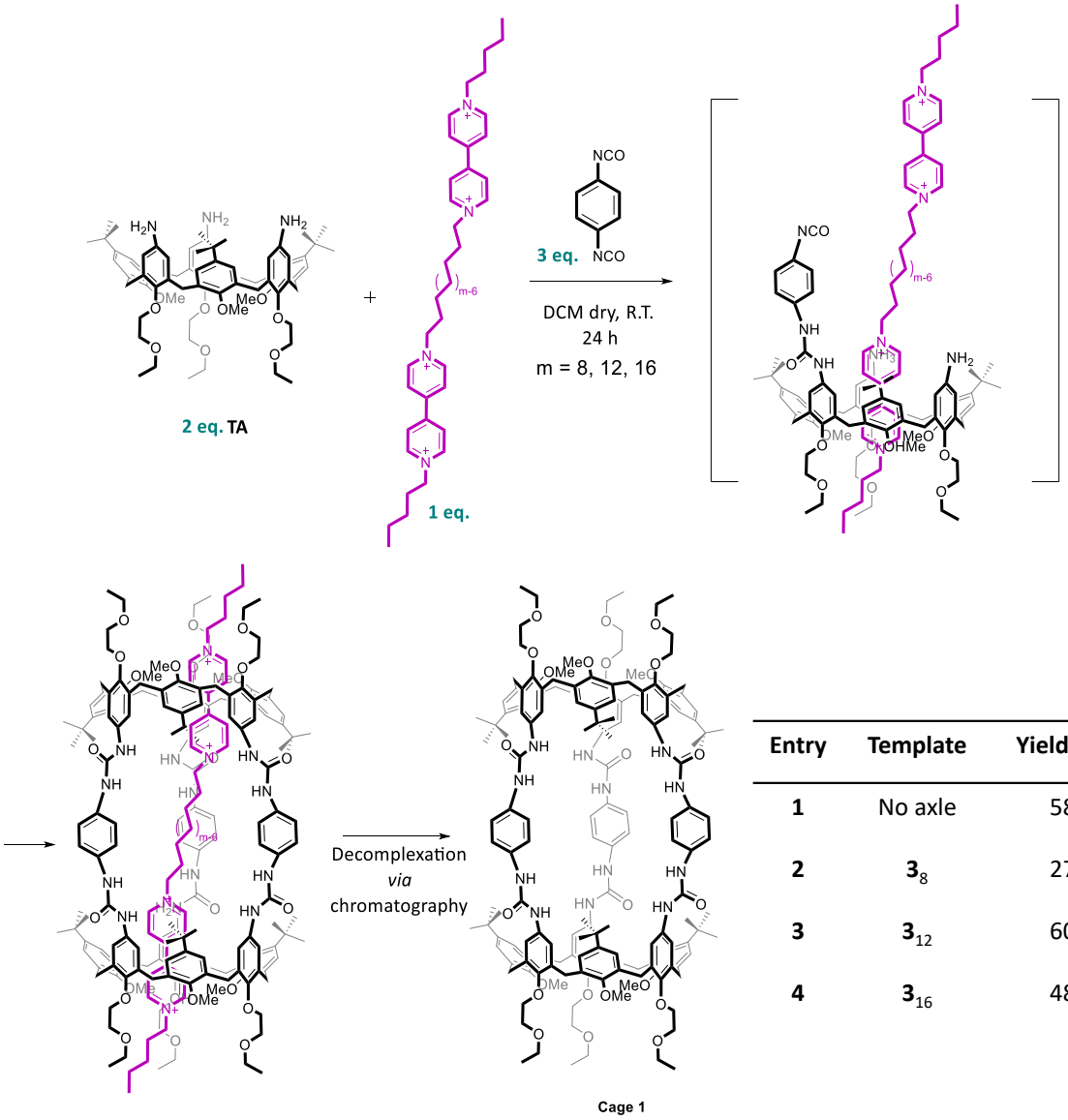

Entry	Template	Yield (%)
1	No axle	58
2	$\mathbf{3}_8$	27
3	$\mathbf{3}_{12}$	60
4	$\mathbf{3}_{16}$	48

Scheme 5.3. Synthesis of **Cage 1**. Tosylate counterions were removed for clarity. Table displaying the yields obtained across the four experimental trials, both in the presence and absence of the template.

The identity of **Cage 1** was confirmed by high-resolution mass spectroscopy (**Figure 5.11**). The peak at m/z = 2698.47593 (z = 1) corresponds to the charged molecular ion, while the peak at m/z = 1349.24114 (z = 2) corresponds to the doubly charged molecular ion. Additional peaks were observed at m/z = 1360.23172 (z = 2), 1372.222569 (z = 2), and 1372.222569 (z = 2), corresponding to adducts with Na^+ and H^+ and with two Na^+ ions, respectively.

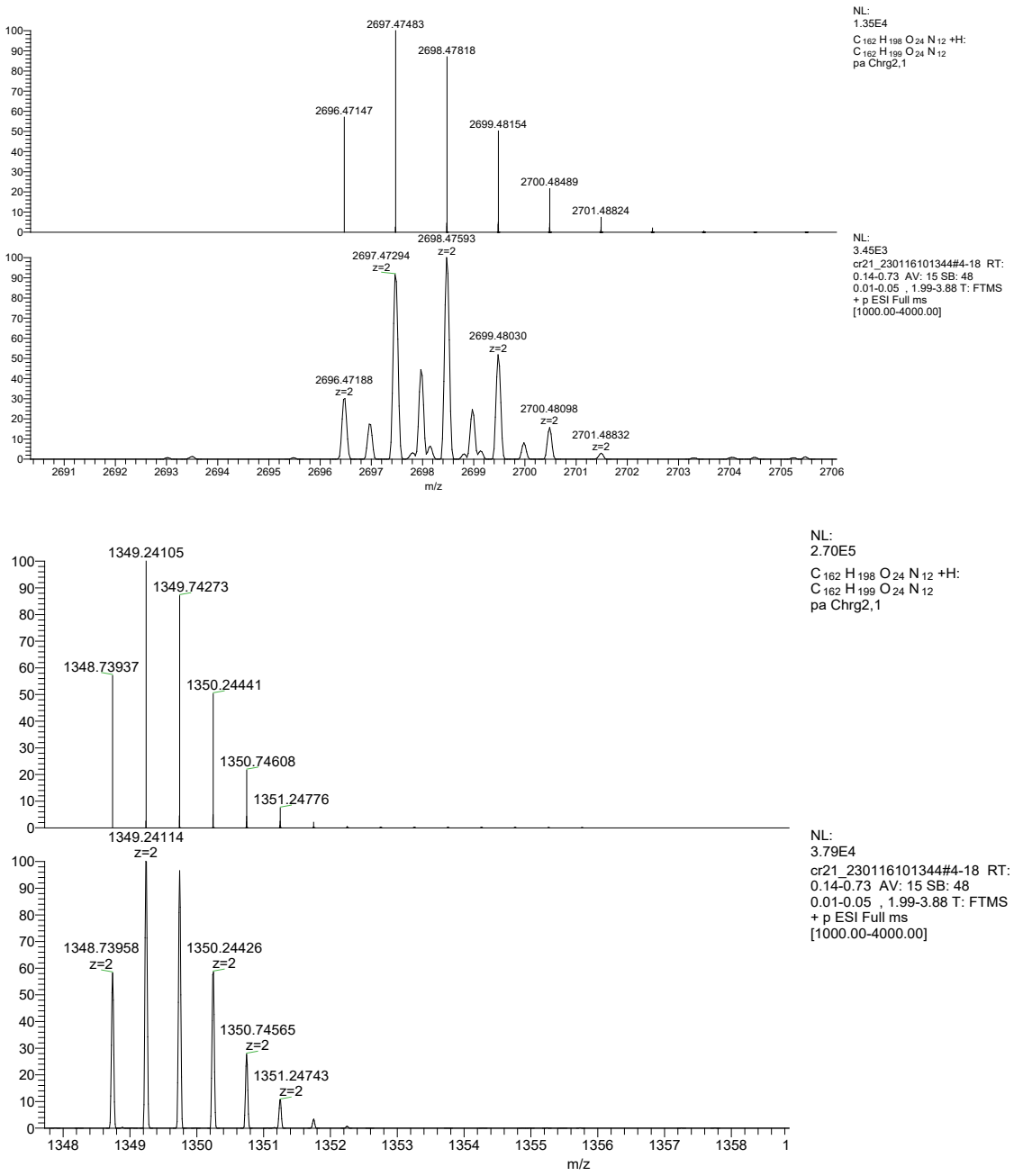

Figure 5.11. Inset of HR-MS (ESI, Orbitrap LQ) spectrum of compound **Cage 1**: experimental and calculated isotopic distribution for the double charged molecular ions. Calculated for $C_{162}H_{199}O_{24}N_{12}$: m/z (z= 1): 2696.47147; found: 2696.47188. Calculated for $C_{162}H_{200}O_{24}N_{12}$: m/z (z= 2): 1348.73937; found: 1348.73958.

NMR measurements were carried out to further characterize **Cage 1**. The ^{1}H NMR spectra were recorded in different deuterated solvents ($CDCl_3$, CD_2Cl_2, TCE-d2, Acetone-d6, ACN-d3), and, surprisingly, no substantial differences in spectral shape were observed across these solvents. In all cases, the NMR spectra were notably broad, indicative of a high structural mobility of **Cage 1** (**Figure 5.12**). Even 2D NMR spectra did not provide clearer structural interpretation, likely due to the dynamic nature of the system.

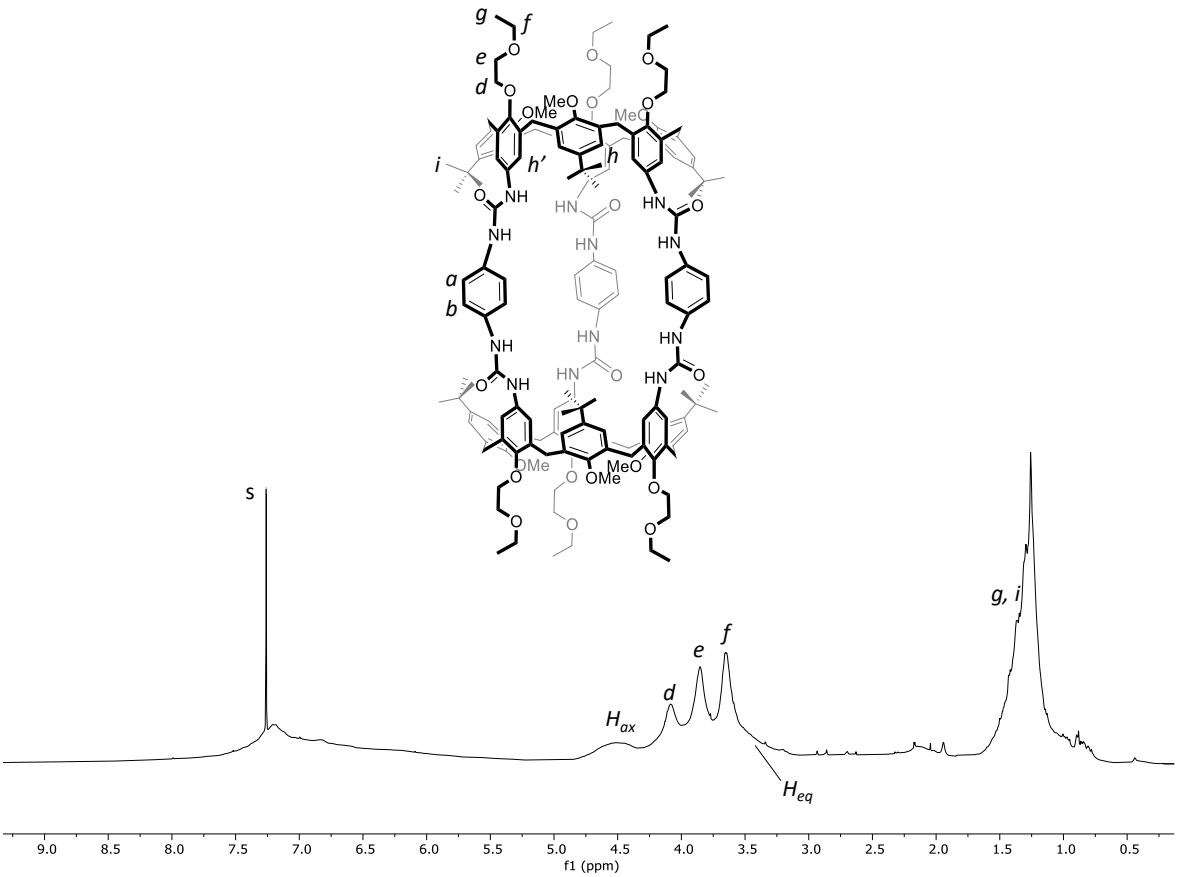

Figure 5.12. ^{1}H NMR spectrum ($CDCl_3$, 400 MHz, 298 K) of **Cage 1**.

We tackled the problem of the poor resolution of the NMR spectra by performing variable temperature (VT) experiments. We expected that lowering the temperature should reduce molecular motion, sharpening the spectral features. **Figure 5.13** shows the result of these measurements. The spectra were recorded in deuterated dichloromethane at temperatures as low as 193 K. Unfortunately, decreasing the temperature only worsened the spectral broadening.

The final approach undertaken to improve the NMR spectrum involved the complexation of **Cage 1** with an organic guest molecule. The rationale behind this strategy was that the complexation might induce a rigidification of the system, thereby enhancing spectral resolution. These attempts are discussed at the end of the chapter.

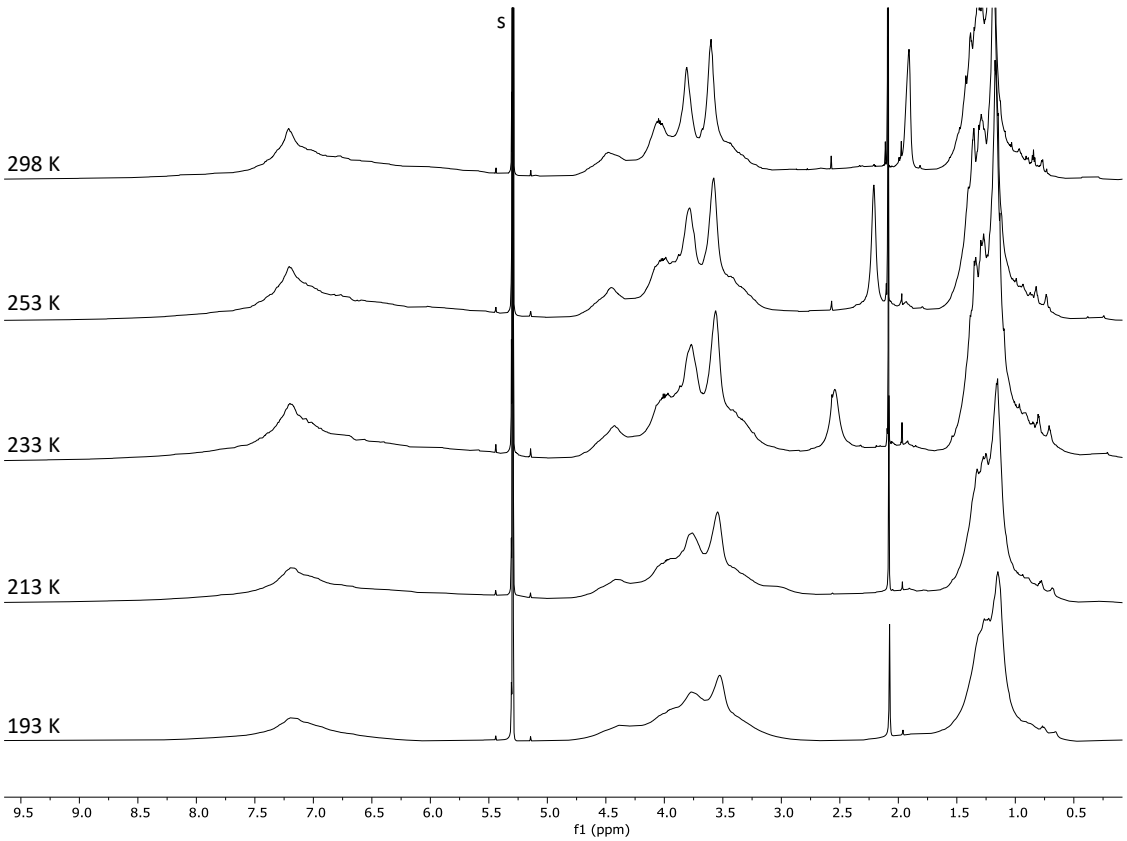

Figure 5.13. ^{1}H NMR stack plot spectra (CD_2Cl_2, 600 MHz) of **Cage 1** at different temperatures.

Synthesis and Characterization of Cage 2

Cage 2 is characterized by a small cavity formed by two calix[6]arene macrocycles, which are linked by three urea-based bridges. Unlike **Cage 1**, no linkers were used in the synthesis of **Cage 2**. Instead, two calix[6]arenes with complementary functional groups were reacted: a tri-amino functionalized calix[6]arenes (**TA**)[4] and a tri-isocyanate calix[6]arene (**TNCO**)[5] (**Scheme 5.4**). This synthetic route, outlined in **Scheme 5.4**, resulted in a 13% yield for **Cage 2**, likely due to the challenge of forming three new urea bonds without inducing side reactions such as oligomerization.

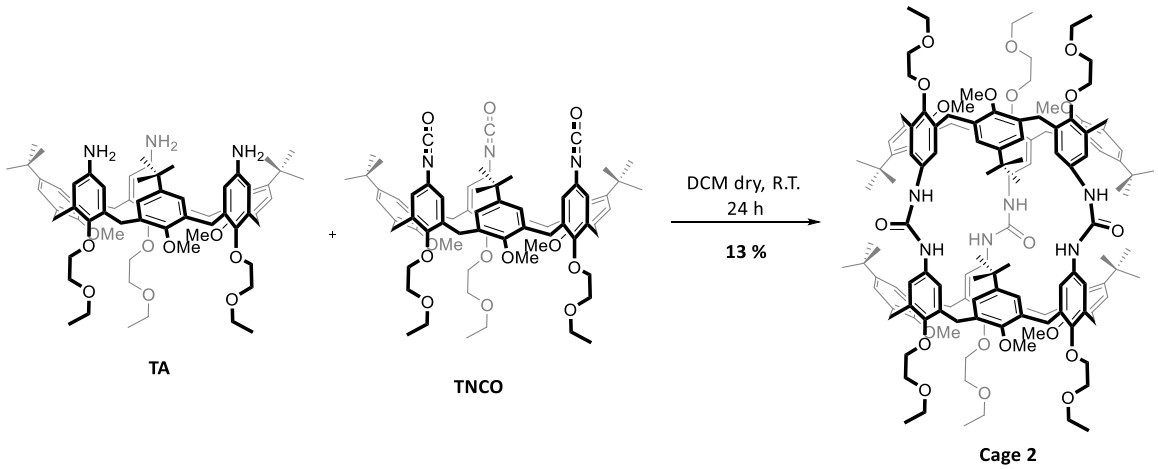

Scheme 5.4. Synthetic route for **Cage 2**.

The higher rigidity of **Cage 2**, compared to **Cage 1**, is evidenced by its ^{1}H NMR spectrum (**Figure 5.14**). Distinct peaks corresponding to the axial and equatorial protons are observed at 4.36 and 3.52 ppm, respectively. Signals for protons *d*, *e*, and *f* of the ethoxy ethyl chains at the macrocycles lower rims are clearly visible at 4.04, 3.83, and 3.65 ppm, respectively. However, the signals related to the aromatic protons remain very broad. The resonance for the aromatic nuclei bearing the *tert*-butyl groups (*h'*) appears as a broad peak at 7.1 ppm, while the signal for protons *h*, which are ortho to the urea groups, is very broad and barely visible around 5.9 ppm. The latter signal is significantly up-field-shifted compared to similar resonances in other *N*-phenylurea-substituted calix[6]arene macrocycles (i.e., **TPU**). Such a shift indirectly confirms the linkage between the macrocycles, as the short bridges impose a trigonal pyramidal shape on **Cage 2**. In this structure, the bridged rings are influenced by the shielding effect of the divergent rings bearing the *tert*-butyl groups. Notably, the NH protons of the urea bridges are not visible in the spectrum, likely due to exchange phenomena in the solvent used.

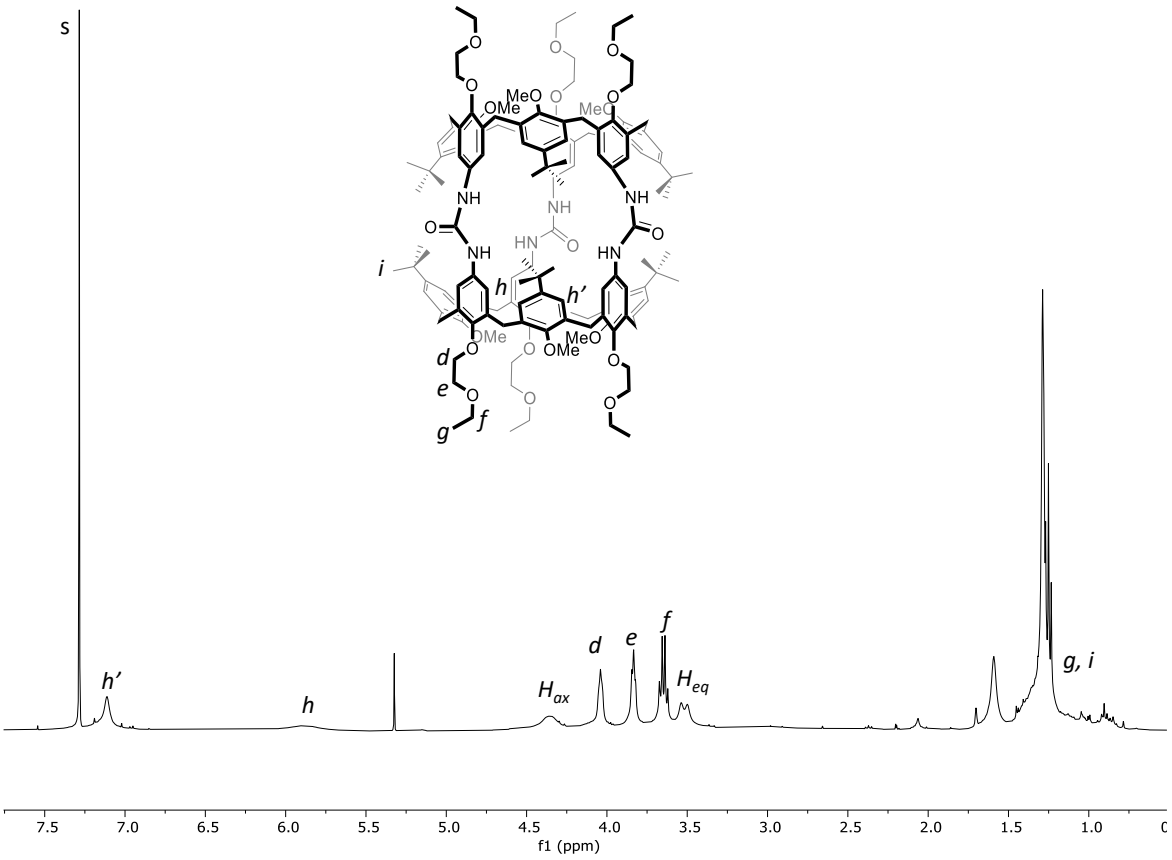

Figure 5.14. ^{1}H NMR spectrum ($CDCl_3$, 400 MHz, 298 K) of **Cage 2**.

A further confirmation of the formation of **Cage 2** was obtained by low-resolution mass spectrometry (LR-MS). The peak observed at m/z = 1148.4 (z = 2) corresponded to the doubly charged molecular ion, while the peak at m/z = 1156.8 (z = 2) was attributed to the adducts of **Cage 2** with H^+ and NH_4^+ ions.

Synthesis and Characterization of Cage 3

The synthesis of **Cage 3** involved a novel calix[6]arene macrocycle featuring three aldehyde functional groups on its upper rim (**TPU-AL**). This novel macrocycle was synthesized as outlined in **Scheme 5.5**.

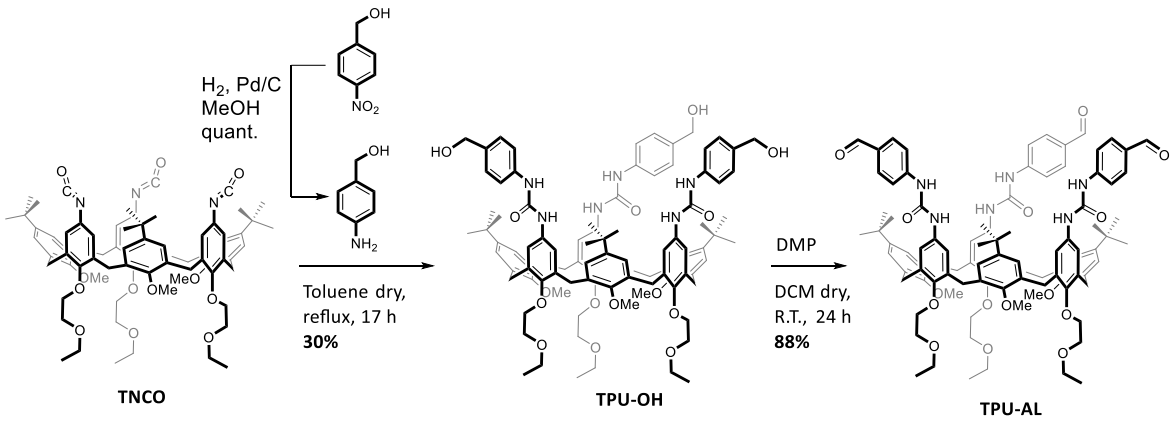

Scheme 5.5. Synthesis of calix[6]arenes **TPU-OH** and **TPU-AL**.

Calix[6]arene **TPU-OH** was obtained from **TNCO**, which was also one of the precursors for **Cage 2**. **TNCO** was reacted with three equivalents of 4-amino-benzyl alcohol, which is a known compound and obtained *via* hydrogenation of 4-nitro-benzyl alcohol over Pd/C[6] (**Scheme 5.5**). The reaction mixture was stirred under reflux in dry toluene for 17 hours. After chromatographic purification, **TPU-OH** was recovered in a 30 % yield as a yellow solid. **TPU-OH** was characterized through NMR and HR-MS (MALDI). The ^{1}H NMR spectrum was recorded in deuterated acetonitrile (**Figure 5.15**, top), with signal assignment confirmed through a 2D HSQC experiment. The aromatic protons were well differentiated, with protons *a* resonating at 7.29 ppm, protons *h* at 7.14 ppm, protons *b* at 7.08 ppm, and protons *h'* displaying a broad singlet at 6.5 ppm. A diagnostic indicator of the free alcohol moiety is observed as a doublet at 4.41 ppm, corresponding to the methylene protons (*c*, circled in red) located at the *para* position relative to the phenylurea groups, along with a triplet at 3.02 ppm, attributed to the hydroxyl groups (*j*, circled in violet). However, the signals corresponding to the bridging methylene protons of the calix[6]arene macrocycle (H_{eq} and H_{ax}) exhibit very broad and nearly indiscernible signals, which suggests significant conformational flexibility and dynamic behavior.

Successively, the target tri-carboxyaldehyde calix[6]arene **TPU-AL** was obtained in 53 % of yield through oxidation of **TPU-OH** with the Dess-Martin periodinane (DMP) in dichloromethane at room temperature (**Scheme 5.5**). **TPU-AL** was characterized using NMR spectroscopy and HR-MS (ORBITRAP LQ). Comprehensive signal assignment was accomplished through a 2D HSQC experiment. The ^{1}H NMR spectrum, recorded in deuterated chloroform, exhibited broad signals

(**Figure 5.15**, bottom); nevertheless, a distinct diagnostic peak at 9.77 ppm was observed, corresponding to the aldehyde protons (*c,* circled in green). Furthermore, the absence of the characteristic signals of **TPU-OH**, specifically the methylene protons at 4.41 ppm (*c*, red circle) and the hydroxyl protons (*j*, violet circle) at 3.02 ppm, further supported the successful conversion to **TPU-AL** calix[6]arene.

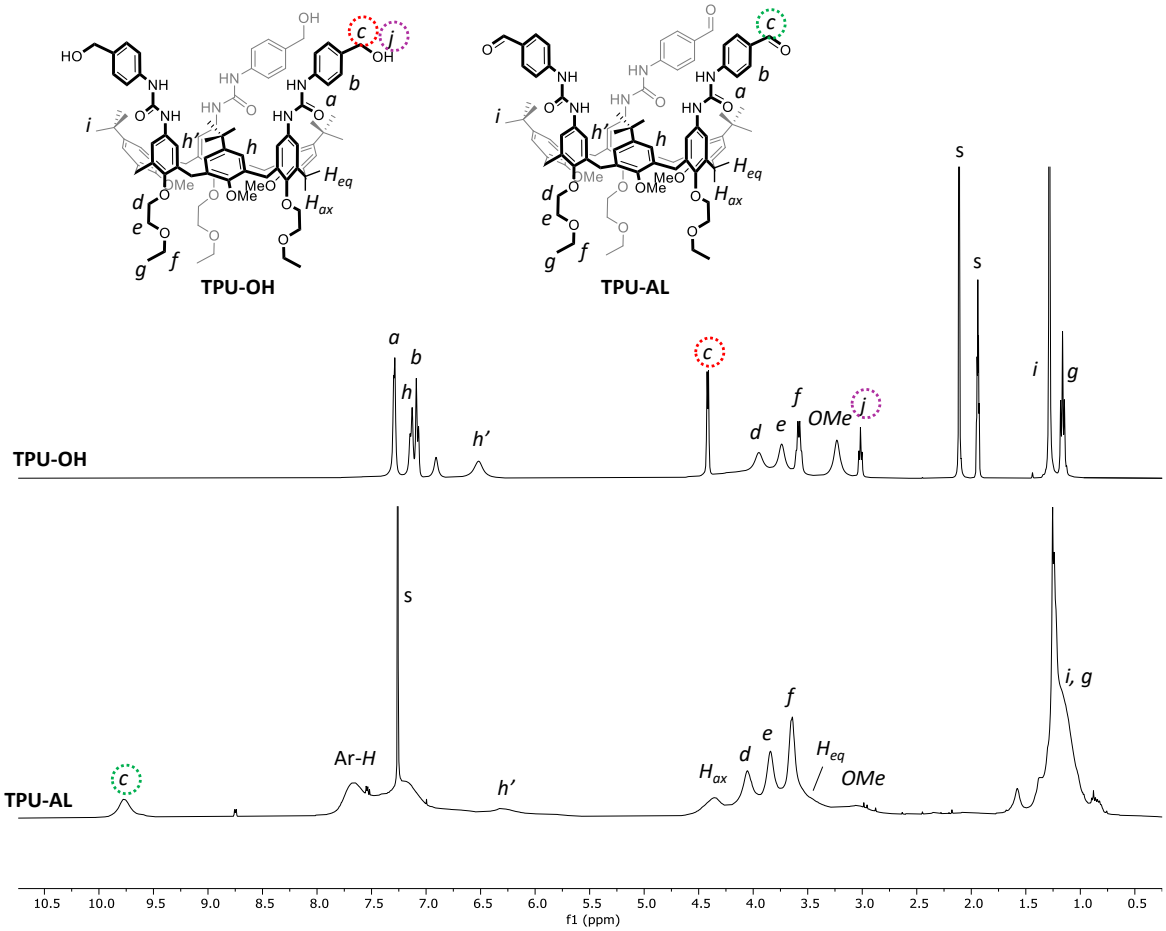

Figure 5.15. ^{1}H NMR stack plot spectra (400 MHz, 298 K) of **TPU-OH** ($CDCN_3$, top) and **TPU-AL** ($CDCl_3$, bottom).

The synthesis of **Cage 3** was accomplished by reacting two equivalents of **TPU-AL** with three equivalents of *p*-phenylenediamine, resulting in the formation of six imine bonds (**Scheme 5.6**). The *p*-phenylenediamine linker was selected due to its rigidity and aromatic structure, which should minimize the probability of intramolecular bridging reactions. The templating effect was studied using the three bis-viologen salts $\mathbf{3}_m$ previously employed for the synthesis of **Cage 1**. The reaction was performed in dichloromethane at room temperature for 24 hours, followed by chromatographic separation using dichloromethane:methanol = 95:5 as the eluent. In the template-assisted synthesis, **TPU-AL** was first equilibrated with the appropriate bis-viologen, after which a dilute solution of the linker was added dropwise to the reaction mixture. The yields of the isolated **Cage 3** were as follows: 48 % without a template, 52% with $\mathbf{3}_8$, 51% with $\mathbf{3}_{12}$, and 50% with

$\mathbf{3}_{16}$. These comparable yields highlight the reversible nature of the imine bond, as discussed in the Introduction.

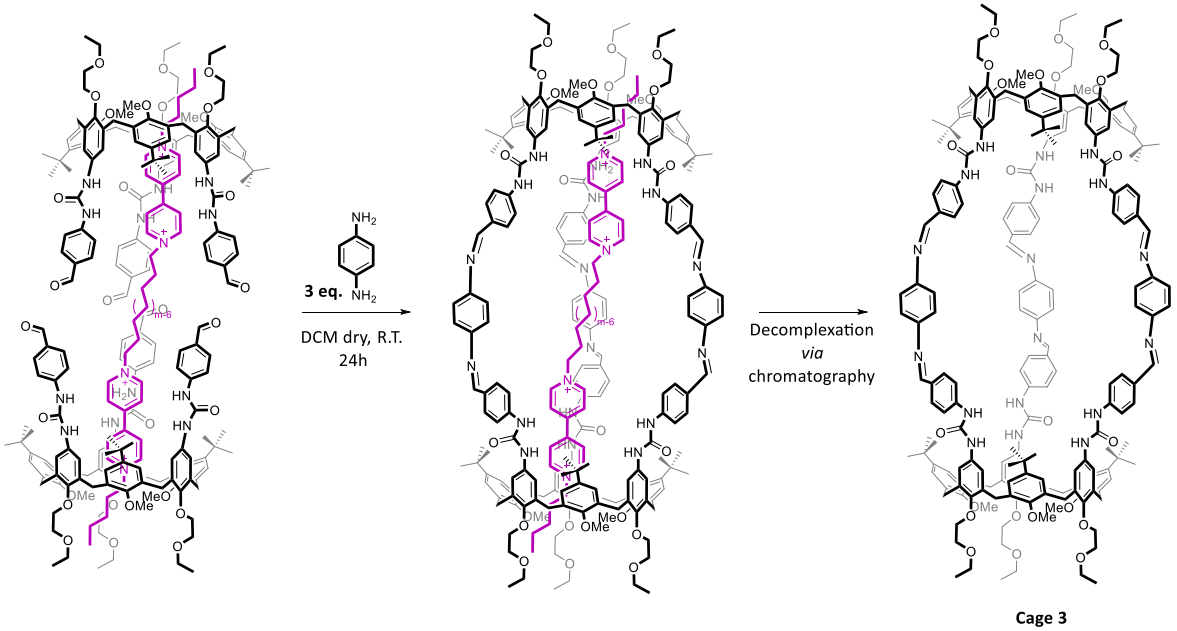

Entry	Template	Yield (%)
1	No axle	48
2	$\mathbf{3}_{8}$	52
3	$\mathbf{3}_{12}$	51
4	$\mathbf{3}_{16}$	50

Scheme 5.6. Synthesis of **Cage 3**.

Cage 3 formation was confirmed by HR-MS (ORBITRAP LQ). The recorded MS spectrum displays a doubly charged molecular ion at m/z 1658.86598, whose isotopic pattern agrees with the doubly charged target molecule (**Figure 5.16**). ^{1}H NMR measurements at different temperatures afforded broad spectra in which the signal assignment was barely possible (**Figure 5.17**). Fortunately, some key features of the calix[6]arene scaffold were detected in the corresponding 2D HSQC spectrum taken in $CDCl_3$ (**Figure 5.18**). In particular, a weak but recognizable cross-peak at *F*2,*F*1 = 8.32,156 ppm corresponds to the six imine protons *c* of the bridges. Due to the high fluxionality of **Cage 3**, these protons are barely seen in the corresponding ^{1}H spectrum (**Figure 5.17**).

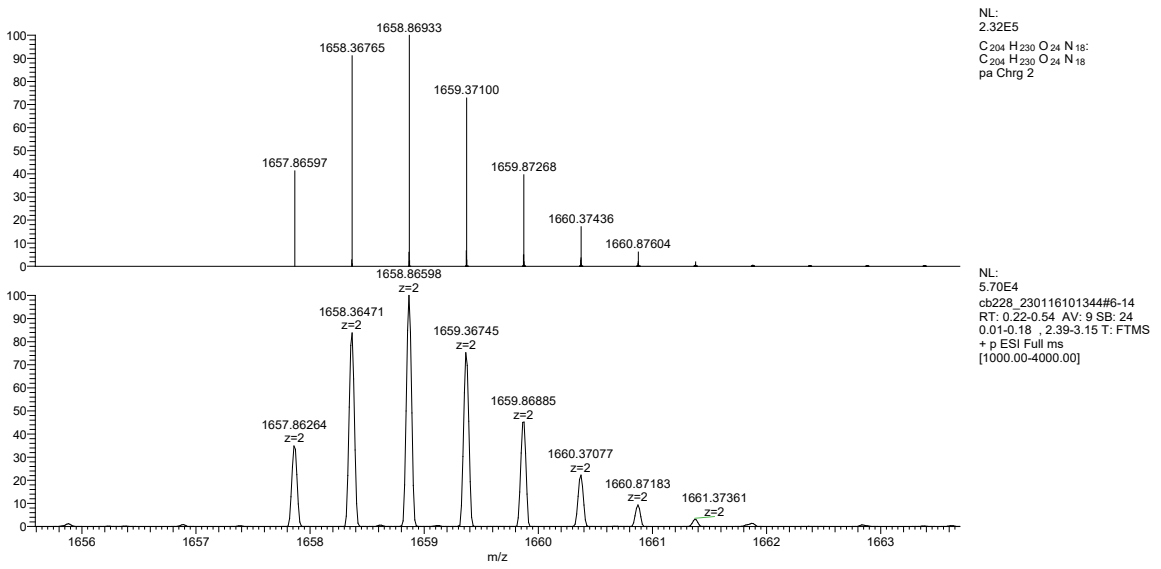

Figure 5.16. Inset of HR-MS (ESI, Orbitrap LQ) spectrum of compound **Cage 3**: calculated (top) and experimental (down) isotopic distribution for the doubly charged molecular ion. Calculated for $C_{204}H_{230}N_{18}O_{24}$: m/z (z = 2): 1657.86597; found: 1657.86264.

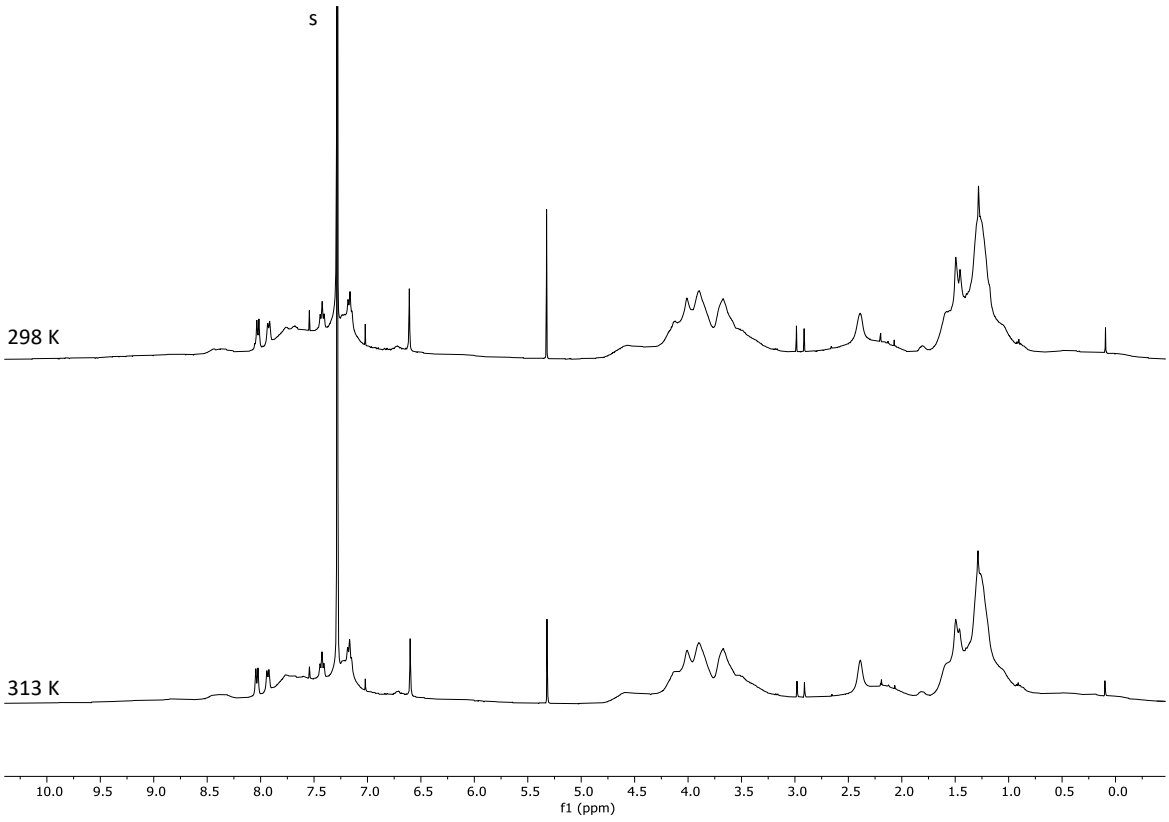

Figure 5.17. ^{1}H NMR stack plot spectra ($CDCl_3$, 400 MHz) of **Cage 3** at 298 K (top) and 313 K (bottom).

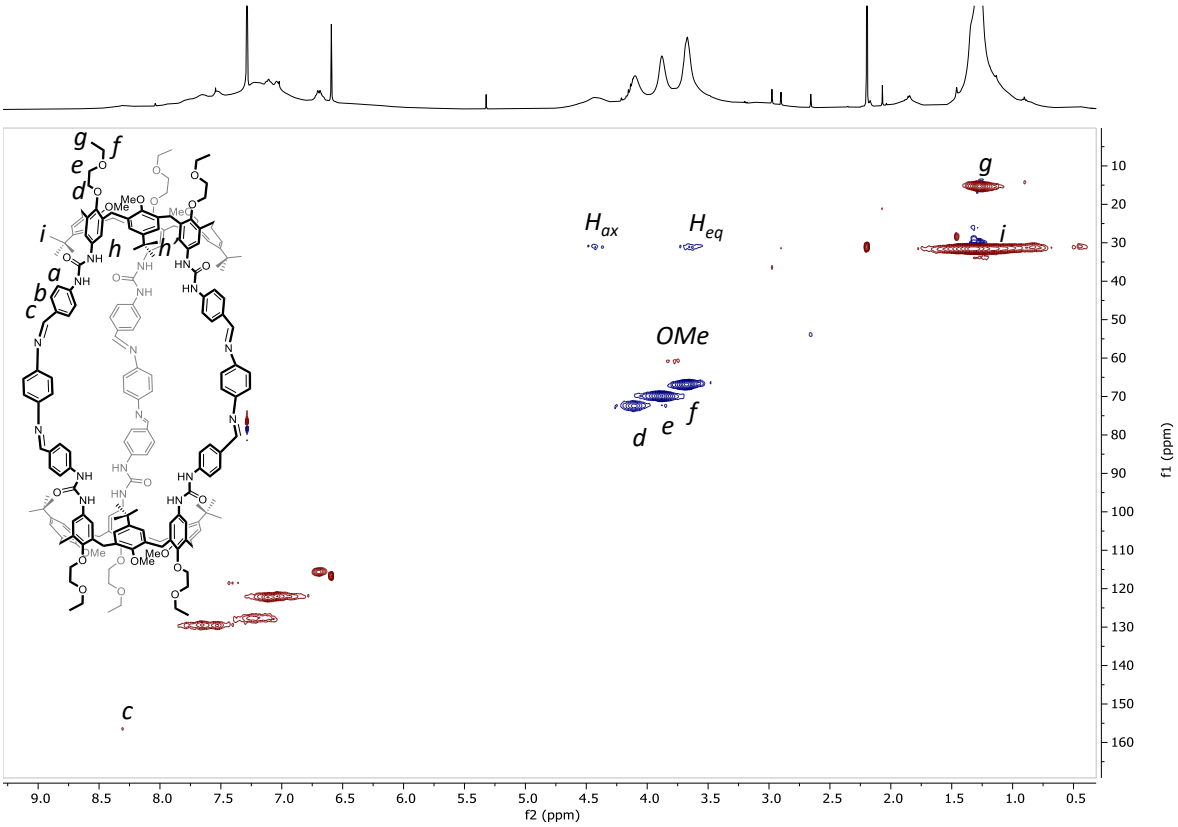

Figure 5.18. Edited HSQC ($CDCl_3$, 400 MHz, 298 K) of **Cage 3**. Positive peaks (CH_3 and CH) are shown in red, while negative ones (CH_2) are in blue.

Different results were observed in the reaction carried out using $\mathbf{3}_{12}$ as the template. The corresponding HR-MS data (**Figure 5.19**) displayed three intense peak clusters, indicating a strong interaction between **Cage 3** and the bis-viologen salt. The first cluster, with a base peak at m/z = 984.55106 (z = 4), corresponds to the quadrly charged complex, i.e., the adduct with $\mathbf{3}_{12}$ having lost all the tosylate counteranions. The second cluster at m/z = 1324.72470 (z = 3) was assigned to the adduct, which has retained an adventitious chloride ion as the counterion. Finally, the third cluster, with a base peak at m/z = 2004.57077 (z = 2), was attributed to the doubly charged complex with two chloride ions as counterions. Therefore, it appears that when bis-viologen salt $\mathbf{3}_{12}$ is employed as a template, its interaction with the cage is sufficiently strong that even chromatographic purification is unable to achieve a complete dethreading of the templating species. The incorporation of axle $\mathbf{3}_{12}$ within **Cage 3** was further validated by the 2D HSQC NMR spectrum recorded in deuterated chloroform. The spectrum, reported in **Figure 5.20**, clearly indicates the presence of the methyl group from the tosylate anions at 2.39 ppm. However, the interpretation of the 2D spectrum results difficult even in the presence of the bis-viologen axle, due to the still high fluxionality.

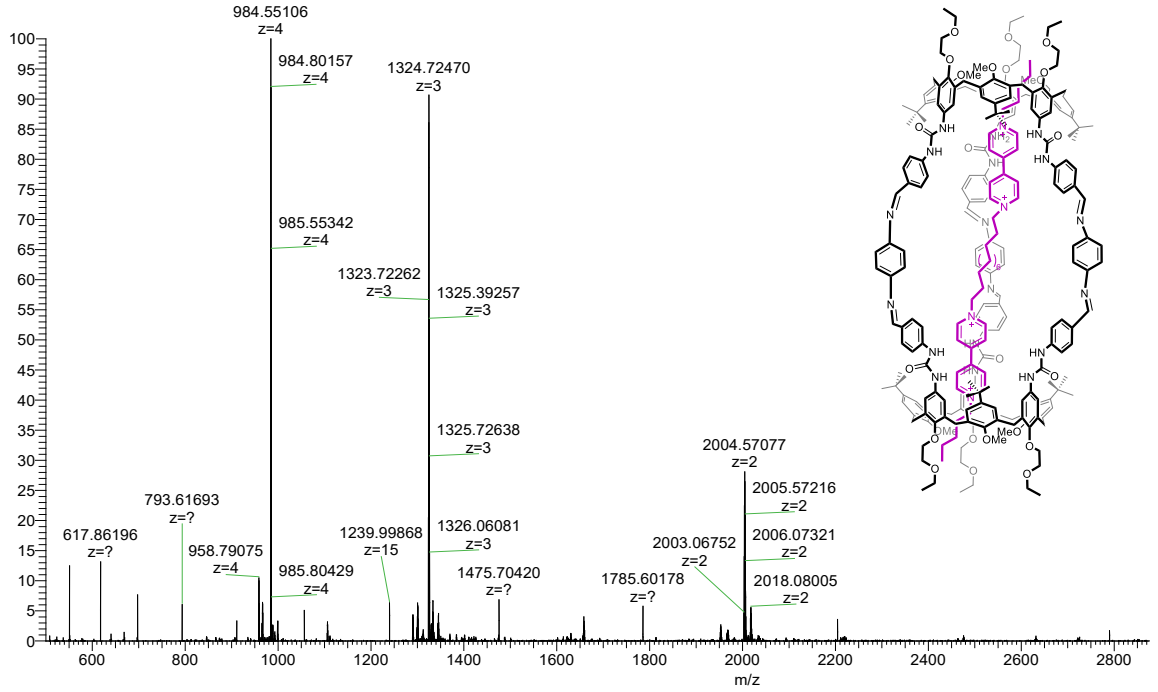

Figure 5.19. HR-MS (ESI, Orbitrap LQ) spectrum of compound **Cage 3** and axle **3**$_{12}$. Calculated for $C_{246}H_{290}N_{22}O_{24}$: m/z (z = 4): 984.55106; found: 984.55484. Calculated for $C_{246}H_{290}N_{22}O_{24}Cl_1$: m/z (z = 3): 1324.39112; found: 1324.39625. Calculated for $C_{246}H_{290}N_{22}O_{24}Cl_2$: m/z (z = 2): 2004.07036; found: 2004.07908.

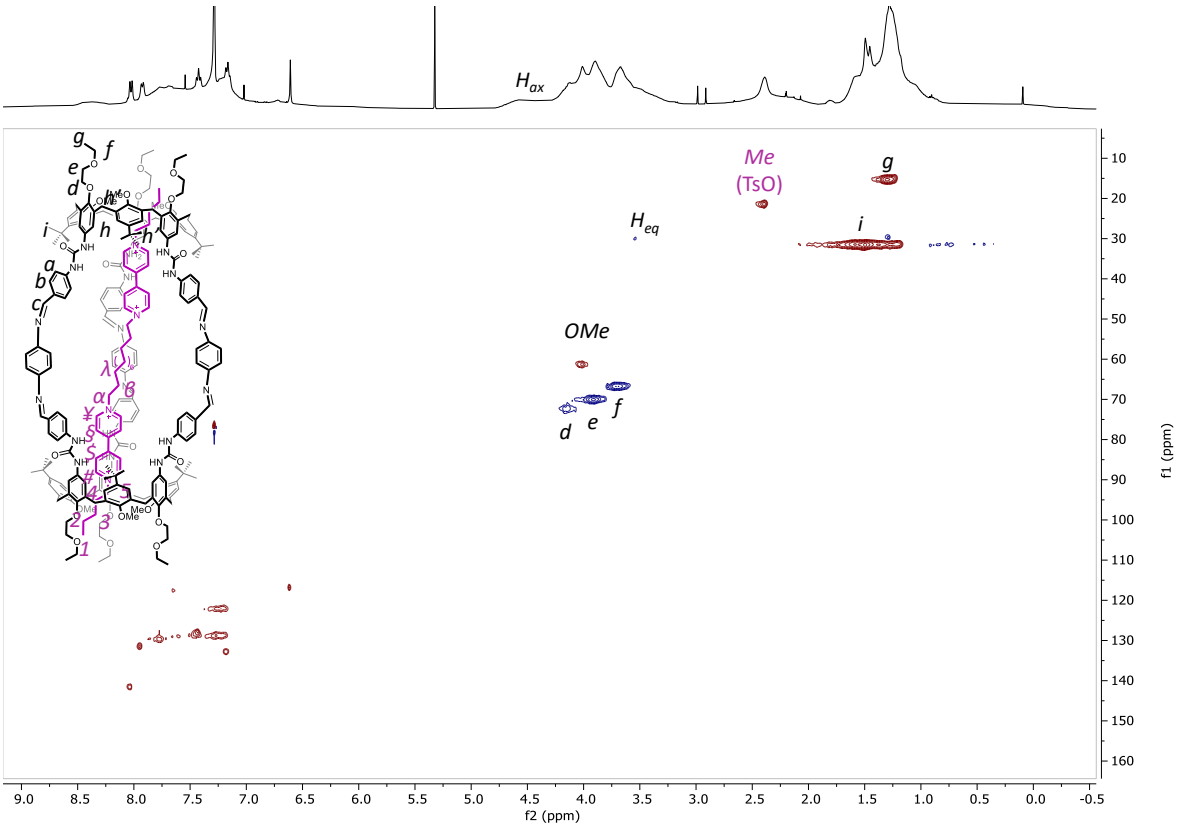

Figure 5.20. Edited HSQC ($CDCl_3$, 400 MHz, 298 K) of **Cage 3** and axle **3**$_{12}$. Positive peaks (CH_3 and CH) are shown in red, while negative ones (CH_2) are in blue.

Synthesis and characterization of Cage 4

Previous cages were characterized by symmetrical structures, which facilitated the synthesis. At this stage of the project, we wanted to take a more challenging approach by synthesizing an asymmetric cage while exploiting the reactivity previously described. The idea was to use **TA** and **TPU-AL** to form a novel imine-based cage. Similarly to **Cage 2**, no linker molecule was needed since the necessary functionalities to form the desired bonds were already present on the upper rim of the two calix[6]arene macrocycles (**Scheme 5.7**). The template effect with $\mathbf{3}_n$ was not investigated in this case since the cavity of the target cage would be too small to host any bis-viologen template.

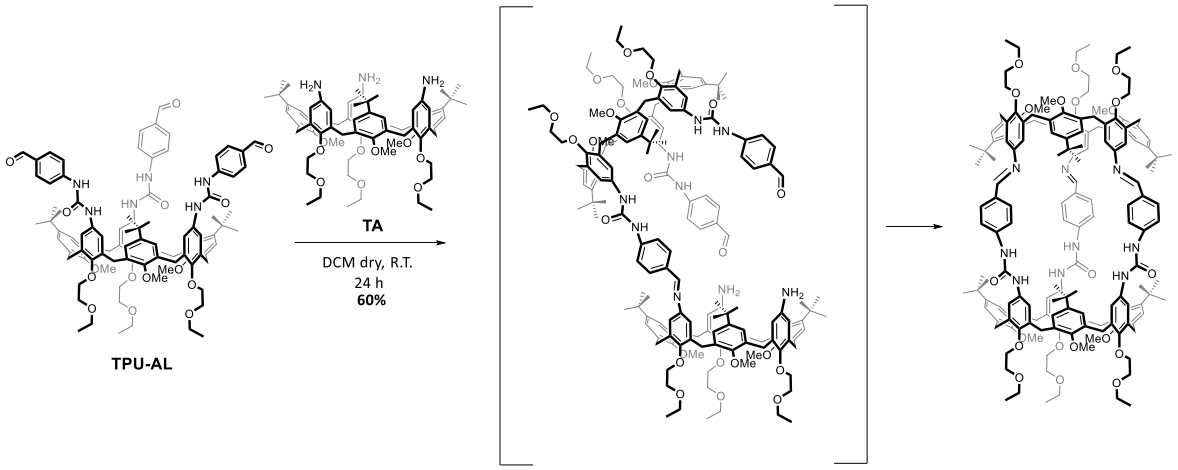

Scheme 5.7. Synthesis of **Cage 4**.

To synthesize **Cage 4**, a 1:1 mixture of the two calix[6]arene macrocycles was prepared in anhydrous dichloromethane and allowed to react under stirring at room temperature for 24 hours. The pure **Cage 4** was isolated *via* column chromatography in a 60% yield. As for **Cage 3**, the promising results of this synthesis are likely due to the formation of a reversible imine bond in the three bridging units. The effective formation of **Cage 4** was initially investigated through NMR spectroscopy. Similar to previous cages, the ^{1}H NMR spectra (**Figure 5.21**), taken in different deuterated solvents, exhibit significant signals broadening, indicative of the dynamic nature of the structure.

Like for other cages, a 2D HSQC NMR experiment in deuterated chloroform (**Figure 5.22**) allowed us to have more information. However, the aromatic proton signals remain unresolved, merging into a large and flat resonance ranging from 7.8 to 7.0 ppm. In contrast, the methoxy group gives rise to several (at least six) ill-defined cross-peaks around 60 ppm in *F*1(^{13}C). Two of these cross-peaks displayed high-field proton resonance at approximately 3.1 and 2.5 ppm, suggesting a cage configuration in which several methoxy groups are still located inside the cavity. Despite the inconclusive nature of the NMR findings, the formation of **Cage 4** was confirmed by LR-MS. The peak observed at m/z = 1303.0 (z = 2) corresponded to the doubly charged molecular ion, while the peak at m/z = 1332.2 was attributed to the adducts of **Cage 4** with K^+ and Na^+ ions.

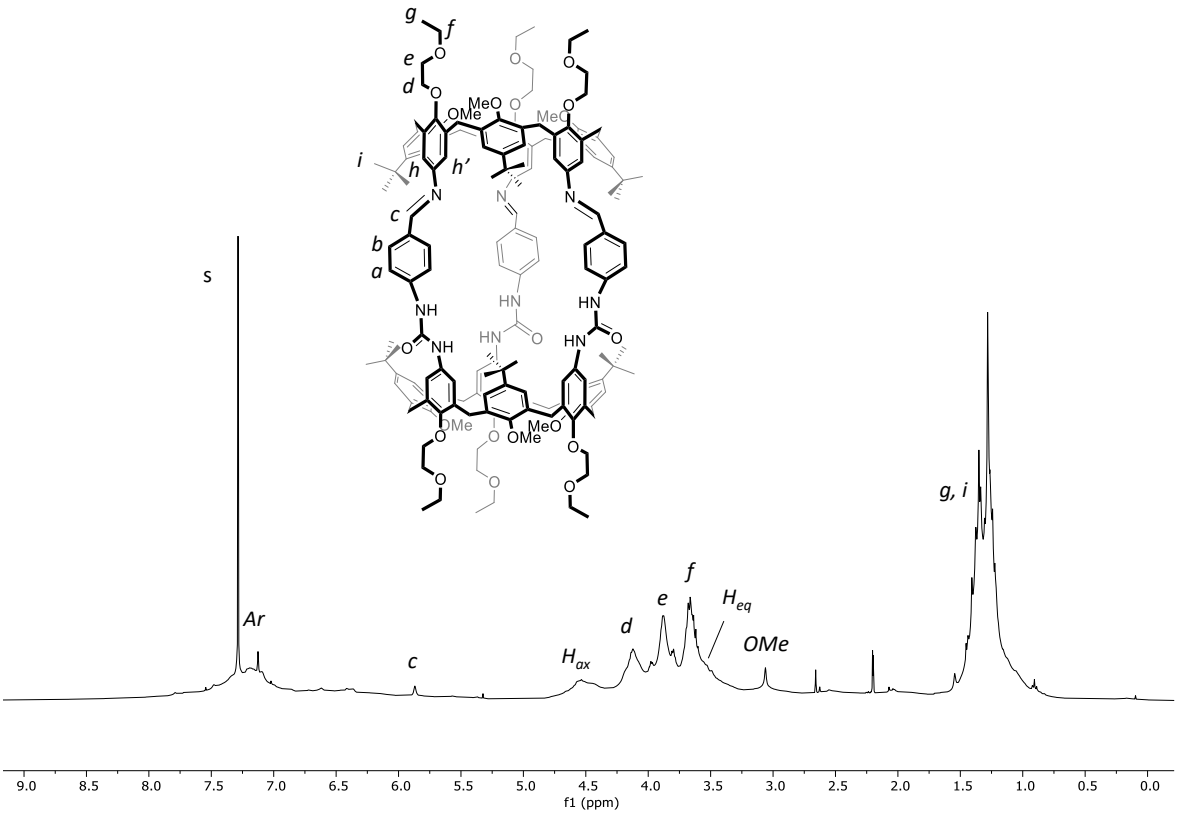

Figure 5.21. ^{1}H NMR spectrum ($CDCl_3$, 400 MHz, 298 K) of **Cage 4**.

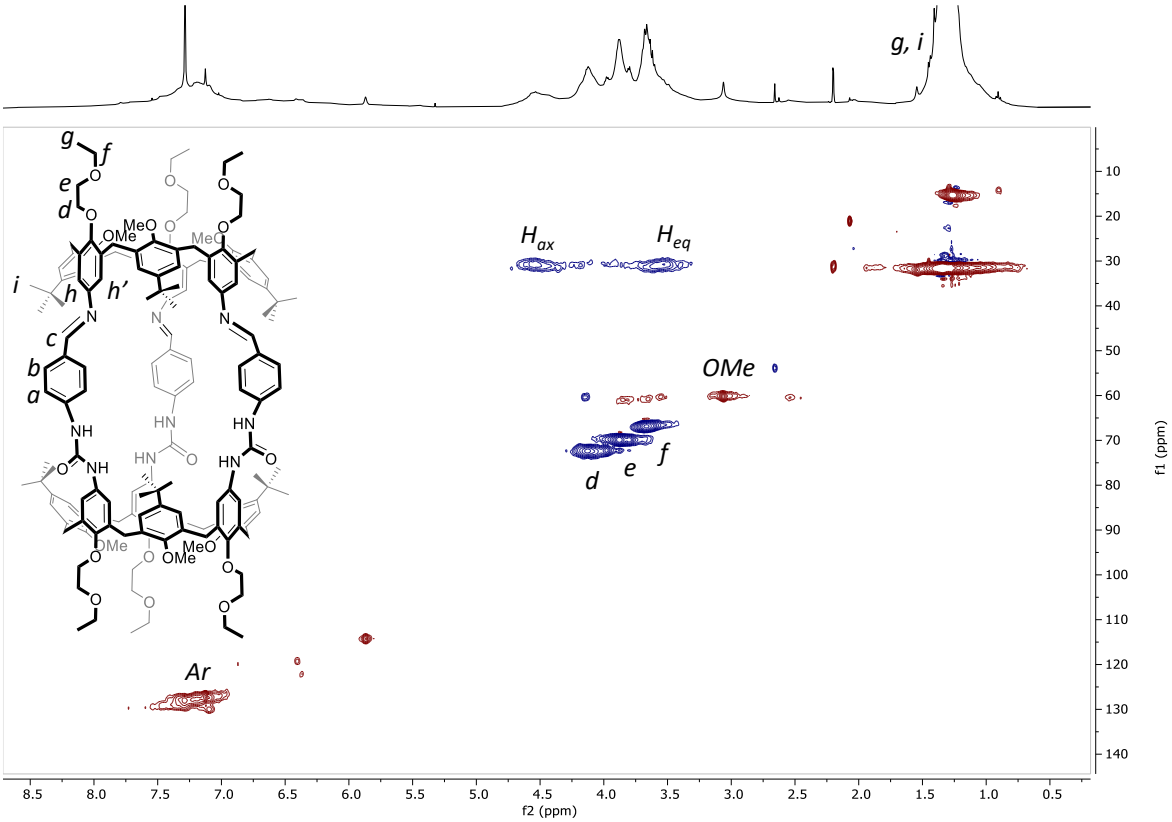

Figure 5.22. Edited HSQC ($CDCl_3$, 400 MHz, 298 K) of **Cage 4**. Positive peaks (CH_3 and CH) are shown in red, while negative ones (CH_2) are in blue.

Complexation studies with viologen and bis-viologen salts

In the second part of this project, we wanted to investigate the recognition abilities of the synthesized cages. **Cage 1** was chosen as a model system, and the *N*,*N*-dioctyl viologen ditosylate **DOV(2TsO)** was selected as the first guest to be investigated since our group has extensively studied the optical and electrochemical properties of this species[7] (**Scheme 5.8**).

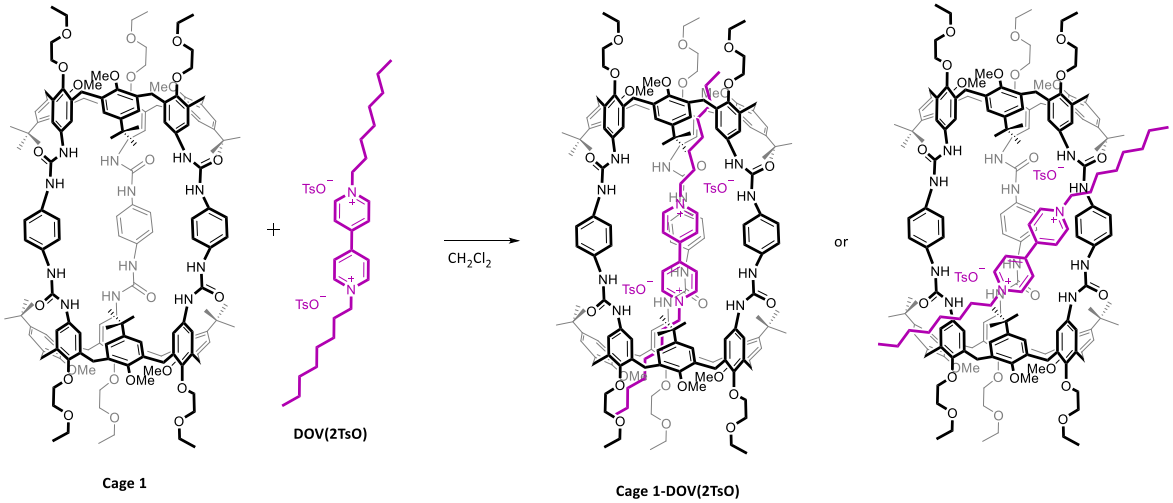

Scheme 5.8. Complexation reaction between **DOV(2TsO)** and **Cage 1**.

The complexation was initially assessed using UV-Vis spectroscopy by simultaneously recording the absorption spectrum of each species separately. **Figure 5.23** shows the "sum" and "mix" spectra for **Cage 1** and **DOV(2TsO)**. These spectra were recorded with the same method described in Chapter 1 (section 1) using a specialized cuvette with a central septum (**Figure 5.23**, top). The "mix" spectrum (green line) exhibits a hyperchromic effect along with a red shift in the maximum absorption compared to the "sum" spectrum (violet line). Additionally, a CT band becomes evident around 450-500 nm (green line in the right panel of **Figure 5.23**), confirming the complex formation.

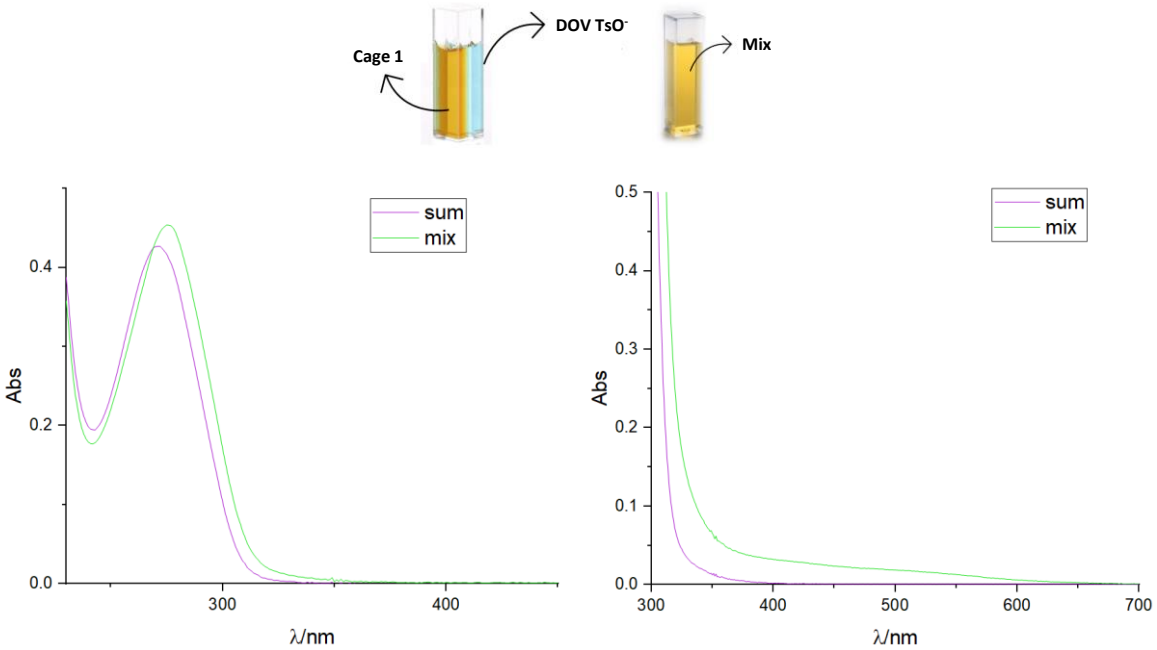

Figure 5.23. Top: representation of the special cuvette used for the "sum" and "mix" experiment; bottom left: sum of the absorption spectra of **Cage 1** (c = 6.23×10^{-6} M) and **DOV(2TsO)** (c = 2.00×10^{-5} M) (violet line) and the absorption spectrum of the mixture of **Cage 1** and **DOV(2TsO)** (green line) (CH_2Cl_2, 298 K); bottom right: expanded region from 300 to 700 nm evidencing the formation of the CT band (**Cage 1** c = 5.93×10^{-5} M and **DOV(2TsO)** c = 1.41×10^{-4} M).

In **Figure 5.24**, the UV-Vis spectra corresponding to the titrations of **DOV(2TsO)** with **Cage 1** in dichloromethane at varying concentrations are presented. The titrations exhibit comparable behavior despite variations in the concentration of the two solutions. At higher concentrations (**Figure 5.24,** panel a), two association constants were determined: $\log K_1$ = 6 and $\log K_2$ = 5, corresponding to 1:1 and 1:2 cage-to-viologen complexes. Lowering the concentration of the interacting species up to 10^{-6} M (**Figure 5.24,** panels b and c) to promote the exclusive formation of the 1:2 complex was not successful as better optical data fittings were obtained when the formation of both 1:1 and 1:2 complexes was considered. Unexpectedly, dilution of the reactants had the only effect of increasing the formation of the 1:2 cage-to-viologen adduct ($\log K_2$ = 6) (**Figure 5.24,** panel c).

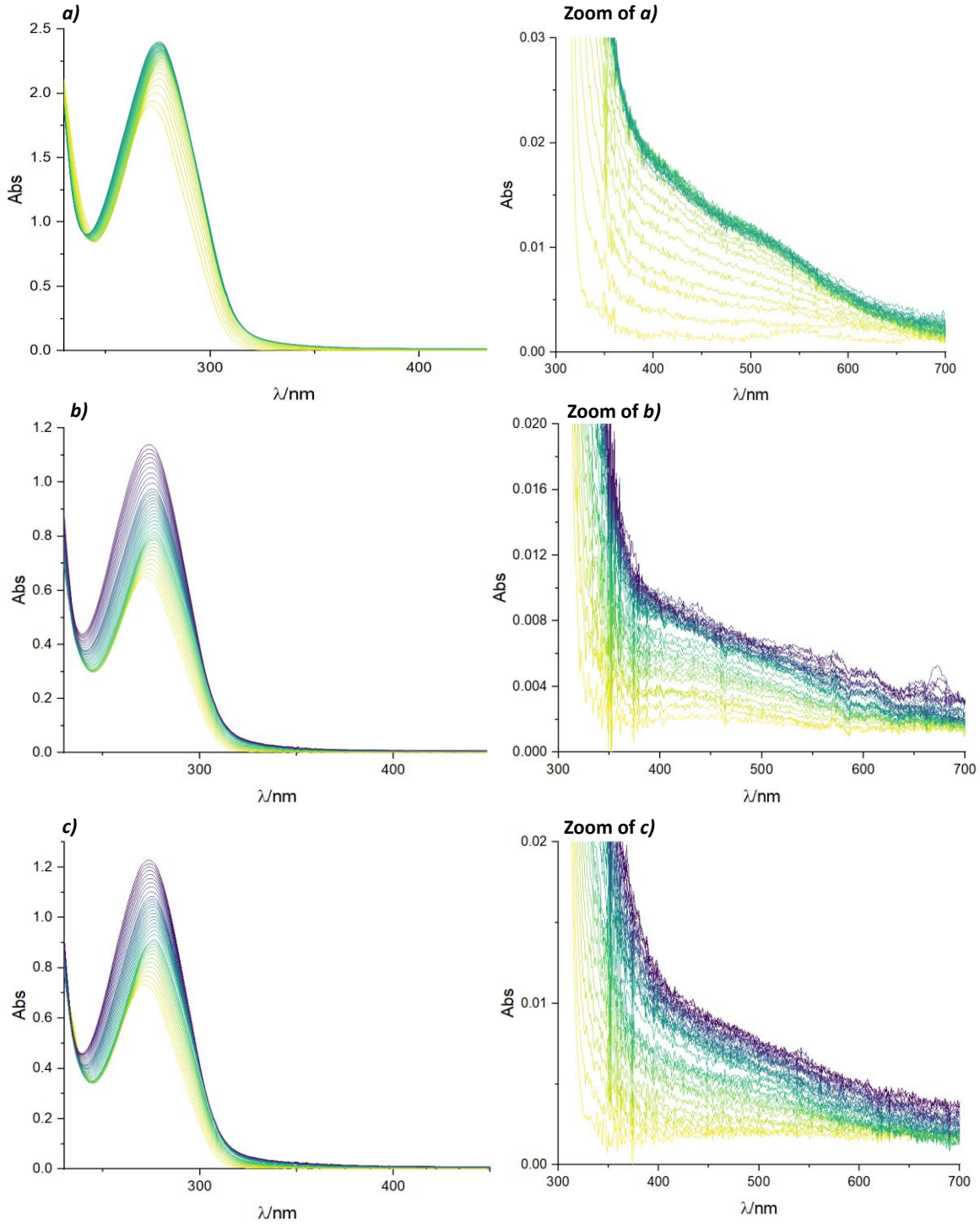

Figure 5.24. Left: UV-Vis titrations plots of **Cage 1** with **DOV(2TsO)** in dichloromethane at different concentrations: *a*) **DOV(2TsO)** (c = 1.15×10^{-4} M) and **Cage 1** (c = 1.94×10^{-5} M); *b*) **DOV(2TsO)** (c = 6.25×10^{-5} M) and **Cage 1** (c = 6.44×10^{-6} M); *c*) **DOV(2TsO)** (c = 6.90×10^{-5} M) and **Cage 1** (c = 7.40×10^{-6} M). Right: expanded region of the spectra showing the CT band.

The above findings were confirmed by comparing the binding isotherms obtained across the three different concentration conditions (**Figure 5.25**). The binding isotherms determined at different wavelengths always exhibited an equivalence point for a cage-viologen equivalents ratio of ca. 1, indicating the predominant formation of a complex with a 1:1 stoichiometry. However, data fitting

was only successful when accounting for the formation of both 1:1 and 1:2 complexes. This suggests that **Cage 1** can interact with either one or two viologen species.

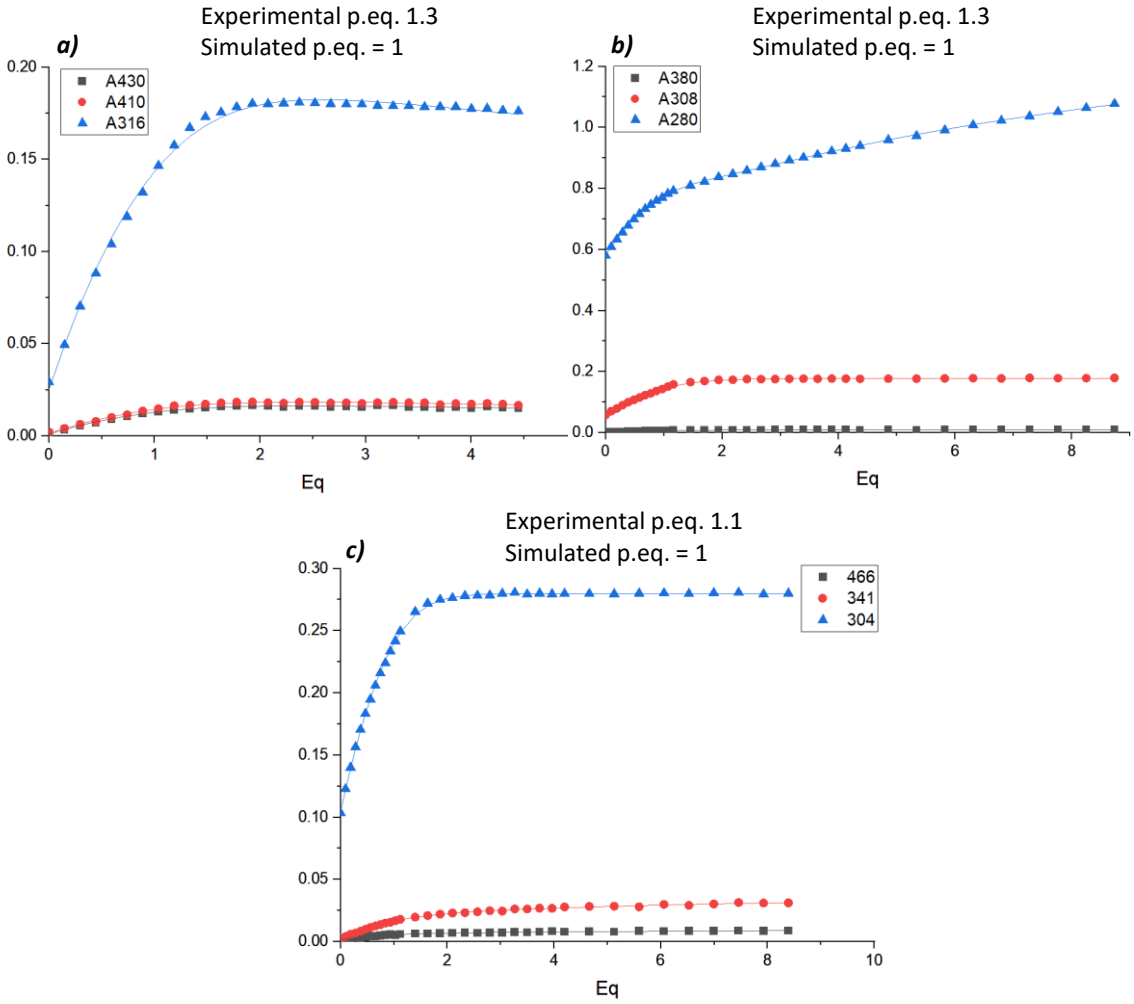

Figure 5.25. Binding isotherms at multiple wavelengths for the complexation of **DOV(2TsO)** and **Cage 1** in dichloromethane: *a*) **DOV(2TsO)** (c = 1.15×10^{-4} M) and **Cage 1** (c = 1.94×10^{-5} M); *b*) **DOV(2TsO)** (c = 6.25×10^{-5} M) and **Cage 1** (c = 6.44×10^{-6} M); *c*) of **DOV(2TsO)** (c = 6.90×10^{-5} M) and **Cage 1** (c = 7.40×10^{-6} M). The experimental points are depicted as black squares, blue triangles, or red circles, the corresponding fitting with continuous lines of the same colors; wavelengths are indicated in the boxes.

To assess the influence of the tosylate anion, which is the counterion of the investigated viologen salt, a titration of **Cage 1** (c = 7.84 × 10^{-6} M) with tetrabutylammonium tosylate (TBATsO) (c = 1.21×10^{-3} M) was conducted. As in Chapter 1 (section 1) TBATsO was chosen as source of tosylate anions. **Figure 5.26** presents the collection of UV-Vis spectra obtained during this titration. Data fitting for the first association yielded a logK_1 = 6, while the second association produced a logK_2 = 3.

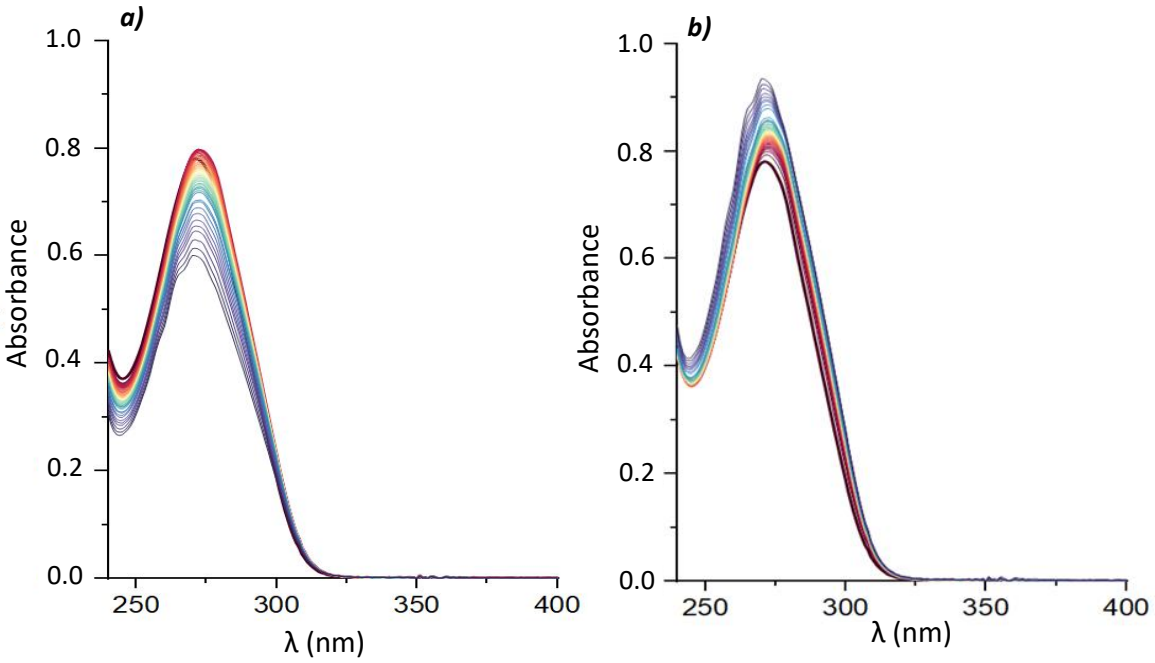

Figure 5.26. UV-Vis titration plots of *a)* **Cage 1** (c = 7.84×10^{-6} M) with TBATsO (c = 1.21×10^{-3} M) in dichloromethane; *b*) UV-Vis spectra corrected by dilution.

To account for whether the observed UV-Vis spectral changes in the **Cage 1-DOV(2TsO)** titrations were effectively due to the interaction with a second **DOV(2TsO)** species or with the tosylate, a solution of **Cage 1** (c = 8.93×10^{-6} M) pre-complexed with 10 equivalents of TBATsO was titrated with **DOV(2TsO)** (c = 1.02×10^{-4} M).

Plotting the equivalents of **DOV(2TsO)** added against the absorbance recorded at 303 nm (**Figure 5.27**, panel c) revealed a change in slope at 1.1 equivalents, indicating the formation of a 1:1 complex. However, the sigmoidal nature of the isotherm in the UV region suggests the formation of a 1:2 complex as well. This confirmed that both complexation modes are present.

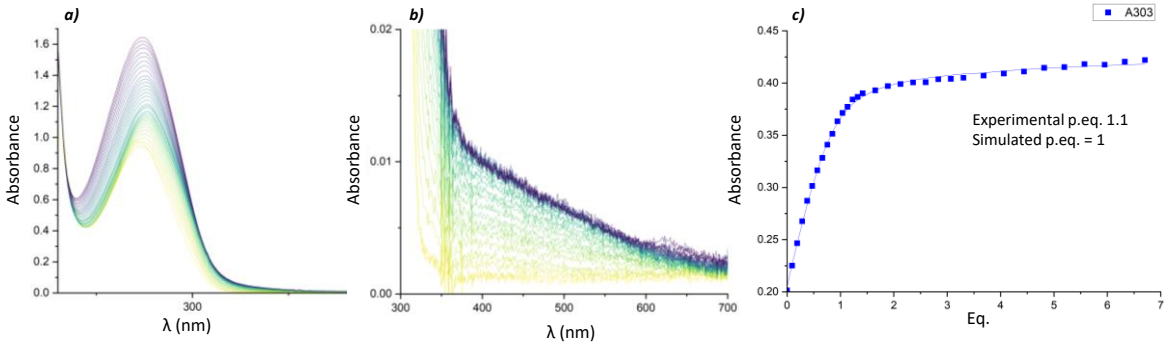

Figure 5.27. UV-Vis titrations plots of *a*) a solution of **Cage 1** (c = 8.93×10^{-6} M) containing 10 equivalents of TBATsO with **DOV(2TsO)** (c = 1.02×10^{-4} M) in dichloromethane; *b*) expanded region between 300-700 nm showing the formation of the CT band; *c*) binding isotherms at 303 nm.

To further investigate the complexation behavior of **Cage 1**, preliminary NMR experiments were carried out to investigate its interaction with a bis-viologen salt (**3**$_{12}$), which was one of the

templates used in the synthesis of this cage. The complexation experiment was performed in deuterated chloroform by mixing **Cage 1** with axle $\mathbf{3}_{12}$ in a 1:1 molar ratio. Upon mixing, $\mathbf{3}_{12}$ became soluble, and the resulting solution turned red, likely due to the formation of a CT band. However, as shown in **Figure 5.28**, the resulting ^{1}H NMR spectrum did not show a significant increase in the cage rigidity compared to the free **Cage 1**, although some changes were observed in the mid-field region, and a new broad signal appears at ~2.4 ppm which was assigned to the methyl group of the tosylate anions.

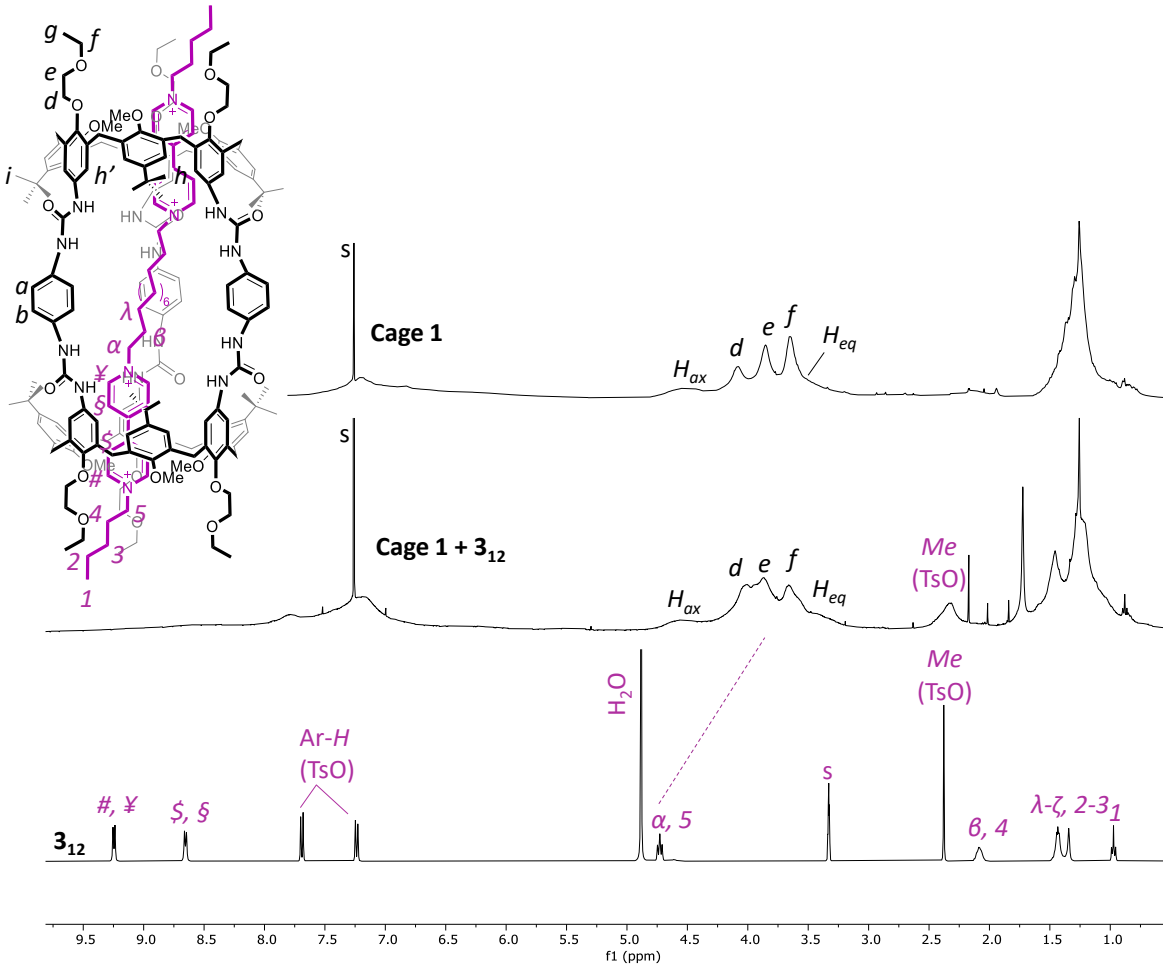

Figure 5.28. ^{1}H NMR stack plot (400 MHz, 298 K) of **Cage 1** ($CDCl_3$, top), 1:1 mixture of **Cage 1** and axle $\mathbf{3}_{12}$ ($CDCl_3$, middle), and axle $\mathbf{3}_{12}$ (CD_3OD, bottom). Tosylate counterions were omitted for clarity.

Complexation studies with organic dyes

The complexation properties of **Cage 1** were also preliminarily investigated using a selected set of organic dyes, previously discussed in earlier chapters. Organic dyes serve as excellent guest molecules for encapsulation studies, as their interactions with the host can be easily monitored through changes in their absorption and emission properties. Encapsulation also improves the photostability of the dyes.[34,35] Three dyes were selected for this study: the stilbazolium dye **NSC1**

(Chapter 1), the cyanine dye **Cy7-Cl** (Chapter 4), and the thiazo[5,4-*d*]thiazole dye **$(C_8)_2Py_2TTz$** (Chapter 2) (**Figure 5.29**).

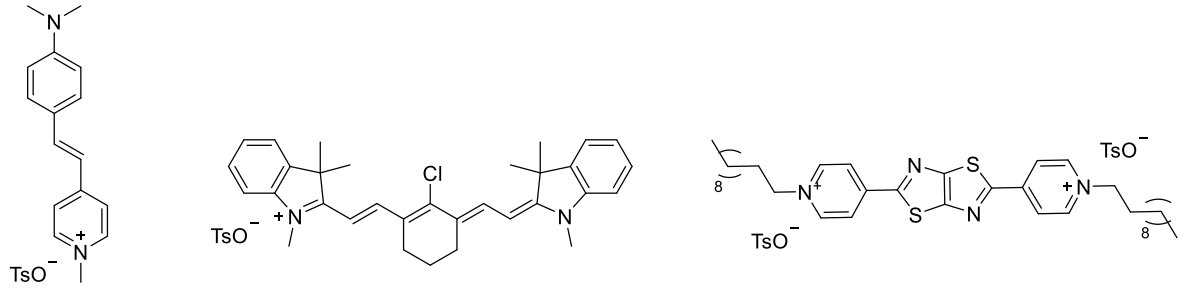

Figure 5.29. Structure of the organic dyes used as guests for **Cage 1**.

Complexation with NSC1

The first dye examined was **NSC1**, which was mixed with **Cage 1** in a 1:1 molar ratio in deuterated chloroform, followed by NMR analysis. **Figure 5.30** shows a stack plot of the ^{1}H NMR spectra for free **Cage 1** (top), free **NSC1** (bottom), and their 1:1 mixture (middle). While the spectrum of the mixture largely resembles that of the free **Cage 1**, most of the dye peaks at lower fields nearly disappear, indicating complex formation. The broadness of the spectrum of the complex could be explained by considering the small size of **NSC1**, which could allow it to move freely within the cage's cavity. Moreover, the dye may access the cavity of **Cage 1** from multiple entry gates, including both the lower rims and the lateral openings between the linkers. Unfortunately, experimental evidence cannot suffragate this hypothesis since the guest signals are not clearly recognizable in the protonic spectrum of the complex. This prevents, for example, from carrying out NMR dynamic experiments such as DOSY.

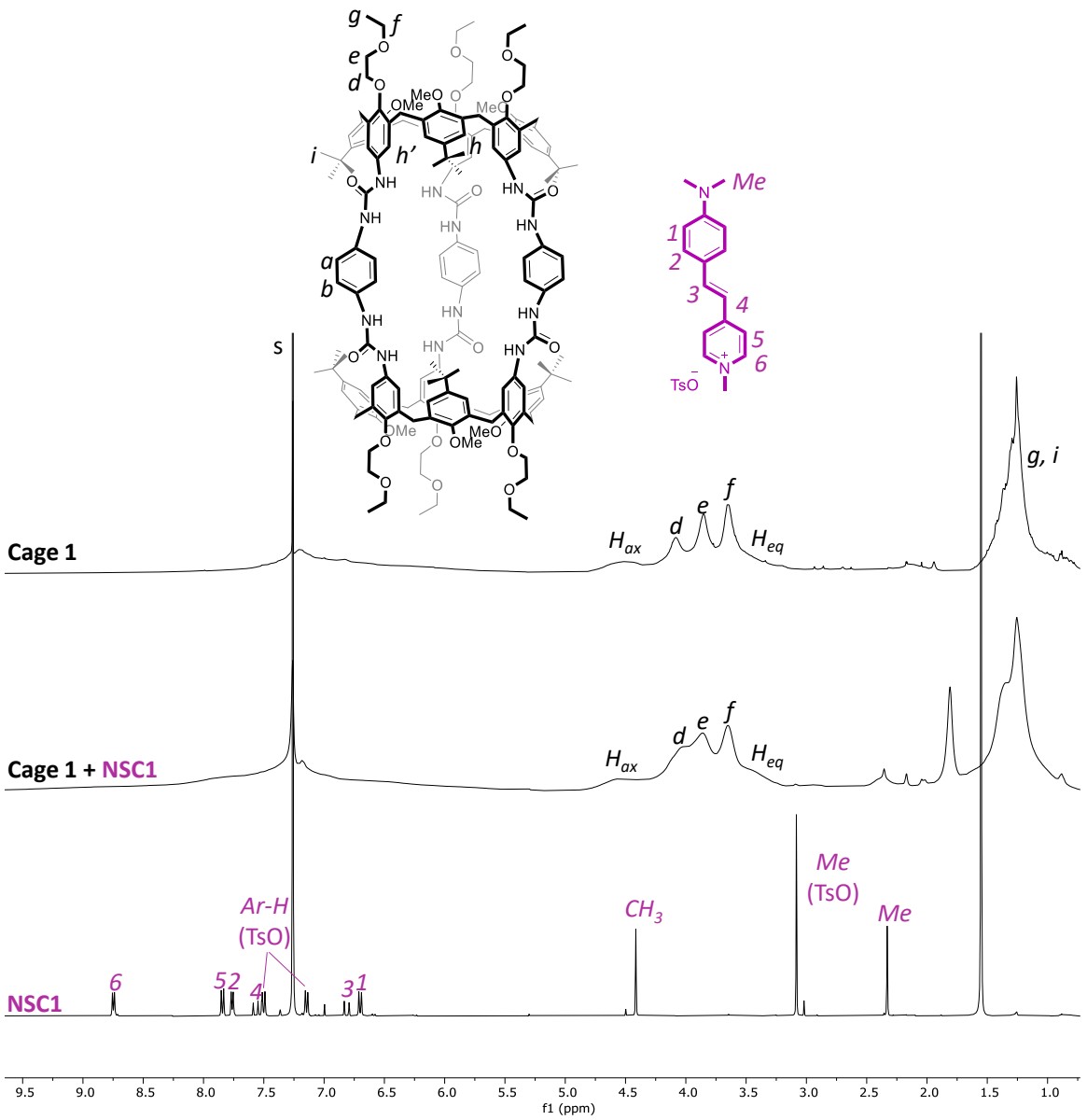

Figure 5.30. ^{1}H NMR stack plot ($CDCl_3$, 400 MHz, 298 K) of **Cage 1** (top), 1:1 mixture of **Cage 1** and **NSC1** (middle), and free **NSC1** (bottom).

To further confirm the interaction between **NSC1** and **Cage 1**, a UV-Vis titration experiment was performed, monitoring the dye's absorbance as successive aliquots of a solution of **Cage 1** were added (**Figure 5.31**). The resulting UV-Vis spectra exhibited a blue shift of the dye's absorbance maximum, indicative of complex formation and the appearance of isosbestic points at around 460 nm. The absorbance value variations were fitted with a 1:1 binding model, yielding a logK_1 of 5.6±0.09. This result provides clear evidence of interaction between the **NSC1** and **Cage 1**.

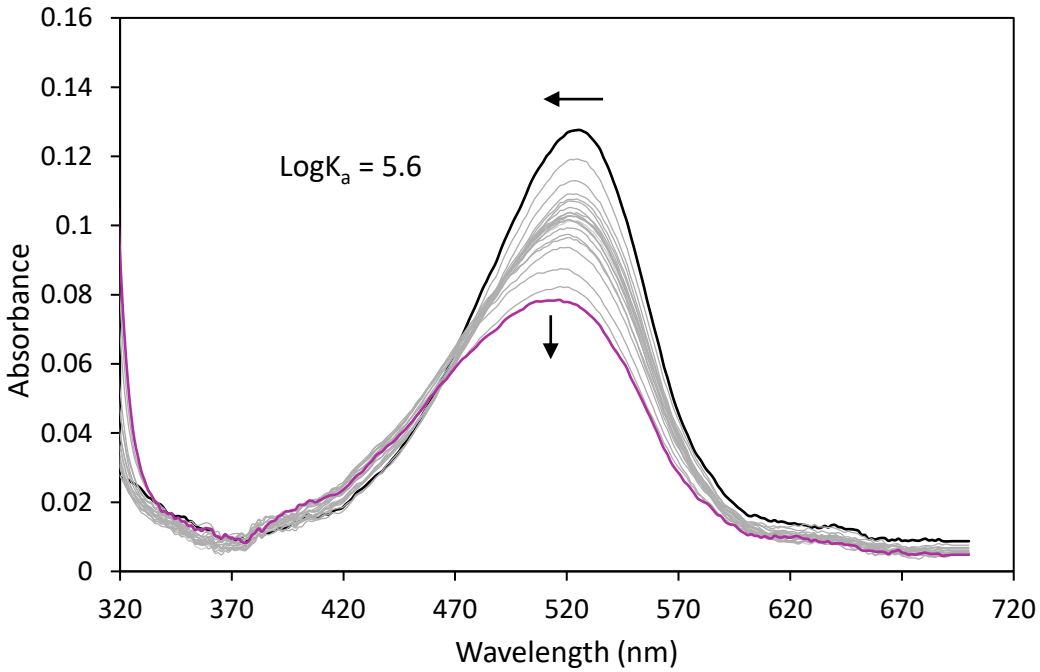

Figure 5.31. Collection of UV-Vis spectra recorded during the titration of **NSC1** (c = 4.39x10^{-6} M) with **Cage 1** (c = 1.52x10^{-4} M) in CH_2Cl_2 at 298 K.

Complexation with Cy7-Cl

A second organic dye, the cyanine **Cy7-Cl**, was selected for its larger size, rigidity, and poor photostability. As with the previous experiments, NMR measurements were performed in deuterated chloroform. **Figure 5.32** reports the ^{1}H NMR stack plot of free **Cage 1** (top), free **Cy7-Cl** (bottom), and their 1:1 mixture (middle). In the latter spectrum, the original broadness of the cage signals did not improve significantly, although interactions between the cage and the dye appear to affect the dye's resonances. Notably, the alkene protons *3* and *4* shifted from 6.27 and 8.30 ppm to 6.06 and 8.25 ppm, respectively. Protons *5* experienced an up-field shift from 3.74 to 3.49 ppm, while protons labeled as *2* shifted from 2.70 to 2.54 ppm, and protons *1* from 1.91 to 1.77 ppm. The methyl protons of the tosylate anion showed little change in chemical shift and became broader. The signals in the aromatic region were overlapping, making any interpretation challenging. Although the observed shifts in the **Cy7-Cl** proton signals provide evidence of interactions with **Cage 1**, the lack of observable changes in the broad resonances of the cage does not fully support the endocavity complexation of the dye. However, the broadening of the tosylate resonances suggests that the anion interacts with the cage cavity in some ways. The NMR data are consistent with a fast exchange process for the cationic part of **Cy7-Cl** on the NMR time scale, while an intermediate exchange seems to be at play for the tosylate. These findings suggest that the cavity of **Cage 1** is not large enough to host the entire dye, which may only partially thread through the cage horizontally. Unfortunately, further NMR experiments (NOESY and ROESY) aimed at investigating

the spatial relationships between the dye and the cage were not possible due to poor signal resolution.

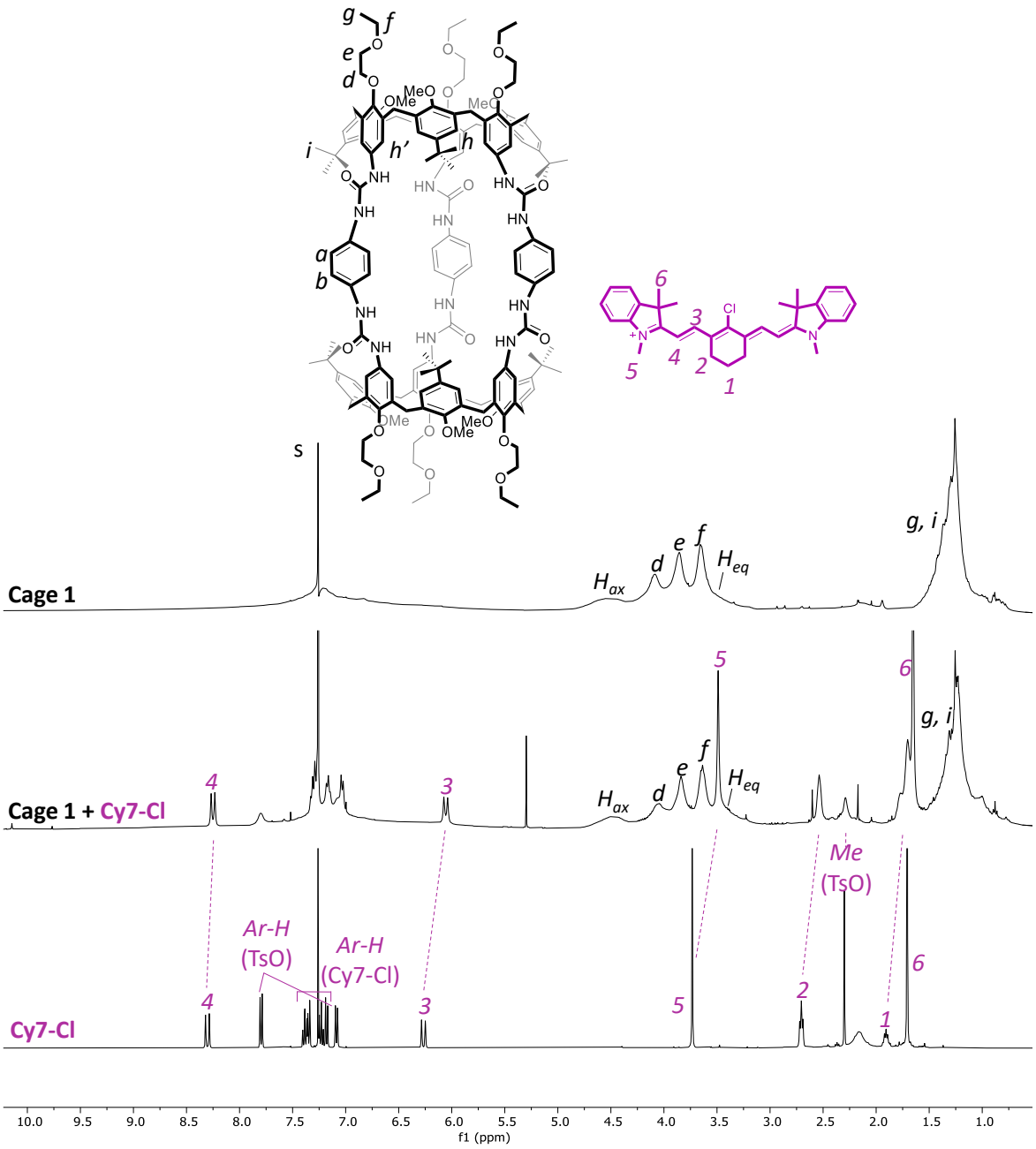

Figure 5.32. ^{1}H NMR stack plot ($CDCl_3$, 400 MHz, 298 K) of **Cage 1** (top), 1:1 mixture of **Cage 1** and **Cy7-Cl** (middle), and free **Cy7-Cl** (bottom). Tosylate counterions were omitted for clarity.

Complexation with $(C_8)_2Py_2TTz$

The dye **$(C_8)_2Py_2TTz(2TsO)$**, first introduced in Chapter 2, was also investigated for its interactions with **Cage 1**. Upon mixing equimolar amounts of **Cage 1** and **$(C_8)_2Py_2TTz(2TsO)$** in deuterated chloroform, the initially insoluble dye became soluble, and the solution's color shifted from fluorescent yellow to brown, indicating the formation of a CT band. **Figure 5.33** displays the ^{1}H NMR stack plot of free **Cage 1** (top), free **$(C_8)_2Py_2TTz(2TsO)$** (bottom), and their 1:1 mixture (middle).

Although the expected improvement in the cage NMR resonances was not observed, all the dye signals, especially those relative to the pyridinium moieties, experienced a significant up-field shift, indicating an intracavity complexation with **Cage 1**. In analogy with the other organic dyes studied (vide supra and infra), the general signal broadness hindered a more detailed analysis of the complexation phenomena; therefore, UV-Vis and fluorescence analyses were employed to further evaluate the extent of the complexation.

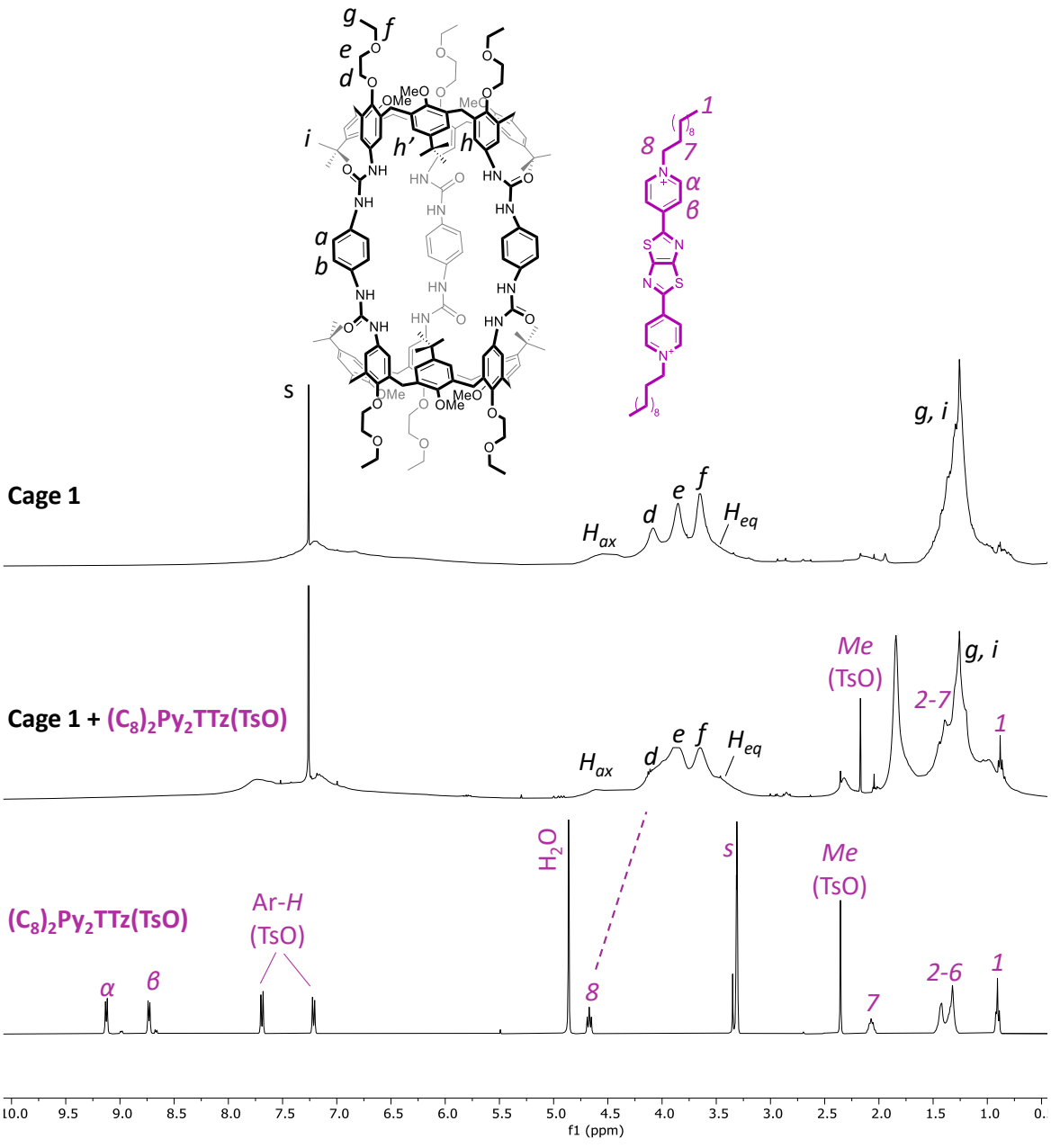

Figure 5.33. ^{1}H NMR stack plot (400 MHz, 298 K) of **Cage 1** (top), 1:1 mixture of **Cage 1** and **$(C_8)_2Py_2TTz$ 2TsO** (middle) in $CDCl_3$, and free **$(C_8)_2Py_2TTz$ 2TsO** (bottom) taken in CD_3OD for solubility reasons. Tosylate counterions were omitted for clarity.

As previously seen with viologen salts, the complexation was qualitatively evaluated by comparing the "sum" and "mix" spectra. For solubility reasons, **$(C_8)_2Py_2TTz(2PF_6)$**, with hexafluorophosphate

counterions instead of tosylates, was used. As usual, the "sum" and "mix" spectra were obtained by using the special cuvette in which the two separate compartments were each filled with a 1:1 solutions of **Cage 1** (c = 1.3×10^{-5} M) and **$(C_8)_2Py_2TTz(2PF_6)$** (c = 2.6×10^{-5} M) in dichloromethane. **Figure 5.34** shows that the "mix" spectrum (red line) experiences a hyperchromic effect for the first band together with a small red shift of the maximum with respect to the "sum" spectrum (black line). The formation of the diagnostic CT band is barely visible at around 500 nm (green arrow).

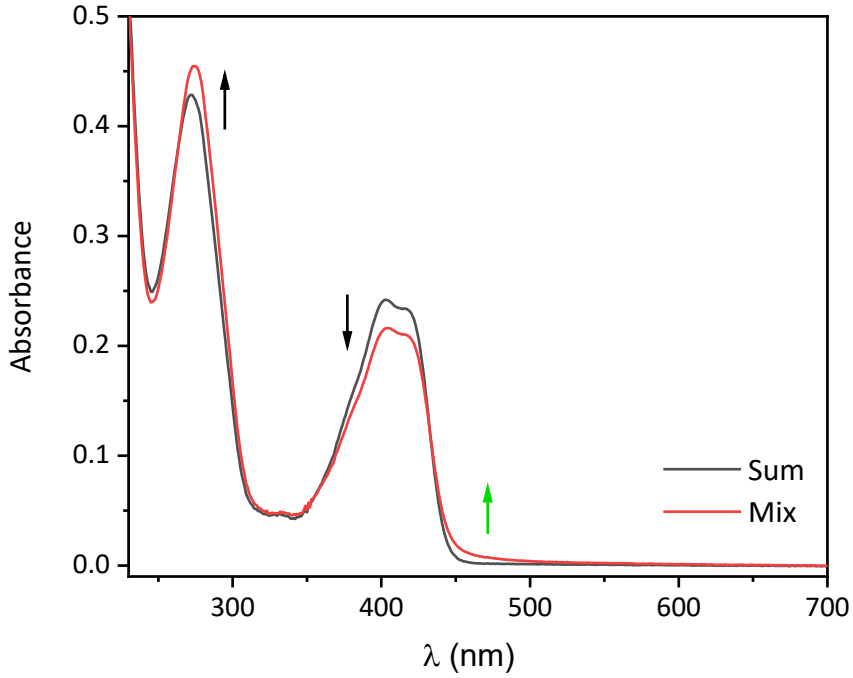

Figure 5.34. Sum (black line) and mix (red line) absorption spectra relative to **Cage 1** and **$(C_8)_2Py_2TTz(2PF_6)$** (CH_2Cl_2, 298 K). The green arrow indicates the CT band.

The association constant and the stoichiometry of the complexation process were examined through the usual UV-Vis titration experiments carried out in dichloromethane by adding aliquots of a **Cage 1** solution (c = 2.0×10^{-4} M) to a solution of **$(C_8)_2Py_2TTz(2PF_6)$** (c = 2.8×10^{-5} M). Plotting the equivalents of **Cage 1** added against the absorbance at 500 nm, a change in curve slope was observed at 2 equivalents, indicating a 2:1 cage-TTz complexation stoichiometry (**Figure 5.35**, left). This stoichiometry of complexation was further confirmed by a fluorescence titration, where the emission of **$(C_8)_2Py_2TTz(2PF_6)$** (c = 2.8×10^{-5} M) was monitored upon the addition of incremental aliquots of a **Cage 1** solution in dichloromethane (**Figure 5.35**, right). The fluorescence intensity at 465 nm decreased progressively until complete quenching was observed. The plot of cage equivalents versus emission intensity also showed a slope change at 2 equivalents of **Cage 1**, corroborating the formation of a 2:1 complex.

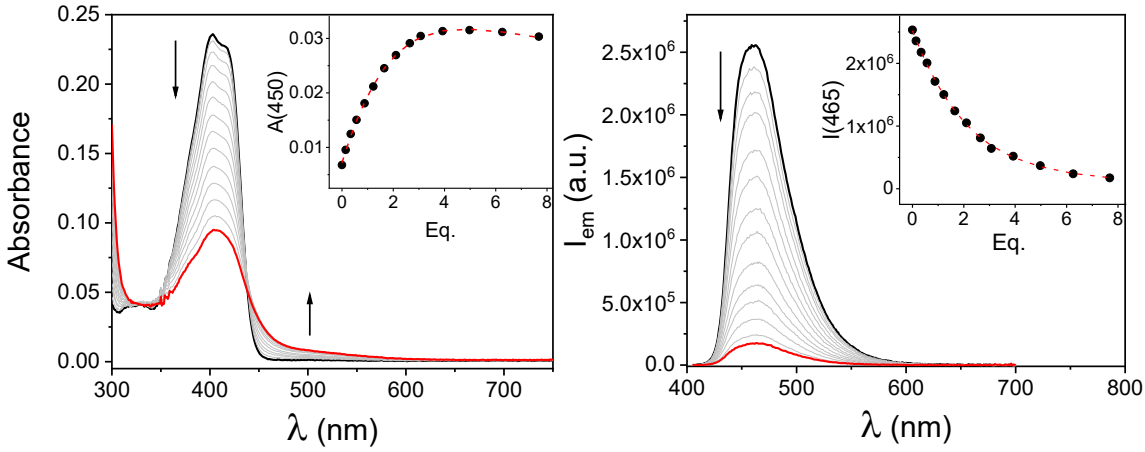

Figure 5.35. Left: collection of absorbance spectra taken during the titration of **$(C_8)_2Py_2TTz(2PF_6)$** solution in CH_2Cl_2 (c = 2.8×10^{-5} M) with a solution of **Cage 1** in CH_2Cl_2 (c = 2.0×10^{-4} M) at 298 K; right: collection of emission spectra taken during the titration of **$(C_8)_2Py_2TTz(2PF_6)$** solution in CH_2Cl_2 (c = 2.8×10^{-5} M, λ_{max}^{ex} = 400 nm) with a solution of **Cage 1** in CH_2Cl_2 (c = 2.0×10^{-4} M) at 298 K.

The data were fitted by assuming a 2:1 stoichiometry, with one equivalent of dye and two equivalents of **Cage 1**. The association constants determined upon experimental data fittings were log K_1 = 4.9 and log K_2 = 5.1. When these values were compared with the association constant calculated for **TPU** calix[6]arene (log K = 4.0) (Chapter 2), a higher complex stability for **Cage 1** was obtained.

Scheme 5.9 illustrates a potential association process. Initially, the dye forms a 1:1 complex with the first molecule of **Cage 1** (K_1). Subsequently, a second molecule of **Cage 1** self-assembles with the previously formed complex (K_2). It is possible to hypothesize that the second interaction may occur in multiple configurations. **Scheme 5.9** depicts two possible adducts configurations: in the first, the calix[6]arene cages are arranged *head-to-head* with the **TTz**-based dye aligned longitudinally and interacting with the aromatic cavities of macrocycles belonging to different cages; in the second, the cages are oriented *side-by-side,* and the dye is threaded orthogonally. The large chemical shifts observed in the dye's protons suggest that the *head-to-head* configuration is more likely. Nevertheless, further studies are needed to explain this unexpected complexing behavior.

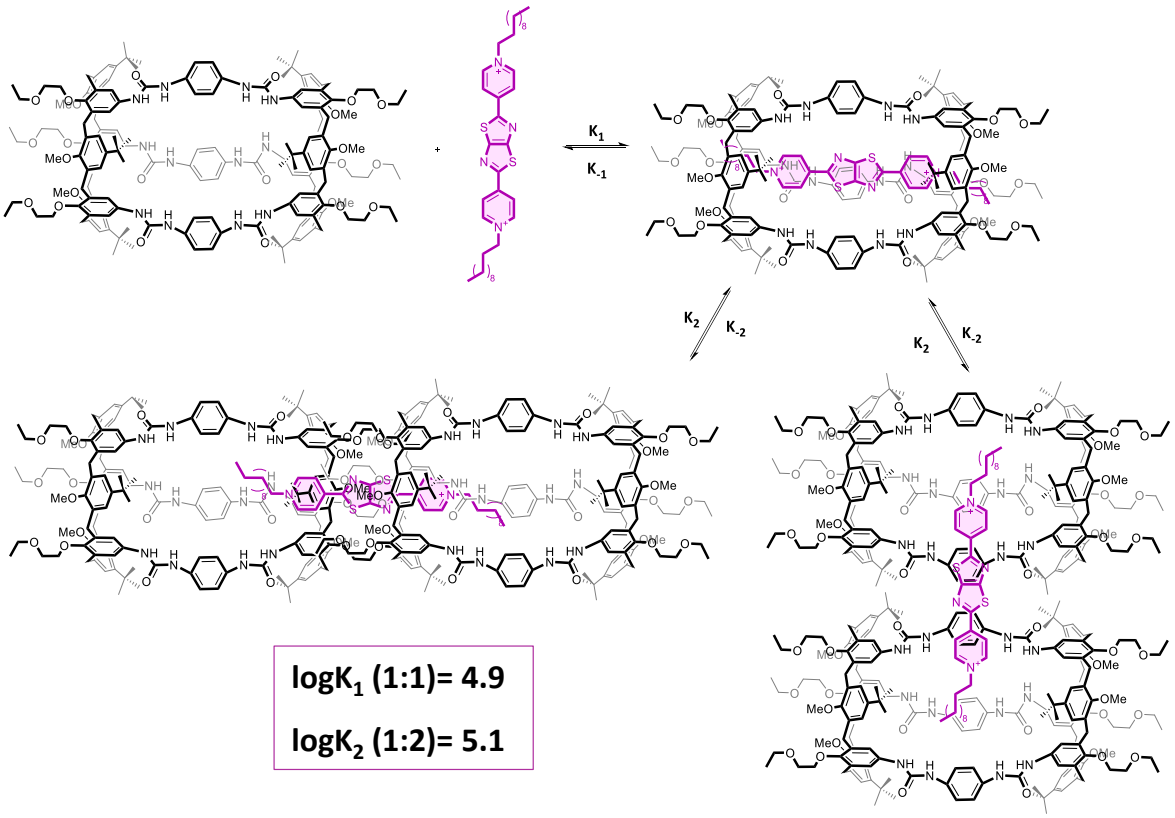

Scheme 5.9. Representation of the association between **$(C_8)_2Py_2TTz(2PF_6)$** and **Cage 1**. The association constants were determined in CH_2Cl_2 by fitting the UV-Vis data as reported in the text. Tosylate counterions were omitted for clarity.

Finally, the kinetics of the complexation were examined using a stopped-flow apparatus. A solution of **Cage 1** (c = 3.6×10^{-5} M) and **$(C_8)_2Py_2TTz(2PF_6)$** (c = 1.5×10^{-5} M) in dichloromethane in 1:1 ratio were mixed, and changes in absorption were monitored over time (**Figure 5.36**). Two kinetic processes were identified, likely corresponding to the two threading events. The fitting of the first process yielded rate constants of k_1 = 1405 $M^{-1}s^{-1}$ and k_{-1} = 0.011 s^{-1}, while the second process had rate constants of k_2 = 135 $M^{-1}s^{-1}$ and k_{-2} = 0.0022 s^{-1}. These results were comparable to those observed with **TPU** (k_1 = 2.7×10^3 $M^{-1}s^{-1}$, see Chapter 2).

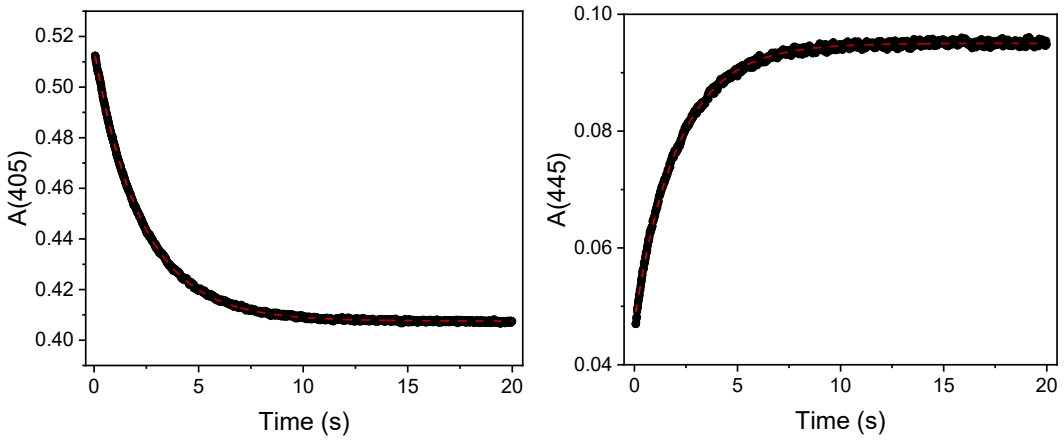

Figure 5.36. Absorption changes at 405 nm (left) and at 445 nm (right) for the 1:1 mixture of **Cage 1** and **$(C_8)_2Py_2TTz(2PF_6)$**.

5 Conclusions

This chapter shows details of the development of novel head-to-head calix[6]arene-based cages. The synthetic approach focused on forming ureido and imine bonds by reacting complementary calix[6]arene macrocycles either with each other or with linker molecules. In certain instances, **Cage 1** and **Cage 3**, the templating effect, achieved through the complexation of calix[6]arene macrocycles with bis-viologen salts, was explored. These templates were intended to preorganize the calix[6]arene macrocycles in a spatial arrangement favorable to cage formation. The final products were obtained in comparable yields in both cases, regardless of whether the templating effect was employed. For **Cage 1**, this outcome is attributed to the inability of the tri-amino calix[6]arene (**TA**) to effectively interact with the template species, rendering the templating effect ineffective. In the case of **Cage 3**, the reversible nature of imine bond formation likely led to repeated assembly and disassembly during synthesis, negating the template effect. Differently from the other two cases, **Cage 2** and **Cage 4** were synthesized by reacting directly calix[6]arene macrocycles decorated on their upper-rim with complementary functionalities to form ureido (**Cage 2**) or imine bonds (**Cage 4**).

All the synthesized cages exhibited significant structural flexibility and limited rigidity, as evidenced by their NMR spectra. Among them, only **Cage 3**, which is characterized by its smaller size and thus improved rigidity, displayed a more defined NMR spectrum. The ability of these cages to complex with electron-deficient dye was limited to **Cage 1** and evaluated using NMR, UV-Vis and fluorescence analyses. The association constants were determined through UV-Vis data fitting, revealing that **Cage 1** tends to form 1:2 stoichiometric complexes with guest molecules.

5 Acknowledgments

Thanks to Dr. Leonardo Andreoni and Dr. Dalila Cafagno (University of Bologna) for UV-Visible and fluorescence measurements. Thanks to Dr. Michele Crepaldi for the help with cage's synthesis.

5 Experimental Section

General Methods

All solvents were dried using standard procedures; all other reagents were of reagent-grade quality obtained from commercial suppliers and used without further purification. Melting points are uncorrected. NMR spectra were recorded at 400 MHz for ^{1}H and 100 MHz for ^{13}C. Chemical shifts are expressed in ppm using the residual solvent signal as an internal reference (7.26 ppm for $CHCl_3$, 7.16 ppm for C_6D_5H, 5.32 for $CHDCl_2$ and 3.31 ppm for CD_2HOD). The terms m, s, d, t and q represent multiplet, singlet, doublet, triplet and quadruplet, respectively; the term "br. s" means a broad signal. Mass spectra were recorded in the ESI mode. Compounds **1**,[8] **TA**,[9] **2$_8$**,[10] **2$_{12}$**,[11] and **2$_{16}$**[12] were synthesised according to published procedures.

Synthetic Procedure and Analytical Data

*General procedure for the synthesis of the tetra-viologen axles **3**$_m$.*

In a sealed 100 mL Schlenk tube, a solution of pentylpyridyl pyridinium tosylate (2.0 eq., 0.6 mmol) and ditosylate (1 eq., 0.3 mmol) in dry acetonitrile (20 mL) was refluxed under vigorous stirring for 4 days. Afterwards, the solution was evaporated to dryness under reduced pressure.

3$_8$: the solid residue of the evaporation was triturated with CH_3CN to afford 0.3 g of pure product **3**$_8$ as a white solid powder (63%).

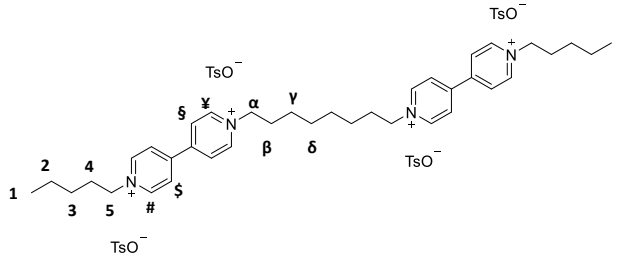

m.p. = 161-163 °C; **^{1}H NMR** (CD_3OD, 400 MHz): δ = 9.25 (d, 8H, *J* = 6.8 Hz, H$_{\#, ¥}$), 8.65 (d, 8H, *J* = 6.6 Hz, H$_{\$, §}$), 7.69 (d, 8H, *J* = 8.2 Hz, H$_{Ar\text{-}H(TsO)}$), 7.24 (d, 8H, *J* = 7.9 Hz, H$_{Ar\text{-}H(TsO)}$), 4.8-4.7 (m, 8H, H$_{α, 5}$), 2.38 (s, 12H, H$_{Me(TsO)}$), 2.1-2.0 (m, 8H, H$_{β, 4}$), 1.5-1.4 (m, 16H, H$_{2\text{-}3, γ\text{-}δ}$), 0.98 (t, 6H, *J* = 6.8 Hz, H$_1$) ppm. **^{13}C NMR** (CD_3OD, 101 MHz): δ = 149.8, 145.6, 142.2, 140.3, 128.5, 126.9, 125.5, 61.9, 31.0, 30.9, 28.3, 27.9, 25.6, 21.8, 19.9, 12.7 ppm. **ESI-MS (+)**: calculated for $C_{59}H_{75}N_4O_9S_3^+$: m/z (z = 1): 1080.5, found: 1080.5.

3$_{12}$: the solid residue of the evaporation was triturated with CH_3CN to afford 0.32 g of product **3**$_{12}$ as a white solid powder (63%).

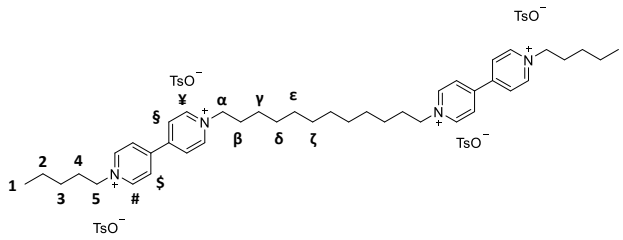

m.p. = 164-166 °C. **^{1}H NMR** (CD_3OD, 400 MHz): δ = 9.25 (d, 8H, *J* = 6.6 Hz, H$_{\#, ¥}$), 8.65 (d, 8H, *J* = 6.5 Hz, H$_{\$, §}$), 7.69 (d, 8H, *J* = 8.3 Hz, H$_{Ar\text{-}H(TsO)}$), 7.24 (d, 8H, *J* = 8.0 Hz, H$_{Ar\text{-}H(TsO)}$), 4.73 (t, 8H, *J* = 7.7 Hz, H$_{α, 5}$), 2.38 (s,

12H, $H_{Me(TsO)}$), 2.1-2.0 (m, 8H, $H_{\beta,4}$), 1.5-1.3 (m, 24H, $H_{2\text{-}3,\gamma\text{-}\zeta}$), 0.96 (t, 6H, *J* = 6.7 Hz, H_1) ppm. **^{13}C NMR** (CD_3OD, 101 MHz): δ = 149.8, 145.6, 142.2, 140.3, 128.5, 126.9, 125.5, 61.9, 31.2, 30.8, 29.2, 29.1, 28.8, 27.9, 25.9, 21.8, 19.9, 12.7 ppm. **ESI-MS (+)**: calculated for $C_{63}H_{83}N_4O_9S_3^+$: m/z (z = 1): 1136.5, found: 1136.5.

3$_{16}$: the solid residue of the evaporation was triturated with CH_3CN to afford 0.34 g of product **3**$_{16}$ as a white solid powder (65%).

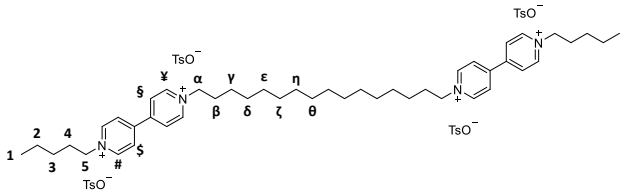

m.p. = 187-189 °C. **^{1}H NMR** (CD_3OD, 400 MHz): δ = 9.28 (d, 8H, *J* = 6.6 Hz, $H_{\#,¥}$), 8.67 (d, 8H, *J* = 6.5 Hz, $H_{\$,§}$), 7.71 (d, 8H, *J* = 8.3 Hz, $H_{Ar\text{-}H(TsO)}$), 7.25 (d, 8H, *J* = 8.0 Hz, $H_{Ar\text{-}H(TsO)}$), 4.75 (t, 8H, *J* = 7.7 Hz, $H_{\alpha,5}$), 2.39 (s, 12H, $H_{Me(TsO)}$), 2.1-2.0 (m, 8H, $H_{\beta,4}$), 1.5-1.3 (m, 32H, $H_{2\text{-}3,\gamma\text{-}\theta}$), 0.98 (t, 6H, *J* = 6.7 Hz, H_1) ppm. **^{13}C NMR** (CD_3OD, 101 MHz): δ = 149.8, 145.6, 142.2, 140.3, 128.5, 126.9, 125.5, 61.9, 31.2, 30.8, 29.7, 29.2, 29.1, 28.8, 28.3, 27.9, 25.9, 21.8, 19.9, 12.7 ppm. **ESI-MS (+)**: calculated for $C_{67}H_{91}N_4O_9S_3^+$: m/z (z = 1): 1192.6, found: 1192.5.

TPU-OH: In a 100 mL two-neck round-bottom flask under nitrogen atmosphere, a solution of triphosgene (70.5 mg, 237.7 µmol, 1.1 eq.) in dry toluene (20 mL) was inserted. A freshly prepared solution of **TA** (265.5 mg, 216.1 µmol, 1.0 eq.) and triethylamine (105 µL, 756.2 µmol, 3.5 eq.) in toluene (10 mL) was added to the reactor. The mixture was stirred at 80 °C for 4 hours. After cooling the reactor at room temperature, a solution of 4-aminobenzylalcohol (106.4 mg, 864.2 µmol, 4.0 eq) in dry toluene (2 mL) was added dropwise, and the reaction was stirred at room temperature for 17 hours. After completion of the reaction, the solvent was evaporated under reduced pressure. The crude product was purified by column chromatography (SiO_2, Hexane/ethyl acetate gradient from 40:60 to 40:60 with 10% of methanol) to afford pure **TPU-OH** as orange solid in 30% yield (111.6 mg, 64.8 µmol).

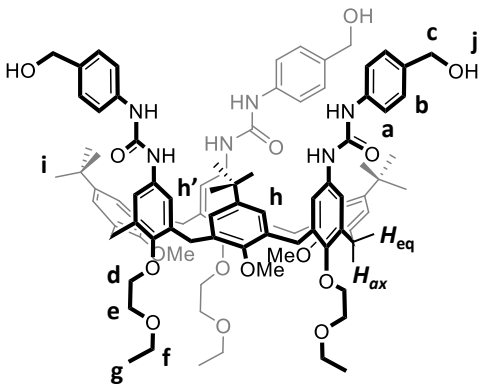

m.p. = 146-148 °C. **^{1}H NMR** (CD_3CN, 400 MHz): δ = 7.3, 7.13, 7.08, 6.9, 6.5 (5 br. s, 30H, $H_{Ar,\ NH}$), 4.4 (d, *J* = 5.2 Hz, 6H, H_c), 3.9 (br. s, 6 H, H_d), 3.7 (br. s, 6H, H_e), 3.6 (br. s, 6H, H_f), 3.2 (br. s, 9H, H_{OMe}), 3.0 (t, *J* = 5.8 Hz, 3H, H_j), 1.3 (s, 27H, H_i), 1.2 (t, *J* = 7 Hz, 9H, H_g) ppm. **^{13}C NMR** (CD_3CN, 101 MHz): δ = 155.8, 154.8, 151.8, 147.6, 139.3, 137.3, 136.4, 135.1, 134.2, 128.7, 128.3, 121.4, 120.4, 73.5, 70.8, 67.3, 64.6, 61.1, 35.0, 31.9, 31.7, 15.7

ppm. **HR-MS (MALDI)** calculated for $C_{93}H_{114}N_6O_{15}Na^+$: m/z (z = 1): 1577.48471; found: 1577.48420. Calculated for $C_{93}H_{114}N_6O_{15}K^+$: m/z (z = 1): 1593.471012; found: 1593.47028.

TPU-AL: In a 25 mL round-bottom flask under a nitrogen atmosphere, **TPU-OH** (50.5 mg, 0.032 mmol, 1.0 eq.) was suspended in 4 mL of dichloromethane, then Dess-Martin periodinane (41 mg, 0.097 mmol, 3.0 eq.) was added. The solution was stirred at room temperature for 24 hours. After completion of the reaction, the solvent was evaporated under reduced pressure. The crude product was purified by column chromatography (SiO_2, hexane/ethyl acetate 50:50 + 2% methanol), affording **TPU-AL** (26.7 mg, 0.017 mmol) as a white solid in 53 % yield.

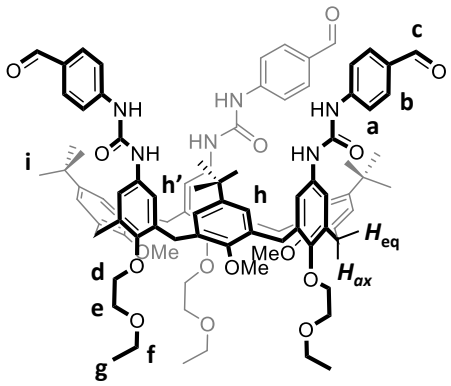

m.p. = 137-139 °C. ^{1}H NMR ($CDCl_3$, 400 MHz): δ = 9.8 (br. S, 3H, H_c), 7.6, 7.2, 6.3 (3 br. s, 30H, $H_{Ar, NH}$), 4.4 (br. s, 6H, H_{Hax}), 4.1 (br. s, 6 H, H_d), 3.9 (br. s, 6H, H_e), 3.7 (br. s, 12H, $H_{Heq, f}$), 3.1 (br. s, 9H, H_{OMe}), 1.5-0.9 (m, 36H, $H_{i, g}$) ppm. **^{13}C NMR** ($CDCl_3$, 101 MHz): δ = 190.8, 131.1, 118.4, 69.8, 66.8, 31.4, 29.6, 15.2 ppm. **HR-MS (ORBITRAP LQ)** calculated for $C_{93}H_{109}N_6O_{15}$: m/z (z = 1): 1549.79454; found: 1549.79250. Calculated for $C_{93}H_{112}N_7O_{15}$: m/z (z = 1): 1566.82109; found: 1566.82178.

General procedure for the synthesis of supramolecular cages

In a three-neck round-bottom flask, under nitrogen atmosphere, the appropriate calix[6]arene (2.0 eq.) and the axle $\mathbf{3}_m$ (1.0 eq.) were suspended in dry CH_2Cl_2 (c = 10^{-3}-10^{-4} M) and the reaction was stirred at room temperature for 15 minutes. A fresh solution of the appropriate linker (3.0 eq.) in dry CH_2Cl_2 was then added to the reaction mixture within 30 minutes. The reaction mixture was stirred at room temperature for 24 hours. After that, the solvent was removed under reduced pressure. The crude solid was dissolved in CH_2Cl_2, adsorbed onto silica, and purified by column chromatography (SiO_2, CH_2Cl_2/MeOH 95:5).

Cage 1

No axle: Cage 1 was synthesized from **TA** (56.6 mg, 51.1 µmol, 2.0 eq.) and 1,4-phenylene diisocianate (12.3 mg, 76.6 µmol, 3.0 eq.) according to general procedure. The pure product was obtained as a pale-yellow solid in 58% yield (39.3 mg, 29.6 µmol).

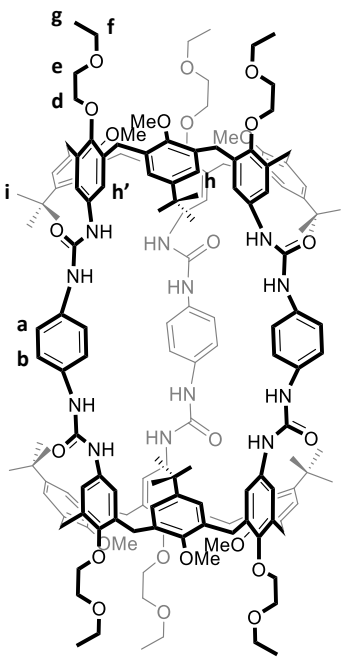

m.p. = 317-320 °C. **^{1}H NMR** ($CDCl_3$, 400 MHz): δ = 7.7-6.3 (br. s, 48H, $H_{ArH,\ NH}$), 4.6 (br. s, 12H, H_{Hax}), 4.1 (br. s, 12H, H_d), 3.9 (br. s, 12H, H_e), 3.7 (br. s, 12H, H_f), 3.6 (br. d, 12H, H_{Heq}), 3.0 (br. s, 18H, H_{OMe}), 1.3, 1.7-0.7 (br. s, m, 66H, $H_{i,\ g}$) ppm. **HR-MS (ESI, Orbitrap LQ)** Calculated for $C_{162}H_{199}O_{24}N_{12}^+$: m/z (z= 1): 2696.47147; found: 2696.47188. Calculated for $C_{162}H_{200}O_{24}N_{12}^{2+}$: m/z (z= 2): 1348.73937; found: 1348.73958.

Axle 3_8: Cage 1 was synthetized from **TA** (54.5 mg, 49.3 µmol, 2.0 eq.), axle $\mathbf{3}_8$ (31.0 mg, 24.7 µmol, 1.0 eq.) and 1,4-phenylene diisocianate (11.8 mg, 73.8 µmol, 3.0 eq.) according to general procedure. The pure product was obtained as pale-yellow solid in 27% yield (18.0 mg, 6.7 µmol).

Axle 3_{12}: Cage 1 was synthetized from **TA** (43.9 mg, 39.6 µmol, 2.0 eq.), axle $\mathbf{3}_{12}$ (25.9 mg, 19.8 µmol, 1.0 eq.) and 1,4-phenylene diisocianate (3.17 mg, 19.8 µmol, 3.0 eq.) according to general procedure. The pure product was obtained as pale-yellow solid in 60% yield (39.8 mg, 11.9 µmol).

Axle 3_{16}: Cage 1 was synthetized from **TA** (33.3 mg, 30.1 µmol, 2.0 eq.), axle $\mathbf{3}_{16}$ (20.5 mg, 15.0 µmol, 1.0 eq.) and 1,4-phenylene diisocianate (7.22 mg, 45.1 µmol, 3.0 eq.) according to general procedure. The pure product was obtained as pale-yellow solid in 48% yield (19.4 mg, 7.19 µmol).

Cage 3

No axle: Cage 3 was synthetized from **TPU-AL** (48.5 mg, 31.3 µmol, 2.0 eq.) and 1,4-phenylenediamine (5.08 mg, 46.9 µmol, 3.0 eq.) according to general procedure. The pure product was obtained as orange-brown solid in 48% yield (25.0 mg, 7.54 µmol).

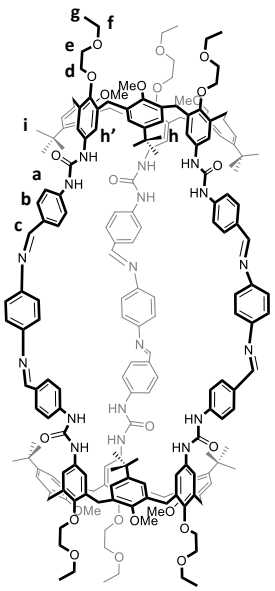

m.p. = 145-147 °C. **^{1}H NMR** (CD_2Cl_2, 400 MHz): δ = 8.3 (br. s, 6H, H_c), 8.9, 7.5, 7.2, 7.1, 6.6 (5 br. s, 72H, $H_{ArH,\ NH}$), 4.4 (br. s, 12H, H_{Hax}), 4.1 (br. s, 12H, H_d), 3.9 (m, 12H, H_e), 3.7 (m, 24H, $H_{f,\ Heq}$), 3.1 (br. s, 18H, H_{OMe}), 1.6-1.0 (m, 72H, $H_{i,\ g}$) ppm. **HR-MS (ESI, Orbitrap LQ)** calculated for $C_{204}H_{230}N_{18}O_{24}^{2+}$: m/z (z = 2): 1657.86597; found: 1657.86264.

Axle 3_8: Cage 3 was synthetized from **TPU-AL** (21.0 mg, 13.5 µmol, 2.0 eq.), axle $\mathbf{3}_8$ (10.0 mg, 6.76 µmol, 1.0 eq.) and 1,4-phenylenediamine (2.2 mg, 20.3 µmol, 3.0 eq.) according to general procedure. The pure product was obtained as an orange-brown solid in 52% yield (11.7 mg, 3.51 µmol).

Axle 3_{12}: Cage 3 was synthetized from **TPU-AL** (87.7 mg, 56.6 µmol, 2.0 eq.), axle $\mathbf{3}_{12}$ (37.0 mg, 28.3 µmol, 1.0 eq.) and 1,4-phenylenediamine (9.2 mg, 84.9 µmol, 3.0 eq.) according to general procedure. The pure product was obtained as an orange-brown solid in 51% yield (47.8 mg, 14.4 µmol).

HR-MS (ESI, Orbitrap LQ) calculated for $C_{246}H_{290}N_{22}O_{24}^{4+}$: m/z (z=4): 984.05316; found: 984.04980. Calculated for $C_{246}H_{290}N_{22}O_{24}Cl^{3+}$: m/z (z=3): 1323.72735; found: 1323.72262. Calculated for $C_{253}H_{297}N_{22}O_{27}S^{3+}$: m/z (z=3): 1369.07493; found: 1369.06860. Calculated for $C_{246}H_{290}N_{22}O_{24}Cl_2^{2+}$: m/z (z=2): 2003.07572; found: 2003.06752.

Axle 3_{16}: Cage 3 was synthetized from **TPU-AL** (13.3 mg, 8.61 µmol, 2.0 eq.), axle $\mathbf{3}_{16}$ (6.85 mg, 4.30 µmol, 1.0 eq.) and 1,4-phenylenediamine (1.40 mg, 12.9 µmol, 3.0 eq.) according to general procedure. The pure product was obtained as an orange-brown solid in 70% yield (10.0 mg, 3.01 µmol).

Cage 2

In a three-neck round-bottom flask, under nitrogen atmosphere, calix[6]arene **TA** (45.0 mg, 40.6 µmol, 1.0 eq.) and calix[6]arene **TNCO** (48.2 mg, 40.6 µmol, 1.0 eq.) were dissolved in dry dichloromethane (9 mL). The reaction mixture was stirred at room temperature for 24 hours. After that, the solvent was removed under reduced pressure. The crude product was dissolved in CH_2Cl_2,

adsorbed onto silica, and purified by column chromatography (SiO_2, CH_2Cl_2/MeOH 95:5) to give pure **Cage 2** as a pale yellow solid in 13% yield (12 mg, 5.2 µmol).

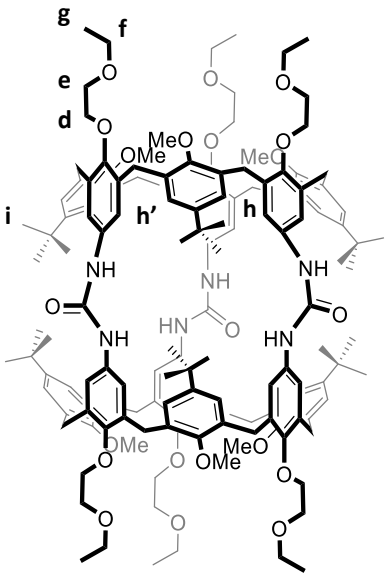

m.p. =313-315 °C. **^{1}H NMR** ($CDCl_3$, 400 MHz): δ = 8.3 (br. s, 15H, H_{ArH}), 5.9 (br. s, 15H, $H_{ArH,\ NH}$), 4.4 (br. s, 12H, H_{Hax}), 4.0 (br. s, 12H, H_d), 3.8 (br. s, 12H, H_e), 3.6 (m, 12H, H_f), 3.5 (br. d, 12H, H_{Heq}), 3.0 (br. s, 18H, H_{OMe}), 1.5, 1.6-1.0 (br. s, m, 66H, $H_{i,\ g}$) ppm. **ESI-MS (+)**: calculated for $C_{141}H_{182}N_6O_{21}^{2+}$: m/z (z = 2): 1148.2, found: 1148.4. Calculated for $C_{141}H_{185}N_7O_{21}^{2+}$: m/z (z = 2): 1156.7, found: 1156.8.

Cage 4

In a three-neck round-bottom flask, under nitrogen atmosphere, **TPU-AL** (51.1 mg, 33.0 µmol, 1.0 eq.) was dissolved in dry dichloromethane (5 mL). Then a solution of **TA** (36.2 mg, 32.7 µmol, 1.0 eq.) in dry dichloromethane (3 mL) was added dropwise. The reaction mixture was stirred at room temperature for 24 hours. After that, the solvent was removed under reduced pressure. The crude product was dissolved in CH_2Cl_2, adsorbed onto silica, and purified by column chromatography (SiO_2, CH_2Cl_2/MeOH 95:5) to give pure **Cage 4** as an orange-brown solid in 60% yield (51.6 mg, 19.8 µmol).

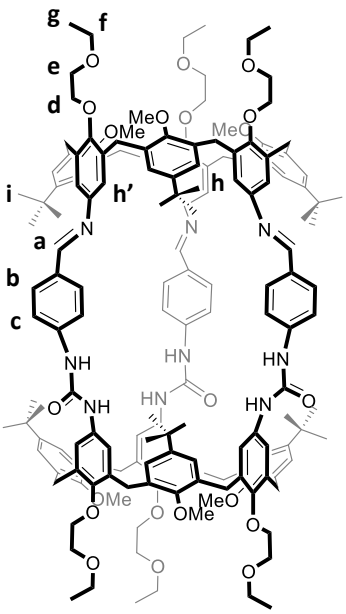

m.p. = 337-340 °C. **^{1}H NMR** ($CDCl_3$, 400 MHz): δ = 7.7-6.3 (m, 42H, H_{ArH}), 5.87 (s, 3H, H_a), 4.6 (br. s, 12H, H_{Hax}), 4.1 (br. s, 12H, H_d), 3.9 (br. s, 12H, H_e), 3.7 (m, 12H, H_f), 3.5 (br. s, 12H, H_{Heq}), 3.06 (s, 18H, H_{OMe}), 1.8-0.7 (m, 66H, $H_{i,\ g}$) ppm. **ESI-MS (+)**: calculated for $C_{162}H_{197}N_9O_{21}^{2+}$: m/z (z = 2): 1303.2, found: 1303.0. Calculated for $C_{162}H_{195}KN_9NaO_{21}^{2+}$: m/z (z = 2): 1333.2, found: 1332.2.

5 Bibliography

(1) Muller, P. Glossary of Terms Used in Physical Organic Chemistry (IUPAC Recommendations 1994). *Pure Appl. Chem.* **1994**, *66* (5), 1077–1184. https://doi.org/10.1351/pac199466051077.

(2) Jin, P.; Dalgarno, S. J.; Atwood, J. L. Mixed Metal-Organic Nanocapsules. *Coord. Chem. Rev.* **2010**, *254* (15–16), 1760–1768. https://doi.org/10.1016/j.ccr.2010.04.009.

(3) Smulders, M. M. J.; Riddell, I. A.; Browne, C.; Nitschke, J. R. Building on Architectural Principles for Three-Dimensional Metallosupramolecular Construction. *Chem. Soc. Rev.* **2013**, *42* (4), 1728–1754. https://doi.org/10.1039/C2CS35254K.

(4) Harris, K.; Fujita, D.; Fujita, M. Giant Hollow MnL2n Spherical Complexes: Structure, Functionalisation and Applications. *Chem. Commun.* **2013**, *49* (60), 6703. https://doi.org/10.1039/c3cc43191f.

(5) MacGillivray, L. R.; Atwood, J. L. A Chiral Spherical Molecular Assembly Held Together by 60 Hydrogen Bonds. *Nature* **1997**, *389* (6650), 469–472. https://doi.org/10.1038/38985.

(6) Steed, J. W.; Atwood, J. L. *Supramolecular Chemistry*; John Wiley & Sons, **2022**.

(7) Little, M. A.; Cooper, A. I. The Chemistry of Porous Organic Molecular Materials. *Adv. Funct. Mater.* **2020**, *30* (41), 1909842. https://doi.org/10.1002/adfm.201909842.

(8) Galan, A.; Ballester, P. Stabilization of Reactive Species by Supramolecular Encapsulation. *Chem. Soc. Rev.* **2016**, *45* (6), 1720–1737. https://doi.org/10.1039/C5CS00861A.

(9) Yu, Y.; Yang, J.-M.; Rebek, J. Molecules in Confined Spaces: Reactivities and Possibilities in Cavitands. *Chem* **2020**, *6* (6), 1265–1274. https://doi.org/10.1016/j.chempr.2020.04.014.

(10) Pappalardo, A.; Puglisi, R.; Trusso Sfrazzetto, G. Catalysis inside Supramolecular Capsules: Recent Developments. *Catalysts* **2019**, *9* (7), 630. https://doi.org/10.3390/catal9070630.

(11) Zhang, G.; Mastalerz, M. Organic Cage Compounds – from Shape-Persistency to Function. *Chem. Soc. Rev.* **2014**, *43* (6), 1934–1947. https://doi.org/10.1039/C3CS60358J.

(12) Liu, W.; Stoddart, J. F. Emergent Behavior in Nanoconfined Molecular Containers. *Chem* **2021**, *7* (4), 919–947. https://doi.org/10.1016/j.chempr.2021.02.016.

(13) Lehn, J. M.; Sauvage, J. P.; Dietrich, B. Cryptates. Cation Exchange Rates. *J. Am. Chem. Soc.* **1970**, *92* (9), 2916–2918. https://doi.org/10.1021/ja00712a053.

(14) Kiggen, W.; Vögtle, F. Functionalized, Oligocyclic Large Cavities — A Novel Siderophore. *Angew. Chem. Int. Ed. Engl.* **1984**, *23* (9), 714–715. https://doi.org/10.1002/anie.198407141.

(15) Quan, M. L. C.; Cram, D. J. Constrictive Binding of Large Guests by a Hemicarcerand Containing Four Portals. *J. Am. Chem. Soc.* **1991**, *113* (7), 2754–2755. https://doi.org/10.1021/ja00007a060.

(16) Lehn, J.-M. Dynamic Combinatorial Chemistry and Virtual Combinatorial Libraries. *Chem. - Eur. J.* **1999**, *5* (9), 2455–2463. https://doi.org/10.1002/(SICI)1521-3765(19990903)5:9<2455::AID-CHEM2455>3.0.CO;2-H.

(17) Mastalerz, M. One-Pot Synthesis of a Shape-Persistent Endo-Functionalised Nano-Sized Adamantoid Compound. *Chem. Commun.* **2008**, No. 39, 4756. https://doi.org/10.1039/b808990f.

(18) Schneider, M. W.; Siegfried Hauswald, H.-J.; Stoll, R.; Mastalerz, M. A Shape-Persistent Exo-Functionalized [4 + 6] Imine Cage Compound with a Very High Specific Surface Area. *Chem. Commun.* **2012**, *48* (79), 9861. https://doi.org/10.1039/c2cc35002e.

(19) Schneider, M. W.; Oppel, I. M.; Mastalerz, M. Exo-Functionalized Shape-Persistent [2+3] Cage Compounds: Influence of Molecular Rigidity on Formation and Permanent Porosity. *Chem. – Eur. J.* **2012**, *18* (14), 4156–4160. https://doi.org/10.1002/chem.201200032.

(20) Liu, X.; Warmuth, R. Solvent Effects in Thermodynamically Controlled Multicomponent Nanocage Syntheses. *J. Am. Chem. Soc.* **2006**, *128* (43), 14120–14127. https://doi.org/10.1021/ja0644733.

(21) Hasell, T.; Wu, X.; Jones, J. T. A.; Bacsa, J.; Steiner, A.; Mitra, T.; Trewin, A.; Adams, D. J.; Cooper, A. I. Triply Interlocked Covalent Organic Cages. *Nat. Chem.* **2010**, *2* (9), 750–755. https://doi.org/10.1038/nchem.739.

(22) Acharyya, K.; Mukherjee, S.; Mukherjee, P. S. Molecular Marriage through Partner Preferences in Covalent Cage Formation and Cage-to-Cage Transformation. *J. Am. Chem. Soc.* **2013**, *135* (2), 554–557. https://doi.org/10.1021/ja310083p.

(23) Kataoka, K.; James, T. D.; Kubo, Y. Ion Pair-Driven Heterodimeric Capsule Based on Boronate Esterification: Construction and the Dynamic Behavior. *J. Am. Chem. Soc.* **2007**, *129* (49), 15126–15127. https://doi.org/10.1021/ja076792f.

(24) Nishimura, N.; Kobayashi, K. Self-Assembly of a Cavitand-Based Capsule by Dynamic Boronic Ester Formation, *Angew. Chem.* **2008**, *120* (33), 6351–6354. https://doi.org/10.1002/ange.200802293.

(25) Christinat, N.; Scopelliti, R.; Severin, K. Multicomponent Assembly of Boronic Acid Based Macrocycles and Cages. *Angew. Chem. Int. Ed.* **2008**, *47* (10), 1848–1852. https://doi.org/10.1002/anie.200705272.

(26) Içli, B.; Christinat, N.; Tönnemann, J.; Schüttler, C.; Scopelliti, R.; Severin, K. Synthesis of Molecular Nanostructures by Multicomponent Condensation Reactions in a Ball Mill. *J. Am. Chem. Soc.* **2009**, *131* (9), 3154–3155. https://doi.org/10.1021/ja809279s.

(27) Zhang, C.; Wang, Q.; Long, H.; Zhang, W. A Highly C_{70} Selective Shape-Persistent Rectangular Prism Constructed through One-Step Alkyne Metathesis. *J. Am. Chem. Soc.* **2011**, *133* (51), 20995–21001. https://doi.org/10.1021/ja210418t.

(28) Okochi, K. D.; Han, G. S.; Aldridge, I. M.; Liu, Y.; Zhang, W. Covalent Assembly of Heterosequenced Macrocycles and Molecular Cages through Orthogonal Dynamic Covalent Chemistry (ODCC). *Org. Lett.* **2013**, *15* (17), 4296–4299. https://doi.org/10.1021/ol4015283.

(29) Galán, A.; Escudero-Adán, E. C.; Ballester, P. Template-Directed Self-Assembly of Dynamic Covalent Capsules with Polar Interiors. *Chem. Sci.* **2017**, *8* (11), 7746–7750. https://doi.org/10.1039/C7SC03731G.

(30) Mastalerz, M. Shape-Persistent Organic Cage Compounds by Dynamic Covalent Bond Formation. *Angew. Chem. Int. Ed.* **2010**, *49* (30), 5042–5053. https://doi.org/10.1002/anie.201000443

(31) Bottino, A.; Cunsolo, F.; Piattelli, M.; Garozzo, D.; Neri, P. Synthesis of 5,5‘-Bicalix[6]Arene and 5,5‘-Bicalix[8]Arene Systems. *J. Org. Chem.* **1999**, *64* (21), 8018–8020. https://doi.org/10.1021/jo9905017.

(32) Arduini, A.; Ferdani, R.; Pochini, A.; Secchi, A. Synthesis of Upper Rim Covalently Linked Double Calix[6]Arenes. *Tetrahedron* **2000**, *56* (43), 8573–8577. https://doi.org/10.1016/S0040-4020(00)00805-X.

(33) Cester Bonati, F.; Bazzoni, M.; Baccini, C.; Zanichelli, V.; Orlandini, G.; Arduini, A.; Cera, G.; Secchi, A. Calix[6]Arene-Based [3]Rotaxanes as Prototypes for the Template Synthesis of Molecular Capsules. *Molecules* **2023**, *28* (2), 595. https://doi.org/10.3390/molecules28020595.

(34) Mitsui, M.; Higashi, K.; Takahashi, R.; Hirumi, Y.; Kobayashi, K. Enhanced Photostability of an Anthracene-Based Dye Due to Supramolecular Encapsulation: A New Type of Photostable Fluorophore for Single-Molecule Study. *Photochem. Photobiol. Sci.* **2014**, *13* (8), 1130–1136. https://doi.org/10.1039/C4PP00065J.

(35) Nishimura, N.; Kobayashi, K. Self-Assembled Boronic Ester Cavitand Capsule as a Photosensitizer and a Guard Nanocontainer against Photochemical Reactions of 2,6-

Diacetoxyanthracene. *J. Org. Chem.* **2010**, *75* (18), 6079–6085. https://doi.org/10.1021/jo101255g.

Chapter 6. Electrochemistry of out-of-equilibrium supramolecular systems

6 Introduction

Out-of-equilibrium system

Endergonic processes are fundamental for numerous biological and chemical systems. In many biological contexts, motor proteins and energy reserves sustain living organisms away from thermodynamic equilibrium.[1–3] Endergonic processes are characterized by a positive Gibbs free energy ($\Delta G > 0$), rendering them thermodynamically unfeasible without an external energy source. In an endergonic process, species distribution is shifted from an equilibrium state to an out-of-equilibrium state thanks to an energy input (**Figure 6.1**). The reverse reaction, where the system dissipates energy as it relaxes towards equilibrium, is also a non-equilibrium process.

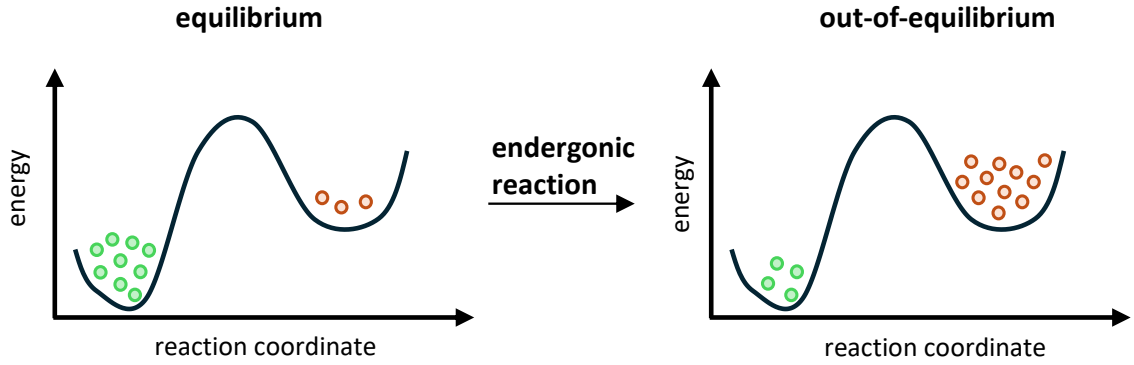

Figure 6.1 Schematic representation of an endergonic reaction driving the system from an equilibrium state to an out-of-equilibrium state.

An endergonic process necessitates a mechanism that facilitates energy transfer from the energy source to the target process. This energy transfer mechanism is known as a ratchet mechanism. A chemical reaction network governed by a ratchet mechanism can be conceptualized as comprising two distinct reactions: a driving reaction, which supplies energy, and a driven reaction, which utilizes part of this energy to facilitate the endergonic reaction. For instance, consider the reaction network depicted in **Scheme 6.1**, where the driven (endergonic) reaction involves the interconversion from a low-energy state L to a high-energy state H. The driving reaction consists of a chemical reaction that provides the necessary energy to drive the L to H interconversion.

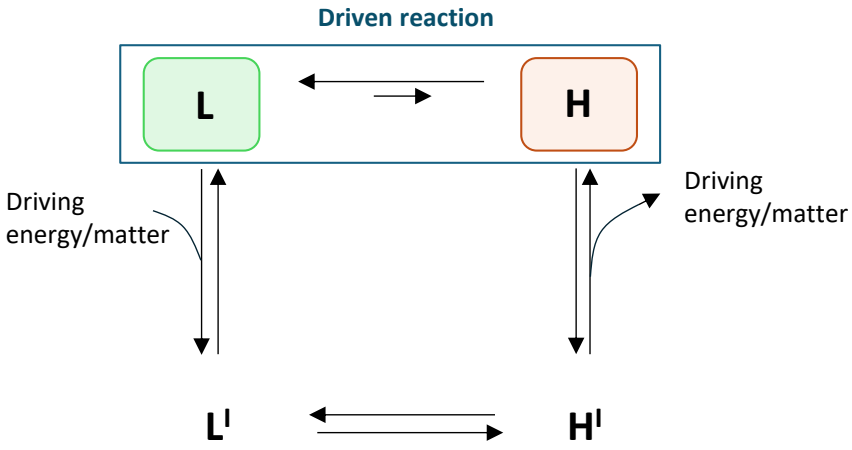

Scheme 6.1 Schematic representation of generic driven reaction (L to H interconversion) and driving cyclic reaction network. Vertical arrows indicate processes of energy exchange with the system.

Ratchet mechanisms can be categorized into two types: energy ratchets and information ratchets. In energy ratchet mechanisms, the energy of the intermediates of the cycle (e.g., L^{I} and H^{I}) determines the directionality of the reaction network. For energy ratchets, the energy source can involve the addition of an acid or a base, a reductant and an oxidant, or the use of light, which can vary over time or space.[2–5] In contrast, in information ratchets, the energy of the intermediates is not a determining factor for directionality. Instead, what matters is the energy of the transition states between the intermediates of the reaction network.[6–8]

This chapter will focus on electrochemically driven energy ratchets mechanisms. As an example, redox stimuli can be exploited in systems involving species such as bipyridinium dications, which, under reductive conditions, are reduced to radical-cationic species capable of engaging in radical-radical interactions.[9] Non-covalent interactions have been extensively used in supramolecular systems for the design of functional materials, and in the last years, radical-radical recognition has also emerged as a significant motif, further expanding the strategies employed in the development of such systems.[10] 4,4'-dipyridinium dications are widely used in supramolecular chemistry for host-guest complexes (see previous Chapters), owing to their π-electron-deficient nature, which facilitates interactions with π-electron-rich macrocycles.[11] These dications serve not only as π-electron-poor acceptors but also participate in radical-radical interaction, also known as pimerization.[12,13] Viologen salts undergo a facile one-electron reduction of their bipyridinium core $\mathbf{V}^{2+}$ to form radical cations $\mathbf{V}^{\bullet+}$ (**Figure 6.2 (*a*)**). At high concentrations, these viologen radical cations can dimerize to form $(\mathbf{V}^{\bullet+})_2$ dimers (**Figure 6.2, (*b*)**). Due to the high concentration (> 1 M) required for this dimerization, it has not been widely utilized in the design of supramolecular systems. In 2010, Stoddart *et al.*[9] leveraged radical-radical recognition to achieve host-guest complexation

using cyclobis(paraquat-*p*-phenylene) (**CBPQT**$^{4+}$), also known as "Blue Box," as host and a viologen salt as the guest. **CBPQT**$^{4+}$ is a macrocycle containing two bipyridinium units, making it π-electron-deficient and capable of interacting with π-electron-rich guest molecules. However, in this study, **CBPQT**$^{4+}$ was employed to exploit the formation of radical-cationic species. Indeed, the radical-cationic species **CBPQT**$^{2(\bullet+)}$ and **V**$^{\bullet+}$, interacting through radical-radical recognition, can form a stable tris-radical tris-cationic complex **CBPQT**$^{2(\bullet+)}\supset$**V**$^{\bullet+}$ (**Figure 6.2, (*c*)**).

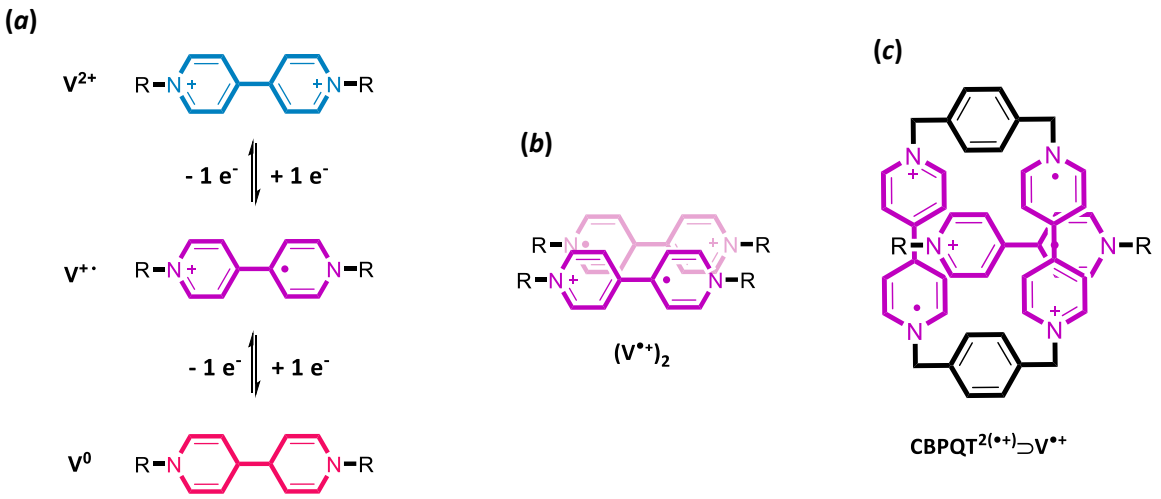

Figure 6.2. (***a***) Schematic representation of the reduction of viologen salts: the first reversible one-electron reduction from **V**$^{2+}$ to **V**$^{\bullet+}$, and the second reversible one-electron reduction from **V**$^{\bullet+}$ to **V**^{0}; (***b***) Representation of dimer species (**V**$^{\bullet+}$)$_2$; (***c***) representation of the tris-radical tris-cationic complex **CBPQT**$^{2(\bullet+)}\supset$**V**$^{\bullet+}$.

The formation of the tris-radical tris-cationic species as **CBPQT**$^{2(\bullet+)}\supset$**V**$^{\bullet+}$ can be monitored through UV-Vis-NIR spectroscopy and spectro-electrochemistry analysis. Indeed, while the radical-cationic species exhibit an absorption band at approximately 600 nm, dimers are characterized by a red-shifted absorption in the near-infrared (NIR) region, around 1100 nm[14,15], and so they can be easily detected.

Artificial molecular machines

In nature, numerous processes are governed by thermodynamically unfavorable reactions. For example, transmembrane protein pumps generate ion concentration gradients, with the stored energy subsequently utilized as an energy source in metabolic processes such as adenosine triphosphate (ATP) synthesis.[16,17] Some proteins can harness external fuel to precisely control the forces exerted on their cargos, driving them energetically uphill. Over the past few decades, significant effort has been devoted to creating artificial molecular systems exhibiting controlled motion. However, the driving force for these systems has typically been to induce molecular motion toward a low-energy equilibrium state. The development of artificial molecular switches capable of driving cargo away from equilibrium has garnered significant interest. In 2014, Stoddart *et al.*[18] introduced a family of artificial supramolecular pumps (AMPs) that facilitated the formation of non-

equilibrium states through redox chemical energy. In particular, a **CBPQT**$^{4+}$ macrocycle was transported from the bulk solution onto an energetically unfavorable dumbbell *via* a redox-controlled energy ratchet mechanism. The structure of the dumbbell was crucial for the process, requiring elements such as a bipyridinium (**BIPY**$^{2+}$) recognition site, a collecting chain, a stopper group, and a so-called "pump head" (**Figure 6.3**).

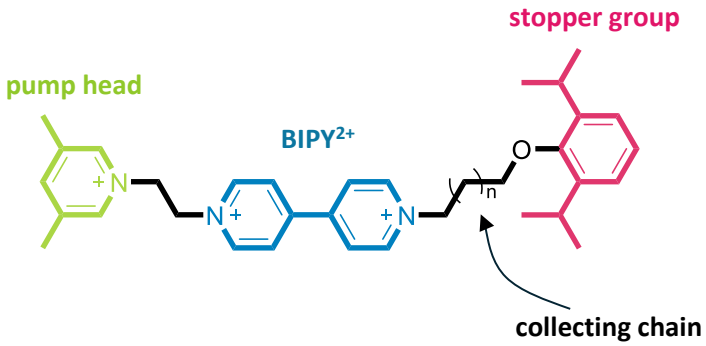

Figure 6.3. Structure of the dumbbell designed by Stoddart *et al.*[18].

In **Scheme 6.2**, the driven and driving reactions of the energy ratchet mechanism are represented. The complexation between the dumbbell and the macrocycle is an equilibrium reaction, predominantly shifted toward the disassembled state due to the Coulombic repulsion between positive charges. To shift the equilibrium towards complexation, we must consider the energetic barriers of each state and utilize an energy ratchet mechanism based on redox reactions to achieve the high-energy state. The initial oxidized species, upon reduction, gain 3 electrons to form the reduced radical-cationic species in solution. Through radical-radical recognition, the threading process gives the tris-radical tris-cationic complex, which is thermodynamically stable and characterized by a low-energy state. Subsequently, oxidation restores the positive charges on the three bipyridinium units, causing the **CBPQT**$^{4+}$ macrocycle to move towards the collecting chain rather than the pump head due to Coulombic repulsion. This process results in the formation of a thermodynamically unstable but kinetically favored high-energy complex. The resulting high-energy complex then dethreads, yielding the free oxidized species in solution, which thereby attains a lower energy state.

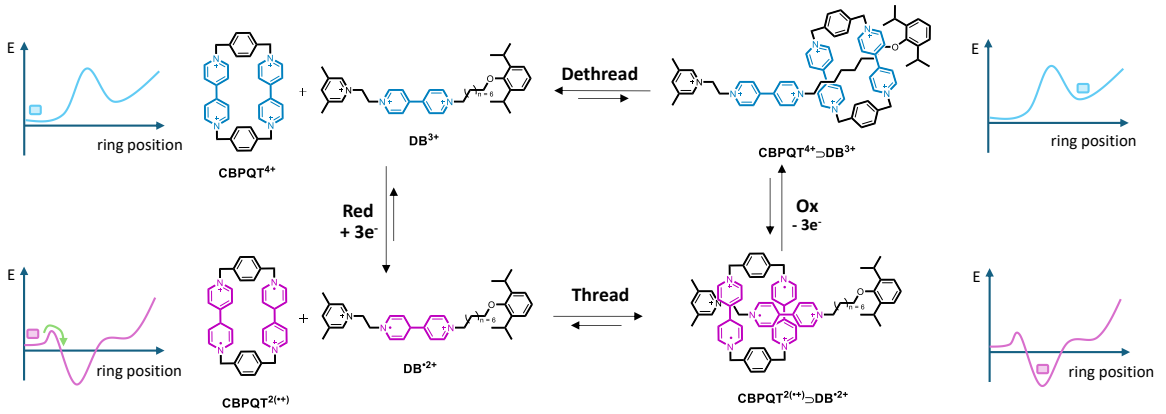

Scheme 6.2. Schematic representation of the energy ratchet network and energy diagrams associated with the formation of a high-energy complex enabled by a redox reaction.

However, this artificial molecular pump lacks the capability for repetitive operation, and the directional motion of the **CBPQT**$^{4+}$ ring is not realized because the entry and exit points coincide. More recently, two new generations of AMPs were designed: **Mark I**[19] and **Mark II**[19] artificial molecular pumps. In their work, Stoddart *et al.*[20] introduce a new component that acts as a steric barrier, effectively preventing the dethreading of the macrocycle and allowing the formation of polyrotaxane species. The initially designed pump, named **Mark I** (**Figure 6.4**), consisted of a dumbbell featuring a viologen recognition site (**V**$^{2+}$) situated between a coulombic barrier (**PY**$^{+}$) and a steric "speed-bump" (**IPP**). The **IPP** unit was connected *via* a triazole ring (**T**) to a collecting chain, which terminated in a bulky stopper group (**S**). The **PY**$^{+}$ and **IPP** units were crucial for the energy ratchet mechanism, facilitating the complexation of the **CBPQT**$^{4+}$ ring with the **V**$^{2+}$ site and enabling its subsequent release upon redox stimuli. Under reducing conditions, both the **V**$^{2+}$ unit and **CBPQT**$^{4+}$ are reduced, leading to a tris-radical tris-cationic complex. Upon the addition of an oxidizing reagent, the positive charges of the **V**$^{2+}$ and the **CBPQT**$^{4+}$ ring are restored. This reoxidation induces Coulombic repulsion, which drives the ring into a kinetic trap during thermal relaxation. If a subsequent reduction is performed, a second ring from the solution can interact with the reduced **V**$^{2+}$ site. Following oxidation and thermal relaxation, it can also be trapped within the collecting chain, forcing its accumulation in a thermodynamically unfavourable state.

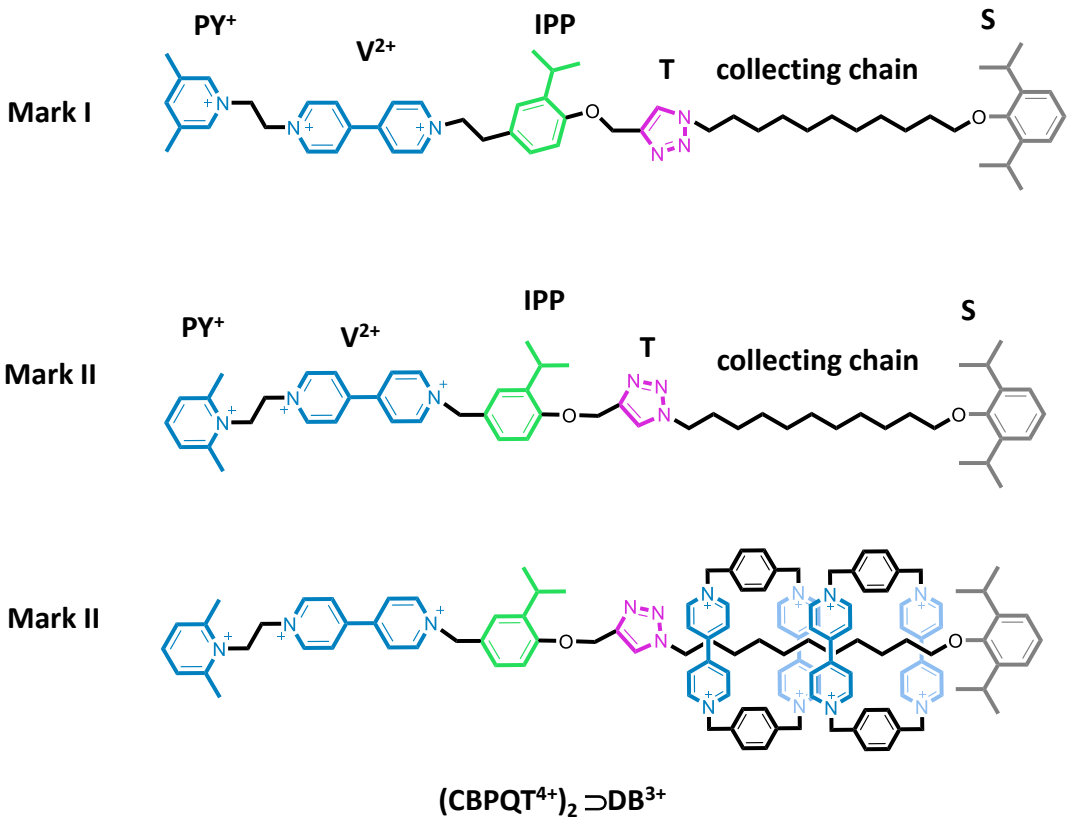

Figure 6.4. Structure of **Mark I** (top) and **Mark II** (middle) artificial molecular pumps. Representation of the [3]pseudorotaxane obtained after two cycles of redox process in **Mark II** pump (bottom).

However, the **Mark I** molecular pump operated too slowly, with the "blue box" reaching the collecting chain only after ca. 2 hours at 42 °C. **Mark II** pump was thus developed to reach a more efficient AMP (**Figure 6.4**). This version retained the same components of the **Mark I** pump but featured a shorter spacer between the $\mathbf{V}^{2+}$ site and **IPP** unit, together with a modified $\mathbf{PY}^{+}$ terminus. These adjustments significantly accelerated the threading kinetics of the "blue box" onto the collecting chain, reducing the operation time to 1 hour at room temperature and seconds at 40 °C. This advancement represented a significant improvement in the development of efficient AMPs.

In 2019,[21] a significant improvement was made with the development of a linear molecular dual pump capable of unidirectional $\mathbf{CBPQT}^{4+}$ transport. In this study, the authors presented a dual pump that could capture and release a $\mathbf{CBPQT}^{4+}$ into the solution through two consecutive redox cycles, using an energy ratchet mechanism, in a unidirectional manner. The molecular design featured two pumps within the same molecule (**Scheme 6.3**). The first pump, identical to the **Mark II** pump, was connected to the second *via* a triazole ring and a collecting chain positioned between the two AMPs. The unidirectional threading and release of the $\mathbf{CBPQT}^{4+}$ ring was governed by the redox-switching properties of the ring and the dumbbell components.

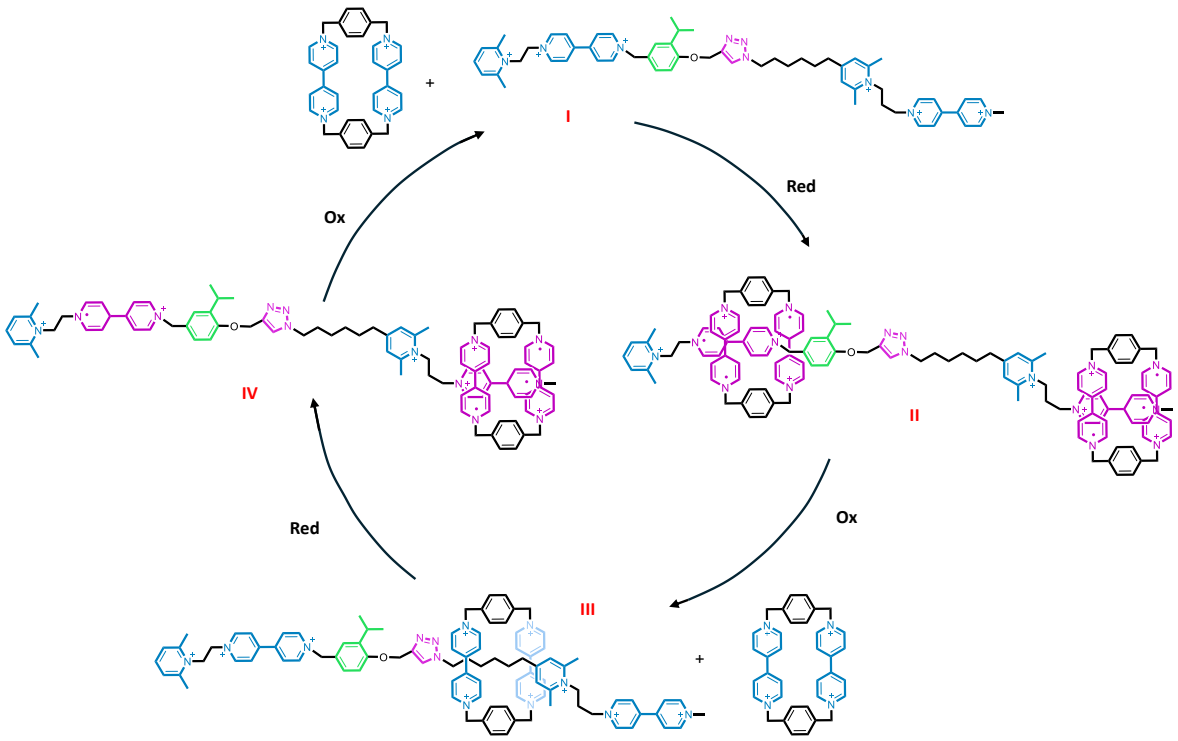

Scheme 6.3. Schematic representation of the energy ratchet mechanism for an AMP capable of unidirectional ring transport.

Initially, the **CBPQT**$^{4+}$ ring and the two **V**$^{2+}$ units did not interact due to Coulombic repulsion (**I**). The presence of a reductant generated radical-cationic species, leading to the formation of thermodynamically stable tris-radical tris-cationic complexes, with the threading of two **CBPQT**$^{4+}$ into the two reduced **V**$^{2\bullet+}$ units, forming two thermodynamically stable tris-radical tris-cationic complexes (**II**). Upon oxidation, one of the rings dethreads due to Coulombic repulsion, going back to the solution. Simultaneously, the other ring was forced by repulsion to translocate through the **IPP** unit forming a kinetically stable [2]rotaxane (**III**). Then, a second reduction event led to the tris-radical tris-cationic complex with the terminal **V**$^{2+}$ unit (**IV**). Finally, after oxidation, the **CBPQT**$^{4+}$ ring was expelled in solution. In this way **CBPQT**$^{4+}$ was trapped and realesed in a unidirectional manner. In 2020, Stoddart *et al.*[22] reported a mechanically interlocked olygomer utilizing the same principle (**Figure 6.5**). The study involved a monomer featuring a **CBPQT**$^{4+}$ macrocycle covalently attached to a pump head *via* a long flexible alkyl chain, as illustrated in **Figure 6.5**. This monomer was employed as a complementary unit for synthesizing a daisy chain oligomer. Upon reduction, the monomer self-assembles into an oligomer through radical-radical interactions. Subsequent oxidation reintroduces the positive charges, resulting in a kinetically trapped daisy chain oligomer (**Figure 6.5**, bottom). The DOSY NMR experiment conducted on the oligomerization crude revealed a diffusion coefficient of 3.57×10^{-7} cm^2/s, which is an order of magnitude lower than the diffusion coefficient observed for **M·7PF$_6$** (4.41×10^{-6} cm^2/s). This significant decrease in diffusion coefficient suggests

that the oligomer product possesses a substantially larger molecular size and weight compared to **M·7PF$_6$**.

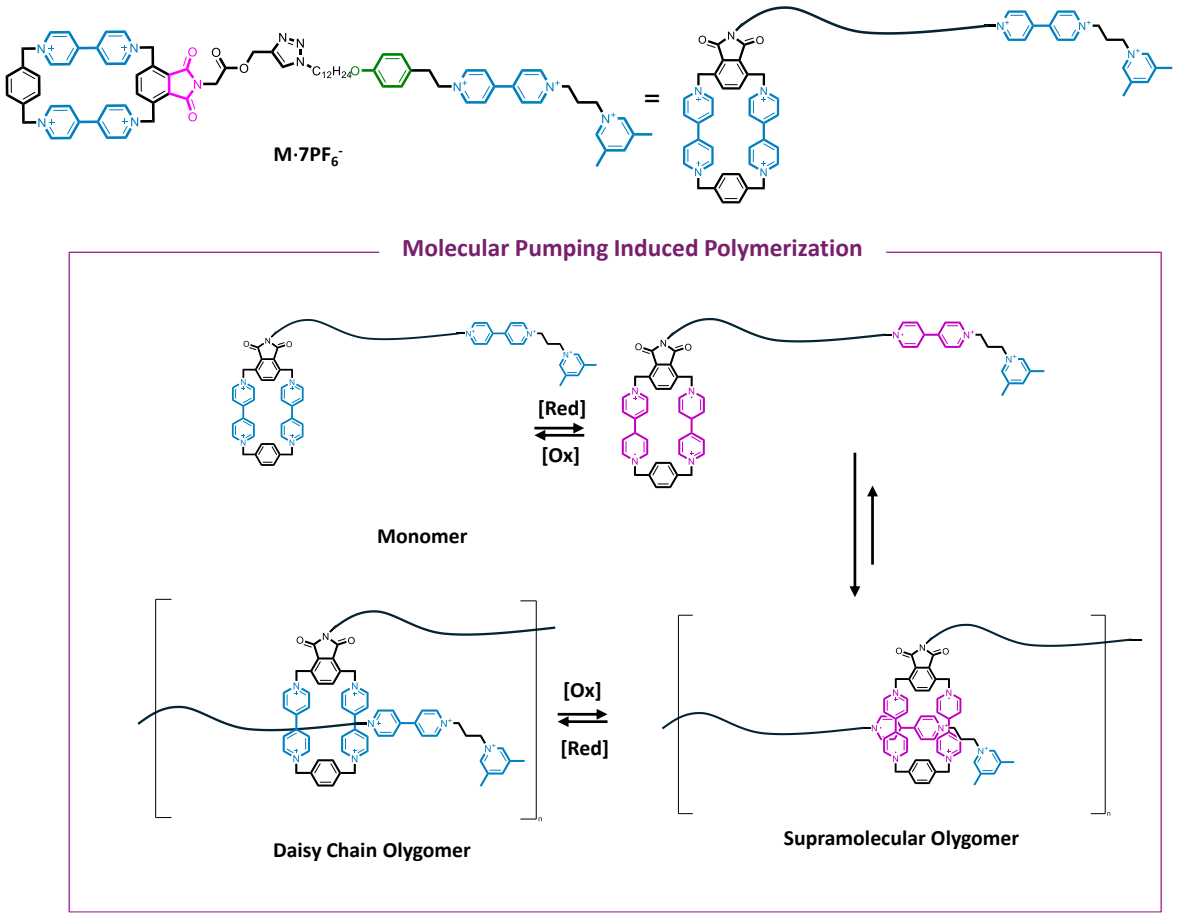

Figure 6.5. Top: structure of the monomer **M·7PF$_6^-$**; bottom: Representation of oligomerization under redox control using the monomer **M·7PF$_6^-$**.

Aim of the project

In this Chapter, out-of-equilibrium systems based on redox reactions were investigated. Multifunctional systems utilizing dumbbells and blue box macrocycles were designed to obtain high-energy structures. Inspired by the work of Stoddart, we wanted to exploit the principles of artificial molecular machines to create high-energy polymers. To promote cross-linking between multifunctional hosts and guests, we designed molecules containing more than one binding site. These multifunctional systems were here analyzed using electrochemical techniques, including cyclic voltammetry (CV) and differential pulse voltammetry (DPV). Moreover, spectro-electrochemistry was used to evaluate the formation of radical-cationic species and the establishment of radical-radical interactions, which are crucial for the operation of the energy ratchet mechanism.

6 Results and Discussion

Investigation of the $M1^{4+}$ and $A1^{3+}$pair

The first system we investigated is well-known in the literature. Its investigation was reported by Stoddart *et al.*[18] in 2014. The "blue box," here referred to as macrocycle **M1**$^{4+}$, and the axle **A1**$^{3+}$, which features a single recognition unit for the host (**H1**) (**Figure 6.6**), were subjected to redox reactions to obtain the high-energy complex. This system was analyzed using CV, DPV, and SEC measurements. All analyses were performed in dry acetonitrile under an argon atmosphere. Firstly, the individual components were investigated. **Figure 6.6** schematizes their redox processes: **M1**$^{4+}$ undergoes two reversible two-electron redox processes, while **A1**$^{3+}$ undergoes two reversible one-electron redox processes.

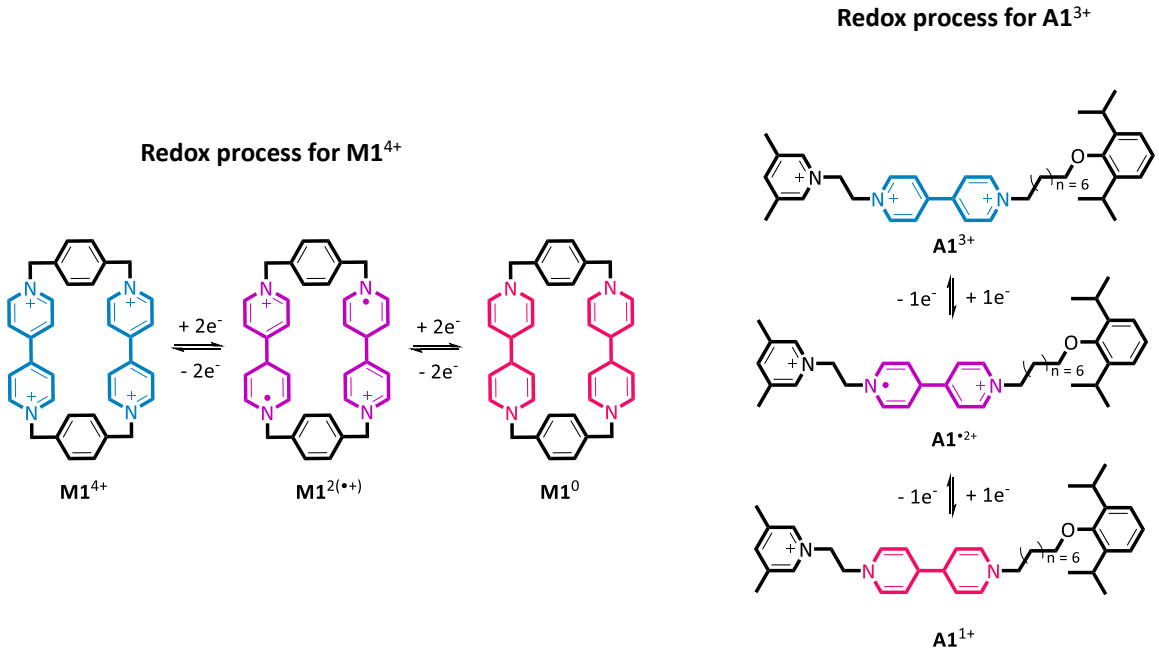

Figure 6.6. Left: redox processes for **M1**$^{4+}$; right: redox processes for **A1**$^{3+}$. All charges are counterbalanced by PF_6^- counter ions, which are not reported for clarity.

The redox potentials obtained correspond to those reported in the literature.[9] From the DPV analysis of **M1**$^{4+}$, a peak corresponding to the first redox process is observed at -0.30 V, while a peak corresponding to the second redox process is observed at -0.73 V (**Figure 6.7**, blue line). Similar values were found for **A1**$^{3+}$, with the first reduction appearing at -0.35 V and the second at -0.75 V (**Figure 6.7**, pink line). The two components were then mixed in a 1:1 ratio and subjected to analysis. In the DPV spectrum, a new peak at -0.05 V was observed (**Figure 6.7**, green line), which was tentatively assigned to the formation of the high energy complex **M1**$^{4+}\supset$**A1**$^{3+}$. **Figure 6.8** shows the CV of the mixture recorded across different potential ranges. The simplified reaction network associated with these redox and self-assembly processes is reported in **Figure 6.2**. The first redox

process is observed at the same potential as the first redox wave of **M1**$^{4+}$ (-0.28 V), while **A1**$^{3+}$ is a bit more negative (-0.35 V above in the DPV, **Figure 6.7**). Based on literature precedents,[9] observations are coherent with **M1**$^{4+}$ being initially reduced to its radical-cationic species **M1**$^{2(\bullet+)}$. Subsequently, it transfers one electron to **A1**$^{3+}$, which, after being reduced to **MA**$^{\bullet 2+}$, can form the tris-radical tris-cationic complex **M1**$^{2(\bullet+)}$⊃**A1**$^{\bullet 2+}$. The second redox process shows two bands at -0.74 V and -0.84 V. The first band likely corresponds to the reduction of free **M1**$^{2(\bullet+)}$ and **A1**$^{\bullet 2+}$ to their fully reduced forms (**M1**^{0} and **A1**$^{+}$), while the second band is presumed to correspond to the reduction of the tris-radical tris-cationic species **M1**$^{2(\bullet+)}$⊃**A1**$^{\bullet 2+}$, leading to the fully reduced complex which rapidly dethreads for lack of interactions. Due to the stabilization from radical-radical pairing, the reduction of this species requires a more negative potential (-0.84 V). When scanning in the oxidation direction, the first oxidation process presents two bands: one relative to the oxidation of the free components, and the other associated with the oxidation of the complex species (-0.80 V). Finally, the band at -0.05 V corresponds to the formation of the high-energy complex **M1**$^{4+}$⊃**A1**$^{3+}$. As anticipated, such an interpretation is coherent with literature data on very similar compounds.[9,23]

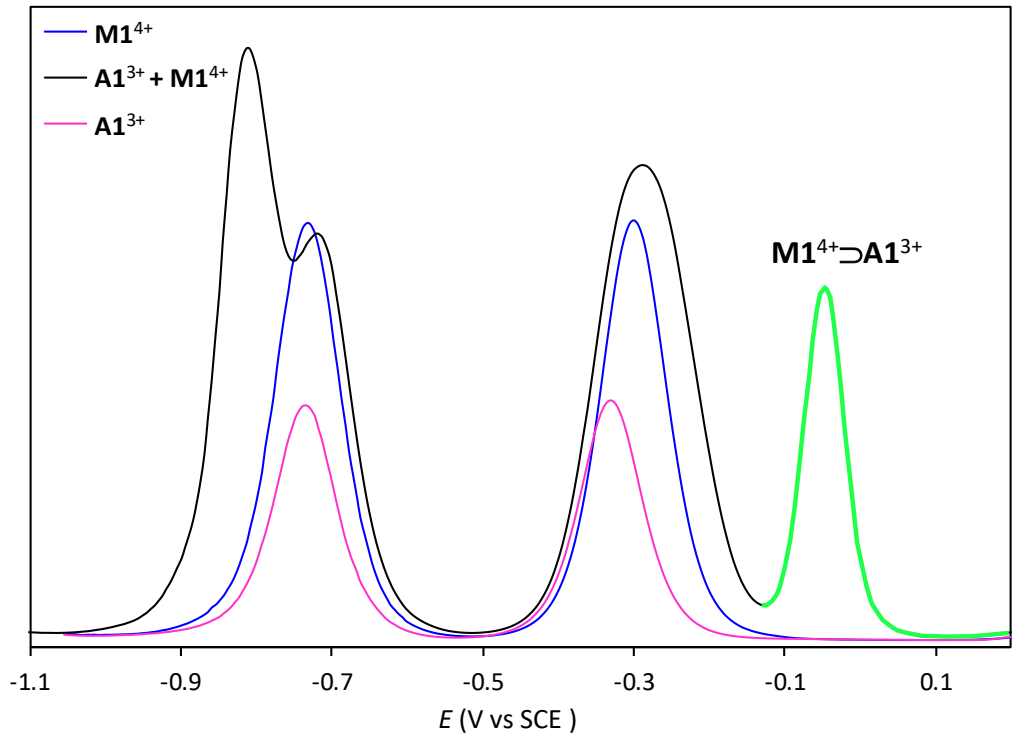

Figure 6.7. DPV in the oxidation direction of 1 mM **M1**$^{4+}$ (blue line), 1 mM **A1**$^{3+}$ (pink line), and the equimolar mixture of 1 mM **M1**$^{4+}$ and 1 mM **A1**$^{3+}$ (black line) in dry ACN (100 mM $TEAPF_6$), (*E*(V) vs SCE = 0.385 V). Peak related to the formation of the high energy complex (**M1**$^{4+}$⊃**A1**$^{3+}$) evidenced in green. The DPV analysis of **M1**$^{4+}$ shows two peaks at -0.30 V and -0.73 V, in agreement with the values found in the CV analysis. The DPV analysis of **A1**$^{3+}$ shows two peaks at -0.35 V and -0.75 V, in agreement with the values found in the CV analysis. The DPV analysis of the 1:1 mixture of **M1**$^{4+}$ and **A1**$^{3+}$ shows four peaks at -0.05 V, -0.28 V, -0.72 V, and -0.81 V, which are consistent with the observations in CV analysis.

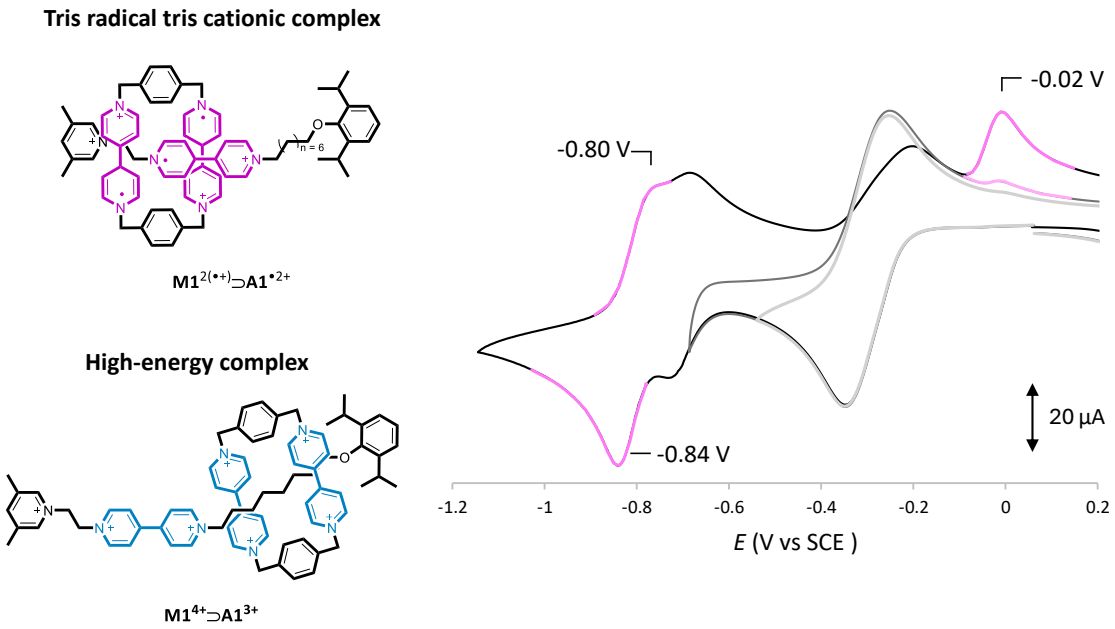

Figure 6.8. Left: structure of the tris-radical tris-cationic complex **M1**$^{2(\bullet+)}$⊃**A1**$^{\bullet 2+}$ and the high-energy complex **M1**$^{4+}$⊃**A1**$^{3+}$; right: cyclic voltammograms (v = 0.1 V·s^{-1}) of the equimolar mixture of 1 mM **M1**$^{4+}$ and 1 mM **A1**$^{3+}$ in dry ACN (100 mM $TEAPF_6$), (*E*(V) vs SCE = 0.385 V) recorded at different potential range: from +0.5 to –1.2 V (black line), from +0.5 to –0.75 V (dark grey line) and from +0.5 to –0.6 V (clear grey line). All charges are counterbalanced by PF_6^- counter ions, which are not reported for clarity.

The formation of the tris-radical tris-cationic complex was further corroborated through spectro-electrochemical (SEC) analysis of a 1 mM solution of a 1:1 mixture of **M1**$^{4+}$ and **A1**$^{3+}$ in dry acetonitrile. UV-Vis-NIR spectra were recorded during the first exhaustive reduction wave of the equimolar mixture, with the potential maintained at -0.5 V to allow the visualization of the absorption bands of radical-cationic species. **Figure 6.9** shows the UV-Vis-NIR spectra recorded at -0.5 V: the band at approximately 260 nm is associated with the initial oxidized species. Upon applying the potential, this band decreases while new bands emerge at about 400, 600, and 1080 nm. The two bands at 400 and 600 nm were attributed to the free radical-cationic species in solution (**M1**$^{2(\bullet+)}$ and **A1**$^{\bullet 2+}$), while the band in the NIR region at about 1080 nm indicates the formation of dimeric species, specifically the tris-radical tris-cationic complex (**M1**$^{2(\bullet+)}$⊃**A1**$^{\bullet 2+}$).

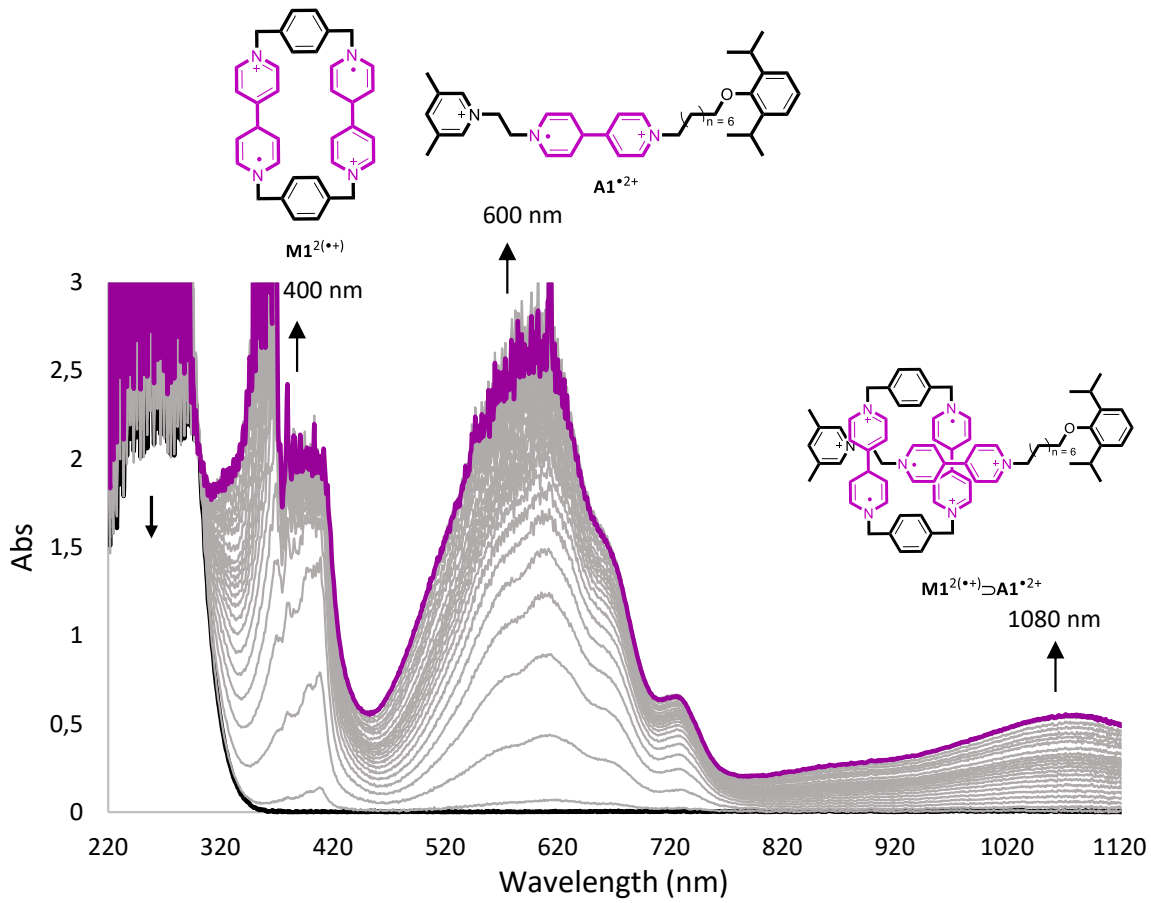

Figure 6.9. Spectro-electrochemistry recorded during the first exhaustive reduction of the equimolar mixture of 1 mM **M1**$^{4+}$ and 1 mM **A1**$^{3+}$ (E_{app} = -0.5 V) in dry ACN (100 mM $TEAPF_6$). PF_6^- counterions were not reported for clarity. All charges are counterbalanced by PF_6^- counter ions, which are not reported for clarity.

Investigation of the M2^{8+} and A1^{3+}pair

Once the formation of the high-energy complex for the **M1**$^{4+}$ and **A1**$^{3+}$ systems was confirmed, we started the investigation of the networks containing the multifunctional structures. In the first moment, we decided to combine a monofunctional component, axle **A1**$^{3+}$, with a bifunctional host, where two derivatives of **M1**$^{4+}$ are linked together in the same molecule, named **M2**$^{8+}$ (**Figure 6.10**). The two **M1**$^{4+}$ units were linked *via* two triazole rings connecting them with an internal polyethylene glycol (PEG) collecting chain of ca. 22 monomer units.

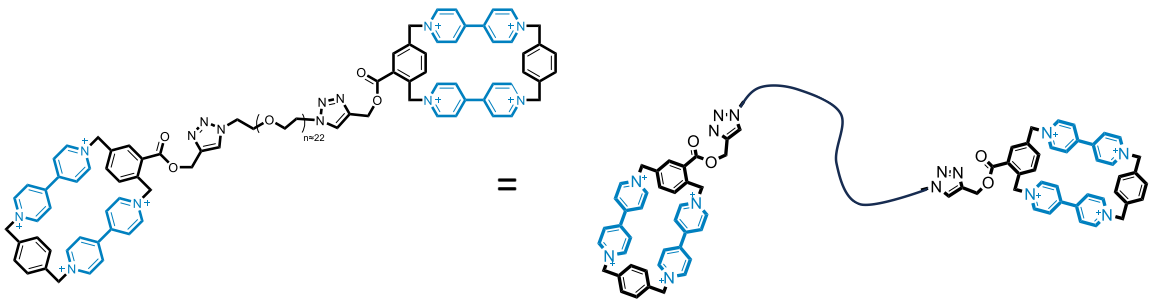

Figure 6.10. Structure of **M2**$^{8+}$. All charges are counterbalanced by PF_6^- counter ions, which are not reported for clarity.

The synthetic strategy involved a click chemistry reaction between a blue box containing an alkyne moiety and a commercial polyethylene glycol chain containing azide groups at the terminations (**Scheme 6.4**). The alkyne-functionalized blue box (**P1**) was synthesized following an improved protocol developed by Ragazzon *et al*.[24] **P1** was reacted with the azide component in the presence of copper(I) tetrakis and TBTA in acetone at reflux for 3 days. This click chemistry approach leads to the formation of the desired product in 20 % yield.

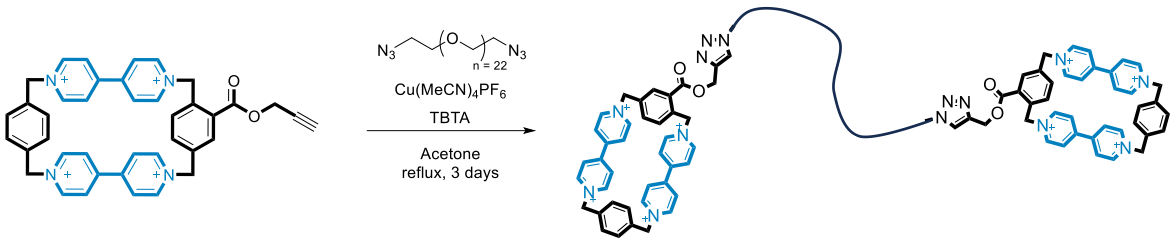

Scheme 6.4. Synthetic scheme of the synthesis of **M2**$^{8+}$. All charges are counterbalanced by PF_6^- counter ions, which are not reported for clarity.

The synthesized **M2**$^{8+}$ was fully characterized by NMR measurements, mass spectrometry and electrochemical analyses. Notably, the CV and DPV spectra appeared similar to those of **M1**$^{4+}$, exhibiting two reversible reduction and oxidation processes at -0.28 V and -0.71 V (see Experimental Part, and **Figure 6.36**-**6.38**). However, the spectro-electrochemical spectrum of **M2**$^{8+}$ was different to **M1**$^{4+}$. **Figure 6.11** shows the evolution of the UV-Vis-NIR spectra recorded at an applied potential of -0.5 V. Three absorption bands can be observed: the two bands at 400 and 600 nm correspond to the formation of free radical species (**M2**$^{4(\bullet+)}$), while the red-shifted band at about 860 nm is indicative of radical-radical dimerization. Absorption bands in the NIR region of the spectrum are generally related to the formation of radical-radical dimers.[25] Thus, it is reasonable to hypothesize that **M2**$^{4(\bullet+)}$ can form homodimer species in solution. In particular, two types of dimers can be considered (**Figure 6.11**): intermolecular dimers, where two **M2**$^{4(\bullet+)}$ molecules interact *via* radical-radical recognition, and intramolecular dimers, where the two **H1**$^{2(\bullet+)}$ units within a single **M2**$^{4(\bullet+)}$ molecule interact with each other *via* radical-radical interaction. The formation of homodimer species can compete with the formation of the tris-radical tris-cationic complex, thereby disfavouring the observation of the desired high-energy complex.

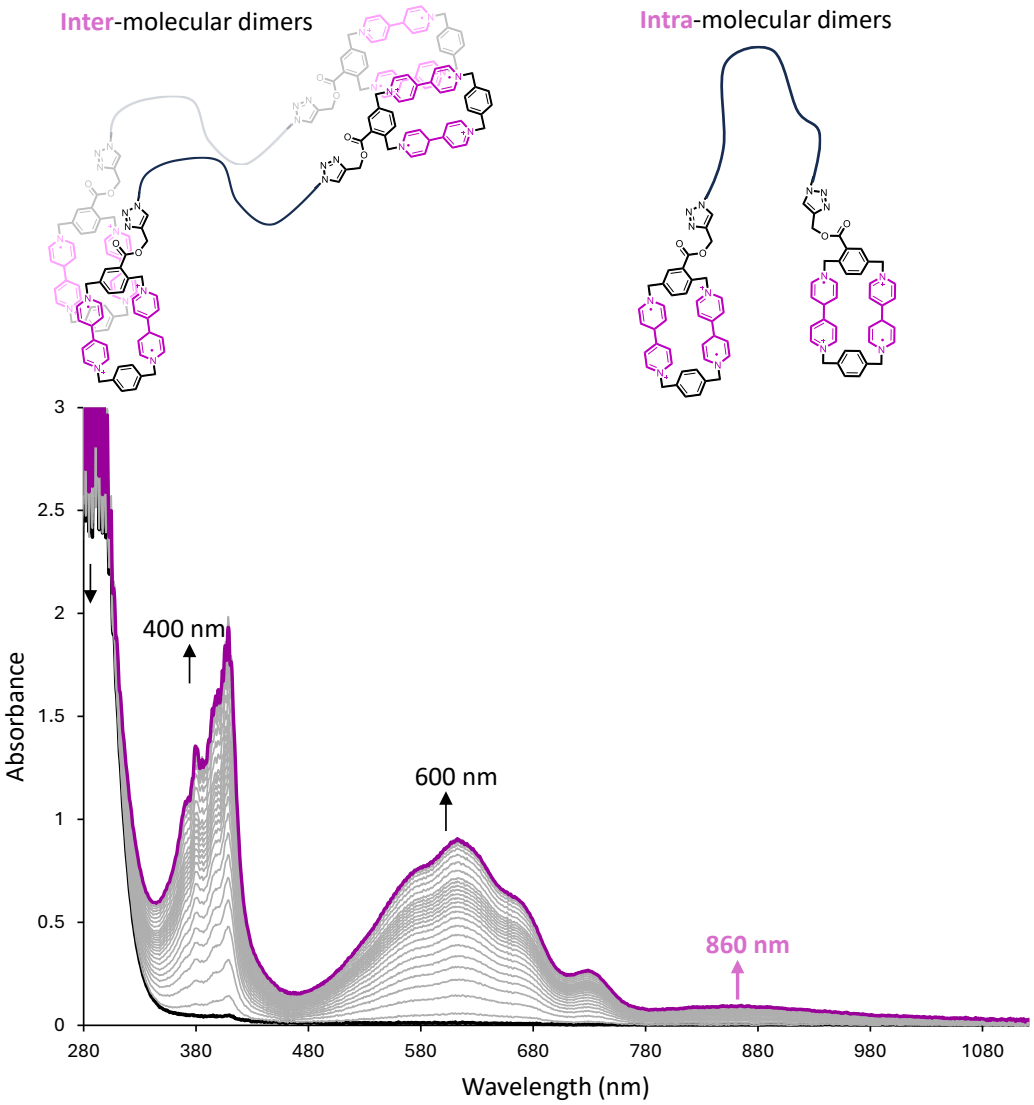

Figure 6.11. Absorption spectra recorded in spectro-electrochemical experiments during the first exhaustive reduction of **M2**$^{8+}$ (c = 1 mM, E_{app} = -0.5 V) in dry ACN (100 mM $TEAPF_6$). Representation of the chemical structures of inter- and intra-molecular dimer species of **M2**$^{8+}$. All charges are counterbalanced by PF_6^- counter ions, which are not reported for clarity.

Successively, we proceeded with the investigation of the mixture of **M2**$^{8+}$ with **A1**$^{3+}$. The bifunctional host **M2**$^{8+}$ enables the interaction with two molecules of **A1**$^{3+}$, potentially leading to the formation of a 1:2 complex. CV and DPV of the 1:1 and 1:2 mixture of **M2**$^{8+}$ and **A1**$^{3+}$ were performed (**Figure 6.12**). The CV and DPV spectra were similar and resembled the spectrum obtained for the 1:1 mixture of **M1**$^{4+}$ and **A1**$^{3+}$. In both mixtures, the formation of the high-energy complex is evidenced by the peak at -0.02 V in the CV spectra. When using 2 equivalents of **A1**$^{3+}$ (purple lines), the current intensity increased, attributed to the higher concentration of redox-active species.

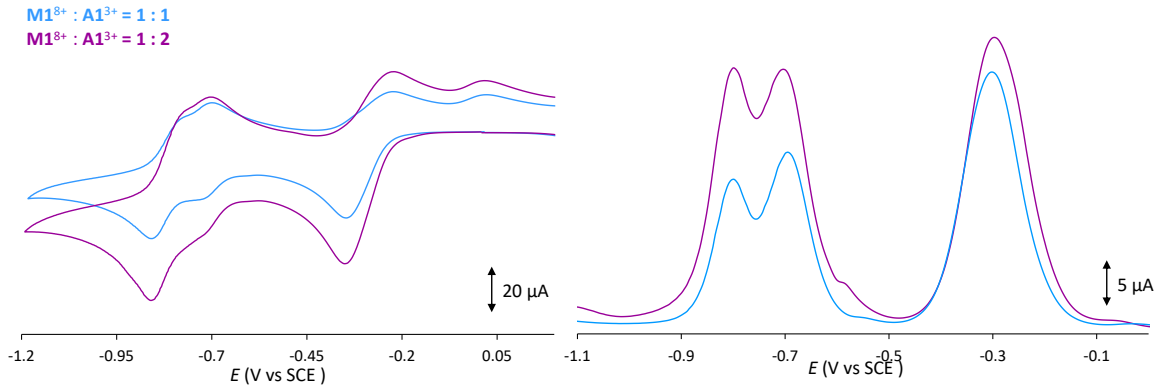

Figure 6.12. Left: Cyclic voltammograms (v = 0.1 V·s^{-1}) of the 1:1 (blue line) and 1:2 (purple line) mixture of **M2**$^{8+}$ and **A1**$^{3+}$ in dry ACN (100 mM $TEAPF_6$), (*E*(V) vs SCE = 0.385 V); right: Differential pulse voltammograms in oxidation direction of 1:1 (blue lines) and 1:2 (purple lines) mixture of **M2**$^{8+}$ and **A1**$^{3+}$ in dry ACN (100 mM $TEAPF_6$), (*E*(V) vs SCE = 0.385 V).

The SEC analysis was particularly noteworthy. **Figure 6.13** shows the collection of UV-Vis-NIR spectra of the equimolar mixture of **M2**$^{8+}$ and **A1**$^{3+}$ recorded at -0.5 V in dry acetonitrile. The spectra consistently show absorption bands at 400 and 600 nm, corresponding to the free radical-cationic species. Additionally, two more absorption bands appear at longer wavelengths. The one at about 860 nm was related to homodimer species of **M2**$^{8+}$, while the 1080 nm band was associated with the tris-radical tris-cationic complex. The presence of **M2**$^{8+}$ homodimer hinders the formation of the desired tris-radical tris-cationic complex, as evidenced by the attenuated intensity of the 1080 nm band.

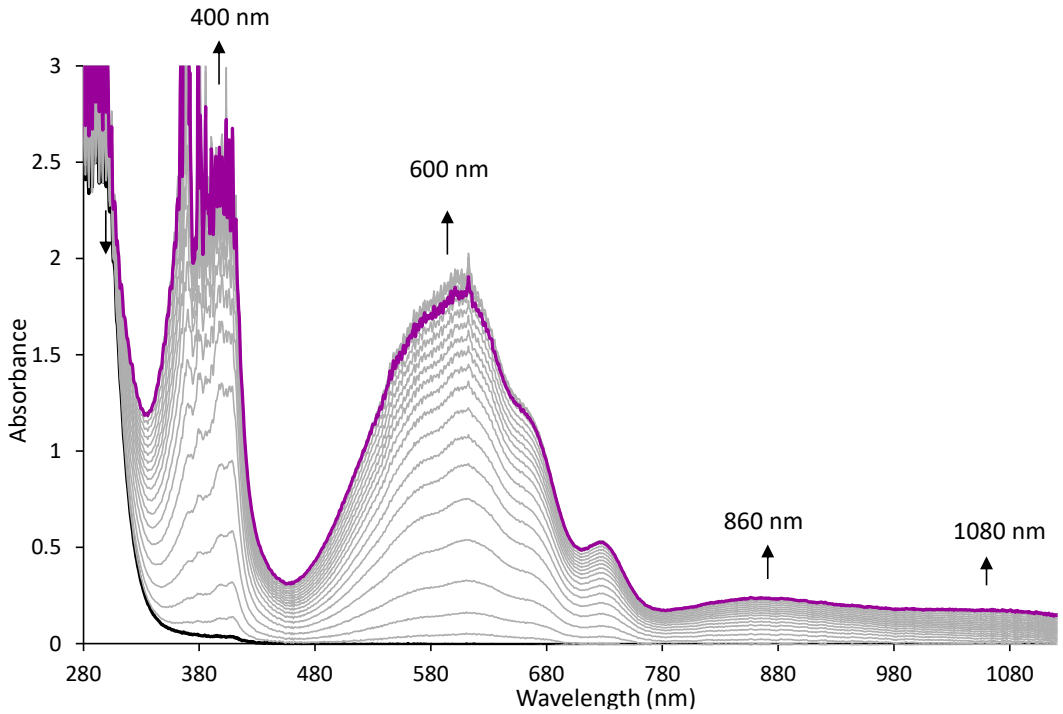

Figure 6.13. Absorption spectra recorded in spectro-electrochemical experiments the first exhaustive reduction of the 1:1 mixture of 1 mM **M2**$^{8+}$ and 1 mM **A1**$^{3+}$ (E_{app} = -0.5 V) in dry ACN (100 mM $TEAPF_6$).

Investigation of the $M1^{4+}$ and $A2^{6+}$ pair

The third system analyzed was the mixture of **M1**$^{4+}$ with a bifunctional axle (**A2**$^{6+}$). This axle contains two viologen units within the same molecule, enabling it to interact with two molecules of **M1**$^{4+}$. The synthetic strategy involved a click reaction, as before seen for the synthesis of **M2**$^{8+}$, where a viologen-containing compound with a terminal alkyne moiety and polyoxyethylene bis(azide) cyclized in the presence of a copper(I)-catalyst, forming a triazole ring (**Scheme 6.5**).

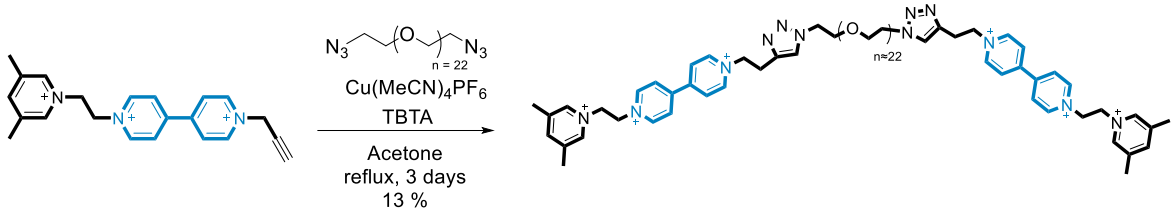

Scheme 6.5. Synthetic scheme of the synthesis of axle **A2**$^{6+}$. All charges are counterbalanced by PF_6^- counter ions, which are not reported for clarity.

The low yield observed in the synthesis of **A2**$^{6+}$ can be attributed primarily to the purification process. NMR analysis of the reaction crude, conducted in deuterated acetonitrile, indicated complete conversion of the starting materials and formation of the target product. This suggested us that the purification step was the critical factor responsible for the reduction of the final yield. The pure axle **A2**$^{6+}$ was then fully characterized using NMR spectroscopy, mass spectrometry, and electrochemical analysis. **Figure 6.14** shows the ^{1}H NMR spectrum of **A2**$^{6+}$, recorded in deuterated acetonitrile. Complete peak assignment was accomplished through 2D NMR experiments, confirming the presence of all signals corresponding to the molecule. In the aromatic region, the protons of the pyridinium moieties, labeled as *f* and *g*, are observed as broad doublets at 8.88 ppm and 8.39 ppm, respectively. Additionally, the signals at 8.49 ppm and 8.27 ppm are attributed to protons *c* and *a*, respectively, from the terminal "pump head" group. A singlet at 7.68 ppm, assigned to protons labeled as *i*, is diagnostic of the triazole ring formation. In the mid-field region of the spectrum, five triplet signals are identified: a triplet at 5.18 ppm assigned to protons *d*, and two overlapping triplets at 5.0 ppm corresponding to protons *e*. The triplets at 4.45 ppm and 3.76 ppm are attributed to the protons of the PEG chain, labeled as *j* and *k*, respectively. Overlapping with these signals, a triplet at 3.46 ppm corresponds to protons *h*. Finally, in the high-field region, a singlet at 2.49 ppm is associated with the methyl group protons labeled as *b*.

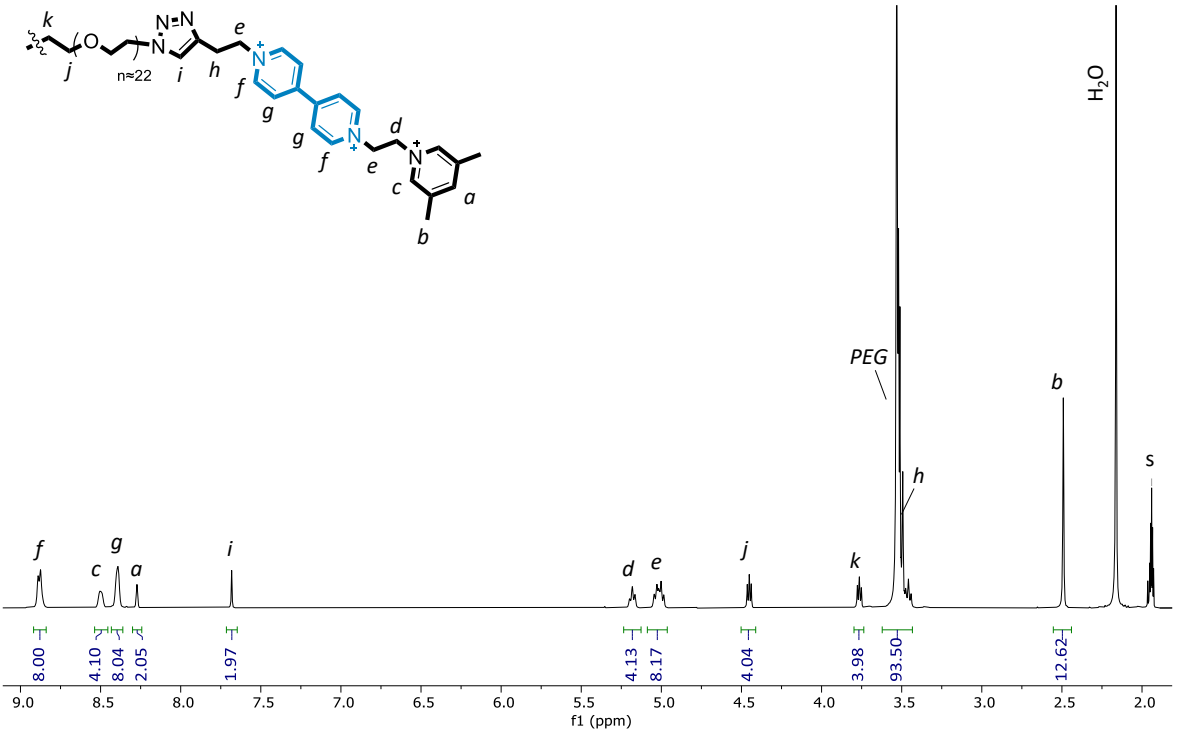

Figure 6.14. ^{1}H NMR spectrum (CD_3CN, 400 MHz, 298 K) of **A2**$^{6+}$. All charges are counterbalanced by PF_6^- counter ions, which are not reported for clarity.

The electrochemical analysis, in particular the CV and DPV spectra, demonstrated the processes' reversibility, with two reductions and oxidations occurring at the same potentials observed for **A1**$^{3+}$ (see Experimental part, **Figures 6.40** and **6.41**). Additionally, the SEC analysis revealed the presence of radical dimers in the solution, similarly to what was observed for **M2**$^{8+}$ (**Figure 6.15** left).

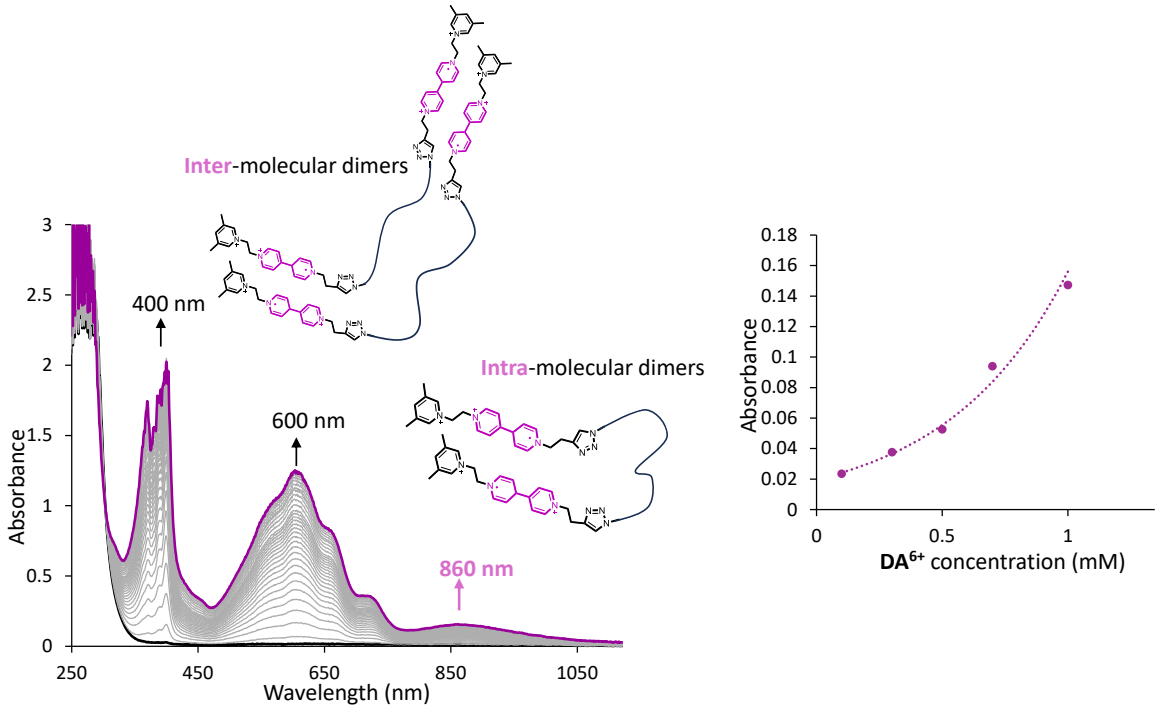

Figure 6.15. Left: absorption spectra recorded in spectro-electrochemical experiments during the first exhaustive reduction of 1 mM **A2**$^{6+}$ (E_{app} = -0.5 V) in dry ACN (100 mM $TEAPF_6$); right: absorbance values (λ =

860 nm) of a solution of **A2**$^{6+}$ at different concentrations recorded by spectro-electrochemistry (E_{app} = -0.5 V) in dry ACN (100 mM $TEAPF_6$). All charges are counterbalanced by PF_6^- counter anions, which are not reported for clarity.

To further investigate the formation mechanism of **A2**$^{6+}$ dimer species, concentration-dependent spectro-electrochemical measurements were conducted. **Figure 6.15** (right) illustrates the absorbance values recorded at 860 nm as a function of **A2**$^{6+}$ concentration. At low concentrations, a linear relationship between absorption intensity and concentration is observed, suggesting that the formation of radical-radical dimers features intramolecular interactions, as these are independent of the concentration.[25] Conversely, at high concentrations, a non-linear component is evident, suggesting the presence of intermolecular radical-radical interactions. These observations would be coherent with the coexistence of both inter- and intra-molecular dimers in solution.

After the **A2**$^{6+}$ was characterized individually, its mixture with **M1**$^{4+}$ was investigated. CV spectra of the 1:2 mixture of **A2**$^{6+}$ and **M1**$^{4+}$ were recorded at different scan rates to gain a deeper understanding of the threading process. **Figure 6.16** shows the CV spectra recorded at three scan rates (comprehensive data for all scan rates can be found in the Experimental Section, **Figures 6.56** and **6.57**): slow scan rate at 0.02 V/s, medium scan rate at 0.1 V/s, and fast scan rate at 10 V/s. Comparing these cases, the peak corresponding to the formation of the high-energy complex was observed only when performing the CV analysis at the medium scan rate (green trace).

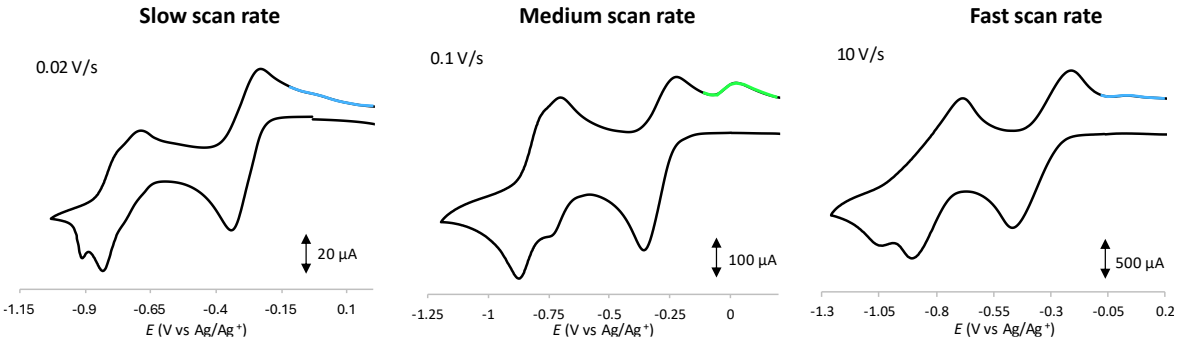

Figure 6.16. Cyclic voltammograms of the 1:2 mixture of 1 mM **A2**$^{6+}$ and 2 mM **M1**$^{4+}$ in dry ACN (100 mM $TEAPF_6$), (E(V) vs SCE = 0.385 V) recorded at different scan rates: left 0.02 V/s, middle 0.1 V/s, and right 10 V/s. In green is evidenced the peak related to the formation of the high-energy complex. The absence of the peak related to the high-energy complex is evidenced in blue.

To rationalize these data, we refer to schemes based on the considerations reported by Stoddart *et al.*[23] for a similar system. Examining the reduction process, we observe three reduction peaks at all scan rates: the first reduction peak corresponds to the formation of free radical-cationic species (**A2**$^{2\bullet 4+}$ and **M1**$^{2(\bullet+)}$). The second band corresponds to the reduction of free **M1**$^{2(\bullet+)}$ and **A2**$^{2\bullet 4+}$ to their fully reduced forms (**M1**^{0} and **A2**$^{2+}$), and the third one at more negative potential is presumed to correspond to the reduction of the tris-radical tris-cationic species **M1**$^{2(\bullet+)}\supset$**A2**$^{2\bullet 4+}$, leading to the fully reduced complex which then dissociates for lack of interactions.

Significant differences are observed in the reoxidation process. When the CV spectrum is recorded at fast scan rates (10 V/s), i.e., through a rapid addition and removal of electrons, the system shifts from the fully reduced state to the radical-cationic state and then to the fully oxidized state without sufficient time for the assembly (**Scheme 6.6**). Since the oxidation process at a fast scan rate is quicker than the threading kinetics, the formation of the high-energy complex is not observed.

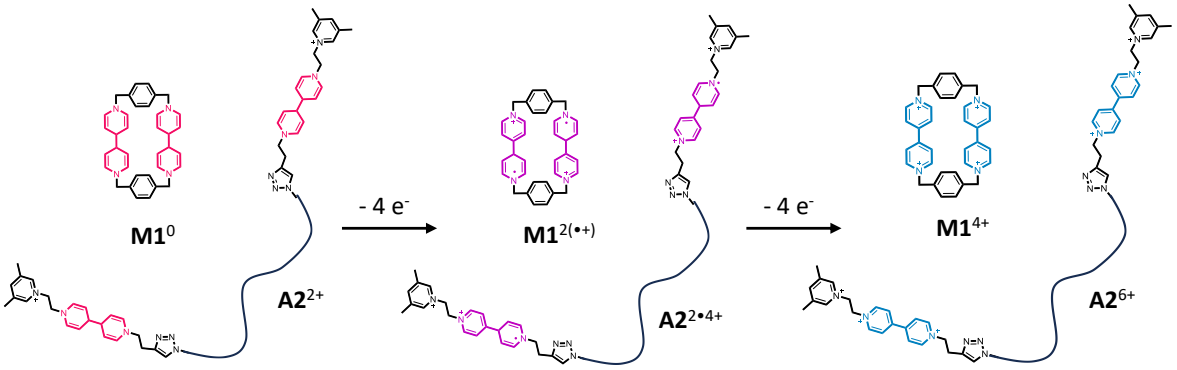

Scheme 6.6. Graphic representation of the oxidation process for the 1:1 mixture of **M1**$^{4+}$ and **A2**$^{6+}$ at a scan rate of 10 V/s. All charges are counterbalanced by PF_6^- counter anions, which are not reported for clarity.

In contrast, at slow scan rates (0.02 V/s), the electrons are slowly removed from the system (**Scheme 6.7**). Starting with the fully reduced disassembled species, during the oxidation process, as the potential becomes more positive, one electron is removed from one of the viologen units, forming a bis-radical bis-cationic complex. At a more positive potential, a second electron is removed, leading to the formation of the tris-radical tris-cationic complex. The third electron is removed from one of the viologen units of **M1**$^{4+}$. It is well known that one of the viologen units of **M1**$^{4+}$ is less involved in the complexation and more prone to oxidation.[9] Since the blue box is only partially oxidized and the Coulombic barrier to be crossed is lowered, the dethreading kinetics are favored over the movement into the collecting chain. As a result, the formation of the high-energy complex was not observed.

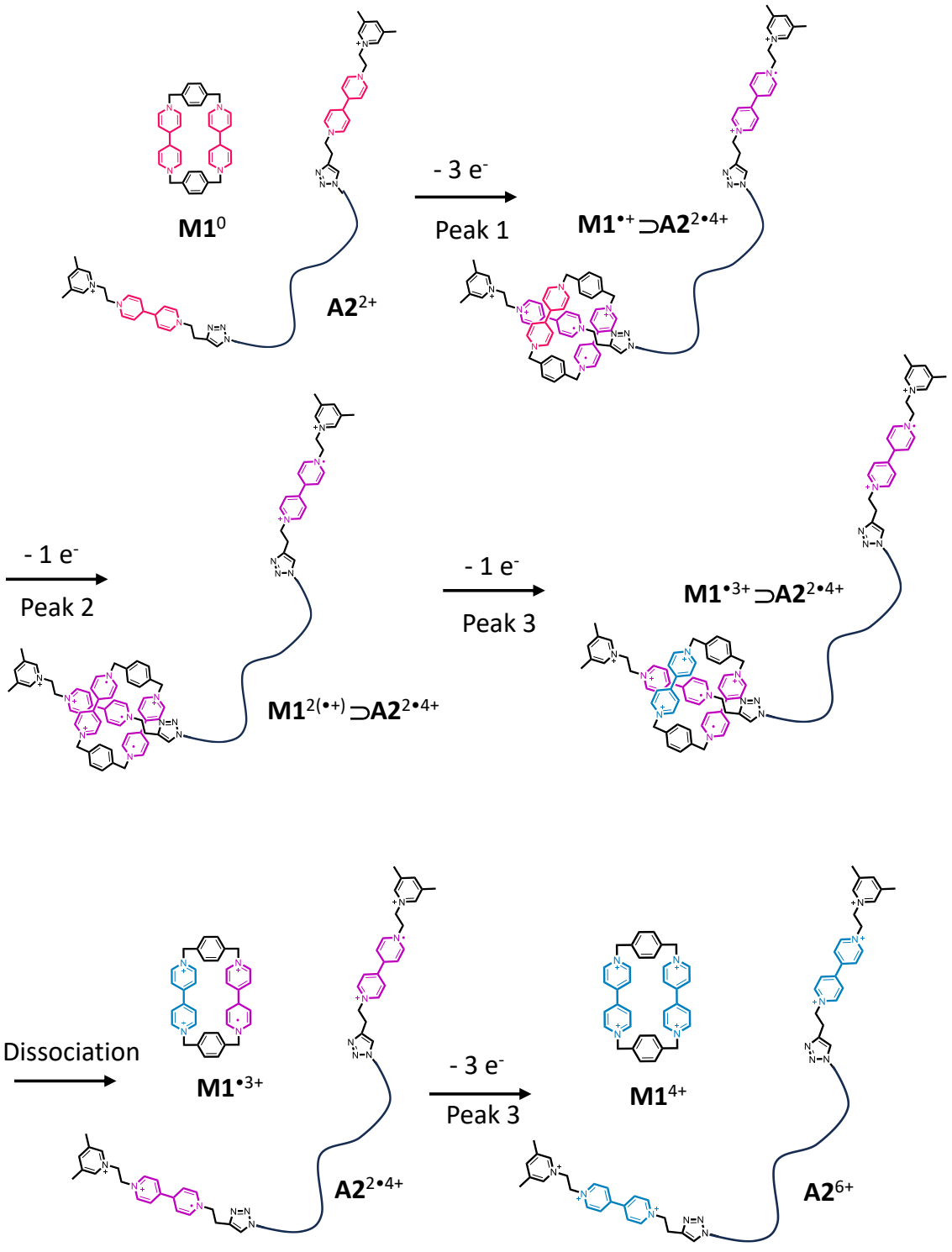

Scheme 6.7. Graphic representation of the oxidation process for the 1:1 mixture of **M1**$^{4+}$ and **A2**$^{6+}$ at a scan rate of 0.02 V/s. All charges are counterbalanced by PF_6^- counter ions, which are not reported for clarity.

When performing the CV analysis at medium scan rates (0.1 V/s), the kinetics of dethreading and the formation of the high-energy complex are competitive, resulting in the observation of the high-energy complex (**Scheme 6.8**). Upon formation of the tris-radical tris-cationic complex, both events can take place: part of the blue box will dethread, while another part will translate into the collecting chain, thereby forming a kinetically trapped state.

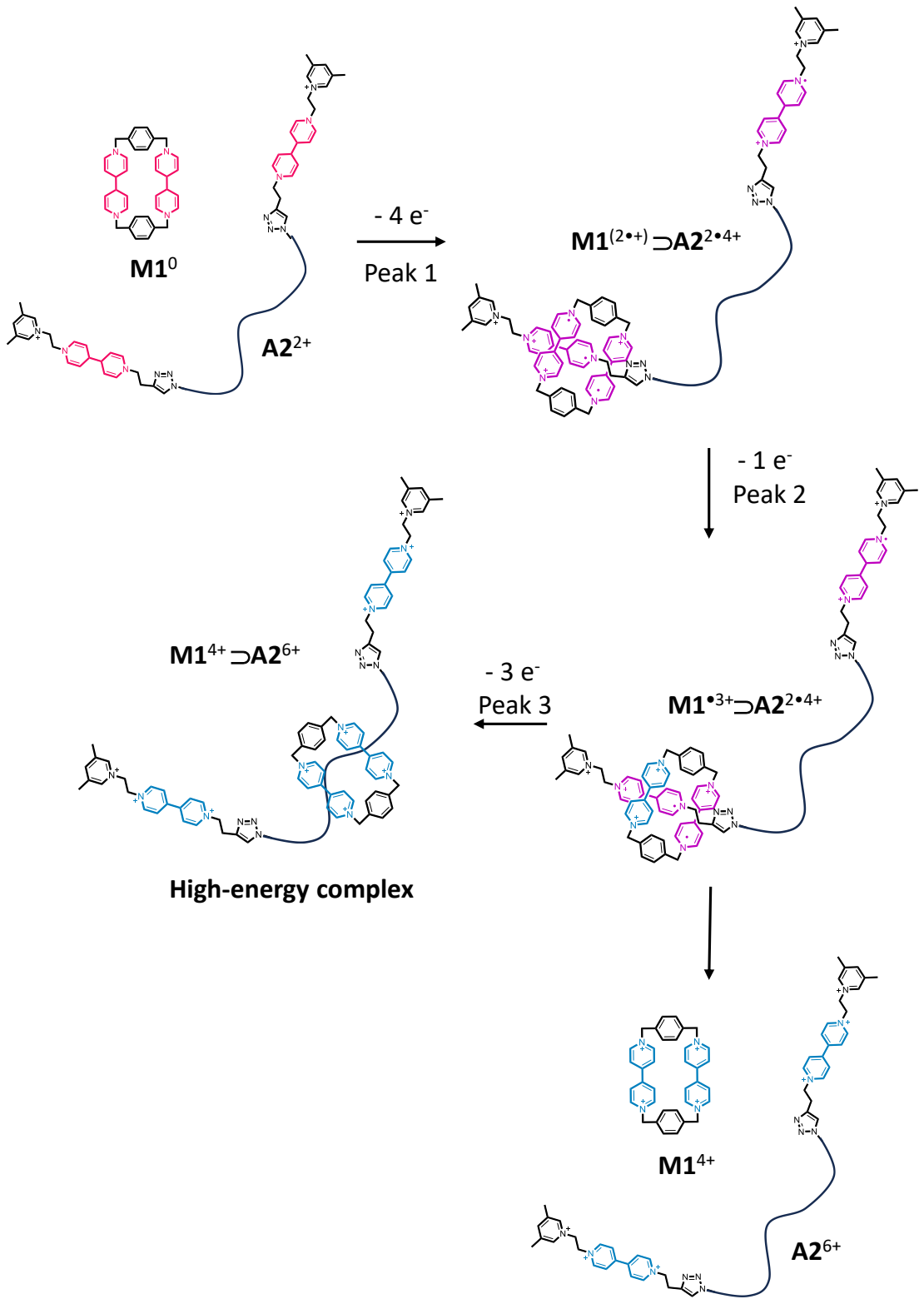

Scheme 6.8. Graphic representation of the oxidation process for the 1:1 mixture of **M1**$^{4+}$ and **A2**$^{6+}$ at a scan rate of 0.1 V/s. All charges are counterbalanced by PF_6^- counter ions, which are not reported for clarity.

Considering a literature precedent of autocatalytic dethreading observed in a related PEG-functionalized derivative,[18] the dethreading process of **A2**$^{6+}$ from **M1**$^{4+}$ may be facilitated by an autocatalytic mechanism involving the PEG chain. In this scenario, following the initial dethreading event, a free **A2**$^{6+}$ molecule is released into the solution. This free **A2**$^{6+}$ may act as a catalyst,

promoting the dethreading of additional **A2**$^{6+}$ molecules. Consequently, the process accelerates as more **A2**$^{6+}$ is liberated, consistent with an autocatalytic behavior. To investigate this possibility, we conducted CV experiments using a mixture of **M1**$^{4+}$ and **A1**$^{3+}$ as a model system (**Figure 6.17**, black line). Following this, an excess of free PEG diazide was introduced into the system, and the CV measurements were repeated under identical conditions (**Figure 6.17**, purple line). A comparison of the two CV spectra revealed no significant differences in peak shape or potential. Given that CV is highly sensitive to the kinetics of molecular processes, it can be inferred that the presence of the free PEG chain does not significantly affect the rate of the threading/dethreading mechanisms. Thus, the dethreading process accelerates only when the PEG chain is covalently attached to the axle.

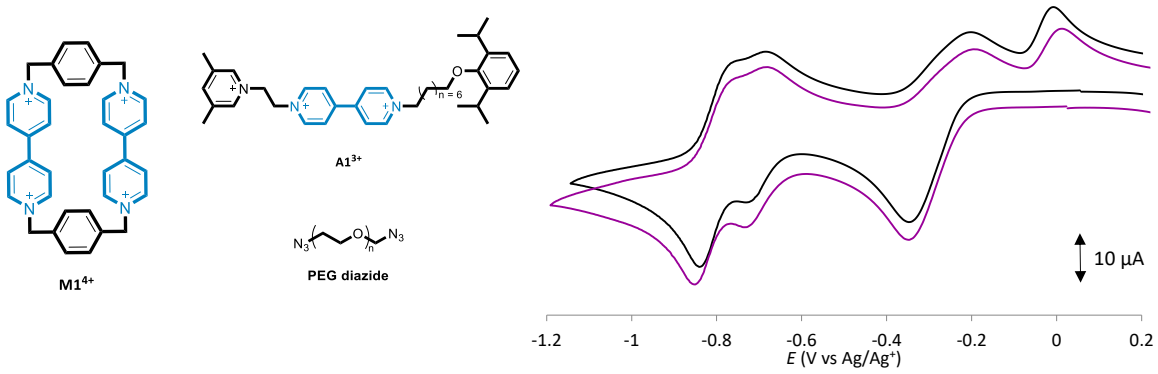

Figure 6.17 Cyclic voltammograms (v = 0.1 V·s^{-1}) of the equimolar mixture of **M1**$^{4+}$ and **A1**$^{3+}$ (c = 1mM, black line) and the 1:1:1 mixture of **M1**$^{4+}$, **A1**$^{3+}$ and PEG-azide chain (c = 1 mM, purple line) in dry ACN (100 mM $TEAPF_6$), (*E*(V) vs SCE = 0.385 V). All charges are counterbalanced by PF_6^- counter ions, which are not reported for clarity.

Investigation of the M2^{8+} and A2^{6+} pair

We then proceeded to combine the bifunctional components **M2**$^{8+}$ and **A2**$^{6+}$. This system was particularly interesting as it may form polymeric structures. The two components were mixed in a 1:1 ratio in dry acetonitrile and subjected to CV and DPV analyses. **Figure 6.18** illustrates the cyclic voltammograms recorded at different scan rates: slow scan rate at 0.02 V/s, medium scan rate at 0.1 V/s, and fast scan rate at 8 V/s (comprehensive data for all scan rates can be found in the Experimental Section, **Figure 6.72**). Notably, in all cases, the peak associated with the formation of the high-energy complex was not observed, even at medium scan rates, which contrasts with the results observed in the previous system involving **A2**$^{6+}$ and **M1**$^{4+}$.

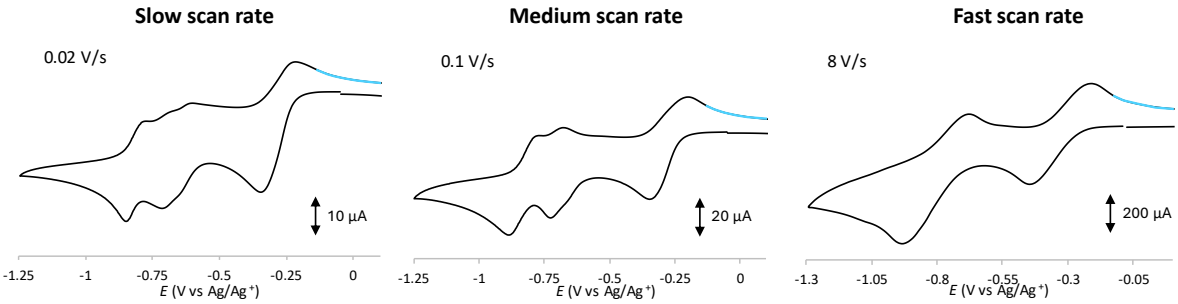

Figure 6.18. Cyclic voltammograms of the 1:1 mixture of 1 mM **A2**$^{6+}$ and 1 mM **M2**$^{8+}$ in dry ACN (100 mM $TEAPF_6$), (E(V) vs SCE = 0.385 V) recorded at different scan rates: left 0.02 V/s, middle 0.1 V/s, and right 8 V/s. The absence of the peak related to the formation of the high-energy complex is evidenced by a blue line.

A SEC analysis was then performed to verify the formation of the tris-radical tris-cationic complex, which is essential for achieving the high-energy state. **Figure 6.19** illustrates the collection of UV-Vis-NIR spectra recorded at the applied potential of -0.5 V. The appearance of the NIR band at 1080 nm, characteristic of dimer species in solution, indicates the formation of the tris-radical tris-cationic complex. Since the SEC analysis confirms the formation of this crucial intermediate necessary for attaining the high-energy state, further analyses were performed to elucidate the behavior of the system.

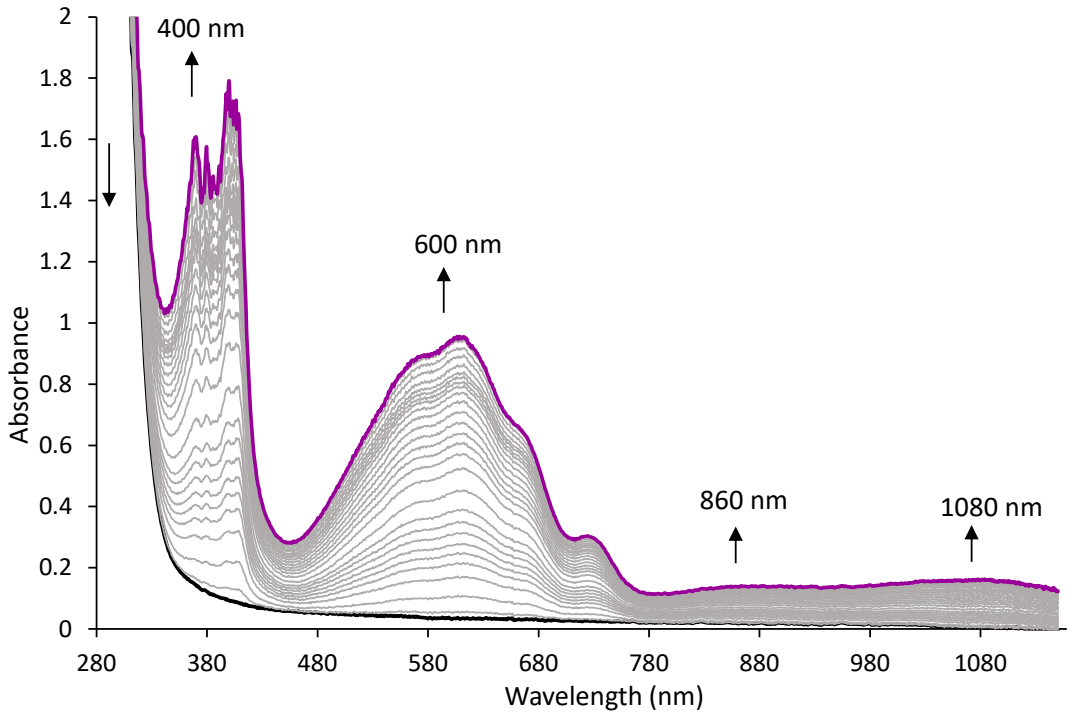

Figure 6.19. Absorption spectra recorded in spectro-electrochemical experiments during the first exhaustive reduction of the 1:1 mixture of 1 mM **M2**$^{8+}$ and 1 mM **A2**$^{6+}$ (E_{app} = -0.5 V) in dry ACN (100 mM $TEAPF_6$).

To gain a better understanding of this system, an adapted Linear Sweep Voltammetry (LSV) was conducted. This technique allows us to linearly scan the potential, and can be combined with intervals where a specific potential is maintained for a predetermined time. An equimolar mixture

of **M2**$^{8+}$ and **A2**$^{6+}$ in dry acetonitrile was subjected to this analysis with a scan rate of 5 V/s. The potential was initially scanned in the reduction direction, from 0 V to -0.7 V. We decided to stop at this potential value – just before the second reduction peak – to ensure the formation of the tris-radical tris-cationic complex. The potential was then kept fixed for varying time delays (**Figure 6.20**). Finally, the potential was scanned in the oxidation direction to return to the fully oxidized state. From the LSV-chronoamperometry data reported in **Figure 6.20**, the formation of a new peak at around -0.06 V was observed upon increasing time delay. Indeed, when the direct analysis was performed (blue line), no peak was observed, while a new peak appeared after a delay of only 60 seconds, which increased its intensity with longer time delays. This means that maintaining the potential at a negative value allows the system to assemble, accumulating the tris radical-tris cationic complex and in turn the high-energy complex.

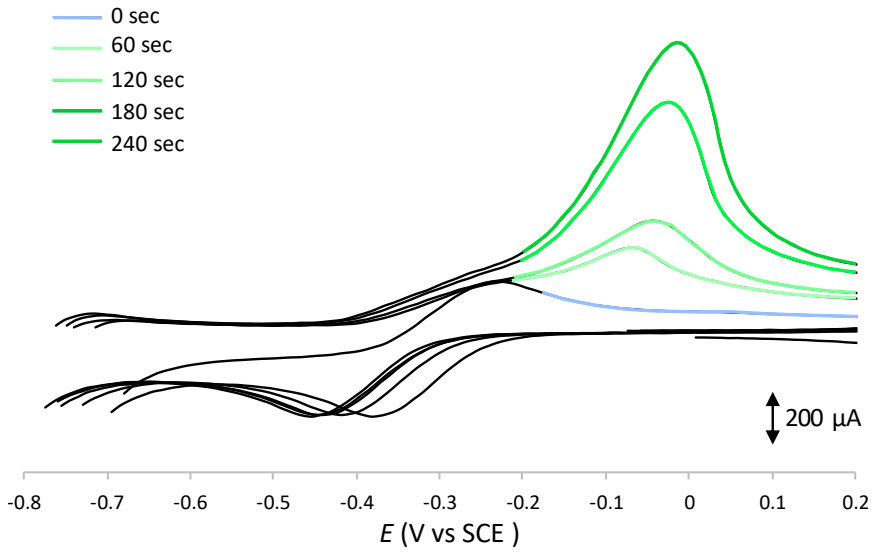

Figure 6.20. LSV of the 1:1 mixture of 1 mM **M2**$^{8+}$ and 1 mM **A2**$^{6+}$ in dry ACN (100 mM $TEAPF_6$), (E(V) vs SCE = 0.385 V) varying the time delay at a fixed potential of -0.7 V. In green is evidenced the peak related to the formation of the high-energy complex.

Based on these results, it can be concluded that in this multifunctional system, the formation of the high-energy complex is kinetically slower than mono-functional counterparts, requiring time to be observed.

Investigation of the A4^{12+} and M1^{4+} pair

To achieve the formation of a cross-linked structure based on the studied energy ratchet mechanism, we designed a novel multifunctional axle, **A4**$^{12+}$, depicted in **Figure 6.21**. This axle features four viologen units, which act as recognition sites for the blue box macrocycle. The synthetic strategy mirrors the one employed for the bis-functionalized axle **A2**$^{6+}$ but uses a tetra azide-terminated polyethylene glycol chain instead of a bis azide-terminated one.

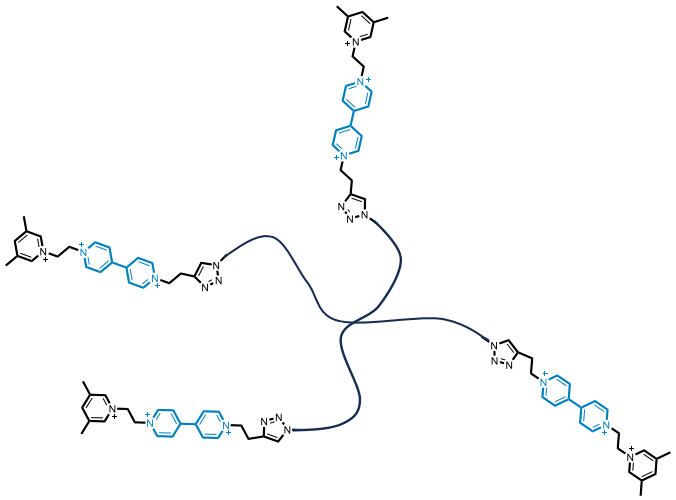

Figure 6.21. Structure of novel tetra-functionalized axle **A4**$^{12+}$. All charges are counterbalanced by PF_6^- counter ions, which are not reported for clarity.

This axle was fully characterized by NMR measurements, mass spectrometry and electrochemical analysis. The CV and DPV spectra were analogous to those observed for **A2**$^{6+}$ (see Experimental Part, **Figures 6.44** and **6.45**). The CV reduction and oxidation peaks are significantly broad, possibly due to a non-optimal solubility of the radical-cationic species in acetonitrile. The spectro-electrochemical analysis of **A4**$^{12+}$ shows the characteristic absorption bands observed for the simple **A1**$^{3+}$ (**Figure 6.22**). UV-Vis-NIR spectra were recorded at different concentrations of **A4**$^{12+}$ to confirm the absence of the band at about 860 nm, which is present in **M2**$^{8+}$ and **A2**$^{6+}$ spectra. The presence of the absorption bands corresponding to homo radical cationic species (400 and 600 nm) indicates that upon reduction of **A4**$^{12+}$, dimer species do not form in solution, which should favor the formation of the desired tris-radical tris-cationic dimers.

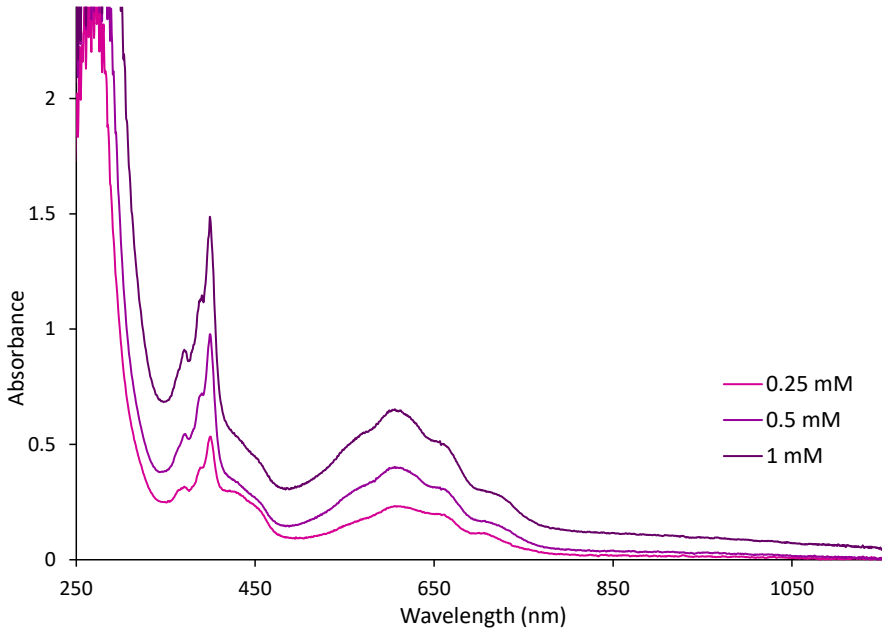

Figure 6.22. Absorption spectra recorded in spectro-electrochemical experiments during the first exhaustive reduction of **A4**$^{12+}$ at different concentrations (E_{app} = -0.5 V) in dry ACN (100 mM $TEAPF_6$).

As in prior studies, CV and DPV analyses of the mixture of **A4**$^{12+}$ and **M1**$^{4+}$ were carried out. In this case, the functionalized axle can potentially interact with four blue box molecules, necessitating CV measurements of the mixture at various ratios of the two components. In all cases, the resulting spectra exhibited broad reduction and oxidation peaks (**Figure 6.23**), indicating similar electrochemical behavior across different mixture ratios.

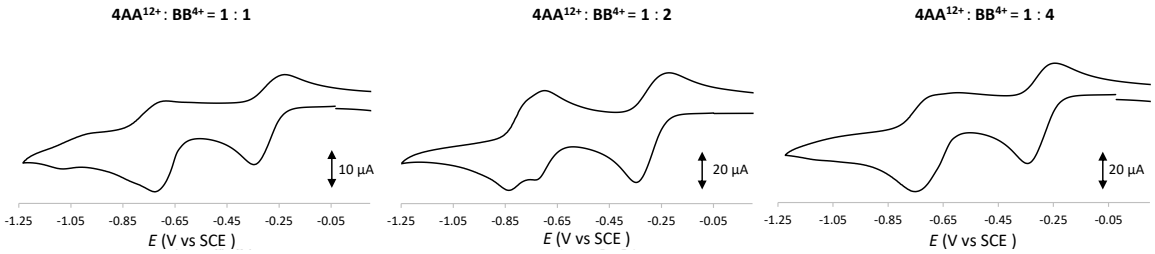

Figure 6.23. Cyclic voltammograms (v = 0.1 V·s^{-1}) of different mixture of **A4**$^{12+}$ and **M1**$^{4+}$ in dry ACN (100 mM $TEAPF_6$), (*E*(V) vs SCE = 0.385 V): left 0.25 mM **A4**$^{12+}$ and 0.25 mM **M1**$^{4+}$, middle 0.25 mM **A4**$^{12+}$ and 0.50 mM **M1**$^{4+}$, and right 0.25 mM **A4**$^{12+}$ and 1.0 mM **M1**$^{4+}$.

Figure 6.24 reported the CV spectra of the 1:2 mixture of **A4**$^{12+}$ and **M1**$^{4+}$ recorded at different scan rates (comprehensive data for all scan rates can be found in the Experimental Section, **Figures 6.80** and **6.82**). Consistent with previous considerations for the **M2**$^{8+}$ and **A2**$^{6+}$ mixture, the peak associated with the formation of the high-energy complex was absent in all cases. This suggests that, as previously noted, the formation of the high-energy complex is a slow process, requiring extended time to be detectable.

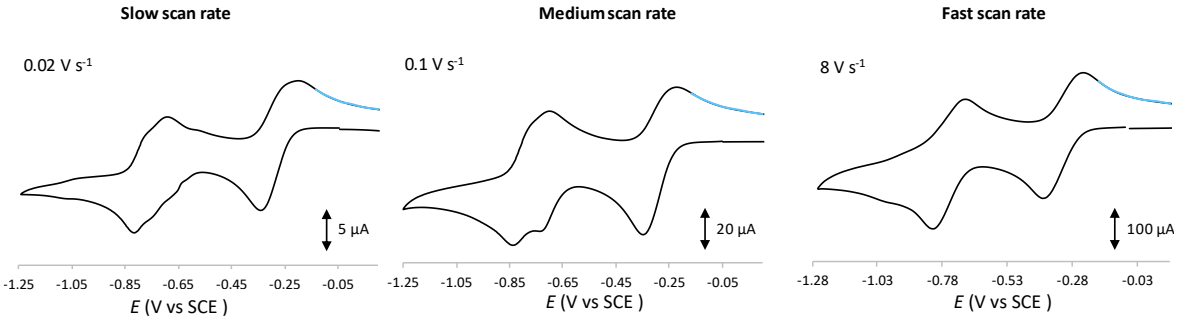

Figure 6.24. Cyclic voltammograms of the 1:2 mixture of 0.25 mM **A4**$^{12+}$ and 0.5 mM **M1**$^{4+}$ in dry ACN (100 mM $TEAPF_6$), (*E*(V) vs SCE = 0.385 V) recorded at different scan rates: left 0.02 V/s, middle 0.1 V/s, and right 8 V/s. The absence of the peak related to the formation of the high-energy complex is evidenced by a blue line.

Firstly, a spectro-electrochemical analysis of the system was performed to confirm the formation of the critical tris-radical tris-cationic complex. **Figure 6.25** reports the collection of UV-Vis-NIR spectra of the 1:1 mixture of **A4**$^{12+}$ and **M1**$^{4+}$ recorded at an applied potential of -0.5 V. In this case, the absence of dimer species, deriving from the interaction of radical-cationic species **A4**$^{4•8+}$ with each other, allows for a clearer observation of the NIR band at about 1080 nm, corresponding to the absorbance of the tris-radical tris-cationic complex.

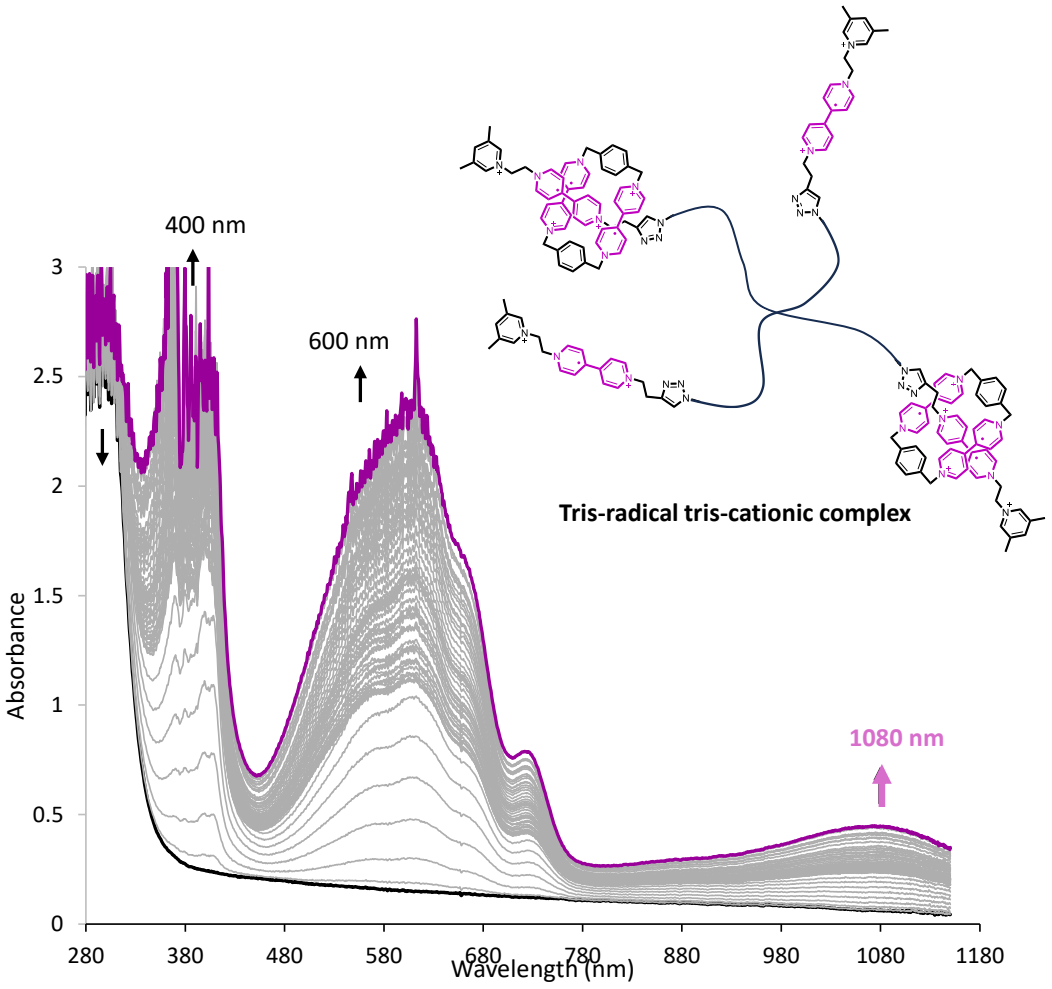

Figure 6.25. Absorption spectra recorded in spectro-electrochemical experiments during the first exhaustive reduction of the 1:1 mixture of 1 mM **A4**$^{12+}$ and 1 mM **M1**$^{4+}$ (E_{app} = -0.5 V) in dry ACN (100 mM $TEAPF_6$). All charges are counterbalanced by PF_6^- counter ions, which are not reported for clarity.

Once the formation of the tris-radical tris-cationic complex was confirmed, LSV-chronoamperometry analysis was performed to observe the peak of the high-energy complex. **Figure 6.26** reports the spectra collected at different time delays ranging from 0 to 300 seconds at an applied potential of -0.7 V, just before the second reduction wave, to assure the formation of the radical-cationic species. At 0 seconds (blue line), no peak is detectable. However, a small band becomes observable with increasing time delay, which is almost imperceptible compared to that obtained for the **M2**$^{8+}$ and **A2**$^{6+}$ mixture.

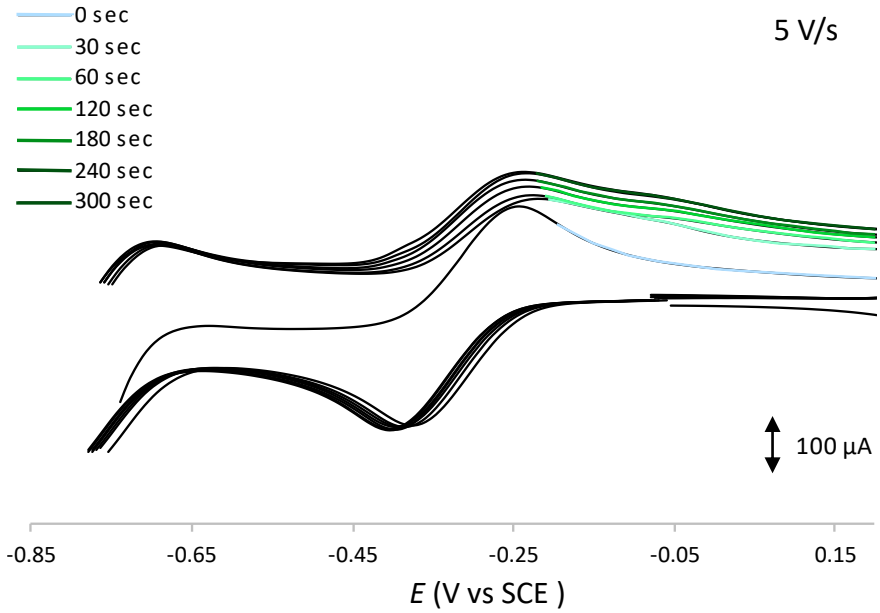

Figure 6.26. LSV of the 1:1 mixture of 1 mM **M1**$^{4+}$ and 1 mM **A4**$^{12+}$ in dry ACN (100 mM $TEAPF_6$), (*E*(V) vs SCE = 0.385 V) varying the time delay at a fixed potential of -0.7 V. In green is evidenced the peak related to the formation of the high-energy complex.

Such behavior resembles the one observed for the **A2**$^{6+}$ and **M1**$^{4+}$ systems, where the high-energy complex was absent at slow and fast scan rates. In the current system, the high-energy complex is also not detected at a medium scan rate. This suggests that, in this instance, dethreading of the axle is facilitated and favored over the formation of the high-energy state at all scan rates.

Investigation of the A4^{12+} and M2^{8+} pair

Finally, the last system investigated derives from combining the tetra-functionalized axle **A4**$^{12+}$ with the bis-functionalized blue box **M2**$^{8+}$. In principle, this system is the most promising one to induce the formation of a cross-linked polymer. The two free species were already characterized. Based on previously collected spectro-electrochemical data for free **A4**$^{12+}$ and **M2**$^{8+}$, it is established that **A4**$^{12+}$ does not form homodimer species in solution, whereas **M2**$^{8+}$ does form homodimers. This suggests that competition with the formation of the tris-radical tris-cationic complex will occur. Indeed, the SEC spectrum of the 1:2 mixture of **A4**$^{12+}$ and **M2**$^{8+}$ (**Figure 6.27**) exhibits the presence of both the homodimer absorption band (880 nm) and the radical-cationic complex band (1080 nm).

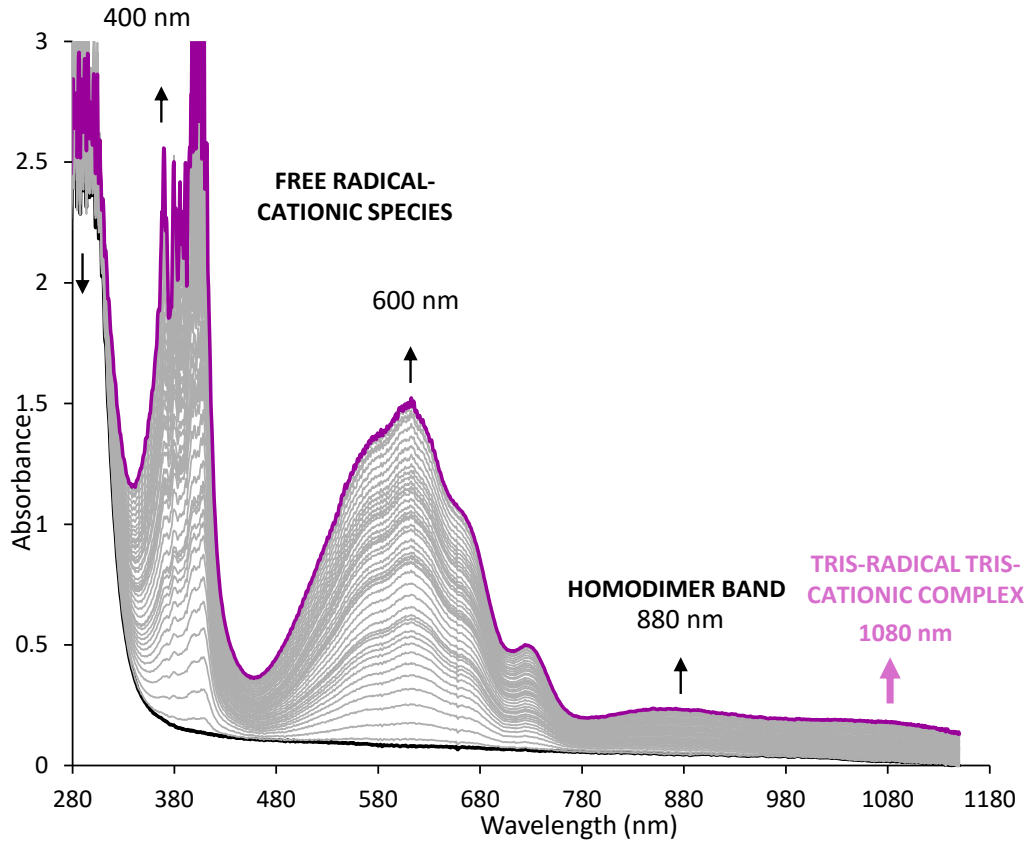

Figure 6.27. Absorption spectra recorded in spectro-electrochemical experiments during the first exhaustive reduction of the 1:2 mixture of 0.25 mM **A4**$^{12+}$ and 0.5 mM **M2**$^{8+}$ (E_{app} = -0.5 V) in dry ACN (100 mM $TEAPF_6$).

CV and DPV data were collected, and the desired peak related to the high-energy complex formation was absent (**Figure 6.28**). The hypothesis, as before, was the slow time required to observe its formation. For this reason, LSV analysis was performed.

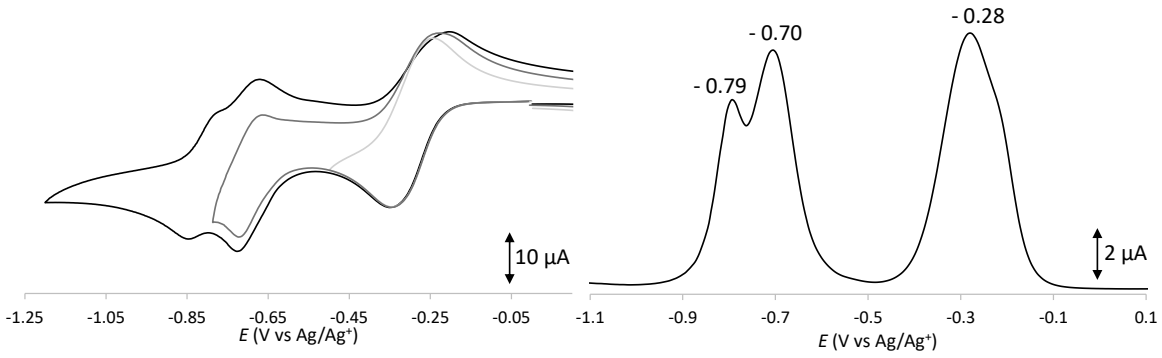

Figure 6.28. Left: cyclic voltammograms (v = 0.1 V·s^{-1}) of the 1:1 mixture of **M2**$^{8+}$ and **A4**$^{12+}$ in dry ACN (100 mM $TEAPF_6$), (E(V) vs SCE = 0.385 V); right: differential pulse voltammograms in oxidation direction of 1:1 mixture of **M2**$^{8+}$ and **A4**$^{12+}$ in dry ACN (100 mM $TEAPF_6$), (E(V) vs SCE = 0.385 V).

Figure 6.29 shows the LSV spectra recorded after varying the time delay at -0.7 V. In this case, the formation of the desired peak was observed after 180 seconds (dark green line), meaning that the formation of the high-energy state is reached within a long time. Upon re-evaluating the obtained

results, it appears that utilizing a multifunctional system containing PEG chains hampers the formation of the high-energy complex. Overall. data suggests that the ratchet mechanism is facilitated kinetically when using small molecules rather than polymeric structures.

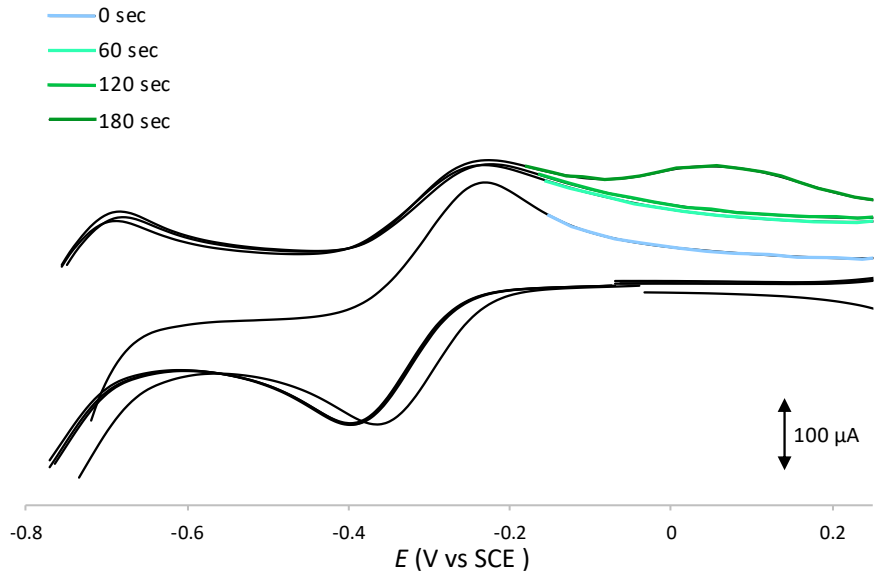

Figure 6.29. LSV of the 1:1 mixture of 1 mM **M2**$^{8+}$ and 1 mM **A4**$^{12+}$ in dry ACN (100 mM $TEAPF_6$), (E(V) vs SCE = 0.385 V) varying the time delay at a fixed potential of -0.7 V. In green is evidenced the peak related to the formation of the high-energy complex.

6 Conclusion

This chapter presents an investigation of multifunctional systems designed to achieve out-of-equilibrium states through an energy ratchet mechanism driven by redox stimuli. The synthesis of novel polyfunctional redox-active molecules is described. Comprehensive characterization of these compounds was performed using electrochemical and spectro-electrochemical techniques. In the case of bis-functionalized components, **M2**$^{8+}$ and **A2**$^{6+}$, the spectro-electrochemical analysis revealed the formation of homodimer species, both intra- and inter-molecular. Conversely, the tetra-functional axle **A4**$^{12+}$ did not exhibit the formation of radical-radical homodimer species. The formation of high-energy kinetically trapped states was examined across several systems, ranging from simple configurations with monofunctional host-guest pairs to more complex systems incorporating multifunctional components. In the simplest case, where the mono-functionalized host **M1**$^{4+}$ and guest **A1**$^{3+}$ were combined, a clear formation of the high-energy complex was observed. This was also the case when the mono-functional guest **A1**$^{3+}$ was combined with the bi-functional host **M2**$^{8+}$. However, when the bi-functional guest **A2**$^{6+}$ was combined with the mono-functional host **M1**$^{4+}$, different behaviors were observed depending on the scan rate. Specifically, the formation of the high-energy complex occurred only at medium scan rates, whereas at both slow and fast scan rates, the dethreading process predominated over the formation of the high-energy complex. Additionally, in systems involving multi-functionalized hosts and guests, the

formation of the high-energy complex was slow, requiring extended time to be detected. These findings contribute to a more comprehensive understanding of these systems and provide an in-depth insight into the redox mechanisms of multifunctional systems. Moving forward, NMR measurements will be conducted under bulk reduction and oxidation conditions to observe and detect the formation of cross-linked networks.

6 Acknowledgments

Thanks to Fabiana Ciocchetti and Ahmad Bachir for mentoring me during my time visiting the Ragazzon Research Group.

6 Experimental part

Synthesis of novel compounds

The synthesis of the novel compounds **M2**$^{8+}$, **A2**$^{6+}$, and **A4**$^{12+}$ was performed by Ahmad Bachir and Fabiana Ciocchetti. As my contribution to this work was limited, a detailed discussion of the synthesis of these compounds is not included in this thesis. The starting material for the synthesis was a commercially available polyoxyethylene bis(azide), which was characterized by an average molecular number (Mn) of 2000, with a molecular weight distribution (Mp) ranging from 1100 to 2200 g/mol, as determined by gel permeation chromatography (GPC). The compounds **M1**$^{4+}$,[26] **A1**$^{3+}$,[18] and **P1**[24] were synthesized following established protocols as reported in the literature.

Electrochemical experiments

Cyclic voltammetry (CV) experiments were measured out at room temperature in Ar-purged ACN, using Autolab PGSTAT100. A glassy carbon working electrode, a Pt wire counter electrode, and an Ag wire as electrodes were employed; ferrocene was present as the internal standard. All analyses were performed in the presence of tetraethylammonium hexafluorophosphate ($TEAPF_6$) as a supporting electrolyte.

M1^{4+}

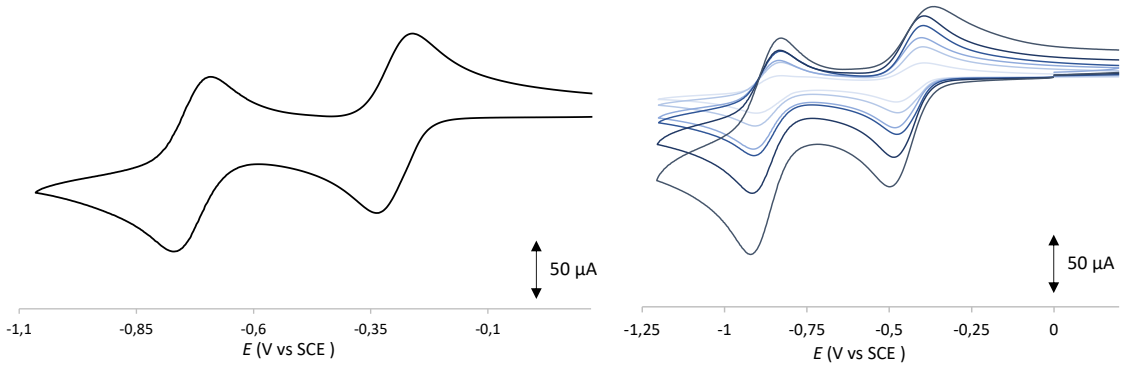

Figure 6.30 Left: Cyclic voltammogram (v = 0.1 V·s^{-1}) of **M1**$^{4+}$ (1 mM) in dry ACN (100 mM $TEAPF_6$), (E(V) vs SCE = 0.385 V); right: Scan rate dependence study of **M1**$^{4+}$ (1 mM) in dry ACN (100 mM $TEAPF_6$), (E(V) vs SCE = 0.385 V). The scan rates vary from 0.05 V·s^{-1} (light blue) through 0.1, 0.2, 0.25, 0.5, leading up to 1 V·s^{-1} (dark blue).

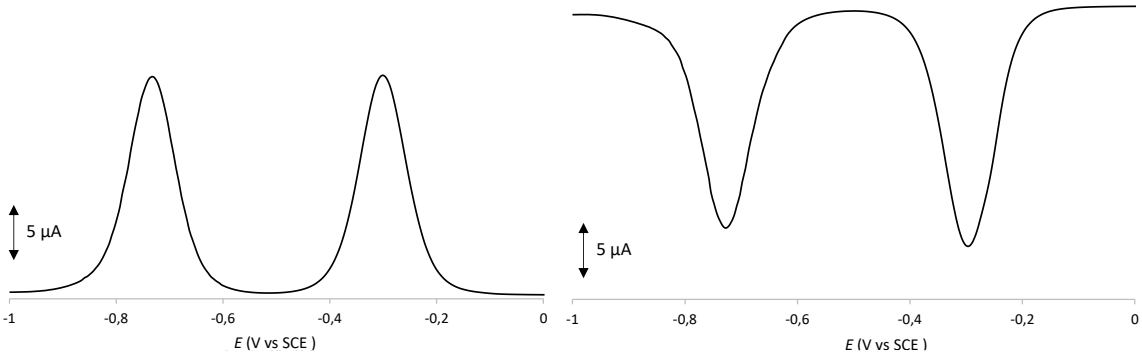

Figure 6.31 Differential pulse voltammograms of **M1**$^{4+}$ (1 mM) in dry ACN (100 mM $TEAPF_6$), (E(V) vs SCE = 0.385 V): left oxidation direction, right reduction direction. The DPV analysis shows two peaks at -0.30 V and -0.73 V, in agreement with the values found in the CV analysis.

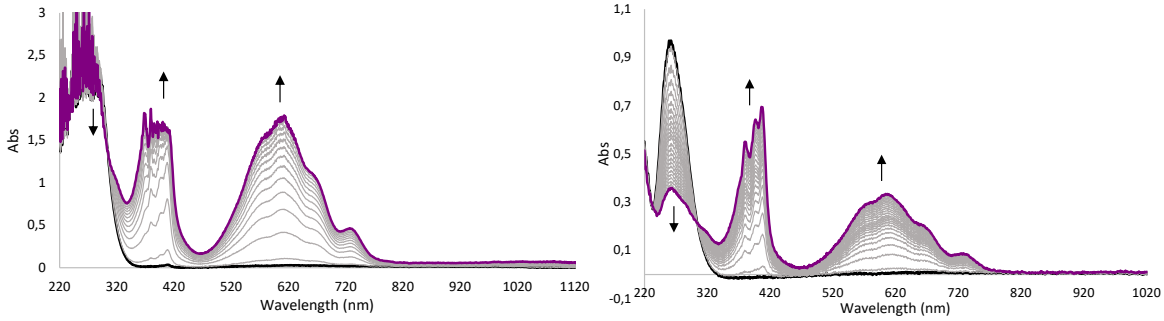

Figure 6.32 Spectro-electrochemistry recorded during the first exhaustive reduction of **M1**$^{4+}$ (E_{app} = -0.5 V) in dry ACN (100 mM $TEAPF_6$): left c = 1 mM, right c = 0.3 mM.

A1^{3+}

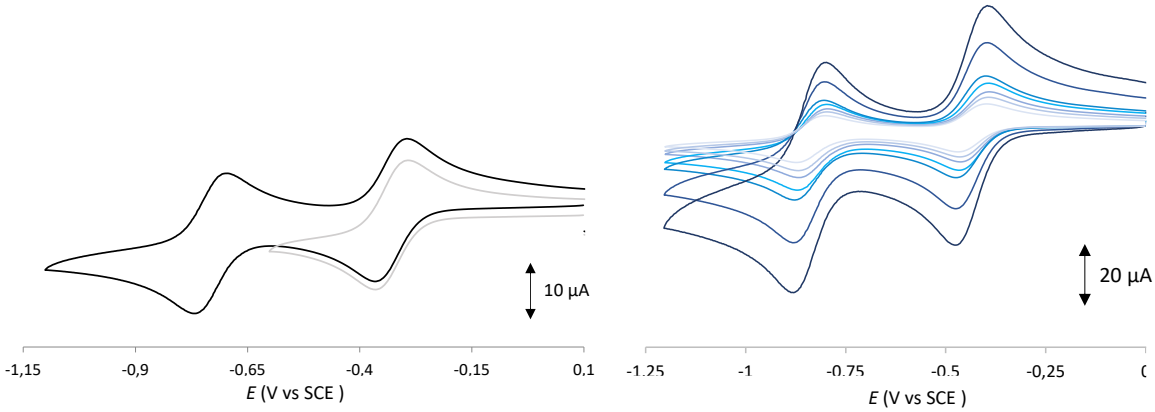

Figure 6.33 Left: Cyclic voltammograms (v = 0.1 V·s^{-1}) of **A1**$^{3+}$ (1 mM) in dry ACN (100 mM $TEAPF_6$), (*E*(V) vs SCE = 0.385 V); right: Scan rate dependence study of **A1**$^{3+}$ (1 mM) in dry ACN (100 mM $TEAPF_6$), (*E*(V) vs SCE = 0.385 V). The scan rates vary from 0.05 V·s^{-1} (light blue) through 0.1, 0.15, 0.2, 0.5, leading up to 1 V·s^{-1} (dark blue).

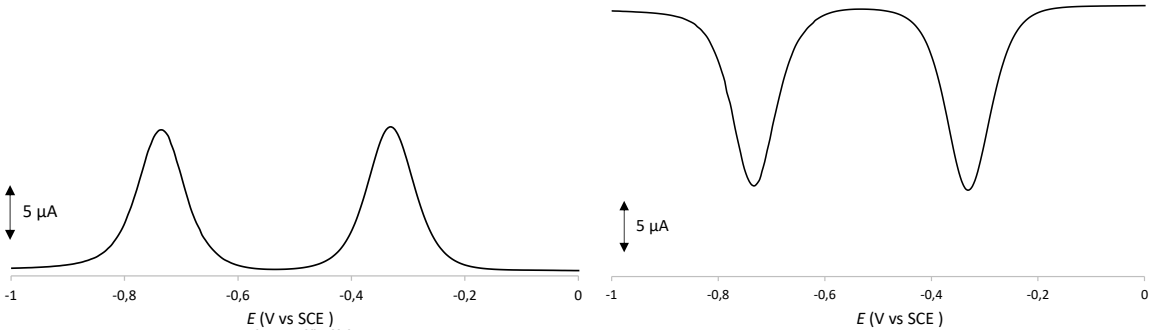

Figure 6.34 Differential pulse voltammograms of **A1**$^{3+}$ (1 mM) in dry ACN (100 mM $TEAPF_6$), (*E*(V) vs SCE = 0.385 V): left oxidation direction, right reduction direction. The DPV analysis shows two peaks at -0.35 V and -0.75 V, in agreement with the values found in the CV analysis.

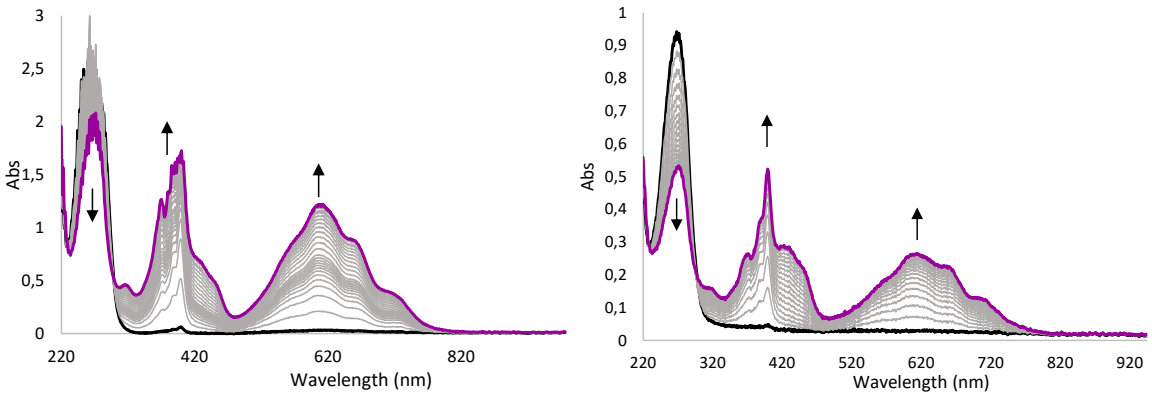

Figure 6.35 Spectro-electrochemistry recorded during the first exhaustive reduction of **A1**$^{3+}$ (E_{app} = -0.5 V) in dry ACN (100 mM $TEAPF_6$): left [**A1**$^{3+}$] = 1 mM, right [**A1**$^{3+}$] = 0.3 mM.

M2^{8+}

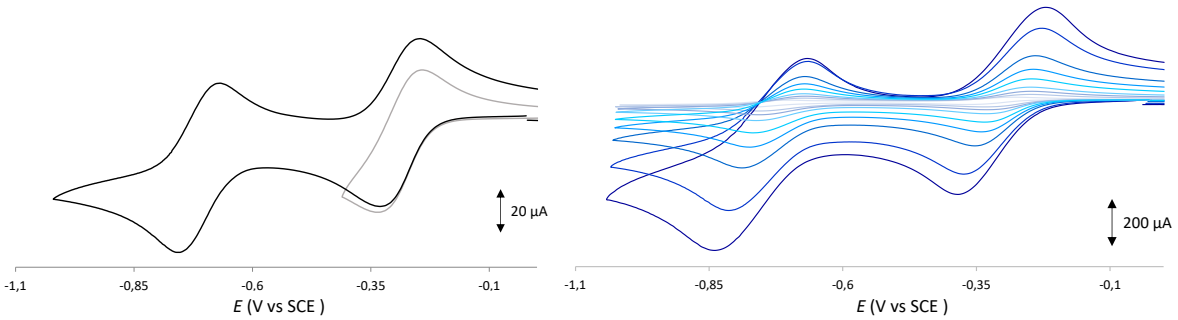

Figure 6.36 Left: Cyclic voltammograms (v= 0.1 V·s^{-1}) of **M2**$^{8+}$ (1 mM) in dry ACN (100 mM $TEAPF_6$), (*E*(V) vs SCE = 0.385 V); right: scan rate dependence study of **M2**$^{8+}$ (1mM) in dry ACN (100 mM $TEAPF_6$), (*E*(V) vs SCE = 0.385 V). The scan rates vary from 0.02 V·s^{-1} (light blue) through 0.05, 0.1, 0.2, 0.5, 1, 2, 5 leading up to 8 V·s^{-1} (dark blue).

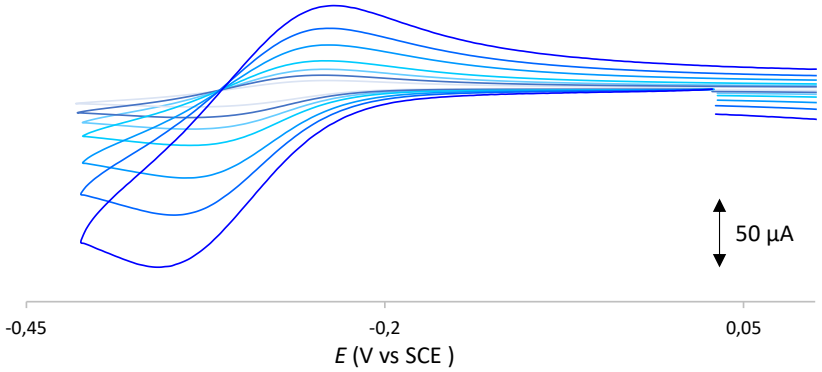

Figure 6.37 Scan rate dependence study of the first exhaustive reduction of **M2**$^{8+}$ (1mM, from +0.6 V to -0.4 V) in dry ACN (100 mM $TEAPF_6$), (*E*(V) vs SCE = 0.385 V). The scan rates vary from 0.02 V·s^{-1} (light blue) through 0.05, 0.1, 0.2, 0.5, 1, 2, 5 leading up to 8 V·s^{-1} (dark blue).

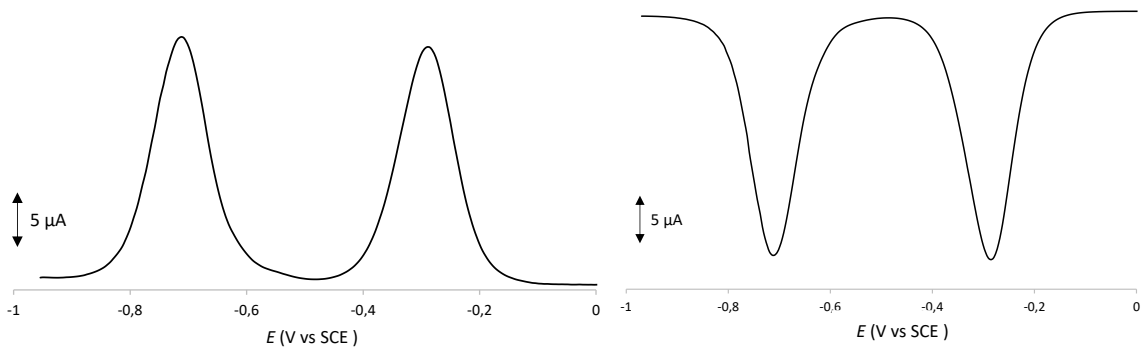

Figure 6.38 Differential pulse voltammograms of **M2**$^{8+}$ (1mM) in dry ACN (100 mM $TEAPF_6$), (*E*(V) vs SCE = 0.385 V): left oxidation direction, right reduction direction. The DPV analysis shows two peaks at -0.28 V and -0.71 V, which agree with the values found in the CV analysis.

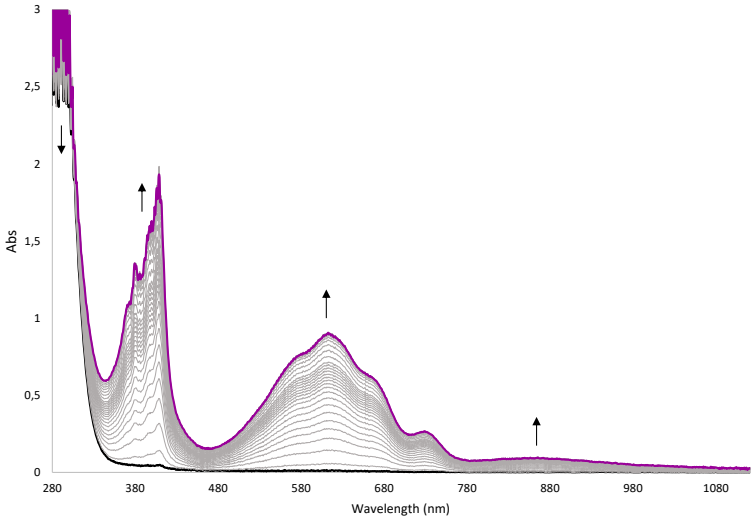

Figure 6.39 Spectro-electrochemistry recorded during the first exhaustive reduction of **M2**$^{8+}$ (1 mM, E_{app} = -0.5 V) in dry ACN (100 mM $TEAPF_6$).

A2^{6+}

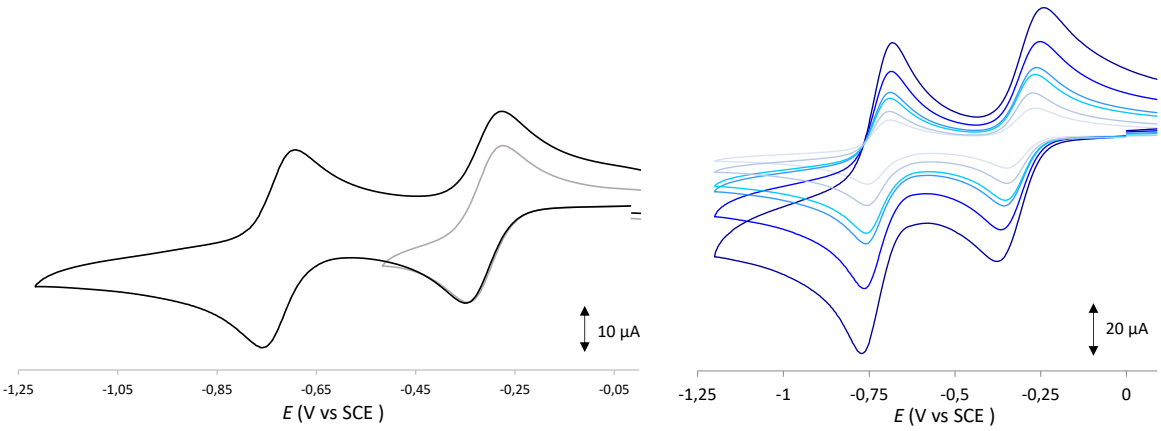

Figure 6.40 Left: Cyclic voltammograms (v= 0.1 V·s^{-1}) of **A2**$^{6+}$ (1mM) in dry ACN (100 mM $TEAPF_6$), (E(V) vs SCE = 0.385 V); right: scan rate dependence study of **A2**$^{6+}$ (1mM) in dry ACN (100 mM $TEAPF_6$), (E(V) vs SCE = 0.385 V). The scan rates vary from 0.05 V·s^{-1} (light blue) through 0.1, 0.2, 0.25, 0.5, leading up to 1 V·s^{-1} (dark blue).

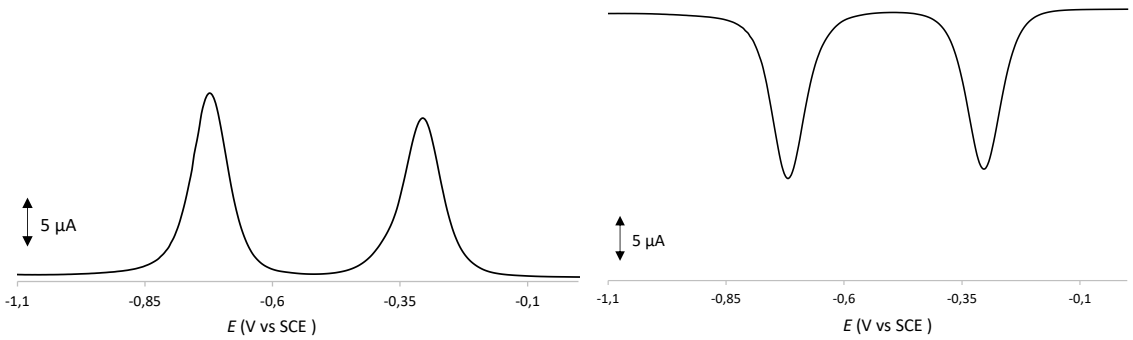

Figure 6.41 Differential pulse voltammograms of **A2**$^{6+}$ (1mM) in dry ACN (100 mM $TEAPF_6$), (E(V) vs SCE = 0.385 V): left oxidation direction, right reduction direction. The DPV analysis shows two peaks at -0.31 V and -0.72 V, which agree with the values found in the CV analysis.

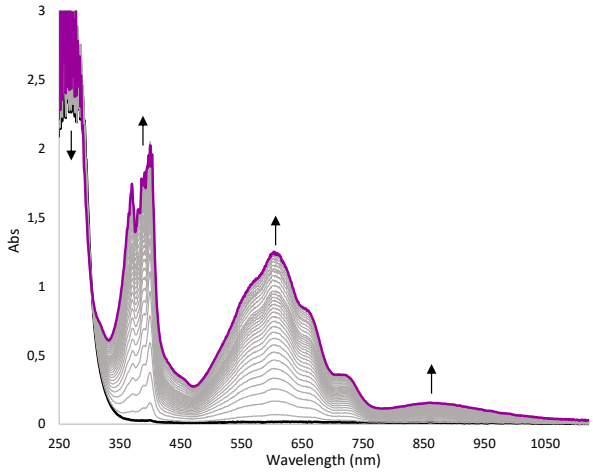

Figure 6.42 Spectro-electrochemistry recorded during the first exhaustive reduction of **A2**$^{6+}$ (1 mM, E_{app} = -0.5 V) in dry ACN (100 mM $TEAPF_6$).

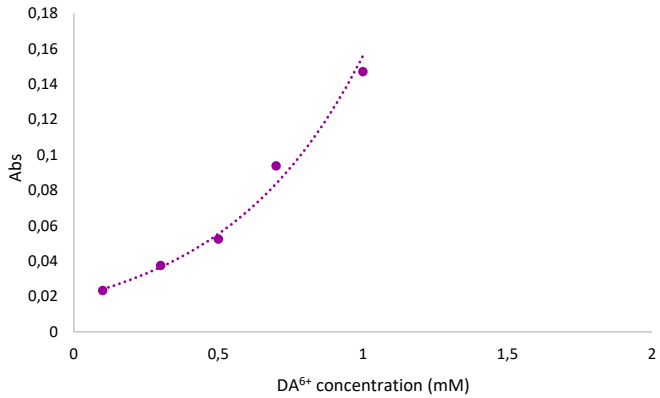

Figure 6.43 Absorbance values (λ = 860 nm) of a solution of **A2**$^{6+}$ at different concentrations recorded by spectro-electrochemistry (E_{app} = -0.5 V) in dry ACN (100 mM $TEAPF_6$).

A4^{12+}

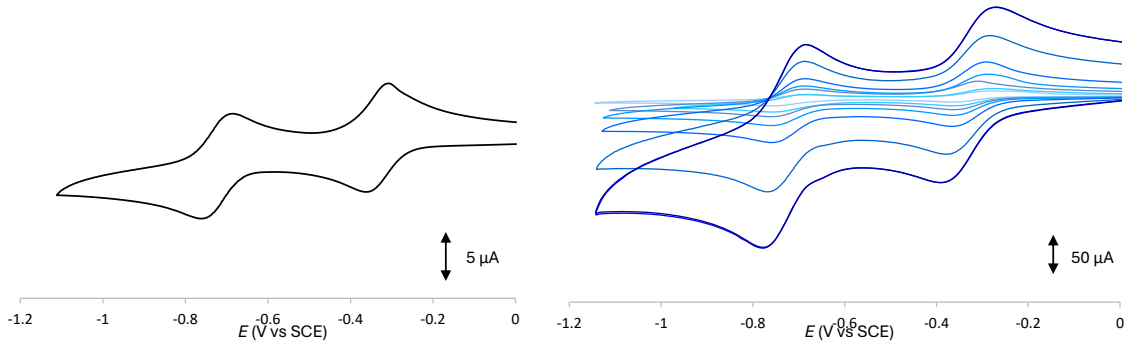

Figure 6.44 Left: cyclic voltammogram (v= 0.1 V·s^{-1}) of **A4**$^{12+}$ (0.25 mM) in dry ACN (100 mM $TEAPF_6$), (E(V) vs SCE = 0.385 V); right: scan rate dependence study of **A4**$^{12+}$ (0.25 mM) in dry ACN (100 mM $TEAPF_6$), (E(V) vs SCE = 0.385 V). The scan rates vary from 0.02 V·s^{-1} (light blue) through 0.05, 0.1, 0.2, 0.5, 1, 2, 5 leading up to 10 V·s^{-1} (dark blue).

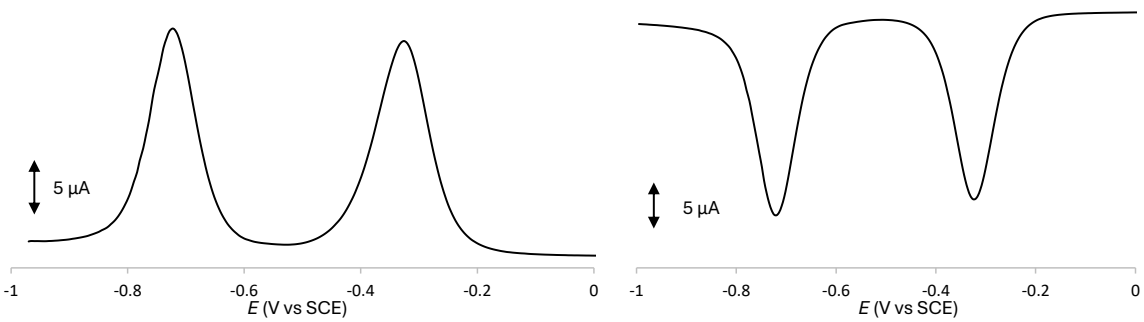

Figure 6.45 Differential pulse voltammograms of **A4**$^{12+}$ (0.25mM) in dry ACN (100 mM $TEAPF_6$), (E(V) vs SCE = 0.385 V): left oxidation direction, right reduction direction. The DPV analysis shows two peaks at -0.33 V and -0.72 V, which agree with the values found in the CV analysis.

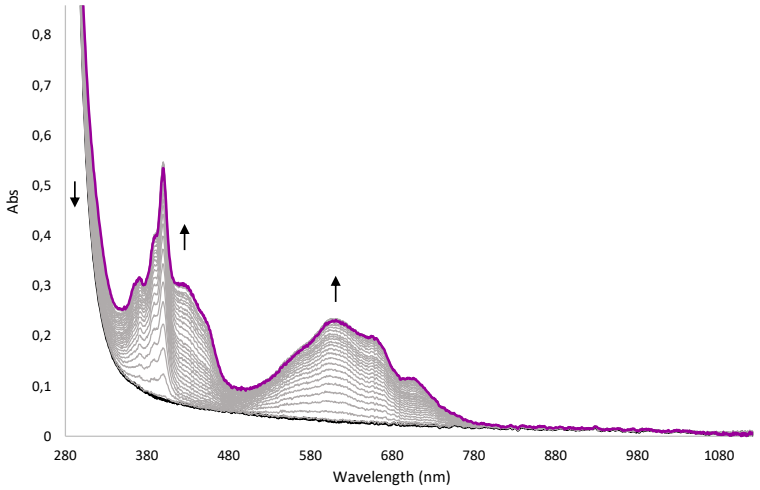

Figure 6.46 Spectro-electrochemistry recorded during the first exhaustive reduction of **A4**$^{12+}$ (0.25mM, E_{app} = -0.5 V) in dry ACN (100 mM $TEAPF_6$).

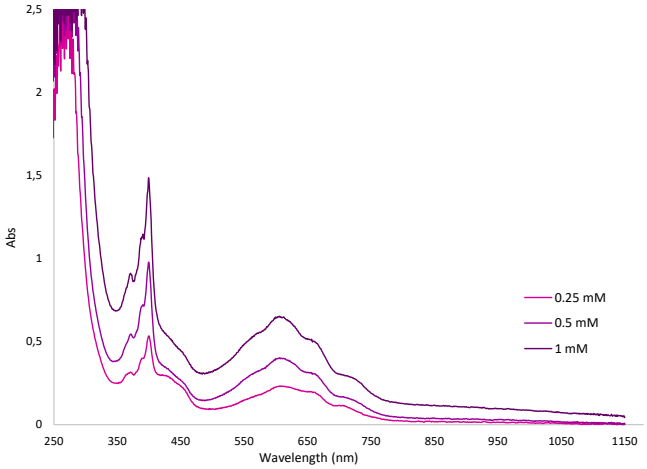

Figure 6.47 Spectro-electrochemistry recorded during the first exhaustive reduction of **A4**$^{12+}$ at different concentrations (E_{app} = -0.5 V) in dry ACN (100 mM $TEAPF_6$).

M1^{4+} and **A1**$^{3+}$

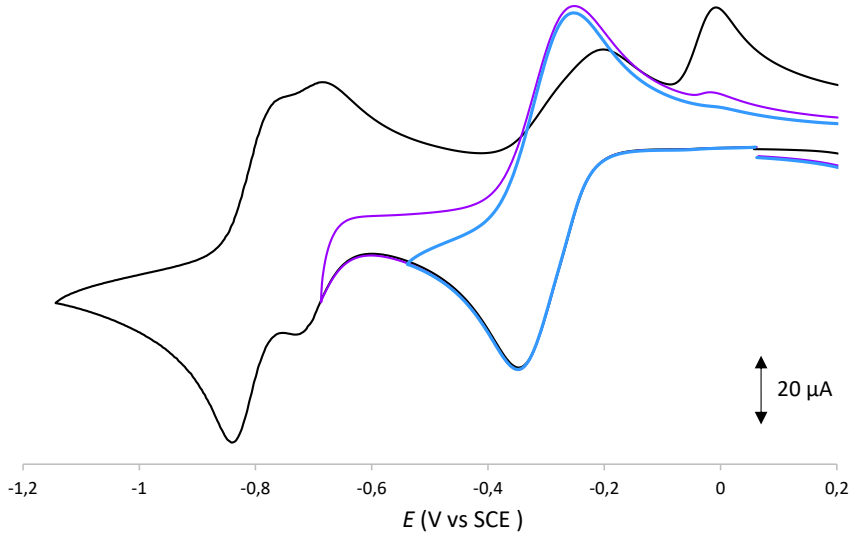

Figure 6.48 Cyclic voltammograms (v = 0.1 V·s^{-1}) of the equimolar mixture of **M1**$^{4+}$ and **A1**$^{3+}$ (1mM in each components) in dry ACN (100 mM $TEAPF_6$), (E(V) vs SCE = 0.385 V) recorded using different potential ranges: from +0.5 to –1.2 V (black line), from +0.5 to –0.75 V (purple line) and from +0.5 to –0.6 V (blue line).

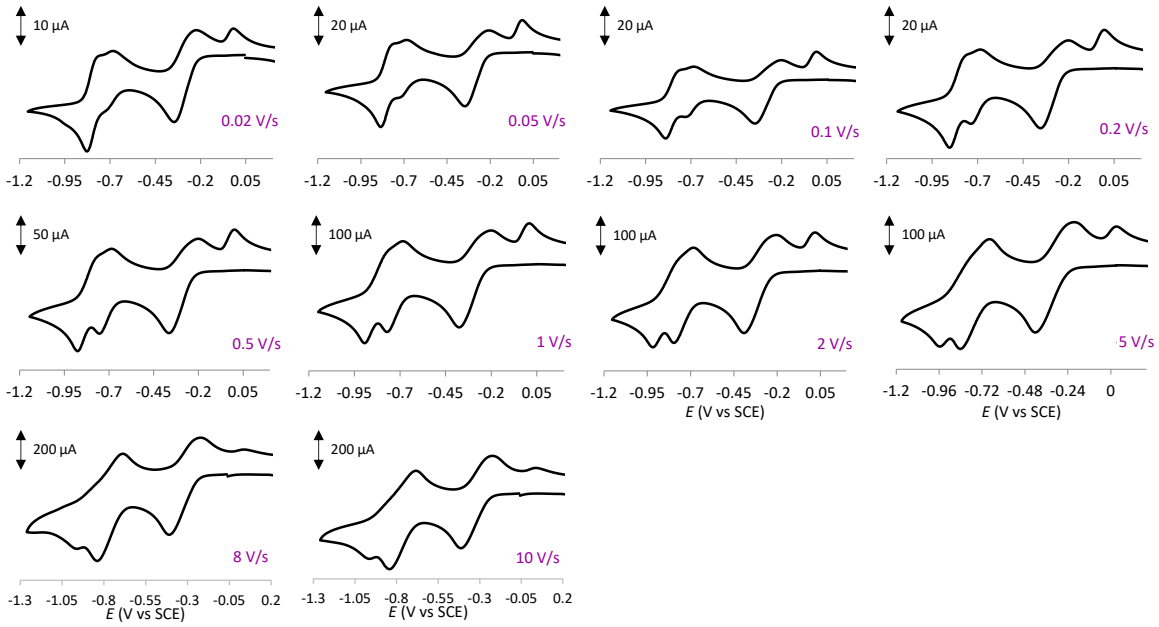

Figure 6.49 Scan rate dependence study of the equimolar mixture of **M1**$^{4+}$ and **A1**$^{3+}$ (1mM in each component) in dry ACN (100 mM $TEAPF_6$), (E(V) vs SCE = 0.385 V). The scan rates vary from 0.02 V·s^{-1} through 0.05, 0.1, 0.2, 0.5, 1, 2, 5, 8 leading up to 10 V·s^{-1}.

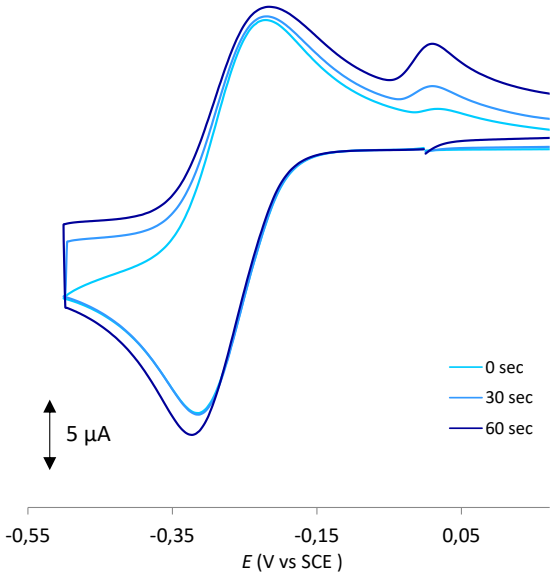

Figure 6.50 Cyclic voltammograms (v = 0.02 V·s^{-1}) of the first exhaustive reduction of the equimolar mixture of **M1**$^{4+}$ and **A1**$^{3+}$ (1mM in each component) in dry ACN (100 mM $TEAPF_6$), (*E*(V) vs SCE = 0.385 V) recorded at different time delay at the applied potential of -0.5 V.

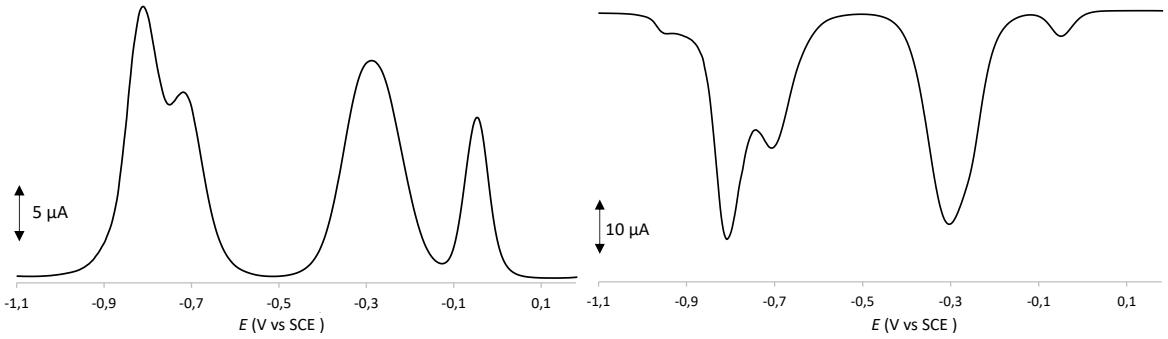

Figure 6.51 Differential pulse voltammograms of the equimolar mixture of **M1**$^{4+}$ and **A1**$^{3+}$ (1mM in each component) in dry ACN (100 mM $TEAPF_6$), (*E*(V) vs SCE = 0.385 V): left oxidation direction, right reduction direction. The DPV analysis shows four peaks at -0.05 V, -0.28 V, -0.72 V and -0.81 V, which are consistent with the observations in the CV analysis.

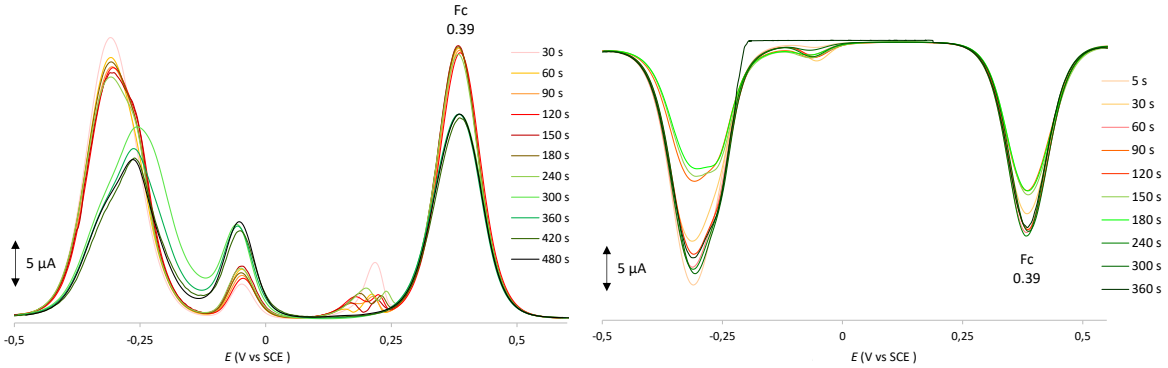

Figure 6.52 Differential pulse voltammograms from -0.5 V and 0.6 V of the equimolar mixture of **M1**$^{4+}$ and **A1**$^{3+}$ (1mM in each component) in dry ACN (100 mM $TEAPF_6$), (*E*(V) vs SCE = 0.385 V) after varying delay at -0.5 V: left oxidation direction, right reduction direction.

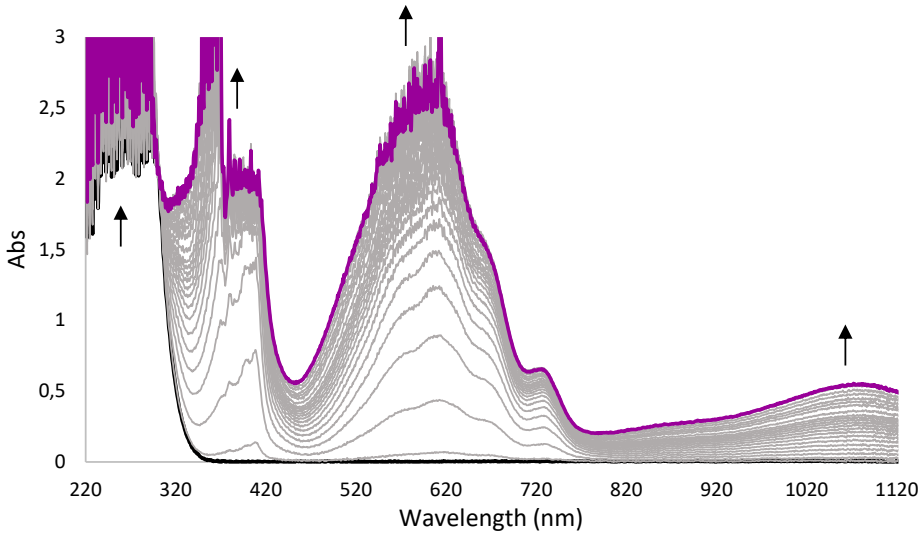

Figure 6.53 Spectro-electrochemistry recorded during the first exhaustive reduction of the equimolar mixture of **M1**$^{4+}$ and **A1**$^{3+}$ (1 mM in each component, E_{app} = -0.5 V) in dry ACN (100 mM $TEAPF_6$).

A2^{6+} and **M1**$^{4+}$

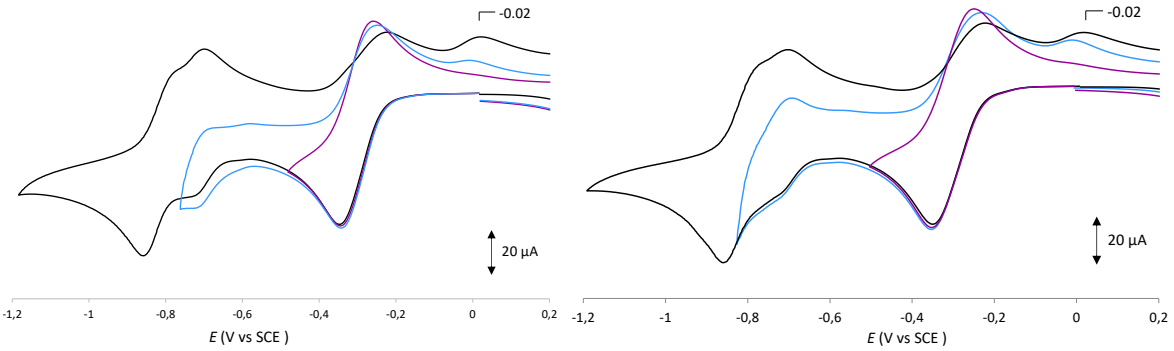

Figure 6.54 Cyclic voltammograms (v = 0.1 $V \cdot s^{-1}$) of the mixture of **M1**$^{4+}$ and **A2**$^{6+}$ in 1:1 ratio (1 mM in each components, left) and 2:1 ratio (2 mM for **M1**$^{4+}$ and 1 mM for **A2**$^{6+}$, right) in dry ACN (100 mM $TEAPF_6$), (*E*(V) vs SCE = 0.385 V) recorded at different potential range: from +0.6 to –1.2 V (black line), from +0.6 to –0.78 V (blue line) and from +0.6 to –0.5 V (purple line).

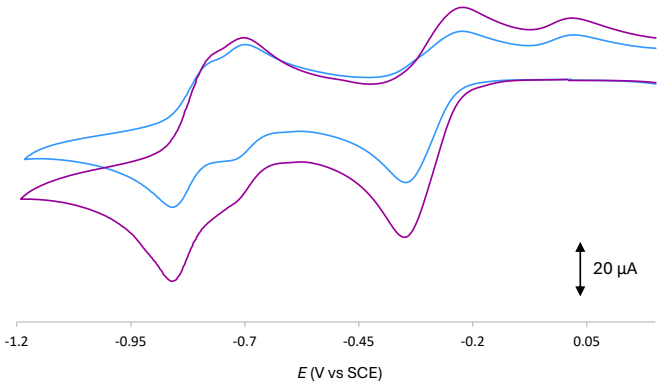

Figure 6.55 Cyclic voltammograms (v = 0.1 $V \cdot s^{-1}$) of the mixture of **M1**$^{4+}$ and **A2**$^{6+}$ in 1:1 ratio (1 mM in each component, blue line) and 2:1 ratio (2 mM for **M1**$^{4+}$ and 1 mM for **A2**$^{6+}$, purple line) in dry ACN (100 mM $TEAPF_6$), (*E*(V) vs SCE = 0.385 V).

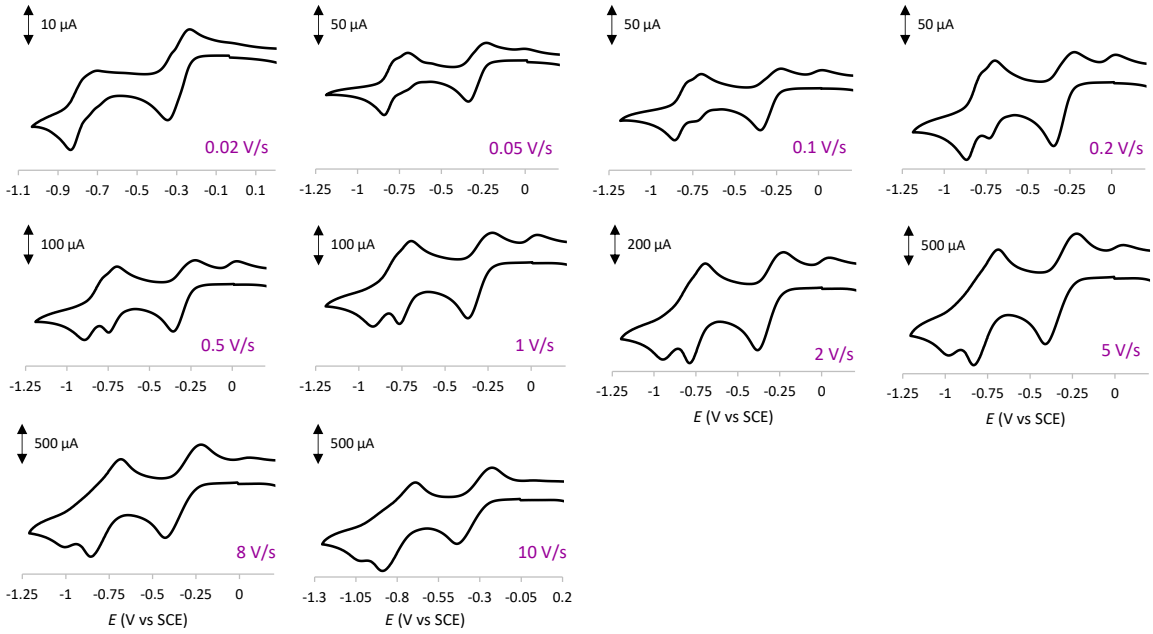

Figure 6.56 Scan rate dependence study of the 1:1 mixture of **M1**$^{4+}$ and **A2**$^{6+}$ (1mM in each component) in dry ACN (100 mM $TEAPF_6$), (E(V) vs SCE = 0.385 V). The scan rates vary from 0.02 V·s^{-1} through 0.05, 0.1, 0.2, 0.5, 1, 2, 5, 8 leading up to 10 V·s^{-1}.

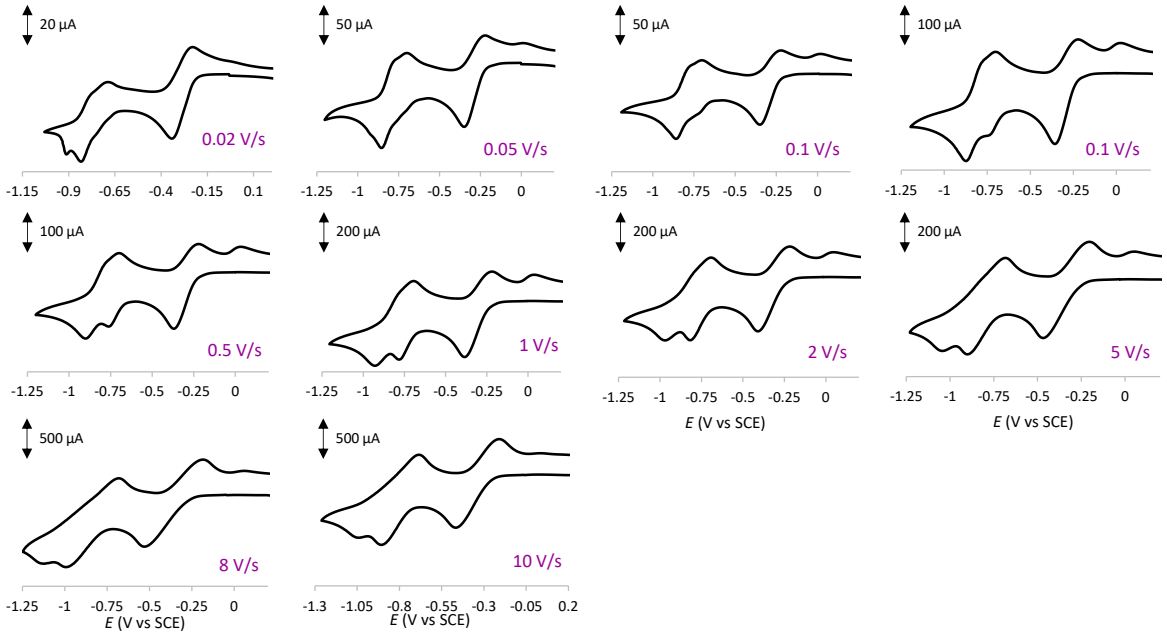

Figure 6.57 Scan rate dependence study of the 2:1 mixture of **M1**$^{4+}$ and **A2**$^{6+}$ (2 mM for **M1**$^{4+}$ and 1 mM for **A2**$^{6+}$) in dry ACN (100 mM $TEAPF_6$), (E(V) vs SCE = 0.385 V). The scan rates vary from 0.02 V·s^{-1} through 0.05, 0.1, 0.2, 0.5, 1, 2, 5, 8 leading up to 10 V·s^{-1}.

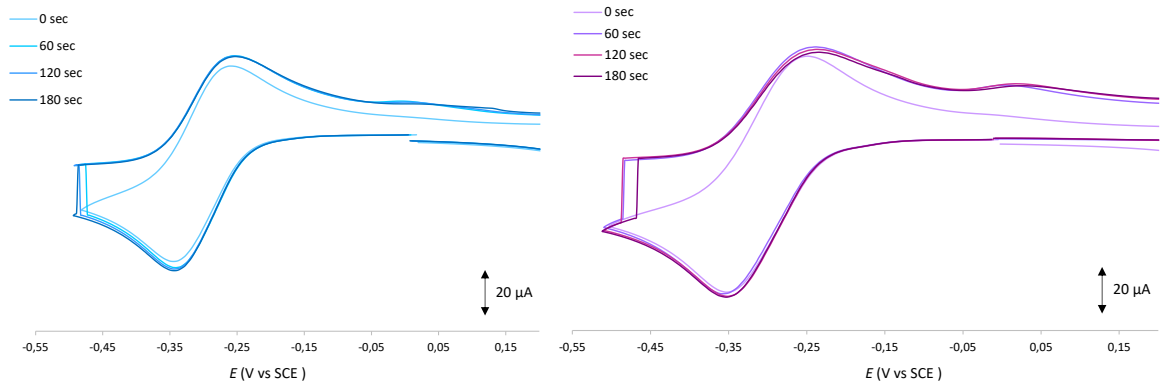

Figure 6.58 Cyclic voltammograms (v = 0.1 V·s^{-1}) of the first exhaustive reduction of the mixture of **M1**$^{4+}$ and **A2**$^{6+}$ in 1:1 ratio (1 mM in each components, left) and 2:1 (2 mM for **M1**$^{4+}$ and 1 mM for **A2**$^{6+}$, right) in dry ACN (100 mM $TEAPF_6$), (*E*(V) vs SCE = 0.385 V) recorded at different time delay at the applied potential of -0.5 V.

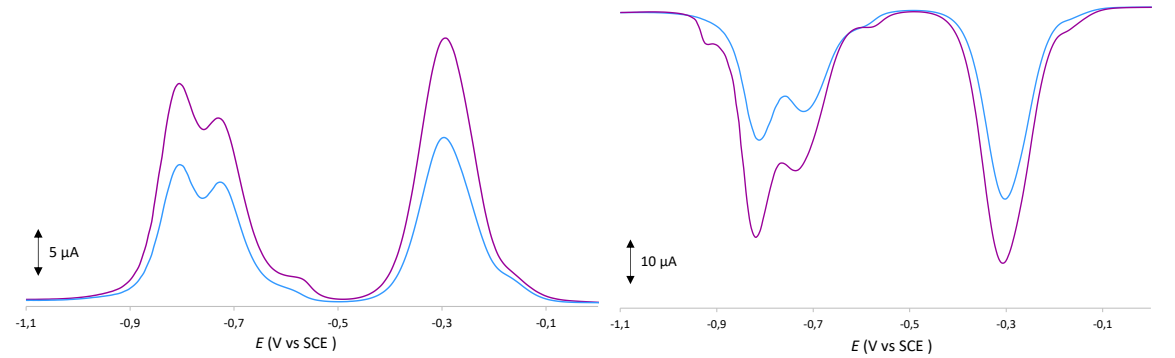

Figure 6.59 Differential pulse voltammograms of 1:1 (1 mM in each component, blue lines) and 2:1 (2 mM for **M1**$^{4+}$ and 1 mM for **A2**$^{6+}$, purple lines) mixture of **M1**$^{4+}$ and **A2**$^{6+}$ in dry ACN (100 mM $TEAPF_6$), (*E*(V) vs SCE = 0.385 V): left oxidation direction, right reduction direction. The DPV analysis shows three peaks at -0.29 V, -0.73 V and -0.80 V, which are consistent with the observations in the CV analysis.

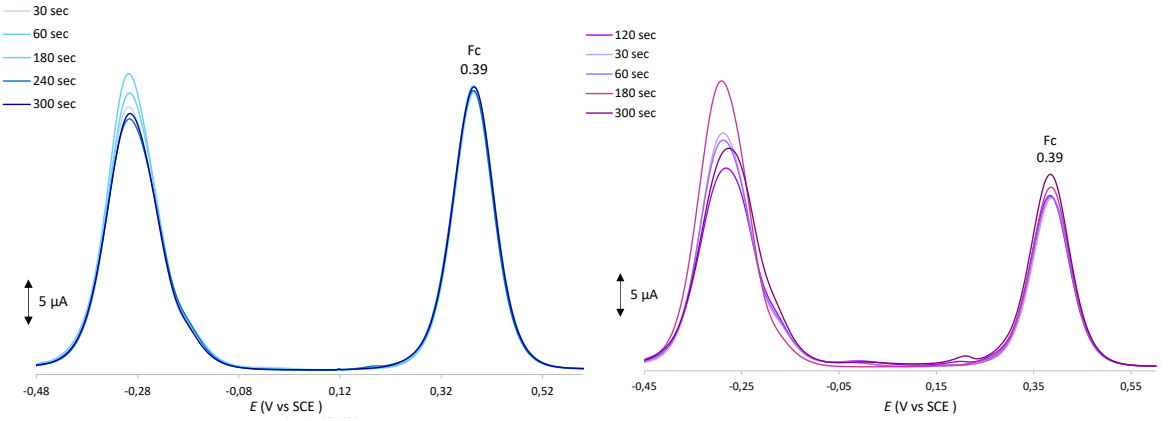

Figure 6.60 Differential pulse voltammograms from -0.5 V and 0.6 V of 1:1 (1 mM in each components, left) and 2:1 (2 mM for **M1**$^{4+}$ and 1 mM for **A2**$^{6+}$, right) mixture of **M1**$^{4+}$ and **A2**$^{6+}$ in dry ACN (100 mM $TEAPF_6$), (*E*(V) vs SCE = 0.385 V), after varying delay time at -0.5 V.

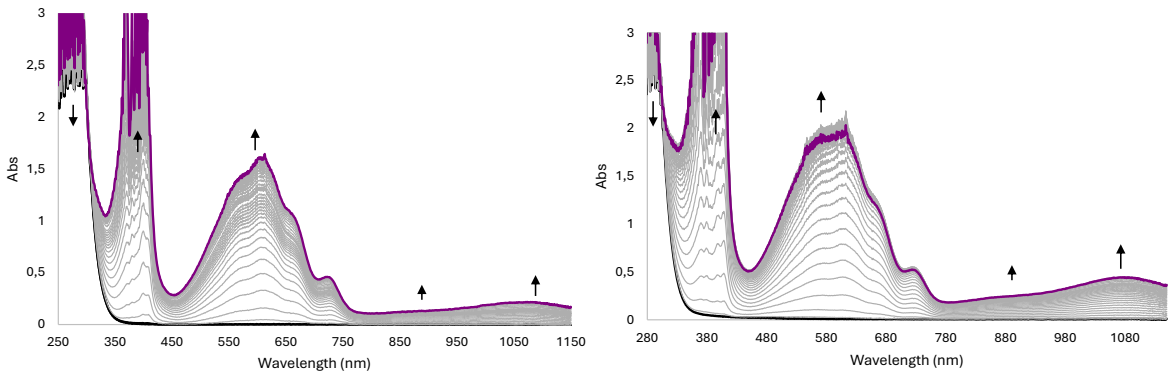

Figure 6.61 Spectro-electrochemistry recorded during the first exhaustive reduction of the mixture of **M1**$^{4+}$ and **A2**$^{6+}$ in 1:1 ratio (1 mM in each component, left) and 2:1 ratio (2 mM for **M1**$^{4+}$ and 1 mM for **A2**$^{6+}$, right) (E_{app} = -0.5 V) in dry ACN (100 mM $TEAPF_6$).

M2^{8+} and **A1**$^{3+}$

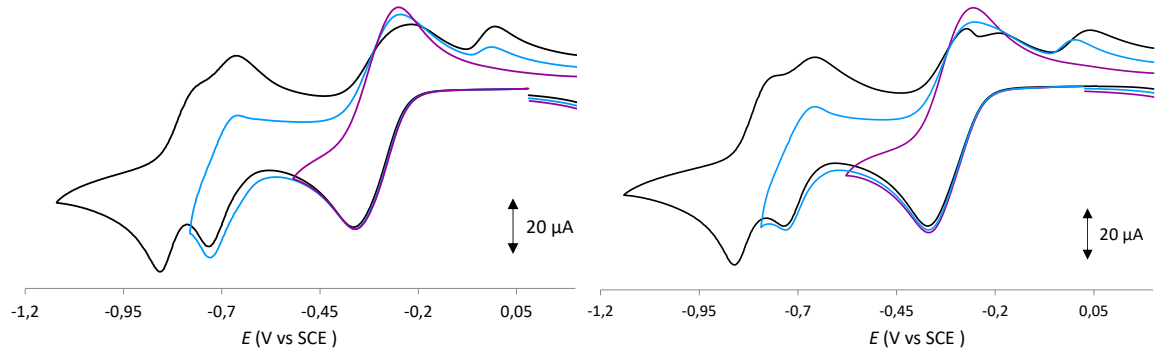

Figure 6.62 Cyclic voltammograms (v = 0.1 V·s^{-1}) of the mixture of **M2**$^{8+}$ and **A1**$^{3+}$ in 1:1 ratio (1 mM in each components, left) and 1:2 ratio (1 mM for **M2**$^{8+}$ and 2 mM for **A1**$^{3+}$, right) in dry ACN (100 mM $TEAPF_6$), (E(V) vs SCE = 0.385 V) recorded at different potential range: from +0.6 to –1.2 V (black line), from +0.6 to –0.78 V (blue line) and from +0.6 to –0.5 V (purple line).

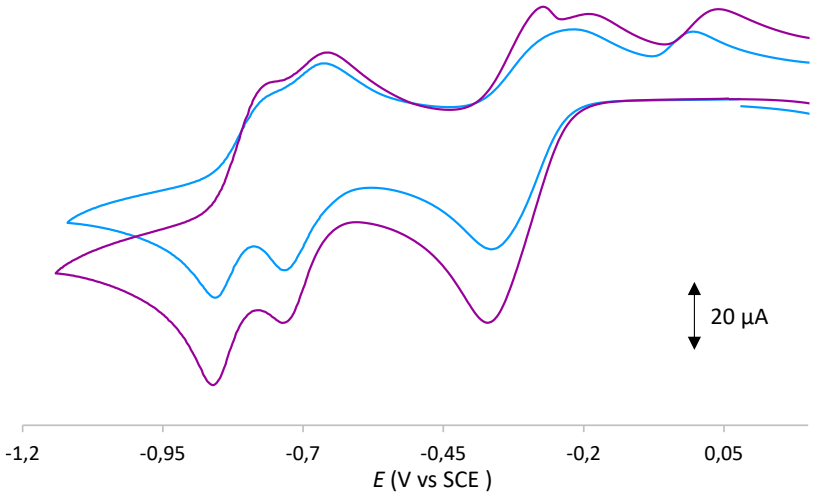

Figure 6.63 Cyclic voltammograms (v = 0.1 V·s^{-1}) of the 1:1 (1 mM in each component, blue line) and 1:2 (1 mM for **M2**$^{8+}$ and 2 mM for **A1**$^{3+}$, purple line) mixture of **M2**$^{8+}$ and **A1**$^{3+}$ in dry ACN (100 mM $TEAPF_6$), (E(V) vs SCE = 0.385 V).

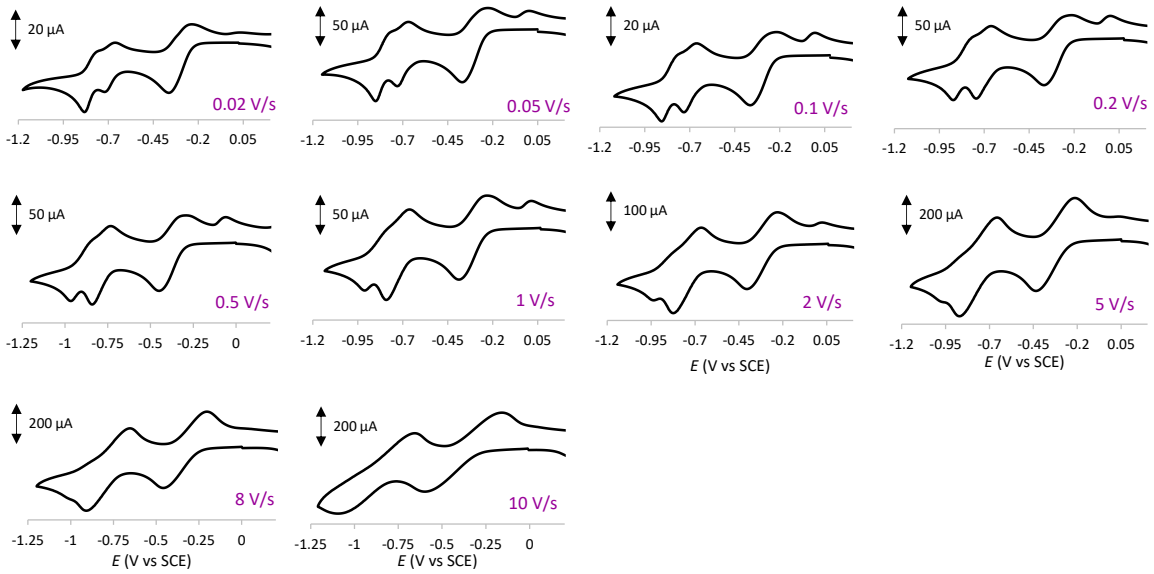

Figure 6.64 Scan rate dependence study of the equimolar mixture of **M2**$^{8+}$ and **A1**$^{3+}$ (1mM in each component) in dry ACN (100 mM $TEAPF_6$), (E(V) vs SCE = 0.385 V). The scan rates vary from 0.02 V·s^{-1} through 0.05, 0.1, 0.2, 0.5, 1, 2, 5, 8 leading up to 10 V·s^{-1}.

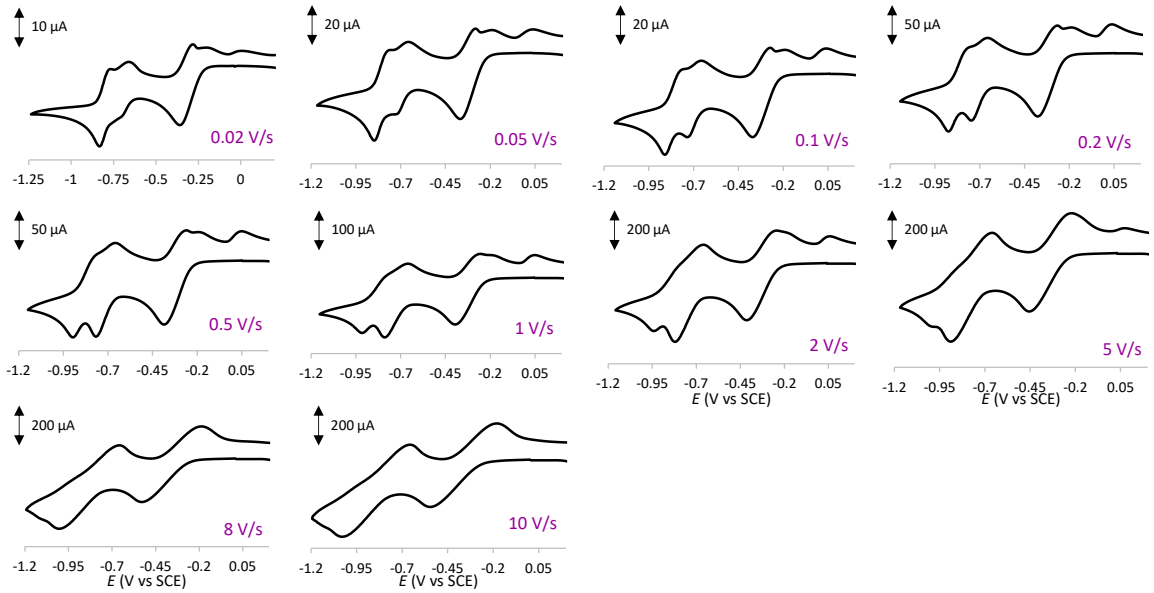

Figure 6.65 Scan rate dependence study of the mixture of **M2**$^{8+}$ and **A1**$^{3+}$ in 1:2 ratio (1 mM for **M2**$^{8+}$ and 2 mM for **A1**$^{3+}$) in dry ACN (100 mM $TEAPF_6$), (E(V) vs SCE = 0.385 V). The scan rates vary from 0.02 V·s^{-1} through 0.05, 0.1, 0.2, 0.5, 1, 2, 5, 8 leading up to 10 V·s^{-1}.

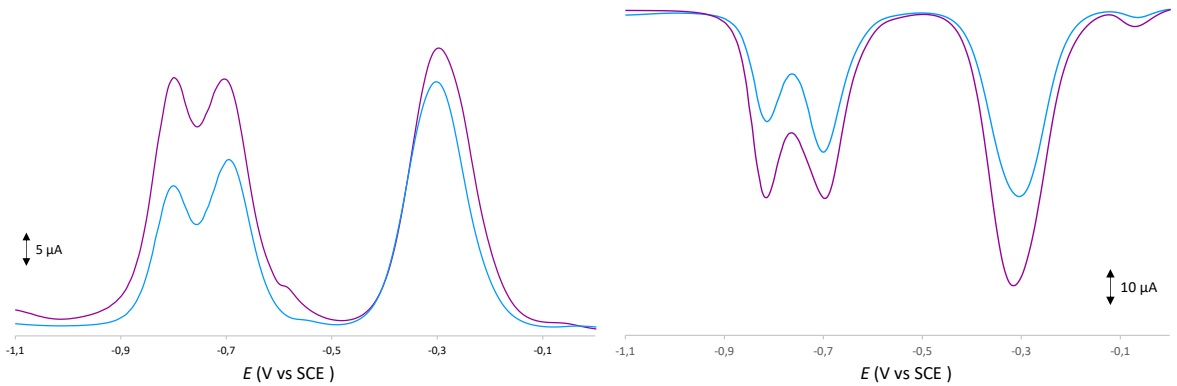

Figure 6.66 Differential pulse voltammograms of 1:1 (1 mM in each component, blue lines) and 1:2 (1 mM for **M2**$^{8+}$ and 2 mM for **A1**$^{3+}$, purple lines) mixture of **M2**$^{8+}$ and **A1**$^{3+}$ in dry ACN (100 mM $TEAPF_6$), (E(V) vs SCE = 0.385 V): left oxidation direction, right reduction direction. The DPV analysis of 1:1 mixture of **M2**$^{8+}$ and **A1**$^{3+}$ shows three peaks at -0.30 V, -0.69 V and -0.79 V, which agree with the values found in the CV analysis. The DPV analysis of 1:2 mixture of **M2**$^{8+}$ and **A1**$^{3+}$ shows three peaks at -0.29 V, -0.70 V and -0.80 V, which are consistent with the observations in the CV analysis.

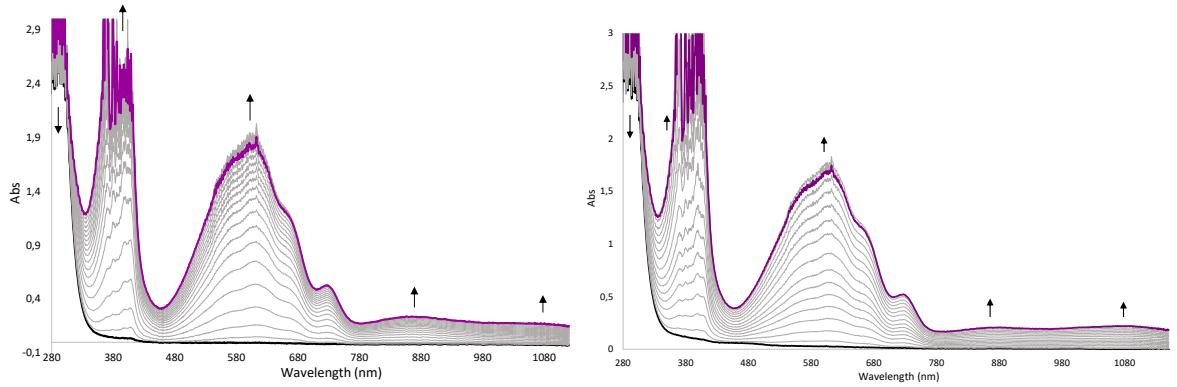

Figure 6.67 Spectro-electrochemistry recorded during the first exhaustive reduction of the mixture of **M2**$^{8+}$ and **A1**$^{3+}$ in 1:1 (1 mM in each component, left) and 1:2 (1 mM for **M2**$^{8+}$ and 2 mM for **A1**$^{3+}$, right) ratio (1 mM, E_{app} = -0.5 V) in dry ACN (100 mM $TEAPF_6$).

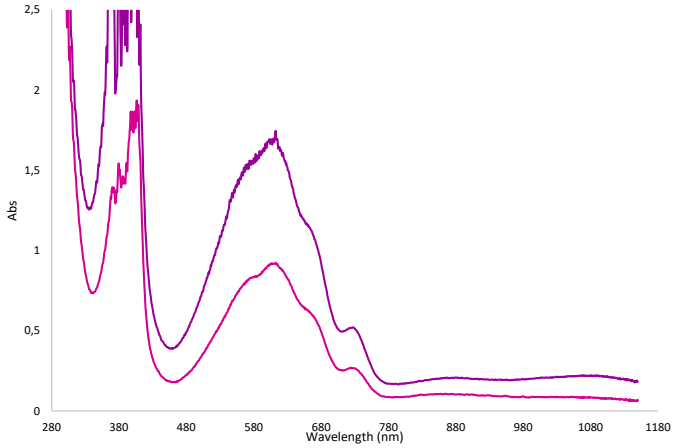

Figure 6.68 Spectro-electrochemistry recorded during the first exhaustive reduction of the mixture of **M2**$^{8+}$ and **A1**$^{3+}$ in 1:1 ratio (1 mM in each components, pink line), and in 1:2 ratio (1 mM for **M2**$^{8+}$ and 2 mM for **A1**$^{3+}$, purple line), (E_{app} = -0.5 V) in dry ACN (100 mM $TEAPF_6$).

M2^{8+} and **A2**$^{6+}$

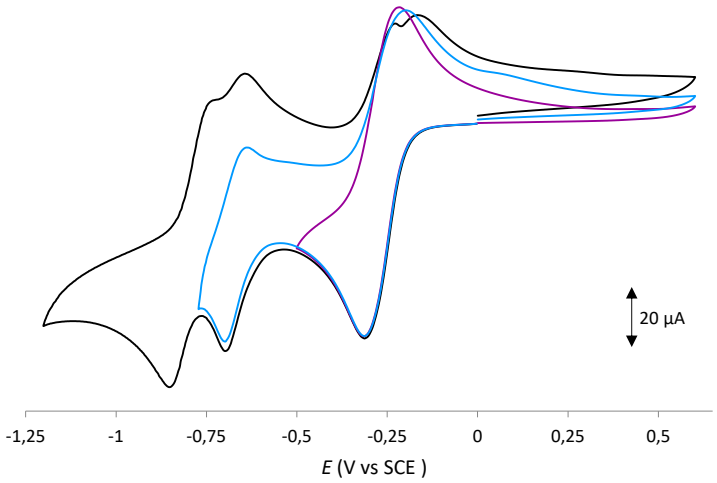

Figure 6.69 Cyclic voltammograms (v = 0.1 V·s^{-1}) of the equimolar mixture of **M2**$^{8+}$ and **A2**$^{6+}$ (1mM in each components) in dry ACN (100 mM $TEAPF_6$), (*E*(V) vs SCE = 0.385 V) recorded at different potential range: from +0.6 to –1.2 V (black line), from +0.6 to –0.78 V (blue line) and from +0.6 to –0.5 V (purple line).

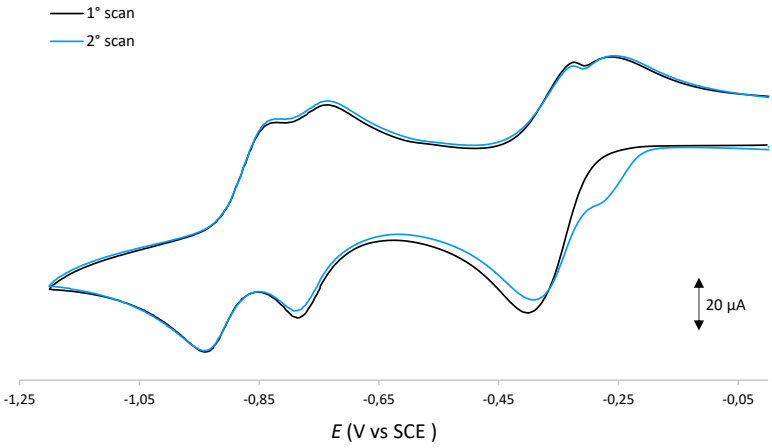

Figure 6.70 Cyclic voltammograms (v = 0.1 V·s^{-1}) of the equimolar mixture of **M2**$^{8+}$ and **A2**$^{6+}$ (1mM in each component) in dry ACN (100 mM $TEAPF_6$), (*E*(V) vs SCE = 0.385 V).

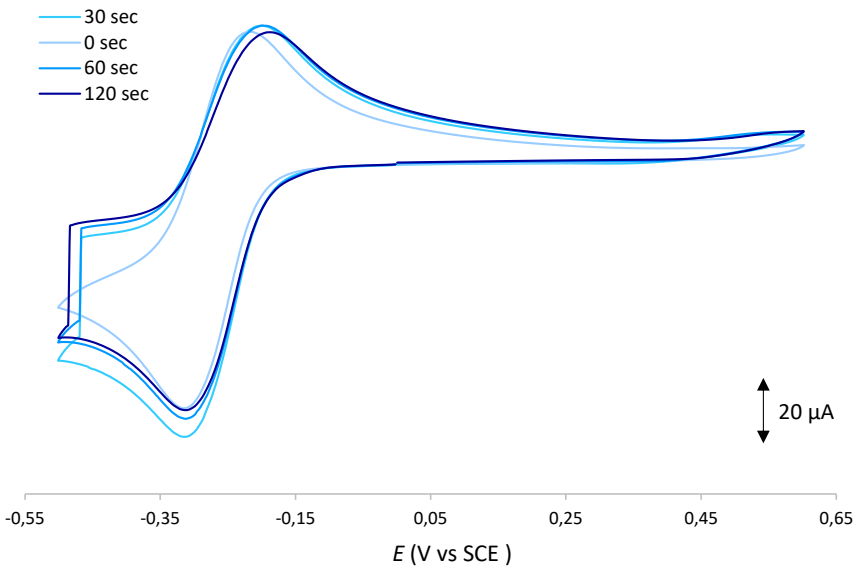

Figure 6.71 Cyclic voltammograms (v = 0.1 V·s^{-1}) of the 1:1 mixture of **M2**$^{8+}$ and **A2**$^{6+}$ (1mM in each component) in dry ACN (100 mM $TEAPF_6$) from +0.6 V to -0.5 V, (*E*(V) vs SCE = 0.385 V) recorded at different time delay at the applied potential of -0.50 V.

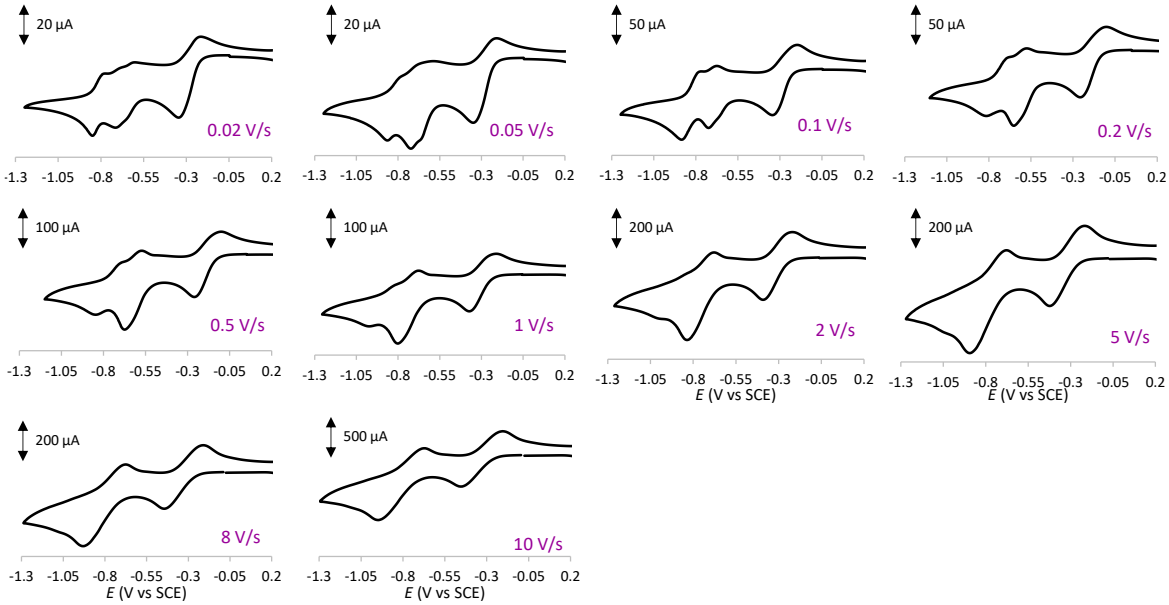

Figure 6.72 Scan rate dependence study of the equimolar mixture of **M2**$^{8+}$ and **A2**$^{6+}$ (1mM in each components) in dry ACN (100 mM $TEAPF_6$), (*E*(V) vs SCE = 0.385 V). The scan rates vary from 0.02 V·s^{-1} through 0.05, 0.1, 0.2, 0.5, 1, 2, 5, 8 leading up to 10 V·s^{-1}.

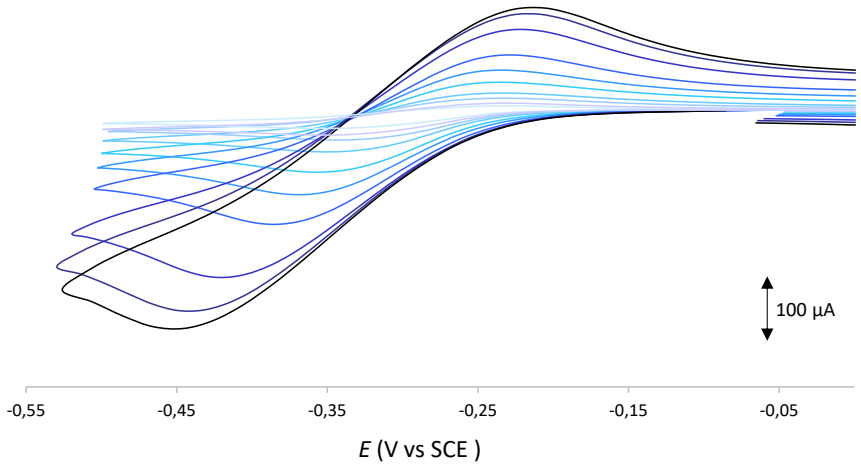

Figure 6.73 Scan rate dependence study of the first exhaustive reduction (from +0.6 V to -0.5 V) of the equimolar mixture of **M2**$^{8+}$ and **A2**$^{6+}$ (1mM in each component) in dry ACN (100 mM $TEAPF_6$), (*E*(V) vs SCE = 0.385 V). The scan rates vary from 0.02 V·s^{-1} through 0.05, 0.1, 0.2, 0.5, 1, 2, 5, 8 leading up to 10 V·s^{-1}.

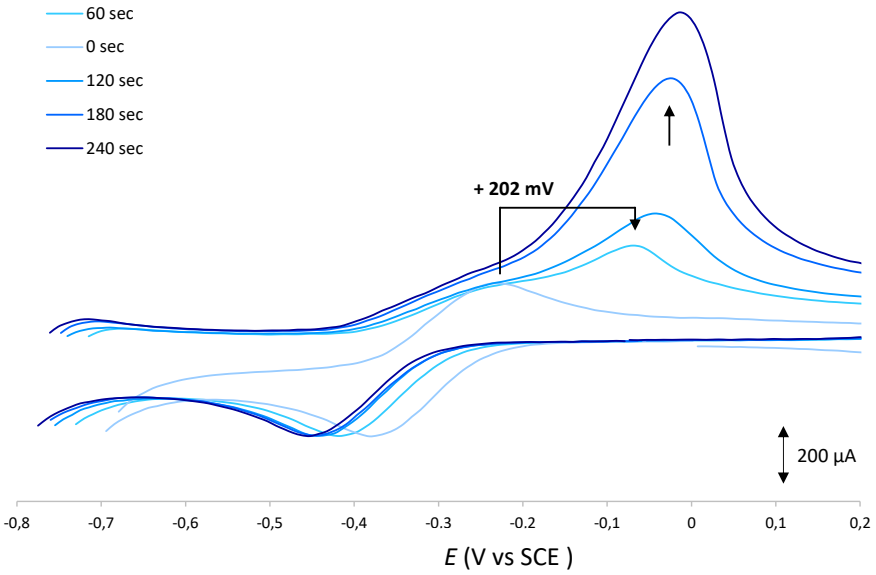

Figure 6.74 Linear sweep voltammetry (ν = 5 V·s^{-1}) of the equimolar mixture of **M2**$^{8+}$ and **A2**$^{6+}$ (1mM in each component) in dry ACN (100 mM $TEAPF_6$), (*E*(V) vs SCE = 0.385 V). Each curve was obtained in four steps: i) scanning from 0 V to -0.7; V ii) maintaining the potential of 0.7 V for a given delay time – indicated in the legend; iii) scanning the potential to 0.6 V; iv) completing the experiment by returning from 0.6 V to 0 V.

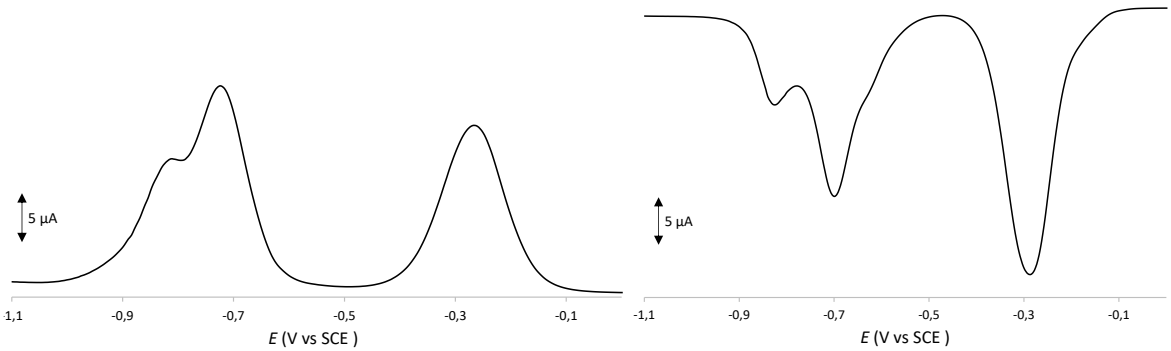

Figure 6.75 Differential pulse voltammograms of the equimolar mixture of **M2**$^{8+}$ and **A2**$^{6+}$ (1 mM in each components) in dry ACN (100 mM $TEAPF_6$), (E(V) vs SCE = 0.385 V): left oxidation direction, right reduction direction. The DPV analysis shows three peaks at -0.26 V, -0.72 V and -0.81 V, which are consistent with the observations in the CV analysis.

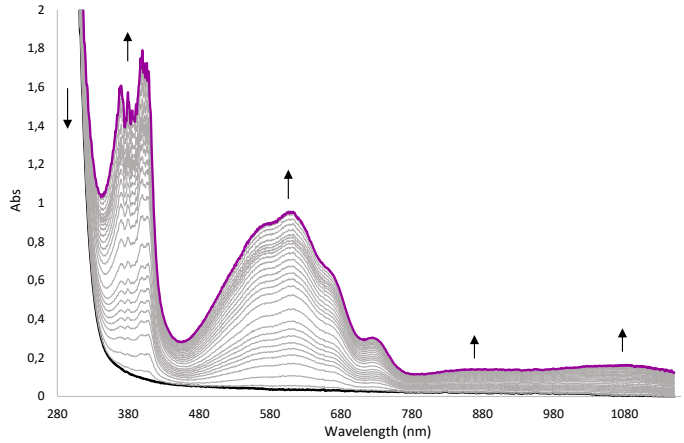

Figure 6.76 Spectro-electrochemistry recorded during the first exhaustive reduction of the equimolar mixture of **M2**$^{8+}$ and **A2**$^{6+}$ (1 mM in each component, E_{app} = -0.5 V) in dry ACN (100 mM $TEAPF_6$).

M1^{4+} and **A4**$^{12+}$

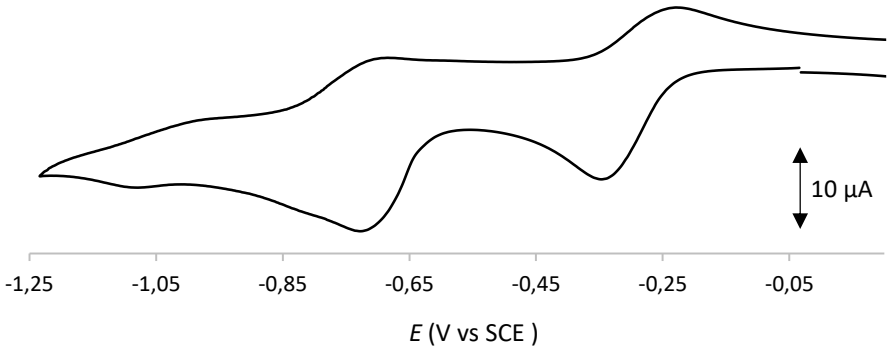

Figure 6.77 Cyclic voltammograms (v = 0.1 V·s^{-1}) of the 1:1 mixture of **A4**$^{12+}$ and **M1**$^{4+}$ (0.25 mM in each component) in dry ACN (100 mM $TEAPF_6$), (*E*(V) vs SCE = 0.385 V).

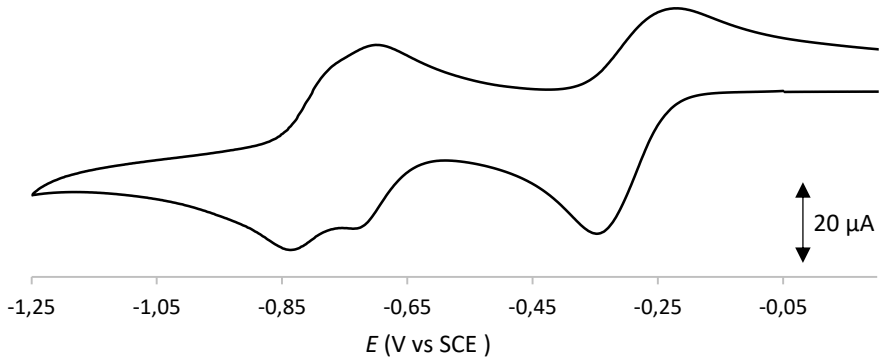

Figure 6.78 Cyclic voltammograms (v = 0.1 V·s^{-1}) of the 1:2 mixture of **A4**$^{12+}$ (0.25 mM) and **M1**$^{4+}$ (0.5 mM) in dry ACN (100 mM $TEAPF_6$), (*E*(V) vs SCE = 0.385 V).

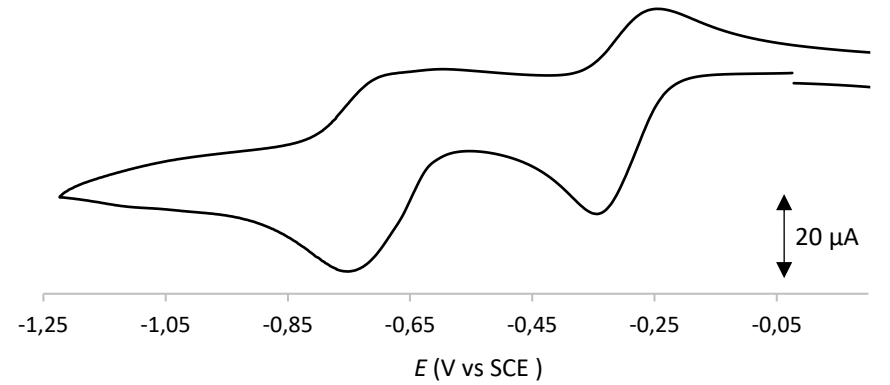

Figure 6.79 Cyclic voltammograms (v = 0.1 V·s^{-1}) of the 1:4 mixture of **A4**$^{12+}$ (0.25 mM) and **M1**$^{4+}$ (1 mM) in dry ACN (100 mM $TEAPF_6$), (*E*(V) vs SCE = 0.385 V).

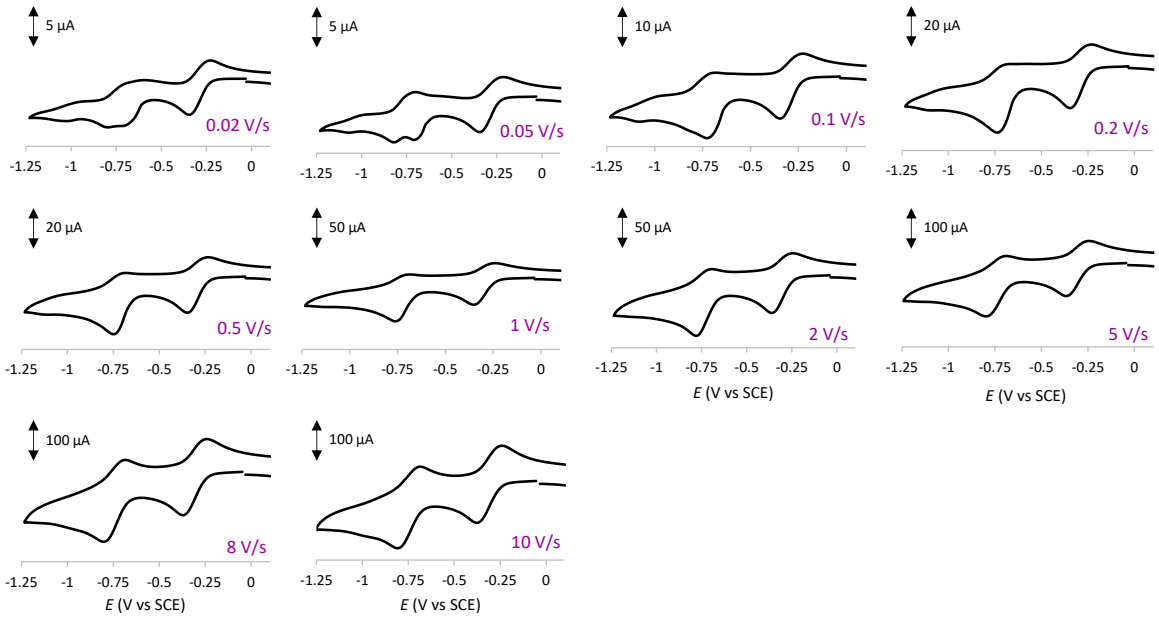

Figure 6.80 Scan rate dependence study of the 1:1 mixture of **A4**$^{12+}$ (0.25 mM) and **M1**$^{4+}$ (0.25 mM) in dry ACN (100 mM $TEAPF_6$), (E(V) vs SCE = 0.385 V). The scan rates vary from 0.02 V·s^{-1} through 0.05, 0.1, 0.2, 0.5, 1, 2, 5, 8 leading up to 10 V·s^{-1}.

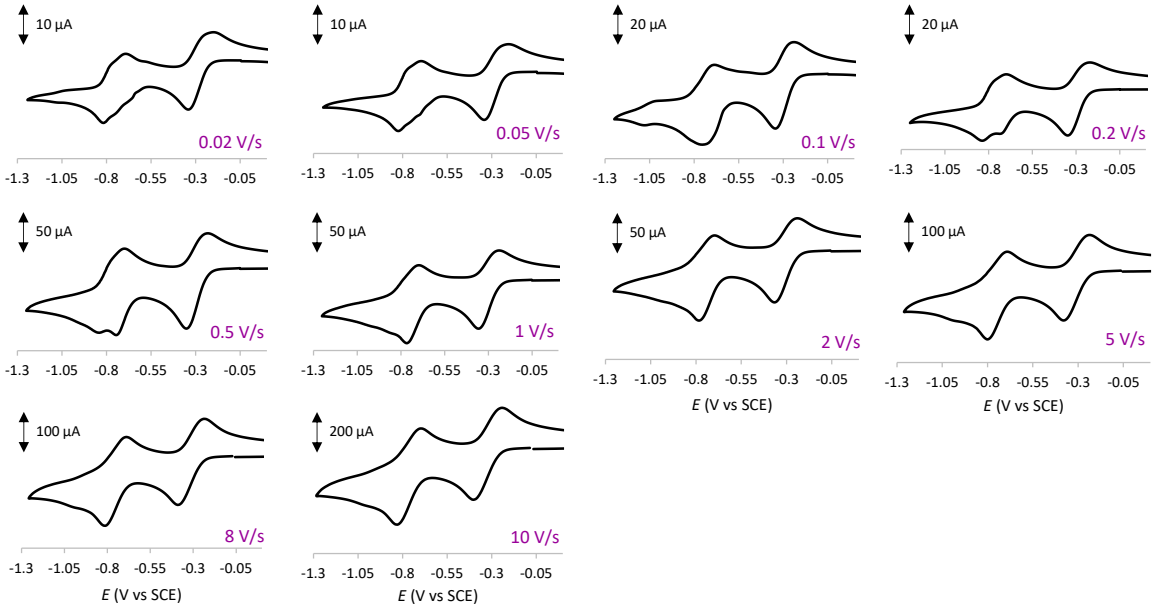

Figure 6.81 Scan rate dependence study of the 1:2 mixture of **A4**$^{12+}$ (0.25 mM) and **M1**$^{4+}$ (0.5 mM) in dry ACN (100 mM $TEAPF_6$), (E(V) vs SCE = 0.385 V). The scan rates vary from 0.02 V·s^{-1} through 0.05, 0.1, 0.2, 0.5, 1, 2, 5, 8 leading up to 10 V·s^{-1}.

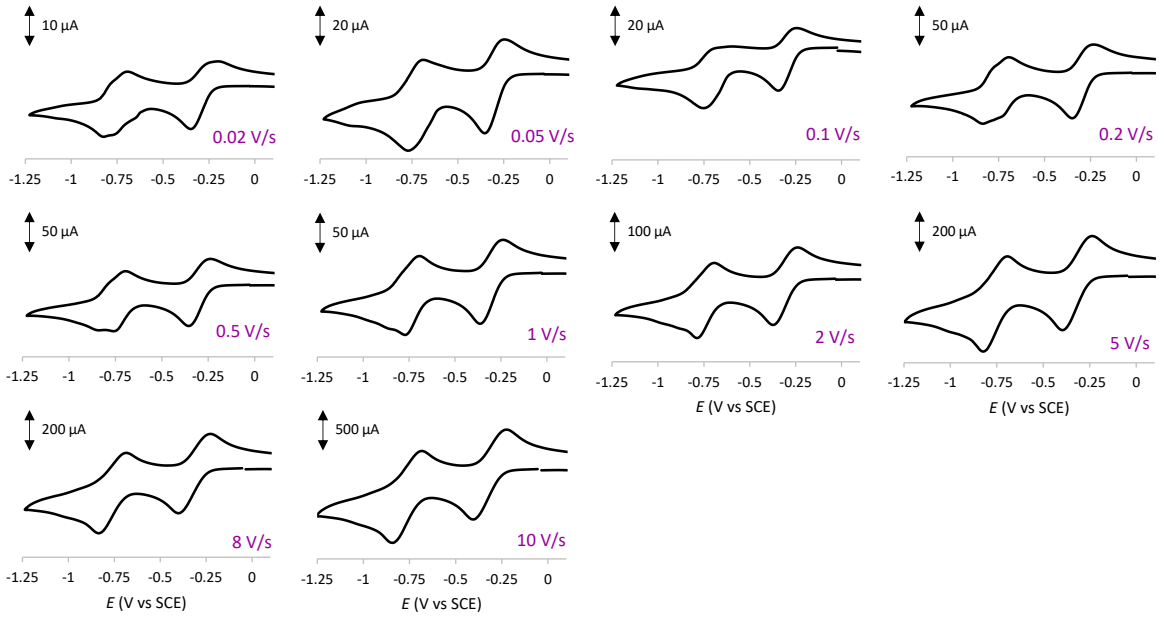

Figure 6.82 Scan rate dependence study of the 1:4 mixture of **A4**$^{12+}$ (0.25 mM) and **M1**$^{4+}$ (1 mM) in dry ACN (100 mM $TEAPF_6$), (*E*(V) vs SCE = 0.385 V). The scan rates vary from 0.02 V·s^{-1} through 0.05, 0.1, 0.2, 0.5, 1, 2, 5, 8 leading up to 10 V·s^{-1}.

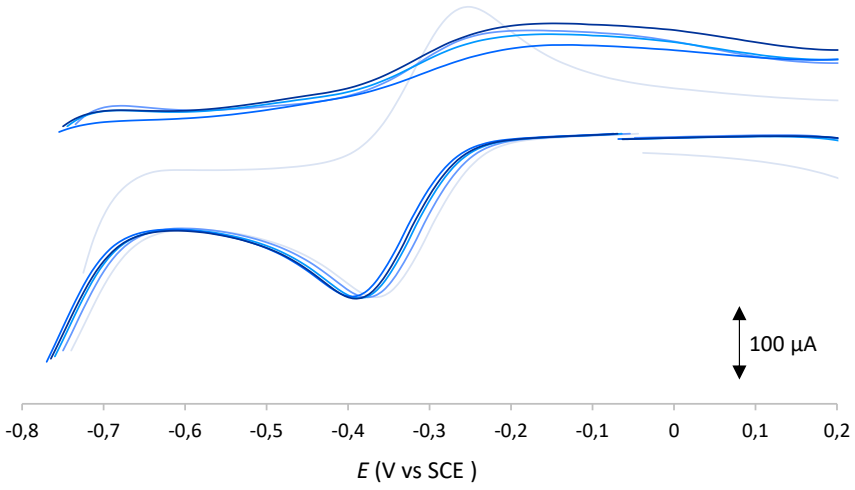

Figure 6.83 Linear sweep voltammetry (v = 5 V·s^{-1}) of the 1:1 mixture of **A4**$^{12+}$ and **M1**$^{4+}$ (0.25 mM in each component) in dry ACN (100 mM $TEAPF_6$), (*E*(V) vs SCE = 0.385 V). Each curve was obtained in four steps: i) scanning from 0 V to -0.7; V ii) maintaining the potential of 0.7 V for a given delay time – indicated in the legend; iii) scanning the potential to 0.6 V; iv) completing the experiment by returning from 0.6 V to 0 V.

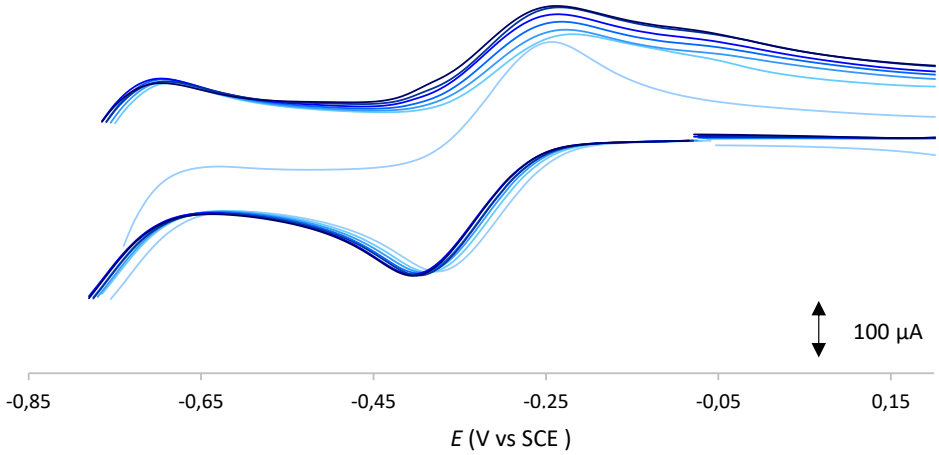

Figure 6.84 Linear sweep voltammetry (v = 5 V·s^{-1}) of the 1:2 mixture of **A4**$^{12+}$ (0.25 mM) and **M1**$^{4+}$ (0.5 mM) in dry ACN (100 mM $TEAPF_6$), (*E*(V) vs SCE = 0.385 V). Each curve was obtained in four steps: i) scanning from 0 V to -0.7; V ii) maintaining the potential of 0.7 V for a given delay time – indicated in the legend; iii) scanning the potential to 0.6 V; iv) completing the experiment by returning from 0.6 V to 0 V.

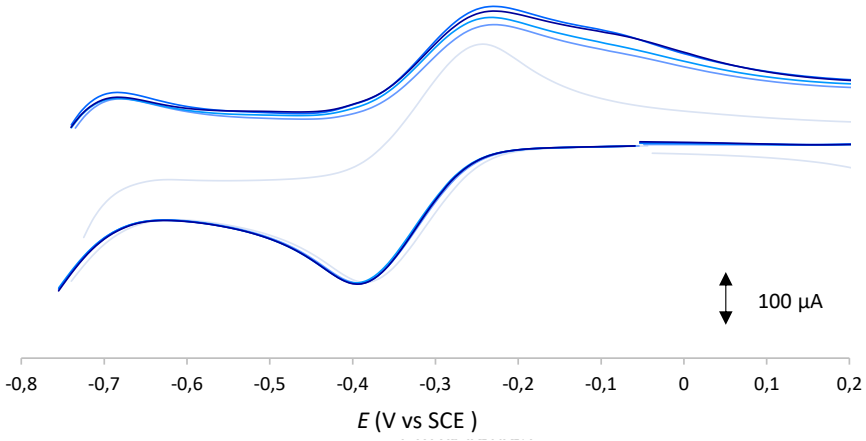

Figure 6.85 Linear sweep voltammetry (v = 5 V·s^{-1}) of the 1:4 mixture of **A4**$^{12+}$ (0.25 mM) and **M1**$^{4+}$ (1 mM) in dry ACN (100 mM $TEAPF_6$), (*E*(V) vs SCE = 0.385 V). Each curve was obtained in four steps: i) scanning from 0 V to -0.7; V ii) maintaining the potential of 0.7 V for a given delay time – indicated in the legend; iii) scanning the potential to 0.6 V; iv) completing the experiment by returning from 0.6 V to 0 V.

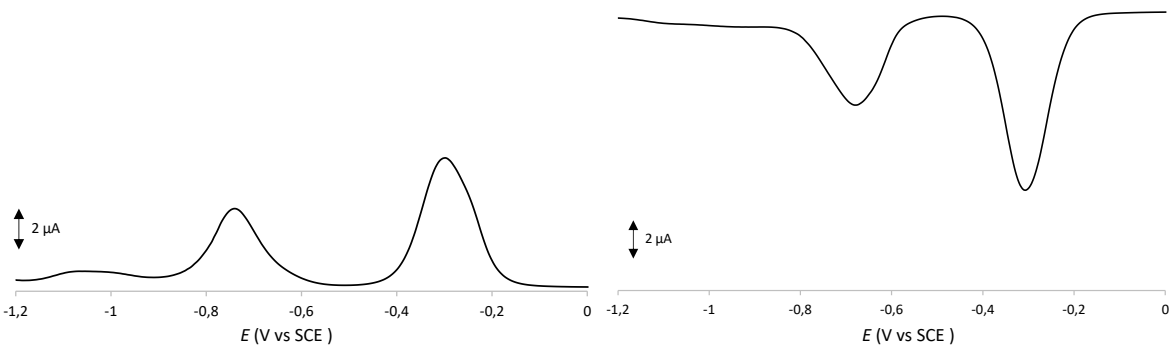

Figure 6.86 Differential pulse voltammograms of the 1:1 mixture of **A4**$^{12+}$ (0.25 mM) and **M1**$^{4+}$ (0.25 mM) in dry ACN (100 mM $TEAPF_6$), (*E*(V) vs SCE = 0.385 V): left oxidation direction, right reduction direction. The DPV analysis shows three peaks at -0.30 V, -0.74 V and -1.05 V, which are consistent with the observations in the CV analysis.

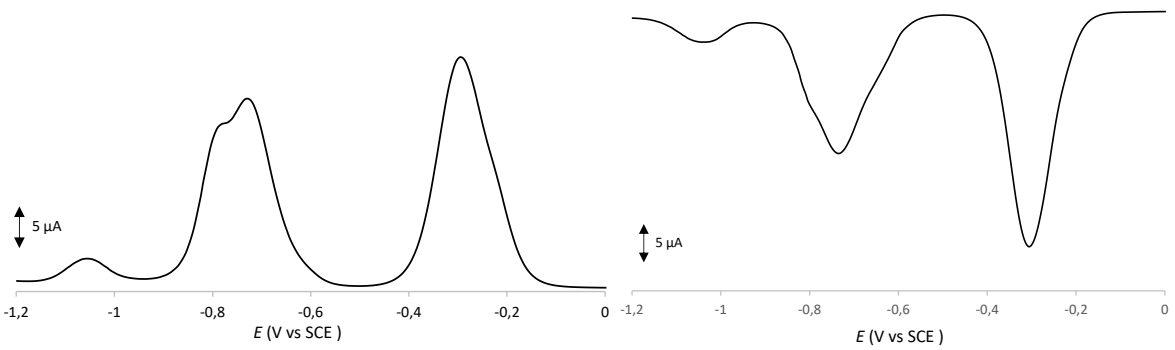

Figure 6.87 Differential pulse voltammograms of the 1:2 mixture of **A4**$^{12+}$ (0.25 mM) and **M1**$^{4+}$ (0.5 mM) in dry ACN (100 mM $TEAPF_6$), (E(V) vs SCE = 0.385 V): left oxidation direction, right reduction direction. The DPV analysis shows four peaks at -0.29 V, -0.73 V, -0.79 and -1.05 V, which are consistent with the observations in the CV analysis.

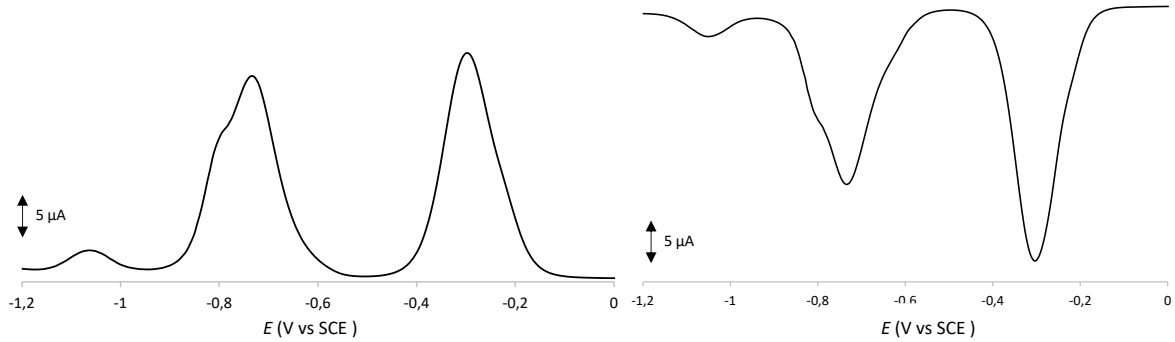

Figure 6.88 Differential pulse voltammograms of the 1:4 mixture of **A4**$^{12+}$ (0.25 mM) and **M1**$^{4+}$ (1 mM) in dry ACN (100 mM $TEAPF_6$), (E(V) vs SCE = 0.385 V): left oxidation direction, right reduction direction. The DPV analysis shows three peaks at -0.30 V, -0.79 and -1.06 V, which are consistent with the observations in the CV analysis.

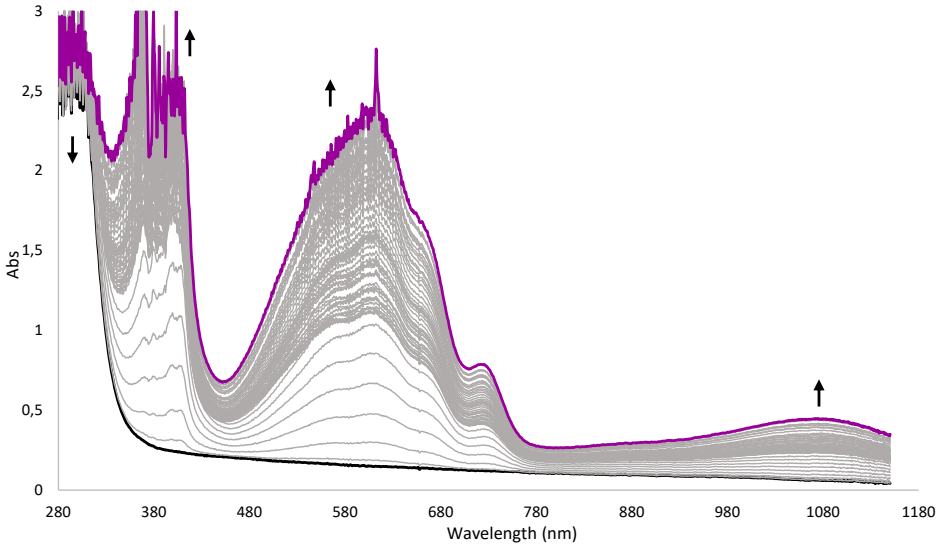

Figure 6.89 Spectro-electrochemistry recorded during the first exhaustive reduction of the mixture of **M1**$^{4+}$ and **A4**$^{12+}$ (1 mM in each component, E_{app} = -0.5 V) in dry ACN (100 mM $TEAPF_6$).

M2^{8+} and **A4**$^{12+}$

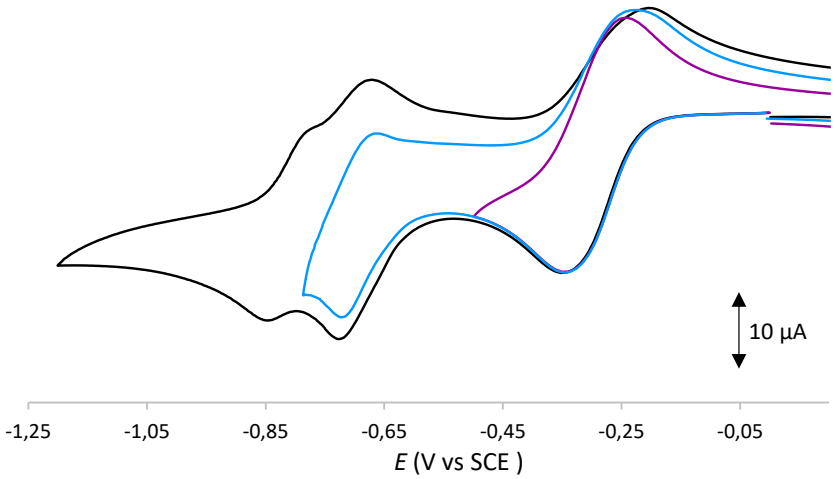

Figure 6.90 Cyclic voltammograms (v = 0.1 V·s^{-1}) of the 1:1 mixture of **A4**$^{12+}$ (0.25 mM) and **M2**$^{8+}$ (0.5 mM) in dry ACN (100 mM $TEAPF_6$), (*E*(V) vs SCE = 0.385 V), recorded at different potential range: from +0.6 to –1.2 V (black line), from +0.6 to –0.78 V (blue line) and from +0.6 to –0.5 V (purple line).

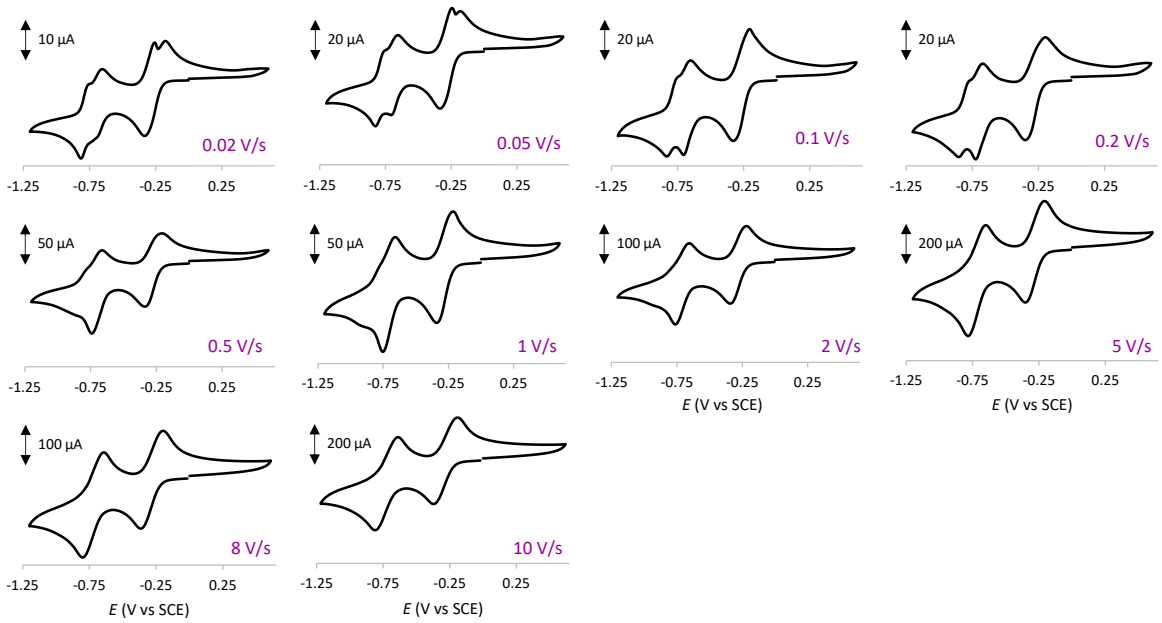

Figure 6.91 Scan rate dependence study of the 1:1 mixture of **A4**$^{12+}$ (0.25 mM) and **M2**$^{8+}$ (0.5 mM) in dry ACN (100 mM $TEAPF_6$), (*E*(V) vs SCE = 0.385 V). The scan rates vary from 0.02 V·s^{-1} through 0.05, 0.1, 0.2, 0.5, 1, 2, 5, 8 leading up to 10 V·s^{-1}.

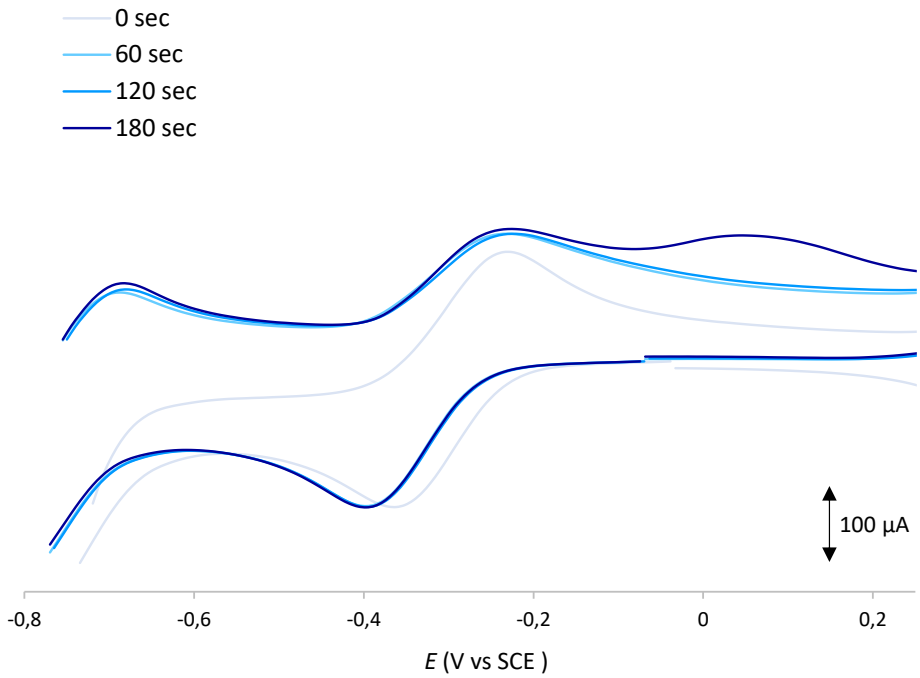

Figure 6.92 Linear sweep voltammetry (v = 5 V·s^{-1}) of 1:1 mixture of **A4**$^{12+}$ (0.25 mM) and **M2**$^{8+}$ (0.5 mM) in dry ACN (100 mM $TEAPF_6$), (*E*(V) vs SCE = 0.385 V). Each curve was obtained in four steps: i) scanning from 0 V to -0.7; V ii) maintaining the potential of 0.7 V for a given delay time – indicated in the legend; iii) scanning the potential to 0.6 V; iv) completing the experiment by returning from 0.6 V to 0 V.

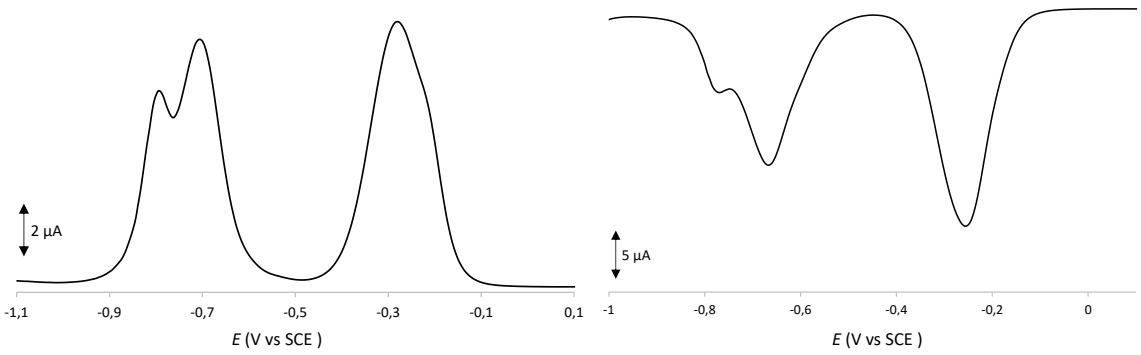

Figure 6.93 Differential pulse voltammograms of the 1:1 mixture of **A4**$^{12+}$ (0.25 mM) and **M2**$^{8+}$ (0.5 mM) in dry ACN (100 mM $TEAPF_6$), (*E*(V) vs SCE = 0.385 V): left oxidation direction, right reduction direction. The DPV analysis shows three peaks at -0.28 V, -0.70 V and -0.79 V, which are consistent with the observations in the CV analysis.

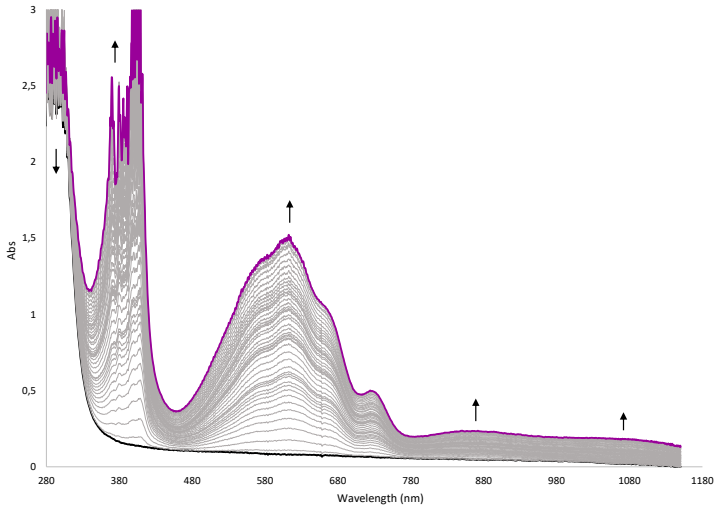

Figure 6.94 Spectro-electrochemistry recorded during the first exhaustive reduction of the mixture of 1mM **M2**$^{8+}$ and 0.5 mM **A4**$^{12+}$ (E_{app} = -0.5 V) in dry ACN (100 mM $TEAPF_6$).

6 Bibliography

(1) Kay, E. R.; Leigh, D. A.; Zerbetto, F. Synthetic Molecular Motors and Mechanical Machines. *Angew. Chem. Int. Ed.* **2007**, *46* (1–2), 72–191. https://doi.org/10.1002/anie.200504313.

(2) Borsley, S.; Leigh, D. A.; Roberts, B. M. W. Molecular Ratchets and Kinetic Asymmetry: Giving Chemistry Direction. *Angew. Chem. Int. Ed.* **2024**, *63* (23), e202400495. https://doi.org/10.1002/anie.202400495.

(3) Erbas-Cakmak, S.; Leigh, D. A.; McTernan, C. T.; Nussbaumer, A. L. Artificial Molecular Machines. *Chem. Rev.* **2015**, *115* (18), 10081–10206. https://doi.org/10.1021/acs.chemrev.5b00146.

(4) Pezzato, C.; Cheng, C.; Stoddart, J. F.; Astumian, R. D. Mastering the Non-Equilibrium Assembly and Operation of Molecular Machines. *Chem. Soc. Rev.* **2017**, *46* (18), 5491–5507. https://doi.org/10.1039/C7CS00068E.

(5) Sangchai, T.; Al Shehimy, S.; Penocchio, E.; Ragazzon, G. Artificial Molecular Ratchets: Tools Enabling Endergonic Processes. *Angew. Chem. Int. Ed.* **2023**, *62* (47), e202309501. https://doi.org/10.1002/anie.202309501.

(6) Wilson, M. R.; Solà, J.; Carlone, A.; Goldup, S. M.; Lebrasseur, N.; Leigh, D. A. An Autonomous Chemically Fuelled Small-Molecule Motor. *Nature* **2016**, *534* (7606), 235–240. https://doi.org/10.1038/nature18013.

(7) Amano, S.; Borsley, S.; Leigh, D. A.; Sun, Z. Chemical Engines: Driving Systems Away from Equilibrium through Catalyst Reaction Cycles. *Nat. Nanotechnol.* **2021**, *16* (10), 1057–1067. https://doi.org/10.1038/s41565-021-00975-4.

(8) Serreli, V.; Lee, C.-F.; Kay, E. R.; Leigh, D. A. A Molecular Information Ratchet. *Nature* **2007**, *445* (7127), 523–527. https://doi.org/10.1038/nature05452.

(9) Trabolsi, A.; Khashab, N.; Fahrenbach, A. C.; Friedman, D. C.; Colvin, M. T.; Cotí, K. K.; Benítez, D.; Tkatchouk, E.; Olsen, J.-C.; Belowich, M. E.; Carmielli, R.; Khatib, H. A.; Goddard, W. A.; Wasielewski, M. R.; Stoddart, J. F. Radically Enhanced Molecular Recognition. *Nat. Chem.* **2010**, *2* (1), 42–49. https://doi.org/10.1038/nchem.479.

(10) Stoddart, J. F. Mechanically Interlocked Molecules (MIMs)—Molecular Shuttles, Switches, and Machines (Nobel Lecture). *Angew. Chem. Int. Ed.* **2017**, *56* (37), 11094–11125. https://doi.org/10.1002/anie.201703216.

(11) Cera, G.; Arduini, A.; Secchi, A.; Credi, A.; Silvi, S. Heteroditopic Calix[6]Arene Based Intervowen and Interlocked Molecular Devices. *Chem. Rec.* **2021**, *21* (5), 1161–1181. https://doi.org/10.1002/tcr.202100012.

(12) ACS+Central+Science+3+(2017)+927−935.Pdf.

(13) Kosower, E. M.; Hajdu, J. Pyridinyl Diradical .Pi.-Mer. Magnesium Iodide Complexes. *J. Am. Chem. Soc.* **1971**, *93* (10), 2534–2535. https://doi.org/10.1021/ja00739a030.

(14) Canton, M.; Groppi, J.; Casimiro, L.; Corra, S.; Baroncini, M.; Silvi, S.; Credi, A. Second-Generation Light-Fueled Supramolecular Pump. *J. Am. Chem. Soc.* **2021**, *143* (29), 10890–10894. https://doi.org/10.1021/jacs.1c06027.

(15) Cheng, C.; Cheng, T.; Xiao, H.; Krzyaniak, M. D.; Wang, Y.; McGonigal, P. R.; Frasconi, M.; Barnes, J. C.; Fahrenbach, A. C.; Wasielewski, M. R.; Goddard, W. A.; Stoddart, J. F. Influence of Constitution and Charge on Radical Pairing Interactions in Tris-Radical Tricationic Complexes. *J. Am. Chem. Soc.* **2016**, *138* (26), 8288–8300. https://doi.org/10.1021/jacs.6b04343.

(16) Walker, J. E. ATP Synthesis by Rotary Catalysis (Nobel Lecture). *Angew. Chem. Int. Ed.* **1998**, *37* (17), 2308–2319. https://doi.org/10.1002/(SICI)1521-3773(19980918)37:17<2308::AID-ANIE2308>3.0.CO;2-W.

(17) Wright, E. M.; Loo, D. D. F.; Hirayama, B. A. Biology of Human Sodium Glucose Transporters. *Physiol. Rev.* **2011**, *91* (2), 733–794. https://doi.org/10.1152/physrev.00055.2009.

(18) Cheng, C.; McGonigal, P. R.; Liu, W.-G.; Li, H.; Vermeulen, N. A.; Ke, C.; Frasconi, M.; Stern, C. L.; Goddard Iii, W. A.; Stoddart, J. F. Energetically Demanding Transport in a Supramolecular Assembly. *J. Am. Chem. Soc.* **2014**, *136* (42), 14702–14705. https://doi.org/10.1021/ja508615f.

(19) Pezzato, C.; Nguyen, M. T.; Cheng, C.; Kim, D. J.; Otley, M. T.; Stoddart, J. F. An Efficient Artificial Molecular Pump. *Tetrahedron* **2017**, *73* (33), 4849–4857. https://doi.org/10.1016/j.tet.2017.05.087.

(20) Cheng, C.; McGonigal, P. R.; Schneebeli, S. T.; Li, H.; Vermeulen, N. A.; Ke, C.; Stoddart, J. F. An Artificial Molecular Pump. *Nat. Nanotechnol.* **2015**, *10* (6), 547–553. https://doi.org/10.1038/nnano.2015.96.

(21) Qiu, Y.; Zhang, L.; Pezzato, C.; Feng, Y.; Li, W.; Nguyen, M. T.; Cheng, C.; Shen, D.; Guo, Q.-H.; Shi, Y.; Cai, K.; Alsubaie, F. M.; Astumian, R. D.; Stoddart, J. F. A Molecular Dual Pump. *J. Am. Chem. Soc.* **2019**, *141* (44), 17472–17476. https://doi.org/10.1021/jacs.9b08927.

(22) Cai, K.; Shi, Y.; Zhuang, G.-W.; Zhang, L.; Qiu, Y.; Shen, D.; Chen, H.; Jiao, Y.; Wu, H.; Cheng, C.; Stoddart, J. F. Molecular-Pump-Enabled Synthesis of a Daisy Chain Polymer. *J. Am. Chem. Soc.* **2020**, *142* (23), 10308–10313. https://doi.org/10.1021/jacs.0c04029.

(23) Jiao, Y.; Qiu, Y.; Zhang, L.; Liu, W.-G.; Mao, H.; Chen, H.; Feng, Y.; Cai, K.; Shen, D.; Song, B.; Chen, X.-Y.; Li, X.; Zhao, X.; Young, R. M.; Stern, C. L.; Wasielewski, M. R.; Astumian, R. D.; Goddard, W. A.; Stoddart, J. F. Electron-Catalysed Molecular Recognition. *Nature* **2022**, *603* (7900), 265–270. https://doi.org/10.1038/s41586-021-04377-3.

(24) Bachir, A.; Ciocchetti, F.; Couto, D. P.; Di Noja, S.; Pezzato, C.; Ragazzon, G. Photochemical Bromination of 2,5-Dimethylbenzoic Acid as Key Step of an Improved Alkyne-Functionalized Blue Box Synthesis**. *Eur. J. Org. Chem.* **2023**, *26* (29), e202300498. https://doi.org/10.1002/ejoc.202300498.

(25) Wang, Y.; Frasconi, M.; Liu, W.-G.; Liu, Z.; Sarjeant, A. A.; Nassar, M. S.; Botros, Y. Y.; Goddard, W. A.; Stoddart, J. F. Folding of Oligoviologens Induced by Radical–Radical Interactions. *J. Am. Chem. Soc.* **2015**, *137* (2), 876–885. https://doi.org/10.1021/ja5111305.

(26) Asakawa, M.; Dehaen, W.; L'abbé, G.; Menzer, S.; Nouwen, J.; Raymo, F. M.; Stoddart, J. F.; Williams, D. J. Improved Template-Directed Synthesis of Cyclobis(Paraquat- *p* -Phenylene). *J. Org. Chem.* **1996**, *61* (26), 9591–9595. https://doi.org/10.1021/jo961488i.